



**HAL**  
open science

# Thermo-hydro-mechanical study of deformable porous media with double porosity in local thermal non-equilibrium

Rachel Gelet

► **To cite this version:**

Rachel Gelet. Thermo-hydro-mechanical study of deformable porous media with double porosity in local thermal non-equilibrium. Materials. Université de Grenoble; University of New South Wales, 2011. English. NNT: 2011GRENI079 . tel-00712459

**HAL Id: tel-00712459**

**<https://theses.hal.science/tel-00712459>**

Submitted on 27 Jun 2012

**HAL** is a multi-disciplinary open access archive for the deposit and dissemination of scientific research documents, whether they are published or not. The documents may come from teaching and research institutions in France or abroad, or from public or private research centers.

L'archive ouverte pluridisciplinaire **HAL**, est destinée au dépôt et à la diffusion de documents scientifiques de niveau recherche, publiés ou non, émanant des établissements d'enseignement et de recherche français ou étrangers, des laboratoires publics ou privés.

## THÈSE

Pour obtenir le grade de

## DOCTEUR DE L'UNIVERSITÉ DE GRENOBLE

Spécialité : **Matériaux, Mécanique, Génie civil, Electrochimie**

Arrêté ministériel : 7 août 2006

Présentée par

**Rachel M. Gelet**

Thèse dirigée par **Benjamin Loret** et  
codirigée par **Nasser Khalili**

préparée au sein du **Laboratoire Sols, Solides, Structures -  
Risques**

dans l'**École Doctorale : Ingénierie – Matériaux Mécanique  
Energétique Environnement Procédé Production**

# Thermo-hydro-mécanique des milieux poreux déformables avec double porosité et non- équilibre thermique local

Thèse soutenue publiquement le **23 Septembre 2011**,  
devant le jury composé de :

**M. Claude Boutin**

Chercheur HDR à l'ENTPE, (Président)

**M. Alessandro Gajo**

Professeur Associé à l'Université de Trento (Rapporteur)

**M. Alain Millard**

Professeur en mécanique des structures à l'ECP (Rapporteur)

**M. Benjamin Loret**

Professeur à Grenoble INP, (Directeur de thèse)

**M. Nasser Khalili**

Professeur à l'Université de Nouvelles-Galles du sud (UNSW), (Co-  
directeur de thèse)





# Abstract

A fully coupled constitutive model is presented for a rigorous analysis of deformation, hydraulic and heat flows in saturated dual porosity media subject to thermo-hydro-mechanical loadings including those able to cause local thermal non-equilibrium. The solid phase is assumed to contain two distinct cavities: the porous blocks and the fissure network. The governing equations are derived based on the equations of conservation of mass, momentum and energy. Solution to the governing equations is obtained numerically using the finite element approach. The capabilities of the model address two energy applications: the stability of a borehole in a thermally enhanced oil recovery context and the heat extraction of enhanced geothermal systems. Substantial differences, particularly in the effective stress response, highlight the major influence of the dual porosity model and the importance of the local thermal non-equilibrium assumption to predict the behaviour of fractured media.

# Resumé

Un modèle constitutif complètement couplé est présenté pour l'analyse rigoureuse de la déformation, de l'écoulement de fluides et de transfert de chaleur dans les milieux poreux saturés à double porosité soumis à des chargements thermo-hydro-mécaniques, y compris ceux induisant un non-équilibre thermique local. La phase solide contient deux cavités distinctes: le bloc poreux et le réseau des fissures. Les équations de champs sont obtenues à partir des équations de conservation de la masse, du mouvement et de l'énergie et sont résolues par une approche par élément finis. Le modèle est utilisé pour deux types d'applications: la stabilité d'un puits de forage stimulée thermiquement pour la récupération de pétrole et l'extraction de chaleur dans un réservoir géothermique fracturé. Les différences substantielles, particulièrement de la contrainte effective, soulignent l'influence majeure de la double porosité et du non-équilibre thermique pour prédire le comportement des milieux fracturés.

All that is hurrying  
soon will be other with;  
only what lasts can bring  
us to the truth.

Young one, don't put your trust  
into the trials of flight,  
into the hot and quick.

All things already rest:  
darkness and morning light,  
flower and book.

Rainer Maria Rilke (1875-1926), translated by Mitchell.

# Acknowledgments

The work described in this thesis was carried out as part of a joined international research partnership (co-cotutelle PhD) between the Sols, Solides, Structures - Risques (3S-R) laboratory at the Institut Polytechnique de Grenoble, France and the School of Civil and Environmental Engineering at the University of New South Wales (UNSW), Sydney, Australia. Financial assistance in the form of a 3 year PhD fellowship provided by the French Ministry of Higher Education is gratefully acknowledged, as is the 6 month financial support from UNSW through the guidance of Prof. Khalili. In addition, the author would like to thank the Association Française des Femmes Diplômées des Universités (AFFDU) and the Institut National Polytechnique de Grenoble for their travel grants.

I would like to thank many members of staff in the Sols, Solides, Structures - Risques laboratory and in the School of Civil and Environmental Engineering. I am indebted to the senior scientists at Grenoble and to Professor David Waite (UNSW) for fostering an outstanding research environment and for welcoming me in the laboratory and in the School. I am enormously grateful to my supervisors Professor Benjamin Loret (3S-R) and Professor Nasser Khalili (UNSW) for sparking my interest in soil mechanics and for their invaluable guidance and encouragement. In particular, I thank Professor Benjamin Loret for his tireless efforts and quick responses to my calls for assistance.

For their friendship and day-to-day support, I thank Ha, Anca, Christina, Elma, Daïki, Ola, Bertrand, Xiangwei, Marcos, Luisa, Séverine, Mark, Jane, Lam, Jessica, Brunella, Wenji, Michal, Jérémy, Hana, Fabrizio, Matias and the boys of the E-building: Cédric, Jean-François, Florent, Jérôme, Stéphane, Rémi, Barthélémy and Guilherme from 3S-R; and Aurélie, Adam, Andrew, Adele, Daniel, Juan Pablo, Yun, Arman, Mohammad, Samaneh, YongJia, Cecilia, Irene, Pattie and Mary from UNSW. I apologise for those left out and I thank them too.

Furthermore, I would like to thank my parents and my brothers for their encouragement and their kindness. I am extremely grateful to my husband, Sylvain Blanvillain, who provided so much support during the last three and a half years, especially the hectic

*Acknowledgments*

---

months prior to completion. This whole experience, including the long separation cemented our bond far beyond expected. Since marriage has already taken place down-under, the next step is yet to come...

Rachel M. Gelet Blanvillain  
Sydney, Australia  
May 2011.



# Contents

<b>Abstract</b>	<b>1</b>
<b>Resumé</b>	<b>2</b>
<b>List of figures</b>	<b>29</b>
<b>List of tables</b>	<b>34</b>
<b>Introduction</b>	<b>35</b>
<b>1 Non-isothermal fluid-saturated porous media: Literature review</b>	<b>40</b>
1.1 Porous media with multi porosity . . . . .	40
1.1.1 Classification of multi porous media . . . . .	41
1.1.2 Definition of dual porous media . . . . .	42
1.2 Poroelastic constitutive framework . . . . .	45
1.2.1 Averaging models . . . . .	45
1.2.2 Recommendation for the mixture theory . . . . .	49
1.3 Poroelastic models for dual porosity . . . . .	50
1.3.1 Coupling in dual porous media: two approaches . . . . .	54
1.3.2 Applications . . . . .	55
1.4 Thermo-hydro-mechanical coupled models . . . . .	57
1.4.1 Models with local thermal equilibrium . . . . .	58
1.4.2 Models with local thermal non-equilibrium . . . . .	59
1.4.3 Models with dual porosity and thermal contribution . . . . .	61
1.4.4 Models with convection . . . . .	63
<b>2 Field and Constitutive equations</b>	<b>66</b>
2.1 General field equations . . . . .	67
2.1.1 Definition . . . . .	68
2.1.2 General form of the balance equation . . . . .	71
2.1.3 Balance of mass . . . . .	73

2.1.4	Balance of momentum . . . . .	75
2.1.5	Balance of energy . . . . .	79
2.1.6	Balance of entropy . . . . .	85
2.1.7	Clausius-Duhem inequality . . . . .	90
2.2	Constitutive equations based on a thermodynamic approach . . . . .	96
2.2.1	Onsager's reciprocity principle versus 'rational' thermodynamics . . . . .	98
2.2.2	Thermo-mechanical constitutive equations . . . . .	103
2.2.3	Diffusion constitutive equations . . . . .	144
2.2.4	Transfer constitutive equations . . . . .	155
2.3	Comprehensive field equations . . . . .	163
2.3.1	Balance of momentum for the mixture . . . . .	164
2.3.2	Balance of mass equation for the fluids . . . . .	166
2.3.3	The comprehensive energy equations . . . . .	169
2.4	Summary of governing equations . . . . .	177
2.5	Parameters identification . . . . .	181
<b>3</b>	<b>Constitutive parameters: interpretation and identification</b> . . . . .	<b>184</b>
3.1	Intensive parameters . . . . .	185
3.1.1	The Young's modulus, the Poisson's ratio and the Lamé's constants . . . . .	185
3.1.2	The drained compressibilities . . . . .	186
3.1.3	The porosities . . . . .	189
3.1.4	The permeabilities . . . . .	190
3.1.5	The aperture factor . . . . .	192
3.2	Extensive parameters . . . . .	193
3.2.1	The thermal expansion coefficients . . . . .	194
3.2.2	The densities . . . . .	195
3.2.3	The dynamic viscosity . . . . .	197
3.2.4	The specific heat capacities . . . . .	197
3.2.5	The thermal conductivities . . . . .	198
3.3	Solid-fluid extensive parameters . . . . .	199
3.3.1	The coefficient of thermo-osmosis . . . . .	199
3.3.2	The coefficients of inter-phase heat transfer . . . . .	200
3.4	The Reynolds, Prandtl, Péclet, Nusselt, Sparrow numbers . . . . .	204
3.4.1	The Reynolds number . . . . .	204
3.4.2	The Prandtl number . . . . .	205
3.4.3	The Péclet number . . . . .	206
3.4.4	The Nusselt number . . . . .	206

3.4.5	The Sparrow number . . . . .	207
<b>4</b>	<b>Finite element method</b>	<b>209</b>
4.1	The finite element method . . . . .	209
4.2	The semi-discrete equations . . . . .	213
4.2.1	The weak formulation . . . . .	213
4.2.2	Definition of the nodal and global unknown vectors . . . . .	215
4.2.3	The (Bubnov-)Galerkin method . . . . .	216
4.2.4	The semi-discrete system . . . . .	216
4.3	The time integration methods for equation solving . . . . .	226
4.3.1	The generalised trapezoidal method . . . . .	227
4.3.2	Predictor multi-corrector algorithms with operator split . . . . .	228
<b>5</b>	<b>Preliminary numerical results</b>	<b>233</b>
5.1	Validation of transient conduction tests . . . . .	234
5.1.1	A one-dimensional application . . . . .	234
5.1.2	Constant heat flux loading . . . . .	235
5.1.3	Fixed temperature loading . . . . .	238
5.2	Thermo-Hydro-Mechanical tests: thermal loading . . . . .	241
5.2.1	A partially coupled THM model in local thermal equilibrium . . . . .	241
5.2.2	A one-dimensional test . . . . .	242
5.2.3	Analytical formulation . . . . .	247
5.2.4	Comparing analytical and numerical results . . . . .	255
5.2.5	The importance of the diffusivity ratio $R$ . . . . .	265
5.2.6	Summary and conclusion . . . . .	269
5.3	Axi-symmetric boundary value problems . . . . .	270
5.3.1	Analytical solutions . . . . .	270
5.3.2	Numerical considerations . . . . .	274
<b>6</b>	<b>A borehole stability analysis: focus on diffusion and mass transfer</b>	<b>279</b>
6.1	Introduction . . . . .	280
6.2	Governing equations . . . . .	282
6.3	Finite element formulation . . . . .	285
6.3.1	The semi-discrete equations . . . . .	285
6.3.2	Time integration . . . . .	287
6.4	Non-isothermal borehole stability analysis . . . . .	289
6.4.1	Boundary conditions . . . . .	291
6.4.2	Characteristic parameters . . . . .	292

6.5	Thermal effects on dual porous media . . . . .	293
6.5.1	Influence of temperature . . . . .	294
6.5.2	Influence of mass transfer . . . . .	295
6.5.3	Time profiles . . . . .	298
6.5.4	Borehole stability analysis . . . . .	299
6.6	Conclusion . . . . .	301
<b>7</b>	<b>The streamline-upwind/Petrov-Galerkin method</b>	<b>303</b>
7.1	Presentation of the SUPG method . . . . .	304
7.1.1	Introduction of the SUPG method . . . . .	305
7.1.2	Origin of the SUPG method: the artificial diffusion . . . . .	306
7.1.3	Standard diffusion-convection formulations . . . . .	307
7.1.4	Weighting the modification : the stabilisation parameter $\tau$ . . . . .	309
7.2	Validation of the SUPG method . . . . .	311
7.2.1	One-dimensional steady state diffusion-convection problems . . . . .	312
7.2.2	One-dimensional transient diffusion-convection problems . . . . .	316
7.2.3	Two-dimensional steady diffusion-convection problems . . . . .	325
7.2.4	Two-dimensional transient diffusion-convection problems . . . . .	329
7.2.5	Stability requirements . . . . .	336
7.3	Beyond SUPG . . . . .	337
7.3.1	Mechanisms of numerical ‘noise’ and spurious oscillations . . . . .	337
7.3.2	The limitations of the SUPG method . . . . .	338
7.3.3	The SUPG method applied to porous media: a short literature review	340
7.3.4	The discontinuity capturing method . . . . .	342
<b>8</b>	<b>Simulation of heat extraction in geothermal reservoirs</b>	<b>348</b>
8.1	The stabilisation process for a THM model . . . . .	349
8.1.1	Stabilisation for a mixture in LTNE . . . . .	350
8.1.2	Stabilisation for a mixture in thermal equilibrium . . . . .	354
8.2	Preliminary results on forced convection in a coupled model . . . . .	357
8.2.1	Problem setup at Soultz-sous-Forêts . . . . .	357
8.2.2	Influence of the thermo-hydro-mechanical couplings . . . . .	362
8.2.3	Influence of the thermal boundary conditions . . . . .	365
8.2.4	Influence of local thermal non-equilibrium . . . . .	370
8.3	A single porosity medium in local thermal non-equilibrium . . . . .	374
8.3.1	Introduction . . . . .	375
8.3.2	The two temperature thermoporoelastoc model . . . . .	377

8.3.3	Finite element discretization . . . . .	380
8.3.4	HDR reservoir analysis . . . . .	385
8.3.5	The double-step pattern of thermal depletion in LTNE . . . . .	389
8.3.6	Fenton Hill HDR reservoir . . . . .	397
8.3.7	Conclusions . . . . .	403
8.4	A dual porosity medium in local thermal non-equilibrium . . . . .	404
8.4.1	Introduction . . . . .	405
8.4.2	Balance equations for the three phase mixture . . . . .	407
8.4.3	Constitutive equations . . . . .	412
8.4.4	The coupled field equations . . . . .	417
8.4.5	Finite element discretization . . . . .	418
8.4.6	HDR reservoir analysis . . . . .	421
8.4.7	Calibration with field data . . . . .	425
8.4.8	Thermo-hydro-mechanical response . . . . .	429
8.4.9	Conclusions . . . . .	438
	<b>Summary and conclusions</b>	<b>440</b>
	<b>A Ray M. Bowen (1970) constitutive model</b>	<b>460</b>
A.1	Bowen Multiple temperature theory . . . . .	460
A.2	Bowen's multiple temperature linear isotropic theory . . . . .	462
	<b>B Pecker and Deresiewicz (1973) constitutive model</b>	<b>471</b>
B.1	The Clausius-Duhem inequality . . . . .	471
B.2	A partial stress/strain formulation . . . . .	473
B.3	The equivalent total stress/strain formulation . . . . .	474
B.4	Reflexion on the physical meaning of the terms $\alpha_{sf}$ and $\alpha_{fs}$ . . . . .	477
	<b>C McTigue (1986) constitutive model</b>	<b>480</b>
	<b>D Appendices of Chapter 2.3.3</b>	<b>482</b>
	<b>E Appendices of Chapter 4</b>	<b>491</b>
E.1	Sub-matrices of the weak formulation . . . . .	491
E.2	Detailed elementary weak formulation . . . . .	493
E.3	Sub-matrices of the effective convection-diffusion matrix . . . . .	496
	<b>F Appendices of Chapter 6</b>	<b>498</b>
F.1	Finite element sub-matrices . . . . .	498

F.2	Definition of the matrices $\mathbf{K}$ and $\mathbf{D}$ in eq. (6.24)	500
<b>G</b>	<b>Appendices of Section 8.3</b>	<b>501</b>
G.1	Definition of the vectors $\mathbb{F}^{\text{grav}}$ and $\mathbb{F}^{\text{surf}}$	501
G.2	Definition of the matrices $\mathbb{K}^e$ and $\mathbb{D}^e$ in eqn (8.77)	501
G.3	An expression for the specific surface	503
G.4	The discontinuity capturing method	504
<b>H</b>	<b>Appendices of Section 8.4</b>	<b>506</b>
H.1	Reduction of the dual porosity model to a single porosity model	506
H.2	Definition of the vectors $\mathbb{F}^{\text{grav}}$ and $\mathbb{F}^{\text{surf}}$	507
H.3	Definition of the element matrices $\mathbb{K}^e$ and $\mathbb{D}^e$	507

# List of Figures

- 1.1 Illustration of the decomposition of a dual porous medium in two overlapping single porous media; the fissure network and the porous block. Mass transfer of fluid, momentum transfer, energy transfer and entropy transfer between the two sub-systems is permitted. . . . . 44
  
- 2.1 Sketch of the exchanges that are accounted for in the multi-species multi-phase open system. For illustration, it is assumed that, at any geometrical point, the species can be segregated in three phases, each of them containing several species. (1) *Transport*: Species of the fluid phases (the fissure phase and the pore phase) are transported to, and from, the boundary by (hydraulic and thermal) diffusion and by forced convection. In addition, the coupling of the hydraulic and thermal diffusion induces thermo-osmosis. (2) *Transfer*: Phases can exchange mass, momentum, energy and entropy. These exchanges are termed transfers. The characteristics of each exchange depend on both the concerned phases (its density, viscosity, chemical potential) and on the nature of the ‘membranes’ that separate the phases. Thus low permeable phases are associated to a large transfer time by contrast with higher permeable phases which are associated to a small transfer time. An infinite transfer time implies impermeability. (3) *Exchanges at the boundary*: If in addition, the system is thermodynamically open, supply and/or removal from the surroundings, of mass, momentum, energy and entropy can take place at each geometrical point. . . . . 69

2.2	Sketch of exchanges that are accounted for in the porous medium with double porosity of a non-isothermal closed system. At each geometrical point, porous media with double porosity are partitioned in three phases; one solid phase and two fluid phases: the fluid of the porous block and the fluid of the fissure network. Within each fluid phase, hydraulic and thermal coupled diffusion occur. Across fluid phases mass transfer occurs due to a chemical potential difference. In between the three phases, energy transfer occurs due to temperature differences, represented by a dashed arrow. . . . .	97
2.3	Total stress decomposition of a representative fissured porous element (Nur and Byerlee, 1971). The stress equilibrium is segregated in two parts: (M) a mechanical stress state and (Th) a thermal stress state. . . . .	113
2.4	Mechanical stress decomposition of a representative fissured porous element. The mechanical stress equilibrium is segregated in four stress states: (I) long-term equilibrium, (II) a medium-term non-equilibrium, (III) a drained isotropic condition and (IV) a drained deviatoric condition. . . . .	114
2.5	Schematic representation of a three phase thermo-elastic porous element, at constant pressures and stresses, subjected to constituent temperature $T_s$ , $T_p$ and $T_f$ . . . . .	117
2.6	Coefficient of thermal expansion $c_T$ of ice and water at atmospheric pressure.	128
2.7	Entropy of water for $K = 1/c_H = 2.2$ GPa, $C_p = 4.18$ KJ/kg/K, and the reference values $p_0 = 0$ Pa, $T_0 = 0^\circ\text{C}$ , $v_0 = 10^{-3}$ m <sup>3</sup> /kg, $S_0 = 0$ J/kg/K, $\mu_0 = 0$ J/kg/K. The left and center contour plots display the linearised and non linear entropies respectively for $K = 2.2$ GPa, and the right contour plot displays the nonlinear entropy for $K = 0.022$ GPa. . . . .	129
2.8	Chemical potential, enthalpy, free energy, and internal energy of water, as a function of temperature and pressure. Same data as Figure 2.7. . . . .	130
2.9	Entropy and chemical potential as a function of temperature and pressure. Same data as Figure 2.7; $K = 0.022$ GPa (involving air bubbles) and using the non linear relations. Comparing the influence of the pressure range. . . . .	131
2.10	Entropy and chemical potential as a function of temperature and pressure. Same data as Figure 2.9 except for the pressure range : $-50$ MPa $< p < 50$ MPa; $K = 0.022$ GPa (involving air bubbles) and using the non linear relations. Comparing the influence of the initial temperature. . . . .	132
2.11	Two types of direct flows through a soil mass: direct fluid flow and direct heat flow. $A$ represents the cross section area normal to the direction of the flow. . . . .	147



2.12 To illustrate the isothermal heat flow phenomenon, a simple case is considered: a system containing only pure fluid is divided into two by a permeable membrane. The two sub-systems (a and b) are homogeneous with themselves, but pressure vary as between the compartments. The experimental arrangements are such that the two sub-systems are maintained at the same temperature (that is,  $\nabla T = 0$ ) by being in intimate contact with a suitable heat source or sink and the volume of the entire system remains constant. Matter moves from a higher pressure to a lower and every unit which passes will convey heat from one to the other. Isothermal heat flow describes flow of heat induced by a pressure gradient. . . . . 151

5.1 Solid temperature  $T_s$  history at (left)  $x = 0$  m and (right)  $x = 2$  m. Comparison between Carslaw's analytical solution eq. (5.4) and the finite element response. The column is composed of an homogeneous solid phase such as  $n_s = 1$  and  $\alpha_{T,s} = 1.25 \times 10^{-6}$  m<sup>2</sup>/s. . . . . 237

5.2 Profile of the solid temperature in the slab for four different times. A constant heat flux is applied at  $x = 0$  m and the initial temperature is imposed at  $x = 3$  m. The column is composed of a single solid phase such as  $n_s = 1$  and  $\alpha_{T,s} = 1.25 \times 10^{-6}$  m<sup>2</sup>/s. . . . . 237

5.3 Contour representation at four different times of a column of solid under a constant heat flux applied at  $x = 0$  m and at initial temperature at  $x = 3$  m. The column is composed of a single solid phase such as  $n_s = 1$  and  $\alpha_{T,s} = 1.25 \times 10^{-6}$  m<sup>2</sup>/s. . . . . 238

5.4 Same as Figure 5.1 for the fluid temperature  $T_p$ . . . . . 238

5.5 Solid temperature  $T_s$  history at (left)  $x = 0$  m and (right)  $x = 2$  m. Comparison between Carslaw's analytical solution eq. (5.7) and the finite element response. The column is composed of an homogeneous solid phase such as  $n_s = 1$  and  $\alpha_{T,s} = 1.25 \times 10^{-6}$  m<sup>2</sup>/s. . . . . 240

5.6 Sketch of the step function  $G_1(t)$  used for the constant temperature loading at the injection point  $x = 0$  m, so that to avoid numerical wiggles. . . . . 245

5.7 (left) Schematic of the mesh used for the numerical applications. (right) Initial boundary conditions: Homogeneous thermal, pressure and displacement equilibrium. . . . . 245

5.8 Illustrations of two types of boundary conditions. (Top) 1. Imposed temperature and i. Drained boundary. (Bottom) 2. Constant heat flux and ii. Undrained boundary. For both tests, a zero vertical displacement is imposed at the top of the column. . . . . 246

- 5.9 (a) Sketch of the mesh and of the boundary conditions applied to the semi-infinite column. (b) Temperature, (c) pressure and (d) displacement histories at  $x = 3\text{ m}$  in the column, for a constant temperature and a drained boundary. The temperature field reaches a steady state. The pressure field displays a peak when the heated boundary is drained. This peak is due to a pressure rise into the pores before a significant dilatation occurs. The pressure propagation is ahead of the thermal front because  $R = 3.9$ . The displacement field shows a dilatation synchronised with the thermal front. . . . . 256
- 5.10 (e) Temperature, (f) pressure and (g) displacement profiles in the column, for a constant temperature and a drained boundary: (left) analytical solution, (right) numerical response. The thermal front has penetrated up to 5 m. A constant pressure peak propagates into the column. The pressure front is ahead of the thermal penetration because  $R = 3.9$ . The dilatation has reached up to 10 m due to pull-on induced by the dilatation below 5 m. . . . . 257
- 5.11 Same as Figure 5.9 for a constant temperature and an *undrained* boundary. The temperature and the displacement fields display a similar behaviour to the drained boundary condition. On the other hand, the pressure field ends by a plateau when the heated boundary is undrained. Locally the fluid is trapped into the pores : the pressure can not dissipate in spite of the dilatation. Note that some numerical disturbances arise in two regions: (i) at early times, these disturbances are induced by the numerical time-dependent loading; (ii) at late times, by the finite property of the implemented column. 258
- 5.12 Same as Figure 5.10 for a constant temperature and an *undrained* boundary. The profile of the temperature remains similar to the drained boundary case. On the other hand, the pressure propagates into the column and is maximum and constant at the undrained boundary. Furthermore, the displacement magnitude is increased compared with the drained boundary case. . . . . 259
- 5.13 (a) Sketch of the mesh and of the boundary conditions applied to the semi-infinite column. (b) Temperature, (c) pressure and (d) displacement histories at  $x = 3\text{ m}$  in the column, for a constant heat flux and a drained boundary. The temperature rises exponentially, i.e. no steady state is reached. The pressure field, although close to the drained boundary, is continuously heated: therefore the pressure does not dissipate easily. The pressure plateau represents this time an equilibrium between hydraulic dissipation and pressure rise induced by thermal excitation. The displacement field shows a dilatation delayed with respect to the thermal front. . . . . 261

5.14	(e) Temperature, (f) pressure and (g) displacement profiles in the column, for a constant heat flux and a undrained boundary: (left) analytical solution, (right) numerical response. The thermal front has penetrated up to 5 m. The pressure propagates into the column. The pressure peak is due to the drained boundary condition. The magnitude of which is increasing with time due to the continuous heating. The dilatation has reached up to 10 m due to pull-on induced by the dilatation below 5 m. . . . .	262
5.15	Same as Figure 5.13 for a constant heat flux and an <i>undrained</i> boundary. The temperature and the displacement fields remain the same as for a drained boundary problem. On the other hand, the pressure field can not dissipate due to the undrained boundary condition. Therefore the pressure rises exponentially induced by continuous thermal excitation. . . . .	264
5.16	Same as Figure 5.14 for a constant heat flux and an <i>undrained</i> boundary. The profile of the temperature remains similar to the drained boundary case. On the other hand, the pressure propagates into the column with a maximum located at the undrained boundary. The magnitude of the maximum pressure is increasing with time due to the continuous heating. Again, the displacement magnitude is slightly larger compared with the drained boundary case. . . . .	265
5.17	Pressure history of (left) abyssal red clay and (right) salt; at $x = 3$ m in the column, for a constant temperature and a drained boundary. For the same loading, the pressure peak in the salt mixture is significantly larger than the pressure in the clay mixture. This is due to the fact that the diffusivity ratio $R$ of the salt is closer to one than the diffusivity ratio of the clay. . . . .	269
5.18	Hollow cylinder subjected to internal and external pressure, $p_1$ and $p_2$ , respectively. . . . .	271
5.19	Profile of the error along the $r$ -direction for the radial displacement, the strain and the stress. Note that with a non-homogeneous mesh, refined at the inner radius $r_1 = 0.5$ mm (on the left-hand-side), the maximum error is not located at $r/r_1 = 0$ mm. For the displacement, the maximum error is located at $r = r_2$ . For the strain, the maximum error is located around $r = 2$ mm. Finally, for the stress, the maximum error is located in the range $1 < r < 1.5$ mm. . . . .	278
6.1	Schematic diagram of a vertical borehole subjected to <i>in-situ</i> stresses (left). 2D representation of the problem with an axi-symmetric mesh in the $r$ - $z$ plane (right). . . . .	290

6.2	Sketch of a semi-permeable hydraulic boundary condition with zero flux at the porous blocks boundary. . . . .	292
6.3	Profiles of pore pressure and fissure pressure, at time 80 s and for three imposed temperature changes $\Delta t$ at the borehole. The leakage parameter is set equal to the average leakage parameter $\eta^* = \eta_{av}^*$ . . . . .	294
6.4	Profiles of radial effective stress and tangential effective stress, at time 80 s and for three imposed temperature changes $\Delta t$ at the borehole. The leakage parameter is set equal to the average leakage parameter $\eta^* = \eta_{av}^*$ . . . . .	295
6.5	Profiles of pore pressure and fissure pressure, at time 80 s, for a thermal loading equal to $T_w - T^0 = 50^\circ\text{C}$ . . . . .	296
6.6	Profiles of effective radial stress and effective tangential stress, at time 80 s, accounting for a <i>permeable</i> boundary. The thermal loading is equal to $T_w - T^0 = 50^\circ\text{C}$ . . . . .	297
6.7	Same as Figure 6.6 for a <i>semi-permeable</i> boundary on the porous blocks. . .	297
6.8	Profiles of pore pressure and fissure pressure for two values of the leakage parameter $\eta^* = 0$ and $\eta^* = \eta_{av}^*$ . The results are presented for three representative times. . . . .	298
6.9	Profiles of effective radial stress and effective tangential stress, for $\eta^* = 0$ and $\eta^* = \eta_{av}^*$ . The results are presented for three representative times. . . .	299
6.10	Effective stress path along dimensionless radial direction $r/r_1$ , in the Mean shear stress $\sqrt{J_2}$ - Mean effective stress $S_p$ plane, for two distinct boundary conditions. The results are presented at time 6 s and with an average leakage parameter $\eta^* = \eta_{av}^*$ . . . . .	300
7.1	The optimal upwind function is approximated by two simplifications: the doubly asymptotic approximation and the critical approximation, Brooks and Hughes (1982, p. 214). . . . .	314
7.2	Relative temperature profile along the horizontal distance $x$ . Comparison of the various stabilisation functions $\tilde{\xi}$ with the exact solution eq. (7.29). While the optimal rule a) gives a nodally exact solution, the doubly asymptotic approximation c) is under-convective and the critical approximation d) is over-convective. b) The comparison between finite element solutions with and without the SUPG method illustrates the spurious oscillations and the efficiency of the method for one-dimensional problems. . . . .	315

7.3 Relative temperature profiles along the horizontal direction  $x$  for four different times and for grid Péclet numbers  $Pe_g$  ranking from 0.34 to 4.3. The characteristic length of the elements  $h$  is equal to 0.086 m and the fluid velocity is set equal to  $v = 2 Pe_g \alpha_T/h$ . The finite element response reproduces well the convection-dominated profile of the analytical solution. The accuracy of the solution is good when using the definition of the artificial diffusivity expressed in eq. (7.31). . . . . 318

7.4 Relative temperature profile along the horizontal direction  $x$  for  $t = 100$  s. The characteristic length of the elements  $h$  is equal to 0.086 m and the fluid velocity is set equal to  $v = 2 Pe_g \alpha_T/h$ . Oscillations arise during the early period due to the sharp temperature gradient applied at the boundary:  $x = 0$  m. When accounting for the SUPG method, these oscillations are larger than the non-stabilised response. This increase of numerical perturbation may induce serious stability and convergence issues in coupled problems. The remedial action to this problem is to add a transient-contribution in the artificial diffusivity formula which is discussed in Section 7.2.2.2. . . . 319

7.5 Relative temperature profile along the horizontal direction  $x$ . The characteristic length of the elements  $h$  is equal to 0.086 m and the fluid velocity is set equal to  $v = 2 Pe_g \alpha_T/h$ . The simulation response for diffusion only is compared with that of diffusion-convection with SUPG and diffusion-convection without SUPG. With no convection, the heat front propagates slowly in the layer and all the curves remain on the left-hand-side. On the other hand, if convection is accounted for, the heat propagates more quickly in the layer. Spurious oscillations arise when the heat front hits the hard boundary  $\varphi(x = 10 \text{ m}) = 0$  and when the SUPG method is not accounted for. The popular SUPG method removes efficiently these unwanted numerical wiggles. Without the SUPG method, the higher the grid Péclet number, the more numerical wiggles arise. . . . . 320

7.6 Integration rule for optimal upwind scheme (Brooks and Hughes, 1982), generic approximation, and modified approximation by Shakib et al. (1991). 321

- 7.7 Relative temperature profiles along the horizontal direction  $x$  for artificial diffusivities  $\tilde{\alpha}_{Ti}$ , for  $i = 1, 6$  (top);  $\tilde{\alpha}_{Ti}$ , for  $i = 7, 10$  (bottom). The grid Péclet number  $Pe_g$  is equal to 2.15. The characteristic length of the elements  $h$  is equal to 0.086 m and the fluid velocity is set equal to  $v = 2 Pe_g \alpha_T/h$ . Along the cold side (right), the parameter  $\tilde{\alpha}_{T1}$  provides a better stabilisation than the other propositions. On the other hand, close to the perturbation (left), the parameters  $\tilde{\alpha}_{T5}$ ,  $\tilde{\alpha}_{T6}$  and  $\tilde{\alpha}_{T9}$ ,  $\tilde{\alpha}_{T10}$  provide a better transition between the transient-dominated period and the convection-dominated period. 323
- 7.8 Relative temperature profile along the horizontal direction  $x$  for  $t = 100$  s. The characteristic length of the elements  $h$  is equal to 0.086 m and the fluid velocity is set equal to  $v = 2 Pe_g \alpha_T/h$ . The streamline upwind diffusivity proposed by Tezduyar and Osawa (2000) in eq. (7.45) reduces significantly the spurious oscillations encountered at early times with respect to the standard streamline upwind diffusivity  $\tilde{\alpha}_{T1}$  (7.39). The ‘transient/short time wiggles’ are now of the same magnitude as the response of convection without SUPG, that is the use of the SUPG method will not induce more spurious oscillations in coupled transient problems compared with the Galerkin method. . . . . 324
- 7.9 Four node parallelogram finite element geometry; definitions of element lengths  $h_x$  and  $h_y$  used in eq. (7.56). For more general quadrilaterals, a proposition is given in Section 7.2.4. . . . . 326
- 7.10 Relative temperature profiles along the vertical direction  $y^*$ , at  $x^* = 5$  and for a convective flow skew to the mesh,  $Pe_g = 10^6$ . The tests are run for three values of  $y_c^*$  which correspond to three angles  $\theta$  of the velocity with the grid lines:  $\theta = 0^\circ$ ,  $\theta = 21.8^\circ$  and  $\theta = 45^\circ$ . The analytical solution is compared with the finite element response with and without SUPG. The SUPG procedure provides satisfactory results and stabilises well the response compared with the Galerkin method (without SUPG). When the angle is  $\theta = 0^\circ$ , the SUPG response is in perfect agreement with the analytical response. As the angle  $\theta$  increases from 0 to  $45^\circ$ , the SUPG response slightly comes away from the step but remains quite smooth in comparison with the non-stabilised response. The stabilisation effect of the SUPG method is mainly visible for  $\theta = 45^\circ$ . . . . . 329

- 7.11 Relative temperature profiles in the plane  $(x^*, y^*)$ , for a convective flow skew to the mesh,  $Pe_g = 10^6$ . E illustrates the exact solution of a convection-dominated problem, from eq. (7.59). SUPG stands for the finite element response accounting for the SUPG method which demonstrates the stabilisation effect of the method. G represents the finite element response with no stabilisation (Galerkin method): spurious wiggles disturb the solution. The SUPG method significantly improves upon the Galerkin method as it efficiently cures the spurious wiggles. In addition, a good agreement with the exact solution is obtained for all the proposed angles. . . . . 330
- 7.12 Relative temperature profiles in the plane  $(x^*, y^*)$ , for a convective flow skew to the mesh and a very high grid Péclet number  $Pe_g = 10^6$ . SUPG stands for the finite element response accounting for the SUPG method; whereas G represents the finite element response with no stabilisation on the weighting function, that is the standard Galerkin method, which displays a heavily disturbed response. The SUPG method using eq. (7.56) produces better results (at all times) than when accounting for a transient contribution eq. (7.68). This is due to the high grid Péclet number  $Pe_g = 10^6$ , which induces the transient contribution of (7.68) to be equal or smaller than the convection contribution. Therefore, for high grid Péclet numbers, the stabilisation parameter with no transient contribution (7.56) is more efficient. . . . . 334
- 7.13 Same as Figure 7.12 for a smaller grid Péclet number:  $Pe_g = 10^2$ . At early times (left), the SUPG method with eq. (7.68) displays a smoother temperature profile than the SUPG method with eq. (7.56), thanks to the transient contribution. On the other, during the intermediate and the late periods, the SUPG method with eq. (7.56) produces smoother results than Tezduyar and Osawa's proposition. The description of the early period is better viewed by using eq. (7.68); whereas the description of the intermediate and of the latter periods is better reproduced with eq. (7.56). No optimum stabilisation parameter exists for two-dimensional transient problems. . . . . 335

- 7.14 Relative temperature profiles for a convective flow skew to the mesh. SUPG stands for the finite element response accounting for the SUPG method. DC1 and DC2 stand for the finite element response with the discontinuity capturing method (added to SUPG) with  $\tau_2 = \tau_{\parallel}$  and  $\tau_2 = \max(0, \tau_{\parallel} - \tau)$ , respectively. The significant improvements of the discontinuity capturing methods over SUPG are manifest: the solutions do not exhibit the overshoots of the SUPG at the downwind boundary; in addition the overshoots at the internal discontinuity are reduced. The DC2 response exhibits less artificial diffusion when  $\mathbf{v} = \mathbf{v}_{\parallel}$  and therefore a smoother response. . . . . 346
- 7.15 Relative temperature profiles for a convective flow skew to the mesh. SUPG stands for the finite element response accounting for the SUPG method. EC1 and EC2 stand for the finite element response with the discontinuity capturing method (added to SUPG) with eq. (7.81) and (7.84), respectively. The overshoots at the downwind boundary are effectively removed with both EC1 and EC2 methods. Minor improvements are observed also at the internal boundary. . . . . 347
- 8.1 Fluid circulation in the geothermal reservoir at Soultz-sous-Forêts after hydraulic stimulation. . . . . 358
- 8.2 Conceptual model of the 2-D circulation test, at Soultz-sous-Forêts, in the horizontal  $x - y$  plane of space. Note that the above sketch is enlarged along the  $y$ -axis. The boundary conditions illustrated on this sketch are properly listed in Table 8.2. . . . . 360
- 8.3 Scaled velocity vectors  $\mathbf{v}_p$  at steady state for an injection pressure equal to 1 MPa at GPK1 and a production pressure equal to -1 MPa at GPK2. The velocity field is non-homogeneous in space in the vicinity of the wells. The horizontal component of the velocity between the wells is equal to  $v_{p,x} = 1.44 \times 10^{-5}$  m/s in average. . . . . 361
- 8.4 (left) Relative temperature profiles and (left) pressure profiles, on the Soultz-sous-Forêts site at  $y = 0$  m. The thermal front propagates towards the production well at a high *unrealistic* rate due to the local thermal equilibrium assumption. The pressure field is undisturbed by the cooling front. Furthermore, the influence of the mechanical couplings on the temperature and on the pressure fields are negligible. . . . . 364
- 8.5 Horizontal displacement profile; on the Soultz-sous-Forêts site at  $y = 0$  m. The horizontal displacement is controlled by the propagation of the cooled thermal front. . . . . 365



- 8.6 Effective stresses profiles  $\bar{\sigma}_x$  (left) and  $\bar{\sigma}_y$  (right) on the Soultz-sous-Forêts site at  $y = 0$  m. Tensile stresses are counted positive. Cooling induces thermal contraction of the solid skeleton, which induces an increase of tensile effective stress. . . . . 365
- 8.7 Scaled velocity vectors  $\mathbf{v}_p$  of a 18 m reservoir with a 36 m piece of formation located at  $(x, 18 < y < 36)$  m. The velocity field is non-monotonic in the vicinity of the wells and the x-component of the velocity between the wells is equal to  $v_{p,x} = 1.44 \times 10^{-5}$  m/s in average. . . . . 368
- 8.8 Relative temperature profiles (left) and horizontal displacement profiles  $u_x$  (right) on the Soultz-sous-Forêts site at  $y = 0$  m, with a piece of formation on the  $y$ -boundary of the reservoir. The hot formation does not modify significantly the temperature profile; whereas the horizontal displacements are significantly reduced compared with Figure 8.4. . . . . 368
- 8.9 Horizontal effective stresses profiles  $\bar{\sigma}_x$  (left) and  $\bar{\sigma}_y$  (right) on the Soultz-sous-Forêts site at  $y = 0$  m, with a piece of formation on the  $y$ -boundary of the reservoir. The hot formation reduces the thermally induced increase in effective stress compared with Figure 8.6. . . . . 369
- 8.10 Contour of the mixture temperature  $T$  [°C], with a piece of formation on the  $y$ -boundary of the reservoir, at 3.81 months. The buffer zone brings a sharp internal layer that requires the use of the SUPG stabilisation method. 369
- 8.11 (left) Gringarten analytical setup for a single crack embedded in a semi-infinite impermeable rock. (right) A continuous single porous medium setup for the finite element analysis. The reservoir is modeled with 30 elements of size  $10 \times 100$  m<sup>2</sup> forming a total volume of  $300 \times 100$  m<sup>2</sup>.  $n_p$  is fixed to 0.003. The imposed fluid velocity along  $x$  is equal to  $v_p = 5 \times 10^{-5}$  m/s. . 371
- 8.12 (Left) Relative outlet temperature versus dimensionless time. (Right) Relative temperature profile at times 3.7 months and 32 years. Gringarten analytical solution is presented in eq. (8.44). LTE stands for local thermal equilibrium and LTNE for local thermal non-equilibrium. The LTNE simulation uses an inter-phase heat transfer  $\kappa_{sp} = 1.0 \times 10^{-2}$  W/m<sup>3</sup>.K found by trial and error to ‘best fit’ the analytical response. The gap between the analytical solution and the LTNE response is attributed to the estimation of the fluid porosity  $n_p$ . In spite of the significant difference between the curves, the LTNE response is closer to the analytical solution compared with the LTE response. . . . . 372

- 8.13 Relative outlet temperatures of the solid and the fluid phases versus dimensionless time. The solid and the fluid phase remain in LTNE until  $t_d = 20$ . . . . . 372
- 8.14 Conceptual representation of the Fenton Hill reservoir, inspired from Zyvoloski et al. (1981, Figure 3-2). The injection well is denoted EE-1 and the production well is denoted GT-2. The extent and the amount of fractures linking the two wells are not precisely known and are indicated here for the illustration. . . . . 375
- 8.15 Representation of a generic HDR reservoir (not at scale). The permeability  $k_f$  of the reservoir depends on the average fracture spacing  $B$  and on the average fracture aperture  $2b$ . The simulations assume a plane strain analysis, in the  $x - z$  plane, and symmetry with respect to  $z$ -axis. . . . . 386
- 8.16 Thermal, hydraulic and mechanical boundary conditions. . . . . 388
- 8.17 Dimensionless temperature outlet  $T_D$  as a function of time for three porosities  $n_f$  and three fracture spacings  $B$ . All results are for  $Z_R = 230$  m,  $v^\infty = 2 \cdot 10^{-4}$  m/s and thermal properties from Table 8.4. In LTNE, time profiles display a double-step pattern, whereas in LTE, time profiles display a continuous pattern. The thresholds between LTE and LTNE are associated with the fracture spacings  $B_T = 6$  m (left),  $B_T = 2.5$  m (middle) and  $B_T = 2$  m (right). The corresponding dimensionless values of  $\eta_D$  are equal respectively to 11, 13 and 10. Therefore, LTE is associated with  $\eta_D$  larger than, say 13, while values of  $\eta_D$  smaller than 13 requires a LTNE analysis. The late overshooting oscillations are numerical artifacts due to an imperfect damping of the convective contribution, see Remark 8.3. . . . . 390
- 8.18 Dimensionless temperature outlet  $T_D$  as a function of time, for a porosity  $n_f = 0.005$ , three flow rates  $v^\infty$  and three fracture spacings  $B$ . All results are for  $Z_R = 230$  m and thermal properties from Table 8.4. In LTNE, time profiles display a double-step pattern, whereas, in LTE ( $B = 0.5$  m), time profiles display a continuous pattern. The thresholds between LTE and LTNE express in terms of fracture spacing  $B_T = 7.5$  m (left),  $B_T = 2.5$  m (middle),  $B_T = 1.5$  m (right). The resulting dimensionless threshold  $\eta_D \simeq 13$  applies to all velocities. . . . . 392

- 8.19 Square of the fracture spacing threshold  $B_T^2$  as a function of the average fluid velocity at steady state  $v^\infty$ , for a porosity  $n_f = 0.005$ , a uniform flow path and an insulated reservoir. All results are for  $Z_R = 230$  m and thermal properties from Table 8.4. The hyperbolic relationship defined by eqn (8.99) is represented by a blue line. It is well captured by the finite element (FE) simulation. . . . . 393
- 8.20 Scaled fluid velocity vectors in the reservoir. Wells (thick horizontal lines) penetrate the reservoir either totally (left) or partially (center, right). The reservoir is insulated from the rock formation (left, center) or exchanges heat with the formation (right). . . . . 394
- 8.21 Same as Fig. 8.19 but for a non-uniform flow path and heat exchange with a formation of 30 m width. The drawdown results correspond to the tip of the production well, i.e.  $x = X_W = 60$  m. A non-linear non-monotonic response is obtained from the finite element (FE) simulations in opposition with the power response suggested by eqn (8.99). Heat exchange between the reservoir and the rock formation requires the use of the SUPG method, Remark 8.5. . . . . 395
- 8.22 Fluid temperature contours for  $v^\infty = 2.0 \cdot 10^{-4}$  m/s, at  $t = 3.18$  years, accounting for heat transfer with the rock formation and for a non-uniform flow field. The Galerkin method (left) displays spurious numerical wiggles, which are partly cured by the SUPG method (right). . . . . 396
- 8.23 Relative temperature outlet  $T_D$  versus time  $t$  along the production well at  $x=60$  m. Experimental data pertain to different depths, namely  $\circ$  2703 m,  $\diamond$  2673 m,  $\times$  2626 m and  $\square$  in the casing 2660 m. *Colors are available on the electronic version.* The experimental temperatures at day one result from the spatial heterogeneity along the production well, see text. (left) Uniform flow field,  $k_f = 8.0 \cdot 10^{-15}$  m<sup>2</sup> and  $n_f = 0.005$ . Optimum specific inter-phase heat transfer coefficient  $\kappa_{sf} = 33.0$  mW/m<sup>3</sup>.K. (right) *Non-uniform* flow field,  $k_f = 2.35 \cdot 10^{-14}$  m<sup>2</sup> and  $n_f = 0.005$ . Optimum specific inter-phase heat transfer coefficient  $\kappa_{sf} = 30.0$  mW/m<sup>3</sup>.K. . . . . 398

- 8.24 Profiles, along the  $z$ -axis at  $x = 60$  m, of fluid temperature (left) and solid temperature (right), with  $n_f = 0.005$ ,  $k_f = 8.0 \cdot 10^{-15} \text{ m}^2$ ,  $\kappa_{sf} = 33.0 \text{ mW/m}^3 \cdot \text{K}$  and a uniform flow field. P.W. stands for production well and I.W. for injection well. The early wiggles near the injection well are numerical artifacts due to an imperfect damping of the convective contribution, see text. The thermal depletion of the fluid phase is significantly ahead of the thermal depletion of the solid phase. . . . . 399
- 8.25 Profiles, along the  $z$ -axis at  $x = 60$  m, of fluid pressure  $p_f$  (left) and relative fluid pressure with respect to the LTE response (right). Same parameters as Fig. 8.24. The fluid pressure reaches quickly steady state and remains undisturbed in spite of the thermal depletion of the fluid phase and of the thermal contraction of the solid phase. . . . . 399
- 8.26 Profiles, along the  $z$ -axis at  $x = 60$  m, of vertical strain (left) and lateral strain (right). Same parameters as Fig. 8.24. Extension is counted positive. The simulations assume a plane strain analysis,  $\epsilon_y = 0$ . Contraction of the solid phase,  $\Delta\epsilon_z < 0$  and  $\Delta\epsilon_x < 0$ , is controlled by the solid temperature response and, thus, develops in the late period. . . . . 400
- 8.27 Profiles, along the  $z$ -axis at  $x = 60$  m, of the induced change in vertical effective stress (left), lateral effective stress (center) and out of plane effective stress (right). Same parameters as Fig. 8.24. Tensile stresses are counted positive. The contraction of the solid phase induces the effective lateral stress to be tensile near the injection well ( $z < 120$  m) and compressive near the production well ( $z > 120$  m). . . . . 401
- 8.28 Same as Fig. 8.27 but with a refined mesh in the vicinity of the injection well. The profile at 31.0 years corresponds to the complete cooling of the reservoir. . . . . 401
- 8.29 Representation of a generic HDR reservoir. The exact convective flow path is unknown and only the average fracture spacing  $B$  and  $n_f$  the porosity of the fracture network are required to obtain the average fracture aperture  $2b$ , eqn (8.165).  $k_p$  and  $k_f$  denote the permeabilities of the porous blocks and of the fracture network, respectively. The simulations assume a plane strain analysis, in the  $x - z$  plane. Symmetry with respect to  $z$ -axis is assumed. . . . . 422
- 8.30 Thermal, hydraulic and mechanical boundary conditions (BC). Symmetry with respect to  $z$ -axis is assumed. . . . . 423

8.31 Relative temperature outlet  $T_D = (T^0 - T_f(z = z_R))/(T^0 - T_{inj})$  versus time in days. LTE stands for local thermal equilibrium and is obtained for  $\kappa_{sf} = 100 \text{ W/m}^3\text{.K}$ . *Colors are available on the electronic version.* (left) Fenton Hill hot dry rock reservoir with  $k_f = 8.0 \cdot 10^{-15} \text{ m}^2$  and  $n_f = 0.005$ . Field data pertain to  $\circ$  2703 m,  $\diamond$  2673 m,  $\times$  2626 m and  $\square$  in the casing 2660 m (Zyvoloski et al., 1981). The optimum specific solid-to-fracture fluid heat transfer coefficient  $\kappa_{sf}$  is equal to  $33 \text{ mW/m}^3\text{.K}$ . (right) Rosemanowes hot dry rock reservoir with  $k_f = 3.2 \cdot 10^{-14} \text{ m}^2$ ,  $n_f = 0.005$ . Field data pertain to  $\circ$  the casing shoe of the production well ( $\approx 2125 \text{ m}$  in true vertical depth) (Kolditz and Clauser, 1998). The optimum specific solid-to-fracture fluid heat transfer coefficient  $\kappa_{sf}$  lies in the range 60 to  $120 \text{ mW/m}^3\text{.K}$ . The late overshooting oscillations for the LTE solution are due to an imperfect damping of the convective contribution (Section 8.3). . . . . 428

8.32 Fenton Hill reservoir, late time ( $t = 1.9 \text{ years}$ ) vertical profiles of the temperatures of solid and pore fluid (top-left), the temperature of fracture fluid (top-right), the pressure of pore fluid (bottom-left), and the pressure of fracture fluid (bottom-right) for  $k_f = 8.0 \cdot 10^{-15} \text{ m}^2$ ,  $n_f = 0.005$ ,  $\kappa_{sf} = 33 \text{ mW/m}^3\text{.K}$  and  $B = 13 \text{ m}$  (Sect. 8.4.7.1). I.W. stands for injection well and P.W. for production well. The responses of the various models match for the temperatures and for the fracture fluid pressure. On the other hand, the pore pressure response of the dual porosity model displays a pressure drop near the injection point. The magnitude of the pressure drop is controlled by the diffusivity ratio  $R_p$  and is larger for smaller pore permeability ( $k_p = 10^{-21} \text{ m}^2$ ). The single porosity model leaves out of account the pore pressure response. Regarding the pore pressure, the dual porosity response for  $k_p = 10^{-18} \text{ m}^2$  is bounded by the dual porosity response for smaller pore permeabilities and by the fracture fluid pressure (1P), close to the injection well  $z/z_R < 0.3$ . . . . . 431

- 8.33 Fenton Hill reservoir, late time ( $t = 1.9$  years) vertical profiles of the changes in vertical effective stress (left), lateral effective stress (middle) and out-of-plane effective stress (right). Tensile stresses are counted positive. Owing to the pore pressure contribution, the stress responses described by the single porosity model (1P) are not equivalent to the responses described by the dual porosity model. The single porosity model predicts a thermally induced tensile stress in the vicinity of the injection well, whereas the dual porosity model predicts a smaller tensile stress ( $\Delta\bar{\sigma}_x$  and  $\Delta\bar{\sigma}_y$ ) and an increase of compressive stress ( $\Delta\bar{\sigma}_z$ ). The pore pressure drop counterbalances the contraction induced by the solid temperature. As expected, the dual porosity response with  $k_p = 10^{-18} \text{ m}^2$  is bounded by the single porosity and by the dual porosity with  $k_p = 10^{-21} \text{ m}^2$  responses, close to the injection well  $z/z_R < 0.3$ . . . . . 432
- 8.34 Fenton Hill reservoir, early time ( $t = 34.72$  days) vertical profiles of fluid temperatures (left), and fluid pressures (right), and jump in scaled chemical potential at early and late times (middle). At early time, the temperature of the fracture fluid decreases, whereas the temperature of the pore fluid remains high. This large difference associated with a negative difference in scaled chemical potentials  $G_p/T_p - G_f/T_f < 0$  induces a large transfer of mass from the fracture network towards the porous blocks, which is characterized by a significant pore pressure drop, while the fracture fluid pressure remains undisturbed as in Figure 8.32. This behavior matches the observations of field experiments Murphy et al. (1981). . . . . 433
- 8.35 Fenton Hill reservoir, late time ( $t = 1.9$  years) vertical profiles of solid and pore fluid temperatures (top-left), fracture fluid temperature (top-right), pore fluid pressure (bottom-left) and fracture fluid pressure (bottom-right) for  $k_f = 8.0 \cdot 10^{-15} \text{ m}^2$ ,  $k_p = 10^{-20} \text{ m}^2$  and  $n_f = 0.005$ . A small fracture spacing  $B$  represents a dense fracture network that overlaps the response of the single porosity model, whereas a large  $B$  represents a sparsely fractured reservoir. The fracture spacing  $B$  controls the departure from *both* hydraulic and thermal equilibria. Hydraulic equilibrium is not recovered unless thermal equilibrium is attained, which takes place only for  $B \rightarrow 0$ . Solely, the fracture fluid pressure is not influenced by the fracture spacing  $B$ . The overshooting oscillations for the temperature solutions near  $z/z_R = 0.2$  are again due to an imperfect damping of the convective contribution, Sec. 8.3, which slightly pollutes the stress and the strain responses (Figures 8.36 and 8.37). . . . . 434

- 8.36 Fenton Hill reservoir, late time ( $t = 1.9$  years) vertical profiles of the changes in vertical effective stress (left), in lateral effective stress (middle) and in out-of-plane effective stress (right) for  $k_f = 8.0 \cdot 10^{-15} \text{ m}^2$ ,  $k_p = 10^{-20} \text{ m}^2$  and  $n_f = 0.005$ . For small fracture spacings  $B \rightarrow 0$ , hydraulic and thermal equilibria are reached and the changes in effective stress are tensile close to the injection area  $z/z_R < 0.3$ . In addition, the single porosity response is well recovered. The dual porosity model reveals that large fracture spacings  $B$  reduce the pore pressure and therefore the effective stress  $\bar{\sigma} = \sigma + \xi_p p_p \mathbf{I} + \xi_f p_f \mathbf{I}$  is more compressive. . . . . 435
- 8.37 Fenton Hill reservoir, late time ( $t = 1.9$  years) vertical profiles of the changes in vertical strain (left) and in lateral strain (right) with the same parameters as in Figure 8.36. For small fracture spacings  $B \rightarrow 0$ , hydraulic and thermal equilibria are reached and negative strains close to the injection area  $z/z_R < 0.3$  characterize a sharp thermally induced contraction. In addition, the single porosity response is well recovered. The dual porosity model reveals that large fracture spacings  $B$  reduce the thermally induced contraction of the rock in the vicinity of the injection well and thereby the potential for aperture enlargement of the micro-fractures or pores. . . . . 435
- 8.38 Scaled chemical potential [J/kg.K.10<sup>3</sup>] as a function of temperature and pressure in a range appropriate to the present analysis. The material data are issued from Tables 8.6 and 8.8. (left): the injection state of the circulation test is taken as reference; (right): the triple point of water is taken as a reference. . . . . 436
- 8.39 Fenton Hill reservoir, late time ( $t = 1.9$  years) vertical profiles of jump in scaled chemical potentials (left), pore fluid pressure (middle), and change in vertical effective stress (right) for  $k_f = 8.0 \cdot 10^{-15} \text{ m}^2$ ,  $k_p = 10^{-20} \text{ m}^2$  and  $n_f = 0.005$ . I.S. : the injection state of the circulation test is used as a reference. T.P.W. : the triple point of water is used as a reference. Mass transfer is larger for T.P.W. Although the pore pressure drop dissipates more effectively for larger mass transfer, the consequences on the reservoir response are quite small. For the pore fluid pressure and the change in vertical effective stress, the T.P.W. and the I.S. responses superpose. . . . . 437

- 
- 8.40 Fenton Hill reservoir close to the injection well  $z/z_R \leq 0.1$ , vertical profiles of pore pressure (left) and change in vertical effective stress (right) for  $k_f = 8.0 \cdot 10^{-15} \text{ m}^2$ ,  $k_p = 10^{-21} \text{ m}^2$ ,  $B = 13 \text{ m}$  and  $n_f = 0.005$ . The hydraulic characteristic time is  $t_H \approx 40$  days. For times close to  $t_H$ , the pore pressure remains high and negative. However, for  $t > t_H$  the excessive pore pressure can dissipate in the fracture network. . . . . 438
- G.1 Contours of fluid temperature for a dimensionless flux  $v^\infty = 9.0 \cdot 10^{-3} \text{ m/s}$  at time  $t = 0.38$  hour, accounting for heat transfer with the surrounding, with the SUPG stabilization (left) and with the SUPG and DC stabilizations (right). The DC stabilization effectively cures some overshootings that are not taken care of by the SUPG method. . . . . 504



# List of Tables

1.1	Summary of poroelastic constants for various porous materials, reproduced from Cowin (2001, p. 23, Chapter 18). Data on bone corresponds to the lacunar-canalicular porosity (PLC). Data on granites represent the range for two granites, and data on sandstones indicate the range across six sandstones. Data are from Detournay and Cheng (1993) and Zhang et al. (1998), where details of specific rocks are given. . . . .	41
1.2	Classification of porous media with respect to void space and solid matrix connectivity, reproduced from Bear and Bachmat (1991). PM = Porous medium, MC = Single multiply-connected domain only, SC = Ensemble of simply-connected domain only, MSC = Combination of MC and SC, IP = Isolated pores, FB = Fluidised bed. . . . .	42
1.3	Fractured media classification based on the comparison of the storage capacity of the two sub-systems (Bai et al., 1993). The porosity of the porous block is denoted $n_p$ and the porosity of the fissure network is denoted $n_f$ . . . . .	43
1.4	Illustration of the effective porous medium approach and of the mixture theory based on the averaging process. The averaging process is represented by dashed lines. The illustration of the effective porous medium is derived from Cowin (2001). . . . .	46
1.5	Illustration of the homogenisation approach and of the statistical approach based on the averaging process. The averaging process is represented by dashed lines. The illustration of the homogenisation approach is derived from Hornung (1997). The illustration of the statistical approach is a three-dimensional representation of a fracture network within a granite block analysed by Ledésert et al. (1993); Adler and Thovert (1999). . . . .	48

1.6	Classification of multi porosity / multi permeability models and recommendations for practical applications from Bai et al. (1993). The porosities are denoted as in Table 1.3. The subscript $T$ refers to a total fluid quantity, that is the sum over all the sub-cavity systems. The permeability of the porous block is denoted $k_p$ and the permeability of the fissure network is denoted $k_f$ . In the last case, the subscript $f1$ refers to natural fractures and $f2$ refers to artificially enhanced fractures or fault gouges. . . . .	53
2.1	Thermodynamical measures of the state. Note that the increment definitions are arbitrary; therefore the total derivative $d(\cdot)$ may be replaced by the gradient operator $\nabla(\cdot)$ or by the partial derivative $\partial(\cdot)$ . . . . .	121
2.2	Some physical properties of pure water, from <a href="http://www.engineeringtoolbox.com">http://www.engineeringtoolbox.com</a> and * from Kestin (1968, p. 541). . . . .	128
2.3	Direct and coupled diffusion phenomena from (Mitchell, 1993, p. 230). The phenomena accounted for in this model are highlighted in bold letters. . . . .	148
2.4	Set of field equations and list of primary unknowns . . . . .	164
2.5	Set of constitutive equations, $k^* = p, f, k = s, p, f$ and $l = p, f, s$ . . . . .	165
2.6	Origins of the coefficients used in equation (2.309). . . . .	173
2.7	Origins of the coefficients used in equation (2.312). . . . .	175
2.8	Origins of the coefficients used in equation (2.313). . . . .	176
2.9	Coefficients of the model . . . . .	179
2.10	Sketch of the repartition of the coupling coefficients in the model. The model displays non symmetry. The diagonal or direct coefficients are not represented here. . . . .	180
3.1	Range of values of various drained Young's moduli from Philipponnat et al. (2003). . . . .	185
3.2	Bulk moduli of typical soil minerals from Gebrande (1982) and Francois (2008). . . . .	187
3.3	Range of values of compressibility ratios for dual porous media. . . . .	188
3.4	Bulk moduli of various fluids, at atmospheric pressure and 20°C. . . . .	189
3.5	Range of values of the porous block porosity $n_p$ and of the fissure network porosity $n_f$ from the literature. . . . .	190
3.6	Range of values of the porous block permeability $k_p$ and of the fissure network permeability $k_f$ from the literature. . . . .	191
3.7	<i>Linear</i> thermal expansion coefficients, of typical clay minerals, for a temperature range between 25°C and 100°C (Horseman and McEwen, 1996). . . . .	194

3.8	Volumetric thermal expansion coefficient of ice and pure water at atmospheric pressure (Kestin, 1968, p. 541).	195
3.9	Density coefficients of various soils (Burger et al., 1985, p. 139).	196
3.10	(left) Density variation with temperature for pure water, at atmospheric pressure, from <a href="http://www.engineeringtoolbox.com">www.engineeringtoolbox.com</a> . (right) Specific volume (inverse density) contour with pressure and temperature as defined in equation (2.158).	196
3.11	Dynamic viscosity of pure water, from <a href="http://www.engineeringtoolbox.com">www.engineeringtoolbox.com</a>	197
3.12	(left) Specific heat capacity of different soils, from <a href="http://www.engineeringtoolbox.com">www.engineeringtoolbox.com</a> . (right) Specific heat capacity of pure water at constant atmospheric pressure (Kestin, 1968, p. 541).	198
3.13	(left) Thermal conductivity of different soils, from <a href="http://www.engineeringtoolbox.com">www.engineeringtoolbox.com</a> . (right) Thermal conductivity of pure water (Burger et al., 1985, p 137).	199
3.14	Thermo-osmosis coefficients for compact clays-water system from the literature.	200
3.15	Specific surface area values for various materials (de Marsily, 1986, p. 22).	201
4.1	Shape functions associated to a four node bilinear quadrilateral reference element. The nodal points are labeled in ascending order corresponding to the counterclockwise direction.	220
4.2	Typical numbers of the generalised trapezoidal methods.	227
5.1	Loading and boundary conditions.	235
5.2	Solid and fluid parameters, representative of granite and water, respectively, at 25°C and atmospheric pressure. The thermal diffusivities are defined in eq. (5.3). The characteristic diffusion times are calculated with eq. (5.2) and $H = 3$ m.	236
5.3	A combination of four boundary conditions is proposed by McTigue (1986).	241
5.4	Loading values. 1: The heat flux is only applied when considering a constant heat flux loading. 2: The imposed temperature is only applied when considering a constant temperature loading.	247
5.5	Material properties of an abyssal red clay (Illite), North Pacific Ocean (McTigue, 1986, p. 9540). *Definitions of these parameters are provided in eq. (5.3) and (5.24), respectively.	247
5.6	Comparison between the hydraulic and the thermal contributions for a diffusivity ratio $R = 1$ . $\delta$ is of order of magnitude of one: $O(10^0)$ and the symbol $\propto$ means ‘proportional to’	267

5.7	Material properties of salt, Salado Formation, Delaware Basin, New Mexico (McTigue, 1986, p. 9540). *Definitions of these parameters are provided in eq. (5.3) and (5.24), respectively. . . . .	268
5.8	Evolution of the integration error on the radial displacement, the deformation and the stress with a <i>homogeneous mesh</i> , at the inner radius $r = r_1$ . Note that the error of the deformation and of the stress is $O(10^i)$ when the error of the displacement is $O(10^{i-1})$ . If an homogeneous mesh is assumed, the number of elements needed to obtain a ‘correct’ error is huge. . . . .	276
5.9	Evolution of the integration error on the radial displacement, the deformation and on the stress with an <i>non-homogeneous mesh</i> , at the inner radius $r = r_1$ . The error on the displacement remains greater or equal to 0.209. This result is probably due to the remaining error along the layer, see Figure 5.19. On the other hand, the accuracy of the strain and of the stress becomes acceptable at the inner radius for 50 elements or more. . . . .	277
6.1	Input parameters representative of a homogeneous isotropic dual porous medium. 1: Nair et al. (2002), 2: Nair et al. (2004) Gulf of Mexico Shale, 3: Wilson and Aifantis (1982) and 4: (Kestin, 1968, p. 541). . . . .	290
6.2	Boundary conditions for a thermal recovery test with an axi-symmetric mesh in the $r$ - $z$ plane. . . . .	291
6.3	Comparison between the diffusivity ratios $R = \sqrt{\alpha_H/\alpha_T}$ of the porous blocks, of the fissure network as parts of dual porosity medium, and of the associated single porosity medium. Note that thermal diffusion is faster than hydraulic diffusion for the pore matrix (2P) while the opposite holds for fissure network (2P) and associated single porosity analysis (A1P). . . . .	293
7.1	Comparison between the stabilisation parameter related to the streamline operator $\tau$ and the stabilisation parameter related to discontinuity-capturing operator $\tau_{  }$ . . . . .	344
8.1	Input parameters representative of the hot dry rock reservoir at Soultz-sous-Forêts (France). 1: Estimated parameters for water and granitic rock, 2: Bataillé et al. (2006) and 3: Evans et al. (2009). *The porosity accounts for the fluid in the fissure network and in the rock matrix. +The permeability describes the interconnected fissure network post-stimulation. . . . .	359
8.2	Boundary conditions used for the circulating model, at Soultz-sous-Forêt. 1 = left, r = right, t = top, b = bottom boundary of Figure 8.2. . . . .	361

8.3	Initial and loading boundary conditions representative of Fenton Hill HDR reservoir, run segment 5. 1: Zyvoloski et al. (1981). 2: Sect.8.3.4.3. 3: Murphy et al. (1977) . . . . .	396
8.4	Input parameters representative of Fenton Hill HDR reservoir, run segment 5. 1: Murphy et al. (1977). 2: Zyvoloski et al. (1981). 3: Elsworth (1989). † Estimated parameters for water and granite. ‡ Although, fluid dynamic viscosity varies much with temperature and with viscosity-increasing additives or propping agents, the fluid dynamic viscosity $\mu_f$ used throughout corresponds to pure water at 95°C, Table A.2.4 in de Marsily (1986). . . . .	397
8.5	Sensitivity of the leakage parameter $\eta$ , the specific solid-to-fracture fluid heat transfer coefficient $\kappa_{sf}$ and the specific pore fluid-to-fracture fluid heat transfer coefficient $\kappa_{pf}$ to the fracture spacing $B$ for a two-dimensional fracture network $n = 2$ endowed with a pore permeability $k_p = 10^{-20} \text{ m}^2$ , a fracture porosity $n_f = 0.005$ and a pore porosity $n_p = 0.05$ . The other material parameters are taken from Table 8.8. . . . .	424
8.6	Initial and loading boundary conditions representative of Fenton Hill HDR reservoir, run segment 5. 1: Zyvoloski et al. (1981). 2: Murphy et al. (1977).	425
8.7	Initial and loading boundary conditions representative of Rosemanowes HDR reservoir, RH12/RH15 system. 1: Hicks et al. (1996). 2: Richards et al. (1994). 3: Bruel (1995). . . . .	425
8.8	Input parameters representative of Fenton Hill HDR reservoir, run segment 5. 1: Murphy et al. (1977). 2: Zyvoloski et al. (1981). 3: Wilson and Aifantis (1982). 4: First estimation owing to the rather high pressure of the overburden rock. 5: Elsworth (1989). 6: Estimated parameters for water. 7: Local thermal equilibrium is enforced between the pore fluid phase and the solid phase owing to the absence of convection, to their similar thermal diffusivities $\alpha_{T,s} \approx \alpha_{T,p} \times 10$ , and to the large specific surface $S_{sp}^s$ . . . . .	426
8.9	Input parameters representative of Rosemanowes HDR reservoir. 1: Bruel (1995). 2: Armstead and Tester (1987). 3: Estimated parameters for water or granite. 4: Wilson and Aifantis (1982). 5: Richards et al. (1994). 6: First estimation owing to the rather high pressure of the overburden rock. 7: Kolditz and Clauser (1998). 8: Local thermal equilibrium is enforced between the pore fluid phase and the solid phase owing to the absence of convection, to their similar thermal diffusivities $\alpha_{T,s} \approx \alpha_{T,p} \times 10$ , and to the large specific surface $S_{sp}^s$ . . . . .	427
8.10	Two possible definitions of the reference thermodynamic potentials. . . . .	436

# Introduction

## Context

Dual or multi-porosity models attempt at a more accurate macroscopic representation of the actual properties of rock formations. Indeed various types of strata, rocks and porous media are naturally fractured. In addition, artificial fracturation is often sought to increase the *in-situ* permeability of a given medium. For example, hydraulic fracturation is used in petroleum engineering and in enhanced geothermal systems (EGS). Other applications of the dual porosity theory include the removal of pollution in ground surface water from agricultural chemicals, prediction of stress in tight reservoirs, stability of wellbores, consolidation of fractured clays, settlements of hazardous waste disposals and influence of clogged pores (unconnected porosity).

The need for dual or multi porosity models is induced by the observation that the behaviour of fractured media is radically different from that of a conventional single porous medium endowed solely with a single intergranular porosity and a single permeability (Bai et al., 1993; Khalili-Naghadeh, 1991; Khalili et al., 1999). Field observations of pressure buildup and depletion history of reservoir (Maury and Zurdo, 1996; Willson et al., 1999) have encouraged studies to accurately characterise the behaviour of fractured reservoirs (Warren and Root, 1963; Kazemi, 1969; Zhang and Roegiers, 2005).

The role of geomechanics in reservoir engineering has become increasingly important as enhanced oil recovery processes and enhanced geothermal systems are undertaken and deeper formations are explored (Lake et al., 1992; Tenzer, 2001). Unfortunately, conventional reservoir modeling fails to describe the stress, fluid pressure and temperature responses encountered at greater depth, which gives rise to inaccurate calibration of *in-situ* well conditions (Chen et al., 1997) and inaccurate thermal output evolution (Armstead and Tester, 1987). In fact, the gap between the purely mechanical point of view and the purely heat transfer point of view has been progressively filled in late years (Hayashi et al., 1999). Hydro-mechanical models are extended to account for thermal contributions and diffusion-convection models are extended to account for stress contributions. Borehole stability problems have motivated the development of more complex constitutive models to

accurately calibrate the drilling mud pressure, density and temperature (McTigue, 1990; Zhang and Roegiers, 2005). On the other hand, these constitutive models can be applied to the understanding of thermal recovery from artificial deep hot dry rock reservoirs.

## **Objective, method and scope**

The objective of this study is to investigate thermo-hydro-mechanical coupled behaviour of dual porosity media in order to gain insight into the effects of fracturation on wellbore stability in tight petroleum reservoirs and on thermal recovery in hot dry rock reservoirs. Particular attention is given to the mass transfer and to the energy transfer phenomena.

A constitutive model is developed that is sufficiently general such that it is suited to all types of dual porosity media. Among the various constitutive frameworks, the theory of mixture appears to be the most appropriate method to implement multi fluid mixtures due to its diffusion-based approach in that the fluxes of the various species are considered at each point of space. A previous poroelastic model (Khalili and Valliappan, 1996) is extended to account for thermal effects within a rational thermodynamic framework of irreversible processes in which the Clausius-Duhem inequality is used to motivate and restrain the constitutive equations (Loret and Khalili, 2000b; Loret, 2008).

From a general point of view, the real needs are: (1) the identification of work conjugate variables for each type of phenomena, that is the thermo-poro-elastic law, the generalised diffusion law and the generalised transfer law; (2) the introduction of forced convection to address convection-dominated problems, such as hot dry rock systems (Willis-Richards and Wallroth, 1995); and (3) the introduction of local thermal non-equilibrium to properly describe the heat transfer between the phases (Aifantis, 1980b). With a mixture in local thermal non-equilibrium various decouplings can then be tested, for example, a pure convective flow in the fissure network coupled to a diffusive flow in the pore matrix.

On the other hand, the identification procedure for the constitutive mechanical coefficients introduces the effective stress concept for a solid permeated with several fluids (Khalili and Valliappan, 1996). The key principle of the effective stress concept is that a single stress entity governs the elastic response of the solid skeleton.

## **Contribution**

The model in local thermal equilibrium is calibrated against analytical results provided for saturated soils subject to a range of thermal loadings and drainage conditions.

The problem of the wellbore stability of a fractured reservoir is solved using the finite

element method in a thermally enhanced oil recovery context. This study highlights the importance of the relative values of the hydraulic and thermal diffusivities. The main conclusion of this study reveals the importance of the dual porosity concept for the prediction of failure in fissured reservoirs: compared with the dual porosity results, the single porosity approach under-estimates the failure potential, for both drained and partially-drained conditions at the wellbore.

Forced convection is stabilised with the streamline-upwind/Petrov-Galerkin method that damps the spurious numerical oscillations observed along sharp temperature gradients. The optimum stabilisation parameter is sought for a multi-dimensional transient problem.

The constitutive model is then applied to the problem of thermal recovery from a fractured medium in local thermal non-equilibrium, simplified to a single porosity mixture. The parameter that characterise thermal non-equilibrium is calibrated with the thermal output of Fenton Hill hot dry rock reservoir. The influence of local thermal non-equilibrium on the fluid temperature outlet is characterised by a double-step curve. For the particular case of a single porosity model, the thermally induced effective stress is found to be tensile and illustrates the dominance of the thermal contributions over the pressure contribution. On the other hand, when accounting for the dual porosity approach in local thermal non-equilibrium, the pressure contributions become significant. The thermally induced effective stress is found to be less tensile with the dual porosity model compared with the single porosity response illustrating the protective effect of the pore pressure contribution; which increases for large fracture spacings. Furthermore, the mechanism of fluid permeation from the fractures towards the porous block is identified.

Throughout the project, a great deal of time was spent in coding the various aspects of the constitutive model, the time marching scheme, the equation solving routines, the stabilisation methods and routines devoted to input and output data, in a home-made FORTRAN program.

## **Thesis structure**

The structure of the thesis is as follows:

Chapter 1 reviews investigations into non-isothermal fluid-saturated porous media, with emphasis placed on the description of dual porosity media. The constitutive models used to describe dual porosity media and other investigations that address coupled thermo-hydro-mechanical models are also reviewed.



Chapter 2 presents the theoretical framework based on the rational thermodynamics of irreversible processes. The field equations are developed as part of the mixture theory and the entropy inequality is defined to illuminate the restrictions that it places on the various constitutive relations. The constitutive equations related to thermo-poro-elasticity, the generalised diffusion and the generalised transfer are considered in turn. Finally, the latter relations are inserted in the field equations to constitute the fully-coupled comprehensive model.

The material parameters of the constitutive model are investigated in Chapter 3. The interpretation and the identification of these parameters are gathered from the literature for typical soils and rocks, and for water.

The finite element discretisation of the problem is proposed in Chapter 4. The weak form and the matrix form of the problem are expressed in detail and the Galerkin approximation is used. The time integration and method of equation solving are also presented. The implementation of the model in a home-made FORTRAN code is part of the project.

The model is evaluated using benchmark applications in Chapter 5, for a single porosity mixture in local thermal equilibrium with no convection. This chapter aims to validate the correct implementation of the thermal contributions in the fully coupled thermo-hydro-mechanical model.

A pure conduction single temperature problem is solved in Chapter 6. The dual porosity approach is compared with a single porosity approach to assess the potential for failure of a wellbore subject to thermal loading, drained and undrained boundary conditions at the well and appropriate stress loading.

Forced convection and its implementation issues are considered in Chapter 7. The streamline-upwind/ Petrov-Galerkin method is introduced and analysed in our context of saturated porous media and typical tests are performed to validate the implementation of the method in the finite element program. For each case, the optimum stabilisation parameters are sought.

The fully-coupled model with local thermal non-equilibrium and forced convection is applied to real field problems in Chapter 8. The problem involves locally two pressures (pores and fractures) and two temperatures (porous block and fracture fluid). The general scheme which allows for distinct temperatures of the solid and pore fluid is not required for the analysis of EGS. The issue of the parameter controlling the thermal non-equilibrium is overcome by calibrating the simulation results against field data. The single porosity approach and the dual porosity approach are both investigated. Particular attention is

given to the effects of pressure contributions on the thermally induced effective stress.

**Nota**

To facilitate the reading, some results are intentionally repeated. These repetitions allow to read the two applicative Chapters 6 and 8, without necessarily reading the Chapters 2, 3 and 4 which establish the model and the finite element discretisation, nor the Chapters 5 and 7 which present preliminary numerical results.

# Chapter 1

## Non-isothermal fluid-saturated porous media: Literature review

The literature review comprises four sections. Section 1.1 provides a general introduction to porous media characterised by multiple porosities and specifies the definition of dual porous media. Section 1.2 compares the various averaging models used to implement the poroelastic constitutive equations and highlights the benefits of using the mixture theory to model mixtures composed of various fluids. Section 1.3 summarises the dual porosity concept and investigates the evolution of poroelastic constitutive models extended to porous media with double porosity. In Section 1.4 constitutive models for soils using thermo-hydro-mechanical coupling and other investigations are discussed.

### 1.1 Porous media with multi porosity

A porous medium can be defined as a material consisting of a solid matrix with interconnected voids. Further, a fractured medium is defined as a porous material endowed with different types of voids. This is also sometimes referred to as a multi porosity / multi permeability porous medium and represents several natural materials such as marble, granite, sandstone, clay, bones, wood and ice.

Let us consider bone as an example of the diversity of and similarities between multi porosity / multi permeability media. According to Cowin (2001), there are three levels of bone porosity containing fluid within cortical bone: the vascular porosity (PV); the lacunar-canalicular porosity (PLC); and the collagen-apatite porosity (PCA). The study of the movement and the interaction of the bone fluid in the PV with that in the PLC is relevant to the understanding of osteocyte nutrition, mechano-sensation and mineral storage and recovery. Although there are three levels of bone porosity, only two of them are considered to be significant with respect to fluid movement; the PV and the PLC.

The vascular permeability dominates that of the PLC cavity and the pressure in the PLC dominates that of the PV. In general, the elastic properties of bones and fluid-saturated porous rocks are comparable (see Table 1.1) and it has been suggested that the dual porosity poroelastic model is appropriate for the study of bone fluid movement and bone fluid pressure.

Parameter	Bone	Marble	Granites	Sandstones
Shear modulus - $G$ [GPa]	5	24	15-19	4.2-13
Drained Poisson's ratio - $\nu$	0.32	0.25	0.25-0.27	0.12-0.20
Undrained Poisson's ratio - $\nu_u$	0.33	0.27	0.30-0.34	0.28-0.33
Drained bulk modulus - $K$ [GPa]	12	40	25-35	4.6-13
Undrained bulk modulus - $K_u$ [GPa]	13	44	41-42	1.3-30
Compressibility coefficient - $B$	0.40	0.51	0.58-0.85	0.50-0.88
Bulk modulus of the solid - $K_s$ [GPa]	14	50	45	31-42
Effective stress parameter - $\xi_p$	0.14	0.19	0.27-0.47	0.65-0.85
Porosity - $n_p$	0.05	0.02	0.01-0.02	0.02-0.26
Intrinsic permeability - $k_p$ [m <sup>2</sup> ] $\times 10^{20}$	1.5	10	10-40	20,000-8.0 $\times 10^7$

Table 1.1: Summary of poroelastic constants for various porous materials, reproduced from Cowin (2001, p. 23, Chapter 18). Data on bone corresponds to the lacunar-canalicular porosity (PLC). Data on granites represent the range for two granites, and data on sandstones indicate the range across six sandstones. Data are from Detournay and Cheng (1993) and Zhang et al. (1998), where details of specific rocks are given.

### 1.1.1 Classification of multi porous media

Two comprehensive classifications of porous (fractured) materials have been proposed within literature and are summarised below. The first classification is based on the connectivity type of each constituent, whereas the second classification refers to the storage capacity of the various cavity types.

Bear and Bachmat (1991, p. 7) proposed the classification of porous media with respect to void space and solid matrix connectivity (Table 1.2). Most geo-materials can be defined as porous media of type  $PM_4$ , that is porous media in which both the solid and the void space are multiply-connected. A domain is multiply-connected if it is bounded from the inside and from the outside by one or more disjoint closed surfaces. In addition to this classification, fractured porous media are described as a portion of space in which the void space is composed of two parts: the fissure inter-connected network and blocks of porous medium, where both are considered multiply-connected. In the case where the fracture widths are large and the pores in the porous blocks are very small, suggestion is made to

regard the fluid in the void space as two apparent phases (Bear and Bachmat, 1991, p. 40).

		Void space		
		MSC	MC	SC
Solid matrix	MSC	PM <sub>1</sub>	PM <sub>2</sub>	
	MC	PM <sub>3</sub>	PM <sub>4</sub>	IP
	SC		FB	

Table 1.2: Classification of porous media with respect to void space and solid matrix connectivity, reproduced from Bear and Bachmat (1991). PM = Porous medium, MC = Single multiply-connected domain only, SC = Ensemble of simply-connected domain only, MSC = Combination of MC and SC, IP = Isolated pores, FB = Fluidised bed.

A classification of fractured (non-reactive) porous media has been proposed by Bai et al. (1993), based on the storage capacity comparison between the fracture network and the pore matrix (Table 1.3). Three types of reservoirs are identified: (1) In the first case, the storage capacity of the porous block appears to be small compared with the storage capacity of the fracture network. During a pumping test, the high initial rates will decline drastically after a short period of time because the fluid has been stored in the fracture system. (2) The second case illustrates a medium where only a small percentage of the total porosity is resident in the fractures. It is assumed that the high matrix block storage would continuously provide the supply to the well through highly permeable fracture channels. (3) The case where the storage capacity is equally distributed in the two sub-systems represents an average situation.

Due to particular interest for geo-materials and for reservoir problems, in which diffusion of fluid mass takes place in both the fissure network and the porous block, the discussion in this study is related primarily to porous media of type PM<sub>4</sub> according to Bear and Bachmat (1991) and to reservoirs with large storage in the matrix according to the classification of Bai et al. (1993).

### 1.1.2 Definition of dual porous media

A medium with double porosity is a porous medium in which two different porosities can be observed, typically pores and fissures. The pores and the fissures are filled up with fluid and the purpose of the pores can be considered as a storage function of the fluid, whereas


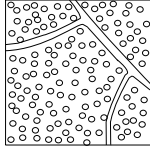
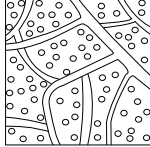
Name	Porosities	Representation	Behaviour
1. Reservoir with all storage in fractures	$n_f \gg n_p$		Sharp decline in production rate after a short period of time
2. Reservoir with large storage in the matrix	$n_p \gg n_f$		Production rate depending on the degree of fracturation
3. Reservoir with equal storage	$n_f \approx n_p$		Smooth production rate

Table 1.3: Fractured media classification based on the comparison of the storage capacity of the two sub-systems (Bai et al., 1993). The porosity of the porous block is denoted  $n_p$  and the porosity of the fissure network is denoted  $n_f$ .

the fissures have a transport function of the fluid through the medium.

Two main hypotheses are made to consider a dual porosity medium:

- i: Spatial scale separation, where it is considered that the average distance separating the pores is small in comparison to the average distance separating the fissures;
- ii: Time scale separation, where two time responses can be observed, the fluid of the fissures is affected by external loading before the fluid of the pores, which become aware of the load after a certain time.

A medium with dual porosity can be delineated in two overlapping entities:

- The porous block represents the part of the medium constituted with interconnected pores surrounded by the solid grains. As far as flow is concerned, unconnected pores may be considered as part of the solid matrix and only the inter-connected pores should be considered.
- The fissure network represents the part of the medium constituted with interconnected fissures.

Figure 1.1 illustrates the decomposition of a fractured porous medium in two coexisting systems of voids: the porous block and the fissure network. The leakage (or mass transfer) represents the ability of the fluid to transfer from one type of porosity to the other.

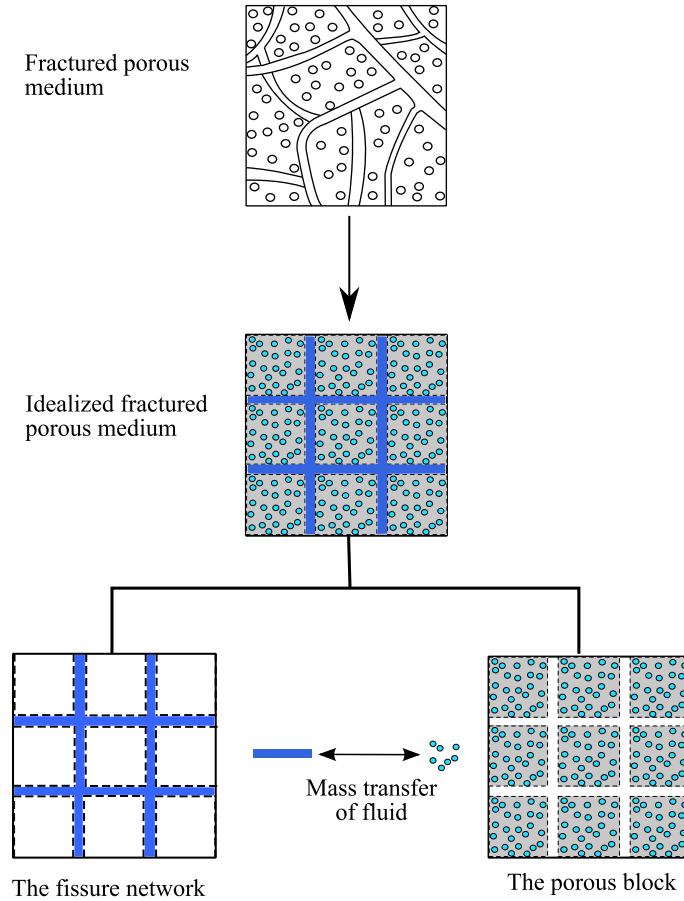


Figure 1.1: Illustration of the decomposition of a dual porous medium in two overlapping single porous media; the fissure network and the porous block. Mass transfer of fluid, momentum transfer, energy transfer and entropy transfer between the two sub-systems is permitted.

As the permeability of the fractured medium is mostly attributed to the fissure network, while most of the storage is held in the porous block, the conceptual model should be constructed so that the fluid in the fractures and the fluid in the porous block are represented by two ‘apparent phases’. In the next section, the various types of approaches to poroelastic models are gathered and compared; and recommendations are sought on the application of these models to multi porous media.

## 1.2 Poroelastic constitutive framework

The derivation of the laws governing macroscopic variables is usually obtained by averaging over volumes or masses containing many pores. Four different approaches to the development of the same basic equations for the theory of poroelasticity are discussed. Each approach is rigorous and consistent with mathematical and physical models for averaging material properties. The difference between each of them lies in the averaging process.

### 1.2.1 Averaging models

1. *The effective medium approach* stems from the field of solid mechanics where the averaging process involves the determination of effective material parameters from a representative volume element (RVE) (Biot, 1941; Nur and Byerlee, 1971; Christensen, 1979; Bear and Bachmat, 1991). This operation leads to values of these parameters at the center of the RVE which are independent of the size of the RVE if the latter satisfies the recommendations of Bear and Bachmat (1991). The RVE is determined so that its length is much larger than the pore scale, but considerably smaller than the length scale of the macroscopic flow. This approach is discussed at length by Bear and Bachmat (1991). For example, let  $u$  be a real valued function on a domain  $\Omega$  which describes any physical quantity with rapid spacial oscillations. By using the effective medium approach, the local average of  $u$  writes,

$$\langle u \rangle (x) = \int_{V(x)} u(y) \, dy, \quad (1.1)$$

where  $V(x)$  is of the same size as the RVE, that is several hundreds or thousands of pores. The effective medium approach suggests that the response of  $u$  at the pore scale describes its properties at a larger scale.

2. *The mixture theory* originates from the traditions of fluid mechanics and thermodynamics. The key principle of this approach (Truesdell and Toupin, 1960) is that each place in a fixed spatial frame of reference may be occupied by several different particles/phases, one for each constituent of the mixture. This diffusion-based approach is an Eulerian approach in that the fluxes of the various species are considered at each point of space with respect to the initial configuration. Truesdell (1957) assigned to each constituent a density, a body force density, partial stress, partial internal energy density, partial heat flux and partial heat density supply. In addition, Truesdell



(1957) allowed the balance of mass, momentum and energy equations to be written for each species of the mixture and postulated the necessary and sufficient closure conditions to satisfy the balances of mass, momentum and energy for the mixture. A comprehensive summary of the subject is provided by Atkin and Craine (1976). The main difference between the mixture approach and the effective medium approach lies in the averaging process; in the mixture theory the averaging is density-weighted on the basis of the density of each constituent of the mixture. For example, if a mixture is composed of three species (referred to as  $s, p$ , and  $f$ ), the definition of the barycentric velocity  $\mathbf{v}$  is

$$\rho \mathbf{v} = \sum_{k=s,p,f} n_k \rho_k \mathbf{v}_k \quad \text{with} \quad \rho = \sum_{k=s,p,f} n_k \rho_k \quad (1.2)$$

where each species  $k$  is endowed with a volume fraction  $n_k$ , an intrinsic density  $\rho_k$  and an absolute velocity  $\mathbf{v}_k$ .

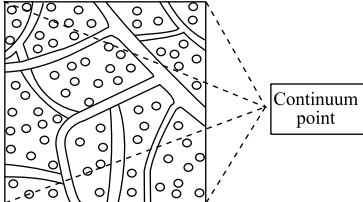
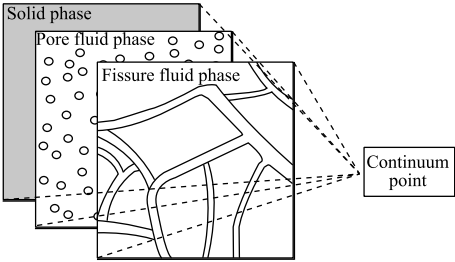
Model	Averaging Process	Schematic Representation
1. The effective medium approach	Volume averaging. A small finite volume (RVE) describes the behaviour at the macroscopic scale.	
2. The mixture theory	Mass averaging. At a fixed continuum point, each constituent of the mixture is considered.	

Table 1.4: Illustration of the effective porous medium approach and of the mixture theory based on the averaging process. The averaging process is represented by dashed lines. The illustration of the effective porous medium is derived from Cowin (2001).

3. The third approach is *the homogenisation theory* introduced by Burridge and Keller (1981). The basic set of poroelastic equations is derived by using a two-space method

of homogenisation. To make it simple, the averaging process used in the homogenisation approach allows to ‘upscale’ the differential equations. Compared with the effective medium approach, the basic idea of homogenisation is somewhat different. Following the explanations of Hornung (1997), a whole family of functions  $u^\epsilon$  is considered where  $\epsilon > 0$  is a spatial length scale parameter, the typical size of a pore. Instead of working with only one situation, the specific problem is imbedded in a family of problems parameterised by the scale parameter  $\epsilon$ . In approximate terms, the averaging process consists in determining the limit,

$$u = \lim_{\epsilon \rightarrow 0} u^\epsilon, \quad (1.3)$$

which is the result of the ‘upscaling’ procedure where the microscale tends to zero. Slattery (1967) and Whitaker (1967) proposed an alternative homogenisation technique based on volume averaging instead of periodical averaging, which is applicable to systems in which the length scale is constrained by  $l < R_0 < L$  (Whitaker, 1969), where  $R_0$  is the radius of the averaging volume,  $L$  is the macroscopic length scale and  $l$  the microscopic length scale.

4. Finally, the fourth approach is *the statistical approach* in which the averaging process is made over an ensemble of possible void structures which are macroscopically equivalent (Nield and Bejan, 2006). This is only possible if statistical homogeneity is assumed when the statistical information about the ensemble is based on a single sample. More information on this approach can be found in (Georgiadis and Catton, 1987; Adler and Thovert, 1999).

At each continuum point, the four approaches lead to the same set of equations (when no fluctuation of the averaged quantities is considered) and the difference between the effective medium approach, the mixture theory, the homogenisation approach and the statistical approach is the averaging process. The characteristics of the four approaches are illustrated in Tables 1.4 and 1.5.

Model	Averaging Process	Schematic Representation
3. The homogenisation approach	<p>‘Upscaling’ by letting the microscale tend to zero, with <math>\epsilon &gt; 0</math> being a scale parameter. <math>x \in \Omega</math> is a spatial coordinate and <math>y</math> is the side of the base cell in a local coordinate system.</p>	
4. The statistical approach	<p>Averaging over a particular void structure from a fractal analysis (Ledésert et al., 1993; Adler and Thovert, 1999).</p>	

Table 1.5: Illustration of the homogenisation approach and of the statistical approach based on the averaging process. The averaging process is represented by dashed lines. The illustration of the homogenisation approach is derived from Hornung (1997). The illustration of the statistical approach is a three-dimensional representation of a fracture network within a granite block analysed by Ledésert et al. (1993); Adler and Thovert (1999).

### 1.2.2 Recommendation for the mixture theory

The subtlety of poroelastic behaviour is better understood because of the various approaches. According to Cowin (2001): “The effective medium approach provides better insight into the nature of the parameters associated with the solid phase; the mixture theory approach provides the mechanisms for averaging over different fluid phases; and the homogenisation approach illuminates the wave propagation characteristics of the theory”.

Compared with the three other approaches, the mixture theory provides a relatively simple general framework for developing a model of multi phase / multi porous mixtures compared with the effective medium approach (Cowin, 1985); an important example being the development of the theory of swelling clays (Gajo and Loret, 2003). The mixture theory is thus employed in this study as presented in Chapter 2.

Bear and Bachmat (1991) proposed to name the various classes of field problems and gave some recommendations on the appropriate model to be used:

- *Zone 1: The very near field.* Interest is focused on diffusion processes within small-scale fissures and the porous block. Problems represented by a single well-defined fracture surrounded by porous rock are considered, see for example (Zhou et al., 2009; Bataillé et al., 2006), and mass transfer between the fracture and the rock is possible.
- *Zone 2: The near field.* Transport of flow is located in a narrow region containing a small number of well-defined fractures surrounded by porous rock. The fissure network needs to be defined either in deterministic (not-random) manner or generated stochastically (based on a real field-site). For more information and a clear example see the work of Ledésert et al. (1993).
- *Zone 3: The far field.* Transport of flow is considered, simultaneously, in two overlapping continua; one composed of the fissure network and the other consisting of the porous block. Exchange of fluid mass between them is taken into account. A comprehensive example is reported in Khalili et al. (1999) on consolidation in fissured clays. Bear and Bachmat (1991) recommend using the ‘two media’ approach (Barenblatt et al., 1960) when facing such conditions in large-scale problems.
- *Zone 4: The very far field.* The entire fractured sample is considered as an ‘equivalent’ single porous medium, which accounts for the properties of all sub-systems.

In this study, applications are narrowed down to transport of flow in large-scale problems. The ‘two media’ approach recommended for *the far field* zone will systematically be

compared with the ‘single medium’ model commonly used in the literature.

### 1.3 Poroelastic models for dual porosity

The initial studies of flow infiltration/seepage in soils were conducted using single porosity models or continuum concepts (Biot, 1941). Evolution in constitutive models introducing a dual porosity concept was initiated by Barenblatt et al. (1960) and Warren and Root (1963):

- Barenblatt et al. (1960) compared the results of theoretical and laboratory tests of transient flow of liquids in fissured rocks, which lead to the conclusion that the single pressure concept associated with the single porosity approach was inadequate. The basic concepts of media with double porosity was introduced by representing two sub-flow systems; the pores and the fissures, which are endowed with a single pressure at each point of space. Mass transfer of fluid between the fissures and the pores was also accounted for. In addition to this important scientific step forward, the mass transfer parameter was intuitively related to the porous block permeability, the inverse of the fluid viscosity, the pressure variation between the pores and the fissures and on certain characteristic of the medium through a dimensionless parameter. Barenblatt et al. (1960) have produced the first contribution to dual porous media by coupling the two fluid flows.
- Warren and Root (1963) extended Barenblatt’s double porosity concept by defining a fissured porous medium as two *completely overlapping* flow regions, named the fissure network and the porous block. In addition, the mass transfer constitutive law is for the first time fully defined through a leakage term *via* a shape factor. The latter is defined in terms of block dimensions and degree of fissuring.
- Aifantis (1977, 1979, 1980a), inspired by Barenblatt’s work, used the mixture theory to propose a double porosity formulation, taking account of the coupling between the deformation and the flows. This formulation is the first rationalised model which involves flow and deformation effects to describe and simulate multi porosity behaviour. However, the main limitation of this work is that the interaction between the pore and fissure volumetric deformations are neglected.
- Alternative solutions to the work of Aifantis were made by Khaled (1980) and Wilson and Aifantis (1982). An important effort has been made to present physical interpretation and experimental determination of the model’s phenomenological coefficients

(Wilson and Aifantis, 1982). In the experimental determination, two distinct approaches are considered. In the first approach, experiments are conducted on both a scale which excludes the fissures and a scale which includes both the pores and the fissures. In the second approach, one set of experiments is conducted over early time scales, and the other over late time scales. A literature survey of the parameter's values is also presented.

- Valliappan and Khalili-Naghadeh (1990) and Khalili-Naghadeh (1991) tried to clarify the mathematical writing of Aifantis, by modifying the parameters of the model, in order to obtain their physical interpretation.
- Elsworth and Bai (1992) presented a significant deviation from dual porosity models by writing the stress-strain relationship for dual porous media based on two overlapping, but *distinct*, single porous media. The original formulation proposed by Elsworth and Bai (1992) is often referred to as ‘the double effective stress laws’ or ‘the separate and overlapping technique’. Distinct total stresses are allocated to each sub-domain along with distinct effective stresses, strains and elasticity matrices. Each sub-domain is regarded as an independent material with a ‘matrix’ and a ‘void space’. The stress-strain relationship for the mixture is obtained by arguing that the changes in total stress within adjacent phases must remain in equilibrium and that the total strain is due to the deformation in each sub-domain. Moreover, like Aifantis’s model the cross-coupling effects between the pore and the fissure fluids are not accounted for.
- The classification of multi porosity / multi permeability models for deformation-dependent flow models have been presented by Bai et al. (1993) based on the mixture theory and Auriault and Boutin (1992, 1993) based on the homogenisation approach. In Bai et al. (1993), special cases of multi porosity / multi permeability formulation are compared and recommendations for practical utilisations are given (Table 1.6).
- Auriault and Boutin (1992, 1993) used a homogenisation technique for periodic structures, which delivers a macroscopic model from the description at the pore and fracture levels. The macroscopic description is sensitive to the ratios between the different scales, where  $l$ ,  $l'$  and  $l''$  are characteristic lengths of the pores, the fractures and the macroscopic medium, respectively. Three cases are successively studied: the first case:  $(l'/l'') = O(l/l')^2$  exhibits a coupling between the flows through the pores and the fractures. The second case:  $(l/l') = O(l/l'')$  exhibits memory effects. The third case:  $(l/l') = O(l/l'')^2$  gives a macroscopic description similar to that of a single

porosity medium. This work allows for the classification of actual models depending on characteristic lengths of the pores, the fissures and the medium. When the pores and the fissures are close enough in size, case 1 appears to be the most appropriate. If the size of the fractures is very large in comparison to the pores size, case 3 is recommended as no seepage from the pores occurs. Case 2 is the most comprehensive as it contains the two previous models, and describes the memory effects due to the leakage of the pores into the fissures when the fractures size is large in comparison to the pore size.

- Khalili and Valliappan (1996) presented a rigorous and unified treatment of the theory of flow and deformation in a dual porous medium. Using the loading decomposition of Nur and Byerlee (1971), a constitutive link is established between the matrix and the pore volumetric deformations. An additional contribution to Aifantis' work is made through a link established between the volumetric deformations of the two pore systems. The latter is considered essential for the proper modeling of flow and deformation in a dual porous medium; which was experimentally demonstrated by Khalili (2003). Consistently, if the deformation link between the two pore systems is ignored, the formulation proposed by Aifantis (1977, 1979, 1980a) is recovered.
- Loret and Rizzi (1999) presented a thermodynamic analysis of anisotropic dual porous media with elastic-plastic solid skeletons. The framework is built so as to address both fissured rocks and partially saturated soils as special cases. The fully coupled model is applied to strain localisation and extends the fact that the onset of strain localization in the three-phase mixture (fissured or unsaturated) is coincident with that of the underlying drained solid to fractured media, that is it is not affected by the details of the effective stress law and of the plastic strain rates. The material parameters of dual porous media are identified thanks to the scale separation property, characteristic to dual porous media. Relevant remarks are provided on the measurements of constitutive moduli for the fluid constituents, the porous block and the fissured medium (the mixture as a whole).

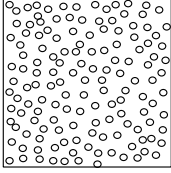
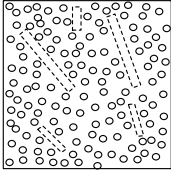
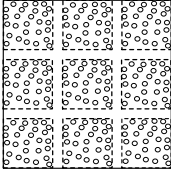
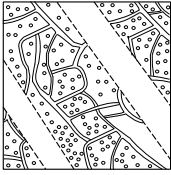
Name	Porosities/ Permeabilities	Idealised Representation	Recommendation
Single porosity / Single permeability	$n_T = n_p + n_f,$ $k_T = k_p + k_f,$ no mass transfer		Suitable for non-fractured reservoir
Dual porosity / Single permeability	$n_p, n_f,$ $k_T = k_p + k_f,$ mass transfer permitted		Suitable for tight reservoir
Dual porosity / Dual permeability	$n_p \gg n_f,$ $k_f \gg k_p,$ mass transfer permitted		Typical for naturally fractured reservoirs
Triple porosity / Triple permeability	$n_p \gg$ $\{n_{f1}, n_{f2}\},$ $k_{f2} \gg k_{f1} \gg$ $k_p,$ multiple mass transfer permitted		Typical for enhanced geothermal systems by hydraulic stimulation

Table 1.6: Classification of multi porosity / multi permeability models and recommendations for practical applications from Bai et al. (1993). The porosities are denoted as in Table 1.3. The subscript  $T$  refers to a total fluid quantity, that is the sum over all the sub-cavity systems. The permeability of the porous block is denoted  $k_p$  and the permeability of the fissure network is denoted  $k_f$ . In the last case, the subscript  $f1$  refers to natural fractures and  $f2$  refers to artificially enhanced fractures or fault gouges.



### 1.3.1 Coupling in dual porous media: two approaches

The effective stress enters the poroelastic constitutive equation of the solid phase and links a change of stress to the fluid pressures. The theory of poroelasticity is based on two crucial assumptions as proposed by Terzaghi (1923), Biot (1941) and Nur and Byerlee (1971): i: The strains can be expressed as linear combinations of the stresses within the elastic range of deformation of the porous solid; ii: The strains are linearly related to pore pressure. The effective stress definition proposed by Biot (1941) for single porous media with compressible matrix is widely accepted by the scientific community. In the literature, a discrepancy of opinion still exists among research teams, on the extension of the effective stress to multi porous media. Two main propositions remain so far: (1) the double effective stress laws (Elsworth and Bai, 1992); and (2) an extension of Biot's relationship to dual porosity (Khalili and Valliappan, 1996). The logical path of each proposal is discussed below.

1. In the double effective stress approach (Elsworth and Bai, 1992; Bai et al., 1995), the effective stress law is regarded as an intermediate expression relating the strain and the effective stress of a single sub-domain. The mixture is separated into two sub-domains, each of them containing a continuum or solid phase; and two effective stress laws are developed, one for each sub-domain. Ultimately, no effective stress law is developed to relate the stress experienced by the solid phase with the pore pressure and the fissure pressure. As a replacement, the authors usually refer to Terzaghi's effective stress, following the advice given by Rice (1977) for inelastic constitutive formulations for fissured rock masses. Finally, the total stresses of each sub-domain are assumed to be in equilibrium. (For porous media, the phases by themselves are not in equilibrium. They interact, and equilibrium is obtained by accounting for the additional momentum supply due to these interactions.) The material parameters required are the compressibility of the porous matrix sub-domain, the compressibility of the fractured sub-domain and the compressibility of the solid phase (grains) (Bai et al., 1995). The compressibility of the fracture sub-domain should be obtained by assuming that the other sub-domain is rigid (Elsworth and Bai, 1992), which may not be applicable in rock media.
2. By using the elastic strain equivalence analysis (Khalili and Valliappan, 1996), the effective stress is developed in a macroscopic sense satisfying the uniqueness theorem for stress boundary problems in elastic solids and following the work of Nur and Byerlee (1971). The material parameters required are the compressibility of the

overall mixture, the compressibility of the porous block (without the fissures) and the compressibility of the solid phase (grains). All these parameters are easily measurable without assuming that the other phases are rigid, provided the fracture network is not too dense, that is if some part of the mixture containing no fissures can be isolated. This approach has the main advantage of representing the solid domain with just one continuum, leading to a single effective stress law (Khalili, 2008). Hence, the effective stress definition is respected and represents the stress experienced by the solid phase.

The interpretation of the pore volumetric changes of dual continua remains under discussion (Chen and Teufel, 1997). The first approach is based on the mixture theory (Wilson and Aifantis, 1982; Bai et al., 1993) and assumes that all the fluid-flow equations in a ‘mixture’ have the same form as that of a single porosity system when the mass transfer term is dropped. In this approach, the phenomenological coefficients are stated first and related to their physical interpretation in a subsequent manner. The second approach (Valliappan and Khalili-Naghadeh, 1990; Khalili and Valliappan, 1996) follows a different route by identifying the couplings parameters and the phenomenological coefficients through stress-dependent rock properties.

Far from providing definitive proof, this discussion aims to compare the approaches with their hypotheses and consequences on the material parameters to be used and on the effective stress definition. From the material parameters point of view, the dual porosity conceptualisation introduced by Valliappan and Khalili-Naghadeh (1990) and formulated by Khalili and Valliappan (1996) is more realistic than the one proposed by Elsworth and Bai (1992). In the double effective stress approach, the definition the effective stress parameters requires the deformation fields of pore and fracture systems to work in series which may not be applicable in real rocks. Furthermore, the resulting definitions of the effective stresses (Elsworth and Bai, 1992; Bai et al., 1995) contradicts the effective stress principle. In other words, not one of the effective stresses represent the stress emanating from the elastic (mechanical) straining of the solid skeleton.

### 1.3.2 Applications

Several authors have presented comprehensive numerical results and applications based on the previous constitutive models. They mainly illustrate field pumping problems, consolidation field problems and wellbore modeling:

- Warren and Root (1963) and Kazemi (1969) were the first to illustrate graphically the time delay, induced by the leakage of the pores into the fractures, on the pressure profile describing a field pumping test. They also discovered that the behaviour of a fractured reservoir moves towards that of an equivalent single porosity system over large time scales. Warren and Root (1963) developed a technique for the analysis of build-up pressure data to evaluate the parameters of the model; whereas Kazemi (1969) focused more on calculating *in-situ* characteristics of the matrix-fracture system, such as pore-volume ratio, over-all capacity of the formation and total storage capacity of the porous matrix.

Later Bourdet and Gringarten (1980) followed the work of Kazemi and added clear explanations on the three distinct periods describing the characteristic pressure response of a pumping test of a dual porous media.

- Khaled et al. (1984) and Khalili et al. (1999) both studied consolidation behaviour through one-dimensional column and two-dimensional half-space problems. Khaled et al. (1984) used the finite element method to illustrate the characteristic response of media with double porosity: Larger displacements and larger pressures were predicted for a dual porosity medium than for an equivalent single porosity medium during early consolidation stages.

Khalili et al. (1999) linked clearly the *in-situ* behaviour of the medium with the three distinct periods of the time-settlement curve. It is shown that in comparison with an equivalent single porosity model, the settlement in a double porosity medium is delayed due to the slow dissipation of the excess pore pressure. The extent of the delay on the ultimate settlement, due to double porosity, is studied through a parametric approach of the rate of fluid transfer between the clay matrix and the fissure network, and through the relative compressibility of the clay matrix.

- Zhang et al. (2003) and Zhang and Roegiers (2005) proposed to apply the model of Bai et al. (1999) to an inclined wellbore in a dual porosity medium. The first reference focused on the borehole stability analysis through several failure criteria with a general plane strain method. The comparison between their dual porosity model and a traditional single porosity one, showed that the former presents a much smaller shear and spalling failure area, and a slightly larger fracturing area. In other words, borehole drilled in a dual-porosity medium is endowed with a larger stable area, a much smaller collapse area, and a slightly larger fracturing area, than in a non-fractured medium. In (Zhang and Roegiers, 2005) similar results were obtained, in particular: (1) pore pressure increases and tensile stress decreases as the fracture

stiffness decreases; and (2) neglecting the double porosity effects, may lead to an underestimation of the pore pressure near the wellbore.

Khalili et al. (2005) presented the modeling of a fully coupled Oil-Gas flow in a dual porosity medium, applied to an inclined wellbore response. Two main concluding remarks are discussed: First, the magnitude of the stresses and pore pressures developed at the borehole wall, which are strongly affected by the fluid compressibilities, are overestimated when assuming that the formation is saturated with a single incompressible fluid. Second, the results obtained from the dual porosity single phase model show that the fluid transfer at early times is affected by the compliance of the secondary medium.

Few references present laboratory experiments to validate the proposed models:

- Callari and Federico (2000) presented a comparison of laboratory tests and a conventional finite element model of a double porosity medium. Special care in including the effects induced by the experimental devices was taken. It was definitively shown that the consolidation process may be strongly delayed by a partially efficient drainage system. The experimental results of consolidation tests on large samples of artificially fissured clays show a good agreement with the compared numerical predictions.
- Khalili (2003) investigated the importance of the coupling effects on the macroscopic response in reference to the consolidation of fissured clays. The importance of the pressure coupling terms is underlined so as to obtain the correct description of the pore and fissure pressures over short time periods. The basic findings of the investigation were validated through a set of laboratory test data.

## 1.4 Thermo-hydro-mechanical coupled models

By drawing the analogy between thermo-elasticity and poro-elasticity, Biot equations were extended by many workers to include thermal effects, for example Schiffman (1971), Brownell et al. (1977), Aktan and Ali (1976), Bear and Corapcioglu (1981) and McTigue (1986). A more exhaustive literature review on the subject can be found in Lewis and Schrefler (1998).

Of course, the models are built to suit a specific range of applications which often allows certain decouplings. Models are accounting for either local thermal equilibrium, which are often hydro-mechanical models extended to include thermal effects, or local thermal non-equilibrium between the phases. Some models have also been developed with both a dual

porosity concept and thermal contributions. Finally, models introducing convection are discussed.

References are restricted to the field of geotechnical engineering applied to reservoir problems and enhanced geothermal systems. The models designed for nuclear waste repositories are not described in this study as they call for elasto-plastic coupled models (Francois, 2008).

### 1.4.1 Models with local thermal equilibrium

In the models presented below, a single temperature is affected to the whole medium and local thermal equilibrium is expected to occur instantaneously.

- McTigue (1986) presented a thermoporoelastic model for fluid saturated porous rock and investigated the heating of a half-space subject to instantaneous temperature change or instantaneous change of heat flux, and for drained and undrained conditions. The thermo-mechanical constitutive behaviour is based on Biot's poroelasticity theory and can be seen as a direct extension of the isothermal theory of Rice and Cleary (1976) thus allowing for compressible fluid and solid constituents, as well as thermal expansion of both phases. Characteristic to the model, the thermal expansion of the porous medium is controlled by the solid skeleton only and the presence of unconnected porosity is taken into account. The diffusion constitutive equations are equivalent to uncoupled Darcy's law and to Fourier's law; and the energy balance equation for the mixture presents a highly reduced form of the complete energy balance; convective transport and thermo-elastic couplings are intentionally neglected. This approach allows the exact solutions of several illustrative problems to be found. The behaviour of these solutions depends critically upon the ratio of hydraulic to thermal diffusivities. The main contribution is the observation that the coupling between heat transport, fluid flow and deformation is strongest for thermal and fluid diffusivity of like order.
- Bai and Abousleiman (1997) investigated thermo-poro-elastic couplings with application to consolidation. The development of a fully coupled thermal-hydraulic-mechanical approach is promoted to minimise potential errors while modeling the behaviour of poro-elastic media under non-isothermal conditions. However, partial couplings are accepted since engineering-orientated analytical solutions are desired. Several simplifications are investigated and recommendations are given: partial decoupling approximations should be discussed, the influence of each coupling term de-

terminated and the omission of such term justified on physical and analytical grounds.

#### 1.4.2 Models with local thermal non-equilibrium

Models accounting for local thermal non-equilibrium raise two issues. The correct identification of the work conjugate variables that will lead to the constitutive coupled laws needs to be identified. The heat transfer constitutive law and the evaluation of the heat transfer parameter, which often remains unclear for porous media, requires scrutiny.

- Bowen and Garcia (1970) introduced a thermo-mechanical theory of a mixture in which each constituent has its own temperature field. Besides the multiple temperature mixture approach, the theory also contains the effects of non-linear elasticity, non-linear heat conduction, non-linear viscosity and diffusion. Bowen and Garcia (1970) provided a general framework consistently ruled by the ‘Rational Thermodynamics’ theories. In addition to the field equations (the balance of mass, linear momentum, moment of momentum, energy and the entropy inequality), the method requires the introduction of the Massieu function for each species. The appropriate thermodynamic restrictions on the constitutive equations are listed. The method leads to six relations that are necessary and sufficient in order that the Clausius-Duhem inequality be satisfied for every admissible thermo-dynamic process. Importantly, the method uses coldness (the inverse of temperature) instead of the usual temperature as an independent variable.

In a subsequent work, Bowen and Chen (1975) specialised their model to a mixture consisting of isotropic elastic solid and an elastic fluid, with diffusion and energy transfer between the constituent. This rather involved model is used to recover several special cases from classical thermoelasticity to the model of Pecker and Deresiewicz (1973). More information on the model presented by Bowen and Chen (1975) is given Appendix A.

- Pecker and Deresiewicz (1973) presented a formulation to account for the effects of temperature on the behaviour of fluid-saturated rocks. The model describes a single porous media in local thermal non-equilibrium, in which each phase is endowed with its own temperature. A partial stress-strain approach is adopted to obtain the stress-strain-temperature relations. The model uses the usual (isobaric) coefficients of thermal expansion for the individual phases; and the *unusual* thermo-elastic coupling coefficients of thermal expansion; that is the strain in the matrix due to a unit

change of temperature in the liquid phase and the dilatation of the fluid due to a unit change in solid temperature. The latter coupled coefficients are usually neglected in most models but are not inappropriate provided experimental measurements. Experimental work is reported to measure the four thermal expansion coefficients for a kerosene-saturated sandstone. The model is then applied to the propagation of plane waves in soils, which is outside the scope of this research. Again, more information on the model presented by Pecker and Deresiewicz (1973) is provided in Appendix B.

- Aifantis and Beskos (1980) applied the work of Bowen and Garcia (1970) to analyse mass and heat transfer with the concept of double temperature. The following hypotheses are made: the solid skeleton experiences no deformation, the fluid is incompressible and has a constant velocity, density and porosity. Therefore, the coupled field equations are the balance of momentum for the fluid, the balance of energy for the solid and the balance of energy for the fluid. Both convection and inter-phase heat transfer phenomena are accounted for, whereas the variation of internal energy of the fluid with respect to pressure changes is neglected. This work is the first concise model which applies local thermal non-equilibrium to saturated porous media.
- De La Cruz and Spanos (1989) applied the procedure of volume averaging to the problem of seismic propagation in saturated porous media. The coupling between temperature variation and mechanical motion is taken into account. Each phase is endowed with its own temperature, which requires the definition of a heat transfer parameter. The latter contributes to equalise the two temperatures and is a function of the averaged thermal conductivity over a microscopic length scale. The definition of the heat transfer parameter seems appropriate if forced convection of heat can be neglected in each phase.
- Hsu (1999) studied transient heat conduction in saturated porous materials with a volumetric average scheme under the assumption of local thermal non-equilibrium. This model presents only the thermal coupling between the solid phase and the fluid phase, that is no mechanical or hydraulic behaviour is accounted for. However, the authors discuss two parameters: the tortuosity term and the interfacial heat transfer term. According to their method, closure modeling is required to identify these parameters. The local thermal non-equilibrium behaviour is found to be particularly significant when the difference in thermal diffusivity of fluid and solid is large. The

closure parameters are found to be dependent on the geometrical microscopic parameters and on the thermal material parameters. Note that the model presented by Hsu (1999) applies only for stagnant heat conduction with no convection.

- Gajo (2002) proposed a non-linear analysis of non-isothermal wave propagation in linear elastic fluid-saturated porous media. Following the work of Pecker and Deresiewicz (1973), the model describes a single porous media in local thermal non-equilibrium, in which each phase is endowed with its own temperature. Furthermore, the fluid temperature is coupled to the thermo-mechanical law based on the propositions of Pecker and Deresiewicz (1973). The introduction of a different reference temperature for the pore fluid is required to account properly for the convection contribution; this issue is discussed later in Subsection 1.4.4. The numerical procedure is validated for a hot fluid injection problem in a steady seepage flow, with no convection. The inter-phase heat transfer parameter is deduced from the measurements made by Pecker and Deresiewicz (1973). Finally, the effects of convection are investigated and the adiabatic property of wave propagation is validated in all cases, that is if convection is accounted for or not, and for a wide range of permeabilities.

Other references (Wakao and Kaguei, 1982; Zanotti and Carbonell, 1984; Kaviany, 1995; Jiang et al., 2006) proposed some relevant discussions on the nature of the heat transfer parameter. A proper study of the heat transfer parameter is provided in Section 3.3.2.

### 1.4.3 Models with dual porosity and thermal contribution

Most constitutive models accounting for both the dual porosity concept and thermal contributions have been developed by using the double effective stress framework (Bai and Rogiers, 1994; Nair et al., 2002, 2004). However, recently, there has been greater interest in using the effective stress approach extended from Biot's theory (Masters et al., 2000; Khalili and Selvadurai, 2003).

- Aifantis (1980b) provided further comments on the problem of heat extraction from hot dry rocks and considered briefly the idea of two temperatures in the transport of heat through fissured rock. One temperature is associated with the pore fluid - solid skeleton and the second temperature with the fissure fluid. In addition, the hypotheses of pure convective flow in the fissure and pure conduction in the pores are made. For convenience, the deformation effects and the variation of internal energy with respect to pressure changes are neglected. Importantly, inter-phase heat transfer



is introduced. This work ends with two uncoupled balance of energy equations and provides the first idea regarding the development of non-isothermal models in fissured media.

- Bai and Rogiers (1994) presented some fully coupled analytical solutions based on a poro-thermo-mechanical formulation for fractured media. This study, which brings quite a complete coupling of the mass balance equations and the balance of momentum equation, displays an uncoupled energy equation. Besides the dual porosity *distinct* concept, the main short coming of this model is that the total stress is related to both the temperature of the solid-pore system and the temperature of the fissure fluid. In other words, the thermal expansion of the mixture is controlled by the whole mixture rather than by the solid skeleton only. In the end, the problem is reduced to four unknowns (the fluid pressures and the solid and the fluid temperatures) in the form of a linear poro-thermo-mechanical system. The radial displacement are directly linked to the four unknowns by assuming that the poro-thermo-mechanical effect primarily occurs in the radial direction, that it is independent of circumferential and vertical orientations, and that it vanishes at infinite boundary. The analytical responses were sought and applied to the cooling of a geothermal reservoir.
- Masters et al. (2000) extended a previous hydro-mechanical dual porosity model (Ghafouri and Lewis, 1996) to account for thermal effects. The model assumes local thermal equilibrium between the phases and accounts for conduction and convection in the theoretical development. The fluid domain is divided in two distinct overlapping porous media and the fissure-network is assumed to be non-deformable. The latter assumption leads to a very simple effective stress law, which is comparable to Terzaghi's formula. Therefore, the pressure of the fissure-network is not linked to the balance of momentum equation, which is a major drawback. The convective terms are accounted for in the balance of energy through fictitious velocities. Finally, the balance of energy is uncoupled with the solid deformation which is a strong approximation. Consistently, two benchmark problems are proposed to validate the model, an isothermal dual porosity problem and a non-isothermal single porosity one. From the latter setup a surprising conclusion is drawn, the pore pressure response is not influenced by thermal loading when no convection is taken into account.
- Khalili and Selvadurai (2003) presented a fully coupled thermo-hydro-mechanical model for fully-saturated elastic dual porous media. The model assumes local thermal non-equilibrium and one temperature is assigned to each phase of the mixture.

The fissured medium is conceptualised by two overlapping single porous media and a consistent effective stress relation is introduced. Hydraulic and thermal diffusion are defined for each phase and the cross-diffusion phenomenon called thermo-osmosis is accounted for. Three balance of energy equations are introduced which are fully coupled with the pressures and the solid deformation. Forced thermal convection is accounted for along with inter-phase heat transfer. Finally, the change of internal energy due to a change of fluid volume is introduced in the balance of energy for the fluid phases. This model presents the advantages of being fully coupled; nevertheless, a theoretical framework (thermodynamics of irreversible processes) should be developed to assure that the Clausius-Duhem inequality is satisfied for every admissible thermodynamical process.

- Nair et al. (2002) and Nair et al. (2004) presented a thermo-hydro-mechanical model extended to dual porosity media. In this work, the thermal equilibrium approach is adopted and both convective and conductive phenomena are incorporated into a finite element formulation. However, the energy conservation equation is not coupled with the mass conservation equations for the fluids. Results are presented on the sensitivity of the thermoelastic response in dual porosity media to fracture spacing, but based on the double effective stress approach (Elsworth and Bai, 1992). The impact of the thermal loading, on the overall purely conductive response, induces an increase of pore pressure along with an increase of tensile effective stress (Terzaghi's effective stress). The magnitude of these increases are significantly higher for the non-isothermal case than for the isothermal one. The effect of the dual porosity parameters are also presented. Note that a direct link between the the fracture spacing and the overall compliance of the medium is assumed. Hence, a decrease of fracture spacing induces an increase of the overall compliance of the medium, which induces an increase in pore pressure in the primary medium. Aside from the use of the separate and overlapping techniques, this work provides the first numerical results on thermal effects in fissured media.

#### 1.4.4 Models with convection

Heat transport can be performed by conduction, convection (forced and free) and by radiation. Conduction is usually taken into account in thermo-hydro-mechanical models as the main transport phenomenon; however, forced convection may also be of some interest specifically in large permeability fissure networks allowing a greater fluid velocity. Free convection may also be observed in soils and in the modeling of the earth crust. Neverthe-

less, free convection and radiation are disregarded in this study. Thus, forced convection is simply referred to as convection.

- Bear and Corapcioglu (1981) developed a mathematical model for consolidation in a thermoelastic aquifer due to hot water injection or pumping which includes the effects of convection. The model aimed at land subsidence owing to temperature and pressure changes in saturated porous media in thermal equilibrium. The comprehensive balance of momentum is obtained with Terzaghi's effective stress relation. The balance of mass of the fluid is simplified for vertical consolidation only, that is the strain contribution is related to the pressure and the temperature. Heat convection is consistently accounted for in the balance of energy for the mixture. The averaging of the model was done over the vertical thickness of an aquifer; to be applied to thermoconsolidation in the vicinity of a single pumping/injection well in a one-dimensional problem along the radial direction. No numerical calculation is proposed; whereas a clear discussion of the various model hypotheses are summarised in the conclusion.
- Kurashige (1989) presented a thermoelastic theory of fully-saturated single porous media which accounts for forced convection. In addition, the difference between the thermal expansibility between the solid phase and the fluid phase is correctly introduced within the change of fluid *mass* per unit volume. By extending the theory of Rice and Cleary (1976), a thermoelastic constitutive law in thermal equilibrium is proposed. Analytical equations of thermal stresses caused by hot or cold water injection are sought for various geotechnical materials: two granitic rocks and three sandstones. Cold water injection induces a drop in pore pressure and an increase in total radial stress in the vicinity of the cavity. If convection is neglected (materials with a low hydraulic diffusivity, such as granitic rocks), the high-temperature high-stress region is restricted to the vicinity of the loaded-cavity for rocks having a diffusivity ratio (thermal over hydraulic) close to one. Conversely when convection is accounted for (high hydraulic diffusivity materials, such as sandstones), the high-stress region penetrates deeper into the semi-infinite rock.

Later, similar conclusions were drawn by Nair et al. (2004) within a sensitivity analysis to study the effect of heat transport *via* conduction and convection as part of a thermo-hydro-mechanical model for single porosity media.

- Pao et al. (2001) presented the extension of a three-phase (water, oil and gas) model to include non-isothermal effects. Various numerical examples are presented and studied. Hot water injection, accounting for conduction and convection is analysed

with a particular focus on the influence of temperature: as the initial fluid viscosity reduces, the pore pressure drops. Significant differences are observed in the pressure and temperature responses when convection is neglected. However, no difference can be seen if the Petrov-Galerkin up-winding scheme is used, which implies that the overall Péclet number is quite small and/or that the far-field boundary condition is a flux-type boundary condition. No information on the overall Péclet number nor on the grid Péclet number is given.

- Gajo (2002) proposed a non-linear analysis of non-isothermal wave propagation in linear elastic fluid-saturated porous media. Forced convection due to large pore fluid displacement is accounted for based on the balance of energy equation, as proposed by McTigue (1986). Thermal forced convection is separated from the balance of energy equation by the introduction of a second reference temperature (a new primary variable) which is linked to the convection contribution to within  $n_f \rho_f C_{f,v}$ . This original contribution is introduced in order to properly account for heat convection; that is the fluid is heated outside of the element and not inside, therefore the reference temperature of the fluid should be that of the injection temperature (as if the fluid temperature was suddenly equal to the injection temperature). However appealing, this new primary variable is only required if the hypothesis raised by Pecker and Deresiewicz (1973) is maintained. Since the latter hypothesis is disregarded in our model (see Remark 2.13, p. 117), a second reference temperature is not needed and the convection contribution remains in the balance of energy equation.

## Chapter 2

# Field and Constitutive equations

This chapter outlines the development of a fully coupled thermo-hydro-mechanical (THM) model for saturated porous media with dual porosity. The equilibrium of the medium is described by the field equations whereas the behaviour of the medium under stress loading is introduced by the constitutive equations.

Section 2.1 presents the *field equations* for a multi-species multi-phase medium. In multi-species media, each species can be considered separately at a macroscopic level. However, as each species is part of a mixture, the summation over the species leads to the whole mixture equation, which is written in an equivalent continuum manner. The interaction phenomena in between species or with the surroundings are better viewed when considering the field equations for each species. Expressing only the mixture relation is very much restrictive as the internal interactions in between the species are elusive. For the sake of generality, the system presented here is *open* to the surroundings. Throughout this section, the balance equations are written for both the species and the mixture as a whole to bring in the light the interactions with other species and with the surroundings. The field equations are recovered by use of the general balance equation. Applying this equation to the appropriate functions allows us to obtain the conservation of mass, the balance of momentum, the balance of energy and the balance of entropy equations. Finally the local Clausius-Duhem inequality is deduced from both the balance of energy and of entropy.

The *mechanical constitutive equations* describe the deformation model which is governed by a thermo-poro-elastic theory through Section 2.2. Focusing on a double porosity model, the relations are restricted to a three-phase *closed* system. A previously presented hydro-mechanical double porosity model is used as a base to be extended. This second section concentrates the light on the description of the direct and coupled behaviour of the phases. Some restrictions and indications on the constitutive equations are deduced from the Clausius-Duhem inequality obtained in Section 2.1. Three types of constitutive

equations are segregated: (1) the thermo-mechanical behaviour equations, (2) the diffusion equations, and finally (3) the transfer equations. Some phases are not involved in all constitutive equation types due to observation of experiments and definitions. In addition, because some uncommon coupled mechanisms are identified, particular attention is given to forecast their influence.

Finally, Section 2.3 introduces the *comprehensive field equations*, which are obtained by including the constitutive equations of Section 2.2 in the general field equations of Section 2.1. The comprehensive equations are expressed in terms of primary variables to facilitate the finite element discretisation performed in Chapter 4.

## 2.1 General field equations

The modeling of deformation (thermo-hydro-mechanical couplings), mass transfer, momentum transfer and heat transfer, that generates generalised diffusion in porous media with double porosity, will assume a continuum mixture framework. For the model to be general, the field equations are written in the context of an *open system*: the surroundings may contribute to the balance equations of mass, momentum, energy and entropy. In addition to these external interaction phenomena, internal interactions occur: other species may also contribute to the balance equations (Figure 2.1).

This thermodynamic analysis stays in the continuity of Eringen and Ingram (1965) paper on mixtures. They provided a detailed derivation of the field balance equations for a chemically reacting continuum in which each phases of the mixture was considered to interact with the other phases *via* transfer. But the whole mixture was considered as a closed system with respect to the surroundings. Considering the work of Eringen and Ingram (1965), this development may appear as an extension. The work of Loret and Simões (2005) is taken as reference, when considering the extension of the model to an open system.

Traditionally in continuum mechanics, all phases are considered equal in importance. By contrast in the theory of mixture, the solid skeleton is assumed to have a special role because it is the reference constituent. Hence, Biot's approach of mixture is preferred to the conventional approach (Biot, 1977).

The aim of this section is to provide the thermodynamic argument that leads to the general field equations form of our mixture problem. First, the definition of the mass, volume and kinematics descriptor needed for the further understanding are introduced. Then the general local balance equation is established, for both a single species of the mixture and for the mixture as a whole. Rewriting the general balance equation using

specific function tensors, the balance of mass, of momentum, of energy and of entropy equations (for an open system) are introduced. Finally, the Clausius-Duhem inequality is recovered.

### 2.1.1 Definition

The developments presented here are intended to be used for a multi-phase / multi-species mixture. A phase may contain several species. For example, a fluid phase may contain two types of fluids of different nature, e.g. water and oil. In order to fix the ideas, the definition of phases and species are introduced:

- *Phases* (e.g. solid(s), fluid of the pores (p) and fluid of the fissures (f)) represent the species when viewed as part of the mixture, also referred to as *porous medium*. In the context of the theory of mixture, the phases are viewed as independent overlapping continua. The solid phase is also referred to as the *solid skeleton*.
- *Species* can be solid or fluids. All species are considered equal in importance, except the solid skeleton which plays a particular role. Within phases, species diffuse. Across phases, a physical reaction occurs, also called transfer, e.g. mass transfer. Mass transfer can be understood as a way for the medium to adapt to physical loadings, by modifying the internal repartition of its species, see Remark 2.1.

**Remark 2.1.** *Let us consider for example a vertical column of saturated porous medium, loaded and drained at the top. The latter will consolidate by releasing fluid on the drained edge. Consolidation is the consequence of an internal rearrangement of the fluid. In the case of a medium with double porosity, the consolidation is delayed because the internal repartition occurs in three time phases: in the first phase the fluid of the fissures is drained out, then a mass transfer of fluid takes place from the pores into the fissures and finally the released fluid is mostly provided by the pores, as presented by (Khalili et al., 1999). Neglecting the mass transfer mechanisms in a porous medium with double porosity may lead to an under-estimated time of consolidation.*

At each point of each phase are defined intrinsic quantities, labeled by subscripts, and apparent or partial quantities, labeled by superscripts. Let us consider a porous medium of volume  $V$ , of surface  $S$ , consisting of  $k$  species in a region. The set of all species is noted  $\mathcal{K}$ . Thanks to the macroscopic approach, at each point of the medium, the species  $k$  is introduced along with its intrinsic properties of mass  $M_k$  and volume  $V_k$ . Each species  $k$

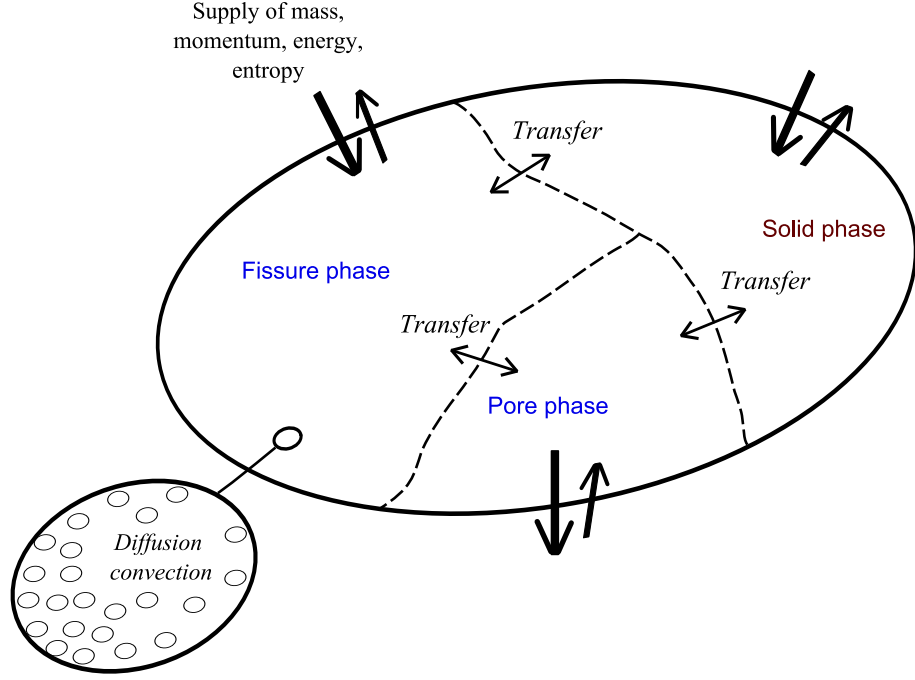


Figure 2.1: Sketch of the exchanges that are accounted for in the multi-species multi-phase open system. For illustration, it is assumed that, at any geometrical point, the species can be segregated in three phases, each of them containing several species. (1) *Transport*: Species of the fluid phases (the fissure phase and the pore phase) are transported to, and from, the boundary by (hydraulic and thermal) diffusion and by forced convection. In addition, the coupling of the hydraulic and thermal diffusion induces thermo-osmosis. (2) *Transfer*: Phases can exchange mass, momentum, energy and entropy. These exchanges are termed transfers. The characteristics of each exchange depend on both the concerned phases (its density, viscosity, chemical potential) and on the nature of the ‘membranes’ that separate the phases. Thus low permeable phases are associated to a large transfer time by contrast with higher permeable phases which are associated to a small transfer time. An infinite transfer time implies impermeability. (3) *Exchanges at the boundary*: If in addition, the system is thermodynamically open, supply and/or removal from the surroundings, of mass, momentum, energy and entropy can take place at each geometrical point.

is endowed with its volume fraction  $n_k$ , its *intrinsic* density  $\rho_k$ , its *partial* density  $\rho^k$  (no summation over the repeated subscript  $k$ ),

$$n_k = \frac{V_k}{V}; \quad \rho_k = \frac{M_k}{V_k}; \quad \rho^k = \frac{M_k}{V} = n_k \rho_k, \quad k \in \mathcal{K}, \quad (2.1)$$

and its absolute velocity  $\mathbf{v}_k$ . For a material point occupying the position  $\mathbf{x}$  at time  $t$ , the absolute velocity  $\mathbf{v}_k$  is defined by,

$$\mathbf{v}_k = \frac{\partial \mathbf{x}}{\partial t}, \quad k \in \mathcal{K}. \quad (2.2)$$



Throughout, the following approximation is used: The surface fraction is considered equal to the volume fraction  $n_k$ .

Following Biot's approach, that is the solid skeleton is paid a special attention and species are viewed as flowing through the solid skeleton, the equations of motion are now introduced. As a consequence, the volume considered is the volume of the solid skeleton  $V_s$ . The motion of a point  $\mathbf{x}$  of the solid is described by the velocity of the solid  $\mathbf{v}_s$  and by the associated deformation gradient  $\mathbf{F}$ .

The *mass flux per unit current area through the solid*  $\mathbf{M}_k$  is defined as the difference of velocity between the species and the solid, and as proportional to the partial density:

$$\mathbf{M}_k = \rho^k (\mathbf{v}_k - \mathbf{v}_s), \quad k \in \mathcal{K}. \quad (2.3)$$

The mixture as a whole is endowed with its own properties like its barycentric velocity  $\mathbf{v}$ . Thus, the *diffusion velocity* with respect to the mass center of the species  $k$  writes,

$$\mathbf{u}_k = \mathbf{v}_k - \mathbf{v}, \quad k \in \mathcal{K}. \quad (2.4)$$

It is worth noting that the diffusion velocity with respect to the mass center does not describe the same flux as the filtration velocity with respect to the solid, introduced in Darcy's law of seepage, nor with the diffusion velocity with respect to the fluid phase, defined in Fick's law of diffusion.

The total mass density of the mixture  $\rho$  is defined by,

$$\rho = \sum_{k \in \mathcal{K}} \rho^k. \quad (2.5)$$

The associated properties of the mixture as a whole are defined by mass averaging, for example its barycentric velocity  $\mathbf{v}$  and its barycentric body force  $\mathbf{b}$ , are

$$\rho \mathbf{v} = \sum_{k \in \mathcal{K}} \rho^k \mathbf{v}_k; \quad \rho \mathbf{b} = \sum_{k \in \mathcal{K}} \rho^k \mathbf{b}_k; \quad k \in \mathcal{K}. \quad (2.6)$$

**Remark 2.2.** *An important remark needs to be done on the following unit detail. Certain properties  $\psi$  of the mixture as a whole are measured per unit volume, where as the corresponding properties  $\psi_k$  attached to the species are measured per unit of mass, for example internal energy, enthalpy, entropy, etc. For these functions, the definition of the property at the mixture level is not  $\rho\psi = \sum_{k \in \mathcal{K}} \rho^k \psi_k$  but  $\psi = \sum_{k \in \mathcal{K}} \rho^k \psi_k$ .*

Carrying equation (2.4) into (2.6) brings,

$$\sum_{k \in \mathcal{K}} \rho^k \mathbf{u}_k = \mathbf{0}, \quad k \in \mathcal{K}. \quad (2.7)$$

Two types of total time derivatives are used in the further analysis,  $D/Dt$  following the mass center and  $d^k/dt$  following the particles of species  $k$ . The total derivative following the solid is noted  $d/dt$  instead of  $d^s/dt$  to simplify the notations. The three total time derivatives of a generic tensor field  $\psi(\mathbf{x}, t)$  in the Eulerian frame are,

$$\begin{aligned} \frac{D\psi}{Dt} &= \frac{\partial\psi}{\partial t} + \nabla\psi \cdot \mathbf{v}, \\ \frac{d^k\psi}{dt} &= \frac{\partial\psi}{\partial t} + \nabla\psi \cdot \mathbf{v}_k, \quad k \in \mathcal{K}, \\ \frac{d\psi}{dt} &= \frac{\partial\psi}{\partial t} + \nabla\psi \cdot \mathbf{v}_s. \end{aligned} \quad (2.8)$$

where  $\nabla$  represents the gradient operator with respect to the coordinates in the deformed configuration  $\mathbf{x}$ .  $\nabla$  is the same for each derivative. The underlying idea is that the position vectors in the actual configuration will coincide for all the phases, as opposed to the velocities which are different for each phase.

### 2.1.2 General form of the balance equation

Let us denote  $s_k$  a volume source per unit current volume and  $\mathbf{i}_k$  a surface source (flux) per unit current area. Considering a single phase medium of a closed system, *the rate of change of a volume integral* of a continuously differentiable function  $\psi_k$  is usually cast as a sum of a total volume source and a flux through the surface  $dS$ ,

$$\underbrace{\frac{d}{dt} \int_{\mathcal{V}} \psi_k dV}_{\text{rate of change}} = \underbrace{\int_{\mathcal{V}} s_k dV}_{\text{Volume source}} + \underbrace{\int_{\mathcal{S}} \mathbf{i}_k dS}_{\text{flux through the surface}}, \quad k \in \mathcal{K}. \quad (2.9)$$

Let us now introduce  $\hat{\psi}_k$ : a volume source due to both mass transfer between phases of the mixture and external mass supply (or deposit representing added mass or extracted mass depending on its sign). Considering a multi-phase medium of an open system, a second volume integral should be added to (2.9), representing the mass transfer between phases and/or the mass deposit due to external supply,

$$\frac{d}{dt} \int_{\mathcal{V}} \psi_k dV = \int_{\mathcal{V}} s_k dV + \int_S \mathbf{i}_k dS + \underbrace{\int_{\mathcal{V}} \hat{\psi}_k dV}_{\text{external mass supply}}, \quad k \in \mathcal{K}. \quad (2.10)$$

The sum over all the species of the net rate supply due to mass transfer and external mass deposit is denoted  $\hat{\psi}$ ,

$$\sum_{k \in \mathcal{K}} \hat{\psi}_k = \hat{\psi}, \quad k \in \mathcal{K}. \quad (2.11)$$

The sum of mass transfer representing the mass exchange in between the phases of the mixture do not appear in  $\hat{\psi}$ . The entity  $\hat{\psi}$  characterises an open system if not equal to zero, and vanishes in absence of external mass deposit (closed system).

In addition, the *generalised Reynold's theorem* states that the rate of change of a volume integral is equal to the rate of change as if the volume was moving with the solid velocity to which should be added the contribution in terms of flux of the individual species,

$$\frac{d}{dt} \int_{\mathcal{V}} \psi_k dV = \underbrace{\int_{\mathcal{V}} \frac{d\psi_k}{dt} + \psi_k \operatorname{div} \mathbf{v}_s dV}_{\text{rate of change following } \mathbf{v}_s} + \underbrace{\int_{\mathcal{V}} \operatorname{div} \left( \frac{\psi_k}{\rho^k} \mathbf{M}_k \right) dV}_{\text{flux contribution of species } k}, \quad k \in \mathcal{K}. \quad (2.12)$$

Substituting equation (2.12) into (2.10) and expressing the result in a local form for a generic volume, provides *the local form of the balance equation of a species k*,

$$\frac{d\psi_k}{dt} + \psi_k \operatorname{div} \mathbf{v}_s + \operatorname{div} \left( \frac{\psi_k}{\rho^k} \mathbf{M}_k \right) - s_k - \operatorname{div} \mathbf{i}_k = \hat{\psi}_k, \quad k \in \mathcal{K}. \quad (2.13)$$

This local balance equation can be written in a different form, using the rate of volume change following the particles  $k$  defined eq. (2.8),

$$\frac{d^k \psi_k}{dt} + \psi_k \operatorname{div} \mathbf{v}_k - s_k - \operatorname{div} \mathbf{i}_k = \hat{\psi}_k, \quad k \in \mathcal{K}. \quad (2.14)$$

**Remark 2.3.** *In contrast with some other works, e.g. Eringen and Ingram (1965), the generic field  $\psi_k$  is assumed to be smooth enough so that no moving discontinuity surface is intersecting the volume  $V$ . In consequence no jump conditions equation is needed.*

The generic relations (2.13) and (2.14) presented in this section are applied in turn for the balance of mass, of momentum, of energy and of entropy.

### 2.1.3 Balance of mass

Considering a closed system, the commonly used balance of mass equation for a continuum introduces the density  $\rho = \rho(\mathbf{x}, t)$  at the location  $\mathbf{x}$  at time  $t$ . The mass contained in a domain  $V$  at time  $t$  is,

$$M = \int_{\mathcal{V}} \rho \, dV. \quad (2.15)$$

The conservation of mass of a *closed* system requires,

$$\frac{DM}{Dt} = 0, \quad (2.16)$$

which can become by use of the generalised Reynolds theorem eq. (2.12),

$$\int_{\mathcal{V}} \frac{DM}{Dt} + \rho \operatorname{div} \mathbf{v} = 0. \quad (2.17)$$

Since the result must hold for an arbitrary domain  $V$ , the integrand must vanish to give,

$$\frac{D\rho}{Dt} + \rho \operatorname{div} \mathbf{v} = 0. \quad (2.18)$$

To introduce the extension of the equation of continuity (balance of mass) to an *open* system, the generic balance equation (2.14) is applied to the density of a body subjected to mass supply. The obtained balance of mass for the species  $k$  leads to the introduction of a new generic balance equation in Remark 2.4. Next, diffusion and mass transfer contributions are identified in the balance of mass for the species. Finally, a summation over species introduces to the balance of mass for the mixture as a whole.

#### 2.1.3.1 The balance of mass for the species

Following the work of Eringen and Ingram (1965), the balance of mass for the species  $k$  is obtained by replacing the following propositions in equation (2.14),

$$\underbrace{\psi_k = \rho^k}_{\text{partial density}}, \quad s_k = 0, \quad \mathbf{i}_k = \mathbf{0}, \quad \underbrace{\hat{\psi}_k = \hat{\rho}^k = \hat{\rho}_{tr}^k + \hat{\rho}_{ex}^k}_{\text{rate of mass supply}}, \quad k \in \mathcal{K}. \quad (2.19)$$

The rate of mass supply is of two types: (1)  $\hat{\rho}_{tr}^k$  represents the mass supply due to mass transfer, commonly due to physical exchanges in between the phases; and (2)  $\hat{\rho}_{ex}^k$  represents the mass supply due to external mass deposition in the case of an open system. The total

rate of mass supply reduces to the sum of the mass supply due to external contribution only, since the contributions due to internal mass transfer sum to zero,

$$\sum_{k \in \mathcal{K}} \hat{\rho}_{tr}^k = 0, \quad \hat{\rho} = \sum_{k \in \mathcal{K}} \hat{\rho}_{ex}^k = \sum_{k \in \mathcal{K}} \hat{\rho}^k, \quad k \in \mathcal{K}. \quad (2.20)$$

The balance of mass equation for the species  $k$  is obtained by inserting equation (2.19) into (2.14),

$$\frac{d^k \rho^k}{dt} + \rho^k \operatorname{div} \mathbf{v}_k = \hat{\rho}^k, \quad k \in \mathcal{K}. \quad (2.21)$$

**Remark 2.4.** The balance equation for a generic function  $\psi_k$  can be re-written in the following form, by use of equation (2.14),

$$\frac{d^k}{dt} \left( \frac{\rho^k \psi_k}{\rho^k} \right) + \psi_k \operatorname{div} \mathbf{v}_k - s_k - \operatorname{div} \mathbf{i}_k = \hat{\psi}_k, \quad k \in \mathcal{K}. \quad (2.22)$$

Let us develop the first term,

$$\rho^k \frac{d^k}{dt} \left( \frac{\psi_k}{\rho^k} \right) + \left( \frac{\psi_k}{\rho^k} \right) \frac{d^k \rho^k}{dt} + \psi_k \operatorname{div} \mathbf{v}_k - s_k - \operatorname{div} \mathbf{i}_k = \hat{\psi}_k, \quad k \in \mathcal{K}; \quad (2.23)$$

and replace  $d^k \rho^k / dt$  using equation (2.21),

$$\rho^k \frac{d^k}{dt} \left( \frac{\psi_k}{\rho^k} \right) + \left( \frac{\psi_k}{\rho^k} \right) \left( \hat{\rho}^k - \rho^k \operatorname{div} \mathbf{v}_k \right) + \psi_k \operatorname{div} \mathbf{v}_k - s_k - \operatorname{div} \mathbf{i}_k = \hat{\psi}_k, \quad k \in \mathcal{K}. \quad (2.24)$$

Rearranging and simplifying leads to the following form of the balance of equation for a generic function  $\psi_k$ ,

$$\rho^k \frac{d^k}{dt} \left( \frac{\psi_k}{\rho^k} \right) - s_k - \operatorname{div} \mathbf{i}_k = \hat{\psi}_k - \frac{\psi_k}{\rho^k} \hat{\rho}^k, \quad k \in \mathcal{K}. \quad (2.25)$$

### 2.1.3.2 Diffusion and mass transfer

In order to highlight the fact that the density change is due to two physical reactions, namely (1) diffusion of species through the solid skeleton and (2) mass transfer (internal and external), the balance of mass for the species  $k$  equation (2.21) may be written with respect to the solid skeleton velocity by use of equation (2.13),

$$\frac{d\rho^k}{dt} + \rho^k \operatorname{div} \mathbf{v}_s = \underbrace{-\operatorname{div} \mathbf{M}_k}_{(1)} + \underbrace{\hat{\rho}_{tr}^k + \hat{\rho}_{ex}^k}_{(2)}, \quad k \in \mathcal{K}. \quad (2.26)$$

This last relation displays (1) the mass flux per unit current area  $\mathbf{M}_k$  which represents the diffusion term, and (2) the mass transfer which is decomposed to visualise the internal and the external contributions.

### 2.1.3.3 Balance of mass for the mixture

Using the definitions of the overall density  $\rho$  and of the barycentric velocity  $\mathbf{v}$  introduced in equations (2.5) and (2.6), the time derivative relations in equation (2.8) and the closure relation of equation (2.20)<sub>1</sub>, the sum of equation (2.21) over species leads to *the balance of mass for the mixture*,

$$\frac{D\rho}{Dt} + \rho \operatorname{div} \mathbf{v} = \hat{\rho}. \quad (2.27)$$

in which  $\hat{\rho}$  characterises an open system if not equal to zero.  $\hat{\rho}$  may be negative or positive depending if the species is increasing or decreasing in mass. The balance of mass for the mixture is written in the same format as for an equivalent single continuum of density  $\rho$ , moving along a barycentric velocity  $\mathbf{v}$  and experiencing an external mass supply rate of  $\hat{\rho}$ .

### 2.1.4 Balance of momentum

The balance of momentum of a *closed* system, also called Newton's law of motion, states that in an initial frame of reference, the material rate of change of the linear momentum of a body is equal to the resultant applied forces. Considering the linear momentum  $\rho \mathbf{v}$  of a body subjected to surface traction  $\boldsymbol{\sigma}$  and body forces per unit volume  $\rho \mathbf{b}$ , Newton's law states that:

$$\frac{d}{dt} \underbrace{\int_{\mathcal{V}} \rho \mathbf{v} dV}_{\text{linear momentum}} = \underbrace{\int_{\mathcal{V}} \rho \mathbf{b} dV + \int_{\mathcal{S}} \boldsymbol{\sigma} \cdot dS}_{\text{applied forces}}, \quad (2.28)$$

which can be written for a generic volume  $\mathcal{V}$ ,

$$\operatorname{div} \boldsymbol{\sigma} + \rho \left( \mathbf{b} - \frac{d\mathbf{v}}{dt} \right) = 0. \quad (2.29)$$

In order to extend Newton's law of motion to an *open* system, the generic equation of balance (2.25) is applied to the linear momentum  $\rho \mathbf{v}$  of a body subjected to surface traction  $\boldsymbol{\sigma}$ , body forces per unit volume  $\rho \mathbf{b}$ , and a momentum supply. The balance of momentum for the species and for the mixture as a whole are considered in turn.

#### 2.1.4.1 Balance of momentum for the species

Following the work of Eringen and Ingram (1965), the balance of momentum for the species  $k$  is obtained by setting,

$$\underbrace{\psi_k = \rho^k \mathbf{v}_k}_{\text{linear momentum}}, \quad \underbrace{s_k = \rho^k \mathbf{b}_k}_{\text{body force}}, \quad \underbrace{\mathbf{i}_k = \boldsymbol{\sigma}^k}_{\text{partial stress}}, \quad \underbrace{\hat{\psi}_k = \hat{\rho}^k \tilde{\mathbf{v}}_k + \hat{\mathbf{p}}_k}_{\text{total momentum supply}}, \quad k \in \mathcal{K}. \quad (2.30)$$

- The term  $\hat{\mathbf{p}}_k$  represents the momentum supply to the species  $k$  by the rest of the mixture and from external momentum supply. The momentum supply may be defined by constitutive equations. An alternative solution is proposed in Remark 2.6.
- The term  $\hat{\rho}^k \tilde{\mathbf{v}}_k$  represents the momentum supply due to mass transfer under the velocity  $\tilde{\mathbf{v}}_k$ , for internal mass transfer and external mass supply.
- The velocities  $\tilde{\mathbf{v}}_k$ ,  $k \in \mathcal{K}$ , are the velocities of the masses just before deposit or transfer. These velocities have to be specified by constitutive equations.

The net momentum supply is only contributed by the surroundings in the external mass supply,

$$\hat{\rho} \tilde{\mathbf{v}} = \sum_{k \in \mathcal{K}} \hat{\rho}^k \tilde{\mathbf{v}}_k + \hat{\mathbf{p}}_k = \sum_{k \in \mathcal{K}} \hat{e}_{\mathcal{M}}^k; \quad (2.31)$$

where  $\hat{e}_{\mathcal{M}}^k$  represents the volume rate of momentum. An example of  $\hat{e}_{\mathcal{M}}^k$  is given in Remark 2.20, p. 156. Equation (2.31) clearly shows that the total momentum supply vanishes if only internal mass transfer takes place.

Replacing the previous propositions of equation (2.30) into the balance generic equation (2.25) and changing sign, brings *the balance of momentum for the species  $k$* ,

$$\operatorname{div} \boldsymbol{\sigma}^k + \rho^k \left( \mathbf{b}_k - \frac{d^k \mathbf{v}_k}{dt} \right) = \underbrace{\hat{\rho}^k (\mathbf{v}_k - \tilde{\mathbf{v}}_k)}_{\text{mass transfer}} - \underbrace{\hat{\mathbf{p}}_k}_{\text{external supply}}, \quad k \in \mathcal{K}. \quad (2.32)$$

The partial or apparent stresses are linked to the intrinsic stresses  $\boldsymbol{\sigma}_k$  of the associated phases through the volume fractions,

$$\boldsymbol{\sigma}^k = n_k \boldsymbol{\sigma}_k, \quad k \in \mathcal{K}. \quad (2.33)$$

**Remark 2.5.** *Note that the interaction momentum due to both mass transfer (internal and external mass deposit), on the left-hand-side of equation (2.32), that contributes to the balance of momentum is not the whole momentum supply. In fact, if the mass supplied is endowed with the velocity of the targeted species  $k$ , that is  $\tilde{\mathbf{v}}_k = \mathbf{v}_k$ , the first term of the interaction momentum vanishes, while the momentum of the mass transferred or deposited itself does not. In general, the interaction momentum  $\hat{\rho}^k (\mathbf{v}_k - \tilde{\mathbf{v}}_k)$  in the balance of momentum equation (2.32) due to mass transfer and external mass deposit does not vanish. Two examples are presented:*

- *Loret and Simões (2005) in a three phase model of articular cartilage define the solid phase and two fluid phases. A species of intrafibrillar phase is assumed to move with the same velocity as the solid. While a species  $k$  in the extrafibrillar phase is endowed with its own velocity  $\tilde{\mathbf{v}}_k = \mathbf{v}_{k,E}$  so as to be able to diffuse in water through the mixture. Thus upon transfer from the extrafibrillar phase to the intrafibrillar phase, the velocity of a species  $k$  undergoes the discontinuity  $\mathbf{v}_s - \mathbf{v}_{k,E}$ .*
- *Khalili and Selvadurai (2003) in a three phase model of saturated soils with double porosity define the solid phase and two fluid phases: one fluid located in the fissure network and the second fluid located in the porous block. In both phases, species are assumed to move with their own intrinsic velocity so as to be able to diffuse in water through the mixture within the phase, namely  $\mathbf{v}_{k,p}$  for the porous block and  $\mathbf{v}_{k,f}$  for the fissure network. Thus, upon transfer from the porous block fluid phase to the fissure network fluid phase, the velocity of the species  $k$  undergoes the discontinuity  $\mathbf{v}_{k,p} - \mathbf{v}_{k,f}$ .*



**Remark 2.6.** *If the momentum supplies  $\hat{\mathbf{p}}_k$  are not provided by the constitutive equations, the generalised diffusion equations are postulated first, based on the Clausius-Duhem inequality. The momentum supplies are then elusive, but, if wished, they can be deduced and identified from the balance of momentum equations.*

#### 2.1.4.2 Balance of momentum for the mixture

Let us introduce the inner part  $\boldsymbol{\sigma}^I$  of the total stress  $\boldsymbol{\sigma}$ , which is obtained by summation of the partial stresses,

$$\boldsymbol{\sigma}^I = \sum_{k \in \mathcal{K}} \boldsymbol{\sigma}^k. \quad (2.34)$$

The balance of momentum for the mixture is obtained by summing the individual balances of momentum (2.32) over all species and using the closure relation (2.31),

$$\operatorname{div} \boldsymbol{\sigma}^I + \rho \mathbf{b} - \sum_{k \in \mathcal{K}} \left( \rho^k \frac{d^k \mathbf{v}_k}{dt} + \hat{\rho}^k \mathbf{v}_k \right) = -\hat{\rho} \tilde{\mathbf{v}}. \quad (2.35)$$

The balance of momentum *for the mixture as a whole*, obtained by summation over species, can be re-written in the following format,

$$\operatorname{div} \boldsymbol{\sigma} + \rho \left( \mathbf{b} - \frac{D\mathbf{v}}{Dt} \right) = \hat{\rho} (\mathbf{v} - \tilde{\mathbf{v}}), \quad (2.36)$$

where  $\mathbf{v}$  and  $\mathbf{b}$  are respectively the barycentric velocity and the overall body force defined by equation (2.6), and  $\boldsymbol{\sigma}$  is the Cauchy stress of the mixture,

$$\boldsymbol{\sigma} = \sum_{k \in \mathcal{K}} \boldsymbol{\sigma}^k - \rho^k \mathbf{u}_k \otimes \mathbf{u}_k. \quad (2.37)$$

The right-hand-side term of the balance of momentum for the mixture will vanish in the case of a closed system (closed from the mass and the momentum point of view). The proof of equation (2.36) is presented in Demonstration 2.1.

---

**Demonstration 2.1.** *The Proof of equation 2.36 is obtained by modifying the derivative of (2.6), namely  $\rho \mathbf{v} = \sum_k \rho^k \mathbf{v}_k$ , to obtain:*

$$\begin{aligned}
\frac{D\rho}{Dt} \mathbf{v} + \rho \frac{D\mathbf{v}}{Dt} &= \sum_{k \in \mathcal{K}} \rho^k \frac{d^k \mathbf{v}_k}{dt} + \frac{d^k \rho^k}{dt} \mathbf{v}_k - \nabla (\rho^k \mathbf{v}_k) \cdot \mathbf{u}_k \quad \text{by (2.4), (2.8)} \\
\hat{\rho} \mathbf{v} - \rho \mathbf{v} \operatorname{div} \mathbf{v} + \rho \frac{D\mathbf{v}}{Dt} &= \sum_{k \in \mathcal{K}} \rho^k \frac{d^k \mathbf{v}_k}{dt} + \hat{\rho}^k \mathbf{v}_k - \rho^k \mathbf{v}_k \operatorname{div} \mathbf{v}_k - \nabla (\rho^k \mathbf{v}_k) \cdot \mathbf{u}_k \\
&\quad \text{by (2.21), (2.27)} \\
\Rightarrow \quad \rho \frac{D\mathbf{v}}{Dt} &= \sum_{k \in \mathcal{K}} \rho^k \frac{d^k \mathbf{v}_k}{dt} + \hat{\rho}^k \mathbf{u}_k - \rho^k \mathbf{v}_k \operatorname{div} \mathbf{u}_k - \nabla (\rho^k \mathbf{v}_k) \cdot \mathbf{u}_k \\
&\quad \text{by (2.6), (2.4)} \\
&= \sum_{k \in \mathcal{K}} \rho^k \frac{d^k \mathbf{v}_k}{dt} + \hat{\rho}^k \mathbf{u}_k - \sum_{k \in \mathcal{K}} \operatorname{div} (\rho^k \mathbf{v}_k \otimes \mathbf{u}_k) \\
&= \sum_{k \in \mathcal{K}} \rho^k \frac{d^k \mathbf{v}_k}{dt} + \hat{\rho}^k \mathbf{u}_k - \sum_{k \in \mathcal{K}} \operatorname{div} (\rho^k \mathbf{u}_k \otimes \mathbf{u}_k) \quad \text{by (2.7)}
\end{aligned}$$

Insertion of this relation in the sum of the individual balances of momentum (2.32) over all the species yields,

$$\operatorname{div} \boldsymbol{\sigma} + \rho \left( \mathbf{b} - \frac{D\mathbf{v}}{Dt} \right) + \sum \hat{\rho}^k (\tilde{\mathbf{v}}_k - \mathbf{v}) + \hat{\mathbf{p}}_k = 0. \quad (2.38)$$

Use of the closure relation (2.31) yields to equation (2.36).

□

**Remark 2.7.** For an open system, the stresses of the mixture may not be symmetric. However in this work, the moment of momentum supplies are assumed to be null, so that the Cauchy stress tensors representing the partial stresses of individual species  $\boldsymbol{\sigma}^k$  and the stress of the mixture  $\boldsymbol{\sigma}$  are symmetric.

### 2.1.5 Balance of energy

The law of conservation of energy governs the motion of a continuum. In an isothermal context, the energy equation is simply the first integral of the equation of motion. If thermal effects become significant, the equation of energy becomes an independent equation to be satisfied.

The first principle of thermodynamics (also called balance of energy) can be stated as follows (Mandel, 1974): Considering a continuum of a *closed system* (no mass, momentum nor energy exchange occurs with the surroundings) which can possibly be in contact with three forms of energy, namely (2) kinetic energy, (3) energy supplied by surroundings and (4) heat supply; there exists a function of state of the continuum called (1) internal energy, such that:

$$\underbrace{d\mathcal{U}}_{(1)} + \underbrace{d\mathcal{C}}_{(2)} = \underbrace{\delta\mathcal{W}_{ext}}_{(3)} + \underbrace{\delta\mathcal{Q}}_{(4)}. \quad (2.39)$$

The differential in front of the internal energy (1) and the kinetic energy (2) is meant to emphasize the fact that these entities are functions of the state of the body ( $d$  being an exact differential), whereas the entities on the right-hand-side are not ( $\delta$  being an increment). Expressing the first principle (2.39) in terms of rate gives,

$$\frac{d}{dt}(\mathcal{U} + \mathcal{C}) = \frac{\delta}{\delta t}\mathcal{W}_{ext} + \frac{\delta}{\delta t}\mathcal{Q}, \quad (2.40)$$

where  $\delta\mathcal{W}_{ext}/\delta t$  and  $\delta\mathcal{Q}/\delta t$  are the rate of change of the energy supplied by the surroundings  $\mathcal{W}_{ext}$  and the heat supply  $\mathcal{Q}$  per unit of time. All forms of energy and work that appear in equation (2.40) are now considered in turn:

(1) The rate of internal energy is defined as a function of the internal energy per unit of mass  $U$  and of the *internal* force per unit mass  $\mathbf{F}_{int}$ , in the form,

$$\frac{d\mathcal{U}}{dt} = \frac{d}{dt} \int_{\mathcal{V}} \rho U \, dV - \int_{\mathcal{V}} \rho \mathbf{F}_{int} \cdot \mathbf{v} \, dV. \quad (2.41)$$

(2) The rate of kinetic energy, contained in a regular domain  $V$  at time  $t$ , relates to the acceleration  $\mathbf{a}$  through,

$$\mathcal{C} = \int_{\mathcal{V}} \frac{1}{2} \rho \mathbf{v}^2 \, dV; \quad \text{and} \quad \frac{d\mathcal{C}}{dt} = \int_{\mathcal{V}} \rho \mathbf{v} \cdot \mathbf{a} \, dV. \quad (2.42)$$

(3) The rate of energy due to external mechanical sources accounts for the *external* force per unit mass  $\mathbf{F}_{ext}$  and for the surface contributions,

$$\frac{\delta\mathcal{W}_{ext}}{\delta t} = \int_{\mathcal{V}} \rho \mathbf{F}_{ext} \cdot \mathbf{v} \, dV + \int_{\partial\mathcal{V}} \boldsymbol{\sigma} \cdot \mathbf{v} \cdot d\mathbf{S}. \quad (2.43)$$

(4) The rate of energy due to heat supply from a volume source  $r$  (due for example to: thermal radiation, electro-chemical reaction etc...) and from a heat flux vector (due for example to: heat conduction)  $\mathbf{h}$  is,

$$\frac{\delta Q}{\delta t} = \int_{\mathcal{V}} r \, dV + \int_{\partial \mathcal{V}} \mathbf{h} \cdot d\mathbf{S}. \quad (2.44)$$

The balance of energy extended to an *open* system is successively written for the species  $k$  and for the mixture. Similarly to Eringen and Ingram (1965), the generic balance equation is used as a base to write the balance of energy for the species. On the other hand, the balance of energy for the mixture as a whole is directly extended from the energy definitions (2.41)-(2.44) to an *open* system.

### 2.1.5.1 The balance of energy for the species

The generic balance equation (2.14) is used to write the balance of energy for the species. Extending the work of Eringen and Ingram (1965) to an open system and applying the propositions of Loret and Simões (2005), let us introduce:

$$\begin{aligned} \psi_k &= \underbrace{\rho^k U_k}_{\text{internal energy}} + \underbrace{\frac{1}{2} \rho^k \mathbf{v}_k^2}_{\text{kinetic energy}}, \\ s_k &= \underbrace{r_k}_{\text{heat source}} + \underbrace{\rho^k \mathbf{b}_k \cdot \mathbf{v}_k}_{\text{mechanical source}}, \\ \mathbf{i}_k &= \underbrace{-\mathbf{q}_k}_{\text{heat flux}} + \underbrace{\boldsymbol{\sigma}^k \cdot \mathbf{v}_k}_{\text{mechanical flux}}, \\ \hat{\psi}_k &= \underbrace{\dot{\rho}^k \left( \tilde{U}_k + \frac{1}{2} \tilde{\mathbf{v}}_k^2 \right)}_{\text{mass supply}} + \underbrace{\hat{\mathbf{p}}_k \cdot \mathbf{v}_k}_{\text{momentum supply}} + \underbrace{\hat{u}_k}_{\text{energy supply}}. \end{aligned} \quad (2.45)$$

**Remark 2.8.** *The sign of the heat fluxes used here is opposite to the work of Eringen and Ingram (1965). It is the same as Loret and Simões (2005) and Mandel (1974).*

Several definitions are introduced within the term  $\hat{\psi}_k$ :

- The rate of energy due to external mass supply (both internal and external).

- Similarly to the balance of momentum equation for the species, the following definition is introduced: just before being transferred or deposit, the masses are endowed with their own internal energy  $\tilde{U}_k$ .
- Finally  $\hat{u}_k$  represents the rate of energy due to energy supply (energy supply to the species  $k$  by the rest of the mixture for example: by contact in between species; and from the surroundings).

The net power supply  $\hat{U}$  is defined by summing over the species the term  $\hat{\psi}_k$  and introduces the volume rate of energy  $\hat{e}_{\mathcal{U}}^k$ , namely,

$$\hat{U} = \sum_{k \in \mathcal{K}} \hat{\rho}^k \left( \tilde{U}_k + \frac{1}{2} \tilde{\mathbf{v}}_k^2 \right) + \hat{\mathbf{p}}_k \cdot \mathbf{v}_k + \hat{u}_k = \sum_{k \in \mathcal{K}} \hat{e}_{\mathcal{U}}^k. \quad (2.46)$$

in which  $\hat{e}_{\mathcal{U}}^k$  is defined in eq. (2.253). If only internal transfer of mass, momentum and energy occur, the net power supply  $\hat{U}$  becomes equal to zero.  $\hat{U}$  characterises an open system when its value is not zero. To obtain the balance of energy for the species  $k$ , the terms of equation (2.45) are introduced into the generic balance equation (2.25),

$$\begin{aligned} \rho^k \frac{d^k}{dt} \left( U_k + \frac{1}{2} \mathbf{v}_k^2 \right) - r_k - \rho^k \mathbf{b}_k \cdot \mathbf{v}_k + \operatorname{div} \mathbf{q}_k - \operatorname{div} \left( \boldsymbol{\sigma}^k \cdot \mathbf{v}_k \right) = \\ \hat{\rho}^k \left( \tilde{U}_k + \frac{1}{2} \tilde{\mathbf{v}}_k^2 \right) + \hat{\mathbf{p}}_k \cdot \mathbf{v}_k + \hat{u}_k - \hat{\rho}^k \left( U_k + \frac{1}{2} \mathbf{v}_k^2 \right), \quad k \in \mathcal{K}. \end{aligned} \quad (2.47)$$

Next, the balance of momentum equation (2.32) for the species  $k$  is multiplied by  $\mathbf{v}_k$ ,

$$\operatorname{div} \left( \boldsymbol{\sigma}^k \cdot \mathbf{v}_k \right) + \rho^k \left( \mathbf{b}_k - \frac{d^k \mathbf{v}_k}{dt} \right) \cdot \mathbf{v}_k = \hat{\rho}^k (\mathbf{v}_k - \tilde{\mathbf{v}}_k) \cdot \mathbf{v}_k - \hat{\mathbf{p}}_k \cdot \mathbf{v}_k, \quad k \in \mathcal{K}. \quad (2.48)$$

Remarking the equality,

$$\frac{d^k}{dt} \left( \frac{1}{2} \mathbf{v}_k^2 \right) = \frac{d^k}{dt} (\mathbf{v}_k) \cdot \mathbf{v}_k, \quad k \in \mathcal{K}, \quad (2.49)$$

the kinetic energy term in eq. (2.47) can be replaced by its expression from (2.48) to obtain *the balance of energy for the species*,

$$\rho^k \frac{d^k U_k}{dt} - \boldsymbol{\sigma}^k : \nabla \mathbf{v}_k + \operatorname{div} \mathbf{q}_k - r_k = \underbrace{\hat{\rho}^k \left( \tilde{U}_k - U_k + \frac{1}{2} (\tilde{\mathbf{v}}_k - \mathbf{v}_k)^2 \right)}_{\text{energy interaction}} + \hat{u}_k, \quad k \in \mathcal{K}. \quad (2.50)$$

**Remark 2.9.** *Similarly to the balance of momentum, the energy supply rate in the balance of energy is not only due to the energy interaction (see Remark 2.5, p. 77).*

### 2.1.5.2 The balance of energy for the mixture

The balance of energy for the mixture is obtained by writing the first principle for an *open* system. This derivation uses as starting point the definitions given in equations (2.41) to (2.44). Each energy contribution is considered in turn and is extended to a multi-phase medium of an open system:

(1) The internal energy  $\mathcal{U}$  of the body is defined in equation (2.41) for a single continuum. Writing this equation for a species  $k$  and summing over the species, leads to:

$$\frac{d\mathcal{U}}{dt} = \sum_{k \in \mathcal{K}} \left[ \frac{d}{dt} \int_{\mathcal{V}} \rho^k U_k dV - \int_{\mathcal{V}} \rho^k \mathbf{b}_{k,int} \cdot \mathbf{v}_k dV \right]. \quad (2.51)$$

The internal energy  $U$  is defined as the mass weighted average of internal energies  $U_k$  of the species measured per unit of mass, namely  $U = \sum_{k \in \mathcal{K}} \rho^k U_k$ . Using the generalised Reynolds theorem presented in equation (2.12) on the first integral term allows us to write the internal energy of the body in the following format:

$$\frac{d\mathcal{U}}{dt} = \int_{\mathcal{V}} \left[ \frac{dU}{dt} + U \operatorname{div} \mathbf{v}_s + \sum_{k \in \mathcal{K}} \left( \operatorname{div} (U_k \mathbf{M}_k) - \rho^k \mathbf{b}_{k,int} \cdot \mathbf{v}_k \right) \right] dV. \quad (2.52)$$

(2) The definition of the kinetic energy has been given in equation (2.42) for a single continuum. Considering this definition for a species  $k$  and summing over the species gives:

$$\frac{d\mathcal{C}}{dt} = \sum_{k \in \mathcal{K}} \int_{\mathcal{V}} \frac{dc_k}{dt} dV, \quad \text{with } c_k = \frac{1}{2} \rho^k \mathbf{v}_k^2. \quad (2.53)$$

Replacing  $c_k$  by using the time derivative equation (2.8) and eq. (2.12) brings,

$$\frac{d\mathcal{C}}{dt} = \sum_{k \in \mathcal{K}} \int_{\mathcal{V}} \frac{\partial c_k}{\partial t} + \operatorname{div} (c_k \mathbf{v}_k) dV, \quad (2.54)$$

which after several transformations, using the equation of balance of momentum for the mixture (2.35) multiplied by  $\mathbf{v}_s$  and the definition of  $\mathbf{M}_k$  in equation (2.3) leads to:

$$\begin{aligned} \frac{d\mathcal{C}}{dt} &= \int_{\mathcal{V}} \left[ -\boldsymbol{\sigma}^I : \nabla \mathbf{v}_s + \mathbf{v}_s \cdot \left( \rho \mathbf{b} + \hat{\rho} \left( \hat{\mathbf{v}} - \frac{\mathbf{v}_s}{2} \right) \right) \right. \\ &\quad \left. + \sum_{k \in \mathcal{K}} \mathbf{M}_k \cdot \frac{d^k \mathbf{v}_k}{dt} + \frac{\hat{\rho}^k}{2} \left( \frac{\mathbf{M}_k}{\rho^k} \right)^2 \right] dV + \int_{\partial \mathcal{V}} \sum_{k \in \mathcal{K}} \operatorname{div} \left( \mathbf{v}_s \cdot \boldsymbol{\sigma}^k \right) \cdot d\mathbf{S} \end{aligned} \quad (2.55)$$

The kinetic energy has been written into this format to allow, later, the introduction of the free enthalpies  $H_k$  in the balance equation of energy for the mixture (2.59). The proof of eq. (2.55) is presented in Demonstration 2.2.

---

**Demonstration 2.2.** *Proof of equation 2.55:*

$$\begin{aligned} \frac{d\mathcal{C}}{dt} &= \sum_{k \in \mathcal{K}} \int_{\mathcal{V}} \frac{\partial c_k}{\partial t} + \operatorname{div} (c_k \mathbf{v}_k) dV = \sum_{k \in \mathcal{K}} \int_{\mathcal{V}} \frac{d^k c_k}{dt} + c_k \operatorname{div} \mathbf{v}_k dV \quad \text{by (2.12) and (2.8)} \\ &= \sum_{k \in \mathcal{K}} \int_{\mathcal{V}} \rho^k \mathbf{v}_k \cdot \frac{d^k \mathbf{v}_k}{dt} + \frac{1}{2} \hat{\rho}^k \mathbf{v}_k^2 dV \quad \text{by (2.21)} \\ &= \sum_{k \in \mathcal{K}} \int_{\mathcal{V}} \mathbf{v}_s \cdot \left( \rho^k \frac{d^k \mathbf{v}_k}{dt} + \hat{\rho}_k \mathbf{v}_k - \hat{\rho}_k \frac{\mathbf{v}_s}{2} \right) + \mathbf{M}_k \cdot \frac{d^k \mathbf{v}_k}{dt} + \frac{\hat{\rho}^k}{2} \left( \frac{\mathbf{M}_k}{\rho^k} \right)^2 dV \quad \text{by (2.20)} \\ &= \int_{\mathcal{V}} \mathbf{v}_s \cdot \left( \operatorname{div} \boldsymbol{\sigma}^I + \rho \mathbf{b} + \hat{\rho} \left( \hat{\mathbf{v}} - \frac{\mathbf{v}_s}{2} \right) \right) + \sum_{k \in \mathcal{K}} \mathbf{M}_k \cdot \frac{d^k \mathbf{v}_k}{dt} + \frac{\hat{\rho}^k}{2} \left( \frac{\mathbf{M}_k}{\rho^k} \right)^2 dV \quad \text{by (2.35)} \\ &= \int_{\mathcal{V}} -\boldsymbol{\sigma}^I : \nabla \mathbf{v}_s + \mathbf{v}_s \cdot \left( \rho \mathbf{b} + \hat{\rho} \left( \hat{\mathbf{v}} - \frac{\mathbf{v}_s}{2} \right) \right) + \sum_{k \in \mathcal{K}} \mathbf{M}_k \cdot \frac{d^k \mathbf{v}_k}{dt} + \frac{\hat{\rho}^k}{2} \left( \frac{\mathbf{M}_k}{\rho^k} \right)^2 dV \\ &\quad + \int_{\partial \mathcal{V}} \sum_{k \in \mathcal{K}} \left( \mathbf{v}_s \cdot \boldsymbol{\sigma}^k \right) \cdot d\mathbf{S} \end{aligned}$$

□

---

(3) Adapting the definition of the rate of energy due to external mechanical sources of equation (2.43) to a species  $k$  and summing over the species, leads to the following relation, for a closed system:

$$\frac{\delta \mathcal{W}_{ext}}{\delta t} = \sum_{k \in \mathcal{K}} \int_{\mathcal{V}} \rho^k \mathbf{b}_{k,ext} \cdot \mathbf{v}_k dV + \sum_{k \in \mathcal{K}} \int_{\partial \mathcal{V}} \mathbf{v}_k \cdot \boldsymbol{\sigma}^k \cdot d\mathbf{S}. \quad (2.56)$$

For an open system the latter relation includes the net power supply  $\hat{U}$  as defined in equation (2.46),

$$\frac{\delta \mathcal{W}_{ext}}{\delta t} = \sum_{k \in \mathcal{K}} \int_{\mathcal{V}} \rho^k \mathbf{b}_{k,ext} \cdot \mathbf{v}_k \, dV + \sum_{k \in \mathcal{K}} \int_{\partial \mathcal{V}} \mathbf{v}_k \cdot \boldsymbol{\sigma}^k \cdot d\mathbf{S} + \int_{\mathcal{V}} \hat{U} \, dV, \quad (2.57)$$

(4) Since external heat is transmitted by conduction  $\mathbf{h}$ , the application of the lemma of the tetrahedron can be used. The latter is obtained in the format  $\mathbf{h} = -\mathbf{q} \cdot \hat{\mathbf{n}}$  where  $\mathbf{q}$  is the heat flux and  $\hat{\mathbf{n}}$  is the local outward unit normal vector to the surface  $dS$ . (The notation  $d\mathbf{A} = dS \hat{\mathbf{n}}$  is used throughout). Hence, the summation over the species of the rate of energy due to heat supply of a species  $k$  is,

$$\frac{\delta \mathcal{Q}}{\delta t} = \sum_{k \in \mathcal{K}} \int_{\mathcal{V}} r_k \, dV - \sum_{k \in \mathcal{K}} \int_{\partial \mathcal{V}} \mathbf{q}_k \cdot d\mathbf{A}. \quad (2.58)$$

The total body force per unit mass for the species  $k$  is defined as the summation of its internal and external contributions  $\mathbf{b}_k = \mathbf{b}_{k,int} + \mathbf{b}_{k,ext}$ . Rewriting the first principle eq. (2.39), by using equations (2.52) to (2.58), gives the following form of *the balance of energy for the mixture* for a generic volume,

$$\begin{aligned} & \frac{dU}{dt} + U \operatorname{div} \mathbf{v}_s - \boldsymbol{\sigma}^I : \nabla \mathbf{v}_s + \sum_{k \in \mathcal{K}} [-r_k + \operatorname{div} \mathbf{q}_k] + \hat{\rho} \mathbf{v}_s \cdot \left( \tilde{\mathbf{v}} - \frac{\mathbf{v}_s}{2} \right) \\ & + \sum_{k \in \mathcal{K}} \operatorname{div} (H_k \mathbf{M}_k) + \sum_{k \in \mathcal{K}} \left[ \mathbf{M}_k \cdot \left( \frac{d^k \mathbf{v}_k}{dt} - \mathbf{b}_k \right) + \frac{\hat{\rho}^k}{2} \left( \frac{\mathbf{M}_k}{\rho^k} \right)^2 \right] = \hat{U}, \end{aligned} \quad (2.59)$$

where the entity  $H_k$  may be called the free enthalpy of the species  $k$  (when the partial stress  $\boldsymbol{\sigma}^k = -p^k \mathbf{I}$  is isotropic),

$$H_k = U_k + \frac{p^k}{\rho^k}, \quad (2.60)$$

in which  $p^k$  is the partial pressure of the species  $k$  equal to  $n_k p_k$ .

### 2.1.6 Balance of entropy

In continuum mechanics, the second principle of thermodynamics (also called the balance of entropy) leads to the definition of the absolute temperature  $T$  related to a thermodynamic function, the entropy  $S$ , so that for a fully reversible transformation of a closed system, the heat supply  $\delta \mathcal{Q}$  received by the system at the temperature  $T$  writes,

$$\frac{1}{T} \frac{\delta \mathcal{Q}}{\delta t} = \frac{dS}{dt}. \quad (2.61)$$



If the transformation is considered *non-reversible*, the second principle states the following inequality:

$$\frac{dS}{dt} \geq \sum \frac{1}{T} \frac{\delta Q}{\delta t}, \quad (2.62)$$

where the right-hand-side term is physically interpreted as a flux of entropy coming from the surroundings. The inequality (2.62) notifies that the entropy of the system is greater than this flux, which implies a production of entropy inside the system. The difference is called *the rate of entropy production*  $\Gamma$ ,

$$\Gamma = \frac{dS}{dt} - \sum \frac{1}{T} \frac{\delta Q}{\delta t} \geq 0. \quad (2.63)$$

This rate of entropy production corresponds to the internal non-reversibilities of the system due to different sources such as mechanical, thermal, physical and chemical sources. For example, the mechanical internal non-reversibilities are internal friction (viscosity, dry friction etc).

Next, the balance of entropy is written for the species and for the mixture in a *multi-temperature context*, extended to an *open* system. A multi-temperature model represents a system in which each species  $k$  is endowed with its own temperature  $T_k$ , for example a model presenting three species displays three temperatures. In addition, each species  $k$  is endowed with its own entropy  $S_k$ . The underlined idea being the introduction of the Clausius-Duhem inequality as proposed in Section 2.1.7. Furthermore, the particular case of a *uniform temperature* system is recovered.

### 2.1.6.1 Balance of entropy for the species

Extending the work of Eringen and Ingram (1965) and Atkin and Craine (1976), the balance of entropy for the species is written using Biot's approach in a multi-temperature context. The second principle may be obtained by replacing in the general balance equation (2.25), the following propositions,

$$\underbrace{\psi_k = \rho^k S_k}_{\text{entropy}}, \quad \underbrace{s_k = \frac{r_k}{T_k} + \rho^k \gamma_k}_{\text{entropy production}}, \quad \underbrace{\mathbf{i}_k = -\frac{\mathbf{q}_k}{T_k}}_{\text{heat flux}}, \quad \underbrace{\hat{\psi}_k = \hat{\rho}^k \tilde{S}_k + \hat{s}_k}_{\text{total entropy supply}}. \quad (2.64)$$

Several definitions are introduced within the term  $\hat{\psi}_k$ :

- The rate of entropy due to external mass supply (both internal and external).
- Similarly to the balance of energy equation for the species, the following definition is introduced: just before being transferred or deposited, the masses are endowed with their own internal entropy  $\tilde{S}_k$ .
- $\hat{s}_k$  represents the rate of entropy due to entropy supply to the species  $k$  by the rest of the mixture and by the surroundings

At a species level, the volume rate of entropy is denoted  $\hat{e}_S^k$ . The net rate of entropy supply, which characterises an open system, is denoted  $\hat{S}$  and is null if only internal transfer occurs,

$$\hat{S} = \sum_{k \in \mathcal{K}} \hat{\rho}^k \tilde{S}_k + \hat{s}_k = \sum_{k \in \mathcal{K}} \hat{e}_S^k. \quad (2.65)$$

Introducing the propositions of equation (2.64) in the general balance equation (2.25) leads to *the balance of entropy for the species  $k$* ,

$$\rho^k \gamma_k = \rho^k \frac{d^k S_k}{dt} - \frac{r_k}{T_k} + \operatorname{div} \frac{\mathbf{q}_k}{T_k} + \underbrace{\hat{\rho}^k (S_k - \tilde{S}_k)}_{\text{entropy interaction}} - \hat{s}_k, \quad k \in \mathcal{K}. \quad (2.66)$$

which implies a rate of entropy production  $\rho^k \gamma_k$  for each species  $k$ . As already remarked for the balance of momentum and of energy, the entropy supply rate is not only due to the entropy interaction (see Remark 2.5, p. 77). Using the balance of mass equation (2.21) and the time derivative relation (2.8), the following form of the balance of entropy for the species can be obtained,

$$\rho^k \gamma_k = \frac{d}{dt} (\rho^k S_k) + \rho^k S_k \operatorname{div} \mathbf{v}_s + \operatorname{div} (S_k \mathbf{M}_k) - \frac{r_k}{T_k} + \operatorname{div} \frac{\mathbf{q}_k}{T_k} - \hat{\rho}^k \tilde{S}_k - \hat{s}_k, \quad k \in \mathcal{K}. \quad (2.67)$$

In the case of a medium containing  $k$  species,  $k$  conditions on the entropy production are required for the model. The second principle is therefore postulated for each species  $k$ ,

$$\rho^k \gamma_k \geq 0, \quad k \in \mathcal{K}. \quad (2.68)$$

This way of writing the second principle is the most demanding. For example, both Eringen and Ingram (1965) and Atkin and Craine (1976) require an entropy inequality for

each species. Hence, this statement is the most restrictive since it requires one inequality per species. By contrast, the second principle may also be written by using the balance of entropy for the mixture, which might appear as less restrictive and more general since a single inequality stands for the whole mixture.

### 2.1.6.2 Balance of entropy for the mixture

The summation over the species of the balance of entropy, equation (2.66), in a *multi-temperature* context is now presented. First, let us introduce the definition of the total entropy  $S$  and of the total production of entropy  $\Gamma$ ,

$$S = \sum_{k \in \mathcal{K}} \rho^k S_k, \quad \Gamma = \sum_{k \in \mathcal{K}} \rho^k \gamma_k. \quad (2.69)$$

The heat source and the heat flux of the mixture are equal to their inner parts,

$$\mathbf{q} = \mathbf{q}^I = \sum_{k \in \mathcal{K}} \mathbf{q}_k, \quad r = r^I = \sum_{k \in \mathcal{K}} r_k. \quad (2.70)$$

Secondly, by use of (2.8)<sub>2</sub> and (2.8)<sub>3</sub> the time rate of the average  $\sum_{k \in \mathcal{K}} \rho^k S_k$  with respect to the solid velocity  $\mathbf{v}_s$  writes,

$$\sum_{k \in \mathcal{K}} \frac{d^s}{dt} (\rho^k S_k) = \sum_{k \in \mathcal{K}} \frac{d^k}{dt} (\rho^k S_k) - \operatorname{div} (\rho^k S_k) (\mathbf{v}_k - \mathbf{v}_s) \quad (2.71)$$

which can be rearranged, by using the balance of mass equation (2.21) multiplied by  $S_k$ ,

$$\sum_{k \in \mathcal{K}} \rho^k \frac{d^k S_k}{dt} = \sum_{k \in \mathcal{K}} \frac{d}{dt} (\rho^k S_k) - \sum_{k \in \mathcal{K}} \left[ \hat{\rho}^k S_k - \operatorname{div} (S_k \mathbf{M}_k) \right] \quad (2.72)$$

By summing the individual balances of entropy (2.67) over all species and by using the closure relation (2.65) and the generalised Reynold's theorem (2.12), *the balance of entropy for the mixture* writes,

$$\int_{\mathcal{V}} \Gamma \, dV = \frac{d}{dt} \int_{\mathcal{V}} S \, dV - \int_{\mathcal{V}} \sum_{k \in \mathcal{K}} \frac{r_k}{T_k} \, dV + \int_{\partial \mathcal{V}} \operatorname{div} \sum_{k \in \mathcal{K}} \frac{\mathbf{q}_k}{T_k} \cdot d\mathbf{A} - \int_{\mathcal{V}} \hat{S} \, dV \geq 0 \quad (2.73)$$

By using the closure relation (2.65) and the previously introduced definitions (2.69)-(2.72) *the second principle for the mixture* and for a generic volume becomes,

$$\Gamma = \frac{dS}{dt} - S \operatorname{div} \mathbf{v}_s + \underbrace{\operatorname{div} \sum_{k \in \mathcal{K}} \left( S_k \mathbf{M}_k + \frac{\mathbf{q}_k}{T_k} \right)}_{\text{total heat flux of entropy}} - \underbrace{\sum_{k \in \mathcal{K}} \frac{r_k}{T_k}}_{\text{total heat source of entropy}} - \hat{S} \geq 0 \quad (2.74)$$

**Remark 2.10.** *The total heat flux and source of entropy may be written in an equivalent form which highlights that the flux of entropy is no longer just the flux due to the inner part of the total heat flux vector, but contains an additional term due to temperature variations among components. A similar statement holds for the heat source of entropy. Considering  $T$  as a reference temperature, the total heat flux and source contribution of entropy write,*

$$\begin{aligned} \operatorname{div} \sum_{k \in \mathcal{K}} \left( S_k \mathbf{M}_k + \frac{\mathbf{q}_k}{T_k} \right) &= \operatorname{div} \left[ \frac{\mathbf{q}^I}{T} + \sum_{k \in \mathcal{K}} \left( S_k \mathbf{M}_k + \mathbf{q}_k \left( \frac{1}{T_k} - \frac{1}{T} \right) \right) \right] \\ \sum_{k \in \mathcal{K}} \frac{r_k}{T_k} &= \left[ \frac{r^I}{T} + \sum_{k \in \mathcal{K}} r_k \left( \frac{1}{T_k} - \frac{1}{T} \right) \right] \end{aligned} \quad (2.75)$$

Note that if the temperature of all components are the same  $T = T_k$  then equation (2.75) reduces to the forms of  $\mathbf{q}$  and  $r$  corresponding to a uniform temperature model.

### 2.1.6.3 A particular case: the temperature is uniform over all phases

In a *uniform temperature* context, the mixture has reached a thermal equilibrium state and the temperatures of each phase are equal, namely  $T = T_k$ . Hence, the balance of entropy for species becomes,

$$\rho^k \gamma_k = \rho^k \frac{d^k S_k}{dt} - \frac{r_k}{T} + \operatorname{div} \frac{\mathbf{q}_k}{T} + \hat{\rho}^k \left( S_k - \tilde{S}_k \right) - \hat{s}_k, \quad k \in \mathcal{K}. \quad (2.76)$$

Similarly, *the second principle for the mixture* after summation over the species reduces to,

$$\Gamma = \frac{dS}{dt} - S \operatorname{div} \mathbf{v}_s + \sum_{k \in \mathcal{K}} \operatorname{div} (S_k \mathbf{M}_k) - \frac{r}{T} + \operatorname{div} \frac{\mathbf{q}}{T} - \hat{S} \geq 0 \quad (2.77)$$

Note that if  $\mathbf{M}_k$  becomes equal to zero (i.e. no fluid mass diffusion occurs) and that no external entropy is supplied ( $\hat{S} = 0$ ), then equation (2.77) reduces to the equation of entropy production of classical continuum mechanics.

### 2.1.7 Clausius-Duhem inequality

The Clausius-Duhem (CD) inequality is obtained by inserting the first principle of thermodynamics (balance of energy) into the second principle of thermodynamics (balance of entropy). Identification and description of the constitutive behaviour of a porous medium under thermo-hydro-mechanical loading is the major issue of the next Section 2.2. In general, the direct behaviour of a single species has already been clearly identified. However, the coupled behaviour of multi-phase multi-species mixtures is not so clear and the CD inequality is needed to identify the global form of the behaviour equations and to bring some restrictions on the constitutive equation couplings.

The balance of entropy and of energy can be written either for each species or for the mixture as a whole by summation over the species. Consequently, both writings are possible for the CD inequality. Although both writings are correct, they do not provide the same restrictions:

- A CD inequality for each species produces some restrictions on the constitutive equations of each species separately. No information is provided on possible interactions or couplings in between species.
- Whereas a CD inequality for the mixture brings restrictive information on the mixture as a whole and therefore indications on possible couplings in between species.

Hence, the writing of a single CD inequality for the mixture as a whole seems more appropriate, since the identification and the description of interactions and coupling phenomena in between phases is the main objective of this study. The Clausius-Duhem inequality is generally, that is to say for a single temperature mixture, obtained by inserting the balance of energy equation into the balance of entropy equation multiplied by  $T$ , the overall temperature of the mixture:

$$T \sum_{k \in \mathcal{K}} \rho^k \gamma_k \geq 0 \quad (2.78)$$

Since  $T$  is a positive value, the restrictions imposed by the inequality (2.78) on the constitutive equations are considered to be unchanged. However, a debate arise when extending the inequality (2.78) to a multi-temperature mixture. The Clausius-Duhem inequality can be written in two different manners: (1) by inserting the balance of energy equation into the balance of entropy equation multiplied by  $T_k$  and summing over the

species; or (2) by inserting the balance of energy equation into the balance of entropy equation and summing over the species *without* multiplying by  $T_k$ :

$$\begin{aligned} (1) \quad & \sum_{k \in \mathcal{K}} T_k \rho^k \gamma_k \geq 0 \\ (2) \quad & \sum_{k \in \mathcal{K}} \rho^k \gamma_k \geq 0 \end{aligned} \tag{2.79}$$

The first solution (1) stems from the assumption that the rate of entropy production is required to be exactly positive on each species  $\rho^k \gamma_k \geq 0$  (Atkin and Craine, 1976) and is more restrictive than the second option (2) which may also be viewed as more general. This choice is strongly related to the multi-temperature assumption. In addition, the latter writing brings some restrictions on the energy transfer constitutive law which are interesting for this study. On the contrary, the former writing leads to the restriction of the entropy transfer constitutive law which is not useful to write the comprehensive energy equation, see Section 2.3. In the following, the CD inequality is presented for the general case of a multi-phase multi-species open system. For future use, the CD inequality is then restricted to a three phase closed system. All CD inequalities are stated in a multi-temperature context.

### 2.1.7.1 Clausius-Duhem inequality for an open system

The writing of the CD inequality for the mixture as a whole, in a detailed form, involves the *free energies* and the *free enthalpies*,

- Where  $E_k$  is the free energy per unit of current volume of the species  $k$ ,

$$E_k = U_k - T_k S_k, \quad k \in \mathcal{K}. \tag{2.80}$$

- In addition, let us introduce  $\rho^k E_k$  the free energy per unit mass of the species  $k$ , which sums up to  $E$  the free energy of the mixture per unit current volume,

$$\rho^k E_k = \rho^k U_k - T_k \rho^k S_k \quad \text{and} \quad E = \sum_{k \in \mathcal{K}} \rho^k E_k, \quad k \in \mathcal{K}; \tag{2.81}$$

- and the free enthalpy (or electro-chemical potentials), per unit mass of the species  $k$ ,

$$G_k = H_k - T_k S_k = E_k + \frac{p^k}{\rho^k}, \quad k \in \mathcal{K}. \quad (2.82)$$

The CD inequality for a multi-temperature mixture is obtained by replacing  $\sum_{k \in \mathcal{K}} -r_k + \text{div } \mathbf{q}_k$  from the first principle for the mixture  $k$  (2.59),

$$\begin{aligned} \sum_{k \in \mathcal{K}} [-r_k + \text{div } \mathbf{q}_k] &= -\frac{dU}{dt} - U \text{div } \mathbf{v}_s + \boldsymbol{\sigma}^I : \nabla \mathbf{v}_s - \hat{\rho} \mathbf{v}_s \cdot \left( \tilde{\mathbf{v}} - \frac{\mathbf{v}_s}{2} \right) \\ &\quad - \sum_{k \in \mathcal{K}} \left[ \mathbf{M}_k \cdot \left( \frac{d^k \mathbf{v}_k}{dt} - \mathbf{b}_k \right) + \frac{\hat{\rho}^k}{2} \left( \frac{\mathbf{M}_k}{\rho^k} \right)^2 \right] \\ &\quad - \sum_{k \in \mathcal{K}} \text{div } (H_k \mathbf{M}_k) + \sum_{k \in \mathcal{K}} \hat{e}_U^k, \end{aligned} \quad (2.83)$$

into the second principle for the mixture (2.74),

$$\begin{aligned} \sum_{k \in \mathcal{K}} \rho^k \gamma_k &= \sum_{k \in \mathcal{K}} \left( \frac{d\rho^k S_k}{dt} - \rho^k S_k \text{div } \mathbf{v}_s + \text{div } (S_k \mathbf{M}_k) \right) \\ &\quad + \sum_{k \in \mathcal{K}} \frac{1}{T_k} \left[ -r_k + \text{div } \mathbf{q}_k - \mathbf{q}_k \frac{\nabla T_k}{T_k} \right] - \sum_{k \in \mathcal{K}} \hat{e}_S^k \geq 0. \end{aligned} \quad (2.84)$$

Let  $dD_i/dt$  represent the sum over the species of the rate of entropy production  $\rho^k \gamma_{k,i}$ , corresponding to the  $i^{\text{th}}$  physical phenomenon,

$$\frac{dD_i}{dt} = \sum_{k \in \mathcal{K}} \rho^k \gamma_{k,i} \geq 0, \quad k \in \mathcal{K}. \quad (2.85)$$

Inserting the definitions of the free energy (2.80) and of the chemical potential (2.82), a detailed CD inequality is obtained in which several substitutions occur:

- The divergence term of  $\mathbf{M}_k$  is eliminated by use of equation (2.26),

$$-\text{div } \mathbf{M}_k = \left( \frac{d\rho^k}{dt} + \rho^k \text{div } \mathbf{v}_s \right) - \hat{\rho}^k, \quad k \in \mathcal{K}. \quad (2.86)$$

- To avoid a possible confusion of notation, Biot's approach to mixtures introduces the mass contents which, unlike the partial densities, are defined per unit reference volume  $m^k$ , namely for species,

$$\rho^k = \frac{1}{\det \mathbf{F}} m^k, \quad k \in \mathcal{K} \quad \text{where} \quad \det \mathbf{F} = \frac{V}{V_0}. \quad (2.87)$$

- The total derivative of the determinant of the deformation gradient  $\mathbf{F}$  can be replaced by,

$$\frac{d}{dt}(\det \mathbf{F}) = \det \mathbf{F} \operatorname{div} \mathbf{v}_s. \quad (2.88)$$

- Finally, the following relation is used,

$$\left( \frac{d\rho^k}{dt} + \rho^k \operatorname{div} \mathbf{v}_s \right) = \frac{1}{\det \mathbf{F}} \frac{dm^k}{dt}, \quad k \in \mathcal{K}. \quad (2.89)$$

The final result of the CD inequality can be separated into three parts associated to different physical phenomena:

- $dD_1/dt$  representing the thermo-mechanical sources,
- $dD_2/dt$  representing the transfer mechanisms (internal and external), and
- $dD_3/dt$  describing the generalised coupled diffusion,

Since the three parts of the CD inequality correspond to different physical phenomena, it is sufficient to require each of them to be greater or equal to zero:  $dD_1 + dD_2 + dD_3 \geq 0$ . In explicit form,

$$\begin{aligned} \frac{dD_1}{dt} &= \sum_{k \in \mathcal{K}} \frac{1}{T_k} \left( -\frac{d(\rho^k E_k)}{dt} + (\boldsymbol{\sigma}^k - \rho^k E_k \mathbf{I}) : \nabla \mathbf{v}_s - \rho^k S_k \frac{dT_k}{dt} \right) \\ &\quad + \sum_{k \in \mathcal{K}^*} \frac{1}{\det \mathbf{F}} \frac{G_k}{T_k} \frac{dm^k}{dt} \geq 0 \end{aligned}$$

$$\begin{aligned} \frac{dD_2}{dt} &= - \sum_{k \in \mathcal{K}^*} \left( G_k + \frac{1}{2} (\mathbf{v}_k - \mathbf{v}_s)^2 - \frac{1}{2} \mathbf{v}_s^2 \right) \frac{1}{T_k} \hat{\rho}^k \\ &\quad - \sum_{k \in \mathcal{K}} \hat{e}_S^k + \frac{1}{T_k} (\hat{e}_{\mathcal{M}}^k \cdot \mathbf{v}_s - \hat{e}_{\mathcal{U}}^k) > 0 \end{aligned}$$



$$\begin{aligned} \frac{dD_3}{dt} &= - \sum_{k \in \mathcal{K}} \mathbf{q}_k \cdot \frac{1}{T_k} \left( \frac{\nabla T_k}{T_k} \right) \\ &\quad - \sum_{k \in \mathcal{K}^*} \mathbf{M}_k \cdot \frac{1}{T_k} \left( S_k \nabla T_k + \nabla G_k + \frac{d^k \mathbf{v}_k}{dt} - \mathbf{b}_k \right) > 0 \end{aligned} \quad (2.90)$$

in which  $\hat{\rho}^k$ ,  $\hat{e}_{\mathcal{M}}^k$ ,  $\hat{e}_{\mathcal{U}}^k$  and  $\hat{e}_{\mathcal{S}}^k$  are the volume supply rates of mass, momentum, energy and entropy as defined by equations (2.20), (2.31), (2.46) and (2.65) respectively,

$$\begin{aligned} \hat{\rho}^k &= \hat{\rho}_{tr}^k + \hat{\rho}_{ex}^k, \\ \hat{e}_{\mathcal{M}}^k &= \hat{\rho}^k \tilde{\mathbf{v}}_k + \hat{\mathbf{p}}_k, \\ \hat{e}_{\mathcal{U}}^k &= \hat{\rho}^k \left( \tilde{U}_k + \frac{1}{2} \tilde{\mathbf{v}}_k^2 \right) + \hat{\mathbf{p}}_k \cdot \mathbf{v}_k + \hat{u}_k, \\ \hat{e}_{\mathcal{S}}^k &= \hat{\rho}^k \tilde{S}_k + \hat{s}_k. \end{aligned} \quad (2.91)$$

The set of species in the mixture as a whole is denoted  $\mathcal{K}$ . The set of all species which diffuses in the solid skeleton is denoted  $\mathcal{K}^*$ . Not all the species are participating to all physical phenomena. One possibility is to consider only the species that transfer or diffuse, and then the set of summation is  $\mathcal{K}^*$ .

- In (2.90)<sub>1</sub> all the species except the solid are concerned by the chemical potential summation, as only the fluid species interact with each other through chemical reactions, consequently the set of summation is  $\mathcal{K}^*$ .
- In (2.90)<sub>2</sub>, the mass transfer term does not involve the solid phase. Within the mixture only the fluid species transfer and the set of summation is  $\mathcal{K}^*$ .
- Finally in (2.90)<sub>3</sub>, the generalised diffusion can be splitted into two terms: a thermal diffusion term where the set of summation is  $\mathcal{K}$ ; and a hydraulic diffusion term, where only the fluid species are concerned and the set of summation is  $\mathcal{K}^*$ .

Note that in the current configuration, the CD inequality features the Eshelby stress, namely  $\boldsymbol{\sigma}^E = (\boldsymbol{\sigma}^k - \rho^k E_k \mathbf{I})$ . The CD inequality can also be written in the reference configuration, see Loret and Simões (2005, eq. 6.14).

### 2.1.7.2 The particular case of a closed system

In the next Section 2.2, the model is restricted to a *closed system* constituted by three phases. Each phase is assumed to contain one species. In order to simplify the establishment of the constitutive equations, the species in the phases are temporarily ignored and each phase is considered as homogeneous.

For a closed system and in absence of surface supply rates, the volume supply rates of mass, momentum, energy and entropy sum to zero,

$$\sum_{k \in \mathcal{K}} \hat{\rho}^k = \sum_{k \in \mathcal{K}} \hat{\rho}_{tr}^k = 0, \quad \sum_{k \in \mathcal{K}} \hat{e}_{\mathcal{M}}^k = 0, \quad \sum_{k \in \mathcal{K}} \hat{e}_{\mathcal{U}}^k = 0, \quad \sum_{k \in \mathcal{K}} \hat{e}_{\mathcal{S}}^k = 0. \quad (2.92)$$

The CD inequality (2.90) is provided as a basic requirement to help with the constitutive equations identification and description presented in Section 2.2:

- The thermo-mechanical behaviour will be constructed in order the first term  $dD_1$  to *exactly vanish*: then the energy dissipation will be due exclusively to transfer of matter and energy between phases, diffusion of fluids through the solid skeleton and to conductive heat<sup>1</sup>;
- On the other hand, the mass, energy and entropy transfer behaviours will be formulated by forcing the second term  $dD_2$  to be positive;
- Similarly, the diffusion constitutive equations will be defined by forcing the third term  $dD_3$  to be positive.

---

<sup>1</sup>However, if the behaviour is thermo-elasto-plastic, energy dissipation occurs by thermo-plastic effects that would imply  $dD_1$  to be *positive*

## 2.2 Constitutive equations based on a thermodynamic approach

In Section 2.1, the field equations of a general *open* multi-species multi-phase system have been introduced. Reducing to a model for porous media with double porosity and to a *closed* system, the mixture is now composed of three phases: the solid skeleton, the pore fluid and the fissure fluid. Each phase is constituted of one species. Although the fluids in the pores and in the fissures are considered of same nature, the two fluid phases are segregated by their physical location. Furthermore, the mixture is assumed to be fully saturated. In the further, the subscript  $k = s$  corresponds to the solid phase,  $k = p$  to the pore fluid and  $k = f$  to the fissure fluid.

The presentation below is a *rational* thermodynamic presentation in which the Clausius-Duhem inequality is used to restrain the constitutive equations (Loret and Khalili, 2000b; Loret, 2008), as opposed to a *manual* presentation which introduces constitutive equations without a prior identification of the appropriate generalised forces and fluxes (Khalili and Selvadurai, 2003). Three types of constitutive equations are required by the thermodynamic theory. (1) The thermo-mechanical constitutive equations describe a reversible process, which is governed by a thermo-poro-elastic theory, and highlight the existence of a potential. The Clausius-Duhem inequalities associated with (2) generalised diffusion and (3) generalised transfer are phrased in terms of thermodynamic functions. The constitutive equations of diffusion and transfer are simplified by assuming symmetry properties, also called Onsager's reciprocity principle.

In Subsection 2.2.1 the thermodynamic theories used to develop and restrict the diffusion and transfer constitutive equations are reviewed. The difficulty of identifying the correct forces and fluxes is highlighted with the generalised diffusion part of the CD inequality (2.90) as example.

In Subsection 2.2.2, the thermo-mechanical constitutive equations are presented based on a thermo-poro-elastic potential that highlights directly a number of symmetry properties and that incorporates the identification procedures for the purely mechanical coefficients (Khalili and Valliappan, 1996). First, the thermo-mechanical behaviour of media with double porosity is introduced, in which two extensions of the classical porous media theory are described: the effective stress relation for a porous medium with double porosity and the influence of the thermal loading on the total stress. For clarity, the purely elastic mechanical contributions are written alone through a mechanical secant form. And finally, the thermal contributions are added to the mechanical contributions to obtain the complete thermo-mechanical secant form.

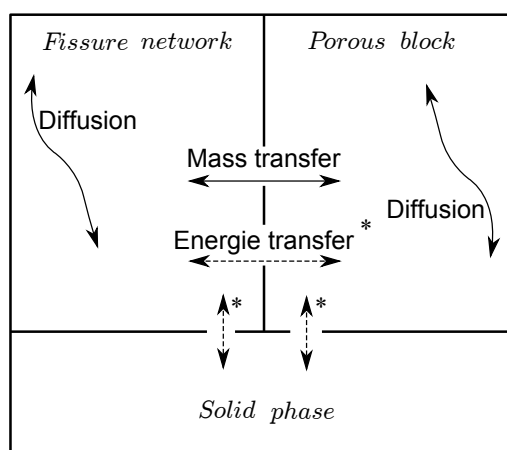


Figure 2.2: Sketch of exchanges that are accounted for in the porous medium with double porosity of a non-isothermal closed system. At each geometrical point, porous media with double porosity are partitioned in three phases; one solid phase and two fluid phases: the fluid of the porous block and the fluid of the fissure network. Within each fluid phase, hydraulic and thermal coupled diffusion occur. Across fluid phases mass transfer occurs due to a chemical potential difference. In between the three phases, energy transfer occurs due to temperature differences, represented by a dashed arrow.

In Subsection 2.2.3, the generalised diffusion constitutive equations are introduced, which involve two types of diffusion mechanisms: the hydraulic diffusion introduced by Darcy and the thermal diffusion introduced by Fourier. The coupled diffusion behaviour presents an extension of Darcy's law and Fourier's law to account for the *thermo-osmosis* and *isothermal flow* coupling phenomena. A discussion is proposed to forecast the influence of these uncommon coupled mechanisms. Finally, a secant relation satisfying the Clausius-Duhem inequality of diffusion is proposed.

In Subsection 2.2.4, the transfer constitutive equations gather two physical mechanisms: mass transfer and energy transfer in between the phases. As a rule, transfer phenomena are assumed to occur at a local geometrical point. The thermo-mechanical properties of fluids are used to accurately depict the chemical potential, which drives the mass transfer. A law describing the mass transfer under thermo-hydro-mechanical stress conditions is proposed. This proposal may be seen as an extension of Barenblatt's law of mass transfer to mixture in local thermal non-equilibrium. Finally, a transfer secant relation is proposed. For simplicity, the mass transfer and the energy transfer mechanisms are assumed to be uncoupled. The generalised diffusion and transfer phenomena are illustrated in Figure 2.2.

### 2.2.1 Onsager's reciprocity principle versus 'rational' thermodynamics

The scope of this section is to give a brief overview of the different theories developed in modern thermodynamics rather than a stance on the best way to proceed. The science of thermodynamics differs from other branches of mathematical physics only in its emphasis on the effects of heating and change of temperature. Its aims are three: (1) construction of the equilibrium theory, (2) reduction of constitutive equations and (3) application. The dissipation inequality (also called entropy inequality) along with the axioms of balance, allows to undertake the task of formulating constitutive equations. Constitutive principles are usually too general when considering a particular system, such as multiphase mixtures. The Clausius-Duhem inequality is therefore used to restrain the constitutive equations describing a specified material.

Lars Onsager (1931) presented a reciprocity principle that systematically assumes symmetry of a given constitutive system of equations. Because of the attractive simplifications and of the easiness of its application, this principle has become very popular among thermodynamical users. However, it should be used with care. Onsager's reciprocity principle has later been very much criticised by Truesdell and its followers (Truesdell, 1984), the 'rational' thermodynamics authors, due to the fact that no 'guide lines' were provided to restrain the constitutive equations and therefore to provide meaningful restrictions.

#### 2.2.1.1 The Onsager's reciprocity principle

The Onsager's reciprocity principle is illustrated by taking the diffusion part of the Clausius-Duhem inequality as example. The irreversible generalised diffusion contributions of the entropy inequality  $dD_3/dt \geq 0$  are phrased in terms of thermodynamic functions,

$$-\sum_{s,p,f} \mathbf{q}_k \cdot \frac{\nabla T_k}{T_k^2} - \sum_{p,f} \mathbf{J}_k \cdot \frac{\nabla p_k}{T_k} \geq 0. \quad (2.93)$$

This expression can be seen as a sum of products of two factors  $X_i Y_i$ : The variables  $Y_i$  represent the rate of transformation or exchange, so called fluxes. The variables  $X_i$  are called forces. Close to the equilibrium, the fluxes  $Y_i$  are defined as linear functions of the forces  $X_i$ ,

$$Y_i = L_{ij} X_j \quad \text{where} \quad X_i = L_{ij}^{-1} Y_j. \quad (2.94)$$

Onsager's reciprocity principle states that the matrix  $L_{ij}$  is symmetric and positive,

$$X_i Y_i = L_{ii} X_i X_i \geq 0. \quad (2.95)$$

Note that the symmetry simplification introduced by Onsager's reciprocity principle is not required to satisfy the entropy inequality. The main limitation of the Onsager's reciprocity principle is that no indication is given on the choice of the forces  $X_i$  and of the fluxes  $Y_i$ . It is worth noting that the delicate choice of forces and fluxes influences the meaning of the stated symmetry. This situation emphasises the need for a definite choice, since without one, the claim of symmetry may be false.

### 2.2.1.2 Rational thermodynamics

In a rational (in a truesdellian perspective) analysis, there are five basic principles that have to be satisfied by constitutive equations, whether for a single body or for mixtures. They are conceived as 'rules to guide us when we come to set up constitutive relations in the first place', (Wang and Truesdell, 1973, p.135). They are briefly stated below from Truesdell (1984, p. 230):

- 1. *Determinism* asserts that natural phenomena can be described and predicted. There exists a set of variables such that the knowledge of their past and present values determines the present response of the mixture.
- 2. *Equipresence* states that any 'quantity present as an independent variable in one constitutive relation must be assumed so present in all', Wang and Truesdell (1973, p. 141). Passman et al. in Truesdell (1984, p. 301) find the principle applicable to single bodies and homogeneous mixtures, but they replace it by the *Principle of phase separation* for inhomogeneous mixtures, also called multiphase mixtures. The latter states that the principle of equipresence applies to individual phases in terms of their own set of independent variables, while interaction and exchange terms follow the general principle of equipresence in terms of all independent variables.
- 3. *Local action* implies that the constitutive response of the species at a point of space depends only of the thermokinetic process in a close neighborhood of that point.
- 4. *Material frame-indifference* requires that the constitutive equations of the species are independent of the observer.
- 5. *Dissipation* requires that some form of the second principle be satisfied for any thermo-kinetic processes.

The first three principles are more metaphysical than mathematical. The fourth and the fifth are of mathematical nature and leads to explicit statements. To these five statements, Wang and Truesdell (1973, p. 135) add a sixth physical principle that allows for specialization, namely,

- 6. *Material symmetry.* There exists a symmetry group, or group of invariance, describing the properties of the body, which leaves unchanged the constitutive equations. The simplest case is that of a mixture of one solid and several inviscid fluids: the mixture inherits the material symmetries of the solid.

When exploiting the dissipation inequality, and developing diffusion constitutive equations, a standard practice is the use of the Onsager reciprocity relations to express the ‘fluxes’ in terms of the ‘forces’ (Groot and Mazur, 1962). Having chosen what the fluxes and the forces are, the fluxes are expressed in terms of the forces *via* a symmetric semi-definite diffusion matrix. Truesdell (1984, p. 365) largely criticises the onsagerist approach, that claims that the definition of the fluxes and the forces is a ‘self-consistent postulate’. All attempts so far to apply this theory to heat conduction, viscosity and diffusion remains on strong further assumptions *ad hoc*.

The dissipation inequality is a powerful tool to develop constitutive equations and to restrict the number of arguments of the constitutive functions. Aside from the statement that certain matrices are or are not symmetric, many matrices are filled up with unknown coupling coefficients in the absence of experiments. The choice of symmetry may therefore be seen as a temporary solution during the absence of experiments to verify or infer these propositions.

### 2.2.1.3 Application to the diffusion problem

As an example, the delicate choice of the forces and the fluxes is applied to our diffusion problem. Let us work with a porous medium restricted to single porosity and to local thermal non-equilibrium  $T_s \neq T_f$ . The fluid diffusion part of the dissipation inequality multiplied by  $T_s$  may be written in the following form;

$$-\mathbf{q}_s \frac{\nabla T_s}{T_s} - \mathbf{q}_f \frac{T_s}{T_f} \frac{\nabla T_f}{T_f} - \mathbf{J}_f \cdot \frac{T_s}{T_f} \nabla p_f \geq 0. \quad (2.96)$$

One needs to choose to whom the dimensionless temperature ratio  $T_s/T_f$  belongs: the forces or the fluxes. This dilemma can be written in a general manner, with the variable  $\alpha \in [0, 1]$ ,

$$-\mathbf{q}_s \frac{\nabla T_s}{T_s} - \underbrace{\mathbf{q}_f \left(\frac{T_s}{T_f}\right)^\alpha}_{\text{flux}} \underbrace{\left(\frac{T_s}{T_f}\right)^{1-\alpha} \frac{\nabla T_f}{T_f}}_{\text{force}} - \underbrace{\mathbf{J}_f \left(\frac{T_s}{T_f}\right)^\alpha}_{\text{flux}} \underbrace{\left(\frac{T_s}{T_f}\right)^{1-\alpha} \nabla p_f}_{\text{force}} \geq 0. \quad (2.97)$$

The *fluxes*: the modified volume flux and the modified heat flux may be linearly related to the modified gradients *forces* through a semi-positive definite diffusion *symmetric* matrix  $\mathbf{L}$ , thanks to Onsager's reciprocity principle,

$$\begin{bmatrix} \mathbf{J}_f \left(\frac{T_s}{T_f}\right)^\alpha \\ \mathbf{q}_s \\ \mathbf{q}_f \left(\frac{T_s}{T_f}\right)^\alpha \end{bmatrix} = - \underbrace{\begin{bmatrix} L_{11} & L_{12} & L_{13} \\ L_{21} & L_{22} & L_{23} \\ L_{31} & L_{32} & L_{33} \end{bmatrix}}_{\mathbf{L}} \begin{bmatrix} \left(\frac{T_s}{T_f}\right)^{1-\alpha} \nabla p_f \\ \frac{\nabla T_s}{T_s} \\ \left(\frac{T_s}{T_f}\right)^{1-\alpha} \frac{\nabla T_f}{T_f} \end{bmatrix}, \quad (2.98)$$

where the symmetric and the semi-positive definiteness holds,

$$\begin{aligned} L_{12} &= L_{21}, & L_{13} &= L_{31}, & L_{23} &= L_{32}, \\ L_{11} &\geq 0, & L_{22} &\geq 0, & L_{33} &\geq 0 \quad \text{and} \quad \det \mathbf{L} \geq 0. \end{aligned} \quad (2.99)$$

The latter relation can be re-written by gathering the dimensionless temperature ratio  $T_s/T_f$  in the matrix. Note that with this writing, the constitutive matrix is *non-symmetric*:

$$\begin{bmatrix} \mathbf{J}_f \\ \mathbf{q}_s \\ \mathbf{q}_f \end{bmatrix} = - \begin{bmatrix} \left(\frac{T_s}{T_f}\right)^{1-2\alpha} L_{11} & \left(\frac{T_s}{T_f}\right)^{-\alpha} L_{12} & \left(\frac{T_s}{T_f}\right)^{1-2\alpha} L_{13} \\ \left(\frac{T_s}{T_f}\right)^{1-\alpha} L_{21} & L_{22} & \left(\frac{T_s}{T_f}\right)^{1-\alpha} L_{23} \\ \left(\frac{T_s}{T_f}\right)^{1-2\alpha} L_{31} & \left(\frac{T_s}{T_f}\right)^{-\alpha} L_{32} & \left(\frac{T_s}{T_f}\right)^{1-2\alpha} L_{33} \end{bmatrix} \begin{bmatrix} \nabla p_f \\ \frac{\nabla T_s}{T_s} \\ \frac{\nabla T_f}{T_f} \end{bmatrix} \quad (2.100)$$

Let us highlight here the importance of imposing the symmetry on the constitutive matrix of equation (2.98) before the rewriting process. It is important to note that the



final constitutive matrix is *non-symmetric* in the general case and that the matrix of equation (2.100) is symmetric for the particular case of  $\alpha = 0.5$  or for  $T_s = T_f$ .

The repartition on the forces or on the fluxes can be influenced by experimental data. The phenomenological coefficients that are experimentally measured are displayed in the diffusion matrix  $\mathbf{D}$ , namely,

$$\begin{bmatrix} \mathbf{J}_f \\ \mathbf{q}_s \\ \mathbf{q}_f \end{bmatrix} = - \underbrace{\begin{bmatrix} D_{11} & D_{12} & D_{13} \\ D_{21} & D_{22} & D_{23} \\ D_{31} & D_{32} & D_{33} \end{bmatrix}}_{\mathbf{D}} \begin{bmatrix} \nabla p_f \\ \frac{\nabla T_s}{T_s} \\ \frac{\nabla T_f}{T_f} \end{bmatrix} \quad (2.101)$$

If  $\alpha = 1$ , the repartition of the temperature ratio is positioned on the *fluxes only*, and the constitutive relation becomes,

$$\begin{bmatrix} \mathbf{J}_f \\ \mathbf{q}_s \\ \mathbf{q}_f \end{bmatrix} = - \begin{bmatrix} \left(\frac{T_s}{T_f}\right)^{-1} L_{11} & \left(\frac{T_s}{T_f}\right)^{-1} L_{12} & \left(\frac{T_s}{T_f}\right)^{-1} L_{13} \\ L_{21} & L_{22} & L_{23} \\ \left(\frac{T_s}{T_f}\right)^{-1} L_{31} & \left(\frac{T_s}{T_f}\right)^{-1} L_{32} & \left(\frac{T_s}{T_f}\right)^{-1} L_{33} \end{bmatrix} \begin{bmatrix} \nabla p_f \\ \frac{\nabla T_s}{T_s} \\ \frac{\nabla T_f}{T_f} \end{bmatrix} \quad (2.102)$$

for instance  $D_{12} = \left(\frac{T_s}{T_f}\right)^{-1} L_{12}$ .

On the other hand, if  $\alpha = 0$  the repartition of the temperature ratio is positioned on the *forces only*, and the constitutive relation becomes,

$$\begin{bmatrix} \mathbf{J}_f \\ \mathbf{q}_s \\ \mathbf{q}_f \end{bmatrix} = - \begin{bmatrix} \left(\frac{T_s}{T_f}\right) L_{11} & L_{12} & \left(\frac{T_s}{T_f}\right) L_{13} \\ \left(\frac{T_s}{T_f}\right) L_{21} & L_{22} & \left(\frac{T_s}{T_f}\right) L_{23} \\ \left(\frac{T_s}{T_f}\right) L_{31} & L_{32} & \left(\frac{T_s}{T_f}\right) L_{33} \end{bmatrix} \begin{bmatrix} \nabla p_f \\ \frac{\nabla T_s}{T_s} \\ \frac{\nabla T_f}{T_f} \end{bmatrix} \quad (2.103)$$

for instance  $D_{12} = L_{12}$ .

It is clear when comparing equations (2.102) and (2.103) that the choice of the position of the temperature ratio deeply influences the meaning of the  $L_{ij}$  coefficients. However, the two relations (2.102) and (2.103) are equivalent as long as the identification of the  $L_{ij}$  coefficients with experimental data eq. (2.101) is done in a correct way.

## 2.2.2 Thermo-mechanical constitutive equations

The presentation below is a thermodynamic presentation based on a thermo-poro-elastic potential that highlights directly a number of symmetry properties (Loret, 2008). While a number of simplifications has been done to linearise the equations about a prescribed state, the construction may be reconsidered and extended to include large perturbations with respect to an initial state that require a non-linear analysis.

This subsection aims to identify the thermo-mechanical elastic secant relation linking the generalised stresses to the generalised strains, *via* a symmetric tensor. First, the thermo-mechanical part of Clausius-Duhem inequality is rewritten in a more useful way, so that the thermo-mechanical forces, or generalised strains, can be related to the thermo-mechanical fluxes, or generalised stresses. Secondly, the thermo-mechanical behaviour of saturated soils with double porosity is described. For instance, the effective and total stress relations, the volume changes relations and the entropy relations are extended to media with double porosity. Furthermore, the thermo-mechanical behaviour of fluids is introduced separately. Last, the *thermo-mechanical* secant relations are presented. For clarity, the *mechanical* secant form simplified to a uniform temperature context and the complete *thermo-mechanical* secant form are presented in turn.

### 2.2.2.1 The Thermo-mechanical part of Clausius-Duhem inequality

The Clausius-Duhem inequality is used to restrain the constitutive equations. In particular, the thermo-mechanical elastic behaviour is constructed in order for the thermo-mechanical part  $dD_1$  of the Clausius-Duhem equation (2.90)<sub>1</sub> to exactly vanish,

$$\begin{aligned} \frac{dD_1}{dt} &= \sum_{k \in \mathcal{K}} \frac{1}{T_k} \left( -\frac{d(\rho^k E_k)}{dt} + (\boldsymbol{\sigma}^k - \rho^k E_k \mathbf{I}) : \nabla \mathbf{v}_s - \rho^k S_k \frac{dT_k}{dt} \right) \\ &+ \sum_{k \in \mathcal{K}^*} \frac{1}{\det \mathbf{F}} \frac{G_k}{T_k} \frac{dm^k}{dt} = 0, \end{aligned} \quad (2.104)$$

in which  $\boldsymbol{\sigma}^E = (\boldsymbol{\sigma}^k - \rho^k E_k \mathbf{I})$  is the Eshelby stress. The aim is to rewrite equation (2.104) in such a way that the thermo-mechanical generalised forces and their related fluxes are

directly available.

The procedure, which aims at linearising some terms around a reference configuration, is held in five steps (Loret, 2008): (1) the CD<sub>1</sub> equality is transposed into the reference configuration. In addition, in order to write equation (2.104) in a form similar to an isothermal system, equation (2.104) is multiplied by  $T_s$ . (2 and 3) The CD<sub>1</sub> equality is expressed for the solid phase and for the fluid phases, separately. (4) The CD<sub>1</sub> equality for the mixture is obtained by summation over the species and is linearised around the reference state. (5) The CD<sub>1</sub> equality for the mixture is transposed back to the actual configuration and the generalised forces and their related fluxes are identified.

(1) The Clausius-Duhem inequality is written in the reference configuration. Upon the multiplication of equation (2.104) by  $\det \mathbf{F} = V/V_0$ , the entities that come into picture are,

- the mass contents  $m^k = \det \mathbf{F} \rho^k$ , rather than the mass densities  $\rho^k$ ,  $k \in \mathcal{K}^*$ ;
- the volume contents  $v^k = \det \mathbf{F} n_k$ , rather than the volume fractions  $n_k$ ,  $k \in \mathcal{K}^*$ ;
- the apparent pressures  $v^k p_k = \det \mathbf{F} p^k$ , rather than the apparent pressures  $n^k p_k = p^k$ ,  $k \in \mathcal{K}^*$ ;
- the Kirchhoff stresses  $\boldsymbol{\tau} = \det \mathbf{F} \boldsymbol{\sigma}$ , and  $\boldsymbol{\tau}^k = \det \mathbf{F} \boldsymbol{\sigma}^k$ , rather than the Cauchy stresses  $\boldsymbol{\sigma}$  and  $\boldsymbol{\sigma}^k$ ,  $k \in \mathcal{K}$ .

In the theoretical developments, the Proposition 2.1 is adopted.

---

**Proposition 2.1.** *When the current configuration is taken as reference, that is  $\det \mathbf{F}$  is set equal to one, these two families of entities are equal. However, their increments and rates are not identical.*

---

Upon multiplication of equation (2.104) by  $T_s$ , the entities that come into picture are.

- the modified free energies  $\underline{E}_k$ , rather than the free energies  $E_k$ ,  $k \in \mathcal{K}^*$ ;
- the modified apparent pressures  $v^k \underline{p}_k$ , rather than the apparent pressures  $v^k p_k$ ,  $k \in \mathcal{K}^*$ ;
- the modified partial Kirchhoff stresses  $\underline{\boldsymbol{\tau}}^k$ , rather than the partial Kirchhoff stresses  $\boldsymbol{\tau}^k$ ,  $k \in \mathcal{K}^*$ ;

- the modified entropies  $\underline{S}_k$ , rather than the entropies  $S_k$ ,  $k \in \mathcal{K}^*$
- the modified chemical potentials  $\underline{G}_k$ , rather than the chemical potentials  $G_k$ ,  $k \in \mathcal{K}^*$ ,

where for all species  $k \in \mathcal{K}^*$ ,

$$\underline{E}_k = E_k \frac{T_s}{T_k}, \quad v^k \underline{p}_k = v^k p_k \frac{T_s}{T_k}, \quad \underline{\boldsymbol{\tau}}^k = \boldsymbol{\tau}^k \frac{T_s}{T_k}, \quad \underline{S}_k = S_k \frac{T_s}{T_k}, \quad \underline{G}_k = G_k \frac{T_s}{T_k}. \quad (2.105)$$

(2) The rate of mechanical entropy production of *the solid species*, upon multiplication by  $T_s \det \mathbf{F}$ , is modified to the following relation,

$$T_s m^s \gamma_{s,1} = -m^s \frac{d}{dt} (E_s) + \boldsymbol{\tau}^s : \nabla \mathbf{v}_s - m^s S_s \frac{dT_s}{dt}. \quad (2.106)$$

The proof of equation (2.106) is provided in Demonstration 2.3, page 108. Note that the rate of the mechanical entropy production of the solid species does not include terms involving a chemical potential.

(3) The rate of mechanical entropy production of *the fluid species*  $k$ , upon multiplication by  $T_s \det \mathbf{F}$ , takes the form of the following equation,

$$T_s m^k \gamma_{k,1} = \frac{d}{dt} \left( v^k \underline{p}_k \right) + \underline{\boldsymbol{\tau}}^k : \nabla \mathbf{v}_s - v^k \frac{d\underline{p}_k}{dt}, \quad k \in \mathcal{K}^*. \quad (2.107)$$

The proof of equation (2.107) is provided in Demonstration 2.4, page 109. Note that the Kirchhoff stress and the modified intrinsic pressure of the fluid  $k$  are related, through the following relation:

$$\underline{\boldsymbol{\tau}}^k = -v^k \underline{p}_k \mathbf{I}, \quad k \in \mathcal{K}^*. \quad (2.108)$$

(4) Finally, upon *summation over the solid phase and all fluid phases* of the rates of entropy production, equation (2.106) and (2.107), respectively, the mechanical part of the rate of entropy production for the mixture multiplied by  $T_s \det \mathbf{F}$  takes the form,

$$T_s \det \mathbf{F} \frac{dD_1}{dt} = -\frac{d\underline{\Psi}}{dt} + \left( \boldsymbol{\tau}^s + \sum_{p,f} \underline{\boldsymbol{\tau}}^k \right) : \nabla \mathbf{v}_s - \sum_{p,f} v^k \frac{d\underline{p}_k}{dt} - m^s S_s \frac{dT_s}{dt}, \quad (2.109)$$

in terms of the modified elastic potential of the mixture  $\underline{\Psi}$  (Remark 2.11) which disregards the contribution of the fluids energies,

$$\underline{\Psi} = \underline{\Psi}(\boldsymbol{\epsilon}, \underline{p}_p, \underline{p}_f, T_s) = m^s E_s - \sum_{p,f} v^k \underline{p}_k, \quad (2.110)$$

with  $\boldsymbol{\epsilon}$  being the infinitesimal strain associated to the deformation gradient  $\mathbf{F}$ .

**Remark 2.11.** *Potential of the mixture  $\underline{\Psi}$  versus Massieu potential  $\Lambda$ : Note that the above derivation is quite different from that proposed by Bowen and Garcia (1970) who introduced a Massieu function for each species,*

$$\Lambda_k = -\frac{\rho^k E_k}{T_k}. \quad (2.111)$$

*They obtain constitutive equations for the internal energies and partial stresses. Each Massieu function is developed up to the second order in terms of main variables, which are the strains of the species and their temperatures. An application to a porous medium including a solid matrix is presented in Bowen and Chen (1975). In contrast, the present derivation aims at highlighting some specific symmetries and decouplings of thermo-mechanical properties as can be observed in equation (2.112).*

Under the assumption of small deformation, the thermo-mechanical behaviour is constructed by setting the entropy production to zero. In the *reference/initial configuration*, the derivation of the potential of the mixture and its consequences on the constitutive equations are written as follows,

$$\left\{ \begin{array}{l} d\underline{\Psi} = \left( \boldsymbol{\tau}^s + \sum_{p,f} \boldsymbol{\tau}^k \right) : d\boldsymbol{\epsilon} - m^s S_s dT_s - \sum_{p,f} v^k d\underline{p}_k \\ \Rightarrow \quad \boldsymbol{\tau} = \frac{\partial \underline{\Psi}}{\partial \boldsymbol{\epsilon}} \quad -m^s S_s = \frac{\partial \underline{\Psi}}{\partial T_s}, \quad -v^k = \frac{\partial \underline{\Psi}}{\partial \underline{p}_k} \quad k = p, f; \end{array} \right. \quad (2.112)$$

where the modified total Kirchoff stress is,

$$\boldsymbol{\tau} = \boldsymbol{\tau}^s + \sum_{k=p,f} \boldsymbol{\tau}^k \mathbf{I}. \quad (2.113)$$

The total Kirchoff stress deduces as,

$$\boldsymbol{\tau} = \boldsymbol{\tau}^s + \sum_{k=p,f} \boldsymbol{\tau}^k \mathbf{I} = \boldsymbol{\tau} - \sum_{k=p,f} v^k (p_k - \underline{p}_k) \mathbf{I}. \quad (2.114)$$

As a first approximation, see Demonstration 2.5 on page 109, the latter relation (2.112)<sub>2</sub> is linearised around *the pressure of reference* (Proposition 2.2) and around *the solid skeleton temperature*. Hence, no difference between the pressure  $p_k$  and the modified pressure  $\underline{p}_k$  is made.

---

**Proposition 2.2.** *The reference stress state is assumed to be in thermal, hydraulic and mechanical equilibrium. The implications on the thermo-mechanical state, on the transfer state and on the diffusion state are, respectively:*

- *The purely mechanical stresses and the pressures are zero. Temperatures are all equal to  $T_0$*
  - *The chemical potential difference and the temperature difference between the pore fluid and the fissure fluid are equal to zero.*
  - *The thermal gradient and the pressure gradient are equal to zero in all phases.*
- 

Hence, the thermo-mechanical part of the CD equation becomes,

$$\left\{ \begin{array}{l} d\Psi = \boldsymbol{\tau} : d\boldsymbol{\epsilon} - m^s S_s dT_s - \sum_{p,f} v^k dp_k, \\ \Rightarrow \quad \boldsymbol{\tau} = \frac{\partial \Psi}{\partial \boldsymbol{\epsilon}} \quad - m^s S_s = \frac{\partial \Psi}{\partial T_s}, \quad -v^k = \frac{\partial \Psi}{\partial p_k} \quad k = p, f. \end{array} \right. \quad (2.115)$$

where  $\Psi$  is the elastic potential of the mixture,

$$\Psi = m^s E_s - \sum_{p,f} v^k p_k. \quad (2.116)$$

(5) As the *current/actual* configuration is taken as reference, if  $\Psi = \det \mathbf{F} \Psi^a$ , equation (2.115) becomes

$$\left\{ \begin{array}{l} d\Psi^a = \boldsymbol{\sigma} : d\boldsymbol{\epsilon} - \rho^s S_s dT_s - \sum_{p,f} n_k dp_k, \\ \Rightarrow \quad \boldsymbol{\sigma} = \frac{\partial \Psi^a}{\partial \boldsymbol{\epsilon}}, \quad -\rho^s S_s = \frac{\partial \Psi^a}{\partial T_s}, \quad -n_k = \frac{\partial \Psi^a}{\partial p_k} \quad k = p, f. \end{array} \right. \quad (2.117)$$

In order to stay consistent with the mechanical elastic behaviour analysis and to use the same primary variables, the complementary potential  $\Psi_c$  is used in stead of  $\Psi^a$ ,

$$\Psi_c = \Psi^a - \boldsymbol{\sigma} : \boldsymbol{\epsilon}. \quad (2.118)$$

Moreover, since this study is restricted to small deformations only, the following assumption is made at this final stage of the derivation,

$$\det \mathbf{F} \approx 1 \quad \Rightarrow \quad v^k = n_k, \quad k = p, f. \quad (2.119)$$

Finally, inserting equations (2.118) and (2.119) into (2.117), allows us to write,

$$\left\{ \begin{array}{l} d\Psi_c = -d\boldsymbol{\sigma} : \boldsymbol{\epsilon} - \rho^s S_s dT_s - \sum_{p,f} v^k dp_k, \\ \Rightarrow \quad \boldsymbol{\epsilon} = -\frac{\partial \Psi_c}{\partial \boldsymbol{\sigma}}, \quad -\rho^s S_s = \frac{\partial \Psi_c}{\partial T_s}, \quad -v^k = \frac{\partial \Psi_c}{\partial p_k} \quad k = p, f. \end{array} \right. \quad (2.120)$$

In equation (2.120), four generalised forces are identified:  $(\boldsymbol{\sigma}, p_p, p_f, T_s)$ , namely the total stress, the pore and fissure fluids pressures and the solid temperature; which are conjugated with four generalised fluxes  $(\boldsymbol{\epsilon}, v^p, v^f, \rho^s S_s)$ , namely the total strain, the volume content of the pore and the fissure fluid, and the entropy of the solid.

**Demonstration 2.3.** *Proof of equation 2.106:*

$$\begin{aligned} T_s m^s \gamma_{s,1} &= \det \mathbf{F} \left( -\frac{d(\rho^s E_s)}{dt} \right) + \det \mathbf{F} (\boldsymbol{\sigma}^s - \rho^s E_s \mathbf{I}) : \nabla \mathbf{v}_s - m^s S_s \frac{dT_s}{dt} \\ &= -\frac{d}{dt} (m^s E_s) + \rho^s E_s \frac{d}{dt} (\det \mathbf{F}) + \det \mathbf{F} (\boldsymbol{\sigma}^s - \rho^s E_s \mathbf{I}) : \nabla \mathbf{v}_s \\ &\quad - m^s S_s \frac{dT_s}{dt} \\ &= -\frac{d}{dt} (m^s E_s) + m^s E_s \operatorname{div} \mathbf{v}_s + \det \mathbf{F} (\boldsymbol{\sigma}^s - \rho^s E_s \mathbf{I}) : \nabla \mathbf{v}_s, \\ &\quad - m^s S_s \frac{dT_s}{dt} \quad \text{by (2.88)} \\ &= -\frac{d}{dt} (m^s E_s) + m^s E_s \operatorname{div} \mathbf{v}_s + \boldsymbol{\tau}^s : \nabla \mathbf{v}_s - m^s E_s \operatorname{div} \mathbf{v}_s - m^s S_s \frac{dT_s}{dt} \\ &= -\frac{d}{dt} (m^s E_s) + \boldsymbol{\tau}^s : \nabla \mathbf{v}_s - m^s S_s \frac{dT_s}{dt} \end{aligned}$$

□

**Demonstration 2.4.** *Proof of equation 2.107:*

$$\begin{aligned}
 T_s m^k \gamma_{k,1} &= \frac{T_s}{T_k} \left( \det \mathbf{F} \left( -\frac{d(\rho^k E_k)}{dt} \right) + \det \mathbf{F} (\boldsymbol{\sigma}^k - \rho^k E_k \mathbf{I}) : \nabla \mathbf{v}_s - m^k S_k \frac{dT_k}{dt} \right. \\
 &\quad \left. + G_k \frac{dm^k}{dt} \right) \\
 &= -\frac{d}{dt} (m^k \underline{E}_k) + m^k E_k \frac{d}{dt} \left( \frac{T_s}{T_k} \right) + \boldsymbol{\tau}^k : \nabla \mathbf{v}_s - m^k \underline{S}_k \frac{dT_k}{dt} + \underline{G}_k \frac{dm^k}{dt} \\
 &\quad \text{by Demonstration (2.3) + eq. (2.105)} \\
 &= -\frac{d}{dt} (m^k \underline{E}_k) + m^k E_k \frac{d}{dt} \left( \frac{T_s}{T_k} \right) + \boldsymbol{\tau}^k : \nabla \mathbf{v}_s - m^k \underline{S}_k \frac{dT_k}{dt} \\
 &\quad + \frac{d}{dt} (m^k \underline{G}_k) - m^k \frac{d\underline{G}_k}{dt}
 \end{aligned}$$

By use of Table 2.1, p. 121, the derivative of the chemical potential writes,

$$d\underline{G}_k = v^k d\underline{p}^k - \underline{S}_k dT_k + E_k d\left(\frac{T_s}{T_k}\right) \quad \text{and} \quad \underline{E}_k = \underline{G}_k - v^k \underline{p}^k$$

$$\begin{aligned}
 T_s m^k \gamma_{k,1} &= \frac{d}{dt} (m^k v^k \underline{p}^k) + \boldsymbol{\tau}^k : \nabla \mathbf{v}_s - m^k v^k \frac{d\underline{p}^k}{dt} \\
 &= \frac{d}{dt} (v^k \underline{p}_k) + \boldsymbol{\tau}^k : \nabla \mathbf{v}_s - v^k \frac{d\underline{p}_k}{dt}
 \end{aligned}$$

□

**Demonstration 2.5.** *Proof of equation 2.115: The temperatures  $T_k$  are linearised around the temperature of the solid  $T_s$  and the pressures  $p_k$  around their reference values  $p_k^0$ , namely,*

$$T_k = T_s + (T_k - T_s) \quad \text{and} \quad p_k = p_k^0 + (p_k - p_k^0). \quad (2.121)$$

The Taylor series of the function  $\frac{1}{1-x}$  which will be used latter for  $x = -\frac{T_k - T_s}{T_s}$  is,

$$\frac{1}{1-x} = \sum_{n=0}^{\infty} x^n \quad \text{for } |x| \leq 1,$$



$$\frac{T_s}{T_k} - 1 = \frac{1}{1 + \left(\frac{T_k - T_s}{T_s}\right)} - 1 = \left( 1 - \underbrace{\frac{T_k - T_s}{T_s}}_{0(\epsilon)} + \underbrace{\left(\frac{T_k - T_s}{T_s}\right)^2}_{0(\epsilon)^2} - 0(\epsilon)^3 \right) - 1, \quad (2.122)$$

where the notation  $0(\epsilon)$  denotes terms of first-order,  $0(\epsilon)^2$  denotes terms of second-order,  $0(\epsilon)^3$  denotes terms of third-order. The total Kirchhoff stress is linearised to bring into picture the high-order terms that can be neglected compared with the first-order terms, namely,

$$\begin{aligned} \boldsymbol{\tau} &= \boldsymbol{\tau}^s + \sum_{p,f} \boldsymbol{\tau}^k \mathbf{I} = \boldsymbol{\underline{\tau}} + \sum_{p,f} v_k \left( \underline{p}_k - p_k \right) \mathbf{I} && \text{by (2.108)}_1 \\ &= \boldsymbol{\underline{\tau}} + \sum_{p,f} v_k p_k \left( \frac{T_s}{T_k} - 1 \right) \mathbf{I} && \text{by (2.108)}_2 \\ &= \boldsymbol{\underline{\tau}} + \sum_{p,f} v_k p_k \left( -\frac{T_k - T_s}{T_s} + 0(\epsilon)^2 \right) \mathbf{I} && \text{by (2.122)} \\ &= \boldsymbol{\underline{\tau}} + \sum_{p,f} v_k \left( p_k^0 + (p_k - p_k^0) \right) \left( -\frac{T_k - T_s}{T_s} + 0(\epsilon)^2 \right) \mathbf{I} && \text{by (2.121)}_2 \\ &= \boldsymbol{\underline{\tau}} + \sum_{p,f} v_k \left[ p_k^0 \left( -\frac{T_k - T_s}{T_s} \right) + 0(\epsilon)^2 \right] \mathbf{I}. \end{aligned}$$

At this stage of the linearisation process, the value of the reference pressures  $p_k^0$  has a strong influence: two cases can be segregated (1) if  $p_k^0$  is not zero, stiffness induced by initial pressures will arise in the thermo-mechanical behaviour matrix and will induce the secant matrix to be non-symmetric; (2) on the contrary if  $p_k^0$  is equal to zero, no stiffness induced by initial stresses is taken into account and the behaviour matrix is symmetric.

Following Proposition 2.2, the reference state will correspond to a mechanically and thermally equilibrate state. Therefore the initial stresses and fluid pressures are considered to be equal to zero. If this assumption is not verified, the proposed thermo-mechanical model holds to within the fact that the rigidity induced by initial state is not accounted for. Since, the initial pressures  $p_k^0$  are assumed to be null, the total Kirchhoff stress becomes,

$$\boldsymbol{\tau} = \boldsymbol{\underline{\tau}} + 0(\epsilon)^2$$

□

### 2.2.2.2 Thermo-Mechanical behaviour of porous media with double porosity

To describe the thermo-mechanical behaviour, the following expressions need to be introduced: (a) the total stress for the mixture, (b) the volume content variation for each species and (c) the entropy variation of the solid species. These expressions are identified for media with double porosity by using a loading decomposition of a planar element (Nur and Byerlee, 1971). All the thermo-mechanical behaviour expressions are expressed as function of the generalised forces previously identified: the total stress  $\boldsymbol{\sigma}$ , the pore fluid pressure  $p_p$ , the fissure fluid pressure  $p_f$  and the temperature of the solid skeleton  $T_s$ .

Due to the physical structure of porous media with double porosity, mechanical anisotropy is encountered. However, the influence of mechanical anisotropy on the global behaviour is not in the scope of this study. As a first approximation, the mechanical properties of porous media with double porosity are assumed isotropic.

(1) First of all, let us introduce some basic entities. The *elastic strain* of the solid skeleton  $\boldsymbol{\epsilon}^e$  is proportional to the effective stress  $\bar{\boldsymbol{\sigma}}$  and to the drained compliance tensor  $\mathbf{C}^{DS}$ ,

$$\boldsymbol{\epsilon}^e = \mathbf{C}^{DS} : \bar{\boldsymbol{\sigma}}. \quad (2.123)$$

The *effective stress* converts a multi-phase, multi-porous medium to a mechanically equivalent, single-phase, single-stress state continuum. The effective stress is expressed as a function of the externally applied stresses and of the internal fluid pressures, which control the mechanical effects of a change in stress.

The relation linking the total stress  $\boldsymbol{\sigma}$  and the effective stress  $\bar{\boldsymbol{\sigma}}$ , for porous media with single porosity of pressure  $p_p$ , has been introduced by Biot (1941). Considering  $c$  as the drained compressibility of the porous medium as a whole and  $c_s$  as the drained compressibility of the solid grains, the effective stress is defined by,

$$\bar{\boldsymbol{\sigma}} = \boldsymbol{\sigma} + \left(1 - \frac{c_s}{c}\right) p_p \mathbf{I}. \quad (2.124)$$

The isotropic part of the total stress is denoted  $p$ , and the isotropic part of the effective stress is denoted  $\bar{p}$ ,

$$p = -\frac{\text{tr } \boldsymbol{\sigma}}{3}, \quad \text{and} \quad \bar{p} = -\frac{\text{tr } \bar{\boldsymbol{\sigma}}}{3}. \quad (2.125)$$

In this model, the fissure network and the porous block are assumed separable, so that the compressibility of the porous block  $c_p$  does not interact with the compressibility of the fissures and only represents the compressibility of the pore space and of the solid grains.

If the drained compressibility of the mixture  $c$  can be considered large enough in front of the drained compressibility of the solid grains  $c_s$ , equation (2.124) reduces to Terzaghi's relationship. However, this approximation is not suitable for rock materials.

In all this development, the assumption of small deformations holds. The strain components  $\epsilon_{ij}$  are related to the vector of the displacement components  $u_i$  by the following expression,

$$\epsilon_{ij} = \frac{1}{2} \left( \frac{\partial u_i}{\partial x_j} + \frac{\partial u_j}{\partial x_i} \right) \quad (2.126)$$

No plasticity nor viscosity is accounted for in this model. In consequence the total strain tensor  $\epsilon$  is equal to the sum of the elastic strain tensor  $\epsilon^e$  and the thermal strain tensor  $\epsilon^T$ ,

$$\epsilon = \epsilon^e + \epsilon^T. \quad (2.127)$$

If  $\Delta T_s = T_s - T^0$  is the temperature variation applied to the solid phase and  $c_T$  is equal to the volumetric thermal expansion of the solid (three times the often reported linear thermal expansion coefficient), then in absence of mechanical loading, the solid undergoes a thermal deformation  $\epsilon^T$  corresponding to,

$$\epsilon^T = c_T \Delta T_s \mathbf{I} \quad \text{and} \quad \epsilon - \epsilon^T = 0 \quad \text{at} \quad \sigma = 0. \quad (2.128)$$

(2) The thermo-mechanical loading decomposition (Nur and Byerlee, 1971) states that the equilibrium of a Representative Planar Element (RPE) loaded under both mechanical stresses and thermal stresses can be separated in two stress states: a mechanical state (M) and a thermal state (Th), as illustrated in Figure 2.3.

- (M) The mechanical stresses are represented by the stress tensor component  $\sigma$  and the fluid pressures,  $p_p$  and  $p_f$ , respectively for the pore fluid and the fissure fluid.
- (Th) The thermal stresses applied to the mixture are the solid temperature  $T_s$ , the pore fluid temperature  $T_p$  and the fissure fluid temperature  $T_f$ . The thermal stress state represents a transient phase, where the mixture has not yet reached thermal equilibrium.

The mechanical state is in turn decomposed based on a Representative Planar Element in equilibrium, loaded under compressive stresses (for the solid skeleton) and pressure

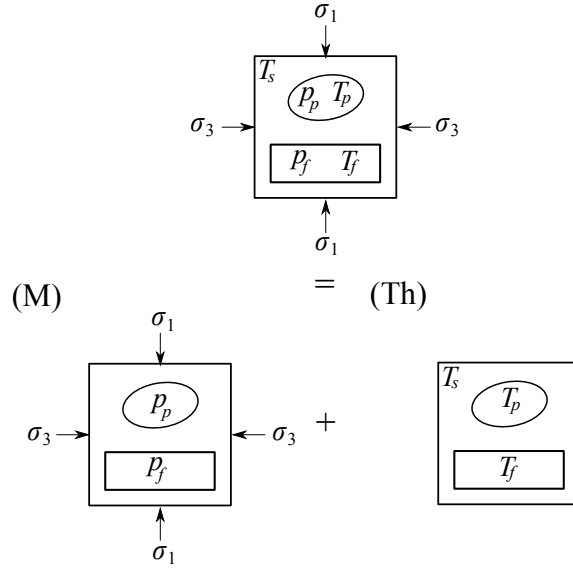


Figure 2.3: Total stress decomposition of a representative fissured porous element (Nur and Byerlee, 1971). The stress equilibrium is segregated in two parts: (M) a mechanical stress state and (Th) a thermal stress state.

stresses (for the fluid phases). In the further development, the mixture is assumed to be in equilibrium during the initial state. This is why the initial stresses, the initial pressures and the initial strains are considered to be zero. However, if the initial state of the system is in equilibrium but the initial pressures and stress values are not null, the additional rigidity implied by the initial state is not accounted for within the model.

The *mechanical* loading decomposition can be segregated in four different stress states, as illustrated in Figure 2.4 (Khalili and Valliappan, 1996). These four stress states (I), (II), (III) and (IV) are loaded under the following conditions<sup>2</sup>,

- (I) The external hydrostatic stresses are equal to  $\sigma_{\text{applied}}^{(I)} = -p_p$  and the fluid pressures to  $p_p$ . This first state represents long-term stress conditions, where the stresses applied to the mixture have reached equilibrium.
- (II) The external hydrostatic stresses are equal to  $\sigma_{\text{applied}}^{(II)} = -(p_f - p_p)$ , the fissure pressure is equal to  $(p_f - p_p)$  and the pore pressure to zero. This second stress state represents medium-term conditions, where the mixture is not in equilibrium: the applied load has not been sensed by the pores yet.

<sup>2</sup>Compressive stresses applied to the continuum are negative. The continuum mechanics sign convention, opposite to the geotechnical sign convention is used. Note that  $p$ , eq. (2.125), is positive when compressive stresses are applied.

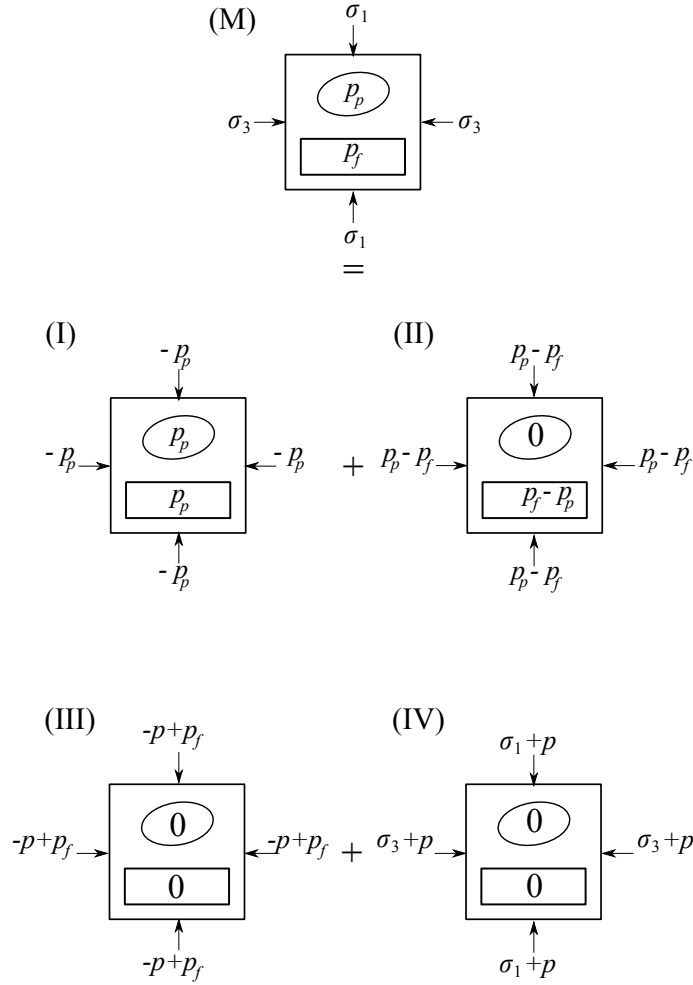


Figure 2.4: Mechanical stress decomposition of a representative fissured porous element. The mechanical stress equilibrium is segregated in four stress states: (I) long-term equilibrium, (II) a medium-term non-equilibrium, (III) a drained isotropic condition and (IV) a drained deviatoric condition.

- (III) The external stresses are equal to  $\sigma_{\text{applied}}^{(\text{III})} = (-p + p_f)$  and the fluid pressures are equal to zero. This third stress state represents drained isotropic conditions, where the pressures in the medium are zero because of free drained limit conditions.
- (IV) The external stresses are equal to  $\sigma_{\text{applied}}^{(\text{IV})} = \mathbf{s} = \boldsymbol{\sigma} + p\mathbf{I}$  and the fluid pressures are equal to zero. This fourth stress state represents drained deviatoric conditions. The drained limit conditions induces zero fluid pressures in both porosities.

These decompositions bring up the following equation of a generic tensor  $\psi^e$ ,

$$\psi^e = \psi^{(\text{M})} + \psi^{(\text{Th})}, \quad \text{and} \quad \psi^{(\text{M})} = \psi^{(\text{I})} + \psi^{(\text{II})} + \psi^{(\text{III})} + \psi^{(\text{IV})}. \quad (2.129)$$

The generic tensor  $\psi^e$  is successively replaced by the strain tensor  $\boldsymbol{\epsilon}$ , by the volume change tensor  $\Delta \mathbf{v}$  and by the entropy variation of the solid phase  $\rho^s \Delta S_s$ .

(3) The effective and total stress relations are now extended to porous media with double porosity. In this development, only the isotropic part is taken into account, in consequence the total stress  $\boldsymbol{\sigma}$  can be replaced by the mean stress  $p$ , eq.(2.125), and the total deformation  $\boldsymbol{\epsilon}$  by its isotropic part  $\text{tr } \boldsymbol{\epsilon}$ .

Let  $\mu^{DS}$  represent the shear modulus of the drained solid (second Lamé's constant). For each stress state, the elastic strain can be expressed as a function of the applied stress, and the corresponding stress-state compressibility, namely,

$$\left\{ \begin{array}{l} \text{tr } \boldsymbol{\epsilon}^{e(\text{I})} = c_s \boldsymbol{\sigma}_{\text{applied}}^{(\text{I})} = c_s (-p_p), \\ \text{tr } \boldsymbol{\epsilon}^{e(\text{II})} = c_p \boldsymbol{\sigma}_{\text{applied}}^{(\text{II})} = c_p -(p_f - p_p), \\ \text{tr } \boldsymbol{\epsilon}^{e(\text{III})} = c \boldsymbol{\sigma}_{\text{applied}}^{(\text{III})} = c (-p + p_f), \\ \text{tr } \boldsymbol{\epsilon}^{e(\text{IV})} = 0, \quad \text{dev } \boldsymbol{\epsilon}^e = \frac{\mathbf{s}}{2\mu^{DS}} \end{array} \right. \quad (2.130)$$

Thus replacing equation (2.130) into (2.129)<sub>1</sub> for  $\psi^e = \text{tr } \boldsymbol{\epsilon}^e$  and rearranging,

$$\begin{aligned} \text{tr } \boldsymbol{\epsilon}^e &= -c p + (c_p - c_s) p_p + (c - c_p) p_f, \\ &= -c(p - \xi_p p_p - \xi_f p_f), \\ &= -c \bar{p}; \end{aligned} \quad (2.131)$$

where  $\xi_p$  and  $\xi_f$  are the effective stress parameters,

$$\xi_p = \frac{c_p}{c} - \frac{c_s}{c} \quad \text{and} \quad \xi_f = 1 - \frac{c_p}{c}. \quad (2.132)$$

Relating equations (2.131)<sub>2</sub> with (2.131)<sub>3</sub> and since the variation between the total stress and the deviatoric stress is isotropic, *the effective stress* writes,

$$\bar{\boldsymbol{\sigma}} = \boldsymbol{\sigma} + \xi_p p_p \mathbf{I} + \xi_f p_f \mathbf{I}. \quad (2.133)$$

**Remark 2.12.** Equation (2.133) can be seen as a generalisation of the formulation introduced by Biot (1941) and Nur and Byerlee (1971) for rock mechanics, equation (2.124).

In order to recover the single porosity expression, one may assume:  $n_f = 0$  (no fissure in the system) which implies  $c = c_p$ . Consequently,  $\xi_f = 0$  and  $\xi_p = 1 - c_s/c$ . Biot's formula is successfully recovered.

The expression of the effective stress extended to double porosity has been presented in eq. (2.133). Let us now write the explicit expression of the total stress as a function of both the total strain and the thermal strain. For a thermo-elastic medium, the stress-strain relationship writes,

$$\begin{aligned}\bar{\boldsymbol{\sigma}} &= \mathbf{K}^{DS} : \boldsymbol{\epsilon}^e, \\ &= [\mathbf{C}^{DS}]^{-1} : (\boldsymbol{\epsilon} - \boldsymbol{\epsilon}^T),\end{aligned}\tag{2.134}$$

where  $\mathbf{K}^{DS}$  is the drained stiffness tensor. The effective stress is expressed as a function of Lamé's constants  $\lambda^{DS}$  and  $\mu^{DS}$ , and both the total strain  $\boldsymbol{\epsilon}$  and the thermal strain  $\boldsymbol{\epsilon}^T$ , in which the thermal strain is described as the volumetric thermal expansion  $c_T$  multiplied by the solid constituent temperature variation  $\Delta T_s$ . The solid constituent temperature variation coefficient  $\gamma_T$  is introduced to highlight the temperature variation  $\Delta T_s$  contribution in the effective stress definition,

$$\begin{aligned}\bar{\boldsymbol{\sigma}} &= \lambda^{DS} (\text{tr } \boldsymbol{\epsilon} - \text{tr } \boldsymbol{\epsilon}^T) \mathbf{I} + 2 \mu^{DS} (\boldsymbol{\epsilon} - \boldsymbol{\epsilon}^T), \\ &= \lambda^{DS} \text{tr } \boldsymbol{\epsilon} \mathbf{I} + 2 \mu^{DS} \boldsymbol{\epsilon} - (\lambda^{DS} \text{tr } \boldsymbol{\epsilon}^T \mathbf{I} + 2 \mu^{DS} \boldsymbol{\epsilon}^T), \\ &= \lambda^{DS} \text{tr } \boldsymbol{\epsilon} \mathbf{I} + 2 \mu^{DS} \boldsymbol{\epsilon} - \underbrace{\left( \lambda^{DS} + \frac{2}{3} \mu^{DS} \right)}_{\gamma_T} c_T \Delta T_s \mathbf{I}.\end{aligned}\tag{2.135}$$

in which  $c_T$  represents both the thermal expansion of the mixture and that of the solid phase, see Remark 2.13. By combining equation (2.135)<sub>3</sub> and (2.133), the explicit expression of *the total stress* is obtained,

$$\begin{aligned}\boldsymbol{\sigma} &= \lambda^{DS} \text{tr } \boldsymbol{\epsilon} \mathbf{I} + 2 \mu^{DS} \boldsymbol{\epsilon} - \xi_p p_p \mathbf{I} - \xi_f p_f \mathbf{I} - \gamma_T \Delta T_s \mathbf{I}, \\ &= \mathbf{K}^{DS} : \boldsymbol{\epsilon} - \xi_p p_p \mathbf{I} - \xi_f p_f \mathbf{I} - \gamma_T \Delta T_s \mathbf{I}.\end{aligned}\tag{2.136}$$

Note that only the isotropic part of the total stress is concerned by the macroscopic thermal and hydraulic contributions, hence,

$$p = -\frac{1}{c} \operatorname{tr} \boldsymbol{\epsilon} + \xi_p p_p + \xi_f p_f + \gamma_T \Delta T_s. \quad (2.137)$$

**Remark 2.13.** *The fact that the deformation undergone by the fissured porous medium is controlled by the solid phase only is highlighted here in contrast with the work of Pecker and Deresiewicz (1973), in which the thermal expansion of the solid skeleton for saturated media is related to a combination of solid and pore fluid temperatures.*

To explore this aspect further, the following thought experiment is proposed. Let us consider an elementary volume of porous medium subjected to constituent temperatures  $T_s$ ,  $T_p$  and  $T_f$ , and constant pressures and stresses (Figure 2.5). The following hypothesis is made: the solid constituent is completely sealed from the thermal effects within the pore space. The energy transfer at the boundaries due to temperature difference are not under concern here.

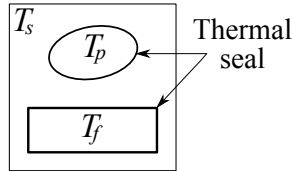


Figure 2.5: Schematic representation of a three phase thermo-elastic porous element, at constant pressures and stresses, subjected to constituent temperature  $T_s$ ,  $T_p$  and  $T_f$ .

Since a continuous grain path relating the solid extremities is considered, the thermal volumetric change of the fissured porous medium (expansion/contraction of the solid skeleton) is independent of the thermal change in the pores and in the fissures. In other words, the volumetric thermal expansion of the solid constituent  $c_{T,s}$  is equal to volumetric thermal expansion of the fissured porous medium  $c_T$ , as the volumetric thermal expansion of the mixture is ruled by the thermal expansion of the solid phase only.

The latter relation  $c_T = c_{T,s}$  is in fact imposed by the thermodynamic theory through the thermo-poro-elastic potential (2.120) which does not account for the fluid temperatures. It is essential to understand that the fluid dilatations do not induce a deformation change of the medium, but induce the fluids to diffuse out of the porous medium.



(4) The relations describing the change in volume content are now extended to porous media with double porosity. The variation of volume content comprise three components: the volume content variation of the porous medium  $\Delta v$ , the volume content variation of the pore voids  $\Delta v^p$  and the volume content variation of the fissure voids  $\Delta v^f$ .

Considering the current volumes of the porous medium  $V$ , of the pore voids  $V_p$ , of the fissure voids  $V_f$  and the total initial volume  $V_0$ , the *dimensionless* volume changes of the porous medium, the pores and the fissures are defined with respect to the initial configuration,

$$\Delta v = \frac{V - V_0}{V_0}, \quad \Delta v^p = \frac{V_p - V_p^0}{V_0} \quad \text{and} \quad \Delta v^f = \frac{V_f - V_f^0}{V_0}. \quad (2.138)$$

Next, the thermo-mechanical decomposition is used to express the volume changes as a function of the four generalised stresses: the mean stress  $p$ , the fluid pressures  $p_p$ , and  $p_f$  and the solid temperature variation  $\Delta T_s$ . Prior to the description of the volume changes, the following propositions are assumed:

- The volume change of the porous medium is equal to the isotropic part of the total strain, namely  $\Delta v = \text{tr } \boldsymbol{\epsilon}$ .
- If the pressure applied to a void is the same as the compression stress applied to the whole porous medium, the volume change of this void is proportional to the volume change of the porous medium by its volume fraction.
- When no pressure is applied in a void, the volume change can not be directly calculated, although it is still proportional to the volume change of the porous medium. In this case, a question mark replaces the unknown coefficient.
- For purely thermal loading  $\Delta T_s \neq 0$ , zero stress and pressure variations  $p = p_p = p_f = 0^3$ , the deformation should be homogeneous throughout the phases; the contribution of each phase is proportional to its volume fraction. In consequence, the thermal volume changes of the pores and the fissures are expressed as a volumetric ratio of the thermal strain of the medium.

Let the generic tensor of equation (2.129)  $\psi^e$  be equal to  $\Delta \mathbf{v}$ . Hence, the volume content changes extended to porous media with double porosity write,

---

<sup>3</sup>Recall that the initial state of stresses and pressures is assumed to be zero in the loading decomposition.

$$\begin{aligned}
 \text{tr } \boldsymbol{\epsilon} &= \text{tr } \boldsymbol{\epsilon}^{e(\text{I})} + \text{tr } \boldsymbol{\epsilon}^{e(\text{II})} + \text{tr } \boldsymbol{\epsilon}^{e(\text{III})} + \text{tr } \boldsymbol{\epsilon}^{e(\text{IV})} + \text{tr } \boldsymbol{\epsilon}^T, \\
 \Delta v^p &= n_p \text{tr } \boldsymbol{\epsilon}^{e(\text{I})} + ? \text{tr } \boldsymbol{\epsilon}^{e(\text{II})} + ? \text{tr } \boldsymbol{\epsilon}^{e(\text{III})} + \text{tr } \boldsymbol{\epsilon}^{e(\text{IV})} + n_p \text{tr } \boldsymbol{\epsilon}^T, \\
 \Delta v^f &= n_f \text{tr } \boldsymbol{\epsilon}^{e(\text{I})} + n_f \text{tr } \boldsymbol{\epsilon}^{e(\text{II})} + ? \text{tr } \boldsymbol{\epsilon}^{e(\text{III})} + \text{tr } \boldsymbol{\epsilon}^{e(\text{IV})} + n_f \text{tr } \boldsymbol{\epsilon}^T.
 \end{aligned} \tag{2.139}$$

(I)                      (II)                      (III)                      (IV)                      (Th)

Note that no strain is observed during the fourth stress state  $\text{tr } \boldsymbol{\epsilon}^{e(\text{IV})} = 0$ . Writing the previous equations in a more explicit form, requires the introduction of three unknown parameters, namely  $\tilde{A}$ ,  $\tilde{B}$  and  $\tilde{C}$ . The unknown parameters have a tilde accent so as to be easily spotted in the further development:

$$\begin{aligned}
 \text{tr } \boldsymbol{\epsilon} &= c_s (-p_p) + c_p (p_p - p_f) + c (-p + p_f) + c_T \Delta T_s, \\
 \Delta v^p &= n_p c_s (-p_p) + \tilde{A} c_p (p_p - p_f) + \tilde{B} c (-p + p_f) + n_p c_T \Delta T_s, \\
 \Delta v^f &= n_f c_s (-p_p) + n_f c_p (p_p - p_f) + \tilde{C} c (-p + p_f) + n_f c_T \Delta T_s.
 \end{aligned} \tag{2.140}$$

(I)                      (II)                      (III)                      (Th)

Consequently, if both the thermal and the mechanical stresses are accounted for, the previous incomplete system can be rearranged to,

$$\begin{aligned}
 \text{tr } \boldsymbol{\epsilon} &= c (-p) + (c_p - c_s) p_p + (c - c_p) p_f + c_T \Delta T_s, \\
 \Delta v^p &= \tilde{B} c (-p) + (\tilde{A} c_p - n_p c_s) p_p + (\tilde{B} c - \tilde{A} c_p) p_f + n_p c_T \Delta T_s, \\
 \Delta v^f &= \tilde{C} c (-p) + n_f (c_p - c_s) p_p + (\tilde{C} c - n_f c_p) p_f + n_f c_T \Delta T_s.
 \end{aligned} \tag{2.141}$$

(5) The solid entropy relation is now extended to porous media with double porosity. As entropy is one of the factors that determines the free energy of the system, its expression is required. The expression of the fluid entropies are defined separately in Section 2.2.2.3. Note that the temperature variations of the two fluid phases do not appear in the mechanical part of the CD equality (2.120).

The entropy of the solid constituent can be defined as a function of the generalised stresses:  $p$ ,  $p_p$ ,  $p_f$  and  $\Delta T_s$  if the generic tensor of equation (2.129)  $\psi^e$  is replaced by  $\rho^s \Delta S_s$ . In addition, for purely thermal loading  $\Delta T_s \neq 0$ , zero stress and pressure variations  $p = p_p = p_f = 0$ , the parameter  $\alpha_{T_s}$  which represents the molecular excitation of the solid constituent due to the temperature variation controls the entropy variation,

$$\rho^s \Delta S_s = ? \text{tr } \boldsymbol{\epsilon}^{e(\text{I})} + ? \text{tr } \boldsymbol{\epsilon}^{e(\text{II})} + ? \text{tr } \boldsymbol{\epsilon}^{e(\text{III})} + ? \text{tr } \boldsymbol{\epsilon}^{e(\text{IV})} + \alpha_{T_s} \Delta T_s. \tag{2.142}$$

(I)                      (II)                      (III)                      (IV)                      (Th)

Again, no strain is observed during the fourth stress state  $\text{tr } \boldsymbol{\epsilon}^{e(\text{IV})} = 0$ . Writing the previous equations in a more explicit form, requires the introduction of three unknown parameters, namely  $\tilde{D}$ ,  $\tilde{E}$  and  $\tilde{F}$ ,

$$\rho^s \Delta S_s = \underset{\text{(I)}}{\tilde{D} (-p_p)} + \underset{\text{(II)}}{\tilde{E} (p_p - p_f)} + \underset{\text{(III)}}{\tilde{F} (-p + p_f)} + \underset{\text{(T)}}{\alpha_{T_s} \Delta T_s}. \quad (2.143)$$

(6) Consequently, if both the thermal stresses and the mechanical stresses are accounted for in a multi-temperature context, the following system can be cast,

$$\begin{aligned} \text{tr } \boldsymbol{\epsilon} &= c (-p) + (c_p - c_s) p_p + (c - c_p) p_f + c_T \Delta T_s \\ \Delta v^p &= \tilde{B} c (-p) + (\tilde{A} c_p - n_p c_s) p_p + (\tilde{B} c - \tilde{A} c_p) p_f + n_p c_T \Delta T_s \\ \Delta v^f &= \tilde{C} c (-p) + n_f (c_p - c_s) p_p + (\tilde{C} c - n_f c_p) p_f + n_f c_T \Delta T_s \\ \rho^s \Delta S_s &= \tilde{F} (-p) + (\tilde{E} - \tilde{D}) p_p + (\tilde{F} - \tilde{E}) p_f + \alpha_{T_s} \Delta T_s \end{aligned} \quad (2.144)$$

This system is said to be complete as it contains the same number of generalised strains,  $\text{tr } \boldsymbol{\epsilon}$ ,  $\Delta v^p$ ,  $\Delta v^f$  and  $\rho^s \Delta S_s$ ; as generalised stresses,  $p$ ,  $p_p$ ,  $p_f$  and  $\Delta T_s$ .

### 2.2.2.3 The thermo-mechanical properties of fluids

Let us start by introducing and defining the thermodynamical potentials: the internal energy, the Helmholtz free energy, the enthalpy and the chemical potential. A fluid alone is considered (in a single temperature context), by contrast with a fluid within a porous medium (in a multi-temperature context). Hence, the non-modified thermodynamics functions are presented. Next, the thermo-mechanical properties for a single fluid species issued from Mandel (1974, p. 102) and Drumheller (1998, p. 321) are presented along with the explicit forms of the thermodynamical potentials for latter use. In addition, the variation of the thermodynamical potentials with pressure and temperature is illustrated. Finally, the thermo-mechanical behaviour of fluids within a porous medium with double porosity in a multi-temperature context is described.

(1) The thermodynamical potentials used here, namely the internal energy  $U$ , the Helmholtz free energy  $E$ , the enthalpy  $H$  and the free enthalpy  $G$  (also called the chemical potential) are measured per unit mass. The knowledge of the internal energy provides the free energy, the enthalpy and the free enthalpy, see Table 2.1. Expressions for all other

thermodynamic energy potentials are derivable *via* Legendre transforms from an expression for  $U$ .

Measure	Variable	Increment
Internal energy	$U = U(v, S)$	$dU = -p dv + T dS$
Free energy	$E = E(v, T) = U - T S$	$dE = -p dv - S dT$
Enthalpy	$H = H(p, S) = U + p v$	$dH = v dp + T dS$
Free enthalpy	$G = G(p, T) = H - T S$	$dG = v dp - S dT$

Table 2.1: Thermodynamical measures of the state. Note that the increment definitions are arbitrary; therefore the total derivative  $d(\cdot)$  may be replaced by the gradient operator  $\nabla(\cdot)$  or by the partial derivative  $\partial(\cdot)$ .

The internal energy is a thermodynamic potential whose natural independent state variables are strain and entropy. The Helmholtz free energy is specified as a function of strain and temperature; the enthalpy is expressed in terms of stress and entropy; and the free enthalpy (or chemical potential) is expressed in terms of stress and temperature. In the case of a fluid, strain is represented by the specific volume  $v$  and stress by the pressure  $p$ .

The variables that are held constant in this process are termed the natural variables of that potential. The natural variables are important not only for the above mentioned reason, but also because if a thermodynamic potential can be determined as a function of its natural variables, all the thermodynamic properties of the system can be found by taking partial derivatives of that potential with respect to its natural variables and this is true for no other combination of variables.

An intensive property (also called a bulk property) of a system is a physical property of the system that does not depend on the system size or on the amount of material in the system. By contrast, an extensive property of a system does depend on the system size or on the amount of material in the system. The volume, the energy, the entropy and the enthalpy are extensive properties; while pressure, temperature and the specific energy (measured per unit mass or unit volume) are intensive properties.

(2) The thermo-mechanical behaviour of a single fluid is now presented. Let  $v = 1/\rho$  be *the specific volume of the fluid*. The properties of liquids subjected to uniform pressure can often be approximated by the assumption of perfect incompressibility. When such an assumption is inadequate, the *coefficient of thermal expansion*  $c_T$  and the *coefficient of the isothermal compressibility*  $c_H$  are introduced,

$$c_T = \frac{1}{v} \frac{\partial v}{\partial T} \Big|_p = -\frac{1}{\rho} \frac{\partial \rho}{\partial T} \Big|_p, \quad c_H = -\frac{1}{v} \frac{\partial v}{\partial p} \Big|_T = \frac{1}{\rho} \frac{\partial \rho}{\partial p} \Big|_T. \quad (2.145)$$

Stability requires that  $c_H$  must be positive, whereas  $c_T$  may be positive or negative. For example at maximum density the coefficient of thermal expansion of water vanishes, and it becomes negative at lower temperatures; it is also negative for ice between absolute zero and about 80 K. The incremental variation of the specific volume for a compressible and dilatable fluid is derived,

$$\frac{dv}{v} = c_T dT - c_H dp, \quad (2.146)$$

which shows that a knowledge of the functions  $c_T(p, T)$  and  $c_H(p, T)$  together with the reference value  $v_0(p_0, T_0)$  is equivalent to the knowledge of the thermal equation of state integrated from equation (2.146). Since  $v$  is a state function, the coefficients of thermal expansion  $c_T$  and of isothermal compressibility  $c_H$  are related through,

$$\frac{\partial c_T}{\partial p} \Big|_T = -\frac{\partial c_H}{\partial T} \Big|_p. \quad (2.147)$$

The preceding compatibility relation demonstrates that the assumption  $c_T = \text{cste}$  and  $c_H = \text{cste}$  is thermodynamically consistent. In this case, the specific volume can be written,

$$v = v_0 \exp(-c_H (p - p_0) + c_T (T - T_0)). \quad (2.148)$$

Let  $\mathcal{L}$  be the *latent heat* with respect to volume of unit [J/kg] and  $C_v$  the *heat capacity at constant volume* of unit [J/kg.K]. The differential of the entropy  $S$  may be written in the format,

$$T dS = \rho \mathcal{L} dv + C_v dT, \quad \text{where} \quad \rho \mathcal{L} = T \frac{\partial p}{\partial T} \Big|_v, \quad C_v = T \frac{\partial S}{\partial T} \Big|_v, \quad (2.149)$$

and by comparing equation (2.149)<sub>2</sub> to equation (2.146), the latent heat is defined as,

$$\rho \mathcal{L} = T \frac{c_T}{c_H}. \quad (2.150)$$

In equation (2.149) the entropy is expressed as a function of the specific volume  $v$  and of the temperature  $T$ . However the entropy may be expressed in terms of other variables once it is known in terms of one couple,

$$T dS = \rho \mathcal{L} dv + C_v dT = \xi dp + C_p dT = \zeta dv + \eta dp, \quad (2.151)$$

in which,

$$C_p - C_v = T v \frac{c_T^2}{c_H}, \quad \xi = -c_T v T, \quad \zeta = \frac{C_p}{c_T v}, \quad \eta = \frac{c_H}{c_T} C_v. \quad (2.152)$$

Note that,

$$\frac{dp}{dv} = -\frac{1}{c_H v} \times \begin{cases} 1 & \text{isothermal process} \\ \gamma & \text{isentropic process} \end{cases}, \quad (2.153)$$

with

$$\gamma = \frac{C_p}{C_v} = 1 + \frac{v c_T^2 T}{c_H C_v} \quad (2.154)$$

being the adiabatic coefficient.  $\gamma$  is close to one for fluids (1 at 4 °C, 1.024 for water at room temperature and 1.08 at 80 °C) and metals, about 1.3 to 1.7 for real gases at room temperature. It is important to note that the properties defined so far in this section are tangent properties, and not secant properties, since they are defined through differentials, and not finite increments. For a fluid which is incompressible ( $c_H = 0$ ) and not dilatible ( $c_T = 0$ ), the previous relations reduce to,

$$\xi = 0, \quad T dS = dU = C dT, \quad \text{and,} \quad C = C_v = C_p = C(T). \quad (2.155)$$

The detailed expressions of the chemical potential  $G$  and of the internal energy  $U$  are sought. The expressions of the enthalpy  $H$  and the free energy  $E$  can be deduced from the  $G$  and  $U$ , through their definitions in Table 2.1. The index 0 refers to the reference state ( $p = p_0, T = T_0$ ). The complete thermodynamic state is known, to within three arbitrary constants only: for example  $v_0, S_0$  and  $G_0$ , see Remark 2.14. The reference potentials express in terms of the quantities  $(p_0, T_0), v_0$  and  $(S_0, G_0)$ ,

$$H_0 = G_0 + T_0 S_0, \quad E_0 = G_0 - p_0 v_0, \quad U_0 = G_0 + T_0 S_0 - p_0 v_0. \quad (2.156)$$

**Remark 2.14.** *The reference value of the chemical potential  $G_0$  may be seen as containing some history of the species. In practice, it can be used as a degree of freedom to ensure chemical equilibrium of a species at interface between two phases.*

The status of the reference entropy  $S_0$  is different. Kestin (1968) discusses at length the issue of reference entropy, see Remark 2.15. He deduces from the third law of thermodynamics that the derivative with respect to temperature of internal energy, free energy, enthalpy and free enthalpy should vanish as the temperature  $T$  tends to 0 K. The third law of thermodynamics does not seem to be much of help at ambient temperature.

**Remark 2.15.** The initial entropy, introduced in equation (2.156) is a priori unknown. Due to the potential nature of the entropy function, it is impossible to attribute a numerical value to  $S_0$ , except a quite arbitrary one.

Kestin (1968) defines the initial entropy by use of thermodynamics. The third law of thermodynamics provides an elegant answer to the definition of equilibrium functions such as standard entropy because it asserts that entropy should vanish at absolute zero of temperature,  $T = 0$  K. This statement induces the specific heat and the thermal expansion coefficient to be temperature dependent, since our soil mechanics applications occur on a small range of temperatures, from  $0^\circ$  C to  $100^\circ$  C, the hypothesis of constant specific heat and thermal dilatation can be preserved. Variation of entropy with temperature for water may be found in, Kestin (1968, p. 472). Note also that in practice Kestin (1968, p. 484) assumes a zero entropy at  $0^\circ$  C.

Regarding the detailed expressions of the thermodynamic potentials, three successive assumptions are proposed (Loret, 2008):

*Assumption 1:* The coefficient of compressibility  $c_H$  is constant, the thermal dilatation coefficient is a function of the temperature only:  $c_T = c_T(T)$ . The integrability condition of the entropy implies,

$$C_v(v, T) = C_v(v_0, T) + \frac{T(v - v_0)}{c_H} \frac{dc_T(T)}{dT}. \quad (2.157)$$

Then,

$$\begin{aligned} v &= v_0 \exp[-c_H(p - p_0) + I(c_T(T))(T, T_0)], \\ S - S_0 &= \frac{c_T}{c_H}(v - v_0) + \int_{T_0}^T \frac{C_v(x)}{x} dx, \\ G - G_0 &= -\frac{v - v_0}{c_H} + -S_0(T - T_0) + \frac{v_0}{c_H} I(c_T(T))(T, T_0) - \int_{T_0}^T \int_{T_0}^T \frac{C_v(x)}{x} dx dy, \end{aligned} \quad (2.158)$$

where,

$$I(c_T(T))(T, T_0) = \int_{T_0}^T c_T(x) dx. \quad (2.159)$$

The complete knowledge of the entropy and of the chemical potential requires the heat capacity  $C_v = C_v(v, T)$  to be prescribed, and the reference values of the specific volume  $v_0$ , the entropy  $S_0$  and of the chemical potential  $G_0$  to be given, see Remarks 2.14 and 2.15.

*Assumption 2:* If, in addition, the heat capacity  $C_v$  is constant,  $C_{v_0} = C_v(v_0, T) = C_v(v_0, T_0)$  then (see Demonstration 2.6 for  $G - G_0$ )

$$\begin{aligned} S - S_0 &= \frac{c_T}{c_H} (v - v_0) + C_{v_0} \ln \frac{T}{T_0}, \\ G - G_0 &= -\frac{v - v_0}{c_H} + (C_{v_0} - S_0) (T - T_0) + \frac{v_0}{c_H} I(c_T(T))(T, T_0) \\ &\quad - C_{v_0} T \ln \frac{T}{T_0}, \\ H - H_0 &= -\frac{(v - v_0)}{c_H} (1 - T c_T) + C_{v_0} (T - T_0) + \frac{v_0}{c_H} I(c_T(T))(T, T_0), \quad (2.160) \\ E - E_0 &= -(p - p_0)v - (p_0 + \frac{1}{c_H})(v - v_0) + (C_{v_0} - S_0) (T - T_0) \\ &\quad + \frac{v_0}{c_H} I(c_T(T))(T, T_0) - C_{v_0} T \ln \frac{T}{T_0}, \\ U - U_0 &= -(p - p_0)v - (p_0 + \frac{1 - c_T T}{c_H})(v - v_0) + C_{v_0} (T - T_0) \\ &\quad + \frac{v_0}{c_H} I(c_T(T))(T, T_0). \end{aligned}$$

Upon linearization at *first* order about the reference state  $(p_0, T_0)$ ,

$$\begin{aligned} v - v_0 &= -v_0 c_H (p - p_0) + v_0 I(c_T(T))(T, T_0), \\ S - S_0 &= -c_T v_0 (p - p_0) + \frac{C'_{p_0}}{T_0} (T - T_0), \\ G - G_0 &= v_0 (p - p_0) - S_0 (T - T_0), \quad (2.161) \\ H - H_0 &= v_0 (1 - T_0 c_T) (p - p_0) + C'_{p_0} (T - T_0), \end{aligned}$$



$$E - E_0 = p_0 v_0 c_H(p - p_0) - S_0(T - T_0) - p_0 v_0 I(c_T(T))(T, T_0),$$

$$U - U_0 = v_0(p_0 c_H - c_T T_0)(p - p_0) + C'_{p_0}(T - T_0) - p_0 v_0 I(c_T(T))(T, T_0).$$

where the secant heat capacity  $C'_{p_0}$  is defined by,

$$C'_{p_0} = C_{v_0} + \frac{v_0 c_T}{c_H} \frac{T_0}{T - T_0} I(c_T(T))(T, T_0). \quad (2.162)$$

It is worth noting that the linearised chemical potential and free energy show an affine dependence on the reference entropy. Similarly, the free energy and the internal energy show an affine dependence on the reference pressure. Entropy is increased by an increase of temperature, and by a decrease of pressure. Conversely pressure increase implies an increase of free energy, free enthalpy and enthalpy. As for the internal energy, the influence of pressure is parameter and reference dependent.

Equation (2.153) induces the pressure increment,

$$p - p_0 = \begin{cases} -\frac{1}{c_H} \frac{v - v_0}{v_0} & + \frac{I(c_T)(T, T_0)}{c_H (T - T_0)} (T - T_0) \\ -\frac{1}{c_{HS=S_0}} \frac{v - v_0}{v_0} & + \frac{T_0 I(c_T)(T, T_0)}{C_v c_H (T - T_0)} (S - S_0) \end{cases} \quad (2.163)$$

to be expressed in terms of volume change and temperature change *via* the isothermal compressibility  $c_H$ , or in terms of volume change and entropy *via* the isentropic (or adiabatic) compressibility  $c_{HS=S_0}$ ,

$$\frac{1}{c_{HS=S_0}} = \frac{1}{c_H} + \frac{1}{c_H^2} \frac{v_0}{C_{v_0}} c_T T_0 \frac{I(c_T)(T, T_0)}{T - T_0} = \frac{C'_{p_0}}{c_H C_{v_0}}. \quad (2.164)$$

*Assumption 3:* If in addition, the fluid is incompressible ( $c_H = 0$ ) and not dilatable ( $c_T = 0$ ), then equation (2.155) implies  $C_p = C_v = C_{v_0} = C$ , and,

$$S - S_0 = C \ln \frac{T}{T_0},$$

$$G - G_0 = v_0(p - p_0) + (C - S_0)(T - T_0) - C T \ln \frac{T}{T_0},$$

$$H - H_0 = v_0(p - p_0) + C(T - T_0), \quad (2.165)$$

$$E - E_0 = (C - S_0)(T - T_0) - c_T \ln \frac{T}{T_0},$$

$$U - U_0 = C(T - T_0)$$

Note that in this limit case the pressure influence survives in the enthalpy and the free energy only.

---

**Demonstration 2.6.** *Proof of equation (2.160)<sub>2</sub>: The incremental of the chemical potential is defined as follows:  $dG = v dp - S dT$ . Hence,*

$$\begin{cases} \frac{\partial G}{\partial T} = -S = -S_0 - \frac{c_T}{c_H}(v - v_0) - C_{v_0} \ln \frac{T}{T_0}, \\ \frac{\partial G}{\partial p} = v = v_0 \exp[-c_H(p - p_0) + I(c_T)(T, T_0)]. \end{cases} \quad (2.166)$$

By integrating equation (2.166)<sub>2</sub> and considering  $f(T)$  as an unknown function of the temperature  $T$ ,  $G - G_0$  becomes,

$$G - G_0 = -\frac{v - v_0}{c_H} + f(T). \quad (2.167)$$

The previous equality is derived in respect to temperature, which is also equal to equation (2.166)<sub>1</sub>,

$$\frac{\partial G}{\partial T} = -\frac{c_T(T)v}{c_H} + \frac{\partial f(T)}{\partial T} = \frac{\partial G}{\partial T} = -S_0 - \frac{c_T(T)}{c_H}(v - v_0) - C_{v_0} \ln \frac{T}{T_0}. \quad (2.168)$$

Therefore, the partial derivative of the unknown function  $f(T)$  is,

$$\frac{\partial f(T)}{\partial T} = -S_0 + \frac{c_T(T)v_0}{c_H} - C_{v_0} \ln \frac{T}{T_0}, \quad (2.169)$$

and  $f(T)$  can be identified by being integrated to,

$$f(T) - f_0(T) = (C_{v_0} - S_0)(T - T_0) + \frac{v_0}{c_H} I(c_T(T))(T, T_0) - C_{v_0} T \ln \frac{T}{T_0}. \quad (2.170)$$

By replacing the latter relation into (2.167), eq. (2.160)<sub>2</sub> is recovered. The other relations of the enthalpy  $H$ , the free energy  $E$  and of the internal energy  $U$  can be deduced from  $G$  and from their definitions, see Table 2.1.

□

---

(3) The variation of thermal properties and of thermodynamical potentials with temperature are now illustrated. Table 2.2 displays some physical properties of water. Its heat capacity is the next largest among liquids after ammonia. Heat capacity of sea water is slightly smaller. The dynamic viscosity of pure water is equal to  $1 \times 10^{-3}$  Pa.s at 20 °C.

The thermal expansion coefficient of water substance undergoes a negative jump at 0 °C (Figure 2.6). It increases monotonically between 0 °C and 100 °C, passing through a null value just below 4 °C (Kestin, 1968, p. 264). In the liquid state, it can be approximated by an affine function for temperature (unit of constant 1/K),

$$c_T(T) = -0.0067 \times 10^{-3} + 0.00819 \times 10^{-3} \times (T - 273), \quad T \in ]273, 373 \text{ K}[ \quad (2.171)$$

Temperature	Density	Heat capacity	Thermal expansion*	Bulk modulus*	Dynamic viscosity
$T$ [°C]	$\rho$ [kg/m <sup>3</sup> ]	$C_p$ [kJ/kg.K]	$c_T$ [10 <sup>-3</sup> /K]	$K$ [GPa]	$\mu$ [10 <sup>-3</sup> Pa.s]
0 (ice)	916.8	—	0.158	—	—
0 (liquid)	999.8	4.210	-0.067	1.97	1.789
2	—	—	-0.031	—	1.52
4	1000.0	—	0.001	—	1.52
25	997.1	4.181	0.256	2.21	0.89
40	992.3	4.179	0.390	2.28	0.653
55	986	4.183	0.493	2.29	0.504
75	975	4.194	0.614	2.25	—
100 (liquid)	958	4.219	0.752	—	0.282

Table 2.2: Some physical properties of pure water, from <http://www.engineeringtoolbox.com> and \* from Kestin (1968, p. 541).

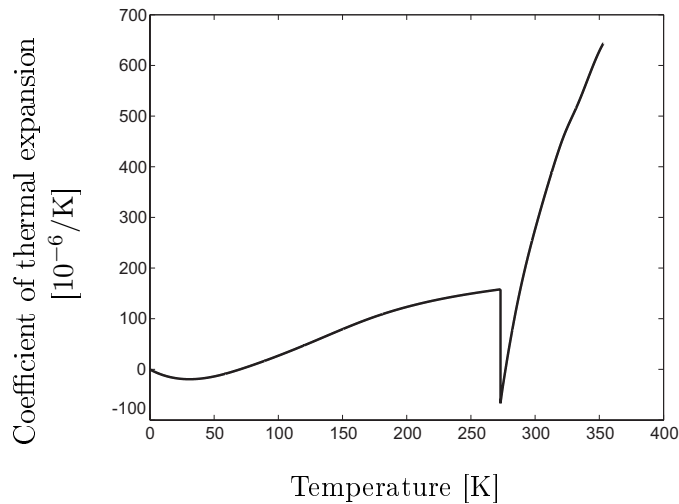


Figure 2.6: Coefficient of thermal expansion  $c_T$  of ice and water at atmospheric pressure.

The variation of the heat capacity  $C_v$  with temperature, as implied by the second term in the right-hand-side of equation (2.157), can now be estimated: for a temperature change of 100 °C, the ratio of this term relative to  $C_v$  is approximately 0.0043.

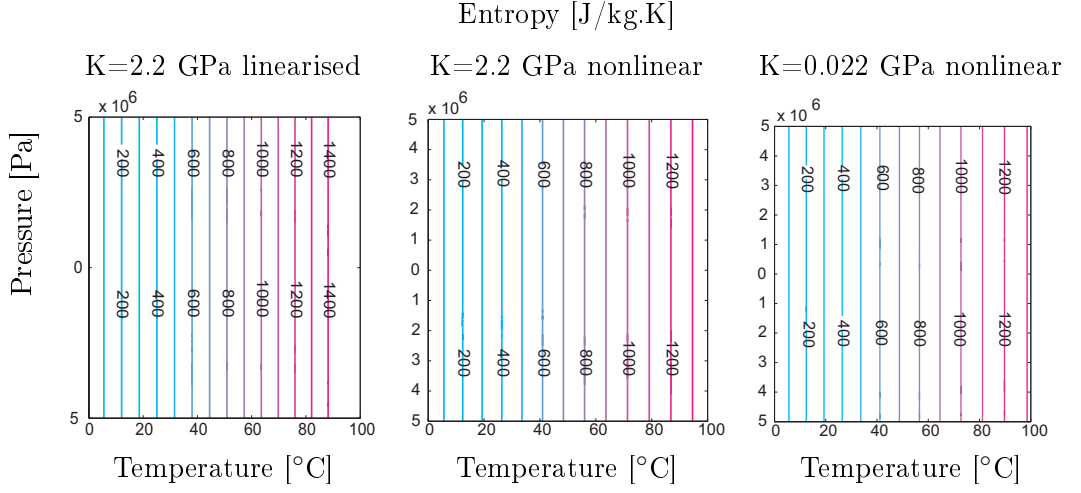


Figure 2.7: Entropy of water for  $K = 1/c_H = 2.2$  GPa,  $C_p = 4.18$  KJ/kg/K, and the reference values  $p_0 = 0$  Pa,  $T_0 = 0$  °C,  $v_0 = 10^{-3}$  m<sup>3</sup>/kg,  $S_0 = 0$  J/kg/K,  $\mu_0 = 0$  J/kg/K. The left and center contour plots display the linearised and non linear entropies respectively for  $K = 2.2$  GPa, and the right contour plot displays the nonlinear entropy for  $K = 0.022$  GPa.

The above data are employed to obtain contour plots of the thermodynamic functions, see Figure 2.7 and 2.8. For pressure variations of a few atmospheres and null initial pressure and temperature, the mechanical contributions to the thermodynamic potentials are largely outweighed by the thermal contribution, so that it comes into picture essentially under isothermal conditions. The plots show that this conclusion holds true even if water contains air bubble that reduces the bulk modulus by two orders of magnitude.

These figures also allow to assess the accuracy of the linearised expressions (2.161) with respect to the nonlinear relations (2.160). The first order linearised expression of the chemical potential appears as a very rough approximation for  $S_0 = 0$ . Moreover, these plots validate the accuracy of the linearised entropy function, which participate to the constitutive behaviour for the fluids.

---

**Proposition 2.3.** *Thermal and mechanical equilibrium*

*The fact that the thermal contribution dominates the mechanical contribution in the chemical potential has an immediate consequence: for temperature in the range of  $[0^\circ\text{C}, 100^\circ\text{C}]$ , and pressures of a few atmospheres, thermal disequilibrium gives rise to much larger forces than mechanical disequilibrium. Trend towards thermal equilibrium is thus stronger than trend towards mechanical equilibrium.*

---

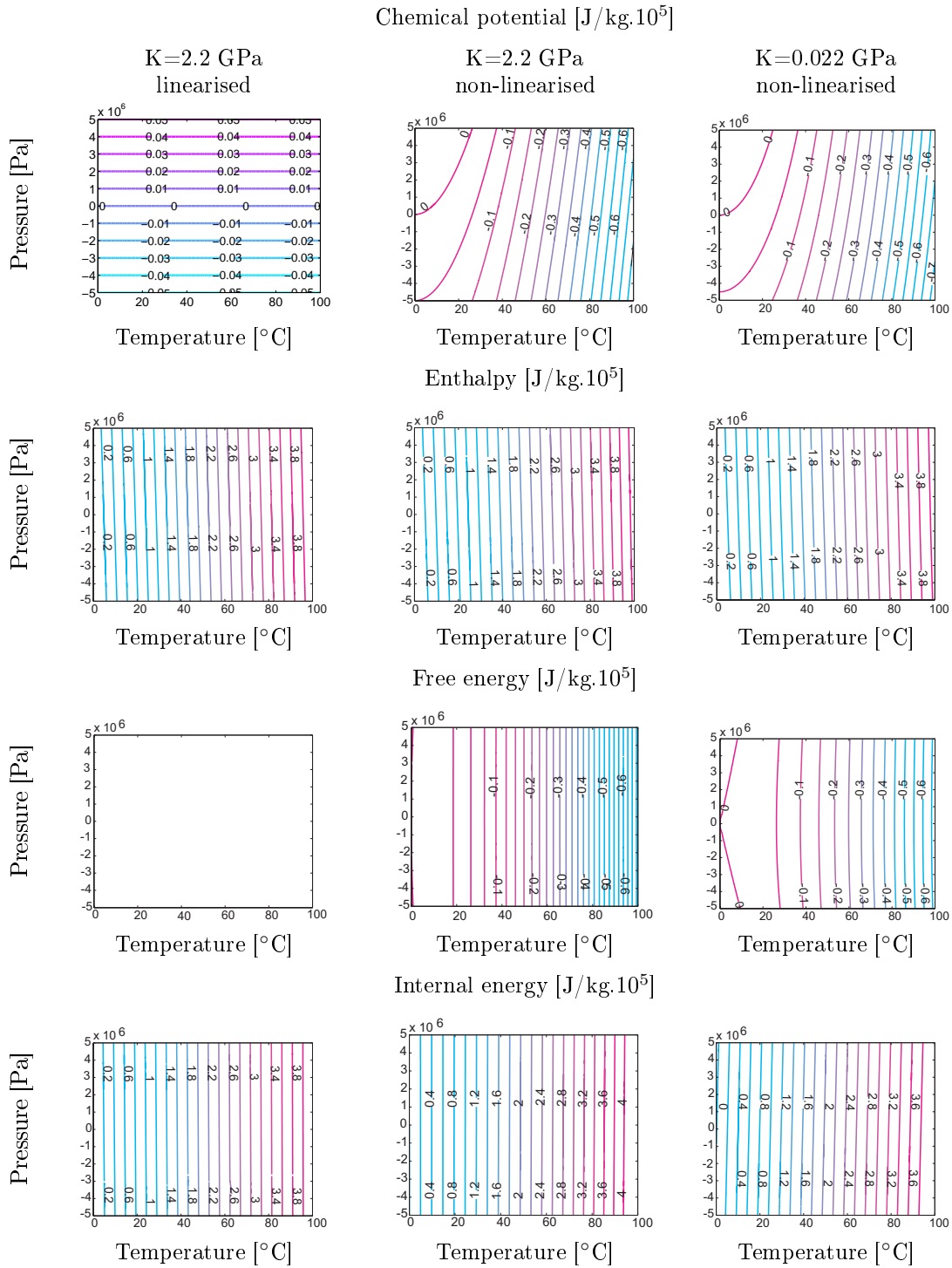


Figure 2.8: Chemical potential, enthalpy, free energy, and internal energy of water, as a function of temperature and pressure. Same data as Figure 2.7.

The influence of the pressure range and of the initial temperature  $T_0$  is analysed on the representation of the entropy and of the chemical potential as a function of temperature and pressure. Due to the fact that in most geotechnical applications air (or gas) bubbles

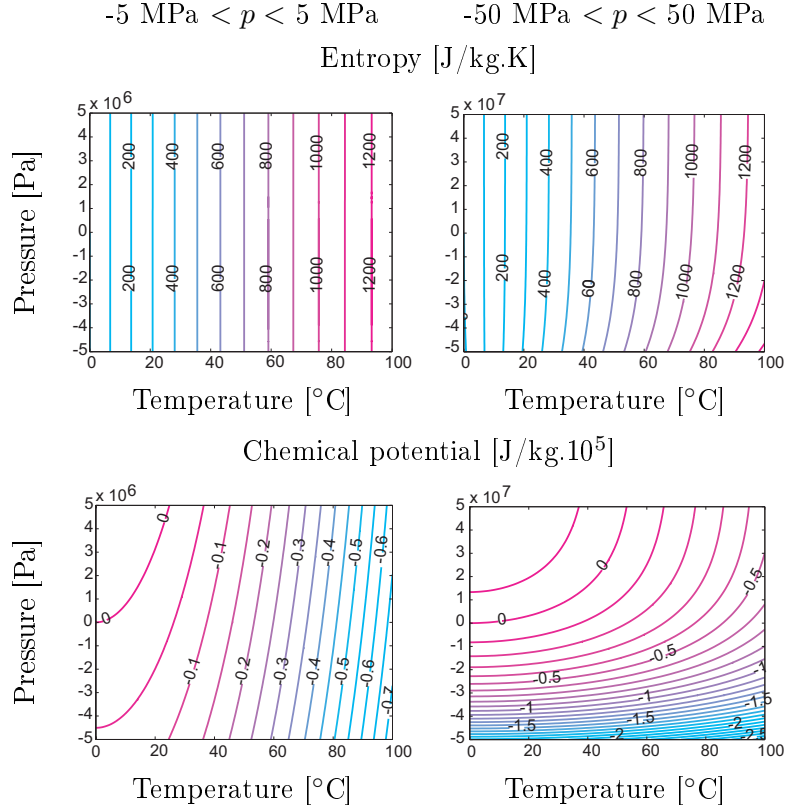


Figure 2.9: Entropy and chemical potential as a function of temperature and pressure. Same data as Figure 2.7;  $K = 0.022$  GPa (involving air bubbles) and using the non linear relations. Comparing the influence of the pressure range.

are trapped in the underground fluid, a bulk modulus  $K$  a hundred times smaller than the one of pure water is used, i.e.  $K = 0.022$  GPa.

Figure 2.9 aims at evaluating the influence of the range of pressure on the entropy and the chemical potential. The thermal contributions are still dominating the mechanical contributions, for the entropy function, when considering a pressure range from -50 MPa to 50 MPa. On the contrary for the chemical potential function, the mechanical contributions are greater than the thermal contributions in the lower-left part of the graph, and the thermal contributions are overwhelming the mechanical contributions in the upper-right part of the graph. The influence of the pressure versus the temperature is better viewed when considering a wider pressure range. Consequently, Proposition 2.3 will remain true only for a certain range of pressure-temperature.

Figure 2.10 presents the influence of the initial temperature on the entropy and on the chemical potential representation. Three initial temperatures are compared:  $T_0 = 0^\circ\text{C}$ ,  $T_0 = 25^\circ\text{C}$  and  $T_0 = 50^\circ\text{C}$ . The range of pressure used for this comparison goes from -50 MPa to 50 MPa, so that to have the most general overview of  $T_0$  influence. When increasing the

initial temperature, both the entropy and the chemical potential contour plot shift to the right. In other words, the higher the initial temperature, the later (at higher temperatures) will the zero line be encountered.

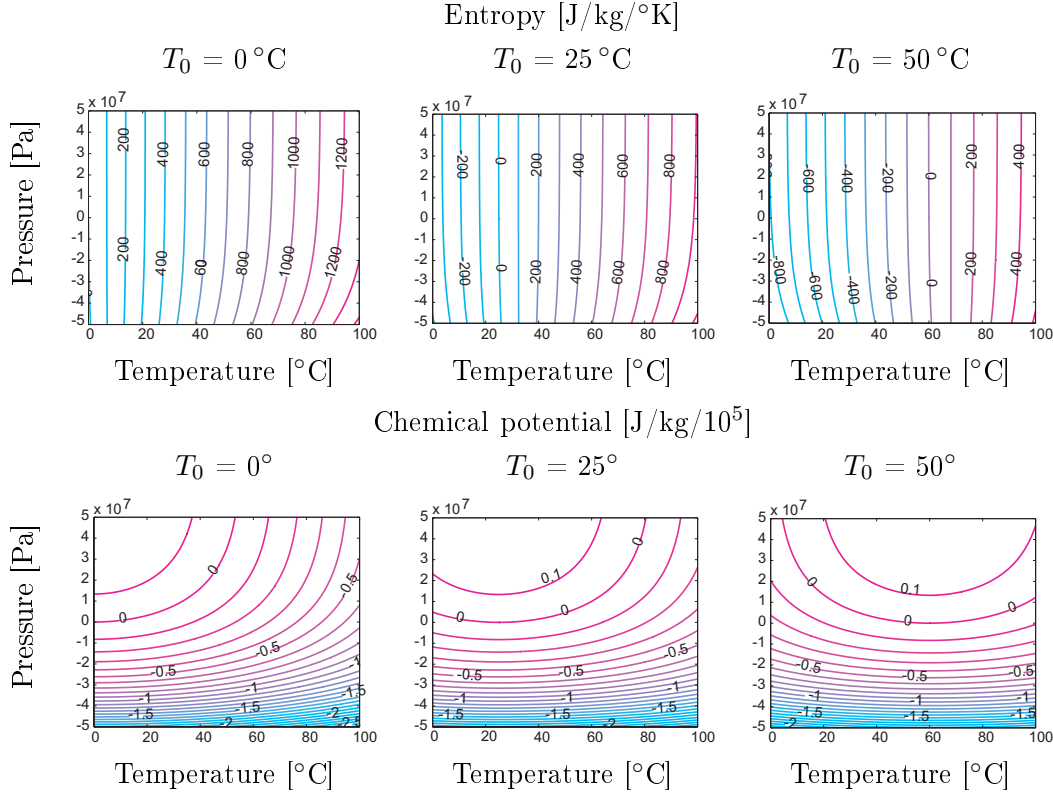


Figure 2.10: Entropy and chemical potential as a function of temperature and pressure. Same data as Figure 2.9 except for the pressure range :  $-50 \text{ MPa} < p < 50 \text{ MPa}$ ;  $K = 0.022 \text{ GPa}$  (involving air bubbles) and using the non linear relations. Comparing the influence of the initial temperature.

(4) The thermo-mechanical behaviour of fluids within a multi-temperature mixture is now examined. Within a dual porosity mixture, the two fluids are assumed to be physically separated, that is to say the pore fluid is in the porous block and the fissure fluid is in the fissure network. The two fluids do not interact except through transfer. In addition, each fluid is endowed with its own *modified* pressure and *modified* temperature. Therefore, each phase of the mixture is saturated with a slightly compressible fluid and can be in a different state in each pore type. Consequently, the fluids densities  $\rho_k$ , the hydraulic compressibilities  $c_{kH}$  and the thermal expansion coefficients  $c_{kT}$  are assumed *different* in each type of void,

$$c_{kH} = \frac{1}{\rho_k} \left. \frac{\partial \rho_k}{\partial p_k} \right|_{T_k}, \quad c_{kT} = -\frac{1}{\rho_k} \left. \frac{\partial \rho_k}{\partial T_k} \right|_{p_k}, \quad k = p, f. \quad (2.172)$$

and the relationship relating the density change of a fluid to a pressure change and to a temperature change,  $\rho_k = f(p_k, T_k)$  is,

$$\frac{1}{\rho_k} \frac{\partial \rho_k}{\partial t} = c_{kH} \frac{\partial p_k}{\partial t} - c_{kT} \frac{\partial T_k}{\partial t}, \quad k = p, f. \quad (2.173)$$

Furthermore, since the two fluids are assumed to be of the same nature, no meniscus is accounted for in the chemical potential differential formulas, see Remark 2.16.

**Remark 2.16.** *A reflection on the influence of the meniscus is now proposed. The meniscus separating the two liquid phases has only a significant contribution when the two liquids are of different nature, e.g. water and oil (Loret and Khalili, 2000b,a). In the further development the fluid phases are assumed to be of same nature and the strain-energy due to the influence of the meniscus is neglected.*

*The presence of menisci modifies the expression of the entropy  $S_k$  of the fluid  $k$ , which becomes  $S_k + G_k^m$ . Therefore the chemical potential expression of the fluid  $k$  is also modified. Accounting for the influence of menisci is recommended if the two fluid phases are of different nature, e.g. water and oil or water and air.*

#### 2.2.2.4 Isothermal Mechanical secant relation

To ease the global understanding, a mixture in local thermal equilibrium is firstly considered. The local thermal non-equilibrium case will be addressed in Subsection 2.2.2.5. The elastic constitutive equation for saturated soils with double porosity links the generalised stresses to the generalised (elastic) strains through a secant formulation (Khalili and Valliappan, 1996). Let us begin by the evaluation of the shear stress and of the pressure stress contributions.

The shear behaviour is accounted for, fully, by the shear modulus  $\mu^{DS}$  of the drained solid skeleton. The fluid does not react to shear stresses. The associated relationship is,

$$\boldsymbol{\epsilon}^e = \mathbf{C}^{DS} : \bar{\boldsymbol{\sigma}} \quad \text{and} \quad \text{tr } \boldsymbol{\epsilon}^e = -c \bar{p}, \quad \text{dev } \boldsymbol{\epsilon}^e = \frac{\text{dev } \bar{\boldsymbol{\sigma}}}{2 \mu^{DS}}. \quad (2.174)$$

On the other hand, the fluids of the pores and of the fissures participate to the isotropic behaviour. The complete mechanical model links the primary variables: total stress, fissure fluid and pore fluid pressures  $\Delta(\boldsymbol{\sigma}, p_p, p_f)$ ; to the dependent variables:  $\Delta(\text{tr } \boldsymbol{\epsilon}^e, v^p, v^f)$  which represent, respectively, the strain of the solid skeleton, the volume changes of the porous block and the fissure network. In our developments in this section, only the isotropic



part is taken into account, in consequence the total stress  $\boldsymbol{\sigma}$  can be replaced by the mean stress  $-p$ , eq. (2.125), and the total elastic deformation  $\boldsymbol{\epsilon}^e$  by its isotropic part  $\text{tr } \boldsymbol{\epsilon}^e$ .

The aim of this analysis is to introduce the link between the generalised stress-strain tensor, through a symmetric tensor  $\mathbf{C}^e$ , the underlying idea being the existence of an elastic potential. In a matrix form,

$$\begin{bmatrix} -\text{tr } \boldsymbol{\epsilon}^e \\ v^p \\ v^f \end{bmatrix} - \begin{bmatrix} -\text{tr } \boldsymbol{\epsilon}_0^e \\ v_0^p \\ v_0^f \end{bmatrix} = \underbrace{\begin{bmatrix} c_{ss} & c_{sp} & c_{sf} \\ c_{ps} & c_{pp} & c_{pf} \\ c_{fs} & c_{fp} & c_{ff} \end{bmatrix}}_{\mathbf{C}^e} \begin{bmatrix} p - p^0 \\ p_p - p_p^0 \\ p_f - p_f^0 \end{bmatrix} \quad (2.175)$$

The proof of the existence of an elastic potential and the identification of the coefficients  $c_{kl}$ ,  $k, l = s, p, f$  proceeds in four steps: (1) First a potential in the form of the differential of the complementary energy  $d\Psi_c^{\text{mech}}$  is introduced. (2) Then, as the complementary energy  $\Psi_c^{\text{mech}}$  is a state function, the properties of state functions and total differentials are resumed. (3) Using the previously introduced properties, the symmetry of the tensor  $\mathbf{C}^e$  is recovered. (4) Finally  $\Psi_c^{\text{mech}}$  is obtained after integration of  $d\Psi_c^{\text{mech}}$ . The existence of the elastic potential allows the secant elastic relation to be established. All the coefficients  $c_{kl}$ ,  $k, l = s, p, f$  are identified.

(1) A thermodynamic property of the mixture, the complementary energy  $\Psi_c^{\text{mech}}$ , is introduced that describes the equilibrium state of the mixture. Since the processed forces are the stress and fluid pressures, the potential defined as the differential of the complementary energy  $\Psi_c^{\text{mech}}(\boldsymbol{\sigma}, p_p, p_f)$  is,

$$d\Psi_c^{\text{mech}} = -d\boldsymbol{\sigma} : \boldsymbol{\epsilon}^e - v^p dp_p - v^f dp_f. \quad (2.176)$$

(2) A summary of the properties of a state function and of a total differential is now proposed. In thermodynamics, a state function, or state quantity, is a property of a system that depends only on the current state of the system, not on the way in which the system got to that state. A state function describes the equilibrium state of a system, for example,

$$d\mathbf{F} = A(x, y) dx + B(x, y) dy. \quad (2.177)$$

The state function  $\mathbf{F}$  is also a differential. This differential is said to be exact (total differential) if the integrand of  $d\mathbf{F}$  is path independent. By way of notation, the symbol  $d(\cdot)$

denotes an exact differential, whereas the symbol  $\partial(\cdot)$  is reserved for inexact differentials, which cannot be integrated without full knowledge of the path.

The total differential of a function of several independent variables, for example  $d\mathbf{F}(x, y)$ , is said to be an exact differential increment. This statement implies that  $d\mathbf{F}(x, y)$  is equal to the sum of its partial differential with respect to each variables,

$$d\mathbf{F} = \left(\frac{\partial\mathbf{F}}{\partial x}\right) dx + \left(\frac{\partial\mathbf{F}}{\partial y}\right) dy. \quad (2.178)$$

Hence, A and B must be of the form,

$$A(x, y) = \frac{\partial\mathbf{F}}{\partial x}, \quad \text{and} \quad B(x, y) = \frac{\partial\mathbf{F}}{\partial y}. \quad (2.179)$$

In three dimensions, a differential  $d\mathbf{F} = A(x, y, z) dx + B(x, y, z) dy + C(x, y, z) dz$  is an exact differential in a simply connected region R of the  $(x, y, z)$  coordinate system if between the functions A, B and C the following relations exist,

$$\left(\frac{\partial A}{\partial y}\right)_{x,z} = \left(\frac{\partial B}{\partial x}\right)_{y,z}; \quad \left(\frac{\partial A}{\partial z}\right)_{x,y} = \left(\frac{\partial C}{\partial x}\right)_{y,z}; \quad \left(\frac{\partial B}{\partial z}\right)_{x,y} = \left(\frac{\partial C}{\partial y}\right)_{x,z}. \quad (2.180)$$

(3) Since the potential  $d\Psi_c^{\text{mech}}$  introduced in equation (2.176) is a total differential which depends only on state variables  $(\boldsymbol{\sigma}, p_p, p_f)$ , the expressions of stress, fluid and pore fluid pressures depending on  $(\text{tr } \boldsymbol{\epsilon}^e, \Delta v^p, \Delta v^f)$  must verify the following conditions,

$$\frac{\partial \boldsymbol{\sigma}}{\partial v^p} = \frac{\partial p_p}{\partial \boldsymbol{\epsilon}^e}, \quad \frac{\partial \boldsymbol{\sigma}}{\partial v^f} = \frac{\partial p_f}{\partial \boldsymbol{\epsilon}^e}, \quad \text{and} \quad \frac{\partial p_p}{\partial v^f} = \frac{\partial p_f}{\partial v^p}. \quad (2.181)$$

Consequently the proof of the symmetry of  $\mathbf{C}^e$  is obtained,

$$c_{sp} = c_{ps}, \quad c_{sf} = c_{fs} \quad \text{and} \quad c_{pf} = c_{fp}. \quad (2.182)$$

(4) The determination of  $\Psi_c^{\text{mech}}$  is recovered by integration. For simplicity, the potential  $\Psi_c^{\text{mech}}(\boldsymbol{\sigma}, p_p, p_f)$  is assumed to be isotropic and quadratic in  $\boldsymbol{\sigma}$ . This hypothesis added to the property (2.179) justifies the following behaviour relationship for the elastic strain and for the volume changes of the pores and the fissures,

$$\boldsymbol{\epsilon}^e = -\frac{\partial \Psi_c^{\text{mech}}}{\partial \boldsymbol{\sigma}}, \quad \Leftrightarrow \text{tr } \boldsymbol{\epsilon}^e = \frac{\partial \Psi_c^{\text{mech}}}{\partial p}, \quad \text{dev } \boldsymbol{\epsilon}^e = -\frac{\partial \Psi_c^{\text{mech}}}{\partial s} = \frac{\mathbf{s}}{2\mu^{DS}} \quad (2.183)$$

$$v^p = -\frac{\partial \Psi_c^{\text{mech}}}{\partial p_p}, \quad v^f = -\frac{\partial \Psi_c^{\text{mech}}}{\partial p_f}. \quad (2.184)$$

The total differential  $\Psi_c^{\text{mech}}$  can be calculated by using the following integration,

$$\Psi_c^{\text{mech}} = \int \frac{\partial \Psi_c^{\text{mech}}}{\partial p} dp + \int \frac{\partial \Psi_c^{\text{mech}}}{\partial p_p} dp_p + \int \frac{\partial \Psi_c^{\text{mech}}}{\partial p_f} dp_f + \int \frac{\partial \Psi_c^{\text{mech}}}{\partial s} ds \quad (2.185)$$

Consequently the integrand of the potential  $d\Psi_c^{\text{mech}}$  can be cast in the following format,

$$\begin{aligned} \Psi_c^{\text{mech}} &= -\frac{1}{2} (c_{ss} p^2 + c_{pp} p_p^2 + c_{ff} p_f^2 + 2 c_{sp} p p_p + 2 c_{sf} p p_f + 2 c_{pf} p_p p_f) \\ &\quad - \frac{1}{4\mu^{DS}} \mathbf{s} : \mathbf{s}. \end{aligned} \quad (2.186)$$

The existence of the potential  $\Psi_c^{\text{mech}}$  has been proved in equation (2.186). Consequently the secant relation can now be established. The latter is detailed as follows: crossing equations (2.183), (2.184) with (2.141) for  $\Delta T_s = 0$ , the secant relation writes,

$$\begin{bmatrix} -\text{tr } \boldsymbol{\epsilon}^e \\ \Delta v^p \\ \Delta v^f \end{bmatrix} = \begin{bmatrix} c & -(c_p - c_s) & -(c - c_p) \\ -\tilde{B} c & \tilde{A} c_p - n_p c_s & \tilde{B} c - \tilde{A} c_p \\ -\tilde{C} c & n_f (c_p - c_s) & \tilde{C} c - n_f c_p \end{bmatrix} \begin{bmatrix} p \\ p_p \\ p_f \end{bmatrix} \quad (2.187)$$

Applying the symmetry conditions of equation (2.182) allows us to identify the unknown parameters  $\tilde{A}$ ,  $\tilde{B}$  and  $\tilde{C}$ .

$$\tilde{A} = \frac{(c_p - c_s)}{c_p} (1 - n_f), \quad \tilde{B} = \frac{(c_p - c_s)}{c}, \quad \text{and} \quad \tilde{C} = \frac{(c - c_p)}{c}. \quad (2.188)$$

Hence, the elastic tensor  $\mathbf{C}^e$  writes in explicit form,

$$\begin{bmatrix} -\text{tr } \boldsymbol{\epsilon}^e \\ \Delta v^p \\ \Delta v^f \end{bmatrix} = \begin{bmatrix} c & -(c_p - c_s) & -(c - c_p) \\ -(c_p - c_s) & c_p (1 - n_f) & n_f (c_p - c_s) \\ -(c - c_p) & -c_s (1 + n_p - n_f) & c - c_p (1 + n_f) \end{bmatrix} \begin{bmatrix} p \\ p_p \\ p_f \end{bmatrix} \quad (2.189)$$

Crucially, the secant relation displays a major symmetry.

**Remark 2.17.** A similar relation to (2.189) can be written with  $(\boldsymbol{\epsilon}^e, p_p, p_f)$  as primary variables, namely the Mixed Secant relation.

### 2.2.2.5 Thermo-Mechanical secant relation

The mechanical elastic secant relation has been defined in Subsection 2.2.2.4. The latter relation is now extended to a thermo-mechanical secant relation (Loret and Khalili, 2000b), using the thermo-mechanical contributions of the Clausius-Duhem inequality, previously introduced in Subsection 2.2.2.1,

$$\left\{ \begin{array}{l} d\Psi_c = -d\boldsymbol{\sigma} : \boldsymbol{\epsilon} - \rho^s S_s dT_s - \sum_{p,f} v^k dp_k, \\ \Rightarrow \quad \boldsymbol{\epsilon} = -\frac{\partial \Psi_c}{\partial \boldsymbol{\sigma}}, \quad -\rho^s S_s = \frac{\partial \Psi_c}{\partial T_s}, \quad -v^k = \frac{\partial \Psi_c}{\partial p_k} \quad k = p, f; \end{array} \right. \quad (2.190)$$

which allowed the constitutive system to be restricted to a set of four primary variables  $\Delta(\boldsymbol{\sigma}, p_p, p_f, T_s)$  related to four dependent variables  $\Delta(\boldsymbol{\epsilon}, v^p, v^f, \rho^s S_s)$ . The thermo-mechanical part of the Clausius-Duhem inequality suggests that the fluid temperatures are not accounted for in the conjugate variables, which recovers the hypothesis that the fluid temperatures do not influence the porous medium thermo-mechanical deformation, see Remark 2.13, p. 117.

The aim is now to introduce the link between the generalised stress-strain tensor, through as symmetric tensor  $\mathbf{C}$ . To do so, the existence of a thermo-elastic potential has to be proved.

$$\begin{bmatrix} -\text{tr } \boldsymbol{\epsilon} \\ v^p \\ v^f \\ \rho^s S_s \end{bmatrix} - \begin{bmatrix} -\text{tr } \boldsymbol{\epsilon}^0 \\ v^{p,0} \\ v^{f,0} \\ \rho^{s,0} S_s^0 \end{bmatrix} = \underbrace{\begin{bmatrix} c_{ss} & c_{sp} & c_{sf} & c_{sT} \\ c_{ps} & c_{pp} & c_{pf} & c_{pT} \\ c_{fs} & c_{fp} & c_{ff} & c_{fT} \\ c_{Ts} & c_{Tp} & c_{Tf} & c_{TT} \end{bmatrix}}_{\mathbf{C}} \begin{bmatrix} p - p^0 \\ p_p - p_p^0 \\ p_f - p_f^0 \\ T_s - T_s^0 \end{bmatrix} \quad (2.191)$$

The proof of the existence of the thermo-elastic potential and the identification of the coefficient  $c_{kl}$ ,  $k, l = s, p, f, T$  is similar to the mechanical elastic behaviour analysis (Subsection 2.2.2.4) in which the potential in the form of the complementary energy  $d\Psi_c(\boldsymbol{\sigma}, p_p, p_f, T_s)$  has already been introduced. Using its total differential properties implies,

$$\boldsymbol{\epsilon} = -\frac{\partial \Psi_c}{\partial \boldsymbol{\sigma}} \quad \Leftrightarrow \quad \text{tr } \boldsymbol{\epsilon} = \frac{\partial \Psi_c}{\partial p}, \quad \text{dev } \boldsymbol{\epsilon} = -\frac{\partial \Psi_c}{\partial \mathbf{s}}$$

$$\rho^s S_s = -\frac{\partial \Psi_c}{\partial T_s} \quad \text{and} \quad v^k = -\frac{\partial \Psi_c}{\partial p_k}, \quad k = p, f. \quad (2.192)$$

In addition to the relations (2.181), the total differential properties of  $d\Psi_c$  bring,

$$\frac{\partial p}{\partial \rho^s S_s} = \frac{\partial T_s}{\partial \text{tr } \boldsymbol{\epsilon}}, \quad \frac{\partial p_p}{\partial \rho^s S_s} = \frac{\partial T_s}{\partial v^p}, \quad \frac{\partial p_f}{\partial (\rho^s S_s)} = \frac{\partial T_s}{\partial v^f}. \quad (2.193)$$

In consequence, the thermo-mechanical tensor linking the generalised stress-strains displays symmetry,

$$c_{Ts} = c_{sT}, \quad c_{Tp} = c_{pT}, \quad \text{and} \quad c_{Tf} = c_{fT} \quad (2.194)$$

The total differential  $\Psi_c$  can be calculated with the following integration,

$$\Psi_c = \Psi_c^{\text{mech}}(\boldsymbol{\sigma}, p_p, p_f) + \int \frac{\partial \Psi_c}{\partial T_s} dT_s \quad (2.195)$$

Considering the result of equation (2.186) as equal to  $\Psi_c^{\text{mech}}(\boldsymbol{\sigma}, p_p, p_f)$ , the thermal modification may be added linearly, to the purely mechanical part with respect to thermal changes,

$$\Psi_c(\boldsymbol{\sigma}, p_p, p_f, T_s) = \Psi_c^{\text{mech}}(\boldsymbol{\sigma}, p_p, p_f) + \int \frac{\partial \Psi_c}{\partial T_s} dT_s \quad (2.196)$$

where,

$$\int \frac{\partial \Psi_c}{\partial T_s} dT_s = -\frac{1}{2} c_{TT} \Delta T_s^2 - \Delta T_s (c_{Ts} p + c_{Tp} p_p + c_{Tf} p_f) + \text{cste} \quad (2.197)$$

Finally, the thermo-elastic potential takes the following form which proves its existence,

$$\begin{aligned} \Psi_c(\boldsymbol{\sigma}, p_p, p_f, T_s) &= -\frac{1}{2} (c_{ss} p^2 + c_{pp} p_p^2 + c_{ff} p_f^2) - c_{sp} p p_p - c_{sf} p p_f \\ &\quad - c_{pf} p_p p_f - \frac{1}{2} c_{TT} \Delta T_s^2 - \Delta T_s (c_{Ts} p + c_{Tp} p_p + c_{Tf} p_f) \\ &\quad - \frac{1}{4\mu^{DS}} \mathbf{s} : \mathbf{s} + \text{cste}. \end{aligned} \quad (2.198)$$

Using equations (2.144), the following secant relation can be established,

$$\begin{bmatrix} -\text{tr } \boldsymbol{\epsilon} \\ \Delta v^p \\ \Delta v^f \\ \Delta (\rho^s S_s) \end{bmatrix} = \begin{bmatrix} c & -(c_p - c_s) & -(c - c_p) & -c_T \\ -\tilde{B} c & \tilde{A} c_p - n_p c_s & \tilde{B} c - \tilde{A} c_p & n_p c_T \\ -\tilde{C} c & n_f (c_p - c_s) & \tilde{C} c - n_f c_p & n_f c_T \\ -\tilde{F} & \tilde{E} - \tilde{D} & \tilde{F} - \tilde{E} & \alpha_{T_s} \end{bmatrix} \begin{bmatrix} p \\ p_p \\ p_f \\ \Delta T_s \end{bmatrix} \quad (2.199)$$

$\tilde{A}$ ,  $\tilde{B}$  and  $\tilde{C}$  have already been identified in equation (2.188). Using the symmetry property of equation (2.193),  $\tilde{D}$ ,  $\tilde{E}$  and  $\tilde{F}$  are in turn deduced.

$$\tilde{D} = c_T (1 - n_f - n_p), \quad \tilde{E} = c_T (1 - n_f), \quad \text{and} \quad \tilde{F} = c_T. \quad (2.200)$$

Hence, the thermo-mechanical elastic secant relation can be cast in the following format,

$$\begin{bmatrix} -\text{tr } \boldsymbol{\epsilon} \\ \Delta v^p \\ \Delta v^f \\ \Delta (\rho^s S_s) \end{bmatrix} = \begin{bmatrix} c & -(c_p - c_s) & -(c - c_p) & -c_T \\ -(c_p - c_s) & [c_p (1 - n_f) \\ & -c_s (1 + n_p - n_f)] & n_f (c_p - c_s) & n_p c_T \\ -(c - c_p) & n_f (c_p - c_s) & c - c_p (1 + n_f) & n_f c_T \\ -c_T & n_p c_T & n_f c_T & \alpha_{T_s} \end{bmatrix} \begin{bmatrix} p \\ p_p \\ p_f \\ \Delta T_s \end{bmatrix} \quad (2.201)$$

Once again, the secant relation displays symmetry. Equation (2.201) is now rewritten to obtain the mixed secant relation, namely the matrix relating  $(p, \Delta v^p, \Delta v^f, \Delta (\rho^s S_s))$  to  $(\text{tr } \boldsymbol{\epsilon}, p_p, p_f, \Delta T_s)$ , as this relation will be needed to write the comprehensive equations of the balances of mass for the fluids,

$$\begin{bmatrix} p \\ \Delta v^p \\ \Delta v^f \\ \Delta (\rho^s S_s) \end{bmatrix} = \begin{bmatrix} -1/c & \xi_p & \xi_f & \gamma_T \\ \xi_p & c_{22} & c_{23} & c_{24} \\ \xi_f & c_{32} & c_{33} & c_{34} \\ \gamma_T & c_{42} & c_{43} & C_p^s/T_s \end{bmatrix} \begin{bmatrix} \text{tr } \boldsymbol{\epsilon} \\ p_p \\ p_f \\ \Delta T_s \end{bmatrix}, \quad (2.202)$$

in which,

$$\begin{aligned}
 c_{22} &= [(\xi_f - n_f)(c_p - c_s) + c_s(\xi_p - n_p)], \\
 c_{33} &= [(\xi_f - n_f)(c_p - c_s) + c_s(\xi_f - n_f)], \\
 c_{23} &= c_{32} = -(\xi_f - n_f)(c_p - c_s), \\
 c_{42} &= c_{24} = (n_p - \xi_p)c_T, \\
 c_{43} &= c_{34} = (n_f - \xi_f)c_T,
 \end{aligned} \tag{2.203}$$

and where  $C_p^s$  is the apparent heat capacity, at constant strain and fluid pressure, of the solid phase, per unit initial volume of porous medium, that is to say the heat capacity  $C_{s,p}$  times the volume fraction  $n_s$ .

**Remark 2.18.** *The actual form of the total secant thermo-elastic matrix depends of the type of the generalised strains. If the volume contents are taken as generalised strains, see equation (2.202), the partial secant thermo-elastic matrix displays symmetry (Loret, 2008). On the contrary, the total secant thermo-elastic matrix, namely the matrix relating the stresses:  $(p, \Delta v^p, \Delta v^f, \Delta(\rho^s S_s), \Delta(\rho^p S_p), \Delta(\rho^f S_f))$  to the strains:  $(\text{tr } \epsilon, p_p, p_f, \Delta T_s, \Delta T_p, \Delta T_f)$ , is however non-symmetric,*

$$\begin{bmatrix} p \\ \Delta v^p \\ \Delta v^f \\ \Delta(\rho^s S_s) \\ \Delta(\rho^p S_p) \\ \Delta(\rho^f S_f) \end{bmatrix} = \begin{bmatrix} -1/c & \xi_p & \xi_f & \gamma_T & 0 & 0 \\ \xi_p & c_{22} & c_{23} & c_{24} & 0 & 0 \\ \xi_f & c_{32} & c_{33} & c_{34} & 0 & 0 \\ \gamma_T & c_{42} & c_{43} & C_p^s/T_s & 0 & 0 \\ 0 & -n_p c_{pT} & 0 & 0 & C_p^p/T_p & 0 \\ 0 & 0 & -n_f c_{fT} & 0 & 0 & C_p^f/T_f \end{bmatrix} \begin{bmatrix} \text{tr } \epsilon \\ p_p \\ p_f \\ \Delta T_s \\ \Delta T_p \\ \Delta T_f \end{bmatrix} \tag{2.204}$$

where lines five and six are obtained by use of equations (2.151), (2.152) and (2.172) and where  $C_p^p$  and  $C_p^f$  are the apparent heat capacities, at constant strain and fluid pressure, of the pore fluid and the fissure fluid, per unit initial volume of porous medium, respectively.

To obtain a symmetric total secant thermo-elastic matrix, the volume content of the fluids,  $v^p$  and  $v^f$  must be replaced by their respective mass content,  $m^p/\rho_p$  and  $m^f/\rho_f$

(Loret and Khalili, 2000b). Indeed using the definitions of fluid mass content and fluid volume content,

$$v^k = \frac{V_k}{V_0} = n^k \frac{V}{V_0}, \quad \text{and} \quad m^k = \frac{M_k}{V_0} = \rho_k v^k \quad (2.205)$$

Their increments ( $d(\cdot) = \Delta(\cdot)$ ) below relate as under the assumption of small deformations,

$$\frac{dm^k}{\rho_k} = d v^k + v^k (c_{kH} dp_k - c_{kT} dT_k) \approx d v^k + n_k (c_{kH} dp_k - c_{kT} dT_k) \quad (2.206)$$

Consequently the total secant thermo-elastic matrix displays symmetry,

$$\begin{bmatrix} p \\ \frac{\Delta m^p}{\rho_p} \\ \frac{\Delta m^f}{\rho_f} \\ \Delta(\rho^s S_s) \\ \Delta(\rho^p S_p) \\ \Delta(\rho^f S_f) \end{bmatrix} = \begin{bmatrix} -1/c & \xi_p & \xi_f & \gamma_T & 0 & 0 \\ \xi_p & c_{22} & c_{23} & c_{24} & [-n_p c_{pT}] & 0 \\ & [+n_p c_{pH}] & & & & \\ \xi_f & c_{32} & c_{33} & c_{34} & 0 & [-n_f c_{fT}] \\ & & [+n_f c_{fH}] & & & \\ \gamma_T & c_{42} & c_{43} & C_p^s/T_s & 0 & 0 \\ 0 & -n_p c_{pT} & 0 & 0 & C_p^p/T_p & 0 \\ 0 & 0 & -n_f c_{fT} & 0 & 0 & C_p^f/T_f \end{bmatrix} \begin{bmatrix} \text{tr } \epsilon \\ p_p \\ p_f \\ \Delta T_s \\ \Delta T_p \\ \Delta T_f \end{bmatrix} \quad (2.207)$$

in which the terms due to the fluid mass contents  $m^k$  are highlighted in brackets.

### 2.2.2.6 The volume fractions

For a future use in the comprehensive energy equations (Subsection 2.3.3), the description of the rate of the volume fractions of each species is required. The relation between the volume fraction  $n_k$  and the volume content  $v^k$  of the species  $k$  is,

$$n_k = \frac{v^k}{\det \mathbf{F}} \quad \text{where} \quad \det \mathbf{F} = \frac{V}{V_0} \quad k = p, f. \quad (2.208)$$

Moreover, the mass content  $m^k$  and the volume content  $v^k$  are related by the density  $\rho_k$ ,

$$m_k = \rho_k v^k \quad \rightarrow \quad n_k = \frac{1}{\det \mathbf{F}} \frac{m^k}{\rho_k} \quad k = p, f. \quad (2.209)$$



The rate of volume fraction for the fluid species and for the solid are considered in turn. The rate of the volume fraction of the fluid  $k$  is obtained from equations (2.208) and (2.209),

$$\begin{aligned}
 \frac{dn_k}{dt} &= -\frac{v^k}{\det \mathbf{F}^2} \frac{d(\det \mathbf{F})}{dt} + \frac{1}{\det \mathbf{F}} \frac{dv^k}{dt}, \\
 &= -\frac{v^k}{\det \mathbf{F}} \frac{d(\text{tr } \boldsymbol{\epsilon})}{dt} + \frac{1}{\det \mathbf{F}} \frac{dv^k}{dt}, \\
 &= -n_k \frac{d(\text{tr } \boldsymbol{\epsilon})}{dt} + \frac{1}{\det \mathbf{F}} \left( \frac{1}{\rho_k} \frac{dm^k}{dt} - \frac{m^k}{\rho_k^2} \frac{d\rho_k}{dt} \right), \\
 &= -n_k \frac{d(\text{tr } \boldsymbol{\epsilon})}{dt} + \frac{n_k}{m_k} \frac{dm^k}{dt} - n_k \frac{1}{\rho_k} \frac{d\rho_k}{dt} \quad k = p, f. \quad (2.210)
 \end{aligned}$$

By use of the thermo-barotropic fluid relation (2.173), the density rate  $1/\rho_k (d\rho_k/dt)$  is expressed in terms of fluid pressure and solid temperature,

$$\frac{dn_k}{dt} = -n_k \frac{d(\text{tr } \boldsymbol{\epsilon})}{dt} + \frac{n_k}{m_k} \frac{dm^k}{dt} - n_k \left( c_{kH} \frac{dp_k}{dt} - c_{kT} \frac{dT_k}{dt} \right) \quad k = p, f. \quad (2.211)$$

Upon insertion of the rate of mass content  $1/\rho_k (dm^k/dt)$  from equation (2.207) and of the small strain assumption ( $\det \mathbf{F} = 1$ ), the rates of volume fraction become,

$$\begin{aligned}
 \frac{dn_p}{dt} &= (\xi_p - n_p) \frac{d(\text{tr } \boldsymbol{\epsilon})}{dt} + c_{22} \frac{dp_p}{dt} + c_{23} \frac{dp_f}{dt} + c_{24} \frac{dT_s}{dt}, \\
 \frac{dn_f}{dt} &= (\xi_f - n_f) \frac{d(\text{tr } \boldsymbol{\epsilon})}{dt} + c_{32} \frac{dp_p}{dt} + c_{33} \frac{dp_f}{dt} + c_{34} \frac{dT_s}{dt}. \quad (2.212)
 \end{aligned}$$

in which the coefficients  $c_{22}$ ,  $c_{23}$ ,  $c_{24}$ ,  $c_{32}$ ,  $c_{33}$  and  $c_{34}$  are defined in equation (2.203). From the effective stress relations (2.133) and (2.134), the thermo-elastic strain writes as a function of the total stress, the fluid pressure and the solid temperature,

$$\text{tr } \boldsymbol{\epsilon} = c(-p + \xi_p p_p + \xi_f p_f) + c_T (T_s - T_0). \quad (2.213)$$

Finally, upon insertion of equation (2.213), the rates of volume fraction are expressed in terms of total stress and fluid pressures only,

$$\begin{aligned}\frac{dn_p}{dt} &= (\xi_p - n_p) c \frac{d}{dt}(p_p - p) + (\xi_p(\xi_f - n_f) - \xi_f(\xi_p - n_p)) c \frac{d}{dt}(p_p - p_f), \\ \frac{dn_f}{dt} &= (\xi_f - n_f) c : \frac{d}{dt}(p_f - p).\end{aligned}\quad (2.214)$$

The rate of volume fraction for the solid skeleton is deduced from equation (2.208),

$$\frac{dn_s}{dt} = -\frac{v^s}{\det \mathbf{F}} \frac{d(\text{tr } \boldsymbol{\epsilon})}{dt} + \det \mathbf{F} \frac{dv^s}{dt}, \quad (2.215)$$

which simplifies under the small strains assumption to,

$$\frac{dn_s}{dt} = -n_s \frac{d(\text{tr } \boldsymbol{\epsilon})}{dt} + \frac{dv^s}{dt}. \quad (2.216)$$

The volume fraction of the solid skeleton is obtained by substituting into the volume fraction of the whole porous medium the fluid volume fractions. Hence, from equations (2.140) and (2.188),

$$\begin{aligned}\Delta v^s &= \Delta v - \Delta v^p - \Delta v^f, \\ &= -c_s p + c_s n_p p_p + c_s n_f p_f + n_s c_T (T_s - T_0).\end{aligned}\quad (2.217)$$

Finally, upon insertion of the volume content (2.217) and elimination of the thermo-elastic strain *via* equation (2.213), the volume fraction of the solid is expressed in terms of the total stress and fluid pressures only,

$$\frac{dn_s}{dt} = (n_s c - c_s) \frac{dp}{dt} + (n_p c_s - n_s \xi_p c) \frac{dp_p}{dt} + (n_f c_s - n_s \xi_f c) \frac{dp_f}{dt}. \quad (2.218)$$

### 2.2.2.7 Comparison with the literature

The aim of this section has been fulfilled; the thermo-mechanical elastic secant relation linking the generalised stresses to the generalised strains has been identified *via* a symmetric tensor eq. (2.201). The constitutive formulation developed as part of this study can be

compared to three studies published in the literature. The developments are presented in appendices:

- Bowen and Garcia (1970) introduced a formulation of a thermo-mechanical theory of a mixture through a *rational* thermodynamic approach (Appendix A);
- Pecker and Deresiewicz (1973) analysed thermal effects on wave propagation in liquid-filled porous media (Appendix B).
- McTigue (1986) studied the thermoelastic response of porous rocks in thermal equilibrium (Appendix C).

### 2.2.3 Diffusion constitutive equations

Diffusion is a mode of passive transport that governs partially the motion in a porous medium of fluid particles, of ionic particles, of chemical species, as well as heat flux in both solids and fluid-saturated porous media. *In-situ* all the direct and indirect diffusion mechanisms occur at the same time. However, some of them are usually prevalent upon the others depending on the application. Although the direct diffusion phenomena have been well studied and quantified, the magnitude of some coupled mechanisms is still an open question.

This study aims to describe the reaction of fractured porous media under combined thermo-hydro-mechanical loadings, therefore the analysis focuses on the hydraulic and heat diffusion mechanisms only. The relative influence of the coupled hydraulic/heat mechanisms is discussed, in spite of the paucity of *in-situ* measurements in saturated media.

Let us begin by writing the diffusion part of the Clausius-Duhem inequality in a more simple form, the underlined idea being the identification of the conjugate variables (Loret, 2008). The fluid and heat flux equations are identified by forcing the diffusion part of the Clausius-Duhem inequality, eq. (2.90)<sub>3</sub>, to be positive,

$$\frac{dD_3}{dt} = - \sum_{s,p,f} \mathbf{q}_k \cdot \frac{\nabla T_k}{T_k^2} - \sum_{p,f} \mathbf{M}_k \cdot \frac{1}{T_k} \left( S_k \nabla T_k + \nabla G_k + \frac{d^k \mathbf{v}_k}{dt} - \mathbf{b}_k \right) \geq 0. \quad (2.219)$$

The chemical potential gradient  $\nabla G_k$  may be decomposed in a hydraulic gradient term and in a thermal gradient term, as if the fluid was a single continuum, while no meniscus is accounted for as the two fluids are assumed to be of same nature, see Remark 2.16 p. 133,

$$\nabla G_k = \frac{\nabla p_k}{\rho_k} - S_k \nabla T_k. \quad (2.220)$$

Recall that the volume flux is defined as  $\mathbf{J}_k = \mathbf{M}_k/\rho_k$ . Replacing equation (2.220) into (2.219), the diffusion part of the Clausius-Duhem inequality may be written,

$$\frac{dD_3}{dt} = - \sum_{s,p,f} \mathbf{q}_k \cdot \frac{\nabla T_k}{T_k^2} - \sum_{p,f} \mathbf{J}_k \cdot \frac{\nabla P_k}{T_k} \geq 0, \quad (2.221)$$

with

$$\nabla P_k = \nabla p_k + \rho_k \left( \frac{d^k \mathbf{v}_k}{dt} - \mathbf{b}_k \right). \quad (2.222)$$

The choice of the fluxes, namely the volume fluxes  $\mathbf{J}_k$  and the heat fluxes  $\mathbf{q}_k$ , is motivated by two reasons: (1) to work with the same volume fluxes as introduced in Darcy's law and (2) to work with the same heat fluxes as used to describe Fourier's law, and incidentally by Bowen and Chen (1975).

Therefore, the *diffusion driving forces* are the thermal gradient  $\nabla T_k/T_k^2$  and the pressure gradient  $\nabla P_k/T_k$ .

The following conjugate variables are identified:

- The volume flux  $\mathbf{J}_k$  is conjugated to the hydraulic gradient  $\nabla P_k/T_k$
- The heat flux  $\mathbf{q}_k$  is conjugated to the thermal gradient  $\nabla T_k/T_k^2$

The scope of this section is to identify the generalised diffusion secant relation, relating the conjugate variables previously identified through (2.221). To write such relation, the fluid and heat flux coupled behaviour equations are presented first. Next Darcy's law and Fourier's law are extended to account for the coupling phenomena in a multi-temperature context. A particular effort is done to relate the introduced parameters with phenomenological coefficients and to evaluate the magnitude of the coupled coefficients. Finally, the generalised diffusion constitutive secant relation is introduced and simplified with Onsager's reciprocity principle.

### 2.2.3.1 Fluid and heat coupled flow behaviour

The coupled relations describing the generalised diffusion behaviour in a porous medium with double porosity are now presented. This subsection includes a review of the physics of

direct and coupled flow processes through soils and their quantification in practical form. Relationships of fluid and heat flows through soils are successively established: each flow rate or flux  $J_i$ , of the  $i^{th}$  flow type, may be linearly related to its corresponding driving force  $X_i$  by the conductivity coefficient of the flow (Mitchell, 1993),

$$J_i = -L_{ii} X_i. \quad (2.223)$$

Specifically for the fluid flow type, Darcy's law relates the fluid flow rate  $q_h$  to the hydraulic gradient  $i_h$  through the *hydraulic conductivity*  $K_h$ ,

$$q_h = -K_h i_h A. \quad (2.224)$$

in which  $A$  represents the cross section area normal to the direction of the flow. The hydraulic conductivity is a property of a type of porosity and its associated fluid and describes the ease with which the fluid can move through pore spaces. The hydraulic conductivity  $K_k$  may be related to the ratio of the *intrinsic permeability*  $k_k$  over the fluid *dynamic viscosity*  $\mu_k$ ,

$$K_k = \rho_k g \frac{k_k}{\mu_k} \quad \left[ \frac{m}{s} \right] \quad (2.225)$$

in which  $g$  is the gravity. Concerning the heat flow, Fourier's law relates the heat flow rate  $q_t$  to the thermal gradient  $i_t$  through the *thermal conductivity*  $K_t$  [W/m.K],

$$q_t = -K_t i_t A \quad (2.226)$$

Figure 2.11 illustrates the analogy between the two flow types. As long as the flow rates and gradients are linearly related, the mathematical treatment of each flow type is the same, and solutions for flow of one type may be used for problems of another type if the property values and boundary conditions are properly represented. A well known practical illustration of this is the correspondence between the Terzaghi theory of consolidation and one-dimensional transient heat flow (Mitchell, 1993).

In many studies, there are simultaneous flows of different types, even when only one type of driving force is acting. For example, when pore water containing a chemical species flows under the action of a hydraulic gradient, there is a concurrent flow of chemical through the soil. This type of chemical transport is sometimes called convection. It has been proved that a gradient of one type can cause a flow of another type according to,

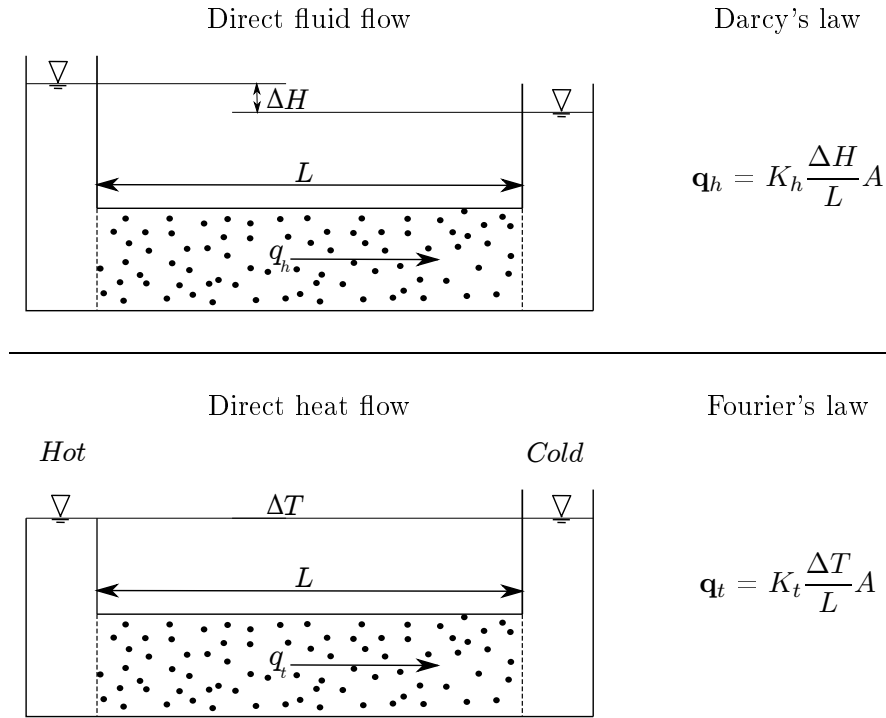


Figure 2.11: Two types of direct flows through a soil mass: direct fluid flow and direct heat flow.  $A$  represents the cross section area normal to the direction of the flow.

$$J_i = - \sum_j L_{ij} X_j \quad (2.227)$$

where  $L_{ij}$  are termed coupling coefficients. Depending on the application, they are properties that may or may not be of significant magnitude in any given porous medium. Direct and coupled diffusion phenomena are listed in Table 2.3. The phenomena that are accounted for in this model are highlighted in bold letters, namely, hydraulic conduction (Darcy's law) and thermal conduction (Fourier's law). Hence two coupling phenomena are primarily identified:

- *Thermo-osmosis* is a water movement under a temperature gradient. McTigue (1986) and Bear (1972) describe this water movement as analogous to the Soret effect, which is ion diffusion due to a thermal gradient.
- *Isothermal heat flow* is flow of heat induced by a pressure gradient, analogous to the Dufour effect, which is heat flux under a chemical concentration gradient. It is also called thermal filtration.

In the particular case of dual porous media, these coupled diffusion mechanisms occur in each phase, i.e. no coupling in between phases is accounted for here, as the two fluids are

Gradient $X$				
Flow $J$	Hydraulic head	Temperature	Electrical	Chemical concentration
Fluid	<b>Hydraulic conduction</b> <i>Darcy's law</i>	<b>Thermo-osmosis</b>	Electro-osmosis	Chemical-osmosis
Heat	<b>Isothermal heat flow</b>	<b>Thermal conduction</b> <i>Fourier's law</i>	Peltier effect	Dufour effect
Current	Streaming current	Thermo-electricity <i>Seebeck effect</i>	Electric conduction <i>Ohm's law</i>	Diffusion and membrane potentials
Ion	Streaming current	Thermal diffusion of electrolyte <i>Soret effect</i>	Eletro-phoresis	Diffusion <i>Fick's law</i>

Table 2.3: Direct and coupled diffusion phenomena from (Mitchell, 1993, p. 230). The phenomena accounted for in this model are highlighted in bold letters.

physically separated in the medium (from the diffusion point of view). Fluid interaction between the two networks is assumed to take place through transfer, which is described in Subsection 2.2.4.

First, the coupled fluid and heat flow behaviour equations, for a dual porous medium in a multi-temperature context, are defined. These expressions may appear as an extension of Darcy's law and Fourier's law. Second, the latter coupled equations are gathered in a coupled diffusion matrix, for a single fluid. The underlined idea is to focus on the thermo-osmosis coupling coefficients and on the consequences of the Onsager's reciprocity principle. Furthermore, a discussion is proposed on the magnitude of the thermo-osmosis coupling phenomena for saturated soils.

(1) The coupled fluid and heat flow behaviour equations presented in this section can be compared with the expressions of heat fluxes and volumes fluxes hidden in the momentum supplies presented by Bowen and Chen (1975, eq. (2.13)-(2.15)). By comparison with the latter reference, less couplings are accounted for here, as the particular case of a porous medium with double porosity is considered. In our model, the two fluids are physically separated in the medium. Hence, no coupling in between the fluid phases is taken into account from the diffusion point of view. Moreover, the heat flux of the solid skeleton is assumed to be independent of the fluid thermal gradients.

a. The *extended Darcy's law* equation describing the hydraulic flux behaviour under combined hydraulic and thermal gradients, may be written as follows,

$$\mathbf{J}_k = -T_k \frac{k_k}{\mu_k} \cdot \left( \frac{\nabla P_k}{T_k} \right) - n_k T_k^2 \Theta_k \cdot \left( \frac{\nabla T_k}{T_k^2} \right), \quad k = p, f; \quad (2.228)$$

where  $k_k$  are the intrinsic permeabilities,  $\mu_k$  are the viscosities of the fluids (temperature dependent) and  $\Theta_k$  are the thermo-osmosis coupling coefficients. The factor  $k_k/\mu_k$  of the pressure gradient is expressed in  $[\text{m}^2/\text{Pa}\cdot\text{s}]$  and the factor  $\Theta_k$  of the temperature gradient is expressed in  $[\text{m}^2/\text{s}\cdot\text{K}]$ .

b. The *extended Fourier's law* describing the heat fluxes behaviour,  $\mathbf{q}_s$  and  $\mathbf{q}_k$ , under combined hydraulic and thermal gradients, may be written as follows,

$$\begin{aligned} \mathbf{q}_s &= -n_s T_s^2 \Lambda_s \cdot \left( \frac{\nabla T_s}{T_s^2} \right), \\ \mathbf{q}_k &= -n_k T_k^2 \Phi_k \cdot \left( \frac{\nabla P_k}{T_k} \right) - n_k T_k^2 \Lambda_k \cdot \left( \frac{\nabla T_k}{T_k^2} \right), \quad k = p, f; \end{aligned} \quad (2.229)$$

where  $\Phi_k$  are called the isothermal heat flow coefficients of unit  $[\text{m}^2/\text{s}\cdot\text{K}]$ ; and  $\Lambda_k$  are the thermal conductivities of unit  $[\text{m}\cdot\text{kg}/\text{s}^3\cdot\text{K}]$ , for  $k = s, p, f$ .

Heat fluxes  $\mathbf{q}_k$  are defined as flows of energy per unit of area of the whole medium. The assumption that the surface fractions are equal to the volume fractions  $n_k$  is used throughout. Hence,  $\mathbf{q}_k = n_k \mathbf{Q}_k$  are in fact *partial* heat fluxes compared with the intrinsic heat fluxes  $\mathbf{Q}_k$ . This explains why the factor  $n_k$  is used in equation (2.229).

Similarly,  $\mathbf{J}_k$  are defined as volume fluxes, per unit current area of the whole porous medium, through the solid skeleton.  $\mathbf{J}_k$  are partial fluxes and not intrinsic fluxes. The factor  $n_k$  is therefore legitimate in equation (2.228). Note that the volume fraction term  $n_k$  is elusive in the definition of the intrinsic permeability,  $k_k$ , see Section 3.1.4.

c. At *thermal equilibrium*, namely  $T_s = T_p = T_f = T$ , Darcy's law and Fourier's law behaviour equations of a porous medium with double porosity reduce to,

$$\mathbf{J}_k = -T \frac{k_k}{\mu_k} \cdot \frac{\nabla P_k}{T} - n_k T^2 \Theta_k \cdot \frac{\nabla T}{T^2} \quad k = p, f, \quad (2.230)$$



$$\mathbf{q} = \mathbf{q}_s + \sum_{k=p,f} \mathbf{q}_k, = - \sum_{k=p,f} n_k T^2 \Phi_k \cdot \frac{\nabla P_k}{T} - T^2 \Lambda \cdot \frac{\nabla T}{T^2}$$

with     $\Lambda = n_s \Lambda_s + \sum_{k=p,f} n_k \Lambda_k,$  (2.231)

in which  $\Lambda$  is the thermal conductivity tensor of the mixture and  $\mathbf{q}$  is the heat flux of the whole medium.

(2) In the particular case of a single fluid  $k$ , the *fluxes*  $\mathbf{Y}$ , the volume flux  $\mathbf{J}_k$  and the heat flux  $\mathbf{q}_k$ , may be linearly related to the modified gradients *forces*  $\mathbf{X}$ , the modified pressure gradient  $-\nabla P_k/T_k$  and the thermal gradient  $-\nabla T_k/T_k^2$ , through a semi-positive definite diffusion matrix  $\mathbf{L}$ ,

$$\mathbf{Y} = -\mathbf{L} \mathbf{X}, \quad \begin{bmatrix} \mathbf{J}_k \\ \mathbf{q}_k \end{bmatrix} = - \begin{bmatrix} L_{mm} & L_{mQ} \\ L_{Qm} & L_{QQ} \end{bmatrix} \begin{bmatrix} \nabla P_k/T_k \\ \nabla T_k/T_k^2 \end{bmatrix}. \quad (2.232)$$

The heat flux unit is  $[\text{kg}/\text{s}^3]$  and the volume flux unit is  $[\text{m}/\text{s}]$ . Since precautions have been taken to measure the fluxes and the forces in the correct way, Onsager's reciprocity principle is valid, and leads to the relation,

$$L_{mQ} = L_{Qm}. \quad (2.233)$$

Thus if the diffusion matrix  $\mathbf{L}$  is semi-positive definite, the following conditions are stated,

$$L_{mm} > 0, \quad L_{QQ} > 0, \quad L_{mm} L_{QQ} - L_{mQ}^2 \geq 0. \quad (2.234)$$

Relating equation (2.232) to (2.228) and (2.229) leads to the identification of the coefficients of the diffusion matrix,

$$\begin{aligned} L_{mm} &= T_k \frac{k_k}{\mu_k} \left[ \frac{\text{m}^3 \cdot \text{s} \cdot \text{K}}{\text{kg}} \right] & L_{QQ} &= n_k T_k^2 \Lambda_k \left[ \frac{\text{kg} \cdot \text{m} \cdot \text{K}}{\text{s}^3} \right] \\ L_{Qm} &= n_k T_k^2 \Phi_k \left[ \frac{\text{m}^2 \cdot \text{K}}{\text{s}} \right] & L_{mQ} &= n_k T_k^2 \Theta_k \left[ \frac{\text{m}^2 \cdot \text{K}}{\text{s}} \right]. \end{aligned} \quad (2.235)$$

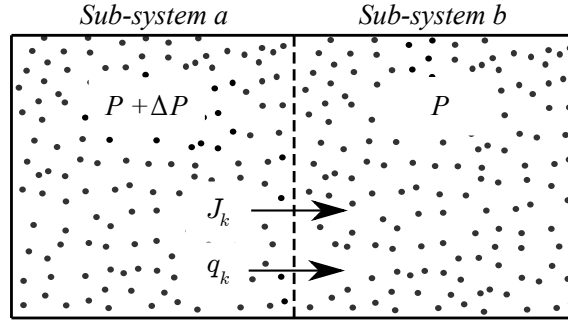


Figure 2.12: To illustrate the isothermal heat flow phenomenon, a simple case is considered: a system containing only pure fluid is divided into two by a permeable membrane. The two sub-systems (a and b) are homogeneous with themselves, but pressure vary as between the compartments. The experimental arrangements are such that the two sub-systems are maintained at the same temperature (that is,  $\nabla T = 0$ ) by being in intimate contact with a suitable heat source or sink and the volume of the entire system remains constant. Matter moves from a higher pressure to a lower and every unit which passes will convey heat from one to the other. Isothermal heat flow describes flow of heat induced by a pressure gradient.

(3) Because of the coupled flows, the measurements of the coupling coefficients require an accurate definition of the experimental system. Three *thought experiments* are proposed to identify the coupling coefficients: i. under isothermal flow, ii. under thermally insulated flow and iii. under the assumption of no flow of matter.

i. *Isothermal flow*,  $\nabla T_k = 0$

Following Spanner's work (1964), a virtual experiment is now proposed (Figure 2.12). Two sub-systems are separated by a membrane and subjected to a pressure difference under isothermal conditions. The membrane may be constituted by any porous material, but may also be aerial or inexistent. The experimental arrangements are made such as each sub-system is maintained at the same temperature by being in intimate contact with a suitable heat source. The flow of each sub-system diffuses through the membrane. The relation (2.232) subjected to an isothermal flow ( $\nabla T_k = 0$ ) reduces to,

$$\begin{cases} \mathbf{J}_k &= -L_{mm} \cdot \nabla P_k / T_k, \\ \mathbf{q}_k &= -L_{Qm} \cdot \nabla P_k / T_k, \end{cases} \quad (2.236)$$

which can be rearranged into,

$$\mathbf{q}_k = \frac{L_{Qm}}{L_{mm}} \mathbf{J}_k. \quad (2.237)$$

The latter equation indicates that the isothermal heat flow of a unit quantity of matter is associated with the flow of  $L_{Qm}/L_{mm}$  units of heat. In other words, it is to be expected

that this quantity of heat has to be supplied experimentally to the first sub-system and removed from the second (per unit of mass passing) to keep their temperatures constant. In addition this equation gives the unit of the fraction  $L_{Qm}/L_{mm}$ , [kg/m.s<sup>2</sup>] equal to a quantity of energy per unit of mass [J/m<sup>3</sup>].

Spanner (1964, p. 246) who was studying irreversible thermodynamical processes in plant cells porous media, in an unsaturated context, proposed to link the proportionality coefficient  $L_{Qm}/L_{mm}$  with the *latent heat of vaporisation*  $\mathcal{L}_{vap}$  of unit [m<sup>2</sup>/s<sup>2</sup>],

$$\mathbf{q}_k = \rho_k \mathcal{L}_{vap} \mathbf{J}_k, \quad \frac{L_{Qm}}{L_{mm}} = \rho_k \mathcal{L}_{vap}. \quad (2.238)$$

At 35 °C for a water fluid,  $\mathcal{L}_{vap} = 2.41710^6$  J/kg,  $\rho_w = 994$ kg/m<sup>3</sup>, so that  $L_{Qm}/L_{mm} = 2.403 \cdot 10^9$  kg/m.s<sup>2</sup>.

Experiments on thermo-osmosis in liquids (water) are reported by Alexander and Wirtz (1950) as well as from Haase and Schönert (1960). These measurements show that thermo-osmosis does not always occur from the cold to the warm side. The sign of the effect depends rather on the type of fluid, on the nature of the membrane, and, finally, on the mean temperature. The measured values of the proportionality coefficient  $L_{Qm}/L_{mm}$  for a system Water-Cellophane at different mean temperatures (from 10.87 to 57.69 °C) variate from 2.43 to 0.016 cal/mol. However, it has often been reported that thermo-osmotic effects are not of a significant magnitude in a wide range of saturated soil applications (McTigue, 1986; Bear and Bachmat, 1991).

In conclusion, the magnitude of the coefficient  $L_{Qm}/L_{mm}$  appears hard to estimate. Taking the latent heat of vaporization  $\mathcal{L}_{vap}$  in an unsaturated context, in which the membrane is chosen to be aerial, seems appropriate. However, in our THM model no phase change (liquid to vapor) is accounted for, and less energy is required for an increase in temperature than for a change of phase. Hence an arbitrary value, proportional to the latent heat of vaporisation but lower, could be proposed to perform a parameter analysis. Further experiments should be done to clarify this point.

ii. *Thermally insulated flow*,  $\mathbf{q}_k = 0$

This experiment would provide the *thermally insulated hydraulic conductivity*, which is the measurement of the hydraulic conductivity in absence of heat flux,

$$\frac{\nabla T_k}{T_k^2} = -\frac{L_{Qm}}{L_{QQ}} \frac{\nabla P_k}{T_k}, \quad \mathbf{J}_k = - \underbrace{\left( L_{mm} - \frac{L_{Qm}^2}{L_{QQ}} \right)}_{\text{equivalent hydraulic conductivity}} \cdot \frac{\nabla P_k}{T_k} \quad (2.239)$$

iii. *No flow of matter*,  $\mathbf{J}_k = 0$

This experiment would provide the *hydraulic open circuit thermal conductivity*, which is the measurement of the thermal conductivity in absence of flux of matter,

$$\frac{\nabla P_k}{T_k} = -\frac{L_{mQ}}{L_{mm}} \cdot \frac{\nabla T_k}{T_k^2}, \quad \mathbf{q}_k = -\underbrace{\left( L_{QQ} - \frac{L_{mQ}^2}{L_{mm}} \right)}_{\text{equivalent thermal conductivity}} \cdot \frac{\nabla T_k}{T_k^2} \quad (2.240)$$

Thus at 35 °C, a gradient of temperature of 1 K gives rise to a gradient of pressure equal to  $-78 \cdot 10^5$  Pa. Note that the signs of the temperature and the pressure gradients are opposite. Once again the use of the latent heat of vaporization brings a non-negligible coupled phenomenon.

### 2.2.3.2 Generalised diffusion secant matrix

The coupled diffusion behaviours have been previously analysed through empirical laws and experiments. Let us now introduce the generalised diffusion secant relation linking the volume fluxes and the heat fluxes to the thermal and hydraulic gradients by using the general form of the diffusion part of the Clausius-Duhem inequality,

$$\frac{dD_3}{dt} = -\sum_{s,p,f} \mathbf{q}_k \cdot \left( \frac{\nabla T_k}{T_k^2} \right) - \sum_{p,f} \mathbf{J}_k \cdot \left( \frac{\nabla P_k}{T_k} \right) \geq 0, \quad (2.241)$$

in which, one can identify the conjugate variables: the heat flux  $\mathbf{q}_k$  with the temperature gradient  $\nabla T_k/T_k^2$ , for  $k = s, p, f$ ; and the volume flux  $\mathbf{J}_k$  with the modified hydraulic gradient  $\nabla P_k/T_k$ , for  $k = p, f$ . The diffusion part of the Clausius-Duhem inequality writes in an expanded form,

$$\begin{aligned} \frac{dD_3}{dt} &= -\mathbf{q}_s \cdot \left( \frac{\nabla T_s}{T_s^2} \right) - \mathbf{q}_p \cdot \left( \frac{\nabla T_p}{T_p^2} \right) - \mathbf{q}_f \cdot \left( \frac{\nabla T_f}{T_f^2} \right) \\ &\quad - \mathbf{J}_p \cdot \left( \frac{\nabla P_p}{T_p} \right) - \mathbf{J}_f \cdot \left( \frac{\nabla P_f}{T_k} \right), \\ &= -\mathbf{X}^T \mathbf{Y} = \mathbf{X}^T \mathbf{L} \mathbf{X} \geq 0. \end{aligned} \quad (2.242)$$

This section aims to introduce the link between the generalised diffusion fluxes to the temperature and hydraulic stress gradients, through the tensor  $\mathbf{L}$ ,

$$\begin{bmatrix} \mathbf{q}_s \\ \mathbf{q}_p \\ \mathbf{q}_f \\ \mathbf{J}_p \\ \mathbf{J}_f \end{bmatrix} = - \underbrace{\begin{bmatrix} L_{ss} & L_{sp} & L_{sf} & H_{sp} & H_{sf} \\ L_{ps} & L_{pp} & L_{pf} & H_{pp} & H_{pf} \\ L_{fs} & L_{fp} & L_{ff} & H_{fp} & H_{ff} \\ \hline G_{ps} & G_{pp} & G_{pf} & K_{pp} & K_{pf} \\ G_{fs} & G_{fp} & G_{ff} & K_{fp} & K_{ff} \end{bmatrix}}_{\mathbf{L}} \begin{bmatrix} \nabla T_s/T_s^2 \\ \nabla T_p/T_p^2 \\ \nabla T_f/T_f^2 \\ \nabla P_p/T_p \\ \nabla P_f/T_f \end{bmatrix}. \quad (2.243)$$

Relating the heat and fluid flow behaviour relations (2.228) and (2.229) to the previous fully coupled diffusion relation (2.243), allows us to simplify the matrix  $\mathbf{L}$  by accounting for only the existing couplings,

$$\mathbf{L} = \begin{bmatrix} L_{ss} & 0 & 0 & 0 & 0 \\ 0 & L_{pp} & 0 & H_{pp} & 0 \\ 0 & 0 & L_{ff} & 0 & H_{ff} \\ \hline 0 & G_{pp} & 0 & K_{pp} & 0 \\ 0 & 0 & G_{ff} & 0 & K_{ff} \end{bmatrix}. \quad (2.244)$$

} Isothermal heat flux  
} Thermo-osmosis

According to Onsager's reciprocity principle, the matrix  $\mathbf{L}$  is assumed to be symmetric,

$$G_{pp} = H_{pp} \quad G_{ff} = H_{ff}, \quad (2.245)$$

and semi-positive definite, i.e. all principal minors have to be non-negative,

$$L_{ss} \geq 0, \quad L_{pp} \geq 0, \quad L_{ff} \geq 0, \quad K_{pp} \geq 0, \quad \text{and} \quad K_{ff} \geq 0, \quad (2.246)$$

$$L_{pp} - G_{pp} K_{pp}^{-1} H_{pp} \geq 0, \quad L_{ff} - G_{ff} K_{ff}^{-1} H_{ff} \geq 0. \quad (2.247)$$

The secant matrix coefficients may be related to physical values by identification with the diffusion coefficients of equations (2.228) and (2.229). As the matrix  $\mathbf{L}$  is symmetric, the thermo-osmosis coefficients are found equal to the isothermal heat flux coefficients, namely,

$$\Theta_p = \Phi_p, \quad \text{and} \quad \Theta_f = \Phi_f. \quad (2.248)$$

The symmetry property is conserved by consistent scalings of the fluxes and driving gradients, see Section 2.2.1. On the other hand, there is no argument why the fluxes themselves should display a symmetric coupling; while in many cases, symmetry is used mainly as a starting convenient assumption, it should *in fine* be verified, or disproved experimentally. Overall, the generalised diffusion secant matrix is identified,

$$\begin{bmatrix} \mathbf{q}_s \\ \mathbf{q}_p \\ \mathbf{q}_f \\ \mathbf{J}_p \\ \mathbf{J}_f \end{bmatrix} = - \begin{bmatrix} n_s T_s^2 \Lambda_s & 0 & 0 & 0 & 0 \\ 0 & n_p T_p^2 \Lambda_p & 0 & n_p T_p^2 \Theta_p & 0 \\ 0 & 0 & n_f T_f^2 \Lambda_f & 0 & n_f T_f^2 \Theta_f \\ \hline 0 & n_p T_p^2 \Theta_p & 0 & T_p k_p / \mu_p & 0 \\ 0 & 0 & n_f T_f^2 \Theta_f & 0 & T_f k_f / \mu_f \end{bmatrix} \begin{bmatrix} \nabla T_s / T_s^2 \\ \nabla T_p / T_p^2 \\ \nabla T_f / T_f^2 \\ \nabla P_p / T_p \\ \nabla P_f / T_f \end{bmatrix} \quad (2.249)$$

where  $\Lambda_s$ ,  $\Lambda_p$  and  $\Lambda_f$  are the direct thermal conductivities of the solid, the pore fluid and the fissure fluid phase, respectively.  $k_p$  and  $k_f$  are the intrinsic permeabilities of the porous block and the fissure network;  $\mu_p$  and  $\mu_f$  are the viscosity of the pore fluid and the fissure fluid;  $\Theta_p$  and  $\Theta_f$  are the coupled thermo-osmosis coefficients of the pore fluid and of the fissure fluid, respectively.

**Remark 2.19.** *The diffusion constitutive behaviour developed by Pecker and Deresiewicz (1973) (Appendix B) is recovered for  $\Theta_p = 0$  and  $\Theta_f = 0$ , i.e. the thermo-osmosis effect and the isothermal heat flux, analogous to the Soret effect and to the Dufour effect, are omitted.*

## 2.2.4 Transfer constitutive equations

Diffusion mechanisms take place within each phase. It is crucial to highlight the fact that transfer mechanisms occur at a local geometrical point, when the flow passes from one phase to the other. *In-situ*, four transfer mechanisms take place at the same time: (1) momentum transfer (Remark 2.20), (2) mass transfer, (3) entropy transfer and (4) energy transfer. Transfer mechanisms are said to be direct when they are induced by a force. On

the contrary, transfer mechanisms are said to be indirect when they are induced by another transfer mechanism.

**Remark 2.20.** *The momentum transfer behaviour can be recovered by substituting Darcy's law (2.222) into the balance of momentum field equation (2.32), namely,*

$$\begin{aligned}\hat{e}_{\mathcal{M}}^k &= \hat{\rho}^k \tilde{\mathbf{v}}_k + \hat{\mathbf{p}}_k \\ \hat{e}_{\mathcal{M}}^k &= \underbrace{\nabla n_k \cdot p_k \mathbf{I}}_{\text{Buoyancy term}} + \underbrace{\nabla P_k \cdot n_k \mathbf{I}}_{\text{Darcy's law}} + \underbrace{\hat{\rho}_{tr}^k \mathbf{v}_k}_{\text{mass transfer}}\end{aligned}\quad (2.250)$$

Therefore, the momentum transfer law is not to be given by the transfer CD inequality.

This section aims to identify the constitutive matrix linking the transfer fluxes to their corresponding driving forces (Loret, 2008). The establishment of a transfer constitutive relation is obtained by forcing the transfer part of the Clausius-Duhem equation (2.90)<sub>2</sub> to be positive. The latter equation (2.90)<sub>2</sub> is now presented to visualise each contribution, namely (2) mass transfer, (3) entropy transfer (Remark 2.21) and (1)+(4) the momentum and energy transfers,

$$\frac{dD_2}{dt} = - \underbrace{\sum_{k=p,f} X_k^{(2)} Y_k^{(2)}}_{(2)} - \underbrace{\sum_{k=s,p,f} \hat{e}_{\mathcal{S}}^k}_{(3)} - \underbrace{\sum_{k=s,p,f} X_k^{(4)} Y_k^{(4)}}_{(1)+(4)} \geq 0 \quad (2.251)$$

where the mass transfer flux  $X_k^{(2)}$  is conjugated with its related force  $Y_k^{(2)}$  defined by,

$$\begin{aligned}X_k^{(2)} &= \hat{\rho}_{tr}^k \\ Y_k^{(2)} &= \left( G_k + \frac{1}{2} (\mathbf{v}_k - \mathbf{v}_s)^2 - \frac{1}{2} \mathbf{v}_s^2 \right) \frac{1}{T_k}\end{aligned}\quad (2.252)$$

One may observe that the whole term  $\hat{e}_{\mathcal{M}}^k \cdot \mathbf{v}_s - \hat{e}_{\mathcal{U}}^k$  appears in the energy comprehensive equation. As the momentum flux  $\hat{e}_{\mathcal{M}}^k$  is known (Remark 2.20), the global energy flux  $X_k^{(4)}$  is assumed to be conjugated with the related force  $Y_k^{(4)}$ , namely,

$$\begin{aligned}X_k^{(4)} &= \hat{e}_{\mathcal{M}}^k \cdot \mathbf{v}_s - \hat{e}_{\mathcal{U}}^k \\ Y_k^{(4)} &= \frac{1}{T_k}\end{aligned}\quad (2.253)$$

The choice of the fluxes, namely the mass transfer  $\hat{\rho}_{tr}^k$ , the entropy transfer  $\hat{e}_{\mathcal{S}}^k$  and the global energy transfer  $X_k^{(4)}$ , is driven by three purposes: (i) so as to take advantage of the

transfer closure relations, (ii) to recover the same mass transfer fluxes when reducing to a hydro-mechanical model (Barenblatt et al., 1960) and (iii) to recover the same energy transfer fluxes when reducing to a single porosity model (Bowen and Garcia, 1970).

**Remark 2.21.** *The rate of entropy transfer, contribution (3), appears to have no work conjugate variable. Hence, no restrictions is provided on the entropy transfer constitutive relation from the thermodynamics theory. In addition, since no dissipation occurs during the entropy transfer, the term (3) sums up to zero as it was presented by the closure relation (2.65),*

$$\sum_{k=s,p,f} \hat{e}_S^k = 0. \quad (2.254)$$

*The constitutive behaviour of  $\hat{e}_S^k$  for each phase will not be described because the transfer of entropy in between phases does not influence the solution of a problem at the boundaries. Any arbitrary behaviour law for  $\hat{e}_S^k$  could be imposed, however it would not change the global results. It is important here to highlight that no constitutive transfer equations is missing.*

To summarise, the CD transfer inequality allows us to write the constitutive equations describing (2) the rate of mass transfer and (4) the rate of global energy transfer *only*. No restrictions on the other transfer constitutive equation is given by the CD inequality. Due to a lack of *in-situ* measurements and as a first approximation, no coupling is assumed between the mass transfer and the energy transfer constitutive equations,

$$-\sum_{k=p,f} \hat{\rho}_{tr}^k Y_k^{(2)} \geq 0 \quad \text{and} \quad -\sum_{k=s,p,f} X_k^{(4)} \frac{1}{T_k} \geq 0. \quad (2.255)$$

For the particular case of non-reactive media, no mass transfer occurs in the solid phase,  $\hat{\rho}_{tr}^s = 0$ . In addition, since a closed system is considered, the fluid mass transfer fluxes satisfy the following closure relation,

$$\sum_{k=p,f} \hat{\rho}_{tr}^k = 0 \quad \Leftrightarrow \quad \hat{\rho}_{tr}^p = -\hat{\rho}_{tr}^f. \quad (2.256)$$

Hence, only one mass transfer flux is needed. Remembering that the closure relations for  $\hat{e}_M^k$  (2.31) and for  $\hat{e}_U^k$  (2.46) sum up to zero for a closed system,

$$\sum_{k=s,p,f} X_k^{(4)} = 0 \quad \Leftrightarrow \quad -X_s^{(4)} = X_p^{(4)} + X_f^{(4)}. \quad (2.257)$$



Similarly to the mass transfer flux, only two global energy transfer fluxes are needed. Consequently, equation (2.255) may be rearranged to let appear the difference of the related mass transfer forces and the coldness (inverse temperature) variation in between the phases, which are the *driving forces* of the transfer mechanisms,

$$-\hat{\rho}_{tr}^p \left( Y_p^{(2)} - Y_f^{(2)} \right) \geq 0 \quad \text{and} \quad -X_p^{(4)} \left( \frac{1}{T_p} - \frac{1}{T_s} \right) - X_f^{(4)} \left( \frac{1}{T_f} - \frac{1}{T_s} \right) \geq 0 \quad (2.258)$$

Once the proper transfer fluxes and forces have been identified, the behaviour laws are required. First, the mass transfer law is extended from the law introduced by Barenblatt et al. (1960) for a hydro-mechanical model in local thermal equilibrium. Second, the energy transfer law is extended from the law proposed by Bowen and Garcia (1970) for a single porosity model. Finally, the transfer secant constitutive relation is defined for dual porous media in local thermal non-equilibrium.

#### 2.2.4.1 Mass transfer behaviour

This subsection aims to identify the mass transfer behaviour relations of media with double porosity, in a thermo-hydro-mechanical context. (1) The mass transfer behaviour is well defined for hydro-mechanical models in which the driving force is the pressure difference between the porous block and the fissure network. (2) On the other hand, in a thermo-hydro-mechanical context the driving force grows up to  $Y_p^{(2)} - Y_f^{(2)}$  and the mass transfer behaviour needs to be clarified.

(1) The mass transfer flux  $\hat{\rho}^k$  for media with double porosity is well known for hydro-mechanical systems. The mass transfer flux was first introduced by Barenblatt et al. (1960) through a *leakage parameter*  $\eta$ . The fluid exchange is assumed to be driven by the pressure difference between the two types of porosities, namely,

$$\hat{\rho}_{tr}^k = (-1)^\alpha \rho_0 \eta (p_p - p_f) \quad \text{where} \quad \begin{cases} \alpha = 1 & \text{if } k = p \\ \alpha = 2 & \text{if } k = f \end{cases} \quad (2.259)$$

The leakage parameter  $\eta$  controls the flow between porous and fissured sub-domains. It is function of the pore fluid viscosity  $\mu_p$ , the porous block permeability  $k_p$  and an aperture factor  $\bar{\alpha}$ . The following relationship has been obtained using a one dimensional analysis with the assumption that a quasi-steady state exists in the blocks of the porous region,

$$\eta = \bar{\alpha} \frac{k_p}{\mu_p} \quad (2.260)$$

The aperture factor  $\bar{\alpha}$ , also called shape factor, is a parameter which represents the fissuration of the medium, its order of magnitude is  $[1/\text{m}^2]$  (Warren and Root, 1963).

While the linear transfer function (2.259) is easily amenable to computational implementation and consistent with a thermodynamic analysis, leading to positive dissipation, it is also known to be inaccurate at early times. The non-linear Vermeulen scheme has been adopted by Zimmerman et al. (1993) in the analysis of fractured geothermal reservoirs where, at each point of the fracture continuum, a porous block of spherical shape is attached: the fluid diffuses in the block and the net flow through its boundary is viewed as a source/sink term for the fracture continuum. Lu and Connell (2007) have devised an one-dimensional semi-analytical scheme that provides the time course of the transferred mass in a gas reservoir. At early times, while the rate of mass transfer in their model tends to vanish, it tends to a constant for the linear transfer scheme and to infinity for the Vermeulen scheme. Correspondingly, the mass transferred depends linearly on time in the linear transfer scheme, but on the square root of time in the schemes of Vermeulen and Lu and Connell, albeit with distinct scaling factors. A simple, accurate while computationally efficient, model of transfer that avoids delving with a convolution product, is yet to come.

(2) The mass transfer behaviour in a thermo-hydro-mechanical context, i.e. the coefficient relating the mass transfer flux  $\hat{\rho}_{tr}^p$  to its conjugated force  $Y_p^{(2)} - Y_f^{(2)}$ , is identified by assuming that for a mixture in local thermal equilibrium, the relation should reduce to the equation (2.259) proposed by Barenblatt et al. (1960). Therefore, the coefficient describing the amount of fluid concerned by the mass transfer flux is the same as the one proposed by Barenblatt et al. (1960) and explicitly identified by Warren and Root (1963):

$$\hat{\rho}_{tr}^k = (-1)^\alpha T_0 \rho_0^2 \eta \left( Y_p^{(2)} - Y_f^{(2)} \right) \quad \text{where} \quad \begin{cases} \alpha = 1 & \text{if } k = p \\ \alpha = 2 & \text{if } k = f \end{cases} \quad (2.261)$$

in which  $T_0$  is the initial temperature of the fluids, which are in local thermal equilibrium in the initial state. Note that the magnitude of the mass transfer flux is homogeneous with the one proposed by Barenblatt et al. (1960).

#### 2.2.4.2 Energy transfer behaviour

The energy transfer behaviour previously introduced for (1) a single porosity model is extended to (2) media with double porosity: in both cases the driving forces are coldness differences.

(1) In a single porosity context, Bowen and Chen (1975, eq. 6.15) define the rate of energy transfer behaviour as,

$$\hat{e}_{\mathcal{U}}^a = \sum_{b=s,p} \Gamma_{ab} \left( \frac{1}{T_b} - \frac{1}{T_0} \right) = \Gamma_{as} \left( \frac{1}{T_s} - \frac{1}{T_0} \right) + \Gamma_{ap} \left( \frac{1}{T_p} - \frac{1}{T_0} \right) \quad a = s, p \quad (2.262)$$

In addition, in order to ensure that equation (2.262) is satisfied for all temperatures, two closure conditions apply (Bowen and Chen, 1975, eq. 6.18 and 6.19),

$$\sum_{b=s,p} \Gamma_{ab} = 0 \quad \rightarrow \quad \Gamma_{as} = -\Gamma_{ap} \quad a = s, p \quad (2.263)$$

$$\sum_{a=s,p} \Gamma_{ab} = 0 \quad \rightarrow \quad \Gamma_{sb} = -\Gamma_{pb} \quad b = s, p \quad (2.264)$$

Consequently, for a single porous medium,

$$-\hat{e}_{\mathcal{U}}^p = \hat{e}_{\mathcal{U}}^s = -\Gamma_{sp} \left( \frac{1}{T_s} - \frac{1}{T_p} \right) \quad (2.265)$$

In the work of Bowen and Chen (1975), the momentum transfer behaviour relation, eq. [6.22], is obtained by a different thermodynamic method, namely a systematic linear expansion. However, the end results are the same.

(2) To extend the energy transfer constitutive relation (2.265) to a medium with double porosity, two additional coefficients of *coldness exchange* are introduced to the one between the solid and the pore fluid  $\gamma_{sp}$ :  $\gamma_{sf}$  and  $\gamma_{pf}$ , respectively, between the solid and the fissure fluid and between the two fluid phases,

$$\begin{aligned} X_s^{(4)} &= - \gamma_{sp} \left( \frac{1}{T_s} - \frac{1}{T_p} \right) - \gamma_{sf} \left( \frac{1}{T_s} - \frac{1}{T_f} \right) - 0 \left( \frac{1}{T_f} - \frac{1}{T_p} \right) \\ X_p^{(4)} &= - \gamma_{sp} \left( \frac{1}{T_p} - \frac{1}{T_s} \right) - 0 \left( \frac{1}{T_f} - \frac{1}{T_s} \right) - \gamma_{pf} \left( \frac{1}{T_p} - \frac{1}{T_f} \right) \\ X_f^{(4)} &= - 0 \left( \frac{1}{T_p} - \frac{1}{T_s} \right) - \gamma_{sf} \left( \frac{1}{T_f} - \frac{1}{T_s} \right) - \gamma_{pf} \left( \frac{1}{T_f} - \frac{1}{T_p} \right) \end{aligned} \quad (2.266)$$

where the coefficients of coldness exchange  $\gamma_{sp}$ ,  $\gamma_{sf}$  and  $\gamma_{pf}$  are positives and of unit: [W.K/m<sup>3</sup>]. Note that eq. (2.266) is in agreement with the closure relation (2.257). According to Bejan (1993, p. 22) and to Kaviany (1995, p. 401), the experimentally measured

values are the coefficients of volumetric inter-phase heat transfer  $\kappa_i$  [W/m<sup>3</sup>.K], for  $i = sp, sf, pf$ . These coefficients can be related to the coefficients of inter-phase coldness exchange  $\gamma_i$  [W.K/m<sup>3</sup>] by,

$$\kappa_{sp} = \frac{\gamma_{sp}}{T_s T_p}, \quad \kappa_{sf} = \frac{\gamma_{sf}}{T_s T_f} \quad \text{and} \quad \kappa_{pf} = \frac{\gamma_{pf}}{T_f T_p} \quad (2.267)$$

Hence, eq. (2.266) can be rearranged with temperature variations as forces instead of the coldness variations,

$$\begin{aligned} X_s^{(4)} &= - \kappa_{sp} (T_p - T_s) - \kappa_{sf} (T_f - T_s) - 0 (T_p - T_f) \\ X_p^{(4)} &= - \kappa_{sp} (T_s - T_p) - 0 (T_s - T_f) - \kappa_{pf} (T_f - T_p) \\ X_f^{(4)} &= - 0 (T_s - T_p) - \kappa_{sf} (T_s - T_f) - \kappa_{pf} (T_p - T_f) \end{aligned} \quad (2.268)$$

This writing recovers well ‘Newton’s law of cooling’ which states that the rate of temperature decrease of a body immersed in a fluid is at all times proportional to the body-fluid temperature difference.

#### 2.2.4.3 Generalised transfer secant matrix

The coupled transfer behaviours have been previously analysed through empirical laws. Let us now introduce the generalised transfer secant matrix relating the transfer rates to the generalised transfer forces.

Recall that the transfer part of the Clausius-Duhem inequality is enforced to be positive and is uncoupled,

$$-\hat{\rho}_{tr}^p (Y_p^{(2)} - Y_f^{(2)}) \geq 0 \quad \text{and} \quad -X_p^{(4)} \left( \frac{1}{T_p} - \frac{1}{T_s} \right) - X_f^{(4)} \left( \frac{1}{T_f} - \frac{1}{T_s} \right) \geq 0 \quad (2.269)$$

The expressions (2.269) may be seen as two scalar products of  $\mathbf{X}$  and  $\mathbf{Y}$  that reduces to zero in equilibrium. Close to the equilibrium,  $\mathbf{Y}$  is a linear function of  $\mathbf{X}$ , through a matrix  $\mathbf{L}_{tr}$ ,

$$\mathbf{Y} = -\mathbf{L}_{tr} \mathbf{X} \quad (2.270)$$

Expanding this last expression leads to,

$$\underbrace{\begin{bmatrix} \hat{\rho}_{tr}^p \\ X_p^{(4)} \\ X_f^{(4)} \end{bmatrix}}_{\mathbf{Y}} = - \underbrace{\begin{bmatrix} L_{11} & L_{12} & L_{13} \\ L_{21} & L_{22} & L_{23} \\ L_{31} & L_{32} & L_{33} \end{bmatrix}}_{\mathbf{L}_{tr}} \underbrace{\begin{bmatrix} Y_p^{(2)} - Y_f^{(2)} \\ T_p^{-1} - T_s^{-1} \\ T_f^{-1} - T_s^{-1} \end{bmatrix}}_{\mathbf{X}} \quad (2.271)$$

The coefficients  $L_{ij}$  related to the energy transfer mechanisms are identified with equation (2.266),

$$\begin{aligned} L_{22} &= \gamma_{sp} + \gamma_{pf} & \text{and} & & L_{33} &= \gamma_{sf} + \gamma_{pf} \\ L_{21} &= 0 & \text{and} & & L_{31} &= 0 \\ L_{23} &= -\gamma_{pf} & \text{and} & & L_{32} &= -\gamma_{pf}. \end{aligned} \quad (2.272)$$

The coefficients  $L_{ij}$  related to the mass transfer mechanism are identified with equation (2.261), extended from Barenblatt's work,

$$L_{11} = T_0 \rho_0^2 \eta, \quad \text{and} \quad L_{12} = L_{13} = 0 \quad (2.273)$$

Hence, the coefficients of the transfer matrix are identified,

$$\begin{bmatrix} \hat{\rho}_{tr}^p \\ X_p^{(4)} \\ X_f^{(4)} \end{bmatrix} = - \begin{bmatrix} T_0 \rho_0^2 \eta & 0 & 0 \\ 0 & \gamma_{sp} + \gamma_{pf} & -\gamma_{pf} \\ 0 & -\gamma_{pf} & \gamma_{sf} + \gamma_{pf} \end{bmatrix} \begin{bmatrix} Y_p^{(2)} - Y_f^{(2)} \\ T_p^{-1} - T_s^{-1} \\ T_f^{-1} - T_s^{-1} \end{bmatrix} \quad (2.274)$$

The restrictive conditions are obtained by replacing equation (2.274) into the dissipation inequalities (2.269). The transfer CD inequalities,

$$T_0 \rho_0^2 \eta \left( Y_p^{(2)} - Y_f^{(2)} \right)^2 \geq 0 \quad (2.275)$$

$$\gamma_{sp} \left( \frac{1}{T_p} - \frac{1}{T_s} \right)^2 + \gamma_{sf} \left( \frac{1}{T_f} - \frac{1}{T_s} \right)^2 + \gamma_{pf} \left( \frac{1}{T_p} - \frac{1}{T_f} \right)^2 \geq 0 \quad (2.276)$$

are satisfied if the coefficients  $\eta$ ,  $\gamma_{sp}$ ,  $\gamma_{sf}$  and  $\gamma_{pf}$  are positive. The rate of mass transfer of the fissure fluid  $\hat{\rho}_{tr}^f$  can be deduced by use of equation (2.256) and the rate of entropy

transfer of the solid  $X_s^{(4)}$  can be calculated by using equation (2.257). The transfer matrix relation can now be rewritten in the global space, in which lines 2 and 3 are deduced from the others.

$$\begin{bmatrix} \hat{\rho}_{tr}^p \\ \hat{\rho}_{tr}^f \\ X_s^{(4)} \\ X_p^{(4)} \\ X_f^{(4)} \end{bmatrix} = - \begin{bmatrix} T_0 \rho_0^2 \eta & -T_0 \rho_0^2 \eta & 0 & 0 & 0 \\ -T_0 \rho_0^2 \eta & T_0 \rho_0^2 \eta & 0 & 0 & 0 \\ 0 & 0 & \gamma_{sp} + \gamma_{sf} & -\gamma_{sp} & -\gamma_{sf} \\ 0 & 0 & -\gamma_{sp} & \gamma_{sp} + \gamma_{pf} & -\gamma_{pf} \\ 0 & 0 & -\gamma_{sf} & -\gamma_{pf} & \gamma_{sf} + \gamma_{pf} \end{bmatrix} \begin{bmatrix} Y_p^{(2)} \\ Y_f^{(2)} \\ T_s^{-1} \\ T_p^{-1} \\ T_f^{-1} \end{bmatrix} \quad (2.277)$$

Note that the transfer behaviour matrix enjoys symmetry in the global space. The inter-phase coldness transfer coefficients  $\gamma_i$ , for  $i = sp, sf, pf$ , are used in this section to relate the global energy forces to their related energy fluxes: from the thermodynamical point of view the  $\gamma_i$  coefficients describe the energy transfer. However, the inter-phase coldness transfer coefficients are not often measured, whereas more values in the literature can be found on the inter-phase heat transfer coefficients  $\kappa_i$ , for  $i = sp, sf, pf$ . This is why, in the following Sections the  $\gamma_i$  coefficients are replaced by the  $\kappa_i$ , according to equation (2.267).

### 2.3 Comprehensive field equations

The comprehensive equations are obtained by introducing the constitutive equations from Section 2.2, into the field equations from Section 2.1. The aim, here, is to express the field equations in terms of the primary unknowns used later in the finite element formulation. Each set of comprehensive field equations involves its own main unknown, e.g. the temperatures for the energy equations. Across the board, interaction terms appear as well, e.g. the permeabilities may be coupled to pressure variations.

The set of comprehensive field equations will consider in turn: 1. the balance of momentum of the whole mixture, 2. the balance of mass of the two fluids and 3. the balance of energy for each phase:

1. A single balance of momentum is required for the mixture as a whole. For each fluid phase, it is complemented by a generalised diffusion equation.

2. The balances of mass equations are written for the two fluid phases only. These two phases are in turn coupled by a leakage term controlling the transfer of fluid between the porous region and the fissure network. The two fluid phases are endowed with their own pressures. The mass of the solid skeleton is assumed to stay constant as no chemical reaction is taken into account, hence the balance of mass of the solid phase is not of interest here.
3. The three phases are assumed to be in local thermal non-equilibrium: the temperatures are *a priori* distinct in the three phases. Consequently, three independent energy equations are needed, one for each phase. Moreover energy transfer is accounted for through conduction, diffusion and heat exchange.

The set of field equations is displayed in Table 2.4, together with the primary unknowns that will be chosen in the finite element formulation. The field equations are coupled through thermo-mechanics, diffusion and transfer constitutive equations. In this table, the unknown attached to each field equation is the one that would appear if they were uncoupled.

Nature of equation	Field equation	Main unknow
1. Balance of momentum of the whole mixture	$\operatorname{div} \boldsymbol{\sigma} = 0$	Displacement vector $\mathbf{u}$
2. Balances of mass for the fluids	$\frac{d^k \rho^k}{dt} + \rho^k \operatorname{div} \mathbf{v}_k = \hat{\rho}^k$	Pressure of the pore fluid $p_p$ Pressure of the fissure fluid $p_f$
3. Balances of energy for the solid and the fluids	$d\mathcal{U} + d\mathcal{C} = \delta\mathcal{W}_{ext} + \delta\mathcal{Q}$	Temperature of the solid $T_s$ Temperature of the pore fluid $T_p$ Temperature of the fissure fluid $T_f$

Table 2.4: Set of field equations and list of primary unknowns

Table 2.5 presents a schematic summary of the constitutive equations. Note that *no* coupling across the constitutive equation types is accounted for in this model. The thermo-mechanical set of constitutive equations enjoys a major symmetry due to the existence of thermo-elastic potential. The generalised diffusion and the transfer constitutive equations display symmetry thanks to Onsager's reciprocity principle.

### 2.3.1 Balance of momentum for the mixture

The balance of momentum equation illustrates a mechanical equilibrium stress state of a representative volume of the medium. In order to express this field equation as a function

Variable	Physical phenomenon	Work conjugate variable
Generalised strain	<b>Coupled thermo-mechanics</b>	Generalised stress
Strain $\text{tr } \boldsymbol{\epsilon}$ of porous medium	Thermo-elasticity	Total stress $\text{tr } \boldsymbol{\sigma}$
Fluid volume changes $\Delta v_{k^*}$	Hydraulic coupling	Fluid pressures $p_{k^*}$
Entropy change of the solid $\Delta S_s$	Entropy exchange	Temperature variation of the solid $\Delta T_s$
Flux relative to fluids	<b>Coupled generalised diffusion</b>	Driving gradient
Flux of mass $\mathbf{J}_{k^*}$	Seepage, thermo-osmosis	Fluid pressures $P_{k^*}$
Flux of heat $\mathbf{q}_k$	Conduction, isothermal Heat flux	Temperatures $T_k$
Nature	<b>Uncoupled transfer</b>	Driving force
Rate of mass $\dot{\rho}^{k^*}$	Mass transfer	Difference of $Y_p^{(2)} - Y_f^{(2)}$
Rate of energy $X_k^{(4)}$	Energy transfer	Coldness differences $T_k^{-1} - T_l^{-1}$

Table 2.5: Set of constitutive equations,  $k^* = p, f$ ,  $k = s, p, f$  and  $l = p, f, s$ .

of the primary variables, the balance of momentum for the mixture as a whole is specified for a closed system,

$$\text{div } \boldsymbol{\sigma} + \rho \left( \mathbf{b} - \frac{D\mathbf{v}}{Dt} \right) = 0 \quad (2.278)$$

and can be further simplified by neglecting the inertial contribution  $\rho D\mathbf{v}/Dt$  (quasi-static analysis),

$$\text{div } \boldsymbol{\sigma} + \rho \mathbf{b} = 0. \quad (2.279)$$

The total stress (2.136) is then expressed as a function of the deformation, the pore and fissure pressures, and the solid temperature,

$$\boldsymbol{\sigma} = \lambda^{DS} \text{tr } \boldsymbol{\epsilon} \mathbf{I} + 2 \mu^{DS} \boldsymbol{\epsilon} - \xi_p p_p \mathbf{I} - \xi_f p_f \mathbf{I} - \gamma_T (T_s - T_0) \mathbf{I} \quad (2.280)$$



By replacing equation (2.280) into equation (2.279), the balance of momentum is written as a function of the effective stress parameters  $\xi_p$  and  $\xi_f$ , the thermal expansion coefficient  $\gamma_T$ , and the Lamé's constants of the drained solid  $\lambda^{DS}$  and  $\mu^{DS}$ ,

$$\lambda^{DS} \frac{\partial \epsilon_{jj}}{\partial x_i} + 2 \mu^{DS} \frac{\partial \epsilon_{ij}}{\partial x_j} - \xi_p \frac{\partial p_p}{\partial x_i} - \xi_f \frac{\partial p_f}{\partial x_i} - \gamma_T \frac{\partial T_s}{\partial x_i} + \rho b_i = 0 \quad (2.281)$$

Furthermore, the small deformation assumption is used to link the deformations to the displacements,

$$\epsilon_{ij} = \frac{1}{2} \left( \frac{\partial u_i}{\partial x_j} + \frac{\partial u_j}{\partial x_i} \right) \quad (2.282)$$

In order to replace the deformation terms  $\epsilon_{ij}$  by the displacements  $u_i$ , the two first terms of equation (2.281) are modified, using the following expression,

$$\lambda^{DS} \frac{\partial \epsilon_{jj}}{\partial x_i} + 2 \mu^{DS} \frac{\partial \epsilon_{ij}}{\partial x_j} = \frac{\lambda^{DS}}{2} \left( 2 \frac{\partial^2 u_i}{\partial x_i \partial x_j} \right) + \mu^{DS} \left( \frac{\partial^2 u_i}{\partial x_j \partial x_j} + \frac{\partial^2 u_j}{\partial x_i \partial x_j} \right) \quad (2.283)$$

Finally the differential equation governing the displacements is obtained and expressed as a function of the primary variables used later in the finite element analysis,

$$\mu^{DS} \frac{\partial^2 u_i}{\partial x_j \partial x_j} + (\lambda^{DS} + \mu^{DS}) \frac{\partial^2 u_j}{\partial x_i \partial x_j} - \xi_p \frac{\partial p_p}{\partial x_i} - \xi_f \frac{\partial p_f}{\partial x_i} - \gamma_T \frac{\partial T_s}{\partial x_i} + \rho b_i = 0 \quad (2.284)$$

Although the balance of momentum could have been written for each species, the description of the balance of momentum for the mixture as a whole is preferred as it brings in the light the influence of the pressure of each fluid and of the solid temperature on the global displacement of the porous medium.

### 2.3.2 Balance of mass equation for the fluids

The balance of mass equations for the fluids are obtained by substituting the generalised Darcy's law and the porosity total derivation with respect to time, in the conservation of fluid mass formula and by using the Lagrangian total derivative concept. Each balance of mass equation introduces a mass transfer term, which is governed by the leakage parameter  $\Gamma$ .

The balance of mass for a species  $k$  may be written in two ways: with respect to the species  $k$  or with respect to the solid skeleton. The second alternative is preferred so as

to describe the balance of mass for the fluids with respect to the same referential. Using the local form of the balance equation for the species  $k$ , (2.13), the balance of mass (2.21) becomes,

$$\frac{d\rho^k}{dt} + \rho^k \operatorname{div} \mathbf{v}_s + \operatorname{div} \mathbf{M}_k = \hat{\rho}^k, \quad k = p, f. \quad (2.285)$$

Replacing the partial density  $\rho^k$  by its definition (2.1)<sub>3</sub> leads to,

$$\frac{d(n_k \rho_k)}{dt} + n_k \rho_k \operatorname{div} \mathbf{v}_s + \operatorname{div} \mathbf{M}_k = \hat{\rho}^k, \quad k = p, f. \quad (2.286)$$

By use of eq. (2.8)<sub>2</sub> and eq. (2.8)<sub>3</sub>, the previous relation is rearranged to,

$$n_k \frac{d^k \rho_k}{dt} + n_k (\mathbf{v}_s - \mathbf{v}_k) \cdot \nabla \rho_k + \rho_k \frac{dn_k}{dt} + n_k \rho_k \operatorname{div} \mathbf{v}_s + \operatorname{div} \mathbf{M}_k = \hat{\rho}^k, \quad k = p, f. \quad (2.287)$$

The porosity  $n_k$  and its total derivative with respect to time are expressed in the following relations:

$$n_k = \frac{V_k}{V} \quad \rightarrow \quad \frac{dn_k}{dt} = \frac{1}{V} \left( \frac{dV_k}{dt} - n_k \frac{dV}{dt} \right) \quad \text{and} \quad \frac{1}{V} \frac{dV}{dt} = \operatorname{div} \mathbf{v}_s \quad (2.288)$$

Replacing equation (2.288) into (2.287), the balance of mass writes,

$$n_k \frac{d^k \rho_k}{dt} + n_k (\mathbf{v}_s - \mathbf{v}_k) \cdot \nabla \rho_k + \frac{\rho_k}{V} \frac{dV_k}{dt} + \operatorname{div} \mathbf{M}_k = \hat{\rho}^k, \quad k = p, f. \quad (2.289)$$

In addition, the rate of the fluid density is now replaced by its definition, eq. (2.173), and equations (2.8)<sub>2</sub> - (2.8)<sub>3</sub> are used to obtain,

$$\begin{aligned} -\operatorname{div} \mathbf{M}_k &= n_k \rho_k c_{kH} \frac{dp_k}{dt} - n_k \rho_k c_{kT} \frac{dT_k}{dt} + \frac{\rho_k}{V} \frac{dV_k}{dt} - \hat{\rho}^k \\ &\quad + n_k (\mathbf{v}_k - \mathbf{v}_s) \cdot (\rho_k c_{kH} \nabla p_k + \rho_k c_{kT} \nabla T_k - \nabla \rho_k), \quad k = p, f; \end{aligned} \quad (2.290)$$

in which the terms on the second line cancel out to zero since in definition of the fluid density (2.173) the partial derivative  $\partial(\cdot)$  may be replaced by the gradient operator  $\nabla(\cdot)$ . The mass flux  $\mathbf{M}_k$ , defined in equation (2.3), relates to the volume flux  $\mathbf{J}_k = n_k (\mathbf{v}_k - \mathbf{v}_s)$  by,

$$\mathbf{M}_k = \rho_k \mathbf{J}_k, \quad k = p, f. \quad (2.291)$$

The idea is now to replace the mass flux  $\mathbf{M}_k$  by the generalised Darcy's law formula (2.249). Dividing by the density  $\rho_k$ , the comprehensive balance of mass for each fluid takes the form of the following equations:

$$\begin{aligned} \frac{\partial}{\partial x_i} \left[ \frac{k_p}{\mu_p} \left( \frac{\partial p_p}{\partial x_i} - \rho_p \mathbf{g} \right) + n_p \Theta_p \frac{\partial T_p}{\partial x_i} \right] &= n_p c_{pH} \frac{dp_p}{dt} - n_p c_{pT} \frac{dT_p}{dt} + \frac{1}{V} \frac{dV_p}{dt} - \frac{\hat{\rho}^p}{\rho_p} \\ \frac{\partial}{\partial x_i} \left[ \frac{k_f}{\mu_f} \left( \frac{\partial p_f}{\partial x_i} - \rho_f \mathbf{g} \right) + n_f \Theta_f \frac{\partial T_f}{\partial x_i} \right] &= n_f c_{fH} \frac{dp_f}{dt} - n_f c_{fT} \frac{dT_f}{dt} + \frac{1}{V} \frac{dV_f}{dt} + \frac{\hat{\rho}^p}{\rho_f} \end{aligned} \quad (2.292)$$

These equations depend on pore and fissure volumetric changes in time, which are not primary variables of the numerical model. They have to be replaced by their respective expressions (2.202), function of the pores and fissures pressures, the displacements and the solid temperature variation,

$$\begin{aligned} \frac{\partial}{\partial x_i} \left[ \frac{k_p}{\mu_p} \left( \frac{\partial p_p}{\partial x_i} - \rho_p \mathbf{g} \right) + n_p \Theta_p \frac{\partial T_p}{\partial x_i} \right] &= a_{pp} \frac{\partial p_p}{\partial t} + a_{pf} \frac{\partial p_f}{\partial t} + \xi_p \frac{\partial^2 u_i}{\partial t \partial x_i} + a_{pT_s} \frac{\partial T_s}{\partial t} \\ &\quad + a_{pT_p} \frac{\partial T_p}{\partial t} + \Gamma, \\ \frac{\partial}{\partial x_i} \left[ \frac{k_f}{\mu_f} \left( \frac{\partial p_f}{\partial x_i} - \rho_f \mathbf{g} \right) + n_f \Theta_f \frac{\partial T_f}{\partial x_i} \right] &= a_{ff} \frac{\partial p_f}{\partial t} + a_{fp} \frac{\partial p_p}{\partial t} + \xi_f \frac{\partial^2 u_i}{\partial t \partial x_i} + a_{fT_s} \frac{\partial T_s}{\partial t} \\ &\quad + a_{fT_f} \frac{\partial T_f}{\partial t} - \Gamma; \end{aligned} \quad (2.293)$$

in which,

$$\begin{aligned} a_{pp} &= n_p c_{pH} + c_{22} = n_p c_{pH} + (\xi_p - n_p) c_s - a_{pf}, \\ a_{ff} &= n_f c_{fH} + c_{33} = n_f c_{fH} + (\xi_f - n_f) c_s - a_{pf}, \\ a_{pf} &= a_{fp} = c_{32} = -(\xi_f - n_f)(c_p - c_s), \\ a_{pT_s} &= c_{24} = (n_p - \xi_p) c_T, \\ a_{pT_p} &= -n_p c_{pT} = -n_p c_{pT}, \\ a_{fT_s} &= c_{34} = (n_f - \xi_f) c_T, \\ a_{fT_f} &= -n_f c_{fT} = -n_f c_{fT}; \end{aligned} \quad (2.294)$$

where the coefficients  $c_{22}$  to  $c_{34}$  are available in equation (2.203). Due to the linearization of  $\rho^p$  around  $\rho_0$  and when neglecting the inertial terms, the mass transfer term  $\Gamma$  is induced by the chemical potential variation scaled by the temperatures,

$$\Gamma = -\frac{\hat{\rho}^p}{\rho_p} = T_0 \rho_p \eta \left( Y_p^{(2)} - Y_f^{(2)} \right) \quad (2.295)$$

$$= T_0 \rho_p \eta \left( \frac{G_p}{T_p} - \frac{G_f}{T_f} \right) \quad (2.296)$$

The latter relation is highly non-linear due to the form of the chemical potential eq. (2.160). The following approximation on  $\Gamma$  can be introduced after several linearisation around the reference configuration, eq. (2.161),

$$\Gamma \approx \rho_p \eta (G_p - G_f) \approx \gamma_{pp} (p_p - p_f) + \gamma_{pT} (T_p - T_f); \quad (2.297)$$

in which the linearised parameters are defined as,

$$\gamma_{pp} = \eta, \quad \text{and} \quad \gamma_{pT} = -\eta \rho_p S_0. \quad (2.298)$$

However, the main problem lies in the fact that the thermal contributions (linearised or not) depend on the value of the initial entropy  $S_0$  which is not directly available. Due to the potential nature of the entropy function, it is impossible to attribute a numerical value to  $S_0$ , except a quite arbitrary one. To assign an arbitrary value to  $S_0$ , a reference state needs to be chosen. The choice of the reference state is discussed in Chapter 8.

Equations (2.293) present the final expressions of the balance of mass for the pore fluid and the fissure fluid in terms of explicit primary unknowns.

### 2.3.3 The comprehensive energy equations

The balance of energy equations describe an equilibrium between the energy released in a system (or phase) and the amount of energy absorbed by the system, either by heat supply or by external work. When writing the balance of energy equation for species, transfer terms are revealed, whereas when writing the balance of energy for the mixture as a whole, they become elusive. As the aim of this study is to model the thermal transient period which occurs before the system reaches thermal equilibrium, it appears natural to consider one balance of energy equation for each phase.

In order to work with a coherent system, the balance of energy equations of each phase are expressed with respect to the solid skeleton. In addition, the balance of energy equations phrased in terms of specific internal energies are transformed to internal energies per unit volume. The starting point is eq. (2.50) for  $k \in \mathcal{K}$ ,

$$\rho^k \frac{d^k U_k}{dt} - \boldsymbol{\sigma}^k : \nabla \mathbf{v}_k + \operatorname{div} \mathbf{q}_k - r_k = \hat{\rho}^k \left( \tilde{U}_k - U_k + \frac{1}{2} (\tilde{\mathbf{v}}_k - \mathbf{v}_k)^2 \right) + \hat{u}_k \quad (2.299)$$

$$\begin{aligned} \frac{d(\rho^k U_k)}{dt} + \operatorname{div}(U_k \mathbf{M}_k) + \rho^k U_k \operatorname{div} \mathbf{v}_s - \boldsymbol{\sigma}^k : \nabla \mathbf{v}_k + \operatorname{div} \mathbf{q}_k - r_k \\ = \hat{\rho}^k \left( \tilde{U}_k + \frac{1}{2} (\tilde{\mathbf{v}}_k - \mathbf{v}_k)^2 \right) + \hat{u}_k \end{aligned} \quad (2.300)$$

There are many different manners to write the balance of energy. One way is to replace directly the internal energy  $d(\rho^k U_k)$  by its formulation as function of the primary variables. If this constitutive relation is not known, as it is the case for the solid phase, the other way is to replace the internal energy by another thermodynamical function, which constitutive relation is known. In our case, the constitutive equation of the entropy is known for both the solid phase and for the fluid phases, see equations (2.202) and (2.151), respectively.

To obtain the final form of the balance of energy equation several substitutions are involved. The complete demonstration is provided in Appendix D. A summary of the procedure is provided below. (1) The solid phase and (2) the fluid phases are considered in turn.

(1) Given the elastic potential in the actual configuration  $\underline{\Psi}^a$ , the internal energy of the solid results from the definition of  $\underline{\Psi}^a$ , equation (2.110),

$$\rho^s U_s = \underline{\Psi}^a + T_s \rho^s S_s + \sum_{p,f} n_k p_k \quad (2.301)$$

and, with help of the elastic potential's derivative, equation (2.117), the rate of internal energy can be related to the rate of entropy through,

$$\frac{d(\rho^s U_s)}{dt} = \frac{\partial \underline{\Psi}^a}{\partial \boldsymbol{\epsilon}} : \frac{d\boldsymbol{\epsilon}}{dt} + T_s \frac{d(\rho^s S_s)}{dt} + \sum_{k \in \mathcal{K}^*} p_k \frac{dn_k}{dt} \quad (2.302)$$

Therefore, *the balance of energy for the solid phase* is obtained by inserting (2.302) into (2.300), namely,

$$T_s \frac{d^s (\rho^s S_s)}{dt} + T_s \rho^s S_s \operatorname{div} \mathbf{v}_s + \sum_{k \in \mathcal{K}^*} p_k \frac{d^s n_k}{dt} + \operatorname{div} \mathbf{q}_s - r_s - \frac{\hat{\rho}^s}{2} \mathbf{v}_s^2 + \underbrace{(\mathbf{v}_s \cdot \hat{e}_{\mathcal{M}}^s - \hat{e}_{\mathcal{U}}^s)}_{\text{energy transfer}} = 0 \quad (2.303)$$

Note that the rate of mass transfer of the solid has been kept for completeness, even if it vanishes in the double porosity model.

(2) As for the fluid  $k$ , insertion of the definition of the rate of internal energy from Table (2.1) into equation (2.300), with help of the balance of mass (2.21) and the balance of momentum (2.32) yields,

$$T_k \frac{d^s (\rho^k S_k)}{dt} + T_k \rho^k S_k \operatorname{div} \mathbf{v}_s + T_k \operatorname{div} (S_k \mathbf{M}_k) - p_k \frac{d^k n_k}{dt} + \operatorname{div} \mathbf{q}_k - r_k + \hat{\rho}^k \left( G_k - \tilde{U}_k - \frac{1}{2} (\tilde{\mathbf{v}}_k - \mathbf{v}_k)^2 \right) - \hat{u}_k = 0 \quad (2.304)$$

This energy equation may be rewritten in a format which involves terms of the rates of entropy production associated to generalised diffusion, mass transfer and energy transfer,

$$\begin{aligned} & T_k \frac{d^s (\rho^k S_k)}{dt} + T_k \rho^k S_k \operatorname{div} \mathbf{v}_s + T_k \operatorname{div} (S_k \mathbf{M}_k) - p_k \frac{d^s n_k}{dt} + \underbrace{\operatorname{div} \mathbf{q}_k}_{\text{diffusion}} - r_k \\ & + \underbrace{\hat{\rho}^k \left( G_k + \frac{1}{2} (\mathbf{v}_k - \mathbf{v}_s)^2 - \frac{1}{2} \mathbf{v}_s^2 \right)}_{\text{mass transfer}} + \underbrace{(\mathbf{v}_s \cdot \hat{e}_{\mathcal{M}}^k - \hat{e}_{\mathcal{U}}^k)}_{\text{energy transfer}} \\ & + \underbrace{\mathbf{J}_k \cdot \left( \nabla p_k + \rho_k \left( \frac{d^k \mathbf{v}_k}{dt} - \mathbf{b}_k \right) \right)}_{\text{convection}} = 0 \end{aligned} \quad (2.305)$$

Equation (2.305) is written in an comprehensive format, since *the mass transfer fluxes*  $\hat{\rho}_k$ , *the energy transfer fluxes*  $(\mathbf{v}_s \cdot \hat{e}_{\mathcal{M}}^k - \hat{e}_{\mathcal{U}}^k)$ , *the heat fluxes*  $\mathbf{q}_k$  and *the hydraulic fluxes*  $\mathbf{J}_k$  are directly available from the constitutive equations. Equation (2.305) can be rearranged by replacing the term,  $T_k \operatorname{div} (S_k \mathbf{M}_k)$ ,

$$\begin{aligned}
& T_k \frac{d^s}{dt} \left( \rho^k S_k \right) + \underbrace{\operatorname{div} \mathbf{q}_k}_{\text{diffusion}} - r_k + \underbrace{\left( \mathbf{v}_s \cdot \hat{e}_{\mathcal{M}}^k - \hat{e}_{\mathcal{U}}^k \right)}_{\text{energy transfer}} + \underbrace{\hat{\rho}^k (H_0)}_{\text{mass transfer}} \\
& - T_k S_k \frac{dm^k}{dt} + T_k \rho^k S_k \operatorname{div} \mathbf{v}_s - p_k \frac{d^s n_k}{dt} \\
& + \underbrace{\hat{\rho}^k \left( (H_k - H_0) + \frac{1}{2} (\mathbf{v}_k - \mathbf{v}_s)^2 - \frac{1}{2} \mathbf{v}_s^2 \right)}_{\text{mass transfer}} + \underbrace{\mathbf{M}_k \cdot \left( \nabla H_k + \left( \frac{d^k \mathbf{v}_k}{dt} - \mathbf{b}_k \right) \right)}_{\text{convection}} = 0
\end{aligned} \tag{2.306}$$

The first order terms are written on the first line and the second order terms are gathered on the second and third lines. All the second order terms are kept for precaution. Although the convection and the mass transfer phenomena are of second order, their influence might be important. The magnitude of their influence will be established later in this document. The comprehensive energy equations for the solid, the pore fluid and the fissure fluid expressed in terms of the primary variables used later in the finite element analysis are now detailed.

**Remark 2.22.** *The balance of energy for the mixture in thermal equilibrium  $T_k = T_s = T$  is obtained by summing up the energy equations over the species and by accounting for the closure relations (2.20), (2.31), (2.46),*

$$\begin{aligned}
& T \frac{dS}{dt} + T S \operatorname{div} \mathbf{v}_s + \operatorname{div} \mathbf{q} - r + \sum_{p,f} \hat{\rho}^k \left( H_k + \frac{1}{2} (\mathbf{v}_k - \mathbf{v}_s)^2 \right) \\
& - \sum_{p,f} T S_k \left( \frac{1}{\det \mathbf{F}} \frac{dm^k}{dt} \right) + \sum_{p,f} \mathbf{M}_k \cdot \left( \nabla H_k + \left( \frac{d^k \mathbf{v}_k}{dt} - \mathbf{b}_k \right) \right) = 0
\end{aligned} \tag{2.307}$$

*The complete demonstration is provided in Appendix D.*

### 2.3.3.1 Energy equation of the solid constituent

Considering that the volume heat source  $r_s$  and the rate of mass transfer  $\hat{\rho}^s$  of the solid skeleton are zero, the comprehensive balance of energy equation for the solid constituent is obtained by replacing the constitutive laws into the balance of energy equation,

	$T_s \, d^s(\rho^s S_s)$	$p_p \, d^s n_p$	$p_f \, d^s n_f$	$T_s \, \rho^s S_s \, d(\text{tr } \epsilon)$
$a_{T_s T_s}$	$= n_s \, C_{s,p}$	$+ p_p \, c_{24}$	$+ p_f \, c_{34}$	$+ 0$
$a_{T_s p}$	$= T_s \, c_{24}$	$+ p_p \, c_{22}$	$+ p_f \, c_{32}$	$+ 0$
$a_{T_s f}$	$= T_s \, c_{34}$	$+ p_p \, c_{23}$	$+ p_f \, c_{33}$	$+ 0$
$a_{T_s \epsilon}$	$= T_s \, K^{DS} \, c_T$	$+ p_p \, (\xi_p - n_p)$	$+ p_f \, (\xi_f - n_f)$	$+ T_s \, \rho^s S_s$

Table 2.6: Origins of the coefficients used in equation (2.309).

$$-\text{div } \mathbf{q}_s = T_s \frac{d(\rho^s S_s)}{dt} + T_s \rho^s S_s \frac{d(\text{tr } \epsilon)}{dt} + p_p \frac{dn_p}{dt} + p_f \frac{dn_f}{dt} + (\mathbf{v}_s \cdot \hat{e}_{\mathcal{M}}^s - \hat{e}_{\mathcal{U}}^s) \quad (2.308)$$

The useful constitutive equations are,

- the heat flux diffusion of the solid phase  $\mathbf{q}_s$ , equation (2.249);
- the thermo-mechanical rate of entropy of the solid skeleton  $d(\rho^s S_s)$ , equation (2.202)<sub>4</sub>; in which the increment  $\Delta(\cdot)$  is assumed equivalent to the rate  $d(\cdot)$  operator;
- the rate of volume fraction of the fluid phases  $dn_k$  for  $k = p, f$ , equation (2.212);
- the rate of energy transfer for the solid skeleton  $(\mathbf{v}_s \cdot \hat{e}_{\mathcal{M}}^s - \hat{e}_{\mathcal{U}}^s)$ , described in equation (2.277)<sub>3</sub>,

Assuming the pore fluid, fissure fluid and solid temperatures are in local thermal non-equilibrium, the energy balance for the solid phase can be written as,

$$\begin{aligned} \frac{\partial}{\partial x_i} \left( n_s \, \Lambda_s \frac{\partial T_s}{\partial x_i} \right) &= a_{T_s T_s} \frac{\partial T_s}{\partial t} + a_{T_s p} \frac{\partial p_p}{\partial t} + a_{T_s f} \frac{\partial p_f}{\partial t} + a_{T_s \epsilon} \frac{\partial^2 u_i}{\partial t \partial x_i} \\ &+ \kappa_{sp} (T_s - T_p) + \kappa_{sf} (T_s - T_f), \end{aligned} \quad (2.309)$$

in which the coefficients are issued from different origins, see Table 2.6, in which the coefficients  $c_{22}$  to  $c_{34}$  are available in equation (2.203). Equation (2.309) accounts for the flux of thermal energy due to conduction, the change in the internal energy of the solid phase due to the solid temperature variation, the pore and the fissure pressure variations, the volume change of the solid skeleton, and the transfer of energy between the solid phase and the pore fluid and between the solid phase and the fissure fluid.



Note that no convection is accounted for into the balance of energy of the solid phase due to the approximation,

$$\frac{\partial(\cdot)}{\partial x_j} \cdot \mathbf{v}_s \ll \frac{\partial(\cdot)}{\partial t} \quad \text{induces} \quad \frac{d(\cdot)}{dt} \approx \frac{\partial(\cdot)}{\partial t} \quad (2.310)$$

which seems realistic since the velocity of the solid phase is in most cases of interest smaller (due to the small deformations assumption) than the other species.

### 2.3.3.2 Energy equation of the fluids

Considering that the volume heat sources of the fluids are zero,  $r_p = r_f = 0$ , and that the inertial terms are neglected, the comprehensive balance of energy for the fluids is obtained by replacing the appropriate constitutive equations into,

$$\begin{aligned} -\operatorname{div} \mathbf{q}_k &= T_k \frac{d}{dt} (\rho^k S_k) - p_k \frac{dn_k}{dt} - T_k \rho^k S_k \left( \frac{1}{n_k} \frac{1}{\rho_k} \frac{dm^k}{dt} - \frac{d(\operatorname{tr} \boldsymbol{\epsilon})}{dt} \right) \\ &\quad + (\mathbf{v}_s \cdot \hat{e}_{\mathcal{M}}^k - \hat{e}_{\mathcal{U}}^k) + \hat{\rho}^k H_k + \mathbf{M}_k \cdot \nabla H_k \end{aligned} \quad (2.311)$$

The useful constitutive equations are,

- the heat flux diffusion of the fluid phases  $\mathbf{q}_k$  for  $k = p, f$ , equation (2.249);
- the thermo-mechanical rate of entropy of the fluids  $d(\rho^k S_k)$  for  $k = p, f$ , eq. (2.204);
- the rate of volume fraction of the fluid phases  $dn_k$  for  $k = p, f$ , equation (2.212);
- the rate of mass content of the fluid phase  $dm_k/\rho_k$  for  $k = p, f$ , equation (2.207);
- the rate of the global energy transfer for the fluid phases  $(\mathbf{v}_s \cdot \hat{e}_{\mathcal{M}}^k - \hat{e}_{\mathcal{U}}^k)$  for  $k = p, f$ , described in equation (2.277),

The energy balance equation for the pore fluid writes,

$$\begin{aligned} \frac{\partial}{\partial x_i} \left( n_p T_p \Theta_p \left( \frac{\partial p_p}{\partial x_i} - \rho_p \mathbf{g} \right) + n_p \Lambda_p \frac{\partial T_p}{\partial x_i} \right) &= a_{T_p T_p} \frac{\partial T_p}{\partial t} + a_{T_p p} \frac{\partial p_p}{\partial t} + a_{T_p f} \frac{\partial p_f}{\partial t} \\ &\quad + a_{T_p \epsilon} \frac{\partial^2 u_i}{\partial t \partial x_i} + a_{T_p T_s} \frac{\partial T_s}{\partial t} \\ &\quad + \kappa_{sp} (T_p - T_s) + \kappa_{pf} (T_p - T_f) \\ &\quad + \hat{\rho}^p H_p + \mathbf{M}_p \cdot \nabla H_p \end{aligned} \quad (2.312)$$

in which the coefficients are issued from different origins (Table 2.7).

	$T_p d^s(\rho^p S_p)$	$p_p d^s n_p$	$T_p \rho_p S_p d^s m_p / \rho_p + T_p \rho^p S_p d^s(\text{tr } \epsilon)$
$a_{T_p T_p}$	$= n_p C_{p,p}$	$+ 0$	$+ T_p \rho_p S_p n_p c_{pT}$
$a_{T_p p}$	$= -T_p n_p c_{pT}$	$- p_p c_{22}$	$- T_p \rho_p S_p c_{22}$ $- T_p \rho_p S_p n_p c_{pH}$
$a_{T_p f}$	$= 0$	$- p_p c_{23}$	$- T_p \rho_p S_p c_{23}$
$a_{T_p \epsilon}$	$= 0$	$- p_p (\xi_p - n_p)$	$- T_p \rho_p S_p \xi_p + T_p \rho^p S_p$
$a_{T_p T_s}$	$= 0$	$- p_p c_{24}$	$- T_p \rho_p S_p c_{24}$

Table 2.7: Origins of the coefficients used in equation (2.312).

Similarly, the energy balance equation for the fissure fluid writes,

$$\begin{aligned}
\frac{\partial}{\partial x_i} \left( n_f T_f \Theta_f \left( \frac{\partial p_f}{\partial x_i} - \rho_p \mathbf{g} \right) + n_f \Lambda_f \frac{\partial T_f}{\partial x_i} \right) &= a_{T_f T_f} \frac{\partial T_f}{\partial t} + a_{T_f p} \frac{\partial p_p}{\partial t} + a_{T_f f} \frac{\partial p_f}{\partial t} \\
&+ a_{T_f \epsilon} \frac{\partial^2 u_i}{\partial t \partial x_i} + a_{T_f T_s} \frac{\partial T_s}{\partial t} \\
&+ \kappa_{sf} (T_f - T_s) + \kappa_{pf} (T_f - T_p) \\
&+ \hat{\rho}^f H_f + \mathbf{M}_f \cdot \nabla H_f
\end{aligned} \tag{2.313}$$

in which the coefficients are issued from different origins (Table 2.8). The coefficients  $c_{22}$  to  $c_{34}$  are available in equation (2.203). Equations (2.312) and (2.313) account for the flux of thermal energy due to conduction, the change in the internal energy of the fluid phases due to the solid and the fluid temperature variations, the pore and the fissure pressure variations, the volume change of the solid skeleton, and the transfer of energy between the solid phase and the fluid and between the two fluid phases.

Note that in both equations (2.312) and (2.313), convection is accounted for through a term of the form  $\mathbf{M}_k \cdot \nabla H_k$ . The convection contributions with the enthalpy gradient formulation (2.160)<sub>3</sub>, the specific volume definition (2.146) and constant thermal expansion coefficients  $c_{Tk}$  write,

$$\begin{aligned}
\mathbf{M}_k \cdot \nabla H_k &= n_k \rho_k (\mathbf{v}_k - \mathbf{v}_s) \cdot \left( \frac{1 - T_0 c_{Tk}}{\rho_k} \nabla p_k + C_{k,p} \nabla T_k \right), \quad \text{for } k = p, f; \\
&= b_{T_k k} (\mathbf{v}_k - \mathbf{v}_s) \cdot \nabla p_k + b_{T_k T_k} (\mathbf{v}_k - \mathbf{v}_s) \cdot \nabla T_k, \quad \text{for } k = p, f; \tag{2.314}
\end{aligned}$$

	$T_f d^s(\rho^f S_f)$	$p_f d^s n_f$	$T_f \rho_f S_f d^s m_f / \rho_f + T_f \rho^f S_f d^s(\text{tr } \epsilon)$
$a_{T_f T_f} =$	$n_f C_{f,p}$	$+ 0$	$+ T_f \rho_f S_f n_f c_{fT}$
$a_{T_f p} =$	$0$	$- p_f c_{32}$	$- T_f \rho_f S_f c_{32}$
$a_{T_f f} =$	$-T_f n_f c_{fT}$	$- p_f c_{33}$	$- T_f \rho_f S_f c_{33}$ $- T_f \rho_f S_f n_f c_{fH}$
$a_{T_f \epsilon} =$	$0$	$- p_f (\xi_f - n_f)$	$- T_f \rho_f S_f \xi_f + T_f \rho^f S_f$
$a_{T_f T_s} =$	$0$	$- p_f c_{34}$	$- T_f \rho^f S_f c_{24}$

Table 2.8: Origins of the coefficients used in equation (2.313).

in which the convective parameters are defined as,

$$\begin{aligned}
b_{T_p p} &= n_p(1 - c_{pT} T_0), & b_{T_f f} &= n_f(1 - c_{fT} T_0), \\
b_{T_p T_p} &= n_p \rho_p C_{p,p}, & b_{T_f T_f} &= n_f \rho_f C_{f,p}.
\end{aligned} \tag{2.315}$$

The influence of the magnitude of these terms will be established latter in this document (Chapter 8). Moreover, the change in the internal energy of the fluid phases due to mass transfer is accounted for through  $\hat{\rho}^k H_k$ . The following approximations on  $\hat{\rho}^p H_p$  and  $\hat{\rho}^f H_f$  can be introduced by use of eq. (2.297) and by several linearisation around the reference configuration,

$$\begin{aligned}
\hat{\rho}^p H_p &\approx -\rho_0 [\gamma_{pp} (p_p - p_f) + \gamma_{pT} (T_p - T_f)] \times \\
&\quad [v_0(1 - T_0 c_{Tp}) (p_p - p_0) + C_{p,p} (T_p - T_0) + H_0], \\
&\approx -\rho_0 \eta [(p_p - p_f) - \rho_0 S_0 (T_p - T_f)] \times [C_{p,p} (T_p - T_0) + H_0], \\
&\approx \gamma_{T_p p} (p_p - p_f) + \gamma_{T_p T_p} (T_p - T_f), \\
\hat{\rho}^f H_f &\approx \gamma_{T_f f} (p_p - p_f) + \gamma_{T_f T_f} (T_p - T_f).
\end{aligned} \tag{2.316}$$

Again, the main problem lies in the fact that the changes in the internal energy of the fluid phases due to mass transfer depend on the value of the initial enthalpy  $H_0$  which is not directly available. Hence, the linearised parameters,

$$\gamma_{T_p p} = \eta \rho_0 \times [C_{p,p} T_0 - H_0] \quad \text{and} \quad \gamma_{T_p T_p} = -\eta \rho_0^2 S_0 \times [C_{p,p} T_0 - H_0], \tag{2.317}$$

$$\gamma_{T_f f} = -\eta\rho_0 \times [C_{f,p}T_0 - H_0] \quad \text{and} \quad \gamma_{T_f T_f} = +\eta\rho_0^2 S_0 \times [C_{f,p}T_0 - H_0], \quad (2.318)$$

require the definitions of the arbitrary initial enthalpy  $H_0$  and of the arbitrary initial entropy  $S_0$ .

## 2.4 Summary of governing equations

The full set of differential equations describing the balance equation, the fluid flow and the heat transfer through deformable fissured porous media with double porosity is presented below.

*The balance of momentum equation for the mixture as a whole, for  $i = 1, 3$*

$$\mu^{DS} \frac{\partial^2 u_i}{\partial x_j \partial x_j} + (\lambda^{DS} + \mu^{DS}) \frac{\partial^2 u_j}{\partial x_i \partial x_j} - \xi_p \frac{\partial p_p}{\partial x_i} - \xi_f \frac{\partial p_f}{\partial x_i} - a_{\epsilon T_s} \frac{\partial T_s}{\partial x_i} + \rho b_i = 0 \quad (2.319)$$

*The balance of mass equations for the fluids*

$$\begin{aligned} \frac{\partial}{\partial x_j} \left( \frac{k_p}{\mu_p} \left( \frac{\partial p_p}{\partial x_j} - \rho_p \mathbf{g} \right) + n_p \Theta_p \frac{\partial T_p}{\partial x_j} \right) &= a_{pp} \frac{\partial p_p}{\partial t} + a_{pf} \frac{\partial p_f}{\partial t} + \xi_p \frac{\partial^2 u_j}{\partial t \partial x_j} + a_{pT_s} \frac{\partial T_s}{\partial t} \\ &\quad + a_{pT_p} \frac{\partial T_p}{\partial t} + \Gamma \end{aligned} \quad (2.320)$$

$$\begin{aligned} \frac{\partial}{\partial x_j} \left( \frac{k_f}{\mu_f} \left( \frac{\partial p_f}{\partial x_j} - \rho_f \mathbf{g} \right) + n_f \Theta_f \frac{\partial T_f}{\partial x_j} \right) &= a_{ff} \frac{\partial p_f}{\partial t} + a_{pf} \frac{\partial p_p}{\partial t} + \xi_f \frac{\partial^2 u_j}{\partial t \partial x_j} \\ &\quad + a_{fT_s} \frac{\partial T_s}{\partial t} + a_{fT_f} \frac{\partial T_f}{\partial t} - \Gamma \end{aligned} \quad (2.321)$$

*The balance of energy equations for solid and the fluids*

$$\begin{aligned} \frac{\partial}{\partial x_j} \left( n_s \Lambda_s \frac{\partial T_s}{\partial x_j} \right) &= a_{T_s T_s} \frac{\partial T_s}{\partial t} + a_{T_s p} \frac{\partial p_p}{\partial t} + a_{T_s f} \frac{\partial p_f}{\partial t} + a_{T_s \epsilon} \frac{\partial^2 u_j}{\partial t \partial x_j} \\ &\quad + \kappa_{sp} (T_s - T_p) + \kappa_{sf} (T_s - T_f) \end{aligned} \quad (2.322)$$

$$\begin{aligned}
\frac{\partial}{\partial x_j} \left( T_p n_p \Theta_p \left( \frac{\partial p_p}{\partial x_j} - \rho_p \mathbf{g} \right) + n_p \Lambda_p \frac{\partial T_p}{\partial x_j} \right) &= a_{T_p T_p} \frac{\partial T_p}{\partial t} + a_{T_p p} \frac{\partial p_p}{\partial t} + a_{T_p f} \frac{\partial p_f}{\partial t} \\
&+ a_{T_p \epsilon} \frac{\partial^2 u_j}{\partial t \partial x_j} + a_{T_p T_s} \frac{\partial T_s}{\partial t} \\
&+ \kappa_{sp} (T_p - T_s) + \kappa_{pf} (T_p - T_f) \\
&+ \hat{\rho}^p H_p + \mathbf{M}_p \cdot \nabla H_p
\end{aligned} \tag{2.323}$$

$$\begin{aligned}
\frac{\partial}{\partial x_j} \left( T_f n_f \Theta_f \left( \frac{\partial p_f}{\partial x_j} - \rho_f \mathbf{g} \right) + n_f \Lambda_f \frac{\partial T_f}{\partial x_j} \right) &= a_{T_f T_f} \frac{\partial T_f}{\partial t} + a_{T_f p} \frac{\partial p_p}{\partial t} + a_{T_f f} \frac{\partial p_f}{\partial t} \\
&+ a_{T_f \epsilon} \frac{\partial^2 u_j}{\partial t \partial x_j} + a_{T_f T_s} \frac{\partial T_s}{\partial t} \\
&+ \kappa_{sf} (T_f - T_s) + \kappa_{pf} (T_f - T_p) \\
&+ \hat{\rho}^f H_f + \mathbf{M}_f \cdot \nabla H_f
\end{aligned} \tag{2.324}$$

The aim of this gathering is to visualise the coupling coefficients which link the model, e.g. the effective stress parameter  $\xi_p$  appears in both the momentum balance equation and in the pore fluid mass balance equation. To ease this summary, the coupling parameters are highlighted in color.

scalar part	first order part		
$\xi_p = (c_p - c_s)/c$			
$\xi_f = (c - c_p)/c$			
$a_{pp} = n_p c_{pH} + c_{22}$			
$a_{ff} = n_f c_{fH} + c_{33}$			
$a_{pf} = c_{32}$			
$a_{pT_s} = c_{24}$			
$a_{pT_p} = -n_p c_{pT}$			
$a_{fT_s} = c_{34}$			
$a_{fT_f} = -n_f c_{fT}$			
$a_{\epsilon T_s} = \gamma T$			
$a_{T_s T_s} = n_s C_{s,p}$	+	$p_p c_{24} + p_f c_{34}$	+ 0
$a_{T_s p} = T_s c_{24}$	+	$p_p c_{22} + p_f c_{32}$	+ 0
$a_{T_s f} = T_s c_{34}$	+	$p_p c_{23} + p_f c_{33}$	+ 0
$a_{T_s \epsilon} = T_s \gamma T$	+	$p_p (\xi_p - n_p)$	+ $T_s \rho^s S_s$
		+ $p_f (\xi_f - n_f)$	
$a_{T_p T_p} = n_p C_{p,p}$	+	0	+ $T_p \rho_p S_p n_p c_{pT}$
$a_{T_p p} = -T_p n_p c_{pT}$	-	$p_p c_{22}$	- $T_p \rho_p S_p (c_{22} + n_p c_{pH})$
$a_{T_p f} = 0$	-	$p_p c_{23}$	- $T_p \rho_p S_p c_{23}$
$a_{T_p \epsilon} = 0$	-	$p_p (\xi_p - n_p)$	- $T_p \rho_p S_p \xi_p$
$a_{T_p T_s} = 0$	-	$p_p c_{24}$	- $T_p \rho_p S_p c_{24}$
$a_{T_f T_f} = n_f C_{f,p}$	+	0	+ $T_f \rho_f S_f n_f c_{fT}$
$a_{T_f p} = 0$	-	$p_f c_{32}$	- $T_f \rho_f S_f c_{32}$
$a_{T_f f} = -T_f n_f c_{fT}$	-	$p_f c_{33}$	- $T_f \rho_f S_f (c_{33} + n_f c_{fH})$
$a_{T_f \epsilon} = 0$	-	$p_f (\xi_f - n_f)$	- $T_f \rho_f S_f \xi_f$
$a_{T_f T_s} = 0$	-	$p_f c_{34}$	- $T_f \rho_f S_f c_{34}$

Table 2.9: Coefficients of the model

Next, the coefficients are written so as to visualise a scalar part and a first order part (Table 2.9). This segregation is due to the reference state assumptions. Upon linearization around the reference state:  $T_0 \neq 0$ ,  $p_0 = 0$  and  $S_0 = 0$ , the coefficients will reduce to the first column only.

Note that the model is non-linear due to the presence of primary variables in the coefficients: the temperatures  $T_s$ ,  $T_p$  and  $T_f$ , the pressures  $p_p$  and  $p_f$ , and the entropies  $S_p$  and  $S_f$ .

This full set of comprehensive equations is *coupled* through several coupling coefficients. Table 2.10 illustrates the couplings which occur in between the six comprehensive equations. Each coupling involves its own coupling coefficient. This table clearly shows the non-symmetry of the model induced by the thermo-hydro-mechanical approach. Only the upper-left area, the hydro-mechanical part, is symmetric.

More precisely, six terms appear to be of second order (upon linearization around the reference state). They appear in Table 2.10 in a black color, namely  $a_{T_p\epsilon}$ ,  $a_{T_f\epsilon}$ ,  $a_{T_p f}$ ,  $a_{T_f p}$ ,  $a_{T_p T_s}$  and  $a_{T_f T_s}$ . If they can be neglected, the above comprehensive set of equations will be form-symmetric (symmetric in form but not symmetric in value).

Note that in local thermal equilibrium, the thermo-hydro-mechanical model still displays non symmetry, for example  $a_{\epsilon T_s} \neq a_{T_s \epsilon}$ . This remark stays valid even if the coefficients are linearised around the reference state.

	Momentum balance	Pore fluid bal. mass	Fiss. fluid bal. mass	Solid bal. energy	Pore fluid bal. energy	Fiss. fluid bal. energy
Momentum balance		$\xi_p$	$\xi_f$	$a_{\epsilon T_s}$		
Pore fluid bal. mass	$\xi_p$		$a_{pf}$	$a_{pT_s}$	$a_{pT_p}$	
Fissure fluid bal. mass	$\xi_f$	$a_{pf}$		$a_{fT_s}$		$a_{fT_f}$
Solid bal. energy	$a_{T_s\epsilon}$	$a_{T_s p}$	$a_{T_s f}$		$\kappa_{sp}$	$\kappa_{sf}$
Pore fluid bal. energy	$a_{T_p\epsilon}$	$a_{T_p p}$	$a_{T_p f}$	$a_{T_p T_s}, \kappa_{sp}$		$\kappa_{pf}$
Fissure fluid bal. energy	$a_{T_f\epsilon}$	$a_{T_f p}$	$a_{T_f f}$	$a_{T_f T_s}, \kappa_{sf}$	$\kappa_{pf}$	

Table 2.10: Sketch of the repartition of the coupling coefficients in the model. The model displays non symmetry. The diagonal or direct coefficients are not represented here.

## 2.5 Parameters identification

The parameters characterising the thermo-hydro-mechanical model are now gathered for identification. To each parameter is associated the corresponding unit expressed in the International System of Units. Two lists are presented: (1) the basic measurable parameters and (2) the coefficients of the governing equations (2.319) to (2.324). Recall that,

$$1 \text{ N} = 1 \frac{\text{kg}\cdot\text{m}}{\text{s}^2} \quad 1 \text{ Pa} = 1 \frac{\text{kg}}{\text{m}\cdot\text{s}^2} \quad 1 \text{ J} = 1 \text{ kg} \frac{\text{m}^2}{\text{s}^2} \quad 1 \text{ W} = 1 \text{ kg} \frac{\text{m}^2}{\text{s}^3}$$

(1) Let us first identify the basic measurable parameters:

- i.  $\lambda^{DS}$  and  $\mu^{DS}$  (unit: Pa) are the Lamé's constant of the drained solid. For an isotropic elastic material, they are completely defined in terms of the drained modulus of elasticity  $E$  and the drained Poisson's ratio  $\nu$ .
- ii.  $c_s$ ,  $c$  and  $c_p$  (unit: 1/Pa) are the the drained compressibilities of the solid grains, of the fissured porous medium and of the porous block, respectively. The drained compressibility  $c$  of the fissured porous medium can be expressed as a function of the elastic drained modulus  $E$  and the drained Poisson's ratio  $\nu$ .
- iii.  $c_{pH}$  and  $c_{fH}$  (unit: 1/Pa) are the hydraulic compressibilities of the pore fluid and of the fissure fluid, respectively.
- iv.  $C_{s,p}$ ,  $C_{p,p}$  and  $C_{f,p}$  (unit: J/m<sup>3</sup>/K) are the volumetric heat capacities at constant strain and fluid pressure of the solid phase, the pore fluid and the fissure fluid, respectively.
- v.  $c_T$  (unit: 1/K) is the volumetric thermal expansion coefficient of the drained skeleton. Similarly,  $c_{pT}$  and  $c_{fT}$  (unit: 1/K) are the volumetric thermal expansion coefficients of the pore fluid and the fissure fluid, respectively. These three parameters are measured at constant pressure.
- vi.  $\kappa_{sp}$ ,  $\kappa_{sf}$  and  $\kappa_{pf}$  (unit: W/m<sup>3</sup>/K) are the coefficients of heat exchange between solid - pore fluid, solid - fissure fluid and pore fluid - fissure fluid, respectively.
- vii.  $\Lambda_s$ ,  $\Lambda_p$  and  $\Lambda_f$  (unit: W/m/K) are the thermal conductivities of the solid, the pore fluid and the fissure fluid.
- viii.  $k_p$  and  $k_f$  (unit: m<sup>2</sup>) are the permeabilities of porous medium with respect to the porous block and to the fissure network.



- ix.  $\mu_p$  and  $\mu_f$  (unit: Pa.s) are the dynamic viscosities of the pore fluid and the fissure fluid, respectively.
- x.  $\Theta_p$  and  $\Theta_f$  (unit:  $\text{m}^2/\text{s}/\text{K}$ ) are coefficients of thermal coupling for the pore fluid flux and the fissure fluid flux, respectively, due to isothermal heat flux and thermo-osmosis hydraulic flow.
- xi.  $\rho_s$ ,  $\rho_p$  and  $\rho_f$  (unit:  $\text{kg}/\text{m}^3$ ) are the densities of the solid skeleton, the pore fluid and the fissure fluid, respectively.
- xii.  $n_s$ ,  $n_p$  and  $n_f$  are dimensionless porosities of the solid skeleton, the porous fluid and the fissure fluid, respectively.

(2) All the following coefficients are related to the basic measurable parameters listed above through relations given in Table 2.9:

- a.  $\xi_p$  and  $\xi_f$  are the dimensionless tangent effective stress parameters, relating the pore fluid and the fissure fluid pressure to the matrix deformation.
- b.  $a_{pp}$  and  $a_{ff}$  (unit:  $1/\text{Pa}$ ) are the apparent compressibilities of the pore fluid and the fissure fluid, respectively.
- c.  $a_{pf}$  (unit:  $1/\text{Pa}$ ) is the coupling coefficient relating the pore fluid to the fissure fluid volumetric deformation due to a change of pressures.
- d.  $a_{\epsilon T_s}$  (unit:  $\text{Pa}/\text{K}$ ) is the thermal expansion coefficient providing the coupling between the deformation and the balance of energy.  $a_{T_s \epsilon}$  (unit:  $\text{Pa}$ ) is its corresponding coupled coefficient providing the coupling between the balance of energy and the deformation. Moreover,  $a_{T_p \epsilon}$  and  $a_{T_f \epsilon}$  (unit:  $\text{Pa}$ ) are the coefficients providing the coupling between the balance of energy of the fluid and the deformation.
- e.  $a_{T_s T_s}$ ,  $a_{T_p T_p}$  and  $a_{T_f T_f}$  (unit:  $\text{Pa}/\text{K}$ ) are the apparent heat capacities of the solid phase, the pore fluid phase and the fissure phase, respectively.
- f.  $a_{p T_s}$ ,  $a_{p T_p}$  (unit:  $1/\text{K}$ ) provide coupling between the pore fluid flow model and the energy balance equations of solid and pore fluid, respectively.  $a_{T_s p}$ ,  $a_{T_p p}$  are their dimensionless corresponding coupled coefficients. Moreover,  $a_{T_f p}$  is the coefficient providing the coupling between the balance of energy of the fissure fluid and the pore pressure volumetric deformation.
- g.  $a_{f T_s}$ ,  $a_{f T_f}$  (unit:  $1/\text{K}$ ) provide coupling between the fissure fluid flow model and the energy balance equations of solid and fissure fluid, respectively.  $a_{T_s f}$ ,  $a_{T_f f}$  are their

dimensionless corresponding coupled coefficients. Moreover,  $a_{T_p f}$  is the coefficient providing the coupling between the balance of energy of the pore fluid and the fissure pressure volumetric deformation.

- h.  $a_{T_p T_s}$ ,  $a_{T_f T_s}$  (unit: Pa/K) provide coupling between the energy balance equations of solid and balance equation of the fluids, respectively.

The full set of comprehensive equations describing the behaviour of a porous medium with double porosity under thermo-hydro-mechanical loading has been presented in this chapter. Each introduced coefficient has been related to a measurable physical entity.

## Chapter 3

# Constitutive parameters: interpretation and identification

This chapter presents the constitutive parameters previously introduced in Chapter 2. The aim is to interpret and identify a range of values of these parameters (for soils, rocks and water) by gathering data from the literature. The constitutive parameters characteristic of dual porous media may be calculated in terms of constants that are measurable through experiments performed at different scales.

Section 3.1 presents intensive parameters. The mechanical parameters such as the Young's modulus, the Poisson's ratio and the drained compressibility are assumed to be invariant over a range of strains (small deformation assumption). In addition, geometrical (hydraulic) parameters such as the porosity and the permeability of each phase are considered intrinsic as they describe physically the mixture. Since the measurement of these parameters in porous media with double porosity is not common, a summary of comprehensive data acquisition is synthesised from the literature. Furthermore, the aperture factor characterising the degree of fissuration of the mixture is defined.

Section 3.2 outlines extensive parameters which may depend on temperature and/or pressure changes. Typically, the thermal expansion coefficients, the densities, the viscosity, the heat capacities and the thermal conductivities of the fluids and the solid are considered.

Section 3.3 describes the solid-fluid extensive parameters which may depend on the nature of both the fluid and the solid, and on other considerations. The coefficient of thermo-osmosis and the coefficient of inter-phase heat transfer are outlined.

Section 3.4 introduces dimensionless numbers used throughout this work such as the Reynolds number, the Prandtl number, the Péclet number, the Nusselt number and the Sparrow number.

### 3.1 Intensive parameters

An *intensive property* is a property that a phase has of itself, independently of other things, including its thermo-hydro-mechanical context. The mechanical and geometrical intensive parameters are considered in turn: (1) First, the Young's modulus and the Poisson's ratio are linked to the Lamé's constants. (2) Next, the drained compressibilities used in the definition of the effective stress parameters and the compressibilities of the fluid phases are considered. Specific to porous media with double porosity, (3) the porosities and (4) the permeabilities and most importantly their role are introduced. (5) Finally, the aperture factor is linked to the degree of fracturation of the medium.

#### 3.1.1 The Young's modulus, the Poisson's ratio and the Lamé's constants

Fractures are naturally oriented. Consequently porous media with double porosity display an anisotropic mechanical behaviour. However, for simplicity mechanical anisotropy is not accounted for in this model and each mechanical property is characterised by a unique isotropic value.

The Young's modulus and the Poisson's ratio are intensive quantities as they are independent of the amount of material under concern and of the amount of stress for small deformations. They can be deduced from a uniaxial compression test. Table 3.1 presents the range of values of the drained Young's modulus  $E^{DS}$  for different type of soils (Philipponnat et al., 2003).

Material	Young's modulus $E^{DS}$ [MPa]
Clay	2 to 30
Sand	10 to 100
Coarse sand	150 to 500
Rock	500 to 10 000

Table 3.1: Range of values of various drained Young's moduli from Philipponnat et al. (2003).

The Poisson's ratio for clay soils and rocks typically ranges between 0.125 and 0.5 (Francois, 2008; Gercek, 2007).

In linear isotropic elasticity, the Lamé's constants are called the Lamé's first parameter, denoted  $\lambda$  and the shear modulus or Lamé's second parameter  $\mu$ , respectively. Hooke's law for homogeneous isotropic materials is expressed in terms of these parameters,

$$\boldsymbol{\sigma} = 2 \mu \boldsymbol{\epsilon} + \lambda \operatorname{tr} \boldsymbol{\epsilon} \mathbf{I}. \quad (3.1)$$

The first parameter  $\lambda$  has no physical interpretation, but serves to simplify the stiffness matrix in Hooke's law. Both parameters constitute a parametrisation of the elastic moduli for homogeneous isotropic media and are named after Gabriel Lamé. The Lamé's constants of *the drained solid*  $\lambda^{DS}$  and  $\mu^{DS}$  are related to the Young's modulus  $E^{DS}$  and the Poisson's ratio  $\nu^{DS}$  by the following relations:

$$\lambda^{DS} = \frac{E^{DS} \nu^{DS}}{(1 + \nu^{DS})(1 - 2\nu^{DS})} \quad \text{and} \quad \mu^{DS} = \frac{E^{DS}}{2(1 + \nu^{DS})}. \quad (3.2)$$

### 3.1.2 The drained compressibilities

The drained compressibilities involved in the definition of the effective stress parameters and the compressibility of the fluid phases are presented in turn.

#### 3.1.2.1 The compressibilities involved in the effective stress parameters

When defining the effective stress parameters  $\xi_p$  and  $\xi_f$  in equation (2.132), three different drained compressibilities have been introduced: (1) the drained compressibility coefficient  $c$ , (2) the drained compressibility of the solid grains  $c_s$  and (3) the drained compressibility of the porous block  $c_p$ . Each of them is considered in turn:

1. Depending on strain conditions, *the drained compressibility coefficient*  $c$  for an isotropic elastic medium can be related to  $E^{DS}$  and  $\nu^{DS}$ , according to the following relationships:

- for one dimensional strain condition:  $\epsilon_{11} = c \sigma_{11}$ ,

$$c = \frac{(1 - 2\nu^{DS})(1 + \nu^{DS})}{(1 - \nu^{DS})E^{DS}}; \quad (3.3)$$

- for two dimensional strain condition:  $\epsilon_{11} + \epsilon_{22} = c (\sigma_{11} + \sigma_{22}) / 2$ ,

$$c = \frac{2(1 - 2\nu^{DS})(1 + \nu^{DS})}{E^{DS}}; \quad (3.4)$$

- for three dimensional strain condition:  $\epsilon_{11} + \epsilon_{22} + \epsilon_{33} = c(\sigma_{11} + \sigma_{22} + \sigma_{33})/3$ ,

$$c = \frac{3(1 - 2\nu^{DS})}{E^{DS}} = \frac{1}{\lambda^{DS} + \frac{2}{3}\mu^{DS}}. \quad (3.5)$$

2. *The drained compressibility of the solid grains  $c_s$*  is a measurable parameter, which represents the compressibility of the solid grains, that is the solid matrix with no pores and no fissures. Its inverse is denoted the bulk modulus of the solid phase  $K_s$  of unit 1/Pa. A large bulk modulus indicates a relative incompressible material. Bulk moduli of various soil minerals are presented in Table 3.2.

Mineral	Bulk modulus
	$K_s = 1/c_s$ [GPa]
Kaolinite	46
Illite	60
Chlorite	127
Quartz	38
Calcite	73
Muscovite	52
Dolomite	94
Anhydrite	55
Pyrite	143

Table 3.2: Bulk moduli of typical soil minerals from Gebrande (1982) and Francois (2008).

3. *The drained compressibility of the porous block  $c_p$*  represents the compressibility of the pores and the solid grains. This parameter is usually not *directly* measurable. As an estimation of its value is needed for the numerical analysis, a percentage of the drained compressibility of the fissured porous medium  $c$  is used.

Table 3.3 presents the magnitude of the compressibility ratios  $c_p/c$  and  $c_s/c_p$  from previous hydro-mechanical studies on porous media with double porosity.

Reference	$\frac{c_p}{c}$	$\frac{c_s}{c_p}$
Paslay and Cheatham (1963)	0.9	0.125
	0.8	0.1875
Kazemi (1969)	1	0
Khalili et al. (1999)	0.9	0

Table 3.3: Range of values of compressibility ratios for dual porous media.

One way to size the compressibility parameters consists in measuring indirectly the effective stress parameters. Hence, when knowing  $\xi_p$  and  $\xi_f$  one can deduce  $c$ ,  $c_p$  and  $c_s$ . Recall that the relationships linking the effective stress parameters to the compressibilities are,

$$\xi_p = \frac{c_p}{c} - \frac{c_s}{c} \quad \text{and} \quad \xi_f = 1 - \frac{c_p}{c}. \quad (3.6)$$

To measure  $\xi_p$  and  $\xi_f$  Wilson and Aifantis (1982) proposed an experimental approach that takes advantage of the time scale separation property of porous media with double porosity. Two measurements are made successively, (a) for early and (b) late times scale, on one sample only.

(a) During the early time scale: one assumes that only the fissures participate in the flow process (while at larger times both the fissures and the pores contribute). Thus during a drained test, one presumes for the short time scale that while the fissure fluid has communicated with the atmosphere ( $p_f = 0$ ), no fluid has yet transferred from the porous block to the fissure network. Measuring the volume of fluid drained out of a unit volume of the sample, which represents only the relative volumetric strain of the fissure fluid  $\theta_f$ , and the dilatation  $\Delta_f$ , the second effective stress parameter  $\xi_f$  is determined:

$$\xi_f = \frac{\theta_f}{\Delta_f}. \quad (3.7)$$

(b) During the late time scale: one assumes that all porosity types have communicated with the atmosphere ( $p_p = p_f = 0$ ). Measuring the total volumetric strain  $\Delta$  and the total dilatation  $\theta$ , the sum of the effective stress parameters is obtained:

$$\xi_p + \xi_f = \frac{\theta}{\Delta}. \quad (3.8)$$

### 3.1.2.2 The fluid compressibility

The compressibility  $c_{kH}$  of the fluid  $k$  is usually presented as the inverse of the bulk modulus. Its unit is 1/Pa. A large bulk modulus indicates a relative incompressible fluid. In most geomechanical applications, one may safely assume that the fluid compressibilities are independent of the temperature and of the pressure variations. Note that fluid compressibilities increase at very high pressures. Bulk moduli of various fluids are presented in Table 3.4 at atmospheric pressure and 20°C.

Material	Bulk modulus $1/c_{kH}$ [GPa]
Water	2.15
Sea water	2.34
SAE 30 Oil	1.5

Table 3.4: Bulk moduli of various fluids, at atmospheric pressure and 20°C.

### 3.1.3 The porosities

Porosity is dimensionless as it is a ratio of volume. Porosity is a fraction between 0 and 1, although it may also be represented in terms of percent, typically ranging from less than 0.01 for igneous rocks to more than 0.5 for clays.

One of the key points when considering media with double porosity is *the storage role of the porous block*. The significance of this storage function arises when comparing the porosity magnitude of the porous block with that of the fissure network: the porosity of the pores  $n_p$  appears to be much larger than the porosity of the fissures  $n_f$ , as illustrated in Table 3.5.

Wilson and Aifantis (1982) proposed two types of experiments to measure the porosities  $n_p$  and  $n_f$ , which take advantage of either (a) the length scale separation or (b) the time scale separation characteristics of porous media with double porosity.

(a) By using the length scale separation property: Two samples are used; one with a short range of investigation so that only the intergranular porosity of the blocks  $n_p$  is measured, and another with a long range of investigation so that the total porosity  $n = n_p + n_f$  is measured. These methods have the advantage of accounting for the deformation of the porosities, the fractures opening and the volume of the fissure network.



Reference	$n_p$	$n_f$
Kazemi (1969)	0.05	0.0012
	0.05	0.0028
	0.08	0.0023
Kazemi (1976)	0.19	0.01
	0.19	0.01
Khalili (1999)	0.54	0.06

Table 3.5: Range of values of the porous block porosity  $n_p$  and of the fissure network porosity  $n_f$  from the literature.

(b) By using the time scale separation property: A fluid (for example mercury) is injected into full-sized core samples, beginning at relatively low pressure, with the amount of injected fluid being recorded for each increment of pressure. When the fluid begins to penetrate the porous block, a sharp increase in the pressure occurs and the porosity of the fissures  $n_f$  is recorded. Injection continues until a second sharp increase of pressure occurs indicating that the total porosity  $n = n_p + n_f$  is filled. This method has a number of drawbacks, among them, the fractures may expand to give incorrect values of  $n_f$ . In addition, as this method fills the porosities (pores and fissures) of the sample from the edges to the center, the value recorded for  $n_f$  might include a certain amount of pores.

### 3.1.4 The permeabilities

The intrinsic permeability  $k_k$  is a measure of the ability of the void-system  $k$  to transmit fluids. Its usual dimension is the meter square  $m^2$ . In petroleum engineering, the millidarcy unit (md) is more frequently used and is equal to  $10^{-15}$  meter square. In some research areas, for example hydrogeology, the permeability is replaced by the hydraulic conductivity  $K_k$  [m/s], which is a property of a type of porosity and its associated fluid that describes the ease with which the fluid can move through pore spaces or fractures. The relationship linking the hydraulic conductivity and the permeability is (de Marsily, 1986, p. 60),

$$K_k = \rho_k g \frac{k_k}{\mu_k}. \quad (3.9)$$

In most hydro-mechanical coupled analyses of dual porous media (Warren and Root, 1963; Kazemi, 1969; Khalili et al., 1999; Khalili, 2003), the permeability of the fissure network used in the model is assumed to be isotropic. This may appear as a strong restriction as the fissure network displays a high anisotropy due to its geometrical form.

However, as the intensity of the fluid transfer is controlled by the porous block permeability, the above approximation does not play a significant role on the accuracy of the fluid transfer magnitude. In any case, additional work should be done to clarify the influence of the anisotropy of the permeability.

In addition to the storage role of the porous block, the crucial point when considering media with double porosity is the fact that fissures play a key role in the transport of the fluid. This role is realised by comparing the permeability magnitude of the porous block with that of the fissure network: the permeability of the fissure network  $k_f$  appears to be much larger than the permeability of the porous block  $k_p$ , as illustrated in Table 3.6.

Reference	$k_p$		$k_f$	
	[md]	[m <sup>2</sup> ]	[md]	[m <sup>2</sup> ]
Kazemi (1969)	0.01	$1.0 \cdot 10^{-17}$	7 236	$7.236 \cdot 10^{-12}$
	0.01	$1.0 \cdot 10^{-17}$	18 098	$1.8098 \cdot 10^{-11}$
	1.0	$1.0 \cdot 10^{-15}$	5 521	$5.521 \cdot 10^{-12}$
Kazemi et al. (1976)	1.0	$1.0 \cdot 10^{-15}$	0.01	$1 \cdot 10^{-11}$
	1.0	$1.0 \cdot 10^{-15}$	21 000	$2.1 \cdot 10^{-11}$
Khalili et al. (1999)	$10^4$	$10^{-11}$	$10^7$	$10^{-8}$
Khalili (2003)	0.013	$1.3 \cdot 10^{-17}$	0.11	$1.1 \cdot 10^{-16}$

Table 3.6: Range of values of the porous block permeability  $k_p$  and of the fissure network permeability  $k_f$  from the literature.

The permeabilities of porous media with double porosity can be either (a) measured experimentally or (b) calculated by using empirical formulas. Each option is briefly presented.

(a) Experimental measurements can be made by using the length scale separation property of media with double porosity as suggested by Wilson and Aifantis (1982): Two direct permeability measurements are made by using Darcy's law; one on a sample representative of the porous block only and one on a sample representative of the overall equivalent permeability. Hence,  $k_p$  and  $k_{eq}$  are measured. For a model which assumes that the fissures are parallel with each other, equally spaced and make an angle  $\theta$  with the flow direction, the equivalent permeability of the medium  $k_{eq}$  can be related to  $k_p$  and  $k_f$ ,

$$k_{eq} = k_p + k_f \cos^2 \theta. \quad (3.10)$$

(b) By using empirically derived formulas: On one hand, the porous block permeabilities  $k_p$  can be physically related to the porous block void ratio  $e$ . A usual starting point for

the derivation of such equation is the law of Poiseuille for flow through a round capillary (Mitchell, 1993, p. 236). Let us denote  $k_p$  the porous block permeability,  $S_0$  the wetted surface per unit volume of particles,  $k_0$  a pore shape factor and  $T$  a tortuosity factor for the porous material without fissures. The well-known Kozeny-Carman equation for the case of full saturation is recovered,

$$k_p = \frac{1}{k_0 T^2 S_0^2} \left( \frac{e^3}{1+e} \right). \quad (3.11)$$

On the other hand, the fissure network permeability  $k_f$  can be related to its aperture  $b$  representing the average distance separating the fissure walls and to the normal distance from one fracture to the other  $d$ , by using the following relationship,

$$k_f = \frac{b^3}{12d}. \quad (3.12)$$

### 3.1.5 The aperture factor

The leakage parameter  $\eta$  controls *fully* the transfer of mass between the porous block and the fissure network in local thermal non-equilibrium. The mass transfer law (2.259) describes well the *in-situ* behaviour of porous media with double porosity in local thermal equilibrium and recovers experimental results. For example Kazemi (1969) obtained some satisfying results on drawdown tests and Khalili et al. (1999) presented some comprehensive results for consolidation of fissured clays.

The leakage parameter  $\eta$  is proportional to the porous block permeability  $k_p$ , to an aperture factor  $\bar{\alpha}$  and to the inverse of the pore fluid viscosity  $\mu_p$ . Hence, for a constant viscosity, the higher the value of  $\eta$  the faster the fluid transfers from one porosity type to the other. The following relationship has been obtained using a one dimensional analysis with the assumption that a quasi-steady state exists in the blocks of the porous region (Barenblatt et al., 1960),

$$\eta = \bar{\alpha} \frac{k_p}{\mu_p}. \quad (3.13)$$

The aperture factor  $\bar{\alpha}$  (also called shape factor) represents the fissuration of the medium, its order of magnitude is  $1/m^2$ . It is a function of the number of fissures  $n$  and of the average distance separating the fissures through the coefficient  $l$  [m]. The following relation was first introduced by Warren and Root (1963),

$$\bar{\alpha} = \frac{4 n (n + 2)}{l^2}. \quad (3.14)$$

Depending on  $n = 1, 2, 3$  the number of normal sets of fissures and  $b_1, b_2, b_3$  the average distance separating the fissures in the directions  $n, l$  can be cast,

$$\begin{aligned} l &= \frac{3 b_1 b_2 b_3}{b_1 b_2 + b_2 b_3 + b_1 b_3}, & \text{if } n &= 3, \\ l &= \frac{2 b_1 b_2}{b_1 + b_2}, & \text{if } n &= 2, \\ l &= b_1, & \text{if } n &= 1. \end{aligned} \quad (3.15)$$

The experimental determination of the leakage parameter  $\eta$  is not straightforward and using the formulation (3.14) introduced by Warren and Root (1963) to calculate  $\eta$  is not always convenient. Uldrich and Ershaghi (1979) proposed a method to determine  $\eta$  experimentally by using the curve of a drawdown test. To this purpose the time scale separation characteristic of porous media with double porosity is used. Drawdown curves are plotted by measuring the wellbore flowing pressure versus logarithm of time. The flow behaviour is characterised by two straight lines, one for early times in which the fissures dominate, and one for late times in which the effect of fluid transfer from the porous blocks to the fissures becomes important. By utilizing an approximate solution to the flow equations, as proposed by Warren and Root (1963),  $\eta$  can be experimentally determined from the drawdown graph.

In the literature, the order of magnitude of the leakage parameter  $\eta$  varies from  $5.3 \cdot 10^{-10}$  1/Pa.s (Kazemi, 1969) to  $1.0 \cdot 10^{-7}$  1/Pa.s (Khalili et al., 1999).

### 3.2 Extensive parameters

An *extensive property* is a property that depends on the surrounding conditions, such as the temperature or the pressure. For example, mass is a physical intensive property of any physical object, whereas weight is an extensive property that varies depending on the strength of the gravitational field in which the respective object is placed.

The extensive parameters which depend on temperature variation are considered in turn, for each phase or for the fluid phases only depending on their nature: (1) First, the thermal expansion coefficients are described. Next, (2) the densities and (3) the viscosities are presented. Furthermore, (4) the specific heat capacities and (5) the thermal conductibilities are introduced.

### 3.2.1 The thermal expansion coefficients

The *volumetric* thermal expansion  $c_{kT}$  measures the ease with which matter changes in volume with a change in temperature, at constant pressure. Its unit is in 1/K. It is equal to three times the often reported *linear* thermal expansion coefficient. (1) Solid and (2) water thermal expansion coefficients are considered in turn:

(1) Due to a lack of experimental data for soils, the linear thermal dilatation coefficient value can be approximated to that of pure silica  $c_T = 1.7 \times 10^{-6}$  1/K. However, if the exact composition of the soil is known, one can estimate the global thermal coefficient by using Table 3.7.

Mineral	Linear thermal expansion coefficient [ $10^{-6}$ 1/°C]	
	$c_T$ [ $10^{-6}$ 1/K]	
	$\perp$ to layering	$\parallel$ to layering
Muscovite	17.8	3.5
Phlogopite	17.8	14
Kaolinite	18.6	5.2
Dickite	14.9	5.9
Halloysite	10.0	6.0
Pyrophyllite	10.2	6.9
Talk	16.3	3.7
Chlorite	9.0	11.1

Table 3.7: *Linear* thermal expansion coefficients, of typical clay minerals, for a temperature range between 25°C and 100°C (Horseman and McEwen, 1996).

(2) Typical values for liquid water and ice are presented in Table 3.8. Although true for pure water and ice, these values may undergo a significant change for unsaturated water, for example water with air bubbles. The thermal expansion coefficient of water substance undergoes a negative jump at 0°C. It increases monotonically between 0°C and 100°C, passing through a null value just below 4°C, (Kestin, 1968, p. 264). In the liquid state, it can be approximated by an affine function with  $T_k$  in Celsius,

$$c_{kT}(T_k) = -0.067 \times 10^{-3} + 0.00819 \times 10^{-3} \times T_k, \quad T_k \in ]0, 100[^\circ\text{C}. \quad (3.16)$$

Temperature $T_k$ [°C]	Thermal expansion coeff. $c_{kT}$ [ $10^{-3}/\text{K}$ ]
0 (ice)	0.158
0 (liquid)	-0.067
2	-0.031
4	0.001
25	0.256
40	0.390
55	0.493
75	0.614
100 (liquid)	0.752

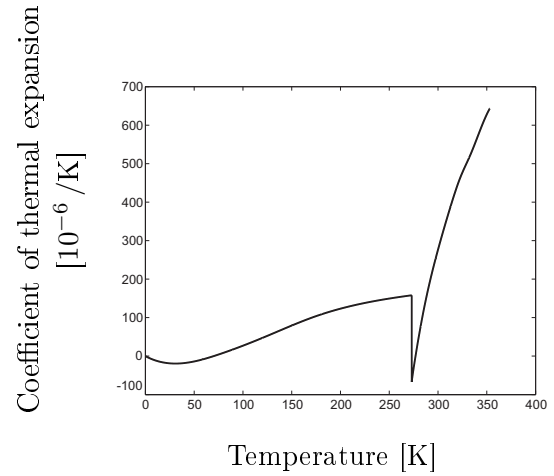


Table 3.8: Volumetric thermal expansion coefficient of ice and pure water at atmospheric pressure (Kestin, 1968, p. 541).

### 3.2.2 The densities

Density is equal to mass per unit volume. The mass is normally measured with an appropriate scale; the volume may be measured directly (from the geometry of the object) or by the displacement of a liquid. A very common instrument for the direct measurement of the density of a liquid is the hydrometer. As a rule, increasing the pressure will always increase the density of a material and increasing the temperature generally decreases the density, but there are notable exceptions to this generalisation. For example, the density of water increases between its melting point at 0 °C and 4 °C. (1) Solid and (2) water densities are considered in turn:

(1) In common geomechanical applications it is reasonable to consider the density of the solid skeleton as constant, since the magnitude of the compressibility coefficient and of the thermal expansion coefficient are small. Hence, the solid density  $\rho_s$  is assumed to be independent of the pressure and temperature changes. Table 3.9 gathers density coefficients of various soil types.

(2) By contrast with the solid skeleton density, water density varies significantly with temperature. The formula relating the density change of a phase  $k$  to a temperature and a pressure change is expressed in equation (2.173). This relation involves two extensive parameters: the hydraulic compressibility  $c_{kH}$  and the thermal expansion coefficient of the phase  $c_{kT}$ ,

Material	Density $\rho_s$ [ $10^3$ kg/m <sup>3</sup> ]
Clay	1.8 to 2.6
Limestone	2.7 to 2.8
Sandstone	2.1 to 2.4
Granite	2.64 to 2.70
Quartz	2.65
Marble	2.80

Table 3.9: Density coefficients of various soils (Burger et al., 1985, p. 139).

$$\frac{1}{\rho_k} \frac{d^k \rho_k}{dt} = c_{kH} \frac{d^k p_k}{dt} - c_{kT} \frac{d^k T_k}{dt}. \tag{3.17}$$

The variation density with temperature change is presented in Table 3.10 for pure water. According to Burger et al. (1985), the variation of water density with temperature in the range of [6°C, 90°C], can be approximated by the following relation (with  $T_k$  in °Celsius),

$$\rho_k = 1000.4 - 0.0478 \times T_k - 3.8810^{-3} \times T_k^2, \quad [\text{kg}\cdot\text{m}^{-3}]. \tag{3.18}$$

Temperature $T_k$ [°C]	Density $\rho_k$ [kg/m <sup>3</sup> ]
0 (ice)	916.8
0 (liquid)	999.8
4	1000.0
10	999.7
20	998.2
30	995.7
50	988.1
70	977.8
100 (liquid)	958

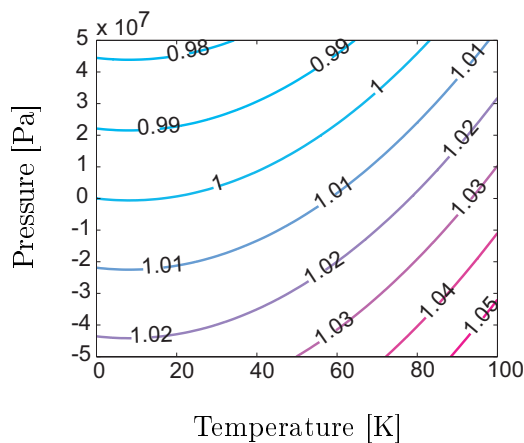


Table 3.10: (left) Density variation with temperature for pure water, at atmospheric pressure, from [www.engineeringtoolbox.com](http://www.engineeringtoolbox.com). (right) Specific volume (inverse density) contour with pressure and temperature as defined in equation (2.158).

### 3.2.3 The dynamic viscosity

The dynamic viscosity describes the internal resistance of a fluid to flow and may be thought of as a measure of fluid friction. Viscosity is independent of pressure (except at very high pressure), but is strongly dependent of the temperature variation (Table 3.11). The SI unit for the dynamic viscosity is Pa.s. The ‘cgs’ physical unit for dynamic viscosity is the poise, 1 P = 0.1 Pa.s. At 20°C the water viscosity is equal to 1.0020 centipoise.

Temperature $T_k$ [°C]	Dynamic viscosity $\mu_k$ [ $10^{-3}$ Pa.s]
0 (liquid)	1.789
2	1.52
4	1.52
20	1.002
40	0.653
55	0.504
70	0.404
100 (liquid)	0.282

Table 3.11: Dynamic viscosity of pure water, from [www.engineeringtoolbox.com](http://www.engineeringtoolbox.com)

According to Burger et al. (1985), the viscosity of water variation, accurate to within 2.5% in the range of [0°C, 370°C], can be approximated by the following relation (with  $T_k$  in Kelvin),

$$\mu_k = 2.414 * 10^{-5} \times 10^{\left(\frac{247.8}{T_k - 140}\right)} \quad [\text{Pa}\cdot\text{s}]. \quad (3.19)$$

### 3.2.4 The specific heat capacities

Heat capacity is a measurable physical quantity that characterises the ability of a body to store heat as it changes in temperature. Its unit is in J/K. Dividing heat capacity by the body mass yields a mass-specific heat capacity J/kg.K, which is a mass-intensive quantity, meaning it is no longer dependent on amount of material, and is now more dependent on the type of material, as well as the physical conditions of heating. (1) Solid and (2) water mass-specific heat capacities are considered in turn:

(1) Traditionally, the solid skeleton specific heat capacity is considered independent of temperature (Table 3.12, left).



(2) Table 3.12, right, presents mass-specific heat capacity variation with temperature for pure water, which indicates a small dependency of the coefficient on the temperature range of 0 to 100 °C. The specific heat capacity of water can therefore be approximated by a constant value.

Material	Specific heat capacity $C_{s,p}$ [J/kg.K]	Temperature $T_k$ [°C]	Specific heat capacity $C_{p,p}$ [kJ/kg.K]
Granite	790	0 (ice)	4.218
Marble	880	0 (liquid)	4.210
Clay	920	10	4.195
Sand	800	20	4.182
Sandstone	920	30	4.179
Limestone	840	50	4.181
		70	4.190
		100 (liquid)	4.219

Table 3.12: (left) Specific heat capacity of different soils, from [www.engineeringtoolbox.com](http://www.engineeringtoolbox.com). (right) Specific heat capacity of pure water at constant atmospheric pressure (Kestin, 1968, p. 541).

### 3.2.5 The thermal conductivities

Thermal conductivity  $\Lambda$  is the property of a material that indicates its ability to conduct heat. It appears primarily in Fourier's law for heat conduction. SI units are W/m.K and English units are Btu.ft/h.ft<sup>2</sup>.°F. To convert between the two, the relation 1 W/m.K = 1.3523 Btu.ft/h.ft<sup>2</sup>.°F is used. (1) Solid and (2) water thermal conductibilities are now outlined in turn:

(1) The thermal conductivity of the solid skeleton is assumed to have an isotropic behaviour in spite of stratification of natural soil deposits and of the presence of fractures. Furthermore, it is considered independent of the temperature for geotechnical applications (Table 3.13, left).

(2) The variation of thermal conductivity of water with temperature is small between 0 °C and 100 °C (Table 3.13, right) and can safely be approximated by a constant.

As the values for soil minerals are higher than those for water and air, it is evident that heat flow must be predominant through the solid in diffusion-dominated flows. The latter statement is erroneous for convection-dominated mixture.

Material	Thermal conductivity $\Lambda_s$ [W/m.K]	Temperature $T_k$ [°C]	Thermal conductivity $\Lambda_k$ [W/m.K]
Granite	1.7 - 4.0	0	0.552
Marble	2.7 - 2.9	10	0.578
Quartz	5.3 - 5.8	20	0.598
Sand, dry	0.35	30	0.614
Sand, saturated	2.7	50	0.641
Limestone	1.26 - 1.33	70	0.661
		100	0.676

Table 3.13: (left) Thermal conductivity of different soils, from [www.engineeringtoolbox.com](http://www.engineeringtoolbox.com). (right) Thermal conductivity of pure water (Burger et al., 1985, p 137).

### 3.3 Solid-fluid extensive parameters

The solid-fluid extensive coefficients which are defined and measured for a particular solid-fluid system are now considered. The coefficients of thermo-osmosis are diffusive coupled phenomena related to Darcy's law and Fourier's law. On the other hand, the volumetric inter-phase heat transfer coefficients control the time difference between local thermal non-equilibrium and local thermal equilibrium.

#### 3.3.1 The coefficient of thermo-osmosis

Thermo-osmosis is the onsagerian coupled process by which groundwater movement is driven by a temperature gradient as defined in equations (2.228) and (2.232). Its unit is  $\text{m}^2/\text{s.K}$ . This thermo-osmosis coefficient depends strongly on the permeability of the medium under concern and on the viscosity of the fluid (and therefore indirectly on its temperature). However, due to the lack of information, the coefficient of thermo-osmosis is assumed independent of temperature variation.

According to Ghassemi and Diek (2002) and Bai (2006), due to the very low permeability (order of nanodarcy) of shales (bedded clays), hydraulic transport is not the dominant form of fluid movement into the formation. In fact, hydraulic fluid transport is often several times smaller than the contribution of chemical and thermal effects. There is evidence that thermo-osmosis can play a significant role on the diffusion behaviour since significant mass transport through clay membranes due to a temperature gradient has been observed in laboratory experiments. Several thermo-osmosis values are gathered in Table 3.14.

Srivastava and Avasthi (1975) showed that, in compact kaolinite subjected to a temperature gradient of  $20^\circ\text{C}/\text{m}$ , the flux of water associated with this effect can reach  $10^{-8}$  m/s

Reference	Thermo-osmosis coefficient $\Theta_k$ [m <sup>2</sup> /s.K]	Material
Dirksen (1969)	$10^{-14} - 3 \times 10^{-13}$	Na-kaolinite
Srivastava and Avasthi (1975)	$2.6 \times 10^{-10}$	kaolinite
Reference	Thermo-osmosis coefficient $\Theta_k$ [m <sup>2</sup> /s.K]	Permeability [m <sup>2</sup> ]
Carnahan (1984)	$2.7 \times 10^{-10}$	$15 \times 10^{-18}$
Zhou et al. (1998)	$6 \times 10^{-11} - 2.7 \times 10^{-10}$	$10^{-17} - 5 \times 10^{-17}$
Ghassemi and Diek (2002)	$6 \times 10^{-11}$	$7.66 \times 10^{-20}$

Table 3.14: Thermo-osmosis coefficients for compact clays-water system from the literature.

(0.5 m/year).

Based on the experimental results of Srivastava and Avasthi (1975), Carnahan (1984) estimated that thermo-osmotic volume flow through kaolinite can be 800 times larger than Darcian flow, that is to say the ratio between the two fluxes could be as great as 3 orders of magnitude. Numerical estimates of the magnitudes of the fluxes associated with the coupling phenomenon have shown that the thermo-osmosis effect could have a significant role in fluid and solute transport only if the thermo-osmosis coefficient is greater than  $10^{-12}$  m<sup>2</sup>/s.K (Soler, 2001).

Thus, thermo-osmosis is likely to be an important near-field mechanism of groundwater movement in low permeability soils, such as clay repository containing heat-emitting wastes.

**Remark 3.1.** *Accounting for the thermo-osmosis effect requires the boundary conditions in terms of flux  $\mathbf{J}_k$  at the interface of the sample to be true for both Darcy's effect and the thermo-osmosis effect.*

### 3.3.2 The coefficients of inter-phase heat transfer

The coefficient of inter-phase heat transfer,  $h_i$  [W/m<sup>2</sup>.K], also known as the particle-to-fluid heat transfer coefficient, influences greatly the rate at which a two phase system (for example solid-fluid or fluid-fluid) will reach thermal equilibrium. The latter coefficient is independent of the geometry of the system under consideration. The higher the coefficient of inter-phase heat transfer, the faster the thermal equilibrium.

The coefficient of *volumetric* or *specific* inter-phase heat transfer  $\kappa_i$  [W/m<sup>3</sup>.K] is proportional to the inter-phase heat transfer coefficient  $h_i$  and to the specific surface  $S_i^{sp}$  [m<sup>2</sup>/m<sup>3</sup>] of the considered two phase system,

$$\kappa_i = h_i \times S_i^{sp}, \quad i = sp, sf, pf. \quad (3.20)$$

On one hand, the inter-phase heat transfer coefficient  $h_i$  depends on the nature of the solid, the fluid and on the dominant heat transport phenomenon. On the other hand, the specific surface represents the geometrical configuration of a particular site,

$$S_i^{sp} = \frac{\text{total surface area of the interstitial voids}}{\text{total volume of the medium}}. \quad (3.21)$$

In hot dry rock applications, heat transport is diffusion-dominant in the solid and in the pore fluid phase; conversely heat transport is convection-dominant in the fissure fluid phase. Thus,  $h_{sp}$  and  $h_{sf}$  should be significantly different in magnitude. As in porous media with double porosity the porous block has a much larger specific surface than the fissure network, namely  $S_{sp}^{sp} \gg S_{sf}^{sp}$ , the coefficient of volumetric inter-phase heat transfer of the solid-pore system should be much larger than the one of the solid-fissure system, namely  $\kappa_{sp} \gg \kappa_{sf}$ .

Consequently, to obtain the *volumetric* coefficient of inter-phase heat transfer  $\kappa_i$ , both the specific surface  $S_i^{sp}$  and the coefficients of inter-phase heat transfer  $h_i$  have to be identified. (1) Specific surface formulas, (2) the solid-pore fluid, (3) the solid-fissure fluid and (4) the pore fluid-fissure fluid coefficients of heat transfer are now considered in turn:

(1) The specific surface area  $S_i^{sp}$  can be measured (Table 3.15) but it is informative to calculate it from empirical formulas. To make this calculation, the interface solid-fluid is estimated from the size and shapes of the solid grains or the pores or the fissures.

Material	Specific surface area $S_i^{sp}$ [m <sup>2</sup> /m <sup>3</sup> ]
Sand	$1.5 \times 10^4$
Fine sandstone	$1.5 \times 10^5$
Montmorillonite (clay)	$1.5 \times 10^9$

Table 3.15: Specific surface area values for various materials (de Marsily, 1986, p. 22).

According to Jiang et al. (2006), the specific surface of a porous medium can be approximated by assuming that the particles are spherical and that their entire surface contributes

to the heat transfer. Consider a porous medium with spherical particles, for example voids of diameter  $d_s$  filled with fluid and of volume fraction  $n_s$ . Then the specific area is,

$$S_i^{sp} = \frac{6 n_s}{d_s}. \quad (3.22)$$

The latter relation is assumed true for coarse material only. If a soil particle is assumed to have a cubed form of length  $L$ , the specific area can be approximated to,

$$S_i^{sp} = \frac{6L^2}{L^3} = \frac{6}{L}. \quad (3.23)$$

Finally, it can be shown that the specific surface area of a plate-shaped soil particle is much larger than that of a cube-shaped particle. Consider the plate-shaped particle as part of a rectangular box ( $L \times H \times 1$ ) cut into many thin slices. For one slice of height  $b$ , the specific area is,

$$S_i^{sp} = \frac{2L \times 1 + 2b \times 1 + 2Lb}{Lb \times 1}. \quad (3.24)$$

(2) The experimental determination of the coefficient of inter-phase heat transfer for the solid-pore system  $h_{sp}$  is reviewed by Kaviany (1995, p. 401) for spherical particles. Wakao and Kaguei (1982) have critically examined the experimental results on  $h_{sp}$  and have selected experiments (steady-state and transient) which they found reliable. They have found a correlation for  $h_{sp}$  for spherical particles; the dimensionless form of it is denoted the Nusselt number  $Nu_d$ ,

$$Nu_d = \frac{h_{sp} d_p}{\Lambda_p} = 2 + 1.1 Re_p^{0.6} Pr_p^{1/3}. \quad (3.25)$$

where  $d_p$  is the pore diameter,  $Re_p = \mathbf{v}_p d_p / \nu_p$  and  $Pr_p = \mu_p c_{p,p} / \Lambda_p$  are the Reynolds number and the Prandlt number associated to the pore fluid. Equation (3.25) gives for the asymptote  $Re \rightarrow 0$  the limit  $Nu_d = 2 = h_{sp} d_p / \Lambda_p$ . Note that the measurement of  $h_{sp}$  becomes more difficult and the experimental uncertainties become much higher as  $Re \rightarrow 0$ .

Pecker and Deresiewicz (1973) also measured experimentally the coefficient of volumetric inter-phase heat transfer of a sandstone sample filled with a conductive aqueous solution (sodium chloride), in a single porosity context. To do so, the fluid of the system was heated electrically, while the rock skeleton itself was electrically insulated. They obtained a value

of  $\kappa_{sp} = 4.309 \times 10^5 \text{ W/m}^3\text{.K}$ . According to de Marsily (1986), the specific surface for sand materials is equal to  $1.5 \times 10^5 \text{ m}^2/\text{m}^3$ ; thus, the result of Pecker and Deresiewicz (1973) leads to an inter-phase heat transfer value of approximately  $2.8 \text{ W/m}^2\text{.K}$ .

Jiang et al. (2006) investigated the heat transfer between solid particles and a fluid in porous media, through experimental and numerical work. The experimental work focused on a porous medium with an average particle diameter of 0.2 mm. The particle-to-fluid heat transfer coefficient was obtained from the experimental data with the lumped capacitance method and a one-dimensional numerical analysis of the experimental data:  $h_{sp} = 12.16 \text{ W/m}^2\text{.K}$ .

(3) Zanotti and Carbonell (1984) proposed a formula to estimate the coefficient of inter-phase heat transfer for a solid-fissure system  $h_{sf}$  from a capillary tube model. Note that the axial conduction in each phase is assumed negligible compared with that in the radial direction. The overall convective heat transfer coefficient is determined to be,

$$\frac{1}{h_{sf}} = \frac{R_i a_3}{2 \Lambda_f} + \frac{R_0^2 - R_i^2 a_4}{2 R_i \Lambda_s}, \quad (3.26)$$

in which the dimensionless constants  $a_i$  are,

$$a_3 = \frac{1}{2} \quad \text{and} \quad a_4 = \frac{4 \left(\frac{R_0}{R_i}\right)^4 \ln \frac{R_0}{R_i} - 3 \left(\frac{R_0}{R_i}\right)^4 + 4 \left(\frac{R_0}{R_i}\right)^2 - 1}{2 \left[\frac{R_0^2}{R_i^2} - 1\right]^3}, \quad (3.27)$$

$R_i$  is the internal radius of the capillary where  $T_f = T_s$  and  $R_0$  is the radius at which  $\partial T_s / \partial r = 0$ ,  $r$  being the direction perpendicular to the axis of the capillary tube. Note that the formula of  $h_{sf}$  in eq. (3.26) is *independent* of the fluid velocity.

(4) The inter-phase heat transfer coefficient of the pore-fissure system  $h_{pf}$  can be approximated by a *conductive heat transfer* phenomenon. Three hypotheses are made:

- i. Although the rate of thermal change is very high, the temperature change at the inter-phase is considered smooth. Consequently, an average temperature  $T_{pf} = (T_p + T_f)/2$  is introduced at the local inter-phase point.
- ii. Let us assume that the fluid is conducting through a thin ‘membrane’ of a round shape cross section. The membrane thermal conductivity is equal to  $\Lambda_{pf} = (\Lambda_p + \Lambda_f)/2$ .

- iii. The characteristic length controlling this heat transfer phenomenon is the radius  $R$  of the thin ‘membrane’.

According to Bejan (1993, p. 33), the conductive heat transfer coefficient, or thermal resistance posed by a sufficiently thin ‘membrane’ is,

$$h_{pf} = \frac{\Lambda_p + \Lambda_f}{2R} = \frac{\Lambda_{pf}}{R}. \quad (3.28)$$

As a first approximation and in absence of available data, the length of the thin ‘membrane’ is assumed equal to a pore radius  $R \approx d_p/2$ . The specific surface of the pore fluid-fissure fluid inter-phase may be approximated by the specific surface of the solid-fissure system weighted by the pore fluid volume fraction, which is assumed to be equal to the pore fluid surface fraction,

$$S_{pf}^{sp} \approx n_p S_{sf}^{sp}. \quad (3.29)$$

In conclusion, the volumetric inter-phase heat transfer coefficient of the solid-pore system should be much larger than the others and the volumetric inter-phase heat transfer coefficient of the solid-fissure system should be larger than that of the pore-fissure system:

$$\kappa_{sp} \gg \kappa_{sf} > \kappa_{pf}.$$

### 3.4 The Reynolds, Prandtl, Péclet, Nusselt, Sparrow numbers

Five dimensionless numbers are now presented. They are often used as indicators of flow rates or of the dominance of certain phenomena over others. In any case, they are very useful to correctly describe a particular flow situation through a mixture.

#### 3.4.1 The Reynolds number

The transition from laminar to turbulent flow is governed by the values of the Reynolds number  $Re$ . The dimensionless Reynolds number is defined *for a cylindrical pipe* by,

$$Re = \frac{V d \rho}{\mu}, \quad (3.30)$$

where  $V$  is the mean velocity of the fluid,  $d$  the diameter of the pipe and  $\mu/\rho$  is the kinematic viscosity. In classical hydraulics, the flow regime is laminar for  $Re < 2000$  and turbulent

for  $Re > 2000$ . However according to Kaviany (1995, p. 48), the turbulent flow limits are different when considering the pore-level measurements of the velocity fluctuation. Dybbs and Edwards (1984) have made point measurement of the three dimensional velocity distributions for flow through hexagonal packing of spheres and for complex arrangements of cylinders. They define a Reynolds number  $Re_d$  that is based on the average pore fluid velocity  $\bar{u}_p$  and on an average characteristic length scale for the pores  $\bar{d}$ ,

$$Re_d = \frac{\bar{u}_p \bar{d} \rho}{\mu}. \quad (3.31)$$

Based on this Reynolds number, they are able to define four distinct flow regimes, presented here,

1.  $Re_d < 1$ , Darcy or creeping-flow regime: The viscous forces dominate over the inertia forces and only the local (pore-level) geometry influences the flow.
2.  $1 - 10 < Re_d < 150$ , inertial-flow regime: Steady nonlinear (inertial forces affected) laminar flow begins between  $Re_d$  from 1 to 10. Boundary layers are more pronounced and uniform-velocity regions are present. As  $Re_d$  increases, the uniform-velocity regions become larger as the boundary thickness decreases.
3.  $150 < Re_d < 300$ , unsteady laminar-flow regime: the flow remains laminar in this regime and displays an instable wake responsible for the transition from laminar steady flows to unsteady flows.
4.  $300 < Re_d$ , unsteady and chaotic-flow regime: The transition to turbulence has been found to take place over Reynolds numbers as large as 300.

### 3.4.2 The Prandtl number

The Prandtl number is a dimensionless number approximating the ratio of momentum diffusivity (kinematic viscosity) and thermal diffusivity. It is defined as:

$$Pr = \frac{\nu}{\alpha} = \frac{\text{viscous diffusion rate}}{\text{thermal diffusion rate}} = \frac{c_p \mu}{\Lambda}, \quad (3.32)$$

where  $\nu$  is the kinematic viscosity [ $m^2/s$ ] and  $\alpha$  is the thermal diffusivity [ $m^2/s$ ],

$$\alpha = \frac{\Lambda}{\rho c_p}, \quad (3.33)$$



defined from the thermal conductivity  $\Lambda$  [W/m.K], the density  $\rho$  [kg/m<sup>3</sup>] and the specific heat capacity at constant pressure  $c_p$  [J/kg.K].

Typical values for Pr are around 7.07 for water, between 100 and 40,000 for engine oil and around 0.02 for mercury, at 20 °C (Bejan, 1993, Appendix C). For mercury, heat conduction is very effective compared with convection: thermal diffusivity is dominant. For engine oil, convection is very effective in transferring energy from an area, compared to pure conduction: momentum diffusivity is dominant.

In heat transfer problems, the Prandtl number controls the relative thickness of the momentum and thermal boundary layers. When Pr is low, heat diffuses very quickly compared with the velocity (momentum); for example, in liquid metals the thickness of the thermal boundary layer is much larger than the velocity boundary layer.

### 3.4.3 The Péclet number

The Péclet number is a dimensionless number relating the rate of forced convection over thermal diffusion for a specific fluid. It is equivalent to the product of the Reynolds number with the Prandtl number in the case of thermal diffusion. For thermal diffusion, the Péclet number is defined as:

$$\text{Pe} = \frac{\text{rate of convection}}{\text{rate of diffusion}} = \text{Re} \times \text{Pr} = \frac{LV}{\alpha}, \quad (3.34)$$

in which  $L$  is a characteristic length (the average characteristic length scale for the pores  $\bar{d}$ ),  $V$  is the velocity of the fluid (the average pore velocity  $\bar{u}_p$ ) and  $\alpha$  is the thermal diffusivity [m<sup>2</sup>/s].

Note that the soils under consideration for waste repositories have extremely low permeabilities and therefore very small pore diameters, so that the Péclet number should be far below one. On the other hand, hot dry rock reservoirs are endowed with large permeabilities (after hydraulic stimulation) and should display large Péclet numbers.

### 3.4.4 The Nusselt number

At a boundary surface of a solid-fluid system, heat transfer occurs when the system is in local thermal non-equilibrium. The dimensionless Nusselt number is the ratio of convective to conductive heat transfer across (normal to) the boundary. If one considers that the convective and conductive heat flows are parallel to each other and to the surface normal

of the boundary surface, and are all perpendicular to the mean fluid flow in the simple case, the Nusselt number may be defined as,

$$Nu_L = \frac{\text{Convective heat transfer}}{\text{Conductive heat transfer}} = \frac{h L}{\Lambda_f}, \quad (3.35)$$

where  $L$  is a characteristic length (the pores diameter  $d_p$ ),  $\Lambda_f$  is the thermal conductivity of the fluid and  $h$  is the coefficient of inter-phase heat transfer [W/m<sup>2</sup>.K].

A Nusselt number close to unity, namely convection and conduction of similar magnitude, is characteristic of laminar flow. A larger Nusselt number corresponds to more active convection, with turbulent flow typically in the 100-1000 range. Wakao and Kaguei (1982) related the Nusselt number to the Reynolds number and to the Prandtl number for spherical particles through,

$$Nu_d = \frac{h_{sp} d_p}{\Lambda_p} = 2 + 1.1 Re_p^{0.6} Pr_p^{1/3}. \quad (3.36)$$

This correlation is based on experimental results of selected experiments for both steady-state and transient tests.

### 3.4.5 The Sparrow number

The dimensionless Sparrow number informs on the existence of local thermal equilibrium (or the absence of), for a porous medium subjected to rapid heating or cooling (Minkowycz et al., 1999). The Sparrow number for a solid-fluid system ( $sf$  subscript) is defined as,

$$Sp_{sf} = \frac{S_{sf}^s h_{sf} L^2}{\Lambda_{sf}}, \quad (3.37)$$

in which  $S_{sf}^s$  is the specific area [1/m],  $h_{sf}$  is the coefficient of inter-phase heat transfer [W/m<sup>2</sup>.K],  $L$  is the thickness of the porous layer [m], and  $\Lambda_{sf}$  is an equivalent thermal conductivity of the solid-fluid system [W/m.K];  $\Lambda_{sf} = n_f \Lambda_f + (1 - n_f) \Lambda_s$ .

The absence of local thermal equilibrium is significant for the ratio of the Sparrow number over the Péclet number  $Sp/4Pe$  smaller than unity (Minkowycz et al., 1999; Nield et al., 2002),

$$\begin{aligned} \frac{Sp}{4Pe} \left[ n_f + (1 - n_f) \frac{\Lambda_s}{\Lambda_f} \right] &< 1 \quad , \\ \frac{Sp}{4Pe} &< 1 \quad , \quad \text{if } \frac{\Lambda_s}{\Lambda_f} \approx 1. \end{aligned} \quad (3.38)$$

3. Parameters magnitude 3.4. The Reynolds, Prandtl, Péclet, Nusselt, Sparrow numbers

Note that the Sparrow number is not yet a widely used tool and is only introduced in a few number of papers.

## Chapter 4

# Finite element method

The complete set of explicit field equations has been derived in Chapter 2. The relation linking the primary unknowns to the applied boundary conditions and body loadings is now developed through a finite element formulation scheme. The main idea is to force the residual, implied by the non-linear first-order semi-discrete equations, to vanish. The actual global effective diffusion matrix is central in the implementation but presents a number of degrees of freedom.

Section 4.1 presents the finite element method through a simple one-dimensional time-independent boundary value problem. In Section 4.2, the field equations and the primary unknowns are gathered to form the problem to be solved: the weak formulation is obtained after integrating by parts and the Galerkin method is used to obtain the semi-discretised set of equations. Crucial for the code implementation, the time integration and the method of equation solving are presented in Section 4.3. The effective diffusion matrix results from the above choices.

The stabilisation of the convective terms will be addressed in Chapter 7.

### 4.1 The finite element method

Finite element methods (FEM) are numerical techniques used for finding *approximate solutions* of partial differential equations as well as of integral equations. The solution approach is based either on reducing the differential equations to a set of linear equations (steady state problems) or to a semi-discrete system of ordinary differential equations (time-dependent problems).

The method to obtain the semi-discrete equations of the problem is now analysed. The time discretisation method is detailed later in Section 4.3. This section taps on the work of (Hughes, 1987a) and we should refer to him for more detailed explanations. Our

explanation proceeds in three steps: (1) The variational or weak statement of the problem is expressed. (2) The Galerkin's approximation method is used to discretise the weak form in a finite dimensional space. (3) A system of coupled linear algebraic equations is obtained within a generic element.

To clarify the concept, let us begin with a one dimensional time-independent problem from which the general method can be extrapolated. The starting point is a partial differential equation for the unknown function  $u = u(x)$ ,

$$\frac{\partial^2 u}{\partial x^2} + f = 0, \quad (4.1)$$

where  $f$  is a given smooth, scalar function defined on the interval  $[0, 1]$ . The complete boundary value problem requires imposing boundary conditions on the function  $u$ . The strong form of the boundary value problem (S) is stated as follows,

$$(S) \begin{cases} \frac{\partial^2 u}{\partial x^2} + f = 0, & \text{on } ]0, 1[, \\ u(1) = g, \\ -\frac{\partial u(0)}{\partial x} = h, \end{cases} \quad (4.2)$$

where  $g$  and  $h$  are constants. This type of boundary condition leads to a boundary value problem of mixed type, the main unknown  $u$  and its derivative being controlled at one point. In the next step, the original boundary value problem is rephrased in its *variational* or *weak form*.

(1) The variational formulation of (S) is the mathematical preparation previous to the spatial discretisation. To do so, two collections of functions are introduced. i. The *trial functions*  $u$  which satisfy  $u(1) = g$  and have square-integrable derivatives. ii. The *variations*  $\delta u$ , also called *weighting functions*, which are required to satisfy the homogeneous counterpart of the  $g$ -boundary condition  $\delta u(1) = 0$  and to have square-integrable derivatives.

The variational formulation of the problem (S) is obtained by multiplying the strong form (4.2) by the *variation*  $\delta u$  and by integrating over the interval  $[0, 1]$ . Finally, integrating by parts provides the variational form,

$$(W) \quad \int_0^1 \frac{\partial \delta u}{\partial x} \frac{\partial u}{\partial x} dx = \int_0^1 \delta u f dx + \delta u(0)h. \quad (4.3)$$

The formulation (W) is often called *virtual work* or *virtual displacement principles*. The functions  $\delta u$  represent virtual displacements. The solution of (W) is called weak or generalised solution.

(2) The second step is the Galerkin's approximation method, where the weak form is discretised in a finite dimensional space. Finite-dimensional *approximations* of the trial functions  $u^h$  and of the *variations*  $\delta u^h$  are introduced with respect to a mesh of characteristic length  $h$ . The approximated functions  $u^h$  and  $\delta u^h$  are subsets of the functions  $u$  and  $\delta u$  and are endowed with the same properties.

Let us rewrite eq. (4.3) in terms of  $u^h$  and  $\delta u^h$ , to obtain an approximate variational formulation,

$$\int_0^1 \frac{\partial \delta u^h}{\partial x} \frac{\partial u^h}{\partial x} dx = \int_0^1 \delta u^h f dx + \delta u^h(0)h. \quad (4.4)$$

Furthermore, the function  $u^h$  is constructed with an 'unknown' part  $v^h$  and a 'known' part  $g^h$ ,

$$u^h = v^h + g^h, \quad (4.5)$$

so that  $v^h$  is a function belonging to the same collection of functions as the approximated variations  $\delta u^h$  and satisfies  $v^h(1) = 0$ , and  $g^h$  is a given function which satisfies  $g^h(1) = g$ . Substitution of (4.5) into (4.4) leads to the (Bubnov-)Galerkin form of the problem,

$$(G) \quad \int_0^1 \frac{\partial \delta u^h}{\partial x} \frac{\partial v^h}{\partial x} dx = \int_0^1 \delta u^h f dx + \delta u^h(0)h - \int_0^1 \frac{\partial \delta u^h}{\partial x} \frac{\partial g^h}{\partial x} dx, \quad (4.6)$$

in which the 'known' contributions are gathered in the right-hand-side. Note that if the functions  $v^h$  do not belong to the collection of approximated variations  $\delta u^h$ , the method is called a Petrov-Galerkin method which is in fact more general than the (Bubnov-)Galerkin method.

(3) The third step leads to system of coupled linear algebraic equations referred to as the matrix problem. The matrix equation requires representations of  $\delta u^h$  and  $v^h$  in terms of basis functions,

$$\delta u^h = \sum_{A=1}^n c_A N_A \quad \text{and} \quad v^h = \sum_{A=1}^n d_A N_A, \quad \text{for } A = 1, 2, \dots, n; \quad (4.7)$$

in which  $N_A$  are *shape functions* which satisfy  $N_A(1) = 0$  and  $c_A$  and  $d_A$  are constants of a generic element.  $g^h$  is now specified to  $g^h = gN_{n+1}$  with  $N_{n+1}(1) = 1$ . Hence,  $u^h$  writes,

$$u^h = \sum_{A=1}^n d_A N_A + g N_{n+1} \quad \text{for } A = 1, 2, \dots, n. \quad (4.8)$$

Substitution of  $\delta u^h$  and  $u^h$  in (4.6) by their discretised form (4.7) and (4.8) and factorising by  $c_A$  leads to,

$$\sum_{A=1}^n c_A \sum_{B=1}^n \int_0^1 \frac{\partial N_A}{\partial x} \frac{\partial N_B}{\partial x} dx d_B - \int_0^1 \left( N_A f - \frac{\partial N_A}{\partial x} \frac{\partial N_{n+1}}{\partial x} g \right) dx = N_A(0)h, \quad (4.9)$$

$$\sum_{A=1}^n c_A \sum_{B=1}^n \mathbb{F}_e^{\text{int}} = \mathbb{F}_e^{\text{surf}}, \quad (4.10)$$

where  $\mathbb{F}_e^{\text{int}}$  is the vector gathering the elementary internal elastic forces and  $\mathbb{F}_e^{\text{surf}}$  is the vector of elementary surface loading. Eq. (4.9) should hold for all values of  $c_A$  for  $A = 1, 2, \dots, n$ . Since the  $c_A$  constants are arbitrary, it is necessary that the remaining functions must be identically zero for each  $A = 1, 2, \dots, n$ , hence,

$$\sum_{B=1}^n \int_0^1 \frac{\partial N_A}{\partial x} \frac{\partial N_B}{\partial x} dx d_B = \int_0^1 N_A f dx + N_A(0)h - \int_0^1 \frac{\partial N_A}{\partial x} \frac{\partial N_{n+1}}{\partial x} g dx. \quad (4.11)$$

Equation (4.11) constitutes a system of  $n$  equations with  $n$  unknowns. The latter relation may be written in a matrix form with a stiffness matrix  $\mathbb{K}$ , a displacement vector  $\mathbb{X} = [d_B]$  for  $B = 1, 2, \dots, n$  and a force vector  $\mathbb{F}$  being equal to the right-hand-side of (4.11),

$$(M) \quad \mathbb{K} \mathbb{X} = \mathbb{F}, \quad (4.12)$$

or in a vectorial form where  $\mathbb{F}^{\text{int}}(V, u^h)$  is the vector gathering the internal elastic forces and  $\mathbb{F}^{\text{surf}}(S, u^h)$  is the vector of surface loading;  $S$  denotes the collective loading surface and  $V$  the total volume,

$$(M) \quad \mathbb{F}^{\text{int}}(V, u^h) - \mathbb{F}^{\text{surf}}(S, u^h) = 0. \quad (4.13)$$

The matrix formulation (M) of the finite dimensional linear problem is obtained whose solution approximately solves the original boundary value problem (S). The three steps leading to the matrix problem are schematically,

$$(S) \equiv (W) \approx (G) \equiv (M). \quad (4.14)$$

In this perspective, the approximate function  $u^h$  is usually considered equal to the unknown function  $u$  from the beginning,

$$\mathbb{F}^{\text{int}}(V, u) - \mathbb{F}^{\text{surf}}(S, u) = 0. \quad (4.15)$$

Note that in the further development, no approximate solution is explicitly introduced and the approximate solution is denoted in the same manner as the exact solution. This notation may appear as non-rigorous compared with the work of Hughes (1987a), although it enhances the clarity of the writing. The finite element procedure developed in Section 4.2 generalises the aforementioned formulation, restricted to time-independent problems, to parabolic problems. The main differences are the introduction of an additional matrix, the diffusion matrix  $\mathbb{D}$ , in the matrix formulation (4.12) and the need for an algorithm to solve systems of ordinary differential equations. The subject is addressed in Section 4.3.

## 4.2 The semi-discrete equations

The finite element method previously presented is used to discretise the constitutive model developed in Chapter 2. The variational or weak formulation is presented in a general context and the nodal and the global vectors are defined. The semi-discretised system is then specified with the Galerkin approximation method.

### 4.2.1 The weak formulation

In a space dimension equal to  $n_{sd}$ , at each point, there are  $n_{sd} + 5$  comprehensive equations to be satisfied, namely,

- the balance of momentum of the whole mixture, equation (2.319),
- the mass balance of the pore fluid, equation (2.320),
- the mass balance of the fissure fluid, equation (2.321),
- the energy balance of the solid, equation (2.322),



- the energy balance of the pore fluid, equation (2.323) and
- the energy balance of the fissure fluid, equation (2.324).

To simplify the variational form, a contracted and parametrised form of the comprehensive equations is introduced,

$$\begin{aligned}
\operatorname{div} \boldsymbol{\sigma} + \rho \mathbf{b} &= 0, \\
\operatorname{div} \mathbf{J}_k + f_k &= 0, \quad \text{for } k = p, f, \\
\operatorname{div} \mathbf{q}_s + g_s &= 0, \\
\operatorname{div} \mathbf{q}_k + g_k + g_k^{\text{conv}} &= 0, \quad \text{for } k = p, f,
\end{aligned} \tag{4.16}$$

where the left-hand-side functions are partitioned into two function types: the thermo-elastic functions  $f_k$ ,  $g_s$  and  $g_k$  and the convective function  $g_k^{\text{conv}}$ , which depends on the solution, namely on the velocities, and on the gradients of pressure and temperature. (*via* the expression of the enthalpy gradient). For example, the pore fluid functions are,

$$\begin{aligned}
f_p &= a_{pp} \dot{p}_p + a_{pf} \dot{p}_f + \xi_p \nabla \cdot \dot{\mathbf{u}} + a_{pT_s} \dot{T}_s + a_{pT_p} \dot{T}_p + \Gamma, \\
\Gamma &= \frac{-\hat{\rho}^p}{\rho_p} = T_0 \rho_p \eta \left( \frac{G_p}{T_p} - \frac{G_f}{T_f} \right) \\
g_p &= a_{T_p T_p} \dot{T}_p + a_{T_p p} \dot{p}_p + a_{T_p f} \dot{p}_f + a_{T_p \epsilon} \nabla \cdot \dot{\mathbf{u}} + a_{T_p T_s} \dot{T}_s + \kappa_{sp} (T_p - T_s) \\
&\quad + \kappa_{pf} (T_p - T_f) + \hat{\rho}^p H_p, \\
\hat{\rho}^p H_p &= T_0 \rho_p^2 \eta \left( \frac{G_p}{T_p} - \frac{G_f}{T_f} \right) H_p \\
g_p^{\text{conv}} &= \mathbf{M}_p \cdot \nabla H_p \\
&= b_{T_p T_p} (\mathbf{v}_p - \mathbf{v}_s) \cdot \nabla p_p + b_{T_p T_p} (\mathbf{v}_p - \mathbf{v}_s) \cdot \nabla T_p \quad \text{from eq. (2.314)}.
\end{aligned} \tag{4.17}$$

Multiplying the field equations by the variations  $\delta \mathbf{u}$ ,  $\delta p$  and  $\delta T$  and integrating by parts over the body  $V$ , provides the weak form of the problem, thanks to Green's theorem. For  $k = p, f$ , the variational formulation of eq. (2.319)-(2.324) is,

$$\begin{aligned}
\int_V \nabla(\delta \mathbf{u}) : \boldsymbol{\sigma} \, dV - \int_V \delta \mathbf{u} \cdot \rho \mathbf{b} \, dV &= \int_{\partial V} \delta \mathbf{u} \cdot \boldsymbol{\sigma} \cdot \hat{\mathbf{n}} \, dS, \\
\int_V \nabla(\delta p) \cdot \mathbf{J}_k \, dV - \int_V \delta p \, f_k \, dV &= \int_{\partial V} \delta p \, \mathbf{J}_k \cdot \hat{\mathbf{n}} \, dS, \\
\int_V \nabla(\delta T) \cdot \mathbf{q}_s \, dV - \int_V \delta T \, g_s \, dV &= \int_{\partial V} \delta T \, \mathbf{q}_s \cdot \hat{\mathbf{n}} \, dS, \\
\int_V \nabla(\delta T) \cdot \mathbf{q}_k \, dV - \int_V \delta T \, (g_k + g_k^{\text{conv}}) \, dV &= \int_{\partial V} \delta T \, \mathbf{q}_k \cdot \hat{\mathbf{n}} \, dS,
\end{aligned} \tag{4.18}$$

where  $\hat{\mathbf{n}}$  is the unit outward normal to the boundary  $\partial V$ . Boundary data can be given in terms of the primary unknowns or in terms of the fluxes that appear in the right-hand-side of the semi-discretised system.

#### 4.2.2 Definition of the nodal and global unknown vectors

The  $n_{sd} + 5$  primary unknowns to be calculated at each *node* are:

- the solid displacement vector  $\mathbf{u} = \begin{bmatrix} u_x \\ u_y \end{bmatrix}$ ,
- the pore fluid pressure  $p_p$ ,
- the fissure fluid pressure  $p_f$ ,
- the solid temperature  $T_s$ ,
- the pore fluid temperature  $T_p$  and
- the fissure fluid temperature  $T_f$ .

Consequently, the unknown *nodal* vector  $\mathbb{X}^e$  used in the discretisation is,

$$[\mathbb{X}^e]^T = [ \mathbf{u}^e \quad \mathbf{p}_p^e \quad \mathbf{p}_f^e \quad \mathbf{T}_s^e \quad \mathbf{T}_p^e \quad \mathbf{T}_f^e ]. \tag{4.19}$$

The size of this vector depends on the number of nodes chosen for the reference elements (*a priori* distinct for each type of unknown). For example, if a two-dimensional four-node reference element is adopted for all the unknowns, the size of  $\mathbb{X}^e$  is  $(n_{sd} + 5) \times 4$ .

The global unknown vector  $\mathbb{X}$  results by assembling of all the element vectors  $\mathbb{X}^e$ :

$$\mathbb{X}^T = [ \mathbf{u} \quad \mathbf{p}_p \quad \mathbf{p}_f \quad \mathbf{T}_s \quad \mathbf{T}_p \quad \mathbf{T}_f ]. \tag{4.20}$$

### 4.2.3 The (Bubnov-)Galerkin method

The (Bubnov-)Galerkin procedure is adopted as far as the same interpolation functions are used for the primary unknowns and for the variations.

If the interpolation functions  $\mathbf{N}_T$  are chosen to interpolate the unknown temperature  $T_k$ , and the interpolation functions  $\mathbf{M}_T$  to interpolate the variation corresponding to the temperature  $\delta T$ ,

$$\left. \begin{aligned} T_k &= \mathbf{N}_T \mathbf{T}_k^e \\ \delta T &= \mathbf{M}_T \delta T^e \end{aligned} \right\} \text{the Bubnov-Galerkin method implies } \mathbf{N}_T = \mathbf{M}_T. \quad (4.21)$$

The presence of convective terms requires modifications with respect to the Bubnov-Galerkin method. Indeed the Petrov-Galerkin method deviates from (4.21). Defining exactly how much different are the weight functions  $\mathbf{M}_T$  from the interpolation functions is a difficult task, which has received only partial answer so far. The issue is of importance in this work since convective heat flow will be shown to control the physical processes to be analysed. Chapter 7 is devoted to analyse the Petrov-Galerkin method.

### 4.2.4 The semi-discrete system

Before writing the semi-discretised system in a vector form and in a matrix form, some finite element notations are introduced, namely, Voigt's notation and the shape functions associated with the reference element.

#### 4.2.4.1 Voigt's notation

Hooke's law uses a symmetric fourth-order stiffness tensor  $\mathbf{K}^{DS}$  with 81 components  $3 \times 3 \times 3 \times 3$ . Voigt's notation enables this tensor to be simplified to a  $6 \times 6$  (pseudo-)matrix. According to our previous notational convention,  $\boldsymbol{\epsilon} = [\epsilon_{ij}]$  is the matrix of strain components. However, no need for this matrix form is required by the FEM and consequently the notation  $\boldsymbol{\epsilon}$  is reserved for the *strain vector*. A similar notational conflict occurs with respect to the *stress vector*  $\boldsymbol{\sigma}$ .

Next, the strain vector and the stress vector are defined for three types of problems: (1) three-dimensional, (2) plane strain and (3) axi-symmetric assumptions are considered in turn.

(1) For a three-dimensional problem, the strain and the stress matrices are simplified into vectors according to Voigt's notation:

$$\boldsymbol{\epsilon} = \begin{bmatrix} \epsilon_{xx} & \epsilon_{xy} & \epsilon_{xz} \\ \epsilon_{yx} & \epsilon_{yy} & \epsilon_{yz} \\ \epsilon_{zx} & \epsilon_{zy} & \epsilon_{zz} \end{bmatrix} \rightarrow \boldsymbol{\epsilon}^{\mathbf{T}} = [ \epsilon_{xx} \quad \epsilon_{yy} \quad \epsilon_{zz} \quad 2 \epsilon_{yz} \quad 2 \epsilon_{xz} \quad 2 \epsilon_{xy} ]; \quad (4.22)$$

$$\boldsymbol{\sigma} = \begin{bmatrix} \sigma_{xx} & \sigma_{xy} & \sigma_{xz} \\ \sigma_{yx} & \sigma_{yy} & \sigma_{yz} \\ \sigma_{zx} & \sigma_{zy} & \sigma_{zz} \end{bmatrix} \rightarrow \boldsymbol{\sigma}^{\mathbf{T}} = [ \sigma_{xx} \quad \sigma_{yy} \quad \sigma_{zz} \quad \sigma_{yz} \quad \sigma_{xz} \quad \sigma_{xy} ]; \quad (4.23)$$

and the constitutive stiffness tensor becomes a  $6 \times 6$  matrix,

$$\mathbf{K}^{DS} = \begin{bmatrix} \lambda^{DS} + 2\mu^{DS} & \lambda^{DS} & \lambda^{DS} & 0 & 0 & 0 \\ \lambda^{DS} & \lambda^{DS} + 2\mu^{DS} & \lambda^{DS} & 0 & 0 & 0 \\ \lambda^{DS} & \lambda^{DS} & \lambda^{DS} + 2\mu^{DS} & 0 & 0 & 0 \\ 0 & 0 & 0 & \mu^{DS} & 0 & 0 \\ 0 & 0 & 0 & 0 & \mu^{DS} & 0 \\ 0 & 0 & 0 & 0 & 0 & \mu^{DS} \end{bmatrix} \quad (4.24)$$

(2) For a plane strain problem, the strain and the stress matrices further reduce to:

$$\boldsymbol{\epsilon} = \begin{bmatrix} \epsilon_{xx} & \epsilon_{xy} & 0 \\ \epsilon_{yx} & \epsilon_{yy} & 0 \\ 0 & 0 & 0 \end{bmatrix} \rightarrow \boldsymbol{\epsilon}^{\mathbf{T}} = [ \epsilon_{xx} \quad \epsilon_{yy} \quad 2 \epsilon_{xy} ]; \quad (4.25)$$

$$\boldsymbol{\sigma} = \begin{bmatrix} \sigma_{xx} & \sigma_{xy} & 0 \\ \sigma_{yx} & \sigma_{yy} & 0 \\ 0 & 0 & \sigma_{zz} \end{bmatrix} \rightarrow \boldsymbol{\sigma}^{\mathbf{T}} = [ \sigma_{xx} \quad \sigma_{yy} \quad \sigma_{xy} ]. \quad (4.26)$$

Note that the stress  $\sigma_{zz}$  is generally not zero. However, it is not considered as an unknown and it can be recalculated by use of equation (4.24). The constitutive stiffness tensor becomes,

$$\begin{bmatrix} \sigma_{xx} \\ \sigma_{yy} \\ \sigma_{xy} \end{bmatrix} = \begin{bmatrix} \lambda^{DS} + 2\mu^{DS} & \lambda^{DS} & 0 \\ \lambda^{DS} & \lambda^{DS} + 2\mu^{DS} & 0 \\ 0 & 0 & \mu^{DS} \end{bmatrix} \begin{bmatrix} \epsilon_{xx} \\ \epsilon_{yy} \\ 2 \epsilon_{xy} \end{bmatrix}; \quad (4.27)$$

where the strain vector can be related to the displacement vector through,

$$\begin{bmatrix} \epsilon_{xx} \\ \epsilon_{yy} \\ 2 \epsilon_{xy} \end{bmatrix} = \begin{bmatrix} \frac{\partial u_x}{\partial x} \\ \frac{\partial u_y}{\partial y} \\ \frac{\partial u_x}{\partial y} + \frac{\partial u_y}{\partial x} \end{bmatrix}. \quad (4.28)$$

(3) For an axi-symmetric analysis, the displacements previously expressed in Cartesian coordinates are now expressed in terms of cylindrical coordinates:

- $u_x = u_r$  = the radial displacement,
- $u_y = u_z$  = the axial displacement and
- $u_z = u_\theta$  = the circumferential displacement.

The basic hypothesis of axi-symmetry is that all functions under consideration are independent of  $\theta$ . That is, they are functions of  $r$  and  $z$  only. In addition, the circumferential displacement is further assumed to be equal to zero  $u_\theta = 0$  and thus,

$$\epsilon_{r\theta} = \epsilon_{z\theta} = 0. \quad (4.29)$$

Note that  $\epsilon_{\theta\theta} = u_r/r$  is generally not zero. Therefore, if the constitutive equations express in the format  $\boldsymbol{\sigma} = \mathbf{K}^{DS} : \boldsymbol{\epsilon}$ , with  $\mathbf{K}^{DS}$  the isotropic stiffness given by (4.24), the shear stresses,

$$\sigma_{r\theta} = \sigma_{z\theta} = 0. \quad (4.30)$$

vanish as well. Hence, for an axi-symmetric analysis,

$$\boldsymbol{\epsilon} = \begin{bmatrix} \epsilon_{rr} & \epsilon_{rz} & 0 \\ \epsilon_{zr} & \epsilon_{zz} & 0 \\ 0 & 0 & \epsilon_{\theta\theta} \end{bmatrix} \rightarrow \boldsymbol{\epsilon}^{\mathbf{T}} = [ \epsilon_{rr} \quad \epsilon_{zz} \quad 2 \epsilon_{rz} \quad \epsilon_{\theta\theta} ]; \quad (4.31)$$

$$\boldsymbol{\sigma} = \begin{bmatrix} \sigma_{rr} & \sigma_{rz} & 0 \\ \sigma_{zr} & \sigma_{zz} & 0 \\ 0 & 0 & \sigma_{\theta\theta} \end{bmatrix} \rightarrow \boldsymbol{\sigma}^{\mathbf{T}} = [ \sigma_{rr} \quad \sigma_{zz} \quad \sigma_{rz} \quad \sigma_{\theta\theta} ]; \quad (4.32)$$

the isotropic stiffness tensor  $\mathbf{K}^{DS}$  takes the form,

$$\begin{bmatrix} \sigma_{rr} \\ \sigma_{zz} \\ \sigma_{rz} \\ \sigma_{\theta\theta} \end{bmatrix} = \begin{bmatrix} \lambda^{DS} + 2\mu^{DS} & \lambda^{DS} & 0 & \lambda^{DS} \\ \lambda^{DS} & \lambda^{DS} + 2\mu^{DS} & 0 & \lambda^{DS} \\ 0 & 0 & \mu^{DS} & 0 \\ \lambda^{DS} & \lambda^{DS} & 0 & \lambda^{DS} + 2\mu^{DS} \end{bmatrix} \begin{bmatrix} \epsilon_{rr} \\ \epsilon_{zz} \\ 2\epsilon_{rz} \\ \epsilon_{\theta\theta} \end{bmatrix} \quad (4.33)$$

where the strain vector can be related to the displacement vector through,

$$\begin{bmatrix} \epsilon_{rr} \\ \epsilon_{zz} \\ 2\epsilon_{rz} \\ \epsilon_{\theta\theta} \end{bmatrix} = \begin{bmatrix} \frac{\partial u_r}{\partial r} \\ \frac{\partial u_z}{\partial z} \\ \frac{\partial u_r}{\partial z} + \frac{\partial u_z}{\partial r} \\ \frac{u_r}{r} \end{bmatrix}. \quad (4.34)$$

Note that the axi-symmetric relations are written in such a way that they are easily transformed into the plane strain relations of the previous paragraph (4.27)-(4.28).

#### 4.2.4.2 Isoparametric reference elements

The  $n_{sd} + 5$  primary unknowns are interpolated, within the generic element  $e$ , in terms of nodal values through *a priori distinct* interpolation functions:  $\mathbf{N}_u$ ,  $\mathbf{N}_p$  and  $\mathbf{N}_T$ .

- the solid displacement vector  $\mathbf{u} = \mathbf{N}_u \mathbf{u}^e$ ,
- the pore and the fissure fluid pressures  $p_k = \mathbf{N}_p \mathbf{p}_k^e$  for  $k = p, f$ , and
- the phase temperatures  $T_k = \mathbf{N}_T \mathbf{T}_k^e$ , for  $k = s, p, f$ .

In this study, *two-dimensional four-node isoparametric elements* are employed to represent the fissured porous medium.

The shape function associated to a given node is equal to one at this node and equal to zero at the other nodes. A four node bilinear quadrilateral reference element is chosen and the associated shape functions are defined in Table 4.1. The nodal points are labeled

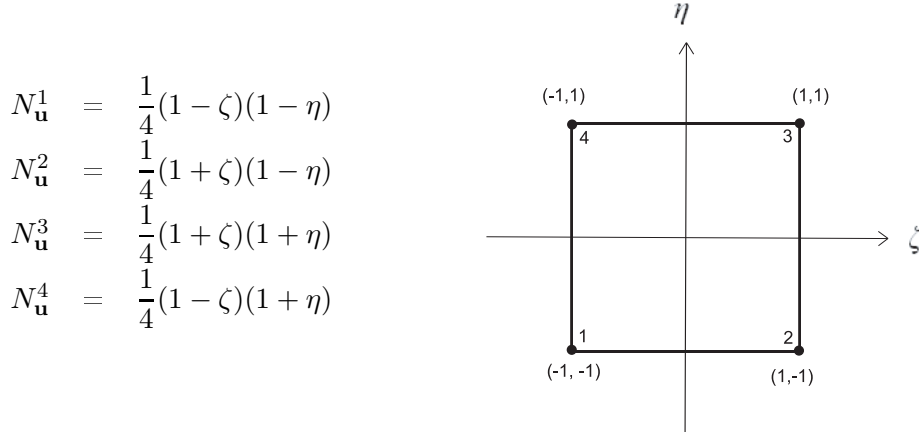


Table 4.1: Shape functions associated to a four node bilinear quadrilateral reference element. The nodal points are labeled in ascending order corresponding to the counterclockwise direction.

in ascending order corresponding to the counterclockwise direction. In the further development displacement, pressure and temperature shape functions are considered identical, namely,

$$\mathbf{N}_{\mathbf{u}} = \mathbf{N}_p = \mathbf{N}_T. \quad (4.35)$$

This approach is satisfactory for hydro-mechanical applications (Khalili-Naghadeh, 1991; Khalili et al., 1999) and for thermo-hydro-mechanical applications (Chapter 5). Mixed interpolation modes have been proposed in the literature (Elsworth and Bai, 1992; Ghafouri and Lewis, 1996; Bai et al., 1999), typically quadratic interpolation for the displacement and linear interpolation for the fluid pressures. In this work, equal-order interpolation for all the unknowns is preferred due its simplicity and ease of computational implementation.

#### 4.2.4.3 The vector form of the semi-discrete system

The internal contributions, of a generic element  $e$ , comprise the thermo-elastic contributions denoted by the vector  $\mathbb{F}_e^{\text{Th-EI}}$  and the convective contributions denoted by the vector  $\mathbb{F}_e^{\text{conv}}$ . On the other hand, the surface loading contributions are gathered into the vector  $\mathbb{F}_e^{\text{surf}}$ ,

$$\underbrace{\mathbb{F}_e^{\text{Th-EI}} + \mathbb{F}_e^{\text{conv}}}_{\text{Internal forces}} - \underbrace{\mathbb{F}_e^{\text{surf}}}_{\text{Surface forces}}. \quad (4.36)$$

The Galerkin method implies that the variations  $\delta \mathbf{u}$ ,  $\delta p$  and  $\delta T$  are interpolated through the functions  $\mathbf{N}_u$ ,  $\mathbf{N}_p$  and  $\mathbf{N}_T$ , respectively. After the spatial discretisation, the elementary contributions to the variational formulation (4.18) are denoted in a vector form,

$$\begin{bmatrix} \int_{V^e} \mathbf{B}_u^T \boldsymbol{\sigma} - \mathbf{N}_u^T \rho \mathbf{b} \, dV^e \\ \int_{V^e} \nabla \mathbf{N}_p^T \mathbf{J}_p - \mathbf{N}_p^T f_p \, dV^e \\ \int_{V^e} \nabla \mathbf{N}_p^T \mathbf{J}_f - \mathbf{N}_p^T f_f \, dV^e \\ \int_{V^e} \nabla \mathbf{N}_T^T \mathbf{q}_s - \mathbf{N}_T^T g_s \, dV^e \\ \int_{V^e} \nabla \mathbf{N}_T^T \mathbf{q}_p - \mathbf{N}_T^T (g_p + g_p^{\text{conv}}) \, dV^e \\ \int_{V^e} \nabla \mathbf{N}_T^T \mathbf{q}_f - \mathbf{N}_T^T (g_f + g_f^{\text{conv}}) \, dV^e \end{bmatrix} = \begin{bmatrix} \int_{\partial V^e} \mathbf{N}_u^T \boldsymbol{\sigma} \cdot \hat{\mathbf{n}} \, dS^e \\ \int_{\partial V^e} \mathbf{N}_p^T \mathbf{J}_p \cdot \hat{\mathbf{n}} \, dS^e \\ \int_{\partial V^e} \mathbf{N}_p^T \mathbf{J}_f \cdot \hat{\mathbf{n}} \, dS^e \\ \int_{\partial V^e} \mathbf{N}_T^T \mathbf{q}_s \cdot \hat{\mathbf{n}} \, dS^e \\ \int_{\partial V^e} \mathbf{N}_T^T \mathbf{q}_p \cdot \hat{\mathbf{n}} \, dS^e \\ \int_{\partial V^e} \mathbf{N}_T^T \mathbf{q}_f \cdot \hat{\mathbf{n}} \, dS^e \end{bmatrix}, \quad (4.37)$$

where  $\mathbf{B}_u$  is the standard strain-displacement matrix (Appendix E). The total stress and the fluxes are expressed in terms of primary unknowns in eq. (2.280) and eq. (2.249), respectively. The generalised transfer constitutive relation is outlined in eq. (2.277). The constitutive equations are introduced into the field equations to form the full set of comprehensive equations in eq. (2.319) to (2.324).

The previous formulation is written in a more detailed form to visualise the primary unknown vectors in eq. (E.18) to (E.23). A contracted form is presented below:

Elementary contribution to the balance of momentum for the mixture:

$$\mathbf{E}_{uu}^e \mathbf{u}^e - \mathbf{C}_{up}^e (\xi_p \mathbf{p}_p^e + \xi_f \mathbf{p}_f^e) - \mathbf{C}_{uT}^e a_{eT_s} \mathbf{T}_s^e - \mathbf{F}_u^e. \quad (4.38)$$

Elementary contribution to the balance of mass for the pore fluid:

$$\begin{aligned} & - \mathbf{J}_{k_p}^e \mathbf{p}_p^e - \mathbf{J}_{\Theta_p}^e \mathbf{T}_p^e - \mathbf{M}_{pp}^e (a_{pp} \dot{\mathbf{p}}_p^e + a_{pf} \dot{\mathbf{p}}_f^e) - \mathbf{M}_{pT}^e (a_{pT_s} \dot{\mathbf{T}}_s^e + a_{pT_p} \dot{\mathbf{T}}_p^e) \\ & - \xi_p \mathbf{C}_{pu}^e \dot{\mathbf{u}}^e - \mathbf{N}_T \mathbf{T}_0^e \rho_p \eta \mathbf{N}_p^T \left[ \frac{G_p(\mathbf{N}_p \mathbf{p}_p^e, \mathbf{N}_T \mathbf{T}_p^e)}{\mathbf{N}_T \mathbf{T}_p^e} - \frac{G_f(\mathbf{N}_p \mathbf{p}_f^e, \mathbf{N}_T \mathbf{T}_f^e)}{\mathbf{N}_T \mathbf{T}_f^e} \right] \\ & - \mathbf{F}_{pp}^e. \end{aligned} \quad (4.39)$$

in which the chemical potential  $G_k(\mathbf{N}_p \mathbf{p}_k^e, \mathbf{N}_T \mathbf{T}_k^e)$  of the fluid  $k$  is defined in eq. (2.160)<sub>2</sub>.



Elementary contribution to the balance of mass for the fissure fluid:

$$\begin{aligned}
& - \mathbf{J}_{k_f}^e \mathbf{p}_f^e - \mathbf{J}_{\Theta_f}^e \mathbf{T}_f^e - \mathbf{M}_{pp}^e (a_{ff} \dot{\mathbf{p}}_f^e + a_{pf} \dot{\mathbf{p}}_p^e) - \mathbf{M}_{pT}^e (a_{fT_s} \dot{\mathbf{T}}_s^e + a_{fT_f} \dot{\mathbf{T}}_f^e) \\
& - \xi_f \mathbf{C}_{pu}^e \dot{\mathbf{u}}^e + \mathbf{N}_T \mathbf{T}_0^e \rho_p \eta \mathbf{N}_p^T \left[ \frac{G_p (\mathbf{N}_p \mathbf{p}_p^e, \mathbf{N}_T \mathbf{T}_p^e)}{\mathbf{N}_T \mathbf{T}_p^e} - \frac{G_f (\mathbf{N}_p \mathbf{p}_f^e, \mathbf{N}_T \mathbf{T}_f^e)}{\mathbf{N}_T \mathbf{T}_f^e} \right] \\
& - \mathbf{F}_{p_f}^e.
\end{aligned} \tag{4.40}$$

Elementary contribution to the balance of energy for the solid phase:

$$\begin{aligned}
& - [\mathbf{Q}_{\Lambda_s}^e + \mathbf{M}_{TT}^e (\kappa_{sp} + \kappa_{sf})] \mathbf{T}_s^e + \mathbf{M}_{TT}^e (\kappa_{sp} \mathbf{T}_p^e + \kappa_{sf} \mathbf{T}_f^e) \\
& - [\mathbf{M}_{pT}^e]^T (a_{T_{sp}} \dot{\mathbf{p}}_p^e + a_{T_{sf}} \dot{\mathbf{p}}_f^e) - a_{T_s T_s} \mathbf{M}_{TT}^e \dot{\mathbf{T}}_s^e - a_{T_s \epsilon} \mathbf{C}_{Tu}^e \dot{\mathbf{u}}^e - \mathbf{F}_{T_s}^e.
\end{aligned} \tag{4.41}$$

Elementary contribution to the balance of energy for the pore fluid:

$$\begin{aligned}
& - [\mathbf{Q}_{\Theta_p}^e + b_{T_{pp}} \mathbf{C}_{T_{p,v_p}}^e] \mathbf{p}_p^e + \mathbf{M}_{TT}^e (\kappa_{sp} \mathbf{T}_s^e + \kappa_{pf} \mathbf{T}_f^e) \\
& - [\mathbf{Q}_{\Lambda_p}^e + b_{T_p T_p} \mathbf{C}_{TT,v_p}^e + \mathbf{M}_{TT}^e (\kappa_{sp} + \kappa_{pf})] \mathbf{T}_p^e \\
& - [\mathbf{M}_{pT}^e]^T (a_{T_{pp}} \dot{\mathbf{p}}_p^e + a_{T_{pf}} \dot{\mathbf{p}}_f^e) - \mathbf{M}_{TT}^e (a_{T_p T_p} \dot{\mathbf{T}}_p^e + a_{T_p T_s} \dot{\mathbf{T}}_s^e) - a_{T_p \epsilon} \mathbf{C}_{Tu}^e \dot{\mathbf{u}}^e \\
& + \mathbf{N}_T \mathbf{T}_0^e \rho_p^2 \eta \mathbf{N}_T^T \left[ \frac{G_p (\mathbf{N}_p \mathbf{p}_p^e, \mathbf{N}_T \mathbf{T}_p^e)}{\mathbf{N}_T \mathbf{T}_p^e} - \frac{G_f (\mathbf{N}_p \mathbf{p}_f^e, \mathbf{N}_T \mathbf{T}_f^e)}{\mathbf{N}_T \mathbf{T}_f^e} \right] H_p (\mathbf{N}_p \mathbf{p}_p^e, \mathbf{N}_T \mathbf{T}_p^e) \\
& - \mathbf{F}_{T_p}^e.
\end{aligned} \tag{4.42}$$

in which the enthalpy  $H_k(\mathbf{N}_p \mathbf{p}_k^e, \mathbf{N}_T \mathbf{T}_k^e)$  of the fluid  $k$  is defined in eq. (2.160)<sub>3</sub>.

Elementary contribution to the balance of energy for the fissure fluid:

$$\begin{aligned}
& - [\mathbf{Q}_{\Theta_f}^e + b_{T_{ff}} \mathbf{C}_{T_{p,v_f}}^e] \mathbf{p}_f^e + \mathbf{M}_{TT}^e (\kappa_{sf} \mathbf{T}_s^e + \kappa_{pf} \mathbf{T}_p^e) \\
& - [\mathbf{Q}_{\Lambda_f}^e + b_{T_f T_f} \mathbf{C}_{TT,v_f}^e + \mathbf{M}_{TT}^e (\kappa_{sf} + \kappa_{pf})] \mathbf{T}_f^e \\
& - [\mathbf{M}_{pT}^e]^T (a_{T_{fp}} \dot{\mathbf{p}}_p^e + a_{T_{ff}} \dot{\mathbf{p}}_f^e) - \mathbf{M}_{TT}^e (a_{T_f T_f} \dot{\mathbf{T}}_f^e + a_{T_f T_s} \dot{\mathbf{T}}_s^e) - a_{T_f \epsilon} \mathbf{C}_{Tu}^e \dot{\mathbf{u}}^e \\
& - \mathbf{N}_T \mathbf{T}_0^e \rho_p^2 \eta \mathbf{N}_T^T \left[ \frac{G_p (\mathbf{N}_p \mathbf{p}_p^e, \mathbf{N}_T \mathbf{T}_p^e)}{\mathbf{N}_T \mathbf{T}_p^e} - \frac{G_f (\mathbf{N}_p \mathbf{p}_f^e, \mathbf{N}_T \mathbf{T}_f^e)}{\mathbf{N}_T \mathbf{T}_f^e} \right] H_f (\mathbf{N}_p \mathbf{p}_f^e, \mathbf{N}_T \mathbf{T}_f^e) \\
& - \mathbf{F}_{T_f}^e.
\end{aligned} \tag{4.43}$$

Note that the terms relative to mass transfer and to the change in internal energy due to mass transfer are not linearised at this stage.

The finite element sub-matrices of the compact weak formulation in equations (4.38) to (4.43) are listed below. The three matrices involved in the elementary contribution to the balance of momentum of the mixture are,

$$\mathbf{E}_{\mathbf{u}\mathbf{u}}^e = \int_{V^e} \mathbf{B}_{\mathbf{u}}^T \mathbf{D}_{\text{el}} \mathbf{B}_{\mathbf{u}} dV^e, \quad (4.44)$$

$$\mathbf{C}_{\mathbf{u}p}^e = \int_{V^e} \nabla \mathbf{N}_{\mathbf{u}}^T \mathbf{N}_p dV^e, \quad \mathbf{C}_{\mathbf{u}T}^e = \int_{V^e} \nabla \mathbf{N}_{\mathbf{u}}^T \mathbf{N}_T dV^e.$$

$$\mathbf{C}_{p\mathbf{u}}^e = \int_{V^e} \mathbf{N}_p^T [1 \quad 1] \nabla \cdot \mathbf{N}_{\mathbf{u}} dV^e, \quad (4.45)$$

$$\mathbf{C}_{T\mathbf{u}}^e = \int_{V^e} \mathbf{N}_T^T [1 \quad 1] \nabla \cdot \mathbf{N}_{\mathbf{u}} dV^e.$$

Next, the matrices describing the hydraulic conductivity and the heat conduction,

$$\mathbf{J}_{k_k}^e = \int_{V^e} \nabla \mathbf{N}_p^T \frac{k_k}{\mu_k} \nabla \mathbf{N}_p dV^e, \quad k = p, f, \quad (4.46)$$

$$\mathbf{Q}_{\Lambda_k}^e = \int_{V^e} \nabla \mathbf{N}_T^T n_k \Lambda_k \nabla \mathbf{N}_T dV^e, \quad k = s, p, f;$$

while the matrices involved in the thermo-osmosis and the isothermal heat flow coupling phenomena are,

$$\mathbf{J}_{\Theta_k}^e = \int_{V^e} \nabla \mathbf{N}_p^T n_k \Theta_k \nabla \mathbf{N}_T dV^e, \quad k = p, f, \quad (4.47)$$

$$\mathbf{Q}_{\Theta_k}^e = \int_{V^e} \nabla \mathbf{N}_T^T T_k n_k \Theta_k \nabla \mathbf{N}_p dV^e, \quad k = p, f.$$

Three mass matrices are required in the general case. Note that they reduce to one matrix if the pressure and the temperature have the same shape functions, namely  $\mathbf{N}_p = \mathbf{N}_T$ .

$$\mathbf{M}_{pp}^e = \int_{V^e} \mathbf{N}_p^T \mathbf{N}_p dV^e, \quad \mathbf{M}_{TT}^e = \int_{V^e} \mathbf{N}_T^T \mathbf{N}_T dV^e, \quad (4.48)$$

$$\mathbf{M}_{pT}^e = \int_{V^e} \mathbf{N}_p^T \mathbf{N}_T dV^e.$$

The convective matrices discretised with the Galerkin method write,

$$\begin{aligned}
\mathbf{C}_{TT,v_p}^e &= \int_{V^e} \mathbf{N}_T^T (\mathbf{v}_p - \mathbf{v}_s) \cdot \nabla \mathbf{N}_T \, dV^e, \\
\mathbf{C}_{TT,v_f}^e &= \int_{V^e} \mathbf{N}_T^T (\mathbf{v}_f - \mathbf{v}_s) \cdot \nabla \mathbf{N}_T \, dV^e, \\
\mathbf{C}_{Tp,v_p}^e &= \int_{V^e} \mathbf{N}_T^T (\mathbf{v}_p - \mathbf{v}_s) \cdot \nabla \mathbf{N}_p \, dV^e, \\
\mathbf{C}_{Tp,v_f}^e &= \int_{V^e} \mathbf{N}_T^T (\mathbf{v}_f - \mathbf{v}_s) \cdot \nabla \mathbf{N}_p \, dV^e.
\end{aligned} \tag{4.49}$$

Finally, the matrices corresponding to the elementary contributions of each equation to the external force vector

$$\begin{aligned}
\mathbf{F}_u^e &= \int_{\partial V^e} \mathbf{N}_u^T \boldsymbol{\sigma} \cdot \hat{\mathbf{n}} \, dS^e + \int_{V^e} \mathbf{N}_u^T \rho \mathbf{b} \, dV^e, \\
\mathbf{F}_{pp}^e &= \int_{\partial V^e} \mathbf{N}_p^T \mathbf{J}_p \cdot \hat{\mathbf{n}} \, dS^e - \int_{V^e} \nabla \mathbf{N}_p^T \frac{k_p}{\mu_p} \rho_p \mathbf{g} \, dV^e, \\
\mathbf{F}_{pf}^e &= \int_{\partial V^e} \mathbf{N}_p^T \mathbf{J}_f \cdot \hat{\mathbf{n}} \, dS^e - \int_{V^e} \nabla \mathbf{N}_p^T \frac{k_f}{\mu_f} \rho_f \mathbf{g} \, dV^e, \\
\mathbf{F}_{Ts}^e &= \int_{\partial V^e} \mathbf{N}_T^T \mathbf{q}_s \cdot \hat{\mathbf{n}} \, dS^e, \\
\mathbf{F}_{Tp}^e &= \int_{\partial V^e} \mathbf{N}_T^T \mathbf{q}_p \cdot \hat{\mathbf{n}} \, dS^e - \int_{V^e} \nabla \mathbf{N}_T^T n_p T_p \Theta_p \rho_p \mathbf{g} \, dV^e, \\
\mathbf{F}_{Tf}^e &= \int_{\partial V^e} \mathbf{N}_T^T \mathbf{q}_f \cdot \hat{\mathbf{n}} \, dS^e - \int_{V^e} \nabla \mathbf{N}_T^T n_f T_f \Theta_f \rho_f \mathbf{g} \, dV^e.
\end{aligned} \tag{4.50}$$

are gathered into the elementary load vector  $\mathbb{F}^e$ ,

$$[\mathbb{F}^e]^T = \left[ \mathbf{F}_u^e \quad \mathbf{F}_{pp}^e \quad \mathbf{F}_{pf}^e \quad \mathbf{F}_{Ts}^e \quad \mathbf{F}_{Tp}^e \quad \mathbf{F}_{Tf}^e \right]. \tag{4.51}$$

#### 4.2.4.4 The matrix form of the semi-discrete system

If a linearisation of the mass transfer terms is authorised, the semi-discretised system writes in a matrix form. For  $n_{el}$  elements, the matrix form of the *linearised* semi-discrete

system can be expressed as a function of the elementary diffusion matrix  $\mathbb{D}^e$ , the elementary stiffness matrix  $\mathbb{K}^e$  and the elementary convection matrix  $\mathbb{C}_{\text{conv}}^e$ , through the assembling process denoted by  $\cup$ ,

$$\bigcup_{e=1}^{n_{el}} \left[ \mathbb{D}^e \left( \frac{d}{dt} \mathbb{X}^e \right) + \mathbb{K}^e \mathbb{X}^e + \mathbb{C}_{\text{conv}}^e \mathbb{X}^e - \mathbb{F}^e \right] = 0, \quad (4.52)$$

in which,  $\mathbb{K}^e$  is of the form,

$$\mathbb{K}^e = \begin{bmatrix} \mathbf{K}_{\mathbf{u} \mathbf{u}}^e & \mathbf{K}_{\mathbf{u} p_p}^e & \mathbf{K}_{\mathbf{u} p_f}^e & \mathbf{K}_{\mathbf{u} T_s}^e & 0 & 0 \\ 0 & \mathbf{K}_{p_p p_p}^e & \mathbf{K}_{p_p p_f}^e & 0 & \mathbf{K}_{p_p T_p}^e & \mathbf{K}_{p_p T_f}^e \\ 0 & \mathbf{K}_{p_f p_p}^e & \mathbf{K}_{p_f p_f}^e & 0 & \mathbf{K}_{p_f T_p}^e & \mathbf{K}_{p_f T_f}^e \\ 0 & 0 & 0 & \mathbf{K}_{T_s T_s}^e & \mathbf{K}_{T_s T_p}^e & \mathbf{K}_{T_s T_f}^e \\ 0 & \mathbf{K}_{T_p p_p}^e & \mathbf{K}_{T_p p_f}^e & \mathbf{K}_{T_p T_s}^e & \mathbf{K}_{T_p T_p}^e & \mathbf{K}_{T_p T_f}^e \\ 0 & \mathbf{K}_{T_f p_p}^e & \mathbf{K}_{T_f p_f}^e & \mathbf{K}_{T_f T_s}^e & \mathbf{K}_{T_f T_p}^e & \mathbf{K}_{T_f T_f}^e \end{bmatrix}, \quad (4.53)$$

$\mathbb{D}^e$  is defined as,

$$\mathbb{D}^e = \begin{bmatrix} 0 & 0 & 0 & 0 & 0 & 0 \\ \mathbf{D}_{p_p \mathbf{u}}^e & \mathbf{D}_{p_p p_p}^e & \mathbf{D}_{p_p p_f}^e & \mathbf{D}_{p_p T_s}^e & \mathbf{D}_{p_p T_p}^e & 0 \\ \mathbf{D}_{p_f \mathbf{u}}^e & \mathbf{D}_{p_f p_p}^e & \mathbf{D}_{p_f p_f}^e & \mathbf{D}_{p_f T_s}^e & 0 & \mathbf{D}_{p_f T_f}^e \\ \mathbf{D}_{T_s \mathbf{u}}^e & \mathbf{D}_{T_s p_p}^e & \mathbf{D}_{T_s p_f}^e & \mathbf{D}_{T_s T_s}^e & 0 & 0 \\ \mathbf{D}_{T_p \mathbf{u}}^e & \mathbf{D}_{T_p p_p}^e & \mathbf{D}_{T_p p_f}^e & \mathbf{D}_{T_p T_s}^e & \mathbf{D}_{T_p T_p}^e & 0 \\ \mathbf{D}_{T_f \mathbf{u}}^e & \mathbf{D}_{T_f p_p}^e & \mathbf{D}_{T_f p_f}^e & \mathbf{D}_{T_f T_s}^e & 0 & \mathbf{D}_{T_f T_f}^e \end{bmatrix}, \quad (4.54)$$

and  $\mathbb{C}_{\text{conv}}^e$  is of the form,

$$\mathbb{C}_{\text{conv}}^e = \begin{bmatrix} 0 & 0 & 0 & 0 & 0 & 0 \\ 0 & 0 & 0 & 0 & 0 & 0 \\ 0 & 0 & 0 & 0 & 0 & 0 \\ 0 & 0 & 0 & 0 & 0 & 0 \\ 0 & \mathbf{C}_{T_p p_p}^e & 0 & 0 & \mathbf{C}_{T_p T_p}^e & 0 \\ 0 & 0 & \mathbf{C}_{T_f p_f}^e & 0 & 0 & \mathbf{C}_{T_f T_f}^e \end{bmatrix}. \quad (4.55)$$

The finite element sub-matrices of the element stiffness matrix  $\mathbb{K}^e$  (4.53), of the element diffusion matrix  $\mathbb{D}^e$  (4.54) and of the element convection matrix  $\mathbb{C}_{\text{conv}}^e$  (4.55) are listed in

Appendix E.3. They can be identified by comparison with equations (4.38) to (4.43), for example:  $\mathbf{K}_{\mathbf{u}\mathbf{u}}^e = \mathbf{E}_{\mathbf{u}\mathbf{u}}^e$ .

The definitions of the elementary matrices represent the contributions gathered in the left-hand-side which can bear some linearisation, as opposed to the contributions of the right-hand-side which can not be linearised nor be represented in a matrix form.

### 4.3 The time integration methods for equation solving

The time integration method based on the general trapezoidal method is a one-step algorithm suitable to find the finite solution of time-independent problems. However, the exact solution of the transient phase is only estimated. The predictor multi-corrector algorithm is a more accurate algorithm to solve parabolic problems (diffusion) and hyperbolic problems (pure convection). In contrast with the general trapezoidal method, the predictor multi-corrector method is suitable to find the exact solution of transient phases, such as problems in fluid-saturated mixtures which involve non-linear terms and whose constituents are not in thermal equilibrium.

Recall that the *linearised* semi-discrete system (4.52) is a parabolic problem which can be written as,

$$\mathbb{D} \mathbb{V} + \mathbb{K} \mathbb{X} + \mathbb{C}_{\text{conv}} \mathbb{X} = \mathbb{F}. \quad (4.56)$$

where  $\mathbb{D}$  is the global diffusion matrix,  $\mathbb{K}$  is the global stiffness matrix,  $\mathbb{C}_{\text{conv}}$  is the global convection matrix and  $\mathbb{F}$  is the global load vector. In addition,  $\mathbb{X}$  is the global unknown vector as defined by equation (4.20) and  $\mathbb{V}$  is the time derivative of  $\mathbb{X}$ .

The system of equations (4.38)-(4.43), assembled over  $n_{el}$  elements, may also be written as a difference between the surface load vector  $\mathbb{F}^{\text{surf}}(\mathbb{S}, \mathbb{X})$ , the vector gathering the internal thermo-elastic forces  $\mathbb{F}^{\text{int}}(\mathbb{X}, \mathbb{V})$  and the vector gathering the convective terms  $\mathbb{F}^{\text{conv}}(\mathbb{X}, \mathbb{V})$ . The residual implied by this semi-discrete system is forced to vanish:

$$\mathbb{F}^{\text{int}}(\mathbb{X}, \mathbb{V}) + \mathbb{F}^{\text{conv}}(\mathbb{X}, \mathbb{V}) - \mathbb{F}^{\text{surf}}(\mathbb{S}, \mathbb{X}) = \mathbb{R} = \mathbb{O}. \quad (4.57)$$

The goal of the equation solving is to find the global unknown vector  $\mathbb{X}$ . Two methods are considered in turn, the generalised trapezoidal method and the iterative predictor corrector method. Henceforth, a time starting from  $t_0$  is adopted. At this starting point  $t = t_0$  the unknown vector is known and is denoted by  $\mathbb{X}_0$ . Between the two calculation

steps  $n$  and  $n + 1$ , the time-step is defined by  $\Delta t = t_{n+1} - t_n$  and is assumed to be independent of  $n$  for the time being.

### 4.3.1 The generalised trapezoidal method

The generalised trapezoidal method is a well known one-step algorithm, commonly use to solve parabolic problems such as the heat equation (Hughes, 1987a, p. 459). The exact solution is found for non-transient infinite equilibrium problems only.

Algorithms belonging to generalised trapezoidal family methods can be represented by the following set of equations:

$$\begin{aligned} \mathbb{D} \mathbb{V}_{n+1} + \mathbb{K} \mathbb{X}_{n+1} + \mathbb{C}_{\text{conv}} \mathbb{X}_{n+1} &= \mathbb{F}_{n+1}, \\ \mathbb{X}_{n+1} &= \mathbb{X}_n + \Delta t \mathbb{V}_{n+\alpha}, \\ \mathbb{V}_{n+\alpha} &= (1 - \alpha) \mathbb{V}_n + \alpha \mathbb{V}_{n+1}, \end{aligned} \tag{4.58}$$

where  $\mathbb{X}_n$  and  $\mathbb{V}_n$  are the approximations to  $\mathbb{X}(t_n)$  and  $\mathbb{V}(t_n)$ , respectively,  $\mathbb{F}_{n+1} = \mathbb{F}(t_{n+1})$  and  $\alpha$  is a parameter taken to be in the interval  $[0,1]$ . Some well-known numbers of the generalised trapezoidal family are identified in Table 4.2.

$\alpha$	Method
0	Forward differences; forward Euler
1/2	Trapezoidal rule; midpoint rule; Crank-Nicolson
1	Backward differences, backward Euler

Table 4.2: Typical numbers of the generalised trapezoidal methods.

To appreciate the computations entailed by the algorithm, a brief overview of the implementational considerations is presented next. The V-form implementation is analysed here. The computational problem is to calculate  $\mathbb{X}_{n+1}$  and  $\mathbb{V}_{n+1}$  given  $\mathbb{X}_n$  and  $\mathbb{V}_n$ . The procedure starts at  $t_0$  with  $\mathbb{X}_0$  and  $\mathbb{V}_0$  known. Note that  $\mathbb{V}_0$  is calculated from equation (4.56):  $\mathbb{D} \mathbb{V}_0 = \mathbb{F}_0 - \mathbb{K} \mathbb{X}_0 - \mathbb{C}_{\text{conv}} \mathbb{X}_0$ .

The *predictor value* of  $\mathbb{X}_{n+1}$  is defined by,

$$\tilde{\mathbb{X}}_{n+1} = \mathbb{X}_n + (1 - \alpha) \Delta t \mathbb{V}_n. \tag{4.59}$$

From equation (4.58), the second and the third lines are combined to obtain,

$$\mathbb{X}_{n+1} = \tilde{\mathbb{X}}_{n+1} + \alpha \Delta t \mathbb{V}_{n+1}. \quad (4.60)$$

Substituting equation (4.60) into (4.58)<sub>1</sub> results into the following equation,

$$(\mathbb{D} + \alpha \Delta t \mathbb{K} + \alpha \Delta t \mathbb{C}_{\text{conv}}) \mathbb{V}_{n+1} = \mathbb{F}_{n+1} - \mathbb{K} \tilde{\mathbb{X}}_{n+1} - \mathbb{C}_{\text{conv}} \tilde{\mathbb{X}}_{n+1}. \quad (4.61)$$

Equation (4.61) may be solved for  $\mathbb{V}_{n+1}$ . Note that the terms on the right-hand-side are known. Once  $\mathbb{V}_{n+1}$  is found,  $\mathbb{X}_{n+1}$  may be calculated thanks to eq. (4.60).

**Remark 4.1.** *In the case of  $\alpha = 0$  the method is said to be explicit. The advantage of this particular case may be seen from equation (4.61): if  $\mathbb{D}$  is diagonal, the solution may be advanced without necessity of equation solving.*

*If  $\alpha \neq 0$ , the method is said to be implicit. In these cases, a system of equations with the coefficient matrix  $(\mathbb{D} + \alpha \Delta t \mathbb{K} + \alpha \Delta t \mathbb{C}_{\text{conv}})$  needs to be solved at each time step to advance the solution.*

### 4.3.2 Predictor multi-corrector algorithms with operator split

More advanced than the general trapezoidal method, the *iterative predictor-corrector* or the *predictor multi-corrector method* is instrumental to calculate the transient response of a time-dependent problem. With these algorithms, several iterations are needed to obtain the correct unknown vector response  $\mathbb{X}_{n+1}$ . In contrast with the general trapezoidal method, the predictor multi-corrector response provides the exact solution at each time step of the problem, if the time step is small enough.

The semi-discretised equations are integrated through a generalised trapezoidal scheme defined by a scalar  $\alpha \in [0, 1]$ . At step  $n + 1$ , the equations are enforced at time  $t_{n+\alpha} = t_n + \alpha \Delta t$ , with  $\Delta t = t_{n+1} - t_n$ , namely,

$$\mathbb{R}_{n+\alpha} = \mathbb{F}^{\text{int}}(\mathbb{X}_{n+\alpha}, \mathbb{V}_{n+\alpha}) + \mathbb{F}^{\text{conv}}(\mathbb{X}_{n+\alpha}, \mathbb{V}_{n+\alpha}) - \mathbb{F}^{\text{surf}}(\mathbb{S}_{n+\alpha}, \mathbb{X}_{n+\alpha}) = \mathbb{O}. \quad (4.62)$$

First, the system to be solved needs to be identified. To do so, the implicit part needs to be segregated from the explicit one. Second, the predictor multi-corrector algorithm for the calculation of the step  $n + 1$  is presented.

### 4.3.2.1 The equation to be solved

Between the iterations  $i$  and  $i + 1$ , the system of equations is solved for the step  $n + 1$ . Before presenting the algorithm, the set of the equations to be solved is subjected to an explicit/implicit partitioning. The iteration  $i$  being known is called *explicit*, denoted by the subscript  $\mathbf{E}$  and the iteration  $i + 1$  being unknown, is called *implicit*, denoted by the subscript  $\mathbf{I}$ . Note that the notion of explicit/implicit partitioning is more general than the known/unknown identification: it accounts for the idea of being active for the implicit part and passive for the explicit part. Active in the sense that implicit terms contribute in the calculation of the effective diffusion matrix.

Two cases arise, when considering the convective contributions, which can be either (1) implicit or (2) explicit. Quite generally, the stability properties of an implicit scheme are stronger than for an explicit scheme.

(1) If the convective forces are considered implicit, one may write,

$$\mathbb{R}_{n+\alpha}^{i+1} = \mathbb{F}_{\mathbf{I}}^{\text{int}}(\mathbb{X}_{n+\alpha}^{i+1}, \mathbb{V}_{n+\alpha}^{i+1}) + \mathbb{F}_{\mathbf{I}}^{\text{conv}}(\mathbb{X}_{n+\alpha}^{i+1}, \mathbb{V}_{n+\alpha}^{i+1}) - \mathbb{F}_{\mathbf{E}}^{\text{surf}}(\mathbb{S}_{n+\alpha}^i, \mathbb{X}_{n+\alpha}^i) = \mathbb{O}. \quad (4.63)$$

The partitioning shown in the above equation is motivated by the following observations:

- the dependence of the vector of external forces on the solution is weak;
- the vector of internal forces and the vector of convective forces depend linearly on the rate vector  $\mathbb{V}$  and on the solution  $\mathbb{X}$ ;
- a non-linearity is observed due to temperature-dependent coefficients.

In the above relation, for  $\mathbb{Z} = \mathbb{X}$  and  $\mathbb{V}$ ,  $\mathbb{Z}_{n+\alpha}^{i+1}$  is defined by,

$$\mathbb{Z}_{n+\alpha}^{i+1} = (1 - \alpha) \mathbb{Z}_n + \alpha \mathbb{Z}_{n+1}^{i+1}. \quad (4.64)$$

The *predictor value* of  $\mathbb{X}_{n+\alpha}^i$  is defined by,

$$i \geq 0 \quad : \quad \tilde{\mathbb{X}}_{n+1}^i = \mathbb{X}_{n+1}^0 + \alpha \Delta t \mathbb{V}_{n+1}^i \quad (= \mathbb{X}_{n+1}^i \quad \text{for } i > 0). \quad (4.65)$$



Note that  $\tilde{\mathbb{X}}_{n+1}^i$  is a known value at iteration  $i$ . The iterative relation between  $i$  and  $i + 1$  is defined as follows,

$$\begin{aligned} \text{initialisation} & \begin{cases} \mathbb{X}_{n+1}^0 &= \mathbb{X}_n + (1 - \alpha)\Delta t \mathbb{V}_n, \\ \mathbb{V}_{n+1}^0 &= \mathbb{V}_n, \end{cases} \\ \text{for } i \geq 0 & \begin{cases} \mathbb{X}_{n+1}^{i+1} &= \mathbb{X}_n + \Delta t \mathbb{V}_{n+\alpha}^{i+1} = \mathbb{X}_{n+1}^0 + \alpha \Delta t \mathbb{V}_{n+1}^{i+1}, \\ &= \tilde{\mathbb{X}}_{n+1}^i + \alpha \Delta t \Delta \mathbb{V}, \\ \mathbb{V}_{n+1}^{i+1} &= \mathbb{V}_{n+1}^i + \Delta \mathbb{V}. \end{cases} \end{aligned} \quad (4.66)$$

To simplify the writing, the notation  $\mathbb{F}^{\text{int+conv}} = \mathbb{F}^{\text{int}} + \mathbb{F}^{\text{conv}}$  is henceforth adopted, since they are both implicit. Hence, equation (4.63) is modified and linearised to obtain the equation to be solved,

$$\begin{aligned} \mathbb{R}_{n+\alpha}^{i+1} &= -\mathbb{F}_{\mathbf{E}}^{\text{surf}}(\mathbb{S}^i, \mathbb{X}_{n+\alpha}^i) + \mathbb{F}_{\mathbf{I}}^{\text{int+conv}}((1 - \alpha)\mathbb{X}_n + \alpha \mathbb{X}_{n+1}^{i+1}, (1 - \alpha)\mathbb{V}_n + \alpha \mathbb{V}_{n+1}^{i+1}) \\ &= -\mathbb{F}_{\mathbf{E}}^{\text{surf}}(\mathbb{S}^i, \mathbb{X}_{n+\alpha}^i) \\ &+ \mathbb{F}_{\mathbf{I}}^{\text{int+conv}}((1 - \alpha)\mathbb{X}_n + \alpha \tilde{\mathbb{X}}_{n+1}^i + \alpha^2 \Delta t \Delta \mathbb{V}, (1 - \alpha)\mathbb{V}_n + \alpha(\mathbb{V}_{n+1}^i + \Delta \mathbb{V})) \\ &\approx -\mathbb{F}_{\mathbf{E}}^{\text{surf}}(\mathbb{S}^i, \mathbb{X}_{n+\alpha}^i) + \mathbb{F}_{\mathbf{I}}^{\text{int+conv}}((1 - \alpha)\mathbb{X}_n + \alpha \tilde{\mathbb{X}}_{n+1}^i, (1 - \alpha)\mathbb{V}_n + \alpha \mathbb{V}_{n+1}^i) \\ &+ \left( \frac{\partial \mathbb{F}_{\mathbf{I}}^{\text{int+conv}}}{\partial \mathbb{X}} \right) ((1 - \alpha)\mathbb{X}_n + \alpha \tilde{\mathbb{X}}_{n+1}^i, (1 - \alpha)\mathbb{V}_n + \alpha \mathbb{V}_{n+1}^i) \alpha^2 \Delta t \Delta \mathbb{V} \\ &+ \left( \frac{\partial \mathbb{F}_{\mathbf{I}}^{\text{int+conv}}}{\partial \mathbb{V}} \right) ((1 - \alpha)\mathbb{X}_n + \alpha \tilde{\mathbb{X}}_{n+1}^i, (1 - \alpha)\mathbb{V}_n + \alpha \mathbb{V}_{n+1}^i) \alpha \Delta \mathbb{V} \\ &\approx -\mathbb{F}_{\mathbf{E}}^{\text{surf}}(\mathbb{S}_{n+\alpha}^i, \mathbb{X}_{n+\alpha}^i) + \mathbb{F}_{\mathbf{I}}^{\text{int+conv}}(\tilde{\mathbb{X}}_{n+\alpha}^i, \mathbb{V}_{n+\alpha}^i) + ([\mathbb{K} + \mathbb{C}]\alpha \Delta t + \mathbb{D})\alpha \Delta \mathbb{V} \\ &\approx \quad \quad \quad -\mathbb{R}_{n+\alpha}^i \quad \quad \quad + \quad \quad \quad \mathbb{C}^* \quad \quad \quad \alpha \Delta \mathbb{V}. \end{aligned} \quad (4.67)$$

Note that the Newton direction  $\Delta \mathbb{V}$  at iteration  $i \geq 0$ , equation (4.67)<sub>2</sub>, is obtained by insertion of the time integrator (4.66) in the residual (4.67)<sub>1</sub>. Finally, when the residual  $\mathbb{R}_{n+\alpha}^{i+1}$  is forced to vanish, the following equation is solved at each iteration,

$$\mathbb{C}^*(\alpha \Delta \mathbb{V}) = \mathbb{R}_{n+\alpha}^i, \quad (4.68)$$

in which *the effective convection-diffusion matrix*  $\mathbb{C}^*$  is expressed in terms of the diffusion matrix  $\mathbb{D}$ , the stiffness matrix  $\mathbb{K}$  and the convective matrix  $\mathbb{C}_{\text{conv}}$ ,

$$\mathbb{C}^* = \underbrace{\left( \frac{\partial \mathbb{F}_{\mathbf{I}}^{\text{int+conv}}}{\partial \mathbb{V}} \right) (\tilde{\mathbb{X}}_{n+\alpha}^i)}_{\mathbb{D}} + \underbrace{\left( \frac{\partial \mathbb{F}_{\mathbf{I}}^{\text{int+conv}}}{\partial \mathbb{X}} \right) (\tilde{\mathbb{X}}_{n+\alpha}^i)}_{\mathbb{K} + \mathbb{C}_{\text{conv}}} \alpha \Delta t, \quad (4.69)$$

where it has been recognised that the derivatives of  $\mathbb{F}_{\mathbf{I}}^{\text{int+conv}}$  do not depend on the rate vector  $\mathbb{V}$ . Note that when the convective terms are considered implicit, they appear in both the calculation of the effective convection-diffusion matrix  $\mathbb{C}^*$  and in the calculation of the residual.  $\mathbb{R}_{n+\alpha}^i$ .

(2) If the convective forces are considered explicit, one may write,

$$\mathbb{R}_{n+\alpha}^{i+1} = \mathbb{F}_{\mathbf{I}}^{\text{int}} (\mathbb{X}_{n+\alpha}^{i+1}, \mathbb{V}_{n+\alpha}^{i+1}) + \mathbb{F}_{\mathbf{E}}^{\text{conv}} (\mathbb{X}_{n+\alpha}^i, \mathbb{V}_{n+\alpha}^i) - \mathbb{F}_{\mathbf{E}}^{\text{surf}} (\mathbb{S}_{n+\alpha}^i, \mathbb{X}_{n+\alpha}^i) = 0. \quad (4.70)$$

To simplify the writing, the notation  $-\mathbb{F}^{\text{surf+conv}} = -\mathbb{F}^{\text{surf}} + \mathbb{F}^{\text{conv}}$  is henceforth adopted, since they are both explicit. This time, equation (4.63) is modified and linearised to obtain,

$$\begin{aligned} \mathbb{R}_{n+\alpha}^{i+1} &\approx -\mathbb{F}_{\mathbf{E}}^{\text{surf+conv}} (\mathbb{S}_{n+\alpha}^i, \mathbb{X}_{n+\alpha}^i, \mathbb{V}_{n+\alpha}^i) + \mathbb{F}_{\mathbf{I}}^{\text{int}} (\tilde{\mathbb{X}}_{n+\alpha}^i, \mathbb{V}_{n+\alpha}^i) - (\mathbb{K} \alpha \Delta t + \mathbb{D}) \alpha \Delta \mathbb{V}, \\ &\approx -\mathbb{R}_{n+\alpha}^i + \mathbb{C}^* \alpha \Delta \mathbb{V}. \end{aligned} \quad (4.71)$$

Finally, when the residual  $\mathbb{R}_{n+\alpha}^{i+1}$  is forced to vanish, the equation to be solved has the same form as equation (4.68). However, this time *the effective diffusion matrix*  $\mathbb{C}^*$  is expressed in terms of the diffusion matrix  $\mathbb{D}$  and of the stiffness matrix  $\mathbb{K}$  and is *independent of the convective matrix*  $\mathbb{C}$ ,

$$\mathbb{C}^* = \underbrace{\left( \frac{\partial \mathbb{F}_{\mathbf{I}}^{\text{int}}}{\partial \mathbb{V}} \right) (\tilde{\mathbb{X}}_{n+\alpha}^i)}_{\mathbb{D}} + \underbrace{\left( \frac{\partial \mathbb{F}_{\mathbf{I}}^{\text{int}}}{\partial \mathbb{X}} \right) (\tilde{\mathbb{X}}_{n+\alpha}^i)}_{\mathbb{K}} \alpha \Delta t. \quad (4.72)$$

The convective terms are confined to the residual vector,

$$\mathbb{R}_{n+\alpha}^i = \mathbb{F}_{\mathbf{E}}^{\text{surf+conv}} (\mathbb{S}_{n+\alpha}^i, \mathbb{X}_{n+\alpha}^i, \mathbb{V}_{n+\alpha}^i) - \mathbb{F}_{\mathbf{I}}^{\text{int}} (\tilde{\mathbb{X}}_{n+\alpha}^i, \mathbb{V}_{n+\alpha}^i). \quad (4.73)$$

Now that the set of equations to be solved is identified, its numerical implementation is presented through the predictor multi-corrector algorithm.

### 4.3.2.2 Algorithm of the predictor multi-corrector method

Algorithms of the predictor multi-corrector family method can be represented by the following equations: at the calculation step  $n + 1$ , the procedure is,

$$\begin{array}{l}
 1. \quad i = 0 \\
 \left. \begin{array}{l} \mathbb{X}_{n+1}^0 = \mathbb{X}_n + (1 - \alpha)\Delta t \mathbb{V}_n \\ \mathbb{V}_{n+1}^0 = \mathbb{V}_n \end{array} \right\} \text{initialisation,} \\
 2. \quad \mathbb{C}^* (\alpha \Delta \mathbb{V}) = \mathbb{R}_{n+\alpha}^i \quad \rightarrow \quad \Delta \mathbb{V}, \\
 \left. \begin{array}{l} \mathbb{X}_{n+1}^{i+1} = \tilde{\mathbb{X}}_{n+1}^i + \alpha \Delta t \Delta \mathbb{V} \\ \mathbb{X}_{n+1}^{i+1} = \mathbb{X}_{n+1}^0 + \alpha \Delta t \mathbb{V}_{n+1}^{i+1} \\ \mathbb{V}_{n+1}^{i+1} = \mathbb{V}_{n+1}^i + \Delta \mathbb{V} \end{array} \right\} \text{corrector,} \\
 3. \\
 4. \quad \text{If } |\text{left-hand-side}| \leq \delta \mathbb{X} \quad \text{and/or} \quad |\text{right-hand-side}| \leq \delta \mathbb{R} \quad \text{then goto 5,} \\
 \quad \text{Else } \quad i = i + 1 \quad \text{and goto 2,} \\
 5. \quad \text{End.}
 \end{array} \tag{4.74}$$

and where  $\delta \mathbb{X}$  and  $\delta \mathbb{R}$  are tolerances associated to the unknown vector and to the residual, respectively. Iterations are stopped when criteria involving both the unknown and the residual are satisfied, which corresponds to step 4. of the algorithm.

Additional information on stability, convergence and accuracy can be found in Hughes (1987a) and Belytschko and Hughes (1983).

## Chapter 5

# Preliminary numerical results

The complete set of explicit field equations, derived in Chapter 2, has been developed through a finite element formulation scheme in Chapter 4. The implementation of the thermo-hydro-mechanical model was added to a previous hydro-mechanical code. The validation of the hydro-mechanical part was performed by Khalili-Naghadeh (1991). The aim of this chapter is to compare the numerical response with analytical results so as to validate the correct implementation of the thermal contributions in the fully coupled thermo-hydro-mechanical model. The influence of convection and local thermal non-equilibrium are disregarded in this work. Their contributions will be analysed in Chapters 7 and 8. Furthermore, only single porous media are considered. The solid phase is endowed with the subscript  $s$  and the fluid phase with the subscript  $p$ .

In Section 5.1, analytical solutions of two transient conduction problems are compared with numerical responses. The mechanical and the hydraulic contributions to the balance of energy equations are disregarded. Correlatively, the balance of momentum for the mixture and the balances of mass of the fluids are not addressed. The numerical model reproduces well the analytical responses for both the solid phase and the fluid phases, which validates the implementation of Fourier's law.

In Section 5.2, the closed form solutions of a partially coupled thermo-hydro-mechanical model proposed by McTigue (1986) are compared with finite element responses. A good match is obtained between the analytical solutions and the numerical responses for all types of loading which validates further the implementation of the thermal contribution. Furthermore, comprehensive information on the diffusion behaviour of thermo-hydro-mechanical mixtures has been observed: the dominance of the hydraulic diffusion on the thermal diffusion, characterised by the diffusivity ratio  $R$ , influences significantly the pore pressure response.

In Section 5.3, an axi-symmetric boundary value problem is analysed in an uncoupled

mechanical context. The errors on the displacement, the strain and the stress in the vicinity of the inner radius are plotted and a logarithmic optimisation of the mesh is proposed to minimise these errors.

Simulations of thermo-hydro-mechanical processes in Chapter 6 which involve coupled diffusion flows within an axi-symmetric analysis will capitalise upon the lessons learned in the elementary instances here.

As a convention, in all the following figures, the plain curves will represent the numerical responses, and the dash curves will represent the analytical responses.

## 5.1 Validation of transient conduction tests

Analytical solutions of transient conduction problems are compared with numerical responses. Two types of thermal loadings are analysed: (1) a constant thermal flux and (2) an imposed temperature. Both loading conditions are applied to the same one-dimensional problem.

### 5.1.1 A one-dimensional application

Transient conduction in a one-dimensional homogeneous body  $k$  is considered alone (uncoupled),

$$\frac{\partial^2 T_k}{\partial x^2} = \frac{1}{\alpha_{T,k}} \frac{\partial T_k}{\partial t}, \quad (5.1)$$

in which  $\alpha_{T,k}$  is the thermal diffusivity defined in eq. (5.3). All numerical tests are done on a vertical column of height  $H = 3$  m. Each one-dimensional sample is composed of a unique phase  $k$  so that  $n_k = 1$ . The vertical column is heated at the bottom ( $x = 0$  m) and maintained at initial temperature  $T_{\text{ini}}$  at the top ( $x = 3$  m). The initial temperature repartition is assumed to be homogeneous and equal to  $T_{\text{ini}}$ . Two types of loadings at the bottom ( $x = 0$  m) are scrutinised; a constant heat flux  $q_k$  loading and an imposed temperature  $T_\infty$ . Each of them is considered in turn.

In addition, the numerical code is tested for two materials; a solid and a fluid which material parameters are presented in Table 5.2. The solid phase is endowed with the subscript  $s$  and the fluid phase with the subscript  $p$ .

The thermal diffusion *characteristic time* is reached when the temperature has ‘penetrated’ through the transversal dimension of the body. This characteristic time is needed

Parameter	Value	Unit
Initial temperature $T_{\text{ini}}$	288	K
Imposed temperature $T_{\infty}$	338	K
Solid heat flux $q_s$	45	W/m <sup>2</sup>
Fluid heat flux $q_p$	9.166	W/m <sup>2</sup>

Table 5.1: Loading and boundary conditions.

to know the time window of the numerical calculation. It is analogous to the consolidation time. For an object of length  $H$ , Bejan (1993, p. 146) defines the characteristic time which distinguishes the early regime from the late regime,

$$t_{k,\text{diff}} = \frac{H^2}{\alpha_{T,k}}, \quad k = s, p, \quad (5.2)$$

where  $\alpha_{T,k}$  is the thermal diffusivity of the phase  $k$ ,

$$\alpha_{T,k} = \frac{\Lambda_k}{\rho_k C_{k,p}}, \quad k = s, p. \quad (5.3)$$

Note that the thermal diffusivity of the solid phase is one order of magnitude higher than that of the fluid phase (Table 5.2). Hence, for the same length  $H$ , the characteristic time of the solid phase is smaller than that of the fluid phase. In other words, the solid phase will reach steady state faster than the fluid phase.

### 5.1.2 Constant heat flux loading

A closed form solution of transient thermal diffusion of an homogeneous phase  $k$  is compared with the numerical output for the particular case of a constant heat flux loading.

#### 5.1.2.1 Analytical solution for a finite sample

The analytical result of a slab with prescribed heat flux  $q_k$  at its surface  $x = H$  and kept at the initial temperature  $T_{\text{ini}}$  at  $x = 0$ , is given by Carslaw and Jaeger (1959, p. 113),

$$T_k(x, t) - T_{\text{ini}} = \frac{q_k x}{\Lambda_k} - \frac{8 q_k H}{\Lambda_k \pi^2} \sum_{n=0}^{\infty} \frac{(-1)^n}{(2n+1)^2} \exp \frac{-\alpha_{T,k}(2n+1)^2 \pi^2 t}{4H^2} \sin \frac{(2n+1)\pi x}{2H}, \quad (5.4)$$

Parameter	Value	Unit
Solid specific heat capacity $C_{s,p}$	800	J/kg.K
Solid density $\rho_s$	2700	kg/m <sup>3</sup>
Solid thermal conductivity $\Lambda_s$	2.7	W/m.K
Solid thermal diffusivity $\alpha_{T,s}$	$1.25 \cdot 10^{-6}$	m <sup>2</sup> /s
Characteristic diffusion time $t_{s,diff}$	$7.2 \times 10^6$	s
	2.69	months
Fluid specific heat capacity $C_{p,p}$	4182	J/kg.K
Fluid density $\rho_p$	999.8	kg/m <sup>3</sup>
Fluid thermal conductivity $\Lambda_p$	0.588	W/m.K
Fluid thermal diffusivity $\alpha_{T,p}$	$1.41 \cdot 10^{-7}$	m <sup>2</sup> /s
Characteristic diffusion time $t_{k,diff}$	$6.4 \times 10^7$	s
	23.9	months

Table 5.2: Solid and fluid parameters, representative of granite and water, respectively, at 25°C and atmospheric pressure. The thermal diffusivities are defined in eq. (5.3). The characteristic diffusion times are calculated with eq. (5.2) and  $H = 3$  m.

for  $0 < x < H$ . Note that no significant change occurs in the calculation of the Taylor series after the summation of 40 terms. This result is restricted to a constant initial temperature repartition over the slab. At the boundaries of time and space eq. (5.4) reduces to,

$$\begin{aligned}
 T_k(x, t) - T_{ini} &= \frac{q_k x}{\Lambda_k} & \text{for } t \rightarrow \infty, \\
 T_k(x, t) - T_{ini} &= 0 & \text{for } x = 0.
 \end{aligned}
 \tag{5.5}$$

For the record, the transition time which corresponds to the two third of the steady conduction limit is,

$$t_{k,diff}^{2/3} = \frac{4H^2}{\alpha_{T,k}\pi^2}, \quad \text{for } T_k(x, t) - T_{ini} = \frac{2}{3} \frac{q_k x}{\Lambda_k}.
 \tag{5.6}$$

### 5.1.2.2 Numerical results

The first test is subjected to a constant heat flux loading. The initial temperature of the vertical column is homogeneous  $T_k(x, t = 0) = T_{ini}$ . A constant heat flux equal to  $q(x = 0, t) = q_k$  is applied on the bottom of a solid column. The top temperature is assumed to remain constant at the initial temperature  $T_k(x = H, t) = T_{ini}$ . The height of the column is equal to  $H = 3$  m.

The solid phase and the fluid phase are considered in turn. History profiles of the solid temperature compare Carslaw's analytical equation, eq. (5.4), with the numerical response (Figure 5.1). A good match is obtained.

The diffusion 'penetration' can be represented by the vertical distribution of the solid temperature in the column, (Figure 5.2) and by contour plots of the whole column at different times (Figure 5.3). Note that for the steady conduction state, the temperature distribution is linear through out the column. This result was expected due to equation (5.5)<sub>1</sub>.

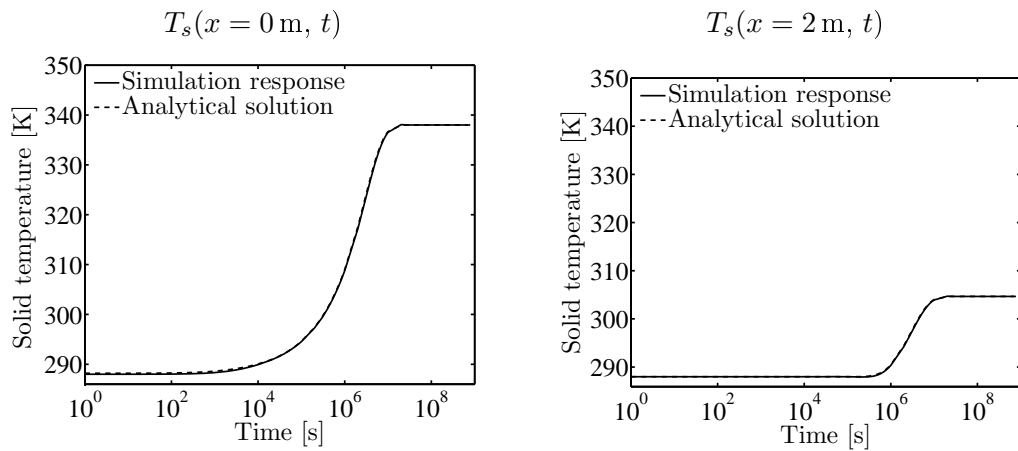


Figure 5.1: Solid temperature  $T_s$  history at (left)  $x = 0$  m and (right)  $x = 2$  m. Comparison between Carslaw's analytical solution eq. (5.4) and the finite element response. The column is composed of an homogeneous solid phase such as  $n_s = 1$  and  $\alpha_{T,s} = 1.25 \times 10^{-6} \text{ m}^2/\text{s}$ .

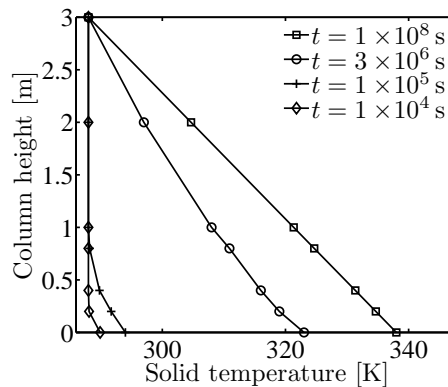


Figure 5.2: Profile of the solid temperature in the slab for four different times. A constant heat flux is applied at  $x = 0$  m and the initial temperature is imposed at  $x = 3$  m. The column is composed of a single solid phase such as  $n_s = 1$  and  $\alpha_{T,s} = 1.25 \times 10^{-6} \text{ m}^2/\text{s}$ .

Transient conduction under constant heat flux loading is also plotted for the fluid phase



(Figure 5.4). The rate of diffusion is different due to a different thermal diffusion value  $\alpha_{T,p}$ . Again a good match between the analytical solution and the finite element response is obtained.

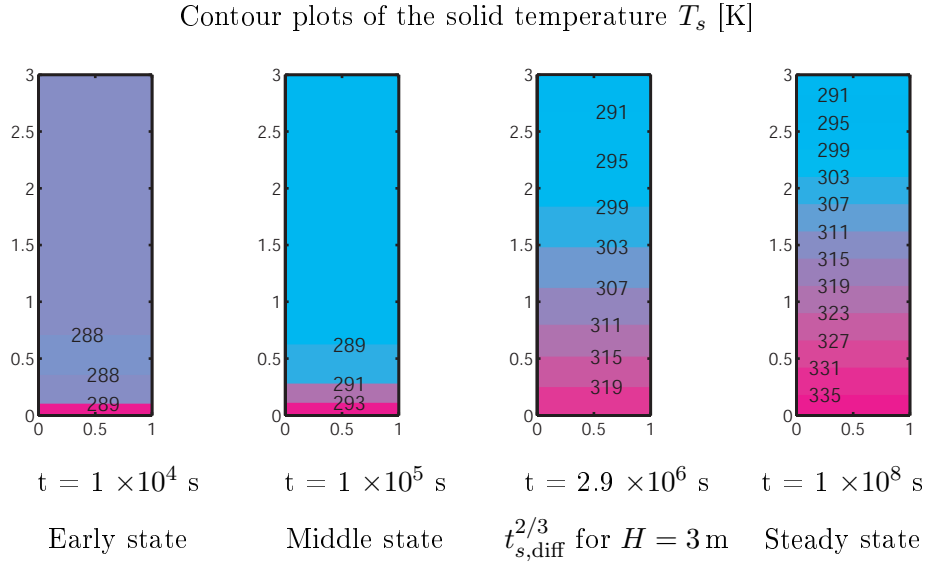


Figure 5.3: Contour representation at four different times of a column of solid under a constant heat flux applied at  $x = 0$  m and at initial temperature at  $x = 3$  m. The column is composed of a single solid phase such as  $n_s = 1$  and  $\alpha_{T,s} = 1.25 \times 10^{-6}$  m<sup>2</sup>/s.

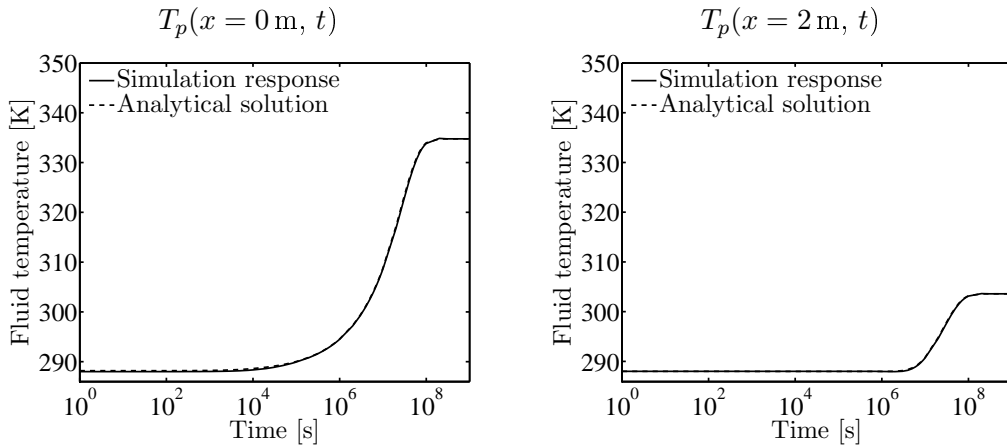


Figure 5.4: Same as Figure 5.1 for the fluid temperature  $T_p$ .

### 5.1.3 Fixed temperature loading

A closed form solution of transient thermal diffusion of an homogeneous phase  $k$  is compared with the numerical output for the particular case of a temperature loading.

### 5.1.3.1 Analytical solution for a finite sample

Carslaw and Jaeger (1959, p. 99-100) proposed an analytical formulation of a finite slab at initial temperature  $T_{\text{ini}}$ , the ends being at constant temperatures. For a region  $0 < x < H$  and in the case in which the end  $x = 0$  m is kept at constant temperature  $T_1$  and the end  $x = H$  m is kept at  $T_2$ , the temperature of the phase  $k$  writes,

$$T_k(x, t) - T_i = v_1 + (v_2 - v_1) \frac{x}{H} + \frac{2}{\pi} \sum_{n=1}^{\infty} \frac{v_2 \cos n\pi - v_1}{n} \sin \frac{n\pi x}{H} \exp \frac{-\alpha_{T,k} n^2 \pi^2 t}{H^2} + \frac{2}{H} \sum_{n=1}^{\infty} \sin \frac{n\pi x}{H} \exp \frac{-\alpha_{T,k} n^2 \pi^2 t}{H^2} \int_0^H T_{\text{ini}} \sin \frac{n\pi x'}{H} dx', \quad (5.7)$$

where  $v_1 = T_1 - T_{\text{ini}}$  and  $v_2 = T_2 - T_{\text{ini}}$ . Note that no significant change occurs in the calculation of the Taylor series after the summation of 10 terms. At the boundaries of time and space eq. (5.7) reduces to,

$$T(x, t) - T_{\text{ini}} = v_1 + (v_2 - v_1) \frac{x}{H} \quad \text{for} \quad t \rightarrow \infty, \quad (5.8)$$

$$T(x, t) - T_{\text{ini}} = v_1 \quad \text{for} \quad x = 0. \quad (5.9)$$

Similarly to the heat flux problem, the characteristic time which corresponds to the two third of the steady conduction limit is identified,

$$t_{k,\text{diff}}^{2/3} = \frac{H^2}{\alpha \pi^2}, \quad \text{for} \quad T(x, t) - T_{\text{ini}} = \frac{2}{3} \left[ v_1 + (v_2 - v_1) \frac{x}{H} \right]. \quad (5.10)$$

The comparison between the analytical response of the temperature history for a column subjected to a constant heat flux, with that subjected to a constant temperature, based on equations (5.6) and (5.10), reveals that the characteristic time  $t_{k,\text{diff}}^{2/3}$  for a given heat flux is four times larger than that for a fixed temperature. This result should be kept in mind when comparing results of different load types.

### 5.1.3.2 Numerical results

In the second test, the finite slab is subjected to a *constant temperature* loading. The initial temperature of the vertical column is homogeneous  $T_k(x, t = 0) = T_{\text{ini}}$ . A constant temperature equal to  $T_k(x = 0, t) = T_{\infty}$  is applied on the bottom side of a solid column (Table 5.1). The top temperature is assumed to remain constant at the initial temperature  $T_k(x = H, t) = T_{\text{ini}}$ . The height of the column is equal to  $H = 3$  m.

The analytical solution given by Carslaw and Jaeger (1959) in equation (5.7) is compared with the numerical result in Figure 5.5, for the solid material. The numerical model reproduces well the analytical response in spite of the Heaviside step function used to apply temperature loading (increase of 2 K per  $10^3$  s). A good match is also obtained for the fluid phase (not shown).

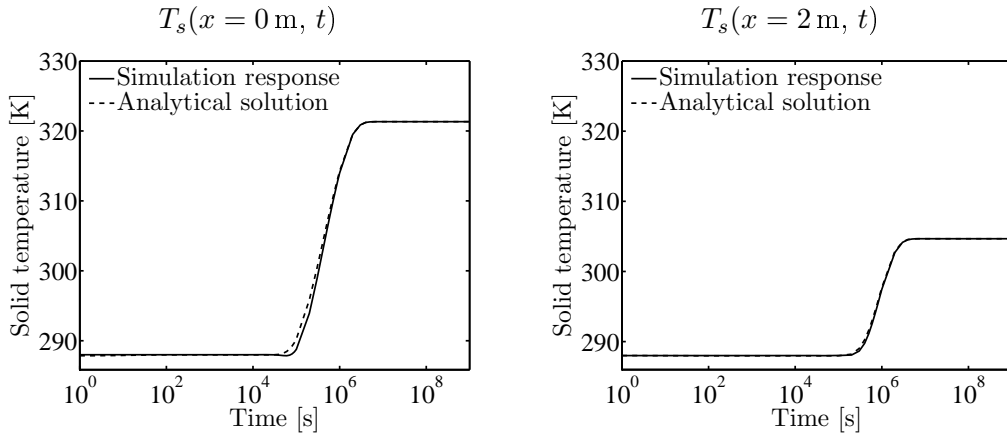


Figure 5.5: Solid temperature  $T_s$  history at (left)  $x = 0$  m and (right)  $x = 2$  m. Comparison between Carslaw’s analytical solution eq. (5.7) and the finite element response. The column is composed of an homogeneous solid phase such as  $n_s = 1$  and  $\alpha_{T,s} = 1.25 \times 10^{-6}$  m<sup>2</sup>/s.

The minimum mesh size from which no significant better results are obtained is 2 elements per meter. Note that a ‘heavy’ refinement is necessary for the temperature function loading between the loading surface and the observed nodes to avoid the disturbance induced by the ‘thermal shock’. Alternatively, the time scheme can be modified with various time-stepping algorithms to artificially damped the disturbance to an acceptable level (Wood and Lewis, 1975).

The implementation of the conduction transient law has been validated throughout this section; the numerical responses provide a good approximation of the analytical results for both types of loadings.

## 5.2 Thermo-Hydro-Mechanical tests: thermal loading

Analytical results provided by McTigue (1986) are compared with numerical responses so as to validate the correct implementation of the thermal contributions in the coupled thermo-hydro-mechanical model. This work focuses on thermo-hydro-mechanical tests induced by thermal loading. Two types of thermal loadings are investigated; in addition to two types of hydraulic boundary conditions. Altogether, four types of tests are performed as presented in Table 5.3.

1. Constant temperature i. Drained boundary	2. Constant heat flux i. Drained boundary
1. Constant temperature ii. Undrained boundary	2. Constant heat flux ii. Undrained boundary

Table 5.3: A combination of four boundary conditions is proposed by McTigue (1986).

This analysis is restricted to a partially coupled thermo-hydro-mechanical model in local thermal equilibrium (Subsection 5.2.1) and is then applied to a one-dimensional setting (Subsection 5.2.2). Next, the analytical formulations of the four loading cases (Table 5.3) are reproduced from McTigue (1986). The validity of the finite element code is then verified by comparison with the foregoing analytical solutions. Finally, the importance of the diffusivity ratio  $R$  is highlighted.

### 5.2.1 A partially coupled THM model in local thermal equilibrium

First, it is worth to reiterate that the THM model considered henceforth is assumed to be in local thermal equilibrium, i.e.  $T_s = T_p = T_f$ . Equations (2.322), (2.323) and (2.324) are added to form only one balance of energy equation for the mixture as a whole.

Four main differences can be identified between the thermoelastic model proposed by McTigue (1986) and the fully coupled model presented in Subsection 2.4. These differences are discussed in detail in Appendix C and are summarised below to facilitate the global understanding.

1. McTigue (1986) proposed a fully coupled thermo-elastic constitutive law, for a single porous medium, in thermal equilibrium. Our comprehensive model can easily be restricted to his proposition by assuming  $n_f = 0$ , see Remark 2.12, p. 115.

2. In addition, the diffusion constitutive equations presented by McTigue (1986) are uncoupled; that is the thermo-osmosis effect and the thermal filtration effect are not accounted for here.
3. Moreover, McTigue (1986) simplifies his model so that the energy equation is uncoupled from the mechanics. Furthermore, he neglects the convection terms  $\mathbf{M}_p \cdot \nabla H_p$  and  $\mathbf{M}_f \cdot \nabla H_f$  in the energy equation.
4. Finally, McTigue (1986) introduces distinctions between two bulk moduli and two expansion coefficients characterizing the solid. Such distinctions are usually ascribed to the presence of unconnected porosity. However, unconnected porosity are disregarded in this Chapter. Hence, the two bulk moduli,  $K'_s$  and  $K''_s$ , and the two expansion coefficients,  $\alpha'_s$  and  $\alpha''_s$ , are assumed to be equal.

For the sake of comparison, the following arrangements are required to reduce the model presented in Subsection 2.4 to McTigue's proposition:

$$1. \left. \begin{array}{l} n_f = 0 \\ c = c_p \\ \hat{\rho}_p = 0 \end{array} \right\} \text{single porosity,} \quad (5.11)$$

$$2. \left. \begin{array}{l} \Theta_p = 0 \\ \Theta_f = 0 \end{array} \right\} \text{no thermo-osmosis \& isothermal heat flow effect,}$$

$$3. \left. \begin{array}{l} a_{T_s p} = 0 \\ a_{T_s \epsilon} = 0 \\ a_{T_p p} = 0 \end{array} \right\} \text{uncoupled energy equation.} \quad (5.12)$$

### 5.2.2 A one-dimensional test

All numerical tests are done on a one-dimensional column. Hence, the deformation is restricted to only one dimension. Such formulation is suitable for considering thermal loading in the  $x$ -direction,

$$\epsilon_y = \epsilon_z = 0, \quad \frac{\partial}{\partial y} = \frac{\partial}{\partial z} = 0. \quad (5.13)$$

The analytical work of McTigue (1986) assumes a *semi-infinite* fluid saturated porous medium, although the finite element implementation requires a finite volume. Hence, the height of the implemented column is ‘large’ with respect to the studied area and is referred to as  $x \rightarrow \infty$ . The actual height of the column is obtained by trial and error in such a way that the initial values of the various fields of interest are not disturbed by the loadings. Furthermore, the following boundary condition for the displacement is assumed valid for all applications,

$$\lim_{x \rightarrow \infty} u_x(x, t) = 0. \quad (5.14)$$

The two types of thermal loadings are detailed below:

1. Constant temperature loading: Consider a semi-infinite mixture, initially at an arbitrary, uniform temperature  $T_0$ , subjected to a sudden increase in temperature at its boundary. The thermal boundary conditions in time and space as are,

$$\begin{aligned} T(x, 0) &= T_0, \\ T(0, t) &= T_i \times G_1(t), \\ \lim_{x \rightarrow \infty} T(x, t) &= T_\infty. \end{aligned} \quad (5.15)$$

2. Constant heat flux loading: For a constant heat flux  $q$  delivered at the boundary of the half-space, the initial and boundary conditions on the temperature field are,

$$\begin{aligned} T(x, 0) &= T_0, \\ \frac{\partial T}{\partial x}(0, t) &= -\frac{q}{\Lambda} \times G_2(t), \\ \lim_{x \rightarrow \infty} T(x, t) &= T_\infty, \end{aligned} \quad (5.16)$$

in which  $G_1(t)$  and  $G_2(t)$  are Heaviside step functions, see Remark 5.1.

For each of the two above thermal loadings, two tests with the following hydraulic boundary conditions are performed:

- i. Drained on both sides: Consider a semi-infinite mixture, of maximum drained path  $H/2$ , the initial and boundary conditions on the pressure field are,

$$\begin{aligned} p_p(x, 0) &= 0, \\ p_p(0, t) &= 0, \\ \lim_{x \rightarrow \infty} p_p(x, t) &= 0. \end{aligned} \tag{5.17}$$

- ii. Undrained at  $x = 0$  m and drained on the semi-infinite side: Consider a semi-infinite mixture, of maximum drained path  $H$ , the initial and boundary conditions on the pressure field are,

$$\begin{aligned} p_p(x, 0) &= 0, \\ \frac{\partial p_p}{\partial x}(0, t) &= 0, \\ \lim_{x \rightarrow \infty} p_p(x, t) &= 0. \end{aligned} \tag{5.18}$$

**Remark 5.1.** *The function  $G_2(t)$  is chosen constant during the test,*

$$G_2(t) = 0 \quad t \leq 0 \quad \text{and} \quad G_2(t) = 1 \quad t > 0. \tag{5.19}$$

*On the contrary, the function  $G_1(t)$  is chosen to be a step function to avoid numerical wiggles, so that,*

$$\begin{aligned} i. \quad T(0, t) &= T_0 = 288 \text{ K} & 1 < t < 1 \times 10^4 \text{ s}, \\ ii. \quad T(0, t) &= T_0 * f(t) & 1 \times 10^4 \text{ s} < t < 5 \times 10^5 \text{ s}, \\ iii. \quad T(0, t) &= T_i = 338 \text{ K} & 5 \times 10^5 \text{ s} < t. \end{aligned} \tag{5.20}$$

*in which the stages i. and iii. are constant and the stage ii. represents a linear increase. The step function  $G_1(t)$  is illustrated in Figure 5.6. Moreover, the time steps in the simulations follow a logarithmic pattern from 1 s to  $10^9$  s.*

The mesh used to reproduce the analytical solution with the finite element method is illustrated in Figure 5.7, left. Note that the height of the column is raised to up to 800 meters so that the numerical response is no too much influenced by the finite boundary

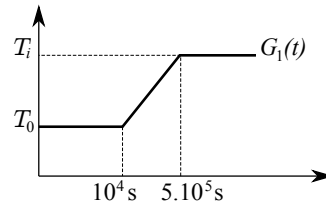


Figure 5.6: Sketch of the step function  $G_1(t)$  used for the constant temperature loading at the injection point  $x = 0$  m, so that to avoid numerical wiggles.

conditions. The numerical response is sought in the first 15 meters area, in which the mesh is refined in a continuous pattern between 0 m and 6 m. A good match with the analytical curves was obtained with two elements per meter (Section 5.1). Therefore, 22 elements and 42 nodes are used to correctly reproduce the semi-infinite curves.

The initial thermo-hydro-mechanical state is illustrated in Figure 5.7, right. The thermal equilibrium is fixed at  $T_0 = 288$  K = 15 °C. The pressure equilibrium is fixed to zero pore pressure. The displacement is referred to the configuration at time  $t = 0$  s.

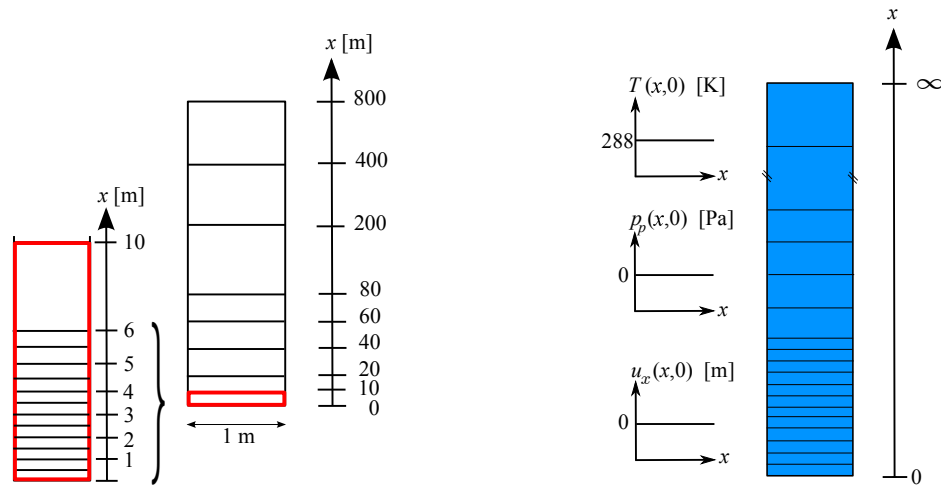


Figure 5.7: (left) Schematic of the mesh used for the numerical applications. (right) Initial boundary conditions: Homogeneous thermal, pressure and displacement equilibrium.

Out of the four types of tests (Table 5.3), two of them are illustrated in Figure 5.8: (top) 1. Imposed temperature and i. Drained boundary; (bottom) 2. Constant heat flux and ii. Undrained boundary. The loading thermal values are detailed in Table 5.4. Each contribution is presented in turn:

- a. Imposed temperature at the top and at the bottom of the column. No lateral thermal flux on the sides.
- b. Imposed zero pore pressure at the top and at the bottom. No lateral hydraulic flux on the sides.



- c. Fixed vertical displacement at the top. Zero lateral displacement on the sides. Zero traction at the bottom.
- d. Imposed temperature at the top and imposed heat flux at the bottom. No lateral thermal flux on the sides.
- e. Imposed zero pore pressure at the top and zero hydraulic flux at the bottom. No lateral hydraulic flux on the sides.

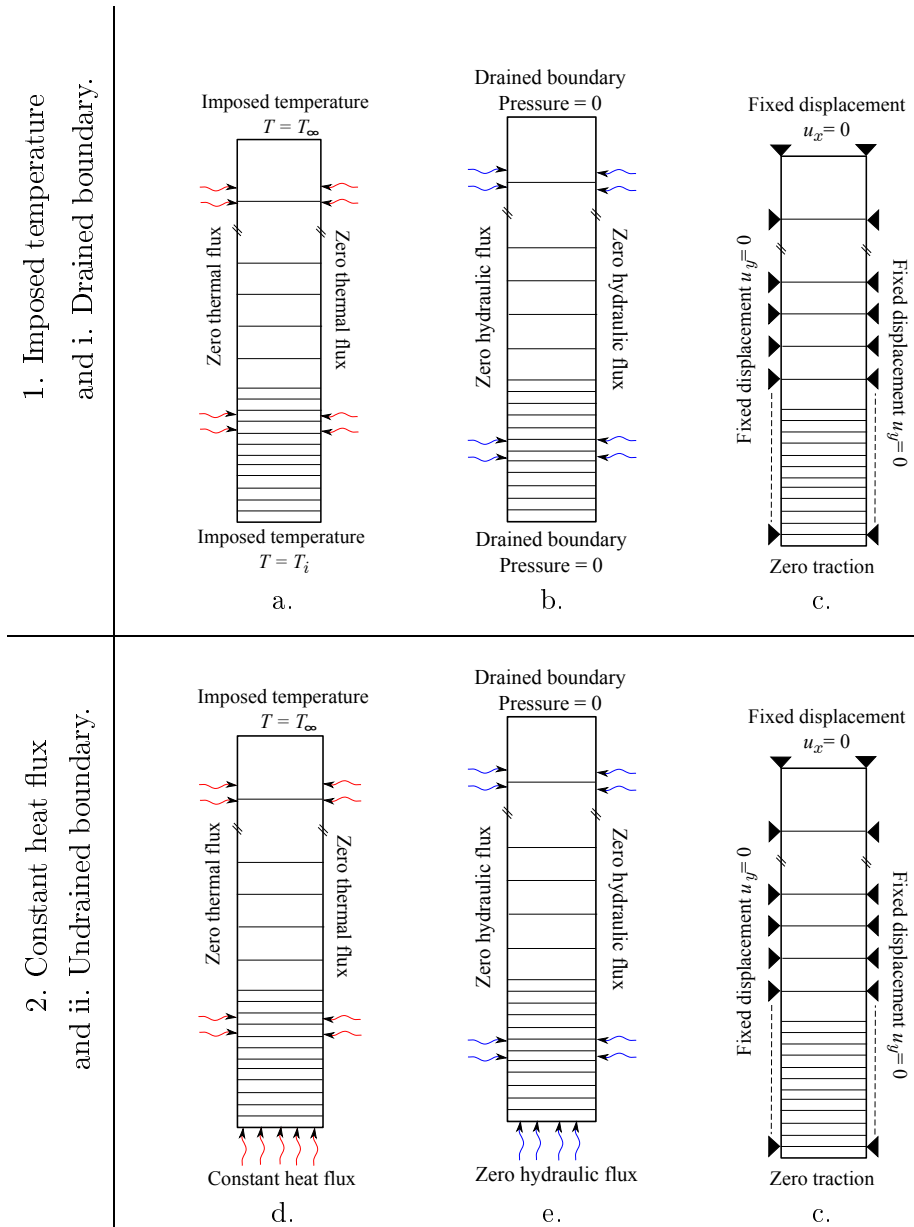


Figure 5.8: Illustrations of two types of boundary conditions. (Top) 1. Imposed temperature and i. Drained boundary. (Bottom) 2. Constant heat flux and ii. Undrained boundary. For both tests, a zero vertical displacement is imposed at the top of the column.

The solid, fluid and mixture parameters are presented in Table 5.5. Since all phases are in thermal equilibrium, thermal parameters are provided for the mixture as a whole.

Parameter	Value	Unit
Initial temperature, $T_0$	288	K
Imposed temperature, $T_\infty$	288	K
Heat flux <sup>1</sup> , $q$	2.55	W/m <sup>2</sup>
Imposed temperature <sup>2</sup> , $T_i$	338	K
Height of the implemented column, $H$	800	m

Table 5.4: Loading values. 1: The heat flux is only applied when considering a constant heat flux loading. 2: The imposed temperature is only applied when considering a constant temperature loading.

Parameter	Value	Unit
Heat capacity, $\rho C_p$	$3.92 \times 10^6$	J/m <sup>3</sup> .K
Conductivity, $\Lambda$	1.02	W/m.K
Solid expansivity, $c_T$	$0.34 \times 10^{-4}$	1/K
Fluid expansivity, $c_{pT}$	$3.0 \times 10^{-4}$	1/K
Drained bulk modulus, $K$	0.02	GPa
Fluid bulk modulus, $K_p$	2	GPa
Solid bulk modulus, $K_s$	50	GPa
Shear modulus, $\mu^{DS}$ (Second Lamé's constant)	0.000072	GPa
Drained Poisson's ratio, $\nu$	0.498	-
Porosity of the porous block, $n_p$	0.71	-
Permeability of the porous block, $k_p$	$3.0 \times 10^{-16}$	m <sup>2</sup>
	0.3	millidarcy
Dynamic viscosity (water), $\mu_p$	$1.5 \times 10^{-3}$	Pa.s
Thermal diffusivity, $\alpha_T^*$	$0.26 \times 10^{-6}$	m <sup>2</sup> /s
Hydraulic diffusivity, $\alpha_H^*$	$4.0 \times 10^{-6}$	m <sup>2</sup> /s
$R = \sqrt{\alpha_H/\alpha_T}$	3.9	-

Table 5.5: Material properties of an abyssal red clay (Illite), North Pacific Ocean (McTigue, 1986, p. 9540). \*Definitions of these parameters are provided in eq. (5.3) and (5.24), respectively.

### 5.2.3 Analytical formulation

The analytical solution to the heating of a half-space mixture is provided from McTigue (1986) for two types of loadings on the boundary  $x = 0$  m. The temperature and the

pressure as a function of space and time are expressed in turn for a constant temperature loading and a constant heat flux loading. Then, the displacement is formulated for each loading case.

### 5.2.3.1 Constant temperature loading

The equation of the temperature history, starting at  $t = 0$  s, near the surface of a semi-infinite mixture, exposed to constant surface temperature  $T_i(x = 0, t)$  is of the form:

$$\frac{T(x, t) - T_0}{T_i - T_0} = \operatorname{erfc} \left( \frac{x}{2\sqrt{\alpha_T t}} \right), \quad (5.21)$$

where  $\alpha_T$  is the thermal diffusivity of the mixture as a whole,  $\alpha_T = \Lambda/\rho C_v$ , and where the function  $\operatorname{erfc}(\cdot)$  is the complementary error function, which is defined by:

$$\operatorname{erfc}(x) = 1 - \operatorname{erf}(x), \quad \text{with} \quad \operatorname{erf}(x) = \frac{2}{\sqrt{\pi}} \int_0^x \exp(-m^2) dm. \quad (5.22)$$

Two hydraulic boundary conditions are considered:

i. Drained boundary: For zero initial pressure and a drained boundary, corresponding to the boundary conditions defined in equation (5.17), the solution for the pressure given by McTigue (1986) is of the form,

$$p = \frac{b' (T_i - T_0)}{1 - R^2} [\operatorname{erf}(\eta) - \operatorname{erf}(R \eta)], \quad (5.23)$$

where  $\eta = x/2\sqrt{\alpha_H t}$ , and  $R^2 = \alpha_H/\alpha_T$ , the ratio of the fluid and thermal diffusivities. The hydraulic diffusivity  $\alpha_H$  is defined by,

$$\alpha_H = \frac{k_p}{\mu_p} \frac{2 \mu^{DS} (1 - \nu)}{1 - 2\nu} \left[ \frac{B^2 (1 + \nu_u)^2 (1 - 2\nu)}{9(1 - \nu_u)(\nu_u - \nu)} \right], \quad (5.24)$$

in which the undrained Poisson's ratio  $\nu_u$  is defined by,

$$\nu_u = \frac{3\nu + B(1 - 2\nu)(1 - K/K_s)}{3 - B(1 - 2\nu)(1 - K/K_s)}, \quad (5.25)$$

and the Skempton coefficient  $B$  is defined by,

$$\frac{1}{B} = 1 + n_p \frac{K(1 - K_p/K_s)}{K_p(1 - K/K_s)}. \quad (5.26)$$

Finally, the coefficient  $b'$  is defined by,

$$b' = \frac{4\mu^{DS}B(1 + \nu_u)}{9(1 - \nu_u)} \left[ c_T + \frac{B(1 - \nu)(1 + \nu_u)}{2(\nu_u - \nu)} n_p (c_{pT} - c_T) \right]. \quad (5.27)$$

The fluid flux at the drained boundary is obtained from equation (5.23) and from the uncoupled Darcy's law,

$$q(0, t) = -\frac{k_p b' (T_i - T_0)}{\mu_p(1 + R)\sqrt{\pi\alpha_H t}}. \quad (5.28)$$

Note that for small times, the fluid flux is infinite, which may induce numerical problems. The pressure field (5.23) exhibits a maximum at  $\eta = \eta^* = x^*/2\sqrt{\alpha_H t}$ ,

$$\eta^* = \left( -\frac{\ln R}{1 - R^2} \right)^{1/2}. \quad (5.29)$$

Thus, a peak of pressure propagates into the semi-infinite mixture, with its location  $x^*$  proportional to  $\sqrt{\alpha_H t}$ . Combining equation (5.29) with (5.23), it is seen that the magnitude of the peak pressure is constant.

ii. Undrained boundary: For an impermeable boundary, corresponding to the boundary conditions defined in equation (5.18), the solution for the pressure given by McTigue (1986) is of the form,

$$p = \frac{b' (T_i - T_0)}{1 - R^2} [\operatorname{erfc}(R\eta) - R \operatorname{erfc}(\eta)]. \quad (5.30)$$

Therefore, the pressure at the boundary is constant,

$$p(0, t) = \frac{b' (T_i - T_0)}{1 + R}. \quad (5.31)$$

### 5.2.3.2 Constant heat flux loading

The equation of the temperature history, near the surface of a semi-infinite mixture, exposed to a constant heat flux  $q(x = 0, t)$ , is of the form:

$$T(x, t) - T_0 = \frac{2q\sqrt{\alpha_T t}}{\Lambda} F_1(R\eta), \quad (5.32)$$

where the function  $F_1(x)$  is defined by,

$$F_1(x) = \frac{1}{\sqrt{\pi}} e^{-x} - x \operatorname{erfc}(x), \quad (5.33)$$

where the function  $\operatorname{erfc}(\cdot)$  is the complementary error function and where  $F_1(0) = 1/\sqrt{\pi}$ .

Two hydraulic boundary conditions are considered:

i. Drained boundary: For zero initial pressure and a drained boundary, corresponding to the boundary conditions defined in equation (5.17), the solution for the pressure given by McTigue (1986) is of the form,

$$p = \frac{2b'q\sqrt{\alpha_T t}}{\Lambda(1-R^2)} [F_1(R\eta) - F_1(\eta)]. \quad (5.34)$$

The flux at the boundary is constant and is equal to,

$$q(0, t) = -\frac{k_p}{\mu_p} \frac{b'q}{\Lambda(1+R)}. \quad (5.35)$$

Again, a peak of pressure propagates into the half space and is located at  $x^* = \eta^* \sqrt{\alpha_H t}$ . Note that this time the magnitude of the pressure peak is not constant.  $\eta^*$  is given implicitly by,

$$R \operatorname{erfc}(R\eta^*) - \operatorname{erfc}\eta^* = 0. \quad (5.36)$$

ii. Undrained boundary: Finally, for an impermeable boundary, the solution for the pressure is of the form,

$$p = \frac{2b'q\sqrt{\alpha_T t}}{\Lambda(1-R^2)} [F_1(R\eta) - R F_1(\eta)]. \quad (5.37)$$

The pressure rise at the boundary is equal to,

$$p(0, t) = \frac{2 b' q \sqrt{\alpha_T t}}{\sqrt{\pi} \lambda (1 + R)}. \quad (5.38)$$

### 5.2.3.3 Formulation of the displacement

The foregoing solutions for the temperature and the pressure are used by McTigue (1986) to find the displacement field. The displacement  $u_x$  is integrated directly from the strain  $\epsilon_x$ ,

$$\epsilon_x = \frac{\partial u_x}{\partial x} \quad \rightarrow \quad u_x(x, t) - u_x(a, t) = \int_a^x \epsilon_x(\xi, t) d\xi, \quad (5.39)$$

in which the limit  $a$  is arbitrary. McTigue (1986) choses the limit  $a$  to be equal to zero. Therefore, one form of the displacement field  $u_x$  is,

$$\begin{aligned} u_x(x, t) = & \frac{3(\nu_u - \nu)}{2GB(1 - \nu)(1 + \nu_u)} \int_0^x p(\xi, t) d\xi + \frac{1 + \nu}{1 - \nu} \frac{c_T}{3} \int_0^x T(\xi, t) d\xi \\ & + \frac{1 - 2\nu}{2G(1 - \nu)} c_1(t) x + c_2(t), \end{aligned} \quad (5.40)$$

where  $c_1(t)$  and  $c_2(t)$  are arbitrary functions of time. These arbitrary functions are found thanks to the boundary conditions and are thus different for each case. The integration of the stress equilibrium equation in one dimension gives,

$$\sigma_x(x, t) = c_1(t). \quad (5.41)$$

One of the boundary conditions common to all cases is that  $\sigma_x(0, t) = 0$ , see Figure 5.8. Hence,  $c_1(t) = 0$  in all the following cases. The function  $c_2(t)$  only remains unknown and can be calculated by heading to the infinite limit  $\lim_{x \rightarrow \infty} u_x(x, t) = 0$ .

As an alternative to McTigue's proposition, the limit  $a$  is chosen equal to  $\infty$  in equation (5.39). The displacement field becomes,

$$\begin{aligned}
u_x(x, t) = & \frac{3(\nu_u - \nu)}{2GB(1 - \nu)(1 + \nu_u)} \int_{\infty}^x p(\xi, t) \, d\xi + \frac{1 + \nu}{1 - \nu} \frac{c_T}{3} \int_{\infty}^x T(\xi, t) \, d\xi \\
& + \frac{1 - 2\nu}{2G(1 - \nu)} \int_{\infty}^x \sigma_x(\xi, t) \, d\xi + u_x(\infty, t), \tag{5.42}
\end{aligned}$$

in which  $u_x(\infty, t)$  is zero thanks to equation (5.14). In addition, if the displacement vanishes at  $x = \infty$ , the prescribed traction  $\sigma_x$  should itself vanish.

The four loading cases are considered in turn:

1.i. Constant temperature and drained boundary: The explicit evaluation of the displacement, for the case of a constant temperature and a drained boundary, is obtained by substituting (5.21) and (5.23) into (5.40) and integrating,

$$\begin{aligned}
u_x = & \frac{3(\nu_u - \nu)}{2GB(1 - \nu)(1 + \nu_u)} \frac{b'(T_i - T_0)}{1 - R^2} 2\sqrt{\alpha_T t} \times \\
& \left[ R \left( \eta \operatorname{erf} \eta - \frac{1}{\sqrt{\pi}} \left( 1 - e^{-\eta^2} \right) \right) - \left( R \eta \operatorname{erf} (R \eta) - \frac{1}{\sqrt{\pi}} \left( 1 - e^{-R^2 \eta^2} \right) \right) \right] \\
& + \frac{1 + \nu}{1 - \nu} \frac{c_T}{3} (T_i - T_0) 2\sqrt{\alpha_T t} \left[ R \eta \operatorname{erfc}(R \eta) + \frac{1}{\sqrt{\pi}} \left( 1 - e^{-R^2 \eta^2} \right) \right] + c_2(t). \tag{5.43}
\end{aligned}$$

In addition, if the following boundary condition is imposed,

$$\lim_{x \rightarrow \infty} u_x(x, t) = 0, \tag{5.44}$$

it follows that,

$$c_2(t) = - \left[ \frac{3(\nu_u - \nu)}{2GB(1 - \nu)(1 + \nu_u)} \frac{b'}{1 + R} + \frac{1 + \nu}{1 - \nu} \frac{c_T}{3} \right] (T_i - T_0) 2\sqrt{\frac{\alpha_T t}{\pi}}. \tag{5.45}$$

in which the second term in brackets is the contribution from the thermoelastic expansion of the drained medium (i.e. without pore pressure effect). The first term is an additional displacement due to the pore pressure. If the thermal loading is positive ( $T_i - T_0 > 0$ ) and  $(\nu_u - \nu) > 0$ , the pressure contribution results in a tensile effective stress and in a stretching of the solid matrix.

Finally, from equations (5.43) and (5.45), the displacement at the boundary is given by,

$$u_x(0, t) = c_2(t). \quad (5.46)$$

1.ii. Constant temperature and undrained boundary: The explicit evaluation of the displacement, for the case of a constant temperature and an undrained boundary, is obtained by substituting (5.21) and (5.30) into (5.42) and integrating,

$$\begin{aligned} u_x(x, t) = & \frac{3(\nu_u - \nu)}{2GB(1 - \nu)(1 + \nu_u)} \frac{b'(T_i - T_0)}{1 - R^2} 2\sqrt{\alpha_T t} \times \\ & \left[ \left( R \eta \operatorname{erfc}(R \eta) - \frac{1}{\sqrt{\pi}} e^{-R^2 \eta^2} \right) - R^2 \left( \eta \operatorname{erfc}(\eta) - \frac{1}{\sqrt{\pi}} e^{-\eta^2} \right) \right] \\ & + \frac{1 + \nu}{1 - \nu} \frac{c_T}{3} (T_i - T_0) 2\sqrt{\alpha_T t} \left[ +R \eta \operatorname{erfc}(R \eta) - \frac{1}{\sqrt{\pi}} e^{-R^2 \eta^2} \right]. \end{aligned} \quad (5.47)$$

The displacement at the boundary is,

$$u_x(0, t) = - \left[ \frac{3(\nu_u - \nu)}{2GB(1 - \nu)(1 + \nu_u)} b' + \frac{1 + \nu}{1 - \nu} \frac{c_T}{3} \right] (T_i - T_0) 2\sqrt{\frac{\alpha_T t}{\pi}}. \quad (5.48)$$

2.i. Constant heat flux and drained boundary: The explicit evaluation of the displacement, for the case of a constant heat flux and a drained boundary, is obtained by substituting (5.32) and (5.34) into (5.42) and integrating,

$$\begin{aligned} u_x = & \frac{3(\nu_u - \nu)}{2GB(1 - \nu)(1 + \nu_u)} \frac{4q \alpha_T t}{\Lambda} \frac{b'}{(1 - R^2)} \times [\operatorname{iF}_1(R \eta) - R \operatorname{iF}_1(\eta)] \\ & + \frac{1 + \nu}{1 - \nu} \frac{c_T}{3} \frac{4q \alpha_T t}{\Lambda} [\operatorname{iF}_1(R \eta)], \end{aligned} \quad (5.49)$$

in which the function  $\operatorname{iF}_1$  is the integral of the function  $F_1$ ,

$$\operatorname{iF}_1(y) = \int_{\infty}^y F_1(Y) dY = - \left[ \left( \frac{1}{4} + \frac{y^2}{2} \right) \operatorname{erfc}(y) \right] + \frac{y}{2\sqrt{\pi}} e^{-y^2}. \quad (5.50)$$



Since  $iF_1(0) = -1/4$  (see Remark 5.2), for a constant heat flux and a drained boundary, the displacement at the boundary  $x = 0$  m is,

$$u_x(0, t) = -\frac{q \alpha_T t}{\Lambda} \left[ \frac{3(\nu_u - \nu)}{2GB(1 - \nu)(1 + \nu_u)} \frac{b'}{1 + R} + \frac{1 + \nu}{1 - \nu} \frac{c_T}{3} \right]. \quad (5.51)$$

**Remark 5.2.** *The complementary function can be approximated by a series expansion which is used to integrate the function  $iF_1$  in equation (5.50). The complementary function is defined by,*

$$\operatorname{erfc}(y) = \frac{2}{\sqrt{\pi}} \int_y^\infty e^{-x^2} dx. \quad (5.52)$$

*Integrating term by term the uniformly convergent series expansion of the exponential yields to a series expansion of the error function itself,*

$$\operatorname{erfc}(y) = \frac{2}{\sqrt{\pi}} \sum_{k=0}^{\infty} \frac{(-1)^k}{k!} \frac{y^{2k+1}}{2k+1} = \frac{2}{\sqrt{\pi}} \left( y - \frac{y^3}{3} + \dots \right). \quad (5.53)$$

*For large  $y$  on the other hand, the complementary function is approximated by the series expansion,*

$$\operatorname{erfc}(y) = \frac{e^{-y^2}}{\sqrt{\pi}} \left( \frac{1}{y} - \frac{1}{2} \frac{1}{y^3} + \dots + (-1)^{n-1} \frac{1 \times 3 \dots \times (2n-3)}{2^{n-1} y^{2n-1}} + \dots \right). \quad (5.54)$$

*Finally, with the help of equation (5.54),  $iF_1(\infty) = 0$  and  $iF_1(0) = 1/4$  are obtained.*

2.ii. Constant heat flux and undrained boundary: The explicit evaluation of the displacement for the case of a constant heat flux and an undrained boundary, is obtained by substituting (5.32) and (5.37) into (5.42) and integrating,

$$\begin{aligned} u_x &= \frac{3(\nu_u - \nu)}{2GB(1 - \nu)(1 + \nu_u)} \frac{4q \alpha_T t}{\Lambda} \frac{b'}{(1 - R^2)} \times [iF_1(R\eta) - R^2 iF_1(\eta)] \\ &+ \frac{1 + \nu}{1 - \nu} \frac{c_T}{3} \frac{4q \alpha_T t}{\Lambda} [iF_1(R\eta)]. \end{aligned} \quad (5.55)$$

Since  $iF_1(0) = -1/4$  (see Remark 5.2), for a constant heat flux and an undrained boundary, the displacement at the boundary  $x = 0$  m is,

$$c_2(t) = -\frac{q \alpha_T t}{\Lambda} \left[ \frac{3(\nu_u - \nu)}{2GB(1 - \nu)(1 + \nu_u)} b' + \frac{1 + \nu c_T}{1 - \nu} \frac{1}{3} \right]. \quad (5.56)$$

#### 5.2.4 Comparing analytical and numerical results

The numerical results are provided for an abyssal red clay whose material properties are provided in Table 5.5. This material appears to have the interesting property that its hydraulic to thermal diffusivity ratio is close to one:  $R = 3.9$ . Therefore, thermo-hydro-mechanical couplings should be strong and easily visible on the pressure and on the displacement fields as suggested by McTigue (1986). For an abyssal red clay, the characteristic time corresponding to thermal diffusion  $t_{\text{diff}}$ , eq. (5.2), at a height of 3 m in the column is equal to  $3.46 \times 10^7$  s which is larger than that corresponding to the hydraulic diffusion:  $2.25 \times 10^6$  s. Hence, the hydraulic front is ahead of the thermal front.

The analytical solutions are *systematically* compared with the numerical responses for 1. a constant temperature loading and a drained boundary, 2. a constant temperature loading and an undrained boundary, 3. a constant heat flux loading and a drained boundary and 4. a constant heat flux loading and an undrained boundary. For each loading case, the history of the temperature, the pressure and the displacement fields are presented at a height of  $x = 3$  m in the column. Furthermore, the profiles of the latter fields are illustrated for four different times, in the vicinity of the loading  $0 < x < 15$  m.

As a convention, in all the following figures, the plain curve will represent the numerical response, and the dash curve will represent the analytical response provided by McTigue (1986) and expressed in Section 5.2.3.

**Remark 5.3.** *The thermoelastic analytical response expressed by McTigue (1986) under a constant temperature boundary describes an instantaneous thermal shock. This loading is smoothed out in the numerical simulations as indicated in Remark 5.1.*

##### 5.2.4.1 Constant temperature loading and a drained boundary

The field histories of the numerical responses and of the analytical curves match satisfactorily (Figure 5.9) for both a constant temperature loading and a drained boundary. The temperature field history is well reproduced in spite of the temperature time-dependent

function replacing the thermal shock. At  $t = 3.46 \times 10^7$  s, the mixture temperature is equal to 311 K, which is equal to 46% of the steady state value. At  $t = 2.25 \times 10^6$  s, the pressure is almost at its peak, no dilatation has occurred yet, and the thermal flux has not been sensed yet by the mixture. Significantly, the peak appears to be *ahead in time* compared with the heat front: This is due to the fact that the hydraulic diffusion is 16 times greater than the thermal diffusion with  $R = 3.9$ . The dilatation behaviour is well reproduced by the numerical model. The difference between the two displacement responses observed for the long term behaviour ( $t > 10^{10}$  s) is due to the fact that our column is not a semi-infinite slab but is a finite column of height equal to 800 m.

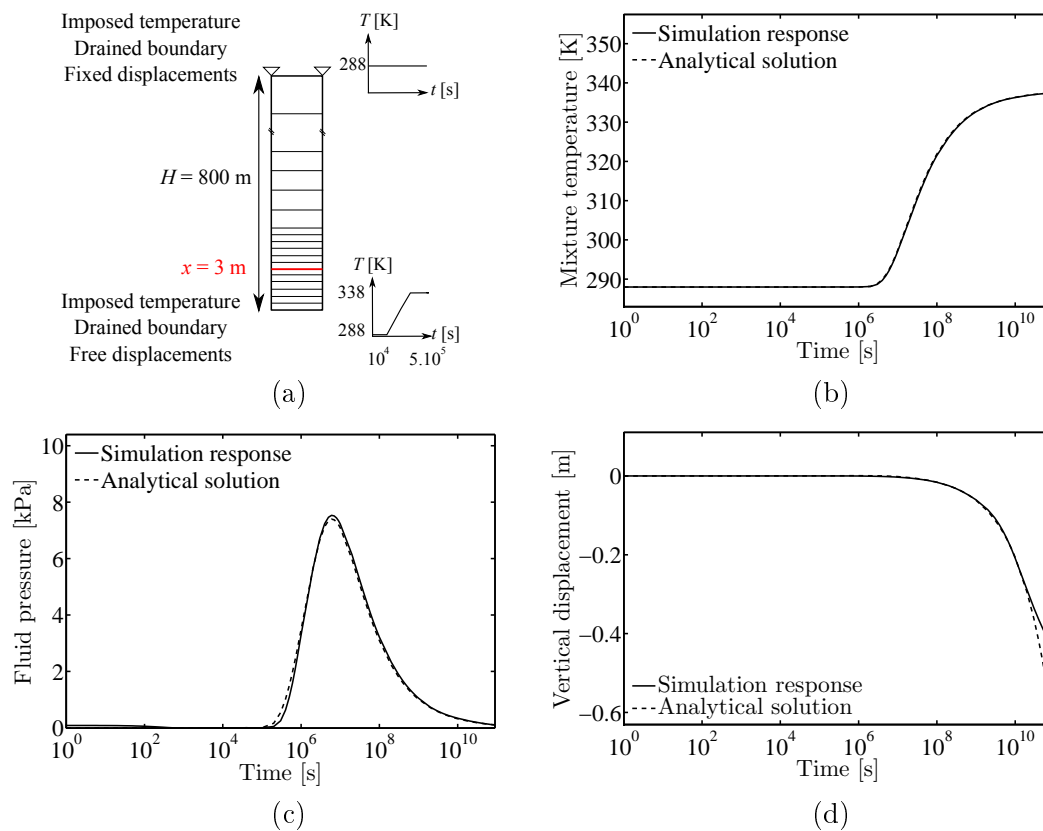


Figure 5.9: (a) Sketch of the mesh and of the boundary conditions applied to the semi-infinite column. (b) Temperature, (c) pressure and (d) displacement histories at  $x = 3$  m in the column, for a constant temperature and a drained boundary. The temperature field reaches a steady state. The pressure field displays a peak when the heated boundary is drained. This peak is due to a pressure rise into the pores before a significant dilatation occurs. The pressure propagation is ahead of the thermal front because  $R = 3.9$ . The displacement field shows a dilatation synchronised with the thermal front.

Similarly to the history curves, the field profiles of the numerical response (Figure 5.10, right) follow very well the profile of the analytical curves (left). The propagation of the heat front reaches 5 m at time  $1 \times 10^7$  s. As expected, a pressure peak propagates into the mixture with time. The magnitude of the peak is constant, which is consistent with

McTigue's conclusions, see eq. (5.29) and eq. (5.23). Note that for lower times, the magnitude of the peak (output of the numerical model) is smaller due to the temperature time-function. The dilation of the mixture increases with time, induced by the temperature contribution. The displacements ahead of the thermal front are induced by the dilatation of the mixture at the thermal front. The phenomenon is denominated pull-on. The magnitude of the pressure peak [kPa] is too small to induce a significant dilatation.

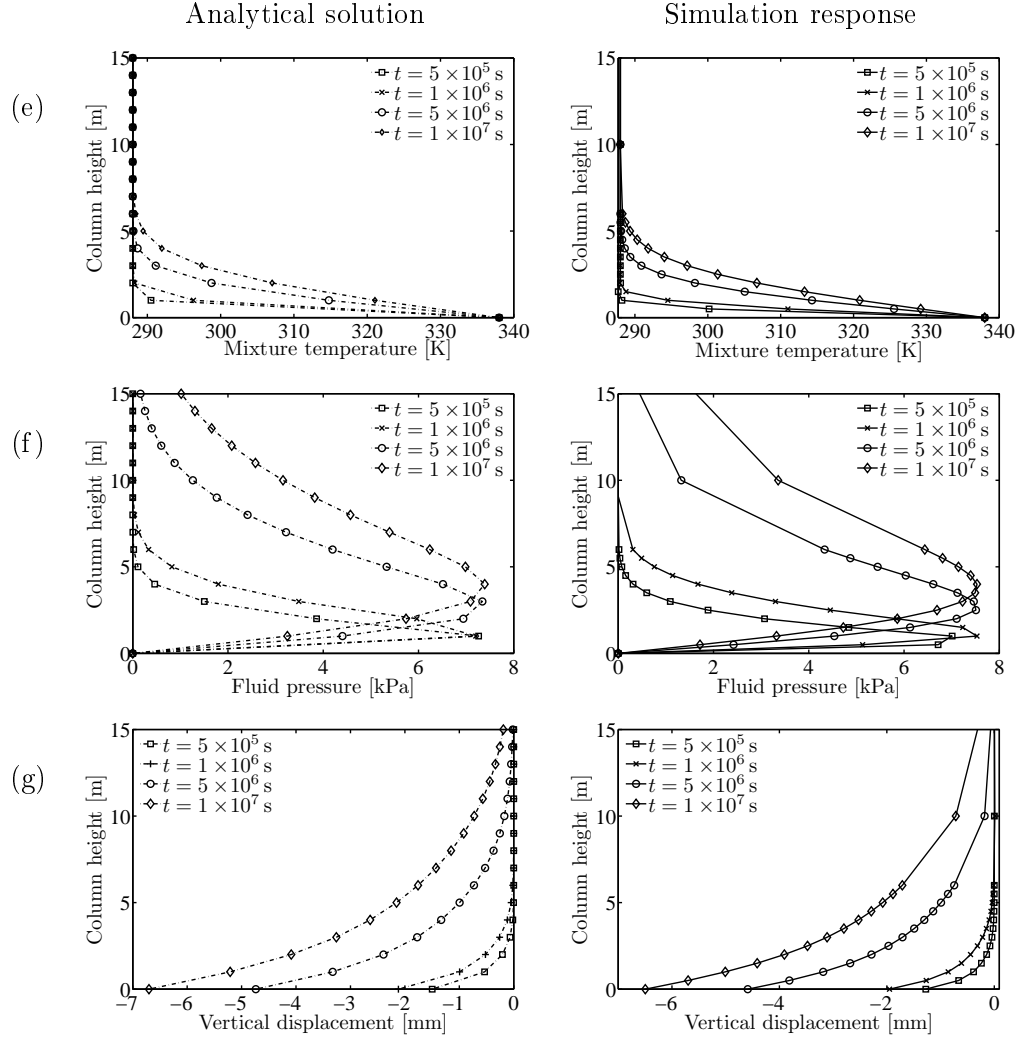


Figure 5.10: (e) Temperature, (f) pressure and (g) displacement profiles in the column, for a constant temperature and a drained boundary: (left) analytical solution, (right) numerical response. The thermal front has penetrated up to 5 m. A constant pressure peak propagates into the column. The pressure front is ahead of the thermal penetration because  $R = 3.9$ . The dilatation has reached up to 10 m due to pull-on induced by the dilatation below 5 m.

### 5.2.4.2 Constant temperature loading and an undrained boundary

Figure 5.11 represents the field history comparison between the numerical responses and the analytical curves for the case with a constant temperature loading and an *undrained* boundary. The temperature and the displacement histories provide a good correspondence between the analytical curves and the numerical responses in spite of the temperature time-dependent function replacing the thermal shock. Their histories are very similar to the drained boundary case. The numerical response of the pressure field history follows the general profile of the analytical curve. This behaviour is induced by the propagation of the pressure front into the mixture and by its impossibility to relax (infinite drained path). The plateau illustrates a steady state behaviour. Note that no reduction of the pore pressure is induced by the dilation of the solid skeleton,  $t > 10^8$  s.

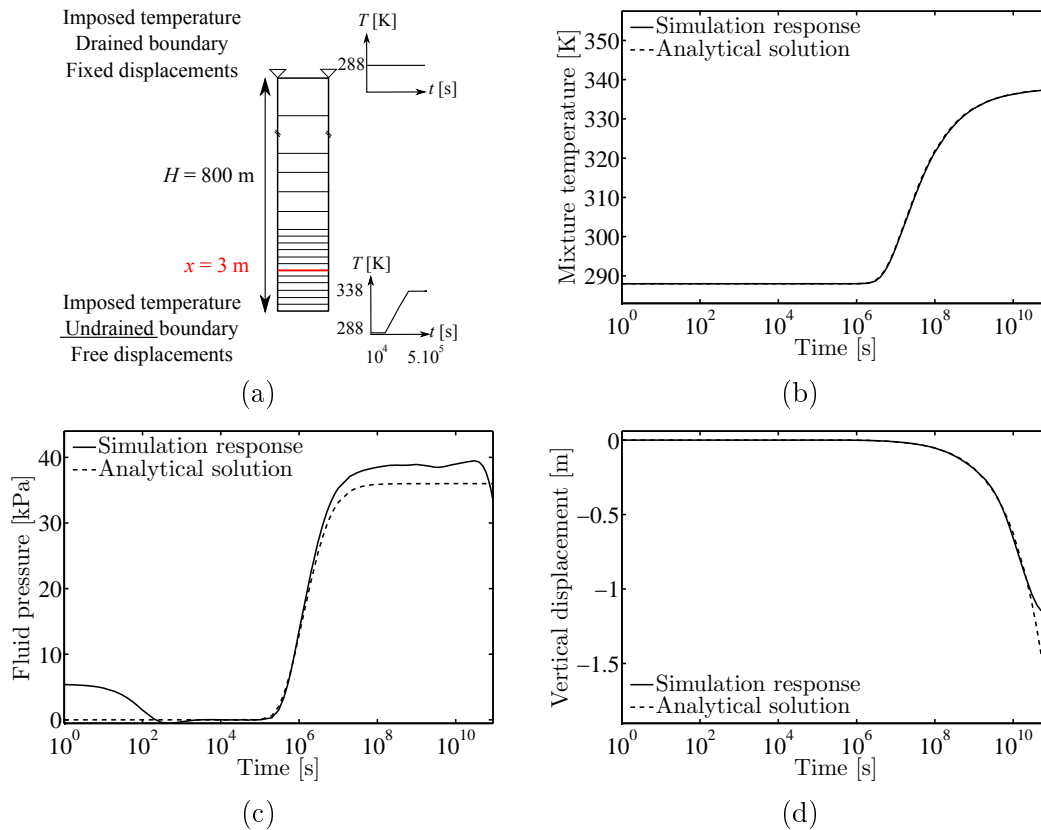


Figure 5.11: Same as Figure 5.9 for a constant temperature and an *undrained* boundary. The temperature and the displacement fields display a similar behaviour to the drained boundary condition. On the other hand, the pressure field ends by a plateau when the heated boundary is undrained. Locally the fluid is trapped into the pores: the pressure can not dissipate in spite of the dilatation. Note that some numerical disturbances arise in two regions: (i) at early times, these disturbances are induced by the numerical time-dependent loading; (ii) at late times, by the finite property of the implemented column.

The numerical disturbances observed at early times and at late times are induced by the coarse mesh at the loading boundary ( $x = 0$  m) and by the finite property of the implemented column, respectively. The undrained boundary condition should lead to a sharp increase of the pressure at the boundary ( $x = 0$  m) up to a constant value, see eq.(5.31). Results should be improved by either an exponential refinement towards the boundary  $x = 0$  m or by the implementation of a time scheme suitable for thermal shocks (Wood and Lewis, 1975).

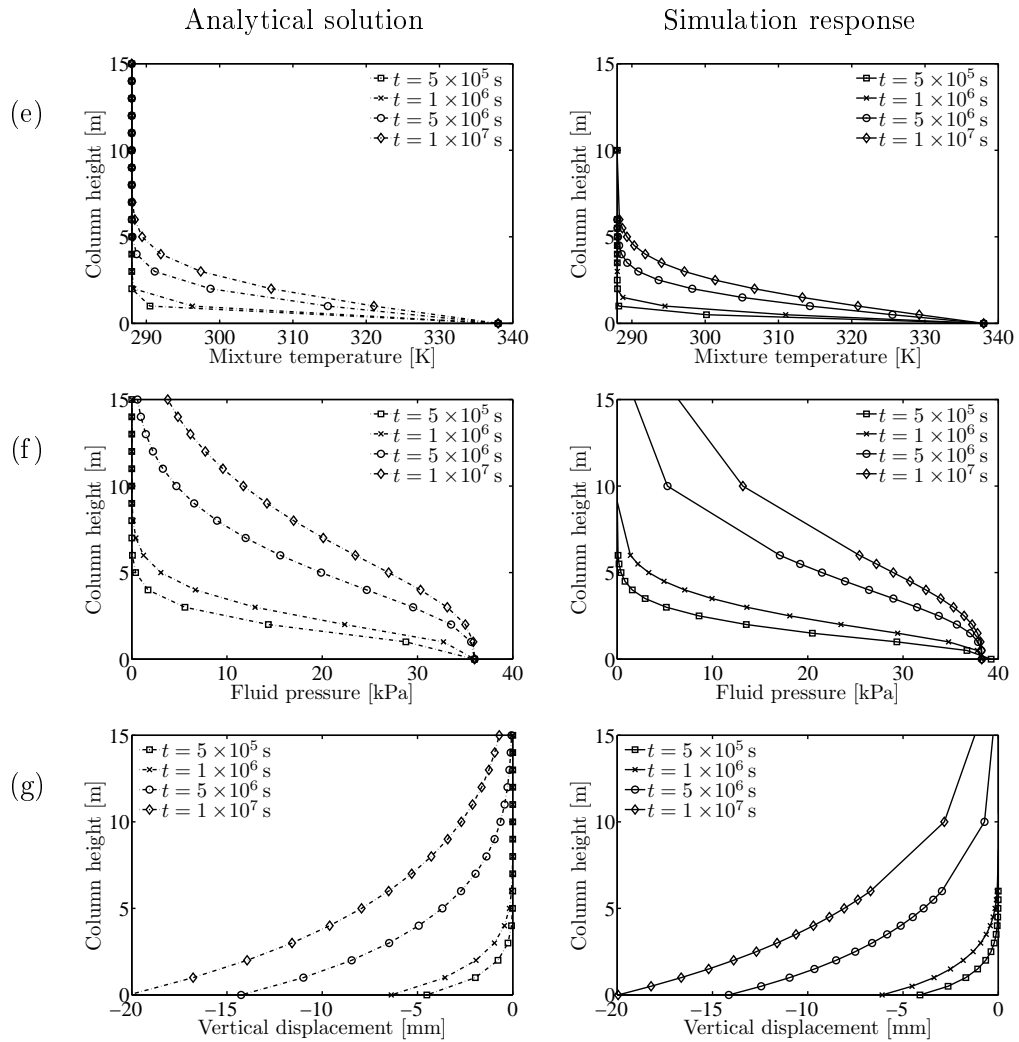


Figure 5.12: Same as Figure 5.10 for a constant temperature and an *undrained* boundary. The profile of the temperature remains similar to the drained boundary case. On the other hand, the pressure propagates into the column and is maximum and constant at the undrained boundary. Furthermore, the displacement magnitude is increased compared with the drained boundary case.

In Figure 5.12, the propagation of the heat front is the same as with a drained boundary condition (in Figure 5.10) and reaches 5 m at time  $1 \times 10^7$  s. Again, the pressure front propagates into the mixture with time, *ahead* compared with the heat front. However,

the magnitude of the pressure at the boundary  $x = 0$  m is constant. Note that for lower times, the magnitude of the pressure from the analytical solution is smaller than that of the simulation response due to the temperature time-function. The profile of the displacement is similar to the drained boundary case but with a larger magnitude due to the pressure contribution.

### 5.2.4.3 Constant heat flux loading and a drained boundary

Figure 5.13 represents the field histories comparison between the numerical responses and the analytical curves for the case of a constant heat flux loading and a drained boundary. A correct match is obtained between the analytical temperature history and the numerical response in spite of our finite column. The latter property induces the numerical front to be slightly ahead of the analytical one. At very large times  $t > 10^{11}$  s, the temperature displays a plateau  $T = T_0$ .

The numerical response of the pressure history follows quite well the profile of the analytical curve to within the fact that the pressure magnitude of the numerical response is larger than the one provided by the analytical response. This is a consequence of the numerical thermal front which is slightly ahead of the analytical one. The very late pressure decrease is due to the fact that our column is not infinite. At late times  $t > 10^{11}$  s, the pressure dissipates completely. The dilatation behaviour is well reproduced by the numerical model and the displacement history is synchronised with the temperature history.

Figure 5.14 compares the field profiles of the numerical response with the analytical solutions, at four different times. A good correspondence is obtained for the temperature profile, although a small magnitude difference is observed. Again, the thermal front penetrates into the mixture, up to at least 5 m at time  $1 \times 10^7$  s. A pressure peak propagates into the mixture, as time increases. The magnitude of the peak is increasing with the temperature penetration. Again, the pressure peak is clearly *ahead in time* compared with the heat front. The numerical curves display the same type of behaviour as the analytical solution, except that the magnitude of the peaks for each time is larger. This is due to finite property of the implemented column which induces the thermal front to be slightly ahead of the analytical response. The dilation of the mixture increases with time. Again the deformations of the numerical test are larger than the analytical response due to finite property of the implemented column.

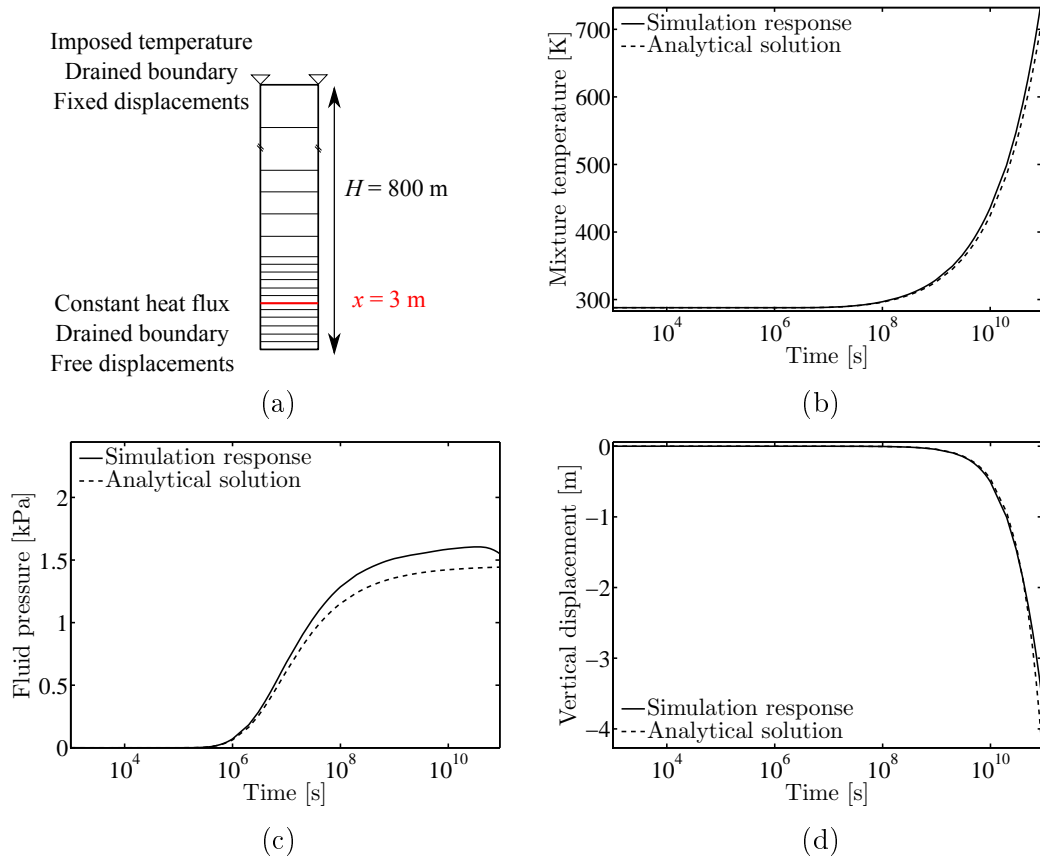


Figure 5.13: (a) Sketch of the mesh and of the boundary conditions applied to the semi-infinite column. (b) Temperature, (c) pressure and (d) displacement histories at  $x = 3$  m in the column, for a constant heat flux and a drained boundary. The temperature rises exponentially, i.e. no steady state is reached. The pressure field, although close to the drained boundary, is continuously heated: therefore the pressure does not dissipate easily. The pressure plateau represents this time an equilibrium between hydraulic dissipation and pressure rise induced by thermal excitation. The displacement field shows a dilatation delayed with respect to the thermal front.

#### 5.2.4.4 Constant heat flux loading and an undrained boundary

For the case of a constant heat flux loading and an *undrained* boundary, the field history comparison between the numerical responses and the analytical curves is presented in Figure 5.15. The temperature and the displacement histories display a correct match between the analytical curve and the numerical response in spite of our finite column. The history curves remain very close to the drained boundary problem. The numerical response of the pressure history follows quite well the profile of the analytical curve to within the fact that the numerical response is a little ahead in time than the one provided by the analytical response.

Figure 5.16 compares the field profiles of the numerical response with the analytical solutions, at four different times. A good correspondence is obtained for the temperature



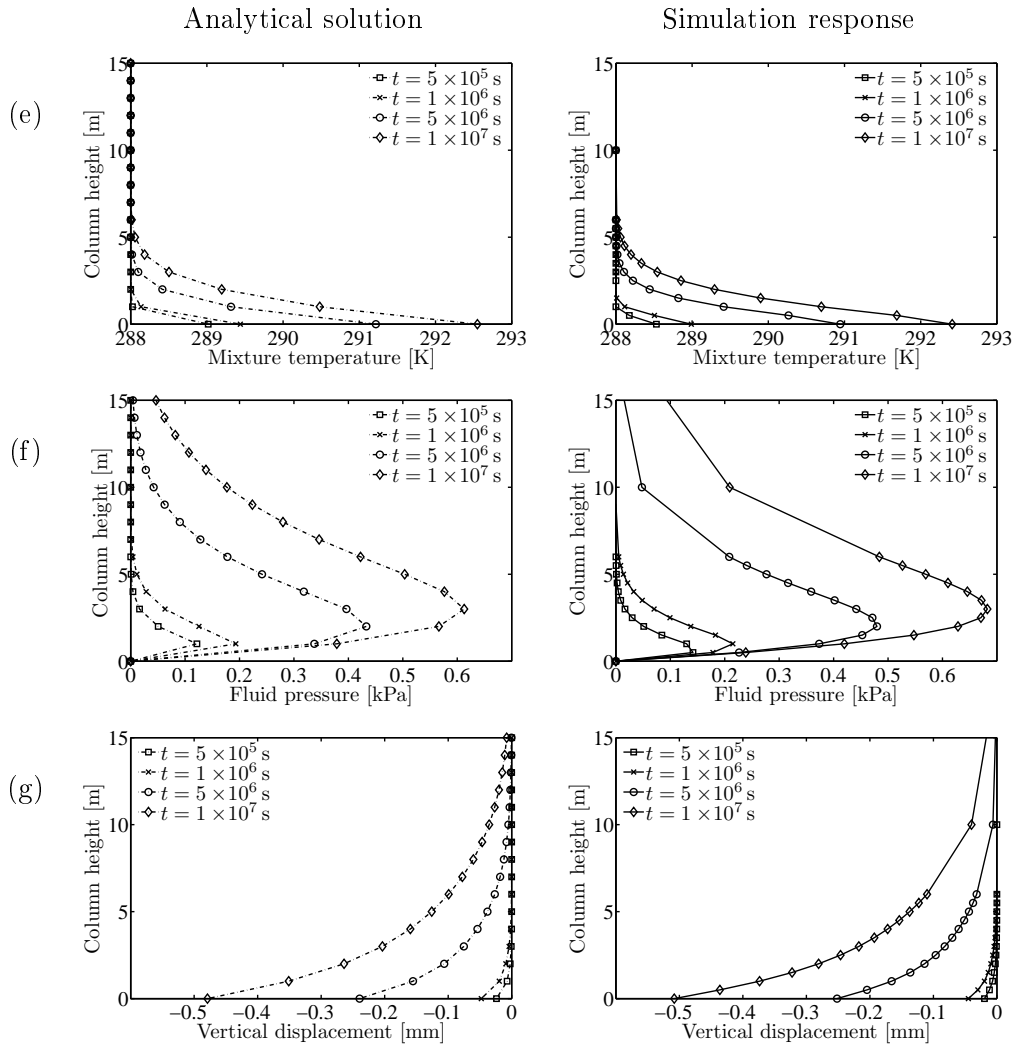


Figure 5.14: (e) Temperature, (f) pressure and (g) displacement profiles in the column, for a constant heat flux and a undrained boundary: (left) analytical solution, (right) numerical response. The thermal front has penetrated up to 5 m. The pressure propagates into the column. The pressure peak is due to the drained boundary condition. The magnitude of which is increasing with time due to the continuous heating. The dilatation has reached up to 10 m due to pull-on induced by the dilatation below 5 m.

profile, although a small magnitude difference is observed. The profile of the temperature is not influenced by the hydraulic boundary condition due to the partially coupled model used by McTigue (1986) (Section 5.2.1). The pressure propagates into the mixture with time. The pressure peak is located at the undrained boundary. The magnitude of the peak is increasing with time. Again, the pressure peak is clearly *ahead in time* compared with the heat front. The numerical curves display the same type of behaviour as the analytical solutions, except that the magnitude of the peaks for each time is larger. Again, the displacement magnitude is slightly increased compared with the drained boundary case due to the pressure contribution. The small variations between the simulation responses

and the analytical solutions are due to the finite property of the implemented column.

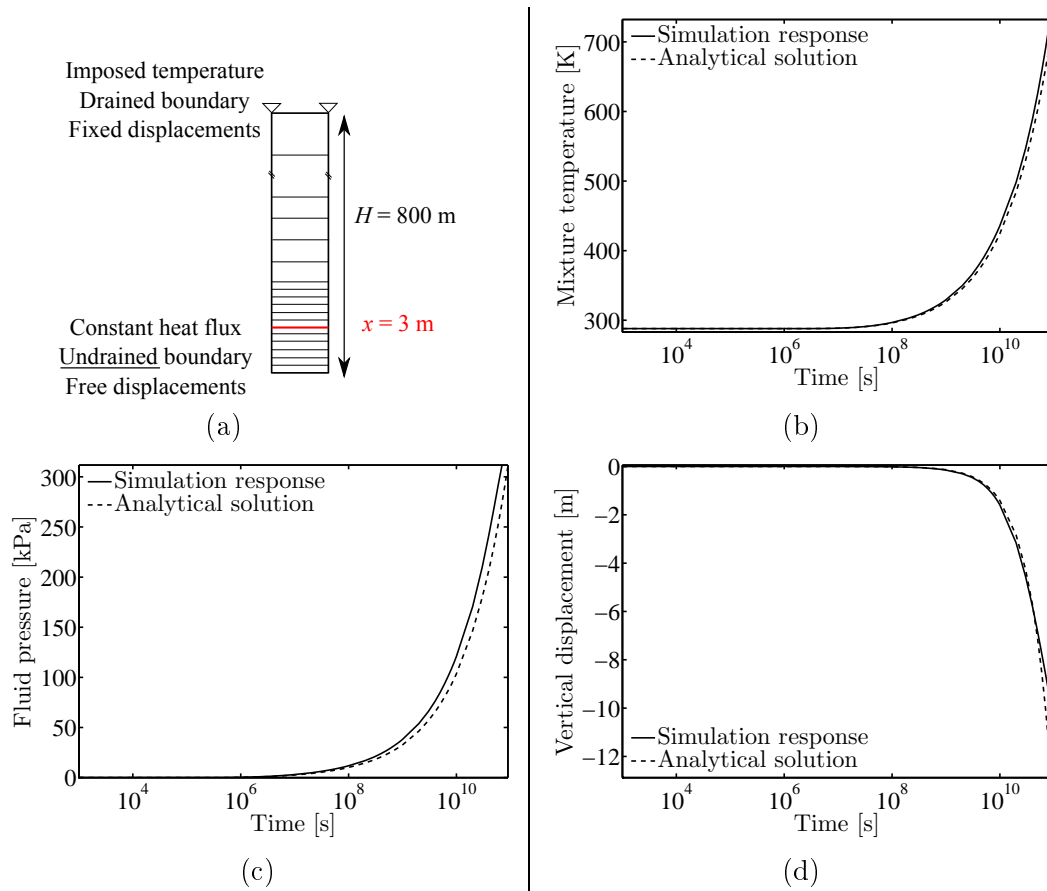


Figure 5.15: Same as Figure 5.13 for a constant heat flux and an *undrained* boundary. The temperature and the displacement fields remain the same as for a drained boundary problem. On the other hand, the pressure field can not dissipate due to the undrained boundary condition. Therefore the pressure rises exponentially induced by continuous thermal excitation.

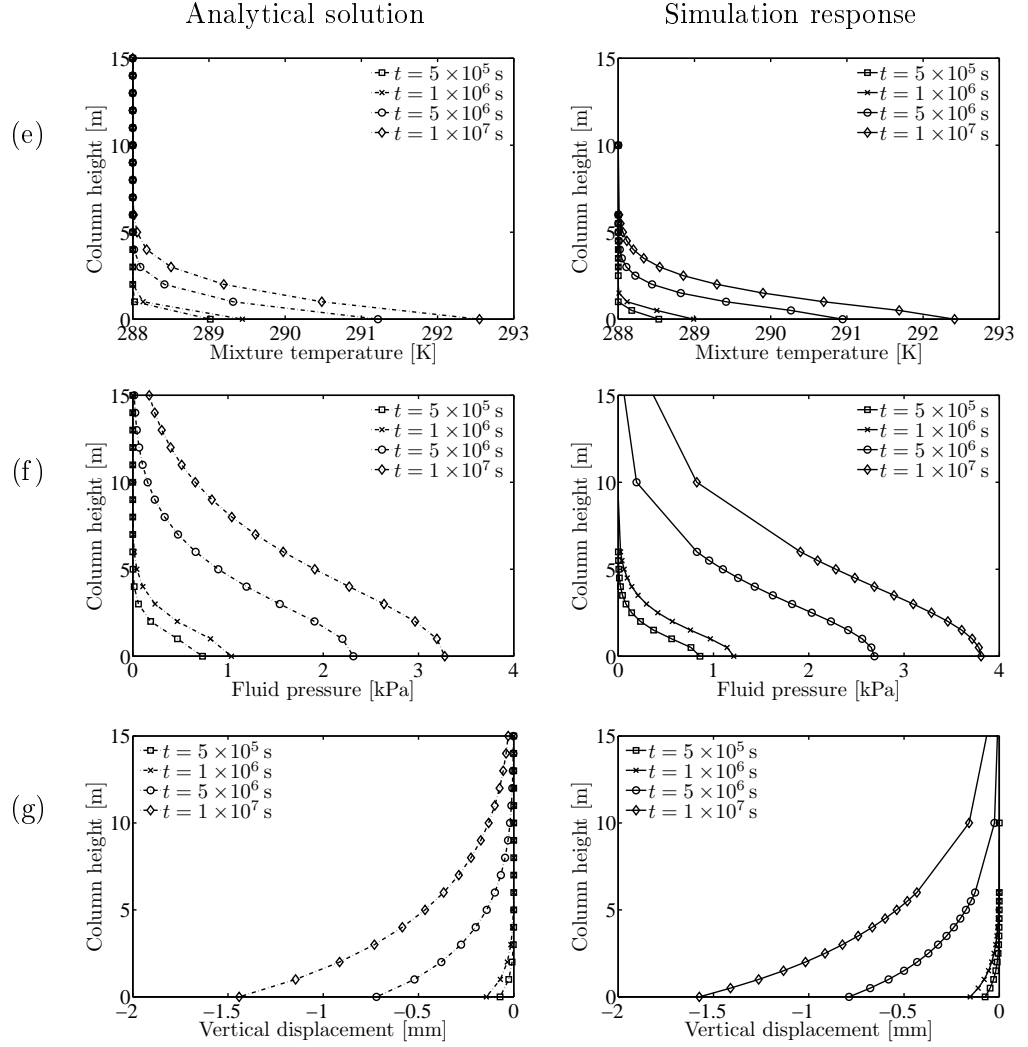


Figure 5.16: Same as Figure 5.14 for a constant heat flux and an *undrained* boundary. The profile of the temperature remains similar to the drained boundary case. On the other hand, the pressure propagates into the column with a maximum located at the undrained boundary. The magnitude of the maximum pressure is increasing with time due to the continuous heating. Again, the displacement magnitude is slightly larger compared with the drained boundary case.

### 5.2.5 The importance of the diffusivity ratio $R$

The importance of the diffusivity ratio  $R$  is first analysed with the analytical solutions. Three limit values are worth investigating:  $R \rightarrow \infty$  characteristic of large permeability porous media,  $R \rightarrow 0$  characteristic of small permeability mixtures and  $R \sim 1$  which is observed in abyssal red clay and rock salt materials. Next, the difference in behaviour of the latter materials is illustrated for the case of a constant temperature loading and a drained boundary. Finally, the conclusions reached in this section are gathered.

### 5.2.5.1 Limits of the diffusivity ratio $R$

The drained and the undrained limits are found to be strongly associated with the ratio of the hydraulic diffusivity and the thermal diffusivity  $R = \sqrt{\alpha_H/\alpha_T}$ . Moreover, the thermo-mechanical coupling appears to be strongest when hydraulic and thermal diffusivities are of equal order (McTigue (1986)). Three cases are discussed below,

1. Drained limit     $R \rightarrow \infty$     ex: large permeability
  2. Undrained limit     $R \rightarrow 0$     ex: small permeability
  3. Like order     $R \sim 1$     ex: abyssal red clay and rock salt materials
- (5.57)

1. Drained limit :  $R \rightarrow \infty$ . When the fluid diffusivity is large in front of the thermal diffusivity:  $\alpha_H \gg \alpha_T$ ; three remarks can be made:

- i. The pore pressure vanishes rapidly in comparison with the rate of temperature change, see eq. (5.23), (5.30), (5.34) and (5.37).
- ii. The fluid flux (at the drained boundary) does not depend on the permeability. In this case, the porous block provides no resistance to the fluid flow, on the time scale of the heating. The fluid flux is limited only by the amount of thermal energy delivered to the medium and by its elastic properties (McTigue, 1986, eq. (38)).
- iii. In the same manner, if  $R \rightarrow \infty$ , one can see that the pore pressure contribution to the displacement field becomes negligible in front of the thermoelastic contribution, eq. (5.43) and (5.45)-(5.46).

In conclusion, for the drained limit case, the medium behaves as a simple thermo-elastic body with properties of the porous skeleton. If a mixture displays a large diffusivity ratio  $R^2 \gg 1$ , a thermo-mechanic uncoupled constitutive law is suitable.

2. Undrained limit :  $R \rightarrow 0$ . The undrained limit is obtained when the thermal diffusivity is large in front of the hydraulic diffusivity, for  $\alpha_H \ll \alpha_T$ . Two observations are made:

- i. The volumetric content is zero: the fluid is trapped locally in the pores, at the time scale of the heating.
- ii. One can see that the pressure contribution to the displacement field, eq. (5.43) and (5.45), is not negligible anymore compared with the thermoelastic contribution. This

Hydraulic contribution		Thermal contribution	
$\text{erf}(\eta)$	$\propto$	$\delta \text{erf}(R\eta)$	eq. (5.23)
$R \text{erfc}(\eta)$	$\propto$	$\delta \text{erfc}(R\eta)$	eq. (5.30)
$\exp(-\eta^2)$	$\propto$	$\delta \exp(-R^2\eta^2)$	eq. (5.34)
$R \exp(-\eta^2)$	$\propto$	$\delta \exp(-R^2\eta^2)$	eq. (5.37)

Table 5.6: Comparison between the hydraulic and the thermal contributions for a diffusivity ratio  $R = 1$ .  $\delta$  is of order of magnitude of one:  $O(10^0)$  and the symbol  $\propto$  means ‘proportional to’

can be illustrated by substituting eq. (5.27) into (5.45), which provides a displacement field highly dependent on undrained parameters,

$$\lim_{R \rightarrow \infty} u_x(0, t) = -\frac{1 + \nu_u}{1 - \nu_u} \frac{c_{T,u}}{3} (T_i - T_0) 2 \sqrt{\frac{\alpha_T t}{\pi}}, \quad (5.58)$$

where,  $c_{T,u}$  is the undrained thermal expansion coefficient,

$$c_{T,u} = c_T + B n_p (c_{pT} - c_T). \quad (5.59)$$

In conclusion, for the undrained limit case, the medium again behaves as a simple thermo-elastic body, but exhibits this time effective properties modified by the presence of the fluid: undrained properties. If a mixture displays a low diffusivity ratio  $R^2 \ll 1$ , a thermo-mechanical uncoupled constitutive law is suitable if undrained coefficients are used.

3. Like magnitude :  $R \sim 1$ . It is crucial to understand that the thermoelastic constitutive coupling of heat flow (thermal conduction), fluid flow (hydraulic diffusion) and deformation is strongest for thermal and hydraulic diffusivities of like order.

- i. The closer  $R \sim 1$ , the closer the thermal and the hydraulic contributions are in magnitude, and therefore the stronger the coupling (Table 5.6).
- ii. The closer  $R \sim 1$ , the closer the pressure and the thermal contributions are in magnitude in the displacement fields equations, and therefore the stronger the coupling, see eq. (5.43) and (5.45).

### 5.2.5.2 Comparing salt and clay

To illustrate the importance of the diffusivity ratio  $R$ , the behaviour of two materials is compared in the case of a constant temperature loading and a drained boundary. Both materials have a diffusivity ratio  $R$  relatively close to one, which ensures a strong coupling between heat conduction and hydraulic conduction.

Comparing Table 5.5 with Table 5.7, one can see that the diffusivity ratio of the salt is closer to one than the diffusivity ratio of the clay:  $R_{\text{clay}} = 3.9 > 1$  and  $R_{\text{salt}} = 0.29 < 1$ . This particularity has an influence on the magnitude of the factor  $1/(1 - R^2)$ , which has a key importance on the pressure and on the displacement magnitude analytically described in Section 5.2.3.

In figure 5.17, the thermo-hydro-mechanical responses of the two materials are compared. The setup is identical to that developed in Subsection 5.1.1 for a constant temperature and a drained boundary. The thermal responses of the two materials are similar in behaviour (not shown). However, the pressure response for the salt rock is significantly larger than the pressure response of the clay. This is due to the diffusivity ratios: the diffusivity ratio of the salt is closer to one,  $|R_{\text{salt}} - 1| = 0.79$ , compared with the clay,  $|R_{\text{clay}} - 1| = 2.9$ .

Material parameter	Value	Unit
Heat capacity, $\rho C_p$	$1.89 \times 10^6$	J/m <sup>3</sup> .K
Conductivity, $\Lambda$	6.60	W/m.K
Solid expansivity, $c_T$	$1.2 \times 10^{-4}$	1/K
Fluid expansivity, $c_{pT}$	$3.0 \times 10^{-4}$	1/K
Drained bulk modulus, $K$	20.7	GPa
Fluid bulk modulus, $K_p$	2	GPa
Solid bulk modulus, $K_s$	23.5	GPa
Shear modulus, $\mu^{DS}$ (Second Lamé's constant)	12.4	GPa
Drained Poisson's ratio, $\nu$	0.25	-
Porosity of the porous block, $n_p$	0.001	-
Permeability of the porous block, $k_p$	$10^{-21}$	m <sup>2</sup>
	1.0	nanodarcy
Dynamic viscosity (water), $\mu_p$	$1.0 \times 10^{-3}$	Pa.s
Thermal diffusivity, $\alpha_T^*$	$3.5 \times 10^{-6}$	m <sup>2</sup> /s
Hydraulic diffusivity, $\alpha_H^*$	$0.16 \times 10^{-6}$	m <sup>2</sup> /s
$R = \sqrt{\alpha_H/\alpha_T}$	0.29	-

Table 5.7: Material properties of salt, Salado Formation, Delaware Basin, New Mexico (McTigue, 1986, p. 9540). \*Definitions of these parameters are provided in eq. (5.3) and (5.24), respectively.

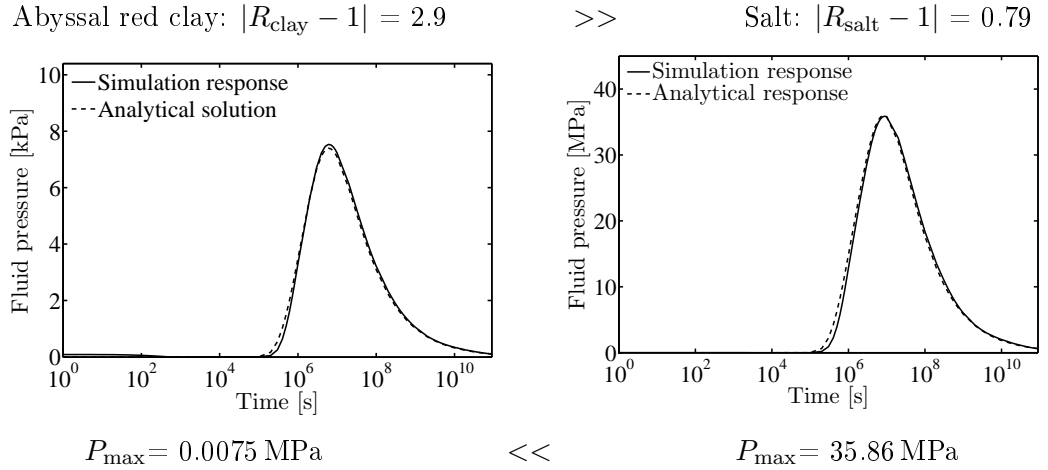


Figure 5.17: Pressure history of (left) abyssal red clay and (right) salt; at  $x = 3 \text{ m}$  in the column, for a constant temperature and a drained boundary. For the same loading, the pressure peak in the salt mixture is significantly larger than the pressure in the clay mixture. This is due to the fact that the diffusivity ratio  $R$  of the salt is closer to one than the diffusivity ratio of the clay.

### 5.2.6 Summary and conclusion

The validity of the numerical model has been checked by comparing the output results with analytical solutions provided by McTigue (1986). A good match is obtained for the two types of loading: constant temperature and constant heat flux; and for the two types of hydraulic boundary conditions; drained and undrained boundary. The discrepancies between the simulation responses and the analytical solutions are attributed to the fact that a finite column is implemented, instead of a semi-infinite mixture, and to the Heaviside step function used for the thermal loading. The disturbance due to the Heaviside step function can be further damped by a refinement of the mesh in the vicinity of the loaded boundary.

Throughout this section, comprehensive information on the diffusion behaviour of thermo-hydro-mechanical mixtures has been observed. The main points are summarised below.

The hydraulic to thermal diffusivity ratio  $R$  informs on the dominance of one type of diffusion on the other. For example the abyssal red clay is endowed with  $R = 3.9$  and the hydraulic diffusivity is larger than the thermal one. As expected, for all loadings and boundary conditions types, the numerical results display a hydraulic front ahead of the thermal one.

A semi-infinite column of mixture subjected to a constant temperature loading has the characteristics to allow the temperature history to reach a steady state distribution into the



column. Keeping this in mind, it is worth noting that the pressure history displays a peak when the heated boundary is drained. This peak is due to a pressure rise into the pores before a significant dilatation occurs. Furthermore, the magnitude of the pressure peak remains constant and propagates into the sample. On the other hand, the pressure history ends by a plateau when the heated boundary is undrained. Locally the fluid is trapped into the pores; the pressure can not dissipate in spite of the solid skeleton dilatation. It is worth noting that the magnitude of the pressure is increased from one order of magnitude between the drained and the undrained cases. In the latter case, the results show that the dilatation of the mixture is not large enough to allow a significant dissipation of the pressure.

A semi-infinite column of mixture subjected to a constant heat flux loading displays a temperature history which increases exponentially. Therefore when the heated boundary is drained, the pressure does not dissipate easily; in fact it displays a plateau due to the exponential heating. Note that it does not mean that the fluid is trapped into the pores, but that the fluid is continuously heated and undergoing dissipation at the same time. Conversely if the heated boundary is undrained, the pressure history follows the exponential behaviour of the temperature history. This time the fluid is trapped into the pores.

### 5.3 Axi-symmetric boundary value problems

In axi-symmetric boundary value problems, errors in the vicinity of the inner radius arise and the mesh requires a special treatment. This section aims to identify the origin of the numerical disturbances and to treat them appropriately, i.e. to minimise the errors. The boundary value problem of a hollow cylinder made of a linear elastic isotropic solid and undergoing infinitesimal strain under static conditions is analysed (Figure 5.18) in an uncoupled mechanical context.

#### 5.3.1 Analytical solutions

A hollow cylinder is subjected to internal and external pressures on its lateral boundaries, and to either a uniform axial displacement or uniform axial traction on its lower and upper bases. The material is linear isotropic elastic, with  $\lambda^{DS}$  and  $\mu^{DS}$  the Lamé's constants of the drained solid.

The motion can then be shown to be compatible with a radial displacement,  $u_r = u_r(r)$  depending only on the radius and an axial displacement  $u_z = u_z(z)$  depending only on the

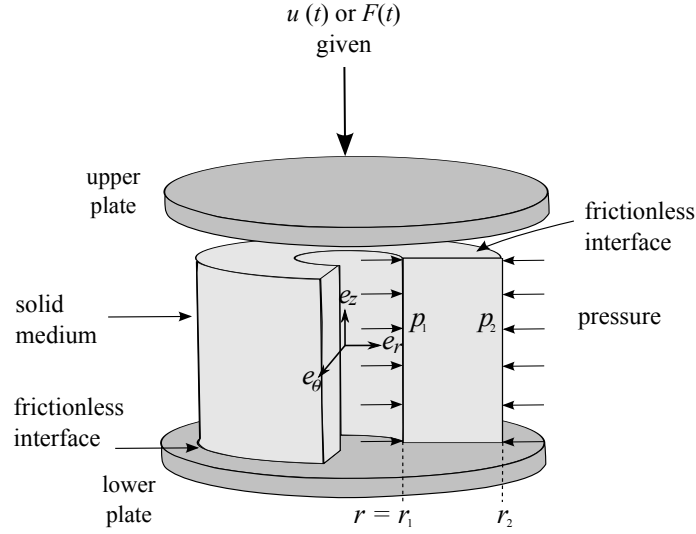


Figure 5.18: Hollow cylinder subjected to internal and external pressure,  $p_1$  and  $p_2$ , respectively.

axial coordinate  $z$  while the tangential displacement  $u_\theta$  vanishes.

Then, the strain tensor is principal in the axes of the cylinder, and so does the stress tensor since the material is isotropic. Therefore, the radial strain  $\epsilon_r$ , the circumferential strain  $\epsilon_\theta$ , axial strain  $\epsilon_z$ , and dilatation  $\text{tr } \epsilon$  simplify to:

$$\epsilon_r = \frac{du_r}{dr}, \quad \epsilon_\theta = \frac{u_r}{r}, \quad \epsilon_z = \frac{du_z}{dz}, \quad \text{tr } \epsilon = \epsilon_r + \epsilon_\theta + \epsilon_z = \frac{1}{r} \frac{d}{dr}(r u_r) + \frac{du_z}{dz}. \quad (5.60)$$

The stress components,

$$\sigma_r = \lambda^{DS} \text{tr } \epsilon + 2\mu^{DS} \frac{du_r}{dr}, \quad \sigma_\theta = \lambda^{DS} \text{tr } \epsilon + 2\mu^{DS} \frac{u_r}{r}, \quad \sigma_z = \lambda^{DS} \text{tr } \epsilon + 2\mu^{DS} \frac{du_z}{dz}, \quad (5.61)$$

should satisfy the balance of momentum equilibrium equations  $\text{div } \boldsymbol{\sigma} = 0$  given in the cylindrical coordinates by Malvern (1969, p. 668),

$$\begin{cases} \frac{d\sigma_{rr}}{dr} + \frac{1}{r} \frac{d\sigma_{\theta r}}{d\theta} + \frac{d\sigma_{zr}}{dz} + \frac{\sigma_{rr} - \sigma_{\theta\theta}}{r} = 0, \\ \frac{d\sigma_{r\theta}}{dr} + \frac{1}{r} \frac{d\sigma_{\theta\theta}}{d\theta} + \frac{d\sigma_{z\theta}}{dz} + \frac{\sigma_{r\theta} + \sigma_{\theta r}}{r} = 0, \\ \frac{d\sigma_{rz}}{dr} + \frac{1}{r} \frac{d\sigma_{\theta z}}{d\theta} + \frac{d\sigma_{zz}}{dz} + \frac{\sigma_{rz}}{r} = 0. \end{cases} \quad (5.62)$$

In fact since the stress tensor is principal in the axes of the cylinder, only two equations are non-trivially satisfied,

$$\begin{cases} \frac{d\sigma_r}{dr} + \frac{\sigma_r - \sigma_\theta}{r} = 0, \\ \frac{d\sigma_z}{dz} = 0. \end{cases} \quad (5.63)$$

Upon insertion of (5.61) into (5.63), the equilibrium equations become,

$$\begin{cases} (\lambda^{DS} + 2\mu^{DS}) \frac{d}{dr} \left( \frac{1}{r} \frac{d}{dr} (r u_r) \right) = 0, \\ (\lambda^{DS} + 2\mu^{DS}) \frac{d}{dz} \left( \frac{d u_z}{dz} \right) = 0. \end{cases} \quad (5.64)$$

Finally, upon integration of (5.64), the equilibrium equations yield the displacements,

$$u_r = A r + \frac{B}{r}, \quad u_z = \epsilon_z z + u_z(0), \quad (5.65)$$

where  $A$  and  $B$  are constants defined by the lateral boundary conditions and  $\epsilon_z$  is the constant axial strain. Calculating the resulting strains,

$$\epsilon_r = A r - \frac{B}{r^2}, \quad \epsilon_\theta = A r + \frac{B}{r^2}, \quad \text{tr } \epsilon = 2A + \epsilon_z \quad (5.66)$$

the volume change is observed to be constant in space, and therefore so is the first stress invariant  $\text{tr } \sigma = 3K^{DS} \text{tr } \epsilon$ , with  $K^{DS} = \lambda^{DS} + 2\mu^{DS}/3$  the bulk modulus.

The values of the constants  $A$  and  $B$  are identified for various boundary conditions. Four cases are considered: (1) the internal and external lateral pressures are different, (2) the internal and external lateral pressures are equal, (3) the internal pressure is null and zero external displacements are prescribed and (4) the internal pressure is fixed and zero external displacements are prescribed at the *infinite* external boundary.

(1) Two different lateral pressures. Let  $\sigma_r(r_1) = -p_1$  and  $\sigma_r(r_2) = -p_2$  be the pressures applied respectively on the internal boundary  $r = r_1$  and external boundary  $r = r_2$ . Then

$$A = -\frac{1}{2} \frac{\lambda^{DS}}{\lambda^{DS} + \mu^{DS}} \epsilon_z - \frac{1}{2} \frac{1}{\lambda^{DS} + \mu^{DS}} \frac{p_2 r_2^2 - p_1 r_1^2}{r_2^2 - r_1^2}, \quad B = \frac{p_1 - p_2}{2\mu^{DS}} \frac{r_1^2 r_2^2}{r_2^2 - r_1^2}. \quad (5.67)$$

The dilatation becomes,

$$\text{tr } \epsilon = \frac{\mu^{DS}}{\lambda^{DS} + \mu^{DS}} \epsilon_z + \frac{\lambda^{DS}}{\lambda^{DS} + \mu^{DS}} \frac{p_1 r_1^2 - p_2 r_2^2}{r_2^2 - r_1^2}. \quad (5.68)$$

The radial and tangential stresses vary radially,

$$\sigma_r = -\frac{p_2 r_2^2 - p_1 r_1^2}{r_2^2 - r_1^2} - \frac{p_1 - p_2}{r^2} \frac{r_1^2 r_2^2}{r_2^2 - r_1^2}, \quad \sigma_\theta = -\frac{p_2 r_2^2 - p_1 r_1^2}{r_2^2 - r_1^2} + \frac{p_1 - p_2}{r^2} \frac{r_1^2 r_2^2}{r_2^2 - r_1^2}, \quad (5.69)$$

where, on the contrary, the axial stress is constant in space,

$$\sigma_z = \frac{\mu^{DS} (3\lambda^{DS} + 2\mu^{DS})}{\lambda^{DS} + \mu^{DS}} \epsilon_z - \frac{\lambda^{DS}}{\lambda^{DS} + \mu^{DS}} \frac{p_2 r_2^2 - p_1 r_1^2}{r_2^2 - r_1^2}. \quad (5.70)$$

(2) The two lateral pressures are equal. If the two pressures are identical,  $p_1 = p_2 = p$ , the constant  $B$  vanishes and strain and stress become homogeneous:

$$\epsilon_r = \epsilon_z = -\frac{1}{2} \frac{\lambda^{DS} \epsilon_z + p}{\lambda^{DS} + \mu^{DS}}, \quad \text{tr } \epsilon = \frac{\mu^{DS} \epsilon_z - p}{\lambda^{DS} + \mu^{DS}}, \quad \sigma_r = \sigma_\theta = -p. \quad (5.71)$$

Note that the radial displacement is linear in  $r$ ,

$$u_r = -\frac{1}{2} \frac{\lambda^{DS} \epsilon_z + p}{\lambda^{DS} + \mu^{DS}} - \frac{1}{2} \frac{1}{\lambda^{DS} + \mu^{DS}} r. \quad (5.72)$$

**Remark 5.4.** *The expression (5.71) holds as well for a solid cylinder ( $r_1 = 0$ ) subjected to the pressure  $p = p_2$  at the outer boundary  $r = r_2$ .*

(3) Fixed internal pressure and zero external displacement. Let  $\sigma_r(r_1) = -p_1$  be the pressure applied on the internal boundary  $r = r_1$  and  $u_r(r_2) = 0$  be the displacement applied to the external boundary  $r = r_2$ . Then

$$\begin{aligned} A &= -\frac{r_1^2}{\lambda^{DS} r_1^2 + \mu^{DS} r_1^2 + \mu^{DS} r_2^2} \frac{p_1 + \lambda^{DS} \epsilon_z}{2}, \\ B &= \frac{r_1^2 r_2^2}{\lambda^{DS} r_1^2 + \mu^{DS} r_1^2 + \mu^{DS} r_2^2} \frac{p_1 + \lambda^{DS} \epsilon_z}{2}. \end{aligned} \quad (5.73)$$

The dilatation is constant in space,

$$\text{tr } \epsilon = \frac{\mu^{DS} (r_1^2 + r_2^2)}{\lambda^{DS} r_1^2 + \mu^{DS} r_1^2 + \mu^{DS} r_2^2} \epsilon_z - \frac{r_1^2}{\lambda^{DS} r_1^2 + \mu^{DS} r_1^2 + \mu^{DS} r_2^2} p_1. \quad (5.74)$$

The radial and tangential stresses vary with  $1/r^2$ ,

$$\begin{aligned} \sigma_r = & \frac{-p_1 r_1^2}{\lambda^{DS} r_1^2 + \mu^{DS} r_1^2 + \mu^{DS} r_2^2} \left( \lambda^{DS} + \mu^{DS} + \frac{\mu^{DS} r_2^2}{r^2} \right) \\ & + \frac{\epsilon_z \lambda^{DS} \mu^{DS} r_2^2}{\lambda^{DS} r_1^2 + \mu^{DS} r_1^2 + \mu^{DS} r_2^2} \left( 1 - \frac{r_1^2}{r^2} \right), \end{aligned} \quad (5.75)$$

$$\begin{aligned} \sigma_\theta = & \frac{-p_1 r_1^2}{\lambda^{DS} r_1^2 + \mu^{DS} r_1^2 + \mu^{DS} r_2^2} \left( \lambda^{DS} + \mu^{DS} - \frac{\mu^{DS} r_2^2}{r^2} \right) \\ & + \frac{\epsilon_z \lambda^{DS} \mu^{DS} r_2^2}{\lambda^{DS} r_1^2 + \mu^{DS} r_1^2 + \mu^{DS} r_2^2} \left( 1 + \frac{r_1^2}{r^2} \right), \end{aligned} \quad (5.76)$$

where, on the contrary, the axial stress is constant in space,

$$\sigma_z = -\frac{\lambda^{DS} r_1^2}{\lambda^{DS} r_1^2 + \mu^{DS} r_1^2 + \mu^{DS} r_2^2} (p_1 + \lambda^{DS} \epsilon_z) + (\lambda^{DS} + 2\mu^{DS}) \epsilon_z. \quad (5.77)$$

(4) Fixed internal pressure and zero displacement at the *infinite* external boundary. Let  $\sigma_r(r_1) = -p_1$  be the pressure applied on the internal boundary  $r = r_1$  and  $u_r(r_2) = 0$  be the displacement applied to the external boundary  $r = r_2 \rightarrow \infty$ . Then the constant  $A$  vanishes, and

$$u_r = \frac{B}{r}, \quad \epsilon_r = -\epsilon_\theta = -\frac{B}{r^2}, \quad \text{tr } \epsilon = \epsilon_z. \quad (5.78)$$

with  $B$  still given by (5.73) where  $r_2 = \infty$ .

### 5.3.2 Numerical considerations

According to Hughes (1987a, p.140), the numerical integration (quadrature) formula of the function  $f(x)$  can be written as follows,

$$\begin{aligned} \int_{\Omega^e} f(r) dr &= \int_{-1}^1 f(r(\xi)) \frac{dr(\xi)}{d\xi} d\xi = \int_{-1}^1 g(\xi) d\xi \\ &= \sum_{l=1}^{n_{\text{int}}} g(\tilde{\xi}_l) W_l + R \end{aligned} \quad (5.79)$$

where  $n_{\text{int}}$  is the number of integration points,  $\tilde{\xi}_l$  is the coordinate of the  $l$ th integration,  $W_l$  is the ‘weight’ of the  $l$ th integration point, and  $R$  is the remainder.

If the number of integration points is equal to two  $n_{\text{int}} = 2$ , the Gaussian quadrature rules yield,

$$\begin{aligned}\tilde{\xi}_1 &= -\frac{1}{\sqrt{3}}, & \tilde{\xi}_2 &= \frac{1}{\sqrt{3}}, \\ W_1 &= W_2 = 1, \\ R &= \frac{g^{(4)}(\bar{\xi})}{135},\end{aligned}\tag{5.80}$$

where  $g^{(4)} = d^4g/d\xi^4$ , and  $\bar{\xi}$  denotes some point in the interval  $[\tilde{\xi}_1, \tilde{\xi}_2]$ . If  $g$  is a constant or linear polynomial this two point integration rule is exact. If  $g$  is a quadratic polynomial then this integration rule is approximate. It is said to be ‘second-order’ accurate.

Unfortunately, if the function  $g$  is proportional to  $\xi^{-1}$ , as in equation (5.78), the remainder is proportional to  $\xi^{-4}$ . The smaller the value of  $\bar{\xi}$  the higher the remainder and the accurate-less the integration rule. Finally, the only way to reduce the error (without changing the integration rule) is to refine the mesh where the value of  $\bar{\xi}$  is small.

Three important questions are addressed below :

1. How much is an acceptable error?
2. What is the influence of the mesh size on the error?
3. How to optimise the mesh so that the error becomes acceptable ?

### 5.3.2.1 Error magnitude

An error lower than 0.001 % will be considered as a very precise result. An error greater than 0.1 % will be considered as an unprecise result. An error lower than 0.1 % and greater than 0.001 % will be considered as acceptable. For all axi-symmetric hollow cylinder tests, the error should be estimated as a function of the mesh.

### 5.3.2.2 Influence of the mesh size on the error

The error is found to be acceptable, if the mesh is sufficiently refined. As refining the mesh is very ‘expansive’ in time calculation, a study is designed to evaluate the evolution of the error as a function of a representative mesh criterion.

If a homogeneous mesh is assumed, the *mesh criterion* is defined as the radial length of one element  $\Delta_r^e$  over the total radial length of the sample:  $r_2 - r_1$ .

The evolution of the error for the displacement, the deformation and for the stress fields is scrutinised, at  $r = r_1 = 0.5$  mm, while  $r_2 = 5.5$  mm (Table 5.8). The case of a hollow cylinder with a fixed internal pressure and a zero external displacement is assumed. Since the error is maximum at  $r = r_1$ , the error analysis focuses on this point. Note that for a plain cylinder  $r = r_1 = 0$  m, additional problems arise in the numerical treatment of the integration method.

mesh criterion	0.1	0.05	0.02	0.002
number of elements per meter	10	20	50	500
% error for $u_r$	8.46	2.73	0.48	0.23
% error for $\epsilon_r$	54.79	35.52	17.13	2.03
% error for $\sigma_r$	41.24	25.06	11.25	1.2

Table 5.8: Evolution of the integration error on the radial displacement, the deformation and the stress with a *homogeneous mesh*, at the inner radius  $r = r_1$ . Note that the error of the deformation and of the stress is  $O(10^i)$  when the error of the displacement is  $O(10^{i-1})$ . If an homogeneous mesh is assumed, the number of elements needed to obtain a ‘correct’ error is huge.

As a conclusion, homogeneous mesh does not seem adequate for axi-symmetric tests since the number of elements needed to obtain an accurate result is huge.

### 5.3.2.3 Mesh optimization

In order to optimise the number of elements for axi-symmetric tests and keeping in mind that the closer to the inner radius  $r = r_1$ , the higher the remainder, the mesh is refined ‘strongly’ at  $r = r_1$  and ‘loosely’ at  $r = r_2$ . In between, the refinement needs to be continuous to avoid additional numerical perturbations.

The following formula is proposed to calculate the ‘external’ radial coordinate  $r(n)$  of the element  $n$ , the maximum number of elements being equal to  $n_e$ ,

$$r(\mathbf{n}) - r_1 = f(\mathbf{n}) \times \frac{r_2 - r_1}{f(\mathbf{ne})}, \quad (5.81)$$

where the function  $f(\mathbf{n})$  is calculated by a home-made algorithm according to a logarithmic rule,

$$f(\mathbf{n}) = \frac{|r_2 - r_1|}{1.2^{\mathbf{ne} - \mathbf{n}}}. \quad (5.82)$$

As a conclusion, optimising the mesh by refining close to the inner radius appears to give out more accurate results *very close to*  $r = r_1$  than a homogeneous mesh (Table 5.9). However, this ‘home-made’ optimisation is not ideal: significant error remains along the layer *not so far from*  $r = r_1$ , see Figure 5.19.

Since mesh optimisation is not the first goal of this work, this ‘home-made’ optimisation is assumed sufficient to reproduce correctly the behaviour at the inner radius.

mesh criterion	0.1	0.05	0.02	0.002	
number of elements per meter	10	20	40	50	100
% error for $u_r$	11.13	0.3420	0.2091	0.2090	0.2087
% error for $\epsilon_r$	61.46	9.445	0.1671	0.0772	0.0643
% error for $\sigma_r$	47.32	5.958	0.0583	0.0083	0.0000

Table 5.9: Evolution of the integration error on the radial displacement, the deformation and on the stress with an *non-homogeneous mesh*, at the inner radius  $r = r_1$ . The error on the displacement remains greater or equal to 0.209. This result is probably due to the remaining error along the layer, see Figure 5.19. On the other hand, the accuracy of the strain and of the stress becomes acceptable at the inner radius for 50 elements or more.



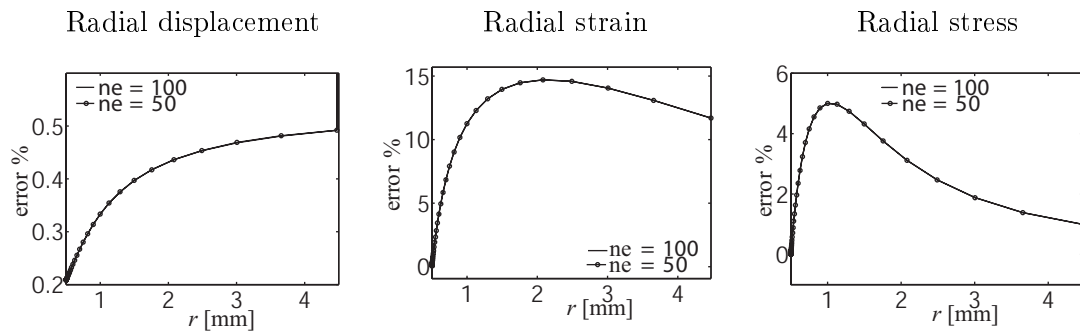


Figure 5.19: Profile of the error along the  $r$ -direction for the radial displacement, the strain and the stress. Note that with a non-homogeneous mesh, refined at the inner radius  $r_1 = 0.5$  mm (on the left-hand-side), the maximum error is not located at  $r/r_1 = 0$  mm. For the displacement, the maximum error is located at  $r = r_2$ . For the strain, the maximum error is located around  $r = 2$  mm. Finally, for the stress, the maximum error is located in the range  $1 < r < 1.5$  mm.

## Chapter 6

# A borehole stability analysis: focus on diffusion and mass transfer

The work presented in this chapter<sup>1</sup> has been submitted to the *International Journal of Rock Mechanics and Mining Sciences* under the title *Diffusion and Mass Transfer in Thermo-poro-elastic Dual Porous Media: A borehole stability analysis*, by the following authors, in order, Rachel Gelet, Benjamin Loret and Nasser Khalili. The paper has been accepted with minor revisions.

The motivation of this first publication is to address a borehole stability problem of a fractured reservoir in a thermally enhanced oil recovery context. Importantly, forced convection is disregarded in this chapter, and diffusion and mass transfer phenomena are considered alone.

The problem of diffusion and mass transfer in dual porous media is considered in a three-phase framework. The solid phase is assumed to contain two distinct cavities filled with fluid. The porous mixture is composed of two overlapping media: the porous blocks and the fissure network. The fluid can transfer between the cavities due to fluid pressure difference. In addition, hydraulic and thermal diffusions take place through the mixture.

The key idea of this study highlights the importance of the difference between the characteristic times of the diffusion phenomena. This work stems from the conclusions drawn by McTigue (1986) detailed in Section 5.2. Specific to dual porous media, the ratio of hydraulic to thermal diffusivity is greater in the fissure network than in the porous block. This particular feature, along with the assumption that the solid phase only is controlling the deformation of the overall mixture (see Remark 2.13, p. 117), rules the behaviour of fractured media when convection is neglected.

The main conclusions of this study reveal the importance of the dual porosity concept for the prediction for failure in fissured reservoirs; since the single porosity approach under-

---

<sup>1</sup>The Remarks were not presented for publication

estimates the failure potential. Due to the absence of confrontation with experimental data, this conclusion remains a strong hypothesis; however such data to the best knowledge of the author and to date remains unavailable.

Section 6.1 introduces the background literature and defines the problem statement. A global understanding of mass transfer, diffusion and deformation is provided. The governing equations associated with these phenomena are presented for a mixture in thermal equilibrium (Section 6.2). The finite element approximation of the governing equations is formulated (Section 6.3) and applied to the stability analysis of a vertical borehole (Section 6.4). A parametric analysis is carried out to evaluate the influence of mass transfer on the pressure profiles of the fluids around the borehole (Section 6.5). Permeable and semi-permeable boundary conditions are compared to predict the potential for failure of the wellbore under drained and partially drained conditions. Finally, the main points of the paper are gathered in Section 6.6.

## 6.1 Introduction

The influence of thermal loading on the behavior of fractured poro-elastic media is relevant to various applications, such as enhanced heavy-oil recovery by steam or hot water injection, thermal and hydraulic stimulations of tight reservoirs, management of nuclear waste disposal in a clay buffer, and geothermal hot dry rock energy extraction. In all these applications, a borehole or a tunnel is required and the stability analysis forms a crucial part of the design (Lake et al., 1992).

Currently borehole stability analyses under thermal loading are scarce and focus mainly on reservoirs represented by saturated rocks with a single porosity (McTigue, 1990, 1986; Wang and Papamichos, 1994; Chen et al., 1997; Chen and Ewy, 2005; Rahman et al., 2000; Zhang et al., 2003; Chen et al., 2003; Abousleiman and Ekbote, 2005; Wang and Dusseault, 2003; Pao et al., 2001). A key factor influencing wellbore stability is the variation of pore pressure on the lining of the wellbore due to mud penetration (Chen et al., 1997; Chen and Ewy, 2005; Rahman et al., 2000). Failure typically occurs when the pore pressure reduces the effective confining pressure below a threshold value (Zhang et al., 2003; Chen et al., 2003).

Closed form solutions for thermally induced fluid flow around a borehole in low permeability media have been presented by a number of investigators, where heat transfer is dominated by conduction (McTigue, 1990, 1986; Wang and Papamichos, 1994; Chen and Ewy, 2005). McTigue (1990, 1986) provided analytical results for the thermoelastic response of saturated porous rocks with a single porosity, highlighting the importance of the

thermal to hydraulic diffusivity ratio and the competition between the heat and the fluid flows. Wang and Papamichos (1994) examined the thermally induced pore fluid pressure around a pumping well for both cold and warm injection processes, underlying the importance of the thermal coupling to accurately estimate the induced fluid flow rate in low permeability media. Chen and Ewy (2005) investigated the thermoporoelastic effect on wellbore stability and analyzed the collapse failure index in the region near the wellbore. Notable contributions have also been made by Abousleiman and Ekbote (2005), Wang and Dusseault (2003) and Pao et al. (2001) on the effects of anisotropy, conductive *versus* convective heat flow, and multi-phase flow on borehole instability.

Based on Biot's theory of mixture (Biot, 1941), thermo-hydro-mechanical models have been extended to account for the dual porosity concept introduced by Barenblatt et al. (1960). However, the existing literature focuses on consolidation (Masters et al., 2000) or on the dominance of convection over conduction phenomena (Khalili and Selvadurai, 2003; Nair et al., 2004). Nair et al. (2004, 2002) presented results on the sensitivity of the thermoelastic response in dual porosity media to fracture spacing, but based on several restrictions. In particular, the deformation field in their dual porosity model was formulated by assigning each cavity system with its own effective stress, deformation and overall compliance, in contradiction of the principle of effective stress where a single stress entity is defined for the entire solid skeleton (Khalili and Valliappan, 1996; Loret and Khalili, 2000b; Khalili and Loret, 2001; Khalili, 2008). Furthermore, in their approach, to define the effective stress parameters the deformation fields of pore and fracture systems are assumed to work in series which may not be applicable in real rocks.

The paper presents a fully coupled finite element formulation for a thermo-poro-elastic dual porous medium under non-isothermal conditions. The fractured porous medium is described as a porous mixture composed of two overlapping continua: the porous blocks and the fissure network. The solid phase has a special role as it provides the matrix skeleton and encloses the fluid phases. The theoretical model of the three-phase mixture is built by postulating constitutive equations for the three phases and by enforcing the balances of mass, momentum and energy. A summary of the governing differential equations is provided in Section 6.2. The formulation presented is specified for a local thermal equilibrium between the phases, saturated soils and for diffusion dominated fluxes (Loret and Khalili, 2000a; Khalili and Selvadurai, 2003). The weak form of the governing equations and the time-integration procedure to solve the coupled equations through a finite element method are detailed in Section 6.3. The primary variables are the displacements, the pore fluid pressure, the pressure of the fluid in the fissures and the temperature of the mixture. The resulting system of equations is used to address the failure potential of a vertical borehole

subjected to both pressure and temperature gradients (Section 6.4). Simulations of heavy-oil recovery through thermal stimulation demonstrate the influences of the dual porosity approach and of the boundary conditions on the borehole stability (Section 6.5). In addition to the stability issue, the study focuses on mass transfer between the pore matrix and the fissure network; and on the difference in diffusivity ratios between the two cavities.

*Notation:* Vector and matrix quantities are identified by boldface letters, for example  $\boldsymbol{\sigma}$  is the total stress.  $\mathbf{I}$  is the identity matrix.  $\text{tr}$ ,  $\nabla(\cdot)$  and  $\text{div}$  denote respectively the trace, the gradient and the divergence operators.

## 6.2 Governing equations

Within a dual porosity conceptual framework (Khalili and Valliappan, 1996; Khalili and Selvadurai, 2003), differential equations describing the deformation, hydraulic and heat flows, and mass transfer through deformable fissured porous media may be expressed as (the convention of summation over repeated mute indices  $i$  and  $j$  is used),

$$\begin{aligned}
\mu \frac{\partial^2 u_i}{\partial x_j \partial x_j} + (\lambda + \mu) \frac{\partial^2 u_j}{\partial x_i \partial x_j} - \xi_p \frac{\partial p_p}{\partial x_i} - \xi_f \frac{\partial p_f}{\partial x_i} - \frac{c_T}{c} \frac{\partial T}{\partial x_i} + F_i &= 0 \\
\frac{\partial}{\partial x_i} \left( \frac{k_p}{\mu_p} \frac{\partial p_p}{\partial x_i} \right) &= a_{pp} \frac{\partial p_p}{\partial t} + a_{pf} \frac{\partial p_f}{\partial t} + \xi_p \frac{\partial^2 u_i}{\partial t \partial x_i} + a_{pT} \frac{\partial T}{\partial t} + \Gamma \\
\frac{\partial}{\partial x_i} \left( \frac{k_f}{\mu_f} \frac{\partial p_f}{\partial x_i} \right) &= a_{ff} \frac{\partial p_f}{\partial t} + a_{pf} \frac{\partial p_p}{\partial t} + \xi_f \frac{\partial^2 u_i}{\partial t \partial x_i} + a_{fT} \frac{\partial T}{\partial t} - \Gamma \\
\frac{\partial}{\partial x_i} \left( \Lambda \frac{\partial T}{\partial x_i} \right) &= T \left( a_{pT} \frac{\partial p_p}{\partial t} + a_{fT} \frac{\partial p_f}{\partial t} + \frac{c_T}{c} \frac{\partial^2 u_i}{\partial t \partial x_i} \right) + a_{TT} \frac{\partial T}{\partial t}
\end{aligned} \tag{6.1}$$

in which,

$$\begin{aligned}
\xi_p &= (c_p - c_s)/c, & \xi_f &= 1 - c_p/c \\
a_{pp} &= n_p c_{H,p} + (\xi_p - n_p) c_s - a_{pf}, & a_{pf} &= -(\xi_f - n_f)(c_p - c_s) \\
a_{ff} &= n_f c_{H,f} + (\xi_f - n_f) c_s - a_{pf}, & a_{pT} &= (n_p - \xi_p) c_T - n_p c_{T,p} \\
a_{fT} &= (n_f - \xi_f) c_T - n_f c_{T,f}, & a_{TT} &= \rho C_p, \\
\Gamma &= \eta (p_p - p_f), & \eta &= \bar{\alpha} k_p / \mu_p, \\
\bar{\alpha} &= 4n(n+2)/l^2 \quad \text{with } n = 1, 2, 3,
\end{aligned} \tag{6.2}$$

where  $u_i$  is the displacement of the solid phase,  $p_p$  is the pressure of the pore fluid,  $p_f$  is the pressure of the fissure fluid and the temperature of the mixture, which is in thermal equilibrium, is denoted  $T$ . The subscripts  $s$ ,  $p$ ,  $f$  refer to the solid skeleton, the pore fluid and the fissure fluid, respectively.

Equation (6.1)<sub>1</sub> uses the Lamé constants of the drained solid  $\lambda$  and  $\mu$ , the body force vector  $F_i$ , the compressibility of the mixture  $c$ , the compressibility of the porous blocks  $c_p$ ,

the compressibility of the solid grains  $c_s$ , and the volumetric thermal expansion coefficient of the solid phase  $c_T$ . Equations (6.1)<sub>2,3</sub> require for each fluid  $k = p, f$  the macroscopic porosity  $n_k$ , the macroscopic intrinsic permeability  $k_k$ , and the dynamic viscosity  $\mu_k$ . The hydraulic compressibility  $c_{H,k}$  and the thermal compressibility  $c_{T,k}$  are defined in eq. (6.11) from the intrinsic density  $\rho_k$  of the fluid  $k$ . A linear mass transfer function  $\Gamma = \eta(p_p - p_f)$  defining the exchange of fluid between the porous blocks and the fissure network is adopted (Barenblatt et al., 1960; Warren and Root, 1963).  $\eta$  is the leakage parameter defined by Warren and Root (1963) through the factor  $\bar{\alpha}$  as a function of the average fissure spacing  $l$  and the number of normal sets of fissures  $n$ . While the linear transfer function is easily amenable to computational implementation and consistent with a thermodynamic analysis, leading to positive dissipation, it is also known to be inaccurate at early times. The non linear Vermeulen scheme has been adopted by Zimmerman et al. (1993) in the analysis of fractured geothermal reservoirs where, at each point of the fracture continuum, a porous block of spherical shape is attached: the fluid diffuses in the block and the net flow through its boundary is viewed as a source/sink term for the fracture continuum. Lu and Connell (2007) have devised a one-dimensional semi-analytical scheme that provides the time course of the transferred mass in a gas reservoir. At early times, while the rate of mass transfer in their model tends to vanish, it tends to a constant for the linear transfer scheme and to infinity for the Vermeulen scheme. Correspondingly, the mass transferred depends linearly on time in the linear transfer scheme, but on the square root of time in the schemes of Vermeulen and Lu and Connell, albeit with distinct scaling factors.

Equation (6.1)<sub>4</sub> involves the overall heat capacity at constant strain and fluid pressure  $C_p$ , the overall density  $\rho$ , and the overall thermal conductivity  $\Lambda$ .

Equations (6.1) are direct consequences of the field equations (balance of momentum for the mixture, balance of mass for each fluid phase, balance of energy for the mixture),

$$-\operatorname{div} \boldsymbol{\sigma} = \mathbf{F}, \quad (6.3)$$

$$-\operatorname{div} \mathbf{J}_k = n_k \frac{1}{\rho_k} \frac{d^k \rho_k}{dt} + \frac{1}{V} \frac{dV_k}{dt} - \frac{\hat{\rho}_{tr}^k}{\rho_k}, \quad k = p, f, \quad (6.4)$$

$$-\operatorname{div} \mathbf{q} = T \frac{d(\rho S)}{dt}, \quad (6.5)$$

where  $\boldsymbol{\sigma}$  is the total stress,  $\mathbf{F}$  is the body force vector,  $\mathbf{J}_k$  is the flux of the fluid  $k$  and  $\mathbf{q}$  is the heat flux of the mixture. The term  $\hat{\rho}_{tr}^k$  represents the mass supply to the cavity  $k$  by the other cavity.

The initial configuration, which is taken as a reference, represents a state in equilibrium in which stress, strain, pressures and temperature can be non-zero. Departure from this reference state is denoted  $\Delta(\cdot)$ . The shear behavior is accounted for, fully, by the shear modulus  $\mu$  of the drained solid skeleton eq. (6.41). The fluid does not react to shear

stresses. The associated relationship links the elastic strain  $\epsilon^{el}$  to the effective stress  $\bar{\sigma}$ ,

$$\text{tr} \epsilon^{el} = c \frac{\text{tr} \bar{\sigma}}{3}, \quad \text{dev} \epsilon^{el} = \frac{\text{dev} \bar{\sigma}}{2\mu} \quad (6.6)$$

in which the deviatoric parts of the elastic strain and of the effective stress are denoted  $\text{dev} \epsilon^{el}$  and  $\text{dev} \bar{\sigma}$ , respectively. The thermo-mechanical constitutive matrix relates the isotropic part of the total stress  $\text{tr} \sigma/3$ , the volume variations of the fluids  $\Delta V_p/V$  and  $\Delta V_f/V$ , and the entropy variation of the solid  $\Delta(\rho^s S_s)$  to the isotropic part of the total strain  $\text{tr} \epsilon$ , the fluid pressures  $p_p, p_f$  and the overall temperature variation  $\Delta T = T - T^0$  from the initial temperature  $T^0$  by,

$$\begin{bmatrix} -\text{tr} \sigma/3 \\ \Delta V_p/V \\ \Delta V_f/V \\ \Delta(\rho^s S_s) \end{bmatrix} = \begin{bmatrix} -1/c & \xi_p & \xi_f & c_T/c \\ \xi_p & a_{pp} - n_p c_{H,p} & a_{pf} & (n_p - \xi_p) c_T \\ \xi_f & a_{pf} & a_{ff} - n_f c_{H,f} & (n_f - \xi_f) c_T \\ c_T/c & (n_p - \xi_p) c_T & (n_f - \xi_f) c_T & \rho^s C_{p,s}/T \end{bmatrix} \begin{bmatrix} \text{tr} \epsilon \\ p_p \\ p_f \\ \Delta T \end{bmatrix} \quad (6.7)$$

in which  $\rho^s$  is the apparent density of the solid equal to  $n_s \rho_s$ ,  $S_s$  is the intrinsic entropy of the solid per unit mass [ $\text{m}^2/\text{s}^2$ ] and  $C_{p,s}$  is the intrinsic heat capacity of the solid, at constant strain and fluid pressure [ $\text{J}/\text{kg.K}$ ].  $\xi_p$  and  $\xi_f$  are the effective stress parameters, which define the hydro-mechanical coupling and  $a_{pf}$  is the coupling term ensuring compatibility of deformation between the two pore systems (Khalili, 2003). The apparent entropy variation of the generic fluid  $k$  is expressed separately as,

$$\Delta(\rho^k S_k) = -n_k c_{T,k} p_k + \rho^k \frac{C_{p,k}}{T} \Delta T, \quad k = p, f. \quad (6.8)$$

By summing the contributions of the three phases, the entropy variation for the mixture introduces the heat capacity of the porous medium  $\rho C_p = \rho^s C_{p,s} + \rho^p C_{p,p} + \rho^f C_{p,f}$ ,

$$\Delta(\rho S) = \frac{c_T}{c} \text{tr} \epsilon + a_{pT} p_p + a_{fT} p_f + \frac{\rho C_p}{T} \Delta T. \quad (6.9)$$

The density of the thermo-barotropic fluid  $k$  varies with its pressure and temperature,

$$\frac{1}{\rho_k} \frac{d^k \rho_k}{dt} = c_{H,k} \frac{d^k p_k}{dt} - c_{T,k} \frac{d^k T}{dt}, \quad k = p, f, \quad (6.10)$$

in which the compressibility  $c_{H,k}$  and the thermal expansion  $c_{T,k}$  are defined as,

$$c_{H,k} = \frac{1}{\rho_k} \left. \frac{d^k \rho_k}{dp_k} \right|_{T_k}, \quad c_{T,k} = -\frac{1}{\rho_k} \left. \frac{d^k \rho_k}{dT} \right|_{p_k}, \quad k = p, f. \quad (6.11)$$

The diffusion constitutive relations are described by uncoupled Darcy's law and Fourier's law,

$$\mathbf{J}_k = -\frac{k_k}{\mu_k} \nabla p_k, \quad k = p, f; \quad \mathbf{q} = -\Lambda \nabla T, \quad (6.12)$$

while the mass transfer uses Barenblatt's quasi-steady relationship (Barenblatt et al., 1960),

$$\hat{\rho}_{tr}^k = (-1)^\alpha \rho_0 \eta (p_p - p_f), \quad (6.13)$$

in which  $\eta$  is the leakage parameter, which controls the mass transfer due to the fluid pressure difference between the two cavities, and  $\alpha = 1$  for  $k = p$ ,  $\alpha = 2$  for  $k = f$ .

This thermo-hydro-mechanical model derives from an effective stress concept, eq. (6.7)<sub>1</sub>,

$$\frac{\text{tr} \boldsymbol{\sigma}}{3} + \xi_p p_p + \xi_f p_f = \frac{\text{tr} \boldsymbol{\epsilon}}{c} - \frac{c_T}{c} \Delta T, \quad (6.14)$$

and accounts for hydraulic fluxes within the two cavities, overall heat flux and fluid exchanges between the two cavities. This model neglects convective effects, the gravity force and the coupled diffusive terms between the hydraulic fluxes and the heat flux. Additional information on the parameters of the model can be found in previous works Khalili and Valliappan (1996), Khalili et al. (1999) and Khalili and Selvadurai (2003).

### 6.3 Finite element formulation

A mixed finite element formulation is developed in which the primary unknowns are the displacements  $\mathbf{u}$ , the pore pressure  $p_p$ , the pressure of the fissure fluid  $p_f$  and the temperature of the porous medium  $T$ . To compact the finite element formulation, it is instrumental to introduce the functions  $f_p$ ,  $f_f$  and  $f_T$  defined as,

$$\begin{aligned} f_p &= a_{pp} \dot{p}_p + a_{pf} \dot{p}_f + a_{pT} \dot{T} + \xi_p \text{div} \dot{\mathbf{u}} + \eta (p_p - p_f), \\ f_f &= a_{fp} \dot{p}_p + a_{ff} \dot{p}_f + a_{fT} \dot{T} + \xi_f \text{div} \dot{\mathbf{u}} - \eta (p_p - p_f), \\ f_T &= T a_{pT} \dot{p}_p + T a_{fT} \dot{p}_f + a_{TT} \dot{T} + T \frac{c_T}{c} \text{div} \dot{\mathbf{u}}, \end{aligned} \quad (6.15)$$

in which the super-imposed dot indicates a partial time derivative.

#### 6.3.1 The semi-discrete equations

Multiplying the field equations by the virtual fields  $\delta \mathbf{u}$ ,  $\delta p$  and  $\delta T$  and integrating by parts over the body  $V$  provides the weak form of the problem, for  $k = p, f$ ,

$$\begin{aligned} - \int_V \nabla(\delta \mathbf{u}) : \boldsymbol{\sigma} dV + \int_V \delta \mathbf{u} \cdot \mathbf{F} dV &= - \int_{\partial V} \delta \mathbf{u} \cdot \boldsymbol{\sigma} \cdot \hat{\mathbf{n}} dS, \\ - \int_V \nabla(\delta p) \cdot \mathbf{J}_k dV + \int_V \delta p f_k dV &= - \int_{\partial V} \delta p \mathbf{J}_k \cdot \hat{\mathbf{n}} dS, \\ - \int_V \nabla(\delta T) \cdot \mathbf{q} dV + \int_V \delta T f_T dV &= - \int_{\partial V} \delta T \mathbf{q} \cdot \hat{\mathbf{n}} dS, \end{aligned} \quad (6.16)$$



where  $\hat{\mathbf{n}}$  is the unit outward normal to the boundary  $\partial V$ . A generalized Galerkin procedure is adopted and the same interpolation functions are used for the primary unknowns and for the variations. The primary unknowns are interpolated, within the generic element  $e$ , in terms of nodal values through the interpolation functions  $\mathbf{N}_{\mathbf{u}}$ ,  $\mathbf{N}_{\mathbf{p}}$ ,  $\mathbf{N}_{\mathbf{T}}$ , respectively,

$$\mathbf{u} = \mathbf{N}_{\mathbf{u}} \mathbf{u}^e; \quad p_k = \mathbf{N}_{\mathbf{p}} \mathbf{p}_k^e, \quad \text{for } k = p, f; \quad T = \mathbf{N}_{\mathbf{T}} T^e. \quad (6.17)$$

The surface loading contributions of a generic element  $e$  are gathered into the vector  $\mathbb{F}_e^{\text{surf}}$  and the internal thermo-poro-elastic contributions into the vector  $\mathbb{F}_e^{\text{int}}$ . The element contributions to the force vectors (6.16) are equal to  $\mathbb{F}_e^{\text{int}} - \mathbb{F}_e^{\text{surf}}$ ,

$$\begin{bmatrix} \int_{V^e} (\mathbf{B}_{\mathbf{u}})^T \boldsymbol{\sigma} - (\mathbf{N}_{\mathbf{u}})^T \mathbf{F} dV^e \\ \int_{V^e} (\nabla \mathbf{N}_{\mathbf{p}})^T \mathbf{J}_p - (\mathbf{N}_{\mathbf{p}})^T f_p dV^e \\ \int_{V^e} (\nabla \mathbf{N}_{\mathbf{p}})^T \mathbf{J}_f - (\mathbf{N}_{\mathbf{p}})^T f_f dV^e \\ \int_{V^e} (\nabla \mathbf{N}_{\mathbf{T}})^T \mathbf{q} - (\mathbf{N}_{\mathbf{T}})^T f_T dV^e \end{bmatrix} - \begin{bmatrix} \int_{\partial V^e} (\mathbf{N}_{\mathbf{u}})^T \boldsymbol{\sigma} \cdot \hat{\mathbf{n}} dS^e \\ \int_{\partial V^e} (\mathbf{N}_{\mathbf{p}})^T \mathbf{J}_p \cdot \hat{\mathbf{n}} dS^e \\ \int_{\partial V^e} (\mathbf{N}_{\mathbf{p}})^T \mathbf{J}_f \cdot \hat{\mathbf{n}} dS^e \\ \int_{\partial V^e} (\mathbf{N}_{\mathbf{T}})^T \mathbf{q} \cdot \hat{\mathbf{n}} dS^e \end{bmatrix}, \quad (6.18)$$

where  $\mathbf{B}_{\mathbf{u}}$  is the standard strain-displacement matrix,  $\boldsymbol{\epsilon} = \mathbf{B}_{\mathbf{u}} \mathbf{u}^e$ . Inserting the total stress (6.7)<sub>1</sub> and the hydraulic and thermal fluxes (6.12) in (6.18) yields a non-linear system of equations including

- an element contribution to the balance of momentum for the mixture,

$$\mathbf{E}_{\mathbf{uu}}^e \mathbf{u}^e - \mathbf{C}_{\mathbf{up}}^e (\xi_p \mathbf{p}_p^e + \xi_f \mathbf{p}_f^e) - \frac{cT}{c} \mathbf{C}_{\mathbf{uT}}^e T^e - \mathbf{R}_{\mathbf{u}}^e, \quad (6.19)$$

- an element contribution to the balance of mass for the pore fluid,

$$\begin{aligned} & - \left[ \mathbf{J}_{\mathbf{k}_p}^e + \eta \mathbf{M}_{\mathbf{pp}}^e \right] \mathbf{p}_p^e + \eta \mathbf{M}_{\mathbf{pp}}^e \mathbf{p}_f^e \\ & - \mathbf{M}_{\mathbf{pp}}^e (a_{pp} \dot{\mathbf{p}}_p^e + a_{pf} \dot{\mathbf{p}}_f^e) - \mathbf{M}_{\mathbf{pT}}^e a_{pT} \dot{T}^e - \xi_p \mathbf{C}_{\mathbf{pu}}^e \dot{\mathbf{u}}^e - \mathbf{R}_{\mathbf{pp}}^e, \end{aligned} \quad (6.20)$$

- an element contribution to the balance of mass for the fissure fluid,

$$\begin{aligned} & - \left[ \mathbf{J}_{\mathbf{k}_f}^e + \eta \mathbf{M}_{\mathbf{pp}}^e \right] \mathbf{p}_f^e + \eta \mathbf{M}_{\mathbf{pp}}^e \mathbf{p}_p^e \\ & - \mathbf{M}_{\mathbf{pp}}^e (a_{ff} \dot{\mathbf{p}}_f^e + a_{pf} \dot{\mathbf{p}}_p^e) - \mathbf{M}_{\mathbf{pT}}^e a_{fT} \dot{T}^e - \xi_f \mathbf{C}_{\mathbf{pu}}^e \dot{\mathbf{u}}^e - \mathbf{R}_{\mathbf{pf}}^e, \end{aligned} \quad (6.21)$$

- an element contribution to the balance of energy for the mixture,

$$- \mathbf{Q}_{\Lambda}^e T^e - \mathbf{M}_{\mathbf{pT}}^{eT} T (a_{pT} \dot{\mathbf{p}}_p^e + a_{fT} \dot{\mathbf{p}}_f^e) - a_{TT} \mathbf{M}_{\mathbf{T}\mathbf{T}}^e \dot{T}^e - T \frac{cT}{c} \mathbf{C}_{\mathbf{Tu}}^e \dot{\mathbf{u}}^e - \mathbf{R}_{\mathbf{T}}^e. \quad (6.22)$$

Details of the element force vectors and matrices are provided in Appendix F.1. The contribution of the element  $e$  to the global set of equations may be cast in a matrix format,

$$\mathbb{K}^e \mathbb{X}^e + \mathbb{D}^e \left( \frac{d\mathbb{X}^e}{dt} \right) - \mathbb{F}^e. \quad (6.23)$$

Here  $\mathbb{K}^e$  is the element stiffness matrix and  $\mathbb{D}^e$  the element diffusion matrix,

$$\mathbb{K}^e = \begin{bmatrix} \mathbf{K}_{\mathbf{u}\mathbf{u}}^e & \mathbf{K}_{\mathbf{u}\mathbf{p}_p}^e & \mathbf{K}_{\mathbf{u}\mathbf{p}_f}^e & \mathbf{K}_{\mathbf{u}\mathbf{T}}^e \\ \mathbf{0} & \mathbf{K}_{\mathbf{p}_p\mathbf{p}_p}^e & \mathbf{K}_{\mathbf{p}_p\mathbf{p}_f}^e & \mathbf{0} \\ \mathbf{0} & \mathbf{K}_{\mathbf{p}_f\mathbf{p}_p}^e & \mathbf{K}_{\mathbf{p}_f\mathbf{p}_f}^e & \mathbf{0} \\ \mathbf{0} & \mathbf{0} & \mathbf{0} & \mathbf{K}_{\mathbf{T}\mathbf{T}}^e \end{bmatrix}, \quad (6.24)$$

$$\mathbb{D}^e = \begin{bmatrix} \mathbf{0} & \mathbf{0} & \mathbf{0} & \mathbf{0} \\ \mathbf{D}_{\mathbf{p}_p\mathbf{u}}^e & \mathbf{D}_{\mathbf{p}_p\mathbf{p}_p}^e & \mathbf{D}_{\mathbf{p}_p\mathbf{p}_f}^e & \mathbf{D}_{\mathbf{p}_p\mathbf{T}}^e \\ \mathbf{D}_{\mathbf{p}_f\mathbf{u}}^e & \mathbf{D}_{\mathbf{p}_f\mathbf{p}_p}^e & \mathbf{D}_{\mathbf{p}_f\mathbf{p}_f}^e & \mathbf{D}_{\mathbf{p}_f\mathbf{T}}^e \\ \mathbf{D}_{\mathbf{T}\mathbf{u}}^e & \mathbf{D}_{\mathbf{T}\mathbf{p}_p}^e & \mathbf{D}_{\mathbf{T}\mathbf{p}_f}^e & \mathbf{D}_{\mathbf{T}\mathbf{T}}^e \end{bmatrix}; \quad (6.25)$$

while  $\mathbb{F}^e$  is the element load vector, and  $\mathbb{X}^e$  the element unknown vector,

$$\mathbb{F}^e = [\mathbf{R}_{\mathbf{u}}^e \quad \mathbf{R}_{\mathbf{p}_p}^e \quad \mathbf{R}_{\mathbf{p}_f}^e \quad \mathbf{R}_{\mathbf{T}}^e]^T, \quad \mathbb{X}^e = [\mathbf{u}^e \quad \mathbf{p}_p^e \quad \mathbf{p}_f^e \quad \mathbf{T}^e]^T. \quad (6.26)$$

All sub-matrices of  $\mathbb{K}^e$  and  $\mathbb{D}^e$  are listed in Appendix F.2. The resulting global non-linear semi-discrete equations (6.18) for the unknown vector  $\mathbb{X}$  imply the residual  $\mathbb{R}$  to vanish,

$$\mathbb{R} = \mathbb{F}^{\text{surf}}(\mathbb{S}, \mathbb{X}) - \mathbb{F}^{\text{int}}\left(\mathbb{X}, \frac{d\mathbb{X}}{dt}\right) = 0, \quad (6.27)$$

in which  $\mathbb{F}^{\text{int}}$  is the vector of internal forces and  $\mathbb{F}^{\text{surf}}$  is the vector of surface loadings denoted collectively by  $\mathbb{S}$ .

### 6.3.2 Time integration

The semi-discrete equations are integrated through a generalized trapezoidal rule defined by a scalar  $\alpha \in ]0, 1]$ . At step  $n + 1$ , the equations are enforced at time  $t_{n+\alpha} = t_n + \alpha \Delta t$ , with  $\Delta t = t_{n+1} - t_n$ , namely

$$\mathbb{R}_{n+\alpha} = \mathbb{F}^{\text{surf}}(\mathbb{S}_{n+\alpha}, \mathbb{X}_{n+\alpha}) - \mathbb{F}^{\text{int}}(\mathbb{X}_{n+\alpha}, \mathbb{V}_{n+\alpha}) = 0. \quad (6.28)$$

In the above relation, we define  $\mathbb{Z} = \mathbb{S}, \mathbb{X}, \mathbb{V}$  as,

$$\mathbb{Z}_{n+\alpha} = (1 - \alpha)\mathbb{Z}_n + \alpha\mathbb{Z}_{n+1}, \quad (6.29)$$

and  $\mathbb{X}_{n+1}$  and  $\mathbb{V}_{n+1}$  are approximations of  $\mathbb{X}(t_{n+1})$  and  $(d\mathbb{X}/dt)(t_{n+1})$  respectively. The system (6.28) is solved iteratively by an explicit/implicit operator splitting, namely at iteration  $i + 1$ ,

$$\mathbb{R}_{n+\alpha}^{i+1} = \mathbb{F}_E^{\text{surf}}(\mathbb{S}_{n+\alpha}, \mathbb{X}_{n+\alpha}^i) - \mathbb{F}_I^{\text{int}}(\mathbb{X}_{n+\alpha}^{i+1}, \mathbb{V}_{n+\alpha}^{i+1}) = 0, \quad (6.30)$$

in which,

$$\begin{aligned}
i = 0 : & \quad \begin{cases} \mathbb{X}_{n+1}^0 = \mathbb{X}_n + (1 - \alpha)\Delta t \mathbb{V}_n \\ \mathbb{V}_{n+1}^0 = \mathbb{V}_n \end{cases} \\
\text{for } i \geq 0 : & \quad \begin{cases} \mathbb{X}_{n+1}^{i+1} = \mathbb{X}_n + \Delta t V_{n+\alpha}^{i+1} = \mathbb{X}_{n+1}^0 + \alpha \Delta t V_{n+1}^{i+1} \\ \quad \quad \quad = \tilde{\mathbb{X}}_{n+1}^i + \alpha \Delta t \Delta \mathbb{V} \\ \mathbb{V}_{n+1}^{i+1} = \mathbb{V}_{n+1}^i + \Delta \mathbb{V} \end{cases} \quad (6.31)
\end{aligned}$$

where  $\tilde{\mathbb{X}}_{n+1}^i$  is defined as the *predictor value* by,

$$i \geq 0 \quad : \quad \tilde{\mathbb{X}}_{n+1}^i = \mathbb{X}_{n+1}^0 + \alpha \Delta t \mathbb{V}_{n+1}^i \quad (= \mathbb{X}_{n+1}^i \text{ for } i > 0). \quad (6.32)$$

and,

$$\mathbb{X}_{n+\alpha}^{i(+1)} = (1 - \alpha)\mathbb{X}_n + \alpha\mathbb{X}_{n+1}^{i(+1)}, \quad \mathbb{V}_{n+\alpha}^{i+1} = (1 - \alpha)\mathbb{V}_n + \alpha\mathbb{V}_{n+1}^{i+1}. \quad (6.33)$$

The partitioning shown in the above equation (6.30) is motivated by two observations: 1. the dependence of the vector of external forces on the solution is weak; 2. the vector of internal forces depends linearly on the rate vector  $\mathbb{V}$  and non-linearly on the solution  $\mathbb{X}$ .

A number of authors, including McTigue (1986), Bear and Corapcioglu (1981) and Nair et al. (2004), have pointed out that the hydro-mechanical terms  $T a_{pT}$ ,  $T a_{fT}$  and  $T c_T/c$  can be neglected in the energy equation (6.22). Indeed, these coefficients may often be of a smaller magnitude than  $a_{TT}$ , particularly in geotechnical materials. The rates of the primary variables in the boundary value problems addressed here have typical magnitudes, namely  $\dot{p}_p = \dot{p}_f \approx O(10^4)$  [Pa/s],  $\dot{u} \approx O(10^{-6})$  [m/s] and  $\dot{T} \approx O(10)$  [K/s]. Therefore, by using Table 6.1,

$$\left. \begin{aligned} T a_{pT} \dot{p}_p &\approx O(10^1) \\ T a_{fT} \dot{p}_f &\approx O(10^0) \\ T c_T/c \text{tr}\dot{\epsilon} &\approx O(10^1) \end{aligned} \right\} \ll a_{TT} \dot{T} \approx O(10^5) \text{ [W/m}^3\text{]}. \quad (6.34)$$

Nevertheless, they are preserved in this formulation for the sake of generality.

The global iteration process uses the full Newton-Raphson procedure as described above. The equation system to be solved is obtained by insertion of the time-integrator (6.31)-(6.33) in the residual (6.30),

$$\mathbb{R}_{n+\alpha}^{i+1} = \mathbb{R}_{n+\alpha}^i - \mathbb{C}^* \alpha \Delta \mathbb{V} = 0 \quad \Leftrightarrow \quad \mathbb{C}^* (\alpha \Delta \mathbb{V}) = \mathbb{R}_{n+\alpha}^i, \quad (6.35)$$

in which the Newton direction  $\Delta \mathbb{V}$  is sought. The *effective diffusion matrix*  $\mathbb{C}^*$  can be expressed in terms of the global diffusion matrix  $\mathbb{D}$  and the global stiffness matrix  $\mathbb{K}$ ,

$$\mathbb{C}^* = \underbrace{\left( \frac{\partial \mathbb{F}_I^{\text{int}}}{\partial \mathbb{V}} \right)}_{\mathbb{D}} (\tilde{\mathbb{X}}_{n+\alpha}^i) + \underbrace{\left( \frac{\partial \mathbb{F}_I^{\text{int}}}{\partial \mathbb{X}} \right)}_{\mathbb{K}} (\tilde{\mathbb{X}}_{n+\alpha}^i) \alpha \Delta t, \quad (6.36)$$

where it has been recognized that the derivatives of  $\mathbb{F}_I^{\text{int}}$  depend linearly on  $\mathbb{V}$  so that the stiffness matrix  $\mathbb{K}$ , and the diffusion matrix  $\mathbb{D}$  do not depend on  $\mathbb{V}$  but only on  $\mathbb{X}$ .

The time step  $\Delta t$  is increased from 1 to 1000 s in order to keep the number of calculated times to a reasonable value. The time integration parameter  $\alpha$  is taken equal to  $2/3$  corresponding to the Galerkin method that provides unconditional stability and first order of accuracy, for linear problems and a single pass. Experience has shown that  $\alpha$  equal to  $2/3$  provides better stability than the Crank-Nicolson method,  $\alpha$  equal to  $1/2$ , in spite of the lower accuracy. With  $\alpha = 1/2$ , the profile of the solution displays some oscillations, particularly in the vicinity of the perturbation (Hughes, 1987a, p. 467). The four-node element (QUAD4) is used to interpolate all unknowns. The number of integration points is equal to two (in each spatial dimension), for all stiffness matrices and all residuals. The finite element code has been developed as part of this research.

## 6.4 Non-isothermal borehole stability analysis

The thermo-hydro-mechanical constitutive equations are now used to assess the stability of a borehole in a heavy-oil recovery context, i.e. a thermally stimulated reservoir.

To this end, a vertical wellbore drilled in a thermo-poro-elastic fractured medium is considered, see Figure 6.1. A unit thickness of the formation ( $h = 1$  m) is analyzed in which, the inner radius  $r_1$  is set to 0.1 m and the far-field radius  $r_2$  is set to 800 m to represent a boundary at a large distance.

We denote the initial (prior to drilling) pore and fissure pressures as  $p_p^0$  and  $p_f^0$ ; and the initial temperature as  $T^0$ . The fully saturated formation is located at a depth of 1000 m and is subjected to the following vertical gradients of *in-situ* stresses, fluid pressures and temperature,

$$\begin{aligned}\partial\sigma_z^0/\partial z &= -29.0 \text{ kPa/m}, \\ \partial\sigma_x^0/\partial z &= \partial\sigma_y^0/\partial z = -23.5 \text{ kPa/m}, \\ \partial p_p^0/\partial z &= \partial p_f^0/\partial z = 9.8 \text{ kPa/m}, \\ \partial T^0/\partial z &= 0.05 \text{ }^\circ\text{C /m}.\end{aligned}\tag{6.37}$$

The fractured reservoir is idealized as a dual porosity medium with the isotropic material properties presented in Table 6.1. Since both the loading conditions display symmetry about the vertical axis of the wellbore an axi-symmetric formulation is employed. To reduce computational time without loss of accuracy, a graded mesh is used and the size of the finite elements is increased along the radial direction (towards  $r_2$  in Figure 6.1) according to a logarithmic rule.

The cap rock on the top of the reservoir is considered to be rigid, constraining the vertical deformation of the reservoir. The initial vertical strain is obtained from equation

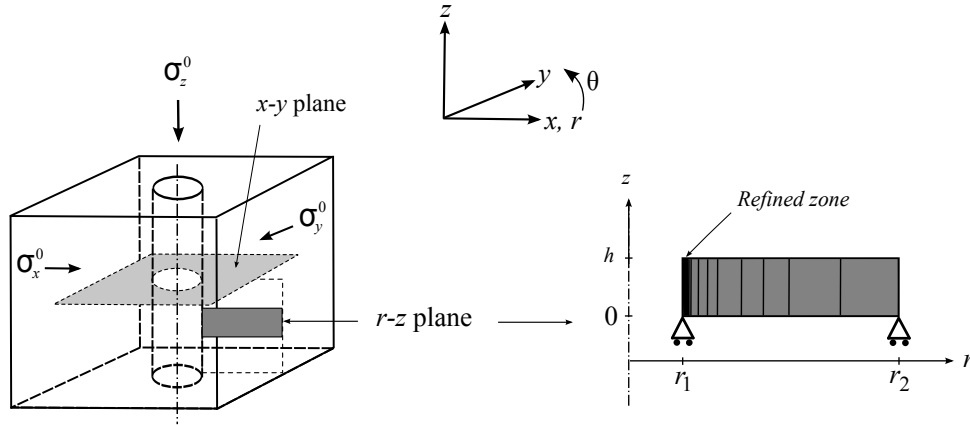


Figure 6.1: Schematic diagram of a vertical borehole subjected to *in-situ* stresses (left). 2D representation of the problem with an axis-symmetric mesh in the  $r$ - $z$  plane (right).

(6.7),

$$\epsilon_z^0 = -\frac{\nu}{E} (\sigma_x^0 + \sigma_y^0) + \frac{1}{E} \sigma_z^0 + \frac{c_p - c_s}{3} p_p^0 + \frac{c - c_p}{3} p_f^0 + \underbrace{\frac{c_T}{3} (T^0 - T^0)}_{= 0}, \quad (6.38)$$

which represents the deformation experienced by the reservoir prior to drilling.

Material parameter	Value	Unit	Ref.
Elastic modulus $E$	9.5	GPa	1
Poisson's ratio $\nu$	0.25	-	1
Bulk modulus of grains $K_s = 1/c_s$	10	GPa	1
Bulk moduli of the fluids $K_k = 1/c_{H,k}$	4.3	GPa	1
Viscosities of the fluids $\mu_p = \mu_f$	$10^{-3}$	Pa.s	1,2
Porous blocks porosity $n_p$	0.15	-	1,2
Porous blocks permeability $k_p$	$5 \times 10^{-20}$	$\text{m}^2$	1,2
Compressibility ratio $c_p/c$	0.9	-	3
Fissure network porosity $n_f$	$0.1 \times n_p$	-	3
Fissure network permeability $k_f$	$10 \times k_p$	$\text{m}^2$	3
Thermal conductivity of the porous medium $\lambda$	2.65	W/m.K	1
Volumetric thermal expansion of the porous medium $c_T$	$1.8 \times 10^{-5}$	1/K	1,2
Volumetric thermal expansion of the fluids $c_{T,p} = c_{T,f}$	$4.5 \times 10^{-4}$	1/K	4
Heat capacity of the porous medium $C_v$	837	J/kg.K	1,2
Density of the porous medium $\rho$	1980	$\text{kg}/\text{m}^3$	1,2

Table 6.1: Input parameters representative of a homogeneous isotropic dual porous medium. 1: Nair et al. (2002), 2: Nair et al. (2004) Gulf of Mexico Shale, 3: Wilson and Aifantis (1982) and 4: (Kestin, 1968, p. 541).

### 6.4.1 Boundary conditions

The boundary conditions at the far-field radius  $r = r_2$ , at the top  $z = h$  and at the bottom  $z = 0$  of the dual porous medium are presented in Table 6.2. To test the stability of the borehole, a constant mud pressure  $p_w = 12.0$  MPa is applied. The boundary conditions on the wellbore radius  $r = r_1$  are handled separately according to two distinct configurations.

$r = r_2$ $z \in [0, h]$	$r \in ]r_1, r_2[$ $z = h$ and $z = 0$
$\sigma_r(r_2, z) = \sigma_r^0$	$\epsilon_z(r, z) = \epsilon_z^0$
$p_p(r_2, z) = p_p^0$	$\mathbf{J}_p(r, z) = \mathbf{0}$
$p_f(r_2, z) = p_f^0$	$\mathbf{J}_f(r, z) = \mathbf{0}$
$T(r_2, z) = T^0$	$\mathbf{q}(r, z) = \mathbf{0}$

Table 6.2: Boundary conditions for a thermal recovery test with an axi-symmetric mesh in the  $r$ - $z$  plane.

Two types of conditions are envisaged at the dual-porosity wellbore wall  $r = r_1$ : a fully permeable boundary condition on both cavities and a semi-permeable boundary condition in which the porous blocks are sealed by the drilling mud cake and have zero outward flux.

a) Permeable boundary. The radial stress, the pressures of the fluid in the two cavities and the temperature are considered to be totally controlled at the wellbore, for any  $z \in [0, h]$ ,

$$\begin{aligned}
 \sigma_r(r_1, z) &= \sigma_r^0 H(-t) - p_w H(t), \\
 p_p(r_1, z) &= p_p^0 H(-t) + p_w H(t), \\
 p_f(r_1, z) &= p_f^0 H(-t) + p_w H(t), \\
 T(r_1, z) &= T^0 H(-t) + T_w H(t),
 \end{aligned} \tag{6.39}$$

where  $H(t)$  is the Heaviside step function (Figure 6.2).

b) Semi-permeable boundary. In this case a mud cake is formed on the borehole wall as the drilling mud infiltrates into the permeable medium. Therefore, a pore matrix endowed with low permeability can be sealed at the inlet by the mud cake. We term this boundary condition a semi-permeable boundary, since the sealing process is applied only to the porous blocks (Figure 6.2). The second relationship in (6.39) is therefore changed to,

$$\mathbf{J}_p(r_1, z) = \mathbf{0}. \tag{6.40}$$

The overall compressibility of the mixture  $c$  and the Lamé constants of the drained solid  $\lambda$  and  $\mu$ , are deduced from the Young's modulus  $E$  and Poisson's ratio  $\nu$  through the elastic relationships,

$$c = \frac{3(1 - 2\nu)}{E}, \quad \lambda = \frac{E\nu}{(1 + \nu)(1 - 2\nu)}, \quad \mu = \frac{E}{2(1 + \nu)}. \tag{6.41}$$

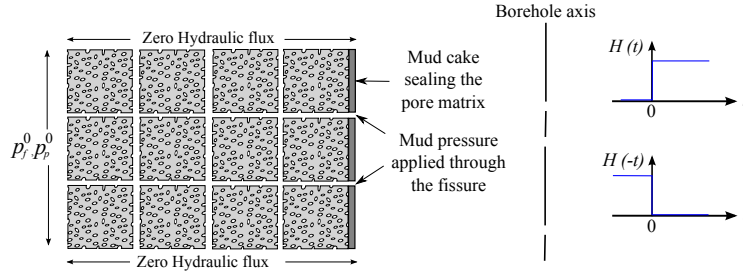


Figure 6.2: Sketch of a semi-permeable hydraulic boundary condition with zero flux at the porous blocks boundary.

### 6.4.2 Characteristic parameters

In a porous medium with a single porosity, the pressure response to a heating/cooling test is controlled by the *diffusivity ratio*  $R = \sqrt{\alpha_H/\alpha_T}$  of the hydraulic diffusivity  $\alpha_H$  over the thermal diffusivity  $\alpha_T$  defined by McTigue (1986),

$$\alpha_T = \frac{\Lambda}{\rho C_v}, \quad \alpha_H = \frac{k_p}{\mu_p} \frac{2\mu(1-\nu)}{1-2\nu} \frac{B^2(1+\nu_u)^2(1-2\nu)}{9(1-\nu_u)(\nu_u-\nu)}, \quad (6.42)$$

in which  $B$  is the Skempton coefficient and  $\nu_u$  is the undrained Poisson's ratio,

$$\frac{1}{B} = 1 + n_p \frac{c_{H,p} - c_s}{c - c_s}, \quad \nu_u = \frac{3\nu + B(1-2\nu)(1 - c_s/c)}{3 - B(1-2\nu)(1 - c_s/c)}. \quad (6.43)$$

In a dual porosity medium (2P), hydraulic diffusion takes place in two spatially separated cavities, and as such *two distinct diffusivity ratios* can be defined. For the porous blocks,  $R$  is typically smaller than one,  $R < 1$  with the thermal diffusion being faster than the hydraulic diffusion. Conversely, for the fissure network  $R$  is greater than one,  $R > 1$  in which the hydraulic flow is faster than the heat flow. Crucial to the understanding of the behavior is the fact that the porous blocks and the fissure network are endowed with opposite characteristics of diffusion dominance.

For the sake of comparison, the diffusivity ratio of the associated single porous medium (A1P) is also analyzed (Table 6.3). For this case, the overall porosity is defined as  $n_{A1P} = n_p + n_f$  and the overall permeability as  $k_{A1P} = k_p + k_f$ . This single porous medium is endowed with only one unknown pressure as the pressure equilibrium between the two pore systems is assumed to hold throughout. For the associated single porous medium (A1P), the thermal diffusivity front is behind the hydraulic diffusion front with  $R_{A1P} = 2.16$ , analogous to the fissure network characteristic.

In addition to the diffusivity ratios, the responses of the behavior of the dual porosity mixture are scrutinized with the help of two other characteristic parameters, namely, a characteristic time  $t^*$  and a characteristic leakage parameter  $\eta^*$ . Both parameters are defined with respect to a point of interest  $r_c \in ]r_1, r_2[$  in the vicinity of the borehole. This point, which defines the boundary of the failure zone, is chosen as equal to ten times the radius of the borehole,  $r_c = 1$  m.

Parameter	Pore matrix (2P)	(A1P)	Fissure network (2P)
Porosity, $n_k$ (-)	0.14	0.154	0.014
Permeability, $k_k$ (m <sup>2</sup> )	$5 \times 10^{-20}$	$5.5 \times 10^{-19}$	$5 \times 10^{-19}$
Hydraulic diffusivity, $\alpha_H$ (m <sup>2</sup> /s)	$6.97 \times 10^{-7}$	$7.48 \times 10^{-6}$	$9.06 \times 10^{-6}$
Thermal diffusivity, $\alpha_T$ (m <sup>2</sup> /s)	$1.6 \times 10^{-6}$	$1.6 \times 10^{-6}$	$1.6 \times 10^{-6}$
Diffusivity ratio, $R$ (-)	0.66 <	1 < 2.16	< 2.38

Table 6.3: Comparison between the diffusivity ratios  $R = \sqrt{\alpha_H/\alpha_T}$  of the porous blocks, of the fissure network as parts of dual porosity medium, and of the associated single porosity medium. Note that thermal diffusion is faster than hydraulic diffusion for the pore matrix (2P) while the opposite holds for fissure network (2P) and associated single porosity analysis (A1P).

A *characteristic time* defined as  $t^* = (r_c - r_1)^2/\alpha$  represents the time that is required for a diffusion front to reach the point of interest  $r_c$  in which  $\alpha$  is a diffusion parameter. For a region of length  $(r_c - r_1)$ , the diffusion time scale distinguishes the early time from the late time responses of the system. The analysis of thermo-hydro-mechanical loading in dual porous media highlights three characteristic times, namely, the end of hydraulic diffusion through the fissures  $8.17 \times 10^4$  s, second the end of thermal diffusion in the mixture  $5.07 \times 10^5$  s, and last the end of hydraulic diffusion through the pores  $1.4 \times 10^6$  s. We chose the characteristic time of the system to be the largest of those three characteristic times; therefore at  $t = t^*$ , all the diffusion fronts should have reached  $r_c$ .

The dimensionless *characteristic leakage parameter*  $\eta^*$  is expressed as in Khalili et al. (1999),

$$\eta^* = \eta \frac{\mu_p r_c^2}{k_p + k_f} \quad (6.44)$$

in which  $\mu_p = \mu_f$  due to thermal equilibrium. For an average fracture spacing  $l$  equal to 0.03 m, one set of fractures  $n = 1$  and the material parameters presented in Table 6.1, the *average characteristic leakage parameter* is equal to  $\eta_{av}^* = 1.1 \times 10^3$  from eq. (6.44).

## 6.5 Thermal effects on dual porous media

Numerical results of thermal effects in a fractured reservoir (Table 6.1) are now presented in the vicinity of the borehole. Two sensitivity analyses are carried out: The influences of the temperature loading  $\Delta T = T_w - T^0$  and of the leakage parameter  $\eta$  on the pressure and stress responses of the system are examined. The variation with time of the effective stresses around the borehole are scrutinized and a stability analysis is conducted at the most unfavorable time.

Results are presented from Figures 6.3 to 6.10 and a continuum mechanics convention is used with compressive stresses taken as negative.



### 6.5.1 Influence of temperature

The effect of thermal loading on a single porosity model has been analyzed by McTigue (1986) who provides analytical responses to a half-plane subjected either to a jump of heat flux or to a jump of temperature. These analytical responses have been used to examine the response of the finite element code in the particular case of a single porosity model.

In what follows, the effect of temperature on a fractured medium is presented and the features of the dual porosity approach are compared with a classic single porosity model. Both heating and cooling tests are performed; the difference between the temperature of the fluid at the wellbore  $T_w$  and the temperature of the *in-situ* fluid  $T^0$  is successively set to  $+50^\circ\text{C}$ ,  $-50^\circ\text{C}$  and  $0^\circ\text{C}$ . The leakage parameter is set equal to the average leakage parameter  $\eta^* = \eta_{av}^*$ . The results are presented for  $t = 80\text{ s}$ , which corresponds to an early time response of the system and where the difference between the three loadings is the largest.

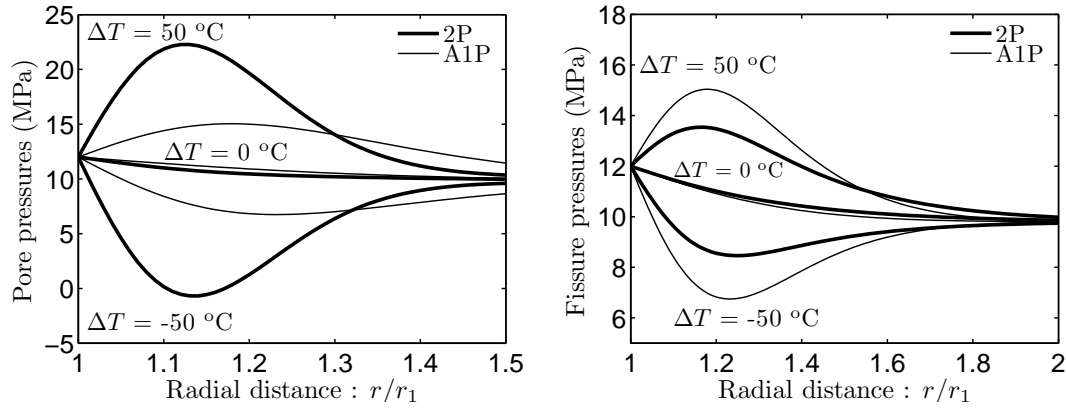


Figure 6.3: Profiles of pore pressure and fissure pressure, at time 80 s and for three imposed temperature changes  $\Delta t$  at the borehole. The leakage parameter is set equal to the average leakage parameter  $\eta^* = \eta_{av}^*$ .

The pore pressure variation under thermal stimulation is due to a factor of 0.04 between the thermal dilatation of the solid skeleton and that of the fluid (Table 6.1). The general trend is that heating,  $T_w - T^0 = 50^\circ\text{C}$ , induces a higher pore pressure and therefore a lower radial effective stress than  $T_w - T^0 = 0^\circ\text{C}$ ; while cooling,  $T_w - T^0 = -50^\circ\text{C}$ , induces the opposite response (Figure 6.3-6.4). A hot thermal stimulation weakens the wellbore, whereas cooling shields against failure.

When considering the two cavities as part of a dual porous medium, the pressure responses (2P) are significantly different from the associated single porosity model (A1P). As expected, such behavior is due to the disparity between the diffusivity ratio of the porous blocks  $R_p = 0.66$  and the diffusivity ratio of the fissure network  $R_f = 2.38$ . In the porous blocks, thermal diffusion is faster than hydraulic diffusion and therefore the pore pressure is unable to dissipate, causing increases or decreases in fluid pressure. On the other hand, in the fissure network, the thermally induced pressure dissipates as soon as it is generated.

The effective stresses, displayed in Figure 6.4 and throughout the paper, are defined by Biot's relationship extended to dual porosity and represent the stresses undergone by the solid skeleton (Khalili and Valliappan, 1996),

$$\bar{\sigma} = \sigma + \xi_p p_p \mathbf{I} + \xi_f p_f \mathbf{I}, \quad (6.45)$$

in which  $\xi_p$  and  $\xi_f$  are the effective stress parameters equal to 0.27 and 0.1, respectively, with the material parameters presented in Table 6.1. Again, compared with the associated single porosity model, the dual porosity approach displays a wider range of effective stress variations related to the pore pressure response (eq. 6.45). The associated single porosity model significantly underestimates the changes of fluid pressures and effective stresses.

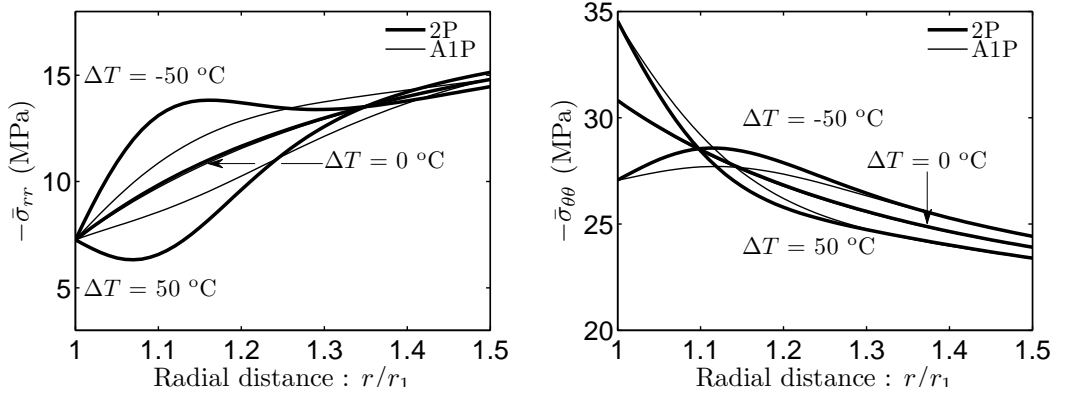


Figure 6.4: Profiles of radial effective stress and tangential effective stress, at time 80 s and for three imposed temperature changes  $\Delta t$  at the borehole. The leakage parameter is set equal to the average leakage parameter  $\eta^* = \eta_{av}^*$ .

### 6.5.2 Influence of mass transfer

In a dual porosity medium, the mass transfer coefficient influences greatly the profiles of the fluid pressures and the effective stresses. A parametric analysis is now conducted to examine the influence of mass transfer and to identify when the dual porosity approach becomes essentially identical to a classical single porosity model.

The characteristic leakage parameter  $\eta_{eq}^*$  is defined as the minimum dimensionless mass transfer to obtain instantaneous hydraulic equilibrium at a time of interest. For  $t = 80$  s,  $\eta_{eq}^*$  is equal to  $1.1 \times 10^6$ . This value was found by trial and error and is specific to the dual porous medium characterized in Table 6.1. Note that  $\eta_{eq}^*$  is a time-dependent parameter.

The influence of mass transfer is illustrated by selecting three representative values of the leakage parameter:  $\eta^*/\eta_{eq}^* = 0$  which represents no mass transfer,  $\eta^*/\eta_{eq}^* = 0.001$  which represents a low mass transfer, and  $\eta^*/\eta_{eq}^* \geq 1$  which corresponds to instantaneous hydraulic equilibrium. The leakage parameter is related to the average fissure spacing and to the porous blocks permeability, and hence represents the ability of the dual porous medium to transfer fluid mass from one cavity to the other. In this section and hereafter, only heating tests  $\Delta T = + 50^\circ\text{C}$  will be considered.

The sensitivity of the fluid pressures to the leakage parameter is presented in Figure 6.5 for two distinct types of boundary condition: (left) permeable boundary and (right) a semi-permeable boundary. A comparison with an associated single porous medium is also presented.

In general, the pore pressure increases due to a combination of low permeability and higher thermal expansion for the fluid than for the solid, whereas the fissure pressure dissipates rapidly due to a higher permeability. For  $\eta^*/\eta_{eq}^* = 0$  the two fluid fields are de-coupled and no mass transfer occurs. For  $\eta^*/\eta_{eq}^* = 0.001$  moderate mass transfer takes place as the pore pressure dissipates into the fissures. Consequently, the pore pressure peak in the porous blocks is lower than the case for  $\eta^*/\eta_{eq}^* = 0$ ; and the pressure in the fissure network is higher than the associated single porosity response. Finally, for  $\eta^*/\eta_{eq}^* \geq 1$  the mass transfer between the pores and the fissures is instantaneous and the two cavities are in hydraulic equilibrium. Note that this equilibrium pressure is not equal to the fissure pressure when  $\eta^*/\eta_{eq}^* = 0$ , but is equal to the pressure response of the associated single porous medium. For  $\eta^*/\eta_{eq}^* \geq 1$ , three curves of the pore pressure, the fissure pressure and the pore pressure of the associated single porosity model are superposed.

For a permeable boundary, the pore pressure maximum is located a short distance away from the wellbore wall due to a flux inward to the formation  $\mathbf{J}_p \geq 0$  for radii larger than  $r/r_1 \geq 1.2$  and a flux outward to the wellbore  $\mathbf{J}_p \leq 0$  for radii smaller than  $r/r_1 \leq 1.1$ . For a semi-permeable boundary, the maximum is located at the borehole itself due to the flux of the porous blocks  $\mathbf{J}_p = 0$ , which induces a zero pore pressure gradient  $\nabla p_p = 0$  at  $r = r_1$ . In addition, the magnitude of the pore pressure maximum is higher for the semi-permeable boundary than for the permeable boundary since the pore fluid can only dissipate internally and through mass transfer. On the other hand, the pore pressure peak is smaller for the permeable boundary due to the direct dissipation the pressure through the wellbore wall.

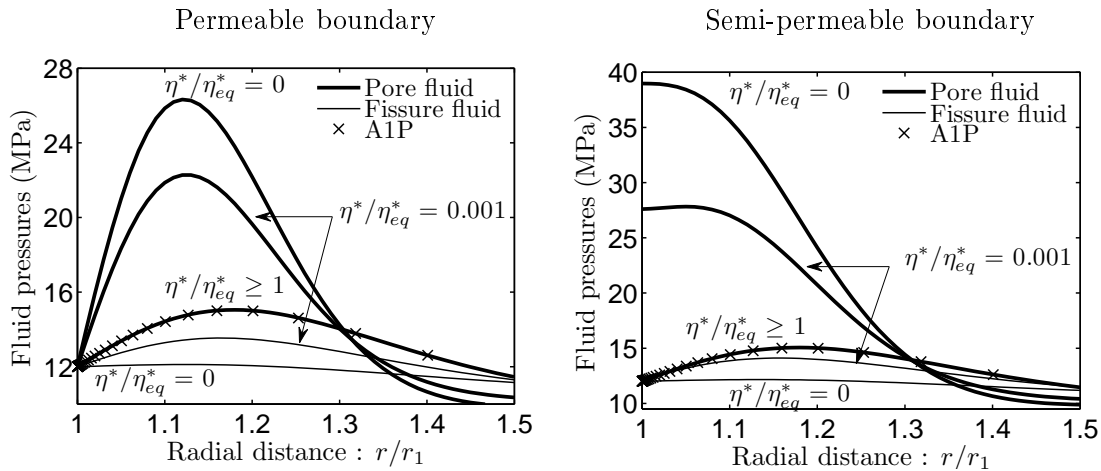


Figure 6.5: Profiles of pore pressure and fissure pressure, at time 80 s, for a thermal loading equal to  $T_w - T^0 = 50^\circ\text{C}$ .

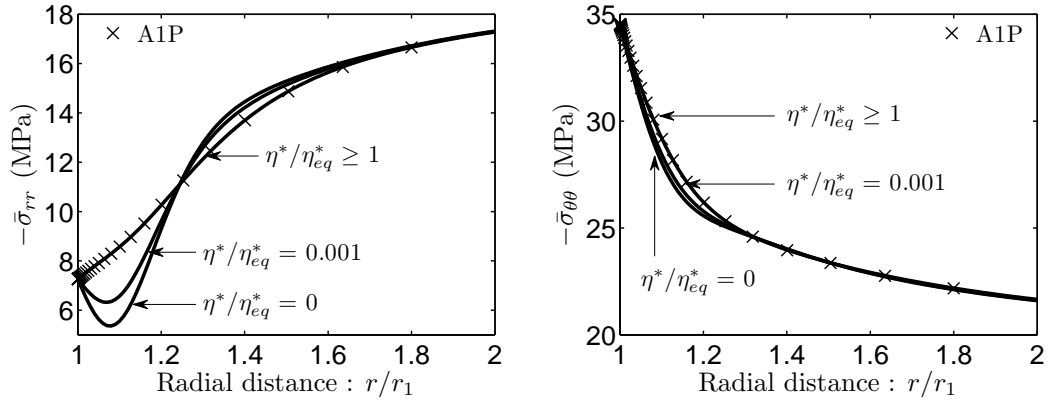


Figure 6.6: Profiles of effective radial stress and effective tangential stress, at time 80 s, accounting for a *permeable* boundary. The thermal loading is equal to  $T_w - T^0 = 50^\circ\text{C}$ .

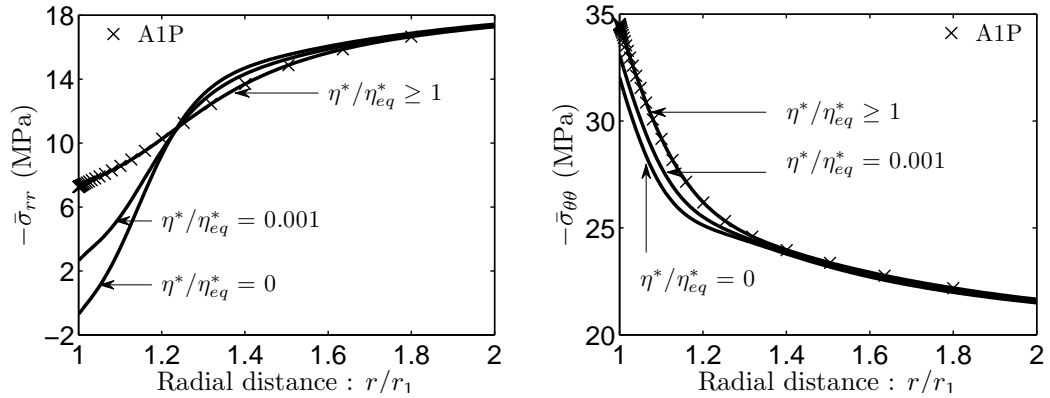


Figure 6.7: Same as Figure 6.6 for a *semi-permeable* boundary on the porous blocks.

The sensitivity of the effective stresses to mass transfer coefficient is illustrated in Figures 6.6 and 6.7. The compressive effective radial stress experiences a significant drop for  $\eta^*/\eta_{eq}^* = 0$ , which tends to diminish for high mass transfer  $\eta^*/\eta_{eq}^* \geq 1$ . By comparing Figures 6.6 and 6.7, the semi-permeable boundary is seen to introduce a greater reduction in effective radial stress than the permeable boundary. For a low leakage parameter (close to zero) the effective radial stress shifts from compressive to tensile. The positive effect of the compressive mud pressure applied at the borehole is annihilated by the thermally induced increase in pore fluid pressure.

Mass transfer from the porous blocks to the fissure network increases the dissipation of the pore pressure and conversely decreases the dissipation of the fissure pressure. This in turn increases the apparent diffusivity ratio of the pore matrix; and decreases the apparent diffusivity ratio of the fissure network. For the intermediate leakage parameters  $\eta^*/\eta_{eq}^* \leq 0.1$ , the dual porosity approach is the only one which can represent correctly the reduction in the effective radial stress induced by the pore pressure response.

### 6.5.3 Time profiles

The variation with time of the fluid pressures gives an indication of the time scale at which the dual porosity model has the largest influence on the effective stress response. The pressure and stress profiles are shown for three representative time intervals; from  $t = 6$  s at very short time  $t/t^* = 4.2 \cdot 10^{-6}$ , to  $t = 80$  s at short time  $t/t^* = 5.5 \cdot 10^{-5}$  and finally  $t = 800$  s at intermediate time  $t/t^* = 5.5 \cdot 10^{-4}$ . Because the characteristic time  $t^*$  is related to the slowest diffusion phenomenon (and does not account for mass transfer effects), the ratio  $t/t^*$  remains small even for the intermediate time. Focusing on a permeable boundary at the wellbore and on a heating test  $T_w - T^0 = 50^\circ\text{C}$ , the results are presented for two values of the dimensionless leakage parameter representing an infinite fracture spacing,  $\eta^* = 0$ , and an average fracture spacing equal to 0.03 m,  $\eta^* = \eta_{av}^*$ .

Over time, the pore pressure front propagates into the formation away from the borehole wall with a diminishing pressure peak (Figure 6.8). As expected, the larger the leakage parameter, the faster the dissipation of the pore pressure. Contrary to the pore pressure behavior, the pressure in the fissure network dissipates more slowly with an increase in the leakage parameter. Note that for the very short time response ( $t = 6$  s), average mass transfer does not play a significant role in the fluid pressure response of the system and pore and fissure fluid pressures, for  $\eta^* = 0$  and  $\eta^* = \eta_{av}^*$ , differ little.

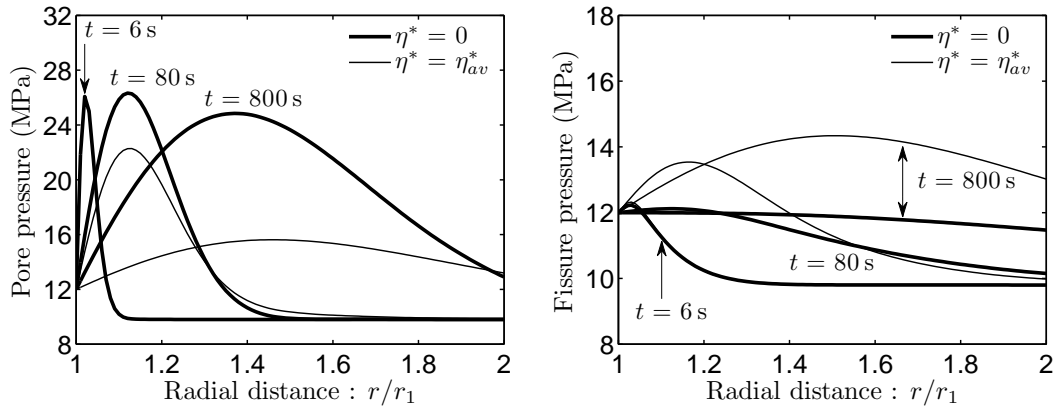


Figure 6.8: Profiles of pore pressure and fissure pressure for two values of the leakage parameter  $\eta^* = 0$  and  $\eta^* = \eta_{av}^*$ . The results are presented for three representative times.

As time elapses, the effective radial stress becomes more compressive as a consequence of diffusion (Figure 6.9). At the time  $t = 6$  s, the effective radial stress displays the highest compressive reduction due to the slow dissipation of the pore pressure. Similarly, there is an uneven reduction in compressive stress for the effective tangential stress at very short time. For both effective stresses at  $t = 6$  s and  $t = 800$  s, the two curves  $\eta^* = 0$  and  $\eta^* = \eta_{av}^*$  are superposed. The effective tangential stress becomes less compressive with time compared with the effective radial stress. The time required for the effective stresses to attain steady state is directly related to the mass transfer coefficient.

At  $t = 6$  s, mass transfer and dissipation have not taken place yet. At the intermediate

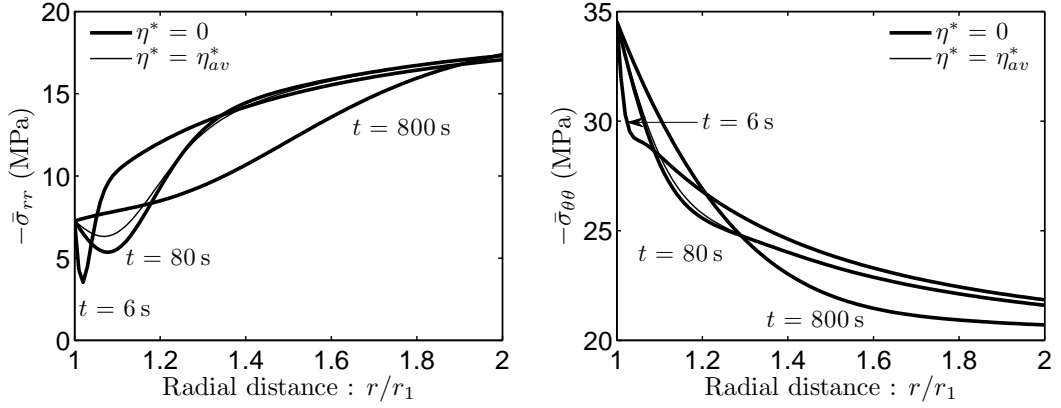


Figure 6.9: Profiles of effective radial stress and effective tangential stress, for  $\eta^* = 0$  and  $\eta^* = \eta_{av}^*$ . The results are presented for three representative times.

time  $t = 800$  s, hydraulic equilibrium has almost been reached for the average mass transfer value  $\eta^* = \eta_{av}^*$ ; however, the influence of the diffusion and the mass transfer in the form of a difference in pore and fissure pressures is still prominent at  $t = 80$  s. The reduction in compressive radial effective stress is maximum at  $t = 6$  s, and hence the borehole failure analysis is most critical at the very short time scale.

#### 6.5.4 Borehole stability analysis

The rise in pore water pressure plays a key role in the stability analysis of boreholes. Failure typically occurs when the pore pressure reduces the effective confining pressure below a critical value (Chen et al., 1997). Thus for an accurate failure prediction, a general understanding of the coupled thermo-hydro-mechanical response of the effective stress, governed by Biot's poroelastic law extended to dual porous media eq. (6.45), is required (Khalili and Valliappan, 1996).

To illustrate the borehole stability analysis, we present the results in the form of the *effective stress path along the radial direction to the wellbore*. The stress path is obtained by evaluating pairs of mean effective stress  $S_p$ , mean shear stress  $\sqrt{J_2}$  for a fixed time along the radial direction. The mean effective stress  $S_p$  and the mean shear stress  $\sqrt{J_2}$  are, respectively, equal to,

$$S_p = -\frac{\bar{\sigma}_{rr} + \bar{\sigma}_{\theta\theta} + \bar{\sigma}_{zz}}{3}, \quad (6.46)$$

and,

$$J_2 = \frac{1}{6} \left[ (\sigma_{rr} - \sigma_{\theta\theta})^2 + (\sigma_{\theta\theta} - \sigma_{zz})^2 + (\sigma_{zz} - \sigma_{rr})^2 \right] + \sigma_{r\theta}^2 + \sigma_{rz}^2 + \sigma_{\theta z}^2. \quad (6.47)$$

To perform the borehole collapse analysis, the Drucker-Prager criterion (Drucker and Prager, 1952) is chosen to represent the failure envelope,

$$\sqrt{J_2} = 3A S_p + D, \quad (6.48)$$

where  $A$  and  $D$  are positive material constants. If the Drucker-Prager yield surface inscribes the Mohr-Coulomb yield surface, these constants can be related to a friction angle  $\phi$  and a cohesion  $\mathcal{C}$  by,

$$3A = \frac{2 \sin \phi}{\sqrt{3}(3 - \sin \phi)}, \quad D = \frac{6\mathcal{C} \cos \phi}{\sqrt{3}(3 - \sin \phi)}. \quad (6.49)$$

Figure 6.10 shows the stress path, along the dimensionless radius  $r/r_1$ , for two distinct boundary conditions at the wellbore: (left) permeable boundary and (right) semi-permeable boundary. The response of a dual porous medium (2P) with an average mass transfer coefficient  $\eta^* = \eta_{av}^*$  is compared with an associated single porous medium (A1P). The results are presented at  $t = 6$  s which corresponds to the maximum reduction in the effective radial stress (Figure 6.9).

The failure criterion line is *calibrated* to intersect the effective stress path representative of the dual porosity approach with a permeable condition on the wellbore; as a first approximation, the following values  $A = 0.1$  and  $D = 8$  MPa are assumed to describe the failure envelope, yielding a friction angle  $\phi$  of  $38^\circ$  and a cohesion  $\mathcal{C}$  of 7 MPa.

The objective is to evaluate if the semi-permeable condition, modeled with the dual porosity approach and compared with the associated single porosity approach, affects the stability of the borehole positively or negatively.

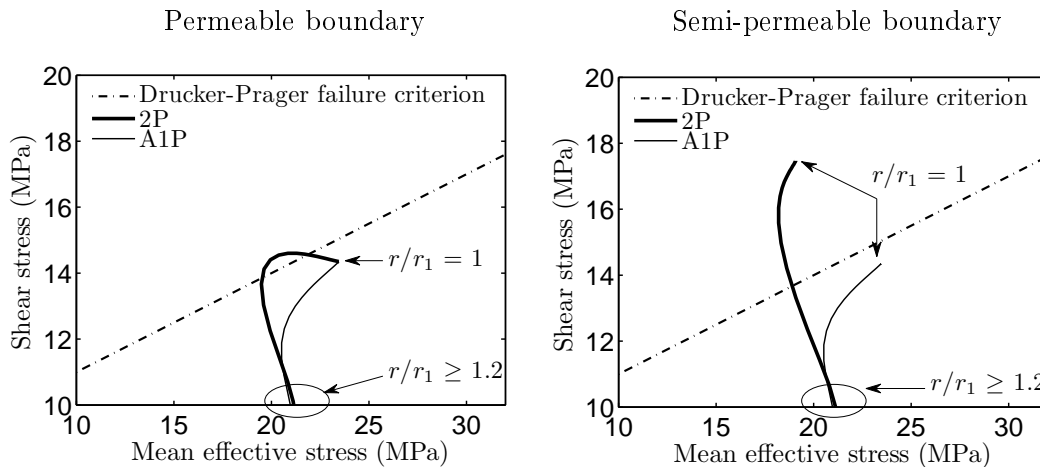


Figure 6.10: Effective stress path along dimensionless radial direction  $r/r_1$ , in the Mean shear stress  $\sqrt{J_2}$  - Mean effective stress  $S_p$  plane, for two distinct boundary conditions. The results are presented at time 6 s and with an average leakage parameter  $\eta^* = \eta_{av}^*$ .

For a permeable boundary at the wellbore, the two stress paths at  $r/r_1 = 1$  are located below the failure criterion. At a distance from the wellbore wall, the (A1P) effective stress path remains inside the failure envelope. In contrast to the (A1P) response, the (2P) effective stress path intersects the failure line and penetrates slightly into the failure domain. On the other hand, the (2P) stress path of the semi-permeable boundary condition is located outside the failure envelope for  $r/r_1 \leq 1.1$ . As expected, the semi-permeable boundary induces a stronger collapse potential at the wellbore wall.

When accounting for a semi-permeable boundary condition, the effective radial stress is greatly reduced by the pore pressure in the vicinity of the wellbore (Figure 6.7) whereas the effective tangential stress remains essentially non affected. Consequently, the mean shear stress  $\sqrt{J_2}$  is significantly increased. In addition, the magnitude of the effective radial stress is lower for a semi-permeable boundary condition, which means a lower magnitude of the mean effective stress.

Figure 6.10 highlights that in the dual porosity model, which contains few fissures and therefore uses a low leakage parameter coefficient, there is a greater potential for failure than in the associated single porosity model. By considering a single porosity model instead of taking the dual porosity approach, it is possible that incorrect drilling mud pressure will be calibrated and unexpected borehole failure will result. Finally, the semi-permeable boundary significantly increases the potential of failure of the borehole.

## 6.6 Conclusion

Diffusion mechanisms and mass transfer between materials with two porosities have been studied in the context of heavy-oil recovery with thermal stimulation. A model describing the behavior of poroelastic dual porous media has been extended to account for thermal loading in a previous work (Khalili and Selvadurai, 2003). The fully coupled thermo-hydro-mechanical system has been specified for mixtures that are in thermal equilibrium and for diffusion dominated media. The governing equations have been presented to characterize thermo-hydro-mechanical coupled behavior. A finite element approximation has been outlined and the nonlinear field equations integrated *via* an implicit time marching scheme and solved using a full Newton-Raphson procedure. This finite element analysis has been employed for a vertical borehole problem.

A parametric analysis has been developed to study the influence of the leakage parameter on the pore pressure, the fissure network pressure and the effective stresses in the vicinity of the wellbore. The rise in the thermally induced pore pressure is more pronounced when the leakage parameter is low, representing a sparsely fissured media; whereas the response of the fissure network pressure is induced by the pore pressure dissipation and is therefore more pronounced for high leakage parameter. The effective stress is mostly controlled by the pore pressure, which induces a reduction in compressive effective stress for low leakage parameter values.

The highest reduction in the compressive effective stress occurs at a very short time after the loading, when the mass transfer has not resulted in the dissipation of excess pore pressure into the fissure network. Below a threshold value of compressive effective stress, collapse of the borehole occurs. It is also shown that dual porosity media display a higher failure potential compared with an associated single porosity medium. In addition, a semi-permeable boundary condition on the porous matrix greatly increases the failure potential compared with a permeable boundary condition at the wellbore lining.

Consequently, the single porosity approach underestimates the failure potential of fissured reservoirs. A consistent dual porosity approach is required for an accurate prediction



of the potential for thermally induced wellbore failure in fractured porous media.

## Chapter 7

# The streamline-upwind/Petrov-Galerkin method

The phenomenon of *forced convection*, also called advection (see Remark 7.1), typically identified by the fluid velocity multiplied with the gradient of the temperature  $\mathbf{v} \cdot \nabla T$  (or the enthalpy or the concentration), requires scrutiny and challenges the usability of numerical methods. Methods being successfully applied in diffusion-dominated flows, where no convection is present, may totally fail when they are applied to convection-dominated problems. This is particularly the case with the widely used Bubnov-Galerkin methods. Using Bubnov-Galerkin methods for the approximation of convection-diffusion differential equations may cause spurious numerical oscillations.

In linear problems, such as heat conduction problems, the application of the Bubnov-Galerkin method leads to symmetric effective diffusion matrices. In these cases, it can be shown that the solutions possess the ‘best approximation’ property (Brooks and Hughes, 1982), that is the difference between the finite element solution and the exact solution is minimised with respect to a certain norm. On the other hand, the ‘best-approximation’ property is lost for non-symmetric effective diffusion matrices describing coupled convection-conduction problems. As a result Bubnov-Galerkin methods applied to these problems are far from ‘optimal’ and even violate basic physical principles like the entropy condition (Hirsch, 1988).

While several Eulerian methods have been proposed to cure these spurious oscillations, for example the Galerkin / Least Squares method (GLS), the Galerkin / Gradient Least Squares method (GGLS) and the Unusual Stabilised Finite Element Method (USFEM); the stabilisation scheme defined by the Streamline-Upwind/Petrov-Galerkin (SUPG) method and introduced by Brooks and Hughes (1982) is preferred. This method adds perturbations which are formulated in terms of modifications of the Galerkin test functions  $\mathbf{N}_T$ , that is the method does not require the introduction of additional test functions. This feature simplifies greatly the implementation of the SUPG method and is most probably the main

reason for the wide success of the SUPG method. In addition, the SUPG method has been extensively studied and is well described in the literature.

**Remark 7.1.** *Definitions of the terms advection and convection. In this work the term advection is used as synonymous with convection. However, in some disciplines a distinction remains:*

- *Many engineers prefer to use the term convection to describe transport by combined molecular and Eddy diffusion (turbulent diffusion), and reserve the usage of the term advection to describe transport with a general (net) flow of the fluid (like in river or pipeline) (Suthersan, 1997, p. 13).*
- *In the ocean and atmospheric sciences, advection is understood as horizontal movement resulting in transport ‘from place to place’, while convection is a vertical ‘mixing’ (Randall, 2000, p. 648).*

In Section 7.1, the SUPG method is briefly introduced and the most important features of the method are highlighted. A special attention is given to the structure of the weak formulation.

In Section 7.2, comparison between analytical solutions and finite element responses for simple problems are illustrated. One-dimensional steady state, one-dimensional transient, two-dimensional steady state and two-dimensional transient diffusion-convection problems are considered. The optimal stabilisation parameter is sought for each problem. Furthermore, stability requirements (or the absence of) for diffusion-convection problems are outlined for various time marching scheme.

In Section 7.3, the mechanisms of spurious oscillations and the limitations of the SUPG method are summarised. Applications in a porous medium context are exposed and the discontinuity capturing method (DCM) is introduced to smoothly resolve sharp layers.

The work presented in this chapter is restricted to diffusion-convection problems *uncoupled* from the hydraulic and the mechanical contributions. Simulations of thermo-hydro-mechanical processes in Chapter 8 which involve coupled diffusion-convection flows will capitalise upon the lessons learned in the elementary instances considered here.

## 7.1 Presentation of the SUPG method

The main characteristics of the SUPG method are introduced with an uncoupled diffusion-convection problem as example. The method originates from the upwind finite differences method which uses the artificial diffusion idea. A ‘classical’ formulation of the convection-diffusion problem is then presented and weak formulations are displayed to enhance the terms which requires stabilisation. The method to determine the stabilisation parameter is summarised to outline the dependency of this parameter on the problem under consideration and on the chosen shape functions. The method taps on the work of Brooks and

Hughes (1982) and the formalism of (Fries and Matthies, 2004), and we should refer to them for more detailed explanations.

### 7.1.1 Introduction of the SUPG method

Here, only the main structure of the SUPG method is shown. The starting point is a generic partial differential equation of a one-dimensional diffusion-convection problem for the unknown  $T$ ,

$$\mathcal{L}T - f = 0, \quad \text{with} \quad \mathcal{L}_{\text{conv}}T = \mathbf{v} \nabla T, \quad (7.1)$$

where  $\mathcal{L}$  is a generic differential operator,  $f$  is the source term,  $\mathcal{L}_{\text{conv}}$  is the convective part of the whole operator  $\mathcal{L}$  and  $\mathbf{v}$  is the convective velocity. The weak form associated with (7.1),

$$\int_V \delta T (\mathcal{L}T - f) \, dV, \quad (7.2)$$

introduces the weight function  $\delta T$ . The finite element method requires to construct finite dimensional approximations of the unknown  $T$  and of the weighting function  $\delta T$ , which should be denoted  $T^h$  and  $\delta T^h$ , respectively. The superscript  $h$  refers to the discretisation of the domain  $V$  with respect to a characteristic length scale  $h$ . Nevertheless, this important notation is dropped in this section to clarify the notation.

Let  $\mathbf{N}_T$  be the interpolation functions chosen to interpolate the unknown temperature  $T$ , and  $\mathbf{W}_T$  the interpolation functions to interpolate the variation corresponding to the temperature  $\delta T$ ,

$$\begin{aligned} T &= \mathbf{N}_T \mathbf{T}^e, \\ \delta T &= \mathbf{W}_T \delta \mathbf{T}^e. \end{aligned} \quad (7.3)$$

By summing the elementary contributions over the total number of elements  $\text{nel}$ , the semi-discretised form of the problem is,

$$\sum_{e=1}^{\text{nel}} [\delta \mathbf{T}^e]^T \int_{V^e} \mathbf{W}_T^T (\mathcal{L}T - f) \, dV^e = 0. \quad (7.4)$$

Choosing the weighting functions equal to the shape functions :  $\mathbf{W}_T = \mathbf{N}_T$  leads to a Bubnov-Galerkin method also called Galerkin method. Any method for which  $\mathbf{W}_T \neq \mathbf{N}_T$  is called a Petrov-Galerkin method. The denomination of the SUPG method implies that  $\mathbf{W}_T$  is chosen differently from  $\mathbf{N}_T$ . The standard Bubnov-Galerkin test functions  $\mathbf{N}_T$  are

modified by a streamline upwind perturbation which does not require the introduction of additional test functions,

$$\begin{aligned}\mathbf{W}_T &= \mathbf{N}_T + \tau \mathcal{L}_{\text{conv}} \mathbf{N}_T, \\ &= \mathbf{N}_T + \tau \mathbf{v} \nabla \mathbf{N}_T,\end{aligned}\tag{7.5}$$

where  $\mathcal{L}_{\text{conv}}$  is the convective part of the whole operator  $\mathcal{L}$  applied to the vector  $\mathbf{N}_T$ , and  $\tau$  is the stabilisation parameter that weights the perturbation.  $\mathbf{N}_T$  is a continuous weighting function and  $\tau \mathbf{v} \nabla \mathbf{N}_T$  is the discontinuous streamline upwind contribution. Both contributions are assumed to be smoothed on the element interiors. Note that the stabilisation contribution is *restricted to the element interiors*,

$$\sum_{e=1}^{\text{nel}} [\delta \mathbf{T}^e]^\text{T} \int_{V^e} (\mathbf{N}_T + \tau \mathcal{L}_{\text{conv}} \mathbf{N}_T)^\text{T} (\mathcal{L}T - f) \, dV^e = 0.\tag{7.6}$$

Crucially, the perturbation  $\tau \mathcal{L}_{\text{conv}} \mathbf{N}_T$  applies to the residual form of the differential equation, that is to *all* the terms of the weak form. This procedure ensures that consistency is enforced from the beginning in that the exact solution also fulfills the stabilised weak form exactly (Fries and Matthies, 2004).

### 7.1.2 Origin of the SUPG method: the artificial diffusion

The SUPG method originates from the upwind finite difference methods, which have been designed to preclude wiggles. Kelly et al. (1980) introduced a ‘balancing dissipation’ in which additional diffusion  $\tilde{\alpha}_T$  [m<sup>2</sup>/s] is added to the one-dimensional problem,

$$\mathcal{L}T = \mathbf{v} \nabla T - (\alpha_T + \tilde{\alpha}_T) \text{div} (\nabla T),\tag{7.7}$$

where  $\tilde{\alpha}_T \rightarrow 0$  as the size of the linear element  $h \rightarrow 0$ . This upwind method is constructed by adding the ‘proper’ amount of artificial diffusivity  $\tilde{\alpha}_T$  to the physical diffusivity, and a conventional (Bubnov-)Galerkin finite element discretisation is employed,

$$\sum_{e=1}^{\text{nel}} [\delta \mathbf{T}^e]^\text{T} \int_{V^e} \mathbf{W}_T^\text{T} \left( \mathbf{v} \frac{\partial T}{\partial x} - (\alpha_T + \tilde{\alpha}_T) \frac{\partial^2 T}{\partial x^2} \right) \, dV^e = 0,\tag{7.8}$$

where the weighting functions and the shape functions are equal  $\mathbf{W}_T = \mathbf{N}_T$ . The divergence theorem is used on the two diffusion terms,

$$\begin{aligned} \sum_{e=1}^{\text{nel}} [\delta \mathbf{T}^e]^T \left[ \int_{V^e} \mathbf{N}_T^T \mathbf{v} \frac{\partial T}{\partial x} dV^e + \int_{V^e} \alpha_T \frac{\mathbf{N}_T^T}{\partial x} \frac{\partial T}{\partial x} dV^e - \int_{\partial V^e} \alpha_T \mathbf{N}_T^T \frac{\partial T}{\partial x} \cdot \hat{\mathbf{n}} dS^e \right. \\ \left. + \int_{V^e} \tilde{\alpha}_T \frac{\mathbf{N}_T^T}{\partial x} \frac{\partial T}{\partial x} dV^e - \int_{\partial V^e} \tilde{\alpha}_T \mathbf{N}_T^T \frac{\partial T}{\partial x} \cdot \hat{\mathbf{n}} dS^e \right] = 0, \end{aligned} \quad (7.9)$$

in which the boundary term of the ‘artificial diffusivity’ vanishes by considering the stabilisation contribution only on the element’s interior:

$$\sum_{e=1}^{\text{nel}} [\delta \mathbf{T}^e]^T \int_{\partial V^e} \tilde{\alpha}_T \mathbf{N}_T^T \frac{\partial T}{\partial x} \cdot \hat{\mathbf{n}} dS^e = 0. \quad (7.10)$$

Then the ‘artificial diffusivity’ term is transformed into a stabilised ‘convective’ term. For a non-zero scalar fluid velocity  $\mathbf{v}$ , eq. (7.9) becomes,

$$\begin{aligned} \sum_{e=1}^{\text{nel}} [\delta \mathbf{T}^e]^T \left[ \int_{V^e} \left( \mathbf{N}_T + \frac{\tilde{\alpha}_T}{\mathbf{v}} \frac{\partial \mathbf{N}_T}{\partial x} \right)^T \mathbf{v} \frac{\partial T}{\partial x} dV^e + \int_{V^e} \alpha_T \frac{\mathbf{N}_T^T}{\partial x} \frac{\partial T}{\partial x} dV^e \right. \\ \left. - \int_{\partial V^e} \alpha_T \mathbf{N}_T^T \frac{\partial T}{\partial x} \cdot \hat{\mathbf{n}} dS^e \right] = 0. \end{aligned} \quad (7.11)$$

One can interpret this artificial diffusion method as a stabilisation of the convective term, where the test functions of the convective term become  $(\mathbf{N}_T + \tilde{\alpha}_T/\mathbf{v} \nabla \mathbf{N}_T)$  instead of only  $\mathbf{N}_T$ .

This technique may be interpreted as ‘balancing diffusion’, in that it balances the under-diffuse response of the Galerkin treatment. In one-dimension, when the artificial diffusivity  $\tilde{\alpha}_T$  is equal to  $\mathbf{v}^2 \tau$  the solution is nodally exact (Brooks and Hughes, 1982). Problems have been noted with the treatment of source terms, transient behaviour, quadratic shape functions and with the generalisation to multi-dimensions: in these cases, pronounced diffusion corrupts the true solution; in the latter case, this has manifested itself by a so-called spurious crosswind diffusion effect (Brooks and Hughes, 1982). The reason for this effect is the inconsistency of the above equation: the exact solution does not satisfy the weak form of the problem with artificial diffusion.

### 7.1.3 Standard diffusion-convection formulations

The extension of the SUPG method from one-dimensional steady diffusion-convection problems to more complex problems, such as transient problems, requires scrutiny; in fact the

stabilisation is not restricted to the convective term. The standard differential operator for the one-dimensional steady diffusion-convection equation with no source term,  $f = 0$ , writes,

$$\mathcal{L}T = \mathbf{v} \nabla T - \alpha_T \operatorname{div}(\nabla T), \quad \text{with} \quad \mathcal{L}_{\text{conv}}T = \mathbf{v} \nabla T. \quad (7.12)$$

With the SUPG method (Brooks and Hughes, 1982; Hughes and Brooks, 1979), the weak form of eq. (7.12) becomes,

$$\sum_{e=1}^{\text{nel}} [\delta \mathbf{T}^e]^\text{T} \left[ \int_{V^e} \mathbf{N}_T^\text{T} \left( \mathbf{v} \frac{\partial T}{\partial x} - \alpha_T \frac{\partial^2 T}{\partial x^2} \right) dV^e + \int_{V^e} \left( \tau \mathbf{v} \frac{\partial \mathbf{N}_T}{\partial x} \right)^\text{T} \left( \mathbf{v} \frac{\partial T}{\partial x} - \alpha_T \frac{\partial^2 T}{\partial x^2} \right) dV^e \right] = 0. \quad (7.13)$$

If the unknowns are interpolated with linear isoparametric shape functions, it implies that  $\partial^2 T / \partial x^2 = 0$  on the element interior. As the stabilisation  $(\tau \mathbf{v} \partial \mathbf{N}_T / \partial x)$  is only required on the element interior, eq. (7.13) reduces to,

$$\sum_{e=1}^{\text{nel}} [\delta \mathbf{T}^e]^\text{T} \left[ \int_{V^e} \mathbf{N}_T^\text{T} \left( \mathbf{v} \frac{\partial T}{\partial x} - \alpha_T \frac{\partial^2 T}{\partial x^2} \right) dV^e + \int_{V^e} \left( \tau \mathbf{v} \frac{\partial \mathbf{N}_T}{\partial x} \right)^\text{T} \left( \mathbf{v} \frac{\partial T}{\partial x} \right) dV^e \right] = 0. \quad (7.14)$$

In this case, it is seen that the streamline upwind modification does not affect the weighting of the diffusion term. Note that equations (7.11) and (7.14) are equivalent for,

$$\tilde{\alpha}_T = \mathbf{v}^2 \tau. \quad (7.15)$$

First order derivatives, however, do not only occur in convective terms, but also in time-dependent terms  $\partial T / \partial t$  of non-stationary problems. The standard differential operator for the one-dimensional *unsteady* diffusion-convection equation with no source term,  $f = 0$ , is,

$$\mathcal{L}T = \frac{\partial T}{\partial t} + \mathbf{v} \nabla T - \alpha_T \operatorname{div}(\nabla T), \quad \text{with} \quad \mathcal{L}_{\text{conv}}T = \mathbf{v} \nabla T. \quad (7.16)$$

Then, in general the same stabilisation as for convective terms has to be implemented for the transient term, which leads to the following weak form when using the SUPG

method and linear shape functions,

$$\sum_{e=1}^{\text{nel}} [\delta \mathbf{T}^e]^T \left[ \int_{V^e} \mathbf{N}_T^T \left( v \frac{\partial T}{\partial x} + \frac{\partial T}{\partial t} - \alpha_T \frac{\partial^2 T}{\partial x^2} \right) dV^e + \int_{V^e} \left( \tau v \frac{\partial \mathbf{N}_T}{\partial x} \right)^T \left( v \frac{\partial T}{\partial x} + \frac{\partial T}{\partial t} \right) dV^e \right] = 0. \quad (7.17)$$

Based on this logic, *all the first order derivatives* of the coupled diffusion-convection formulations should have a similar stabilised weak form.

#### 7.1.4 Weighting the modification : the stabilisation parameter $\tau$

The stabilisation parameter  $\tau$  is chosen so that the solution to the *one-dimensional steady state* diffusion-convection problem be exact at all nodes. The solution proceeds in two steps: (1) The weak form of the one-dimensional steady diffusion-convection problem is further discretised in space. (2) The exact solution of the problem and the linear shape and test functions (for a regular mesh) are combined to express the stabilisation parameter  $\tau$ .

(1) The starting point is the weak form of the one-dimensional steady diffusion-convection problem eq. (7.14),

$$\sum_{e=1}^{\text{nel}} [\delta \mathbf{T}^e]^T \left[ \int_{V^e} \mathbf{N}_T^T \left( v \frac{\partial T}{\partial x} - \alpha_T \frac{\partial^2 T}{\partial x^2} \right) dV^e + \int_{V^e} \left( \tau v \frac{\partial \mathbf{N}_T}{\partial x} \right)^T \left( v \frac{\partial T}{\partial x} \right) dV^e \right] = 0. \quad (7.18)$$

The spatial discretisation of the solution  $T = \mathbf{N}_T \mathbf{T}^e$  through the shape function vector  $\mathbf{N}_T$  leads to,

$$\sum_{e=1}^{\text{nel}} [\delta \mathbf{T}^e]^T \left[ \int_{V^e} \mathbf{N}_T^T \left( v \frac{\partial \mathbf{N}_T}{\partial x} - \alpha_T \frac{\partial^2 \mathbf{N}_T}{\partial x^2} \right) dV^e + \int_{V^e} \tau v^2 \left( \frac{\partial \mathbf{N}_T}{\partial x} \right)^T \frac{\partial \mathbf{N}_T}{\partial x} dV^e \right] \mathbf{T}^e = 0. \quad (7.19)$$

(2) The exact vector of element nodal values  $\mathbf{T}^{\text{ex}}$  is known for this problem (Fries and Matthies, 2004) to within two element constants  $C_1$  and  $C_2$ ,

$$\mathbf{T}^{\text{ex}} = C_1 \exp \left( \frac{v \mathbf{x}}{\alpha_T} \right) + C_2. \quad (7.20)$$



where  $\mathbf{x}$  is the vector constraining the nodal positions. By replacing eq. (7.20) into (7.19), the stabilisation parameter  $\tau$  can be rearranged to,

$$\tau = -\frac{\sum_{e=1}^{\text{nel}} [\delta \mathbf{T}^e]^T \left[ \int_{V^e} \mathbf{N}_T^T \left( v \frac{\partial \mathbf{N}_T}{\partial x} - \alpha_T \frac{\partial^2 \mathbf{N}_T}{\partial x^2} \right) dV^e \right] \mathbf{T}^{\text{ex}}}{\sum_{e=1}^{\text{nel}} [\delta \mathbf{T}^e]^T \left[ \int_{V^e} v^2 \frac{\partial \mathbf{N}_T}{\partial x} \frac{\partial \mathbf{N}_T}{\partial x} dV^e \right] \mathbf{T}^{\text{ex}}}, \quad \text{for } v \neq 0. \quad (7.21)$$

The second term of the numerator is expanded by use of the divergence theorem,

$$\begin{aligned} \sum_{e=1}^{\text{nel}} [\delta \mathbf{T}^e]^T \left[ \int_{V^e} \mathbf{N}_T^T \frac{\partial^2 \mathbf{N}_T}{\partial x^2} dV^e \right] \mathbf{T}^{\text{ex}} &= \sum_{e=1}^{\text{nel}} [\delta \mathbf{T}^e]^T \left[ - \int_{V^e} \frac{\partial \mathbf{N}_T}{\partial x} \frac{\partial \mathbf{N}_T}{\partial x} dV^e \right. \\ &\quad \left. + \int_{\partial V^e} \mathbf{N}_T^T \frac{\partial \mathbf{N}_T}{\partial x} \cdot \hat{\mathbf{n}} dS^e \right] \mathbf{T}^{\text{ex}}, \end{aligned} \quad (7.22)$$

in which the boundary term cancels out on the element's interior, for a one-dimensional problem with linear interpolation functions. Hence, the stabilisation parameter  $\tau$  reduces to,

$$\begin{aligned} \tau &= -\frac{\sum_{e=1}^{\text{nel}} [\delta \mathbf{T}^e]^T \left[ v \int_{V^e} \mathbf{N}_T^T \frac{\partial \mathbf{N}_T}{\partial x} dV^e \right] \mathbf{T}^{\text{ex}}}{\sum_{e=1}^{\text{nel}} [\delta \mathbf{T}^e]^T \left[ v^2 \int_{V^e} \frac{\partial \mathbf{N}_T}{\partial x} \frac{\partial \mathbf{N}_T}{\partial x} dV^e \right] \mathbf{T}^{\text{ex}}} \\ &\quad - \frac{\sum_{e=1}^{\text{nel}} [\delta \mathbf{T}^e]^T \left[ \alpha_T \int_{V^e} \frac{\partial \mathbf{N}_T}{\partial x} \frac{\partial \mathbf{N}_T}{\partial x} dV^e \right] \mathbf{T}^{\text{ex}}}{\sum_{e=1}^{\text{nel}} [\delta \mathbf{T}^e]^T \left[ v^2 \int_{V^e} \frac{\partial \mathbf{N}_T}{\partial x} \frac{\partial \mathbf{N}_T}{\partial x} dV^e \right] \mathbf{T}^{\text{ex}}} \end{aligned} \quad (7.23)$$

$$\tau = -\frac{\sum_{e=1}^{\text{nel}} [\delta \mathbf{T}^e]^T \left[ v \int_{V^e} \mathbf{N}_T^T \frac{\partial \mathbf{N}_T}{\partial x} dV^e \right] \mathbf{T}^{\text{ex}}}{\sum_{e=1}^{\text{nel}} [\delta \mathbf{T}^e]^T \left[ v^2 \int_{V^e} \frac{\partial \mathbf{N}_T}{\partial x} \frac{\partial \mathbf{N}_T}{\partial x} dV^e \right] \mathbf{T}^{\text{ex}}} - \frac{\alpha_T}{v^2}, \quad \text{for } v \neq 0. \quad (7.24)$$

From there, one can evaluate the remaining integrals explicitly for linear shape and test functions and a regular mesh. The details are presented in Fries and Matthies (2004,

p. 22). The result is,

$$\begin{aligned}\tau &= \frac{h}{2v} \frac{\sinh\left(\frac{vh}{\alpha_T}\right)}{\cosh\left(\frac{vh}{\alpha_T}\right) - 1} - \frac{\alpha_T}{v^2}, \quad \text{for } v \neq 0 \\ &= \frac{h}{2v} \left( \coth \text{Pe}_g - \frac{1}{\text{Pe}_g} \right) \quad [\text{s}], \quad \text{for } v \neq 0,\end{aligned}\tag{7.25}$$

where  $\text{Pe}_g$  is the grid Péclet number,

$$\text{Pe}_g = \frac{vh}{2\alpha_T}, \quad \text{for } \alpha_T \neq 0,\tag{7.26}$$

and  $h$  is the point spacing. Consequently, the stabilisation parameter (7.25) required to obtain a *nodally exact solution* for one-dimension steady diffusion-convection problems, with linear elements and a regular node distribution, is known. Notice however that it is not guaranteed that this stabilisation parameter provides a nodally exact solution for one-dimensional transient diffusion-convection problems or for two-dimension steady diffusion-convection problems (with bilinear shape functions). In fact, in general, it doesn't.

The stabilisation parameter  $\tau = h/2v$  is sometimes called the *convective time* or the *intrinsic time* which represent the time for a particle to travel the distance  $h/2$  at a speed equal to  $v$  for convection-dominated cases, that is  $(\coth \text{Pe}_g - 1/\text{Pe}_g) \rightarrow 1$  for  $\text{Pe}_g > 10$  (see Figure 7.1).

Results for one-dimensional cases are very much satisfying. The generalisation to multidimensional problems remains delicate and should be adapted to each application. The optimal choice of the stabilisation parameter  $\tau$  for more complex problems remains an open question.

## 7.2 Validation of the SUPG method

The implementation of the SUPG method requires the modification of the weighting functions and therefore the introduction of the stabilisation parameter  $\tau$  or of the artificial diffusivity  $\tilde{\alpha}_T$  (Section 7.1). The artificial diffusivity  $\tilde{\alpha}_T$  is preferred to the stabilisation parameter  $\tau$  since no non-zero condition on  $v$  is required for  $\tilde{\alpha}_T$ . However both writings are correct and describe the same stabilisation to within  $v^2$ , see eq. (7.15). The denomination of artificial diffusivity is misleading since the SUPG method is improved upon the upwind method. However the denomination is kept owing to the dimensions.

The effective diffusion matrix  $\mathbb{C}^*$  is now dependent on the fluid velocity  $\mathbf{v}$  in one-dimension or  $\mathbf{v} = [v_x, v_y]$  in two-dimension at each time and at each iteration: the problem

to be solved is highly non-linear. Additional finite element details are given in Remarks 7.2 and 7.3, respectively on the Gauss quadrature and on the the fluid velocity used throughout.

**Remark 7.2.** *In this work, a two-by-two Gauss quadrature is used for all weighting and shape functions, including the one defined for the SUPG method. Note that the same quadrature rule is used for the residual and the effective diffusion matrices, including the convective contributions. The details regarding the implementation of the convective contributions are gathered in Section 8.1. Finally, all meshes are discretised with bilinear quadrilateral elements (Q4).*

**Remark 7.3.** *The fluid velocity is denoted  $\mathbf{v}$  in 2-dimension or  $v$  in one-dimension. In this chapter, the fluid velocity is a given value, constant in time and uniform in space. However in Chapter 8, the fluid velocity will be calculated from the balance of mass of the appropriate fluid and will lose the constant in time and uniform in space properties.*

For a single phase medium composed of one fluid, simple problems are presented in turn in which the finite element response is systematically compared with the appropriate analytical solution (if applicable). The ability of the SUPG method to cure spurious wiggles is demonstrated for: (1) one-dimensional steady state diffusion-convection problems, (2) one-dimensional *transient* diffusion-convection problems, (3) two-dimensional steady state diffusion-convection problems with flow skew to the mesh and (4) two-dimensional *transient* diffusion-convection problems with flow skew to the mesh.

Furthermore, the optimum stabilisation parameters  $\tau$  (or the artificial diffusivities  $\tilde{\alpha}_T$ ) are sought for each case. Extensions from the exact form obtained for one-dimensional steady state diffusion-convection problems are proposed based on two ideas: i. the addition of a transient contribution to damp the stabilisation at early times so as to address transient problems and ii. the segregation of the convection contributions depending on their directions.

### 7.2.1 One-dimensional steady state diffusion-convection problems

Following the work of Brooks and Hughes (1982), the accuracy of the SUPG method is illustrated with a one-dimensional steady state problem. The implementation of the SUPG method in the finite element code developed as part of this research is also validated. Consider the one-dimensional diffusion-convection equation,

$$\alpha_T \operatorname{div} (\nabla T) = \mathbf{v} \nabla T, \quad \text{with} \quad \alpha_T = \frac{\Lambda}{\rho C_v}, \quad (7.27)$$

in which  $\mathbf{v}$  is the velocity,  $T$  the temperature and  $\alpha_T$  the thermal diffusivity of the fluid. Both  $\mathbf{v}$  and  $\alpha_T$  are assumed constant and positive. The problem of finding  $T$  satisfying eq. (7.27) and the following boundary conditions,

$$\begin{aligned} T &= T_0 \quad \text{at } x = 0, \\ T &= T_L \quad \text{at } x = L; \end{aligned} \tag{7.28}$$

is solved by the exact solution,

$$\varphi(x) = \frac{T(x) - T_0}{T_L - T_0} = \frac{1 - \exp\left(\frac{\text{Pe } x}{L}\right)}{1 - \exp(\text{Pe})}, \tag{7.29}$$

where  $\text{Pe}$  is the global Péclet number,

$$\text{Pe} = \frac{v L}{\alpha_T}. \tag{7.30}$$

For a one-dimensional case, with constant data, the SUPG solution with a continuous space discretisation will converge to the solution if the artificial diffusivity  $\tilde{\alpha}_T$  from eq. (7.15) and (7.25) is equal to,

$$\tilde{\alpha}_T = \frac{v h}{2} \tilde{\xi}(\text{Pe}_g), \quad \text{with} \quad \tilde{\xi}(\text{Pe}_g) = \coth \text{Pe}_g - \frac{1}{\text{Pe}_g}, \quad \text{and} \quad \text{Pe}_g = \frac{v h}{2 \alpha_T}, \tag{7.31}$$

in which  $h$  is a characteristic length of the element (point spacing) and  $\text{Pe}_g$  is the *grid Péclet number* which determines whether the problem is locally <sup>1</sup> convection-dominated or diffusion-dominated (Note the division by two compared with the global Péclet number). The limits of the function  $\tilde{\xi}(\text{Pe}_g)$  are,

$$\begin{aligned} \text{Pe}_g \rightarrow \infty \quad &\text{convection-dominated} \quad \tilde{\xi}(\text{Pe}_g) \rightarrow 1, \\ \text{Pe}_g \rightarrow 0 \quad &\text{diffusion-dominated} \quad \tilde{\xi}(\text{Pe}_g)/\text{Pe}_g \rightarrow 1/3. \end{aligned} \tag{7.32}$$

In an effort to improve computational efficiency, Brooks and Hughes (1982) introduced two alternative approximations to the function  $\tilde{\xi}$  (Figure 7.1): the doubly asymptotic approximation,

$$\tilde{\xi}(\text{Pe}_g) = \begin{cases} \text{Pe}_g/3, & -3 \leq \text{Pe}_g \leq 3, \\ \text{sgn } \text{Pe}_g, & |\text{Pe}_g| > 3; \end{cases} \tag{7.33}$$

and the critical approximation,

---

<sup>1</sup>The global Péclet number informs on the dominance of convective heat transport over diffusive heat transport for a domain of length  $L$ . Similarly, the grid Péclet number informs on the dominance of convection over diffusion for a sub-domain/element of length  $h/2$ . Therefore, the dominant heat transport mechanisms may be different depending on the scale under consideration.

$$\tilde{\xi}(\text{Pe}_g) = \begin{cases} -1 - 1/\text{Pe}_g, & \text{Pe}_g < -1, \\ 0, & -1 \leq \text{Pe}_g \leq 1, \\ 1 - 1/\text{Pe}_g, & 1 < \text{Pe}_g. \end{cases} \quad (7.34)$$

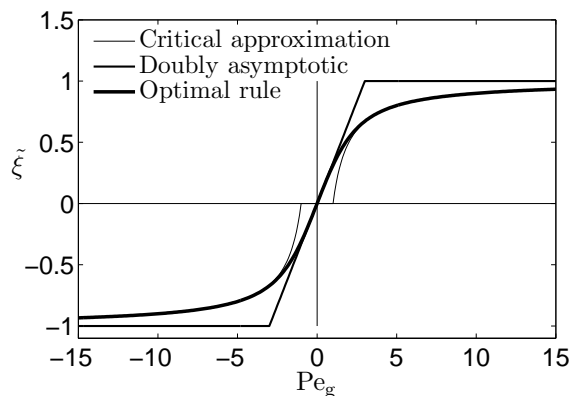


Figure 7.1: The optimal upwind function is approximated by two simplifications: the doubly asymptotic approximation and the critical approximation, Brooks and Hughes (1982, p. 214).

### 7.2.1.1 Simulation results: The stabilisation function $\tilde{\xi}$

To cure the unwanted wiggles, the stabilisation function  $\tilde{\xi}$  is implemented in three different ways as illustrated in Figure 7.1. Finite element responses using (7.31), (7.33) and (7.34) for a grid of 10 elements are compared with the exact solution eq. (7.29) in Figure 7.2. The convective terms are treated implicitly:

- a) The optimal rule solution gives a nodally exact solution.
- b) The finite element response without the use of the SUPG method is easily seen - spurious oscillations, or ‘wiggles’, occur at grid Péclet greater than 1, rendering the solution useless.
- c) The doubly asymptotic approximation is under-convective (or over-diffusive) for a grid Péclet number greater than 1, as if the velocity was underestimated.
- d) The critical approximation is over-convective for a grid Péclet greater or equal to 1, that is the influence of the velocity is overestimated.

These results validate the implementation of the popular SUPG method in the finite element code developed as part of this thesis for one-dimensional uncoupled problems. In the following work, the optimal rule will be preferred to the two alternative formulations proposed earlier to ensure a good accuracy on the finite element results.

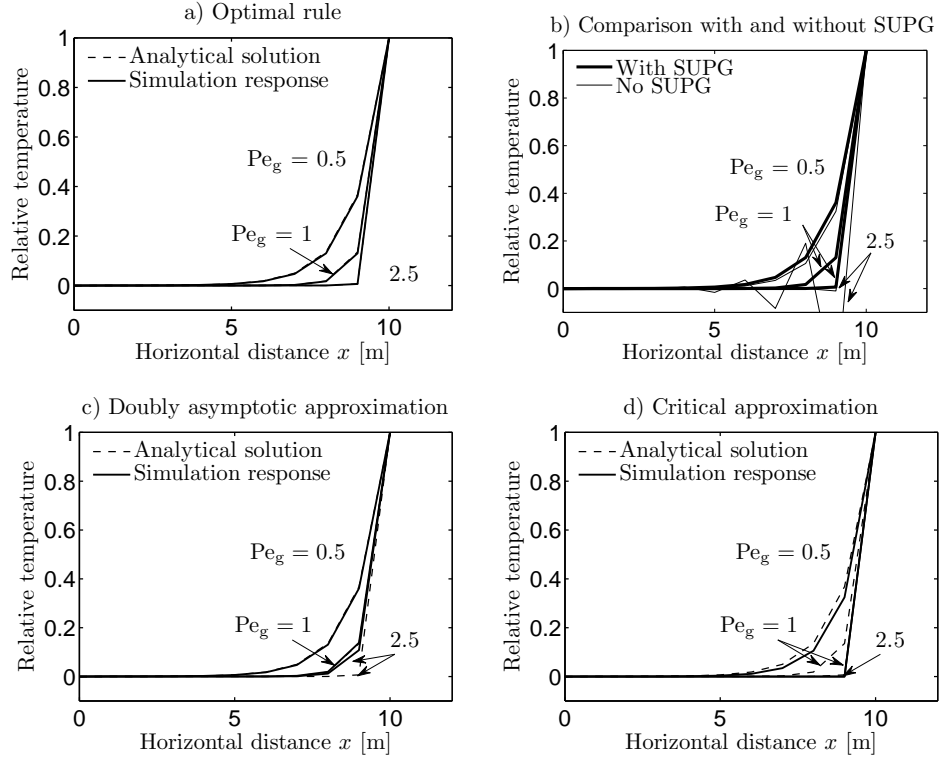


Figure 7.2: Relative temperature profile along the horizontal distance  $x$ . Comparison of the various stabilisation functions  $\tilde{\xi}$  with the exact solution eq. (7.29). While the optimal rule a) gives a nodally exact solution, the doubly asymptotic approximation c) is under-convective and the critical approximation d) is over-convective. b) The comparison between finite element solutions with and without the SUPG method illustrates the spurious oscillations and the efficiency of the method for one-dimensional problems.

### 7.2.1.2 Implicit versus explicit treatment of convection

When the convective term is treated implicitly, eq. (4.69), the convergence of the residual is very good for the optimal rule, the double asymptotic approximation and the critical approximation. Conversely, when the convective term is treated explicitly, eq. (4.72), the convergence of the residual fails for grid Péclet numbers  $Pe_g$  greater than 0.3. This threshold was obtained by performing tests on a one-dimensional, 10 meters length mesh, composed of 10 elements, equally distributed.

Since the explicit treatment of the convective term leads to divergence, for one-dimensional problems endowed with an artificial diffusivity  $\tilde{\alpha}_T$  leading to a nodally exact approximation, the explicit treatment of the convective contribution developed in Subsection 4.3.2 is not pursued further in this work.

### 7.2.1.3 Refining the mesh

Note that the results presented in Figure 7.2 are mesh-independent. In other words if the mesh is refined, the simulation response is more smooth but remains the same as the

analytical result. When the mesh is refined, the point spacing  $h$  is reduced along with the value of the grid Péclet number  $Pe_g$  eq. (7.31); and the smaller the grid Péclet number the less numerical wiggles arise, i.e. the less the SUPG method is needed.

Therefore, for large fluid velocities, the grid Péclet number can be lowered by refining the mesh. This can be useful to avoid the implementation of the SUPG method for problems close to the diffusive-convective limit.

#### 7.2.1.4 Element versus nodal stabilisation

The stabilisation parameter  $\tau = \tilde{\alpha}_T/v^2$  can be calculated for each node or for each element and is then labeled  $\tau^e$ . In practice, for the finite element method, often the element stabilisation is preferred due to the assembling process of elementary matrices. If the mesh is homogeneous, i.e.  $h$  is constant and the fluid velocity  $\mathbf{v}$  is constant, element stabilisation and nodal stabilisation become equal. Both are nodally exact and have a local character, as they are independent of the boundary conditions and of any node positions.

If the mesh is heterogeneous with a constant fluid velocity, element stabilisation and nodal stabilisation become different. For irregular node distribution it is impossible to obtain nodally exact results with element stabilisation, because then the information of the relative up and downstream positions of the neighboring nodes is needed and this cannot be obtained from only one element. For irregular node distribution, the only way to obtain a nodally exact solution is to perform a nodal stabilisation.

In this work, irregular node distributions are avoided in favor of homogeneous meshes. However, the implemented stabilisation is a *nodal* stabilisation since the fluid velocity  $\mathbf{v}$  is assumed to be, in the most general case, non-uniform in space (Remark 7.3). Hence, the fluid velocity  $\mathbf{v}$  can be different for each node inside one element, alike the stabilisation parameter  $\tau$ .

### 7.2.2 One-dimensional transient diffusion-convection problems

The optimal artificial diffusivity  $\tilde{\alpha}_T$  is sought for a one-dimensional *transient* diffusion-convection problem. Two different types of numerical perturbations are observed in transient cases. Undershootings arise due to the stiff thermal boundary condition, near the perturbation. On the other hand, spurious wiggles arise when the heat front hits a ‘hard’ boundary (a boundary condition imposed on the temperature). Hence, the artificial diffusion should smooth both perturbations to be considered optimum.

The partial differential equation of the problem with constant velocity  $\mathbf{v}$  and thermal diffusivity  $\alpha_T$  writes,

$$\alpha_T \operatorname{div} (\nabla T) = \mathbf{v} \cdot \nabla T + \frac{\partial T}{\partial t}. \quad (7.35)$$

The problem of finding  $T$  satisfying eq. (7.35) and the following boundary conditions,

$$\begin{aligned} T &= T_L \quad \text{at } x = 0, \\ T &= T_0 \quad \text{at } x = L; \end{aligned} \tag{7.36}$$

is solved by the exact solution (Carslaw and Jaeger, 1959),

$$\varphi(x) = \frac{T(x) - T_0}{T_L - T_0} = \frac{1}{2} \left[ \operatorname{erfc} \left( \frac{X}{2\sqrt{t^*}} - \frac{\sqrt{t^*}}{2} \right) + e^X \operatorname{erfc} \left( \frac{X}{2\sqrt{t^*}} + \frac{\sqrt{t^*}}{2} \right) \right], \tag{7.37}$$

in which  $\varphi$  denotes the relative temperature; and  $X$  and  $t^*$  are dimensionless parameters defined by,

$$X = \frac{x v}{\alpha_T}, \quad t^* = \frac{v^2 t}{\alpha_T}. \tag{7.38}$$

Figure 7.3 presents the dimensionless temperature profiles along the horizontal distance  $x$  for various times and for four grid Péclet numbers  $\text{Pe}_g$  ranking from 0.34 to 4.3. The mesh is composed of 100 elements of equal length  $h = 0.086$  m. The artificial diffusivity used for the finite element calculation is defined in equation (7.31). The finite element method reproduces well the profile of the analytical solution. An acceptable accuracy is obtained for all grid Péclet numbers.

The difference in accuracy between the simulation response and the analytical solution is most probably due to the choice of the artificial diffusivity  $\tilde{\alpha}_T$ . According to Section 7.1.4, the artificial diffusivity used here does not lead to a nodally exact solution for transient diffusion-convection problems unlike the steady diffusion-convection case.

In transient problems, undershooting arise due to the stiff thermal boundary condition applied on the left-hand-side ( $x = 0$  m) at the very beginning of the simulation. This undershooting is larger when accounting for the SUPG method compared with a non-stabilised response (Figure 7.4). This numerical disturbance has already been described in the literature (Yin et al., 2010). Reducing this excessive undershooting (or overshooting for cooling test) at the beginning of the calculation is crucial to the stability and the accuracy of the overall response. One way to avoid such numerical problem is to account for a transient-contribution in the artificial diffusivity. The issue of the definition of the artificial diffusivity for transient problems is discussed later in Section 7.2.2.2.

### 7.2.2.1 The SUPG method : a cure for spurious oscillations

To illustrate the numerical spurious oscillations induced by the convection term and the curative effect of the SUPG method, the simulation responses are compared for diffusion without convection, diffusion-convection with SUPG and diffusion-convection without



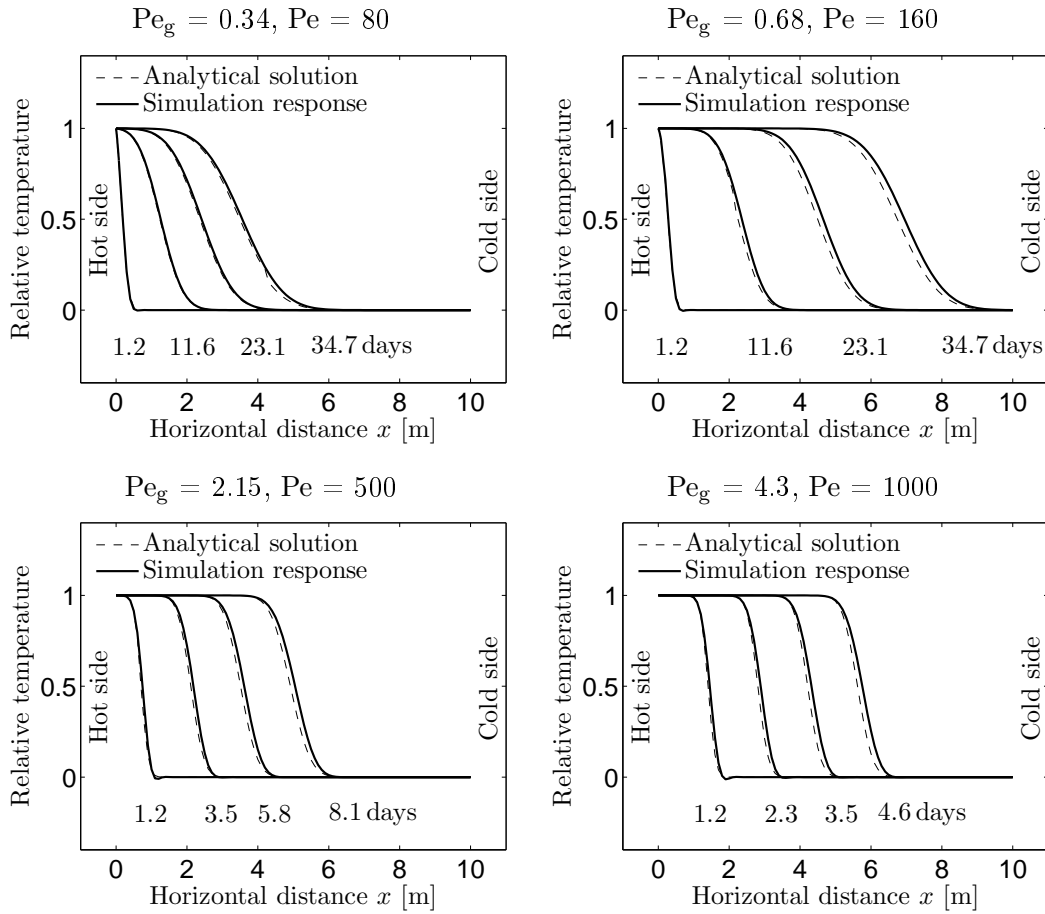


Figure 7.3: Relative temperature profiles along the horizontal direction  $x$  for four different times and for grid Péclet numbers  $Pe_g$  ranking from 0.34 to 4.3. The characteristic length of the elements  $h$  is equal to 0.086 m and the fluid velocity is set equal to  $v = 2Pe_g \alpha_T / h$ . The finite element response reproduces well the convection-dominated profile of the analytical solution. The accuracy of the solution is good when using the definition of the artificial diffusivity expressed in eq. (7.31).

SUPG in Figure 7.5. Spurious oscillations arise for grid Péclet numbers  $Pe_g > 1$  and when the heat front reaches a sharp boundary condition.

The comparison is presented for two grid Péclet numbers :  $Pe_g = 2.15$  and  $Pe_g = 36.6$  (Figure 7.5). The mesh is composed of 100 elements of uniform length  $h$ . The evolution of the grid Péclet numbers represents a pure increase of fluid velocity  $v$ . With diffusion only, the heat is penetrating very slowly in the layer. For all the proposed times, the transition between the maximum and the minimum of the relative temperature,  $\varphi = 1$  and  $\varphi = 0$ , remains very close to the heated side. When convection is added to diffusion, heat propagates faster in the layer than the response without convection. Without accounting for the SUPG method, wiggles arise when the heat front hits the boundary condition  $\varphi(x = 10\text{ m}) = 0$ . These spurious oscillations render the solution useless. If the SUPG method is used to stabilise the transient diffusion-convection problem, wiggles are suppressed. For semi-infinite problems, that is with no sharp boundary condition blocking the heat front

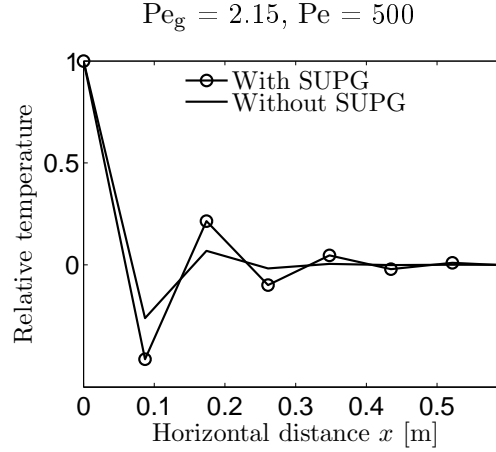


Figure 7.4: Relative temperature profile along the horizontal direction  $x$  for  $t = 100$  s. The characteristic length of the elements  $h$  is equal to 0.086 m and the fluid velocity is set equal to  $v = 2Pe_g \alpha_T / h$ . Oscillations arise during the early period due to the sharp temperature gradient applied at the boundary:  $x = 0$  m. When accounting for the SUPG method, these oscillations are larger than the non-stabilised response. This increase of numerical perturbation may induce serious stability and convergence issues in coupled problems. The remedial action to this problem is to add a transient-contribution in the artificial diffusivity formula which is discussed in Section 7.2.2.2.

propagation, the SUPG method is not needed as no spurious wiggles are likely to appear. An example of such problems is treated in Nair et al. (2004).

### 7.2.2.2 Influence of the artificial diffusivity

In order to find the optimum stabilisation correction factor for a one-dimensional *transient* diffusion-convection problem, the temperature profiles are compared for different artificial diffusivities  $\tilde{\alpha}_{T_i}$ , for  $i = 1, 10$ . These definitions are compared in Figure 7.7 and defined throughout this section.

Brooks and Hughes (1982) refer to the work of Raymond and Garder (1976) who proposed a stabilisation parameter to maximise accuracy near boundary layers. Combinations of the definitions of  $\tilde{\alpha}_T$  with Raymond and Garder's proposition (Raymond and Garder, 1976) are proposed throughout.

- For steady state diffusion-convection problems, Brooks and Hughes (1982) introduced the optimal function  $\tilde{\xi}_{\text{opt}}$  along with the artificial diffusivity  $\tilde{\alpha}_{T1}$ ,

$$\tilde{\xi}_{\text{opt}}(Pe_g) = \coth Pe_g - 1/Pe_g, \quad \tilde{\alpha}_{T1} = \frac{hv}{2} \tilde{\xi}_{\text{opt}}(Pe_g). \quad (7.39)$$

For a transient purely convective problem ( $\alpha_T = 0$ ), Raymond and Garder (1976) proposed to modify the denominator of equation (7.39) to  $\sqrt{15}$ . With this optimum choice, the phase accuracy is improved from fourth order to sixth order according

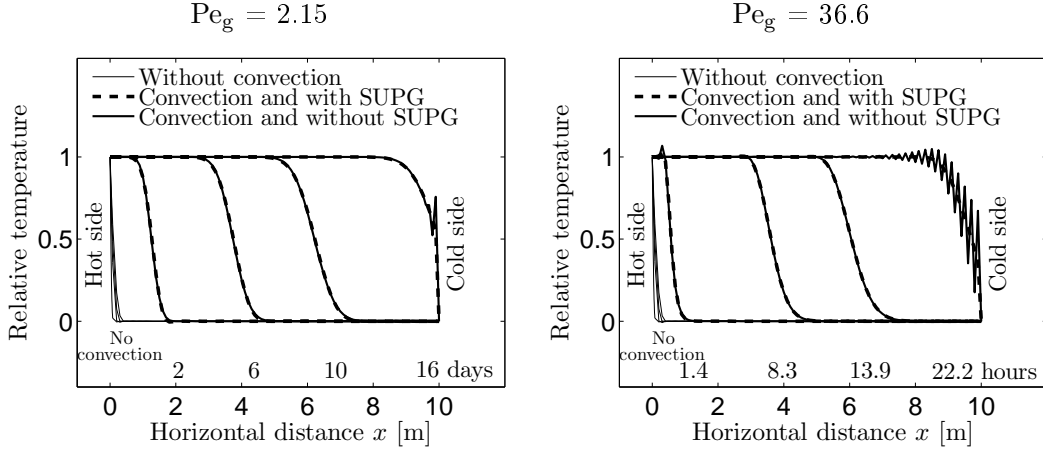


Figure 7.5: Relative temperature profile along the horizontal direction  $x$ . The characteristic length of the elements  $h$  is equal to 0.086 m and the fluid velocity is set equal to  $v = 2 \text{Pe}_g \alpha_T / h$ . The simulation response for diffusion only is compared with that of diffusion-convection with SUPG and diffusion-convection without SUPG. With no convection, the heat front propagates slowly in the layer and all the curves remain on the left-hand-side. On the other hand, if convection is accounted for, the heat propagates more quickly in the layer. Spurious oscillations arise when the heat front hits the hard boundary  $\varphi(x = 10\text{m}) = 0$  and when the SUPG method is not accounted for. The popular SUPG method removes efficiently these unwanted numerical wiggles. Without the SUPG method, the higher the grid Péclet number, the more numerical wiggles arise.

to the method of Dendy (1974). As proposed by Brooks and Hughes (1982), this proposition is extended to a transient diffusion-convection problem ( $\alpha_T \neq 0$ ),

$$\tilde{\alpha}_{T2} = \frac{h\nu}{\sqrt{15}} \tilde{\xi}_{\text{opt}}(\text{Pe}_g). \quad (7.40)$$

- A general design of  $\tilde{\alpha}_T$  is proposed by Shakib et al. (1991) in a space-time Galerkin /least-squares variational formulation. Two additional forms of the function  $\tilde{\xi}(\text{Pe}_g)$  (also named the diffusion correction factor) are introduced (Figure 7.6). Hence, two additional forms of the artificial diffusivity are inferred: a. from the general design conditions:

$$\tilde{\xi}_{\text{gen}}(\text{Pe}_g) = \left(1 + \frac{1}{\text{Pe}_g^2}\right)^{(-1/2)}, \quad \tilde{\alpha}_{T3} = \frac{h\nu}{2} \tilde{\xi}_{\text{gen}}(\text{Pe}_g), \quad (7.41)$$

and b. from a modified definition of  $\tilde{\xi}_{\text{gen}}(\text{Pe}_g)$ :

$$\tilde{\xi}_{\text{mod}}(\text{Pe}_g) = \left(1 + \frac{9}{\text{Pe}_g^2}\right)^{(-1/2)}, \quad \tilde{\alpha}_{T\text{mod}} = \frac{h\nu}{2} \tilde{\xi}_{\text{mod}}(\text{Pe}_g). \quad (7.42)$$

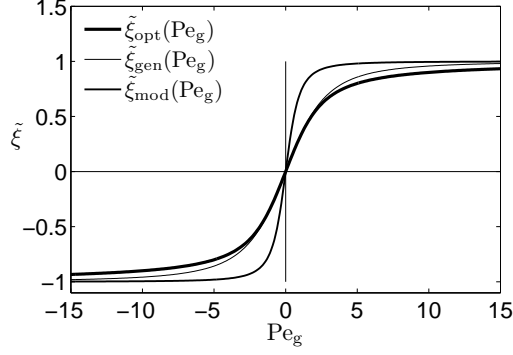


Figure 7.6: Integration rule for optimal upwind scheme (Brooks and Hughes, 1982), generic approximation, and modified approximation by Shakib et al. (1991).

By using the generic diffusion correction factor  $\tilde{\xi}_{\text{gen}}$ ,  $\tilde{\alpha}_{T3}$  writes,

$$\tilde{\alpha}_{T3} = \left[ \underbrace{\left(\frac{2}{v h}\right)^2}_{\text{convective limit}} + \underbrace{\left(\frac{4\alpha_T}{v^2 h^2}\right)^2}_{\text{diffusive limit}} \right]^{(-1/2)}. \quad (7.43)$$

in which the two terms on the right-hand-side can be interpreted as the convection-dominated and diffusion-dominated limits (Tezduyar and Osawa, 2000). Towards the convection-dominated limit, the dependency on the mesh size  $h$  is  $\tilde{\alpha}_{T3} \approx hv/2$ , hence  $O(h)$ , while it is  $\tilde{\alpha}_{T3} \approx h^2v^2/4\alpha_T$  towards the diffusion-dominated limit, hence  $O(h^2)$ . Fortunately, the mesh dependency of convection is smaller than that of diffusion.

Combining the modified function  $\tilde{\xi}_{\text{mod}}(\text{Pe}_g)$  with the proposition of Raymond and Garder (1976) leads to,

$$\tilde{\alpha}_{T4} = \frac{hv}{\sqrt{15}} \tilde{\xi}_{\text{mod}}(\text{Pe}_g). \quad (7.44)$$

- Tezduyar and Osawa (2000) proposed some new ways of computing the artificial diffusivity based on the element-level matrices and vectors. In one-dimension, the extension of  $\tilde{\alpha}_{T3}$  (7.43) to transient problems is,

$$\tilde{\alpha}_{T5} = \left[ \underbrace{\left(\frac{2}{v h}\right)^2}_{\text{convective limit}} + \underbrace{\left(\frac{2}{v^2 \Delta t}\right)^2}_{\text{transient limit}} + \underbrace{\left(\frac{4\alpha_T}{v^2 h^2}\right)^2}_{\text{diffusive limit}} \right]^{(-1/2)}. \quad (7.45)$$

Note that towards transient-dominated limit,  $\tilde{\alpha}_{T5} \approx v^2 \Delta t / 2$  and there is a relation of  $O(v^2 \Delta t)$ : the artificial diffusivity is mesh independent but becomes dependent on the time step  $\Delta t$ . The second term on the right-hand-side of eq. (7.45) mimics the convective contribution. For clarity the reasoning is performed with the stabilisation parameter  $\tau_5$ : having an operator  $v \partial T / \partial x$ , the convection contribution to  $\tau_5$  can be estimated by  $h / 2v$ . Hence having  $\partial T / \partial t$  brings the following contribution to  $\tau_5$ :  $\Delta t / 2$ . Since  $\tilde{\alpha}_{T5} = v^2 \tau_5$ , each contribution is multiplied by  $v^2$ .

Again, combining  $\tilde{\alpha}_{T5}$  with the proposition of Raymond and Garder (1976) leads to:

$$\tilde{\alpha}_{T6} = \left[ \left( \frac{\sqrt{15}}{v h} \right)^2 + \left( \frac{\sqrt{15}}{v^2 \Delta t} \right)^2 + \left( \frac{2\sqrt{15} \alpha_T}{v^2 h^2} \right)^2 \right]^{(-1/2)}. \quad (7.46)$$

- Earlier, Tezduyar and Ganjoo (1986) proposed for transient diffusion-convection problems to use the *algorithmic courant number*  $C_{2\tau}$  or the *element courant number*  $C_{\Delta t}$ ,

$$C_{2\tau} = \frac{2 \tilde{\alpha}_T}{h v} = \frac{2 \tau v}{h}, \quad C_{\Delta t} = \frac{\Delta t v}{h}, \quad (7.47)$$

to weight the stabilisation which leads to the following definitions of the artificial diffusivity,

$$\begin{aligned} \tilde{\alpha}_{T7} &= \tilde{\alpha}_{T1} \times C_{2\tau}(\tilde{\alpha}_{T1}), & \tilde{\alpha}_{T8} &= \tilde{\alpha}_{T2} \times C_{2\tau}(\tilde{\alpha}_{T2}), \\ \tilde{\alpha}_{T9} &= \tilde{\alpha}_{T1} \times C_{\Delta t}, & \tilde{\alpha}_{T10} &= \tilde{\alpha}_{T2} \times C_{\Delta t}, \end{aligned} \quad (7.48)$$

the idea being that the smaller the convective time  $\tau$  [s] or the time step  $\Delta t$  [s], the smaller the artificial diffusivities and conversely.

As pointed out by Brooks and Hughes (1982, p. 215), the structure of the streamline upwind weighting function ( $\mathbf{W}_T$  in Section 7.1) is far more important than the precise value of the artificial diffusivity  $\tilde{\alpha}_T$ . The response obtained with the artificial diffusivity  $\tilde{\alpha}_{T1}$  provides a smoother response along the cold side, that is a better stabilisation, than all the other propositions  $\tilde{\alpha}_{Ti}$  for  $i = 2, 10$  (Figure 7.7). Nevertheless, the transition between the transient-dominated period and the convection-dominated period is better represented by the parameters  $\tilde{\alpha}_{T5}$ ,  $\tilde{\alpha}_{T6}$  and  $\tilde{\alpha}_{T9}$ ,  $\tilde{\alpha}_{T10}$ .

These parameters have in common to account for the time step  $\Delta t$ . In transient calculations, the time step is not constant and varies from small values, for example 1s,

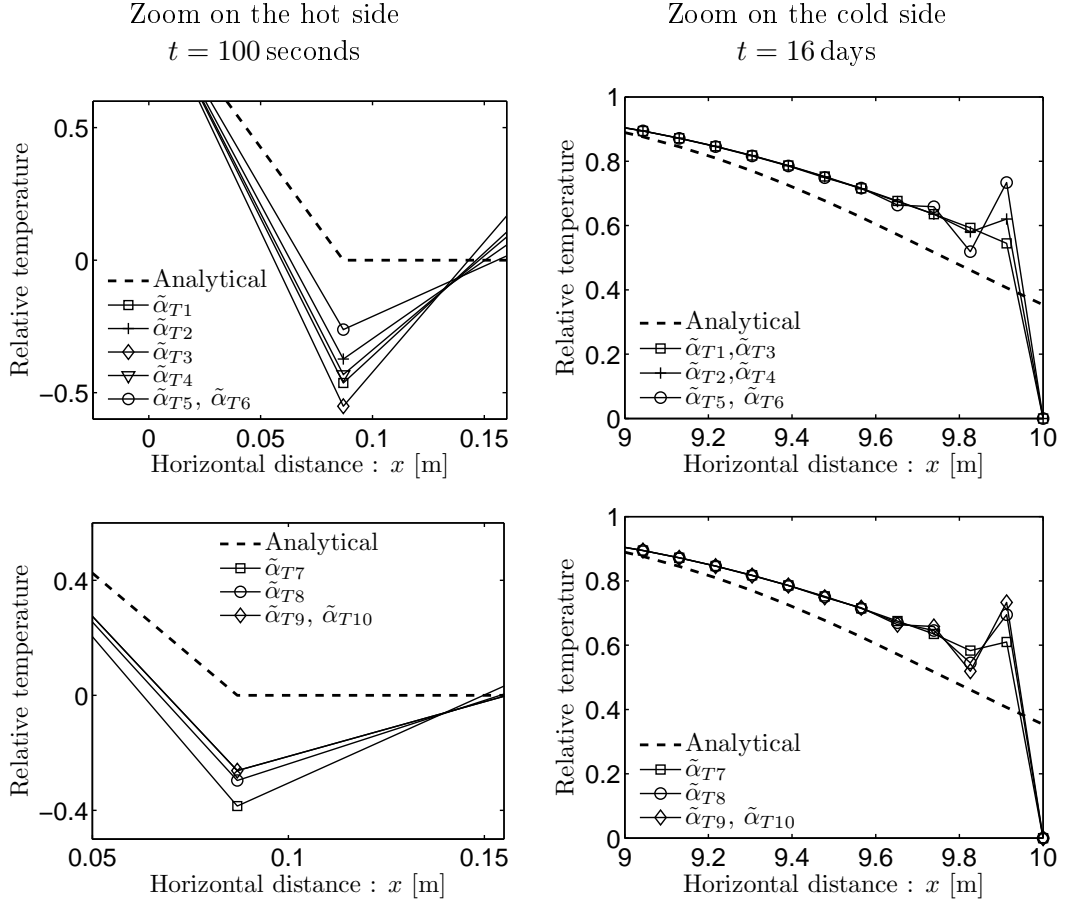


Figure 7.7: Relative temperature profiles along the horizontal direction  $x$  for artificial diffusivities  $\tilde{\alpha}_{T_i}$ , for  $i = 1, 6$  (top);  $\tilde{\alpha}_{T_i}$ , for  $i = 7, 10$  (bottom). The grid Péclet number  $Pe_g$  is equal to 2.15. The characteristic length of the elements  $h$  is equal to 0.086 m and the fluid velocity is set equal to  $v = 2Pe_g \alpha_T/h$ . Along the cold side (right), the parameter  $\tilde{\alpha}_{T1}$  provides a better stabilisation than the other propositions. On the other hand, close to the perturbation (left), the parameters  $\tilde{\alpha}_{T5}, \tilde{\alpha}_{T6}$  and  $\tilde{\alpha}_{T9}, \tilde{\alpha}_{T10}$  provide a better transition between the transient-dominated period and the convection-dominated period.

to a maximum value, for example  $10^6$  s. This time step repartition is required to perform thermal loading tests with a Heaviside step function. Hence, the parameters  $\tilde{\alpha}_{T5}, \tilde{\alpha}_{T6}, \tilde{\alpha}_{T9}$  and  $\tilde{\alpha}_{T10}$  tend to reduce the artificial diffusivity during the transient-dominated period and to maximise it during the convection-dominated period.

Stability and convergence of the coupled model are closely related to the transition between the transient-dominated and the convection-dominated periods. Therefore, for transient problems, the artificial diffusivity  $\tilde{\alpha}_{T5}$  is used henceforth in the absence of an optimum parameter.

To summarise, the SUPG method is necessary to damp oscillations that occur in the neighborhood of a sharp boundary condition, for large grid Péclet numbers. The method has still its shortcomings in the transient case (Figure 7.4) in which the use of standard stabilisation parameters leads to undershooting oscillations at early times in the neighbor-

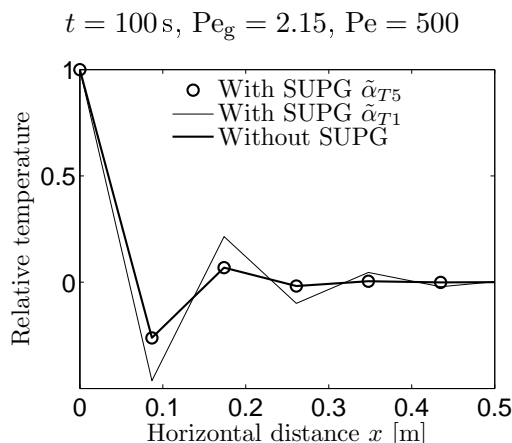


Figure 7.8: Relative temperature profile along the horizontal direction  $x$  for  $t = 100 \text{ s}$ . The characteristic length of the elements  $h$  is equal to  $0.086 \text{ m}$  and the fluid velocity is set equal to  $v = 2 \text{Pe}_g \alpha_T / h$ . The streamline upwind diffusivity proposed by Tezduyar and Osawa (2000) in eq. (7.45) reduces significantly the spurious oscillations encountered at early times with respect to the standard streamline upwind diffusivity  $\tilde{\alpha}_{T1}$  (7.39). The ‘transient/short time wiggles’ are now of the same magnitude as the response of convection without SUPG, that is the use of the SUPG method will not induce more spurious oscillations in coupled transient problems compared with the Galerkin method.

hood of the loading boundary. The modification of the SUPG method including a transient contribution alleviates the issue. The end result is displayed in Figure 7.8.

**Remark 7.4.** *The maximum time step  $\Delta t_{\max}$  needs to be calibrated so as not to compromise the effect of the stabilisation parameter during the convection-dominated period.*

*The time step  $\Delta t$  is defined to vary exponentially towards a maximum  $\Delta t_{\max}$  in the form:  $1, 1, \dots, 10, 10, \dots, \Delta t_{\max}, \dots, \Delta t_{\max}$ . This feature allows the computation of long-term applications, over several years, with a precise loading phase, over several hours.*

*The definition of the stabilisation parameter (Tezduyar and Osawa, 2000) includes a contribution related to the transient-dominated period,*

$$\tau_5 = \left[ \underbrace{\left(\frac{2v}{h}\right)^2}_{\text{convection limit}} + \underbrace{\left(\frac{2}{\Delta t}\right)^2}_{\text{transient limit}} + \underbrace{\left(\frac{4\alpha_T}{h^2}\right)^2}_{\text{diffusion limit}} \right]^{(-1/2)} \quad (7.49)$$

*in which the time step  $\Delta t$  is used. If the maximum time step allowed is too small, this transient contribution will remain large enough to disturb the efficiency of the stabilisation parameter  $\tau_5$  during the convection-dominated period, which inevitably leads to a convergence failure at large time steps. Therefore, unlike the classic practice to reduce the maximum time step when divergence appears, the maximum time step must be increased to allow a good convergence during the convection-dominated period (at large time steps  $\gg \Delta t_{\max}$ ).*

One way to calibrate the maximum time step  $\Delta t_{\max}$  is to ensure that,

$$\left(\frac{2}{\Delta t_{\max}}\right)^2 \ll \left(\frac{2v}{h}\right)^2 + \left(\frac{4\alpha_T}{h^2}\right)^2, \quad \rightarrow \quad \Delta t_{\max} \geq \delta \sqrt{\frac{h^4}{h^2v^2 + 4\alpha_T^2}} \quad (7.50)$$

in which  $\delta$  is higher or equal to 4. In addition, the maximum time step should also satisfy the stability requirements (see Section 7.2.5),

$$\Delta t_{\max} \leq \frac{L^2}{\alpha_T}, \quad (7.51)$$

so that by combining the lower bound (7.51) and the upper bound (7.50) an additional constrain on the mesh size  $h$  arise,

$$\delta^2 \alpha_T^2 h^4 + L^4 v^2 h^2 + 4L^4 \alpha_T^2 \geq 0 \quad (7.52)$$

which provides one positive lower bound to  $h$

$$h \geq \left( \frac{-L^4 v^2 + \sqrt{L^8 v^4 - 16L^4 \alpha_T^4 \delta^2}}{2\delta^2 \alpha_T^2} \right)^{0.5} \quad (7.53)$$

Fortunately, this lower bond tends to zero since  $L^8 v^4 \gg 16^2 L^4 \alpha_T^4$  for  $\delta = 4$  and water  $\alpha_T \approx 1 \times 10^{-7}$ .

### 7.2.3 Two-dimensional steady diffusion-convection problems

A unique optimal artificial diffusivity is sought for a two-dimensional steady diffusion-convection problem based on the differentiation of the convection magnitude in the  $x$ -direction and in the  $y$ -direction. The simulation response is compared with the analytical solution for a flow skew to the mesh and for high Péclet numbers. The influence of the angle between the velocity and the mesh is analysed.

The partial differential equation of the problem writes,

$$v_x \frac{\partial T}{\partial x} + v_y \frac{\partial T}{\partial y} = \alpha_T \left( \frac{\partial^2 T}{\partial x^2} + \frac{\partial^2 T}{\partial y^2} \right), \quad (7.54)$$

in which  $x$  and  $y$  are the space directions. Following the notation of Section 7.1, the weak formulation of the above problem when using the SUPG method and bilinear shape functions becomes,



$$\sum_{e=1}^{\text{nel}} [\delta \mathbf{T}^e]^\top \left[ \int_{V^e} \mathbf{N}_T^\top \left( v_x \frac{\partial T}{\partial x} + v_y \frac{\partial T}{\partial y} - \alpha_T \frac{\partial^2 T}{\partial x^2} - \alpha_T \frac{\partial^2 T}{\partial y^2} \right) dV^e + \int_{V^e} \tau \left( v_x \frac{\partial \mathbf{N}_T}{\partial x} + v_y \frac{\partial \mathbf{N}_T}{\partial y} \right)^\top \left( v_x \frac{\partial T}{\partial x} + v_y \frac{\partial T}{\partial y} \right) dV^e \right] = 0, \quad (7.55)$$

where the stabilisation parameter  $\tau = \tilde{\alpha}_T / \|\mathbf{v}\|^2$  addresses both space directions at once.

### 7.2.3.1 Multidimensional artificial diffusivity

For bilinear isoparametric quadrilaterals, one generalisation of equation (7.31) was proposed by Brooks and Hughes (1982),

$$\begin{aligned} \tilde{\alpha}_T &= \frac{v_x h_x \tilde{\xi}_x + v_y h_y \tilde{\xi}_y}{2}, \\ \tilde{\xi}_x &= \coth \text{Pe}_{g_x} - \frac{1}{\text{Pe}_{g_x}}, & \tilde{\xi}_y &= \coth \text{Pe}_{g_y} - \frac{1}{\text{Pe}_{g_y}}, \\ \text{Pe}_{g_x} &= \frac{v_x h_x}{2 \alpha_T}, & \text{Pe}_{g_y} &= \frac{v_y h_y}{2 \alpha_T}, \\ v_x &= \mathbf{e}_x \cdot \mathbf{v}, & v_y &= \mathbf{e}_y \cdot \mathbf{v}, \end{aligned} \quad (7.56)$$

in which the unit vectors  $\mathbf{e}_x$  and the  $\mathbf{e}_y$ , and element lengths  $h_x$  and  $h_y$  are defined in Figure 7.9, and the components  $v_x$  and  $v_y$  of the velocity vector are evaluated at each Gauss point, while the diffusion property  $\alpha_T$  is isotropic.

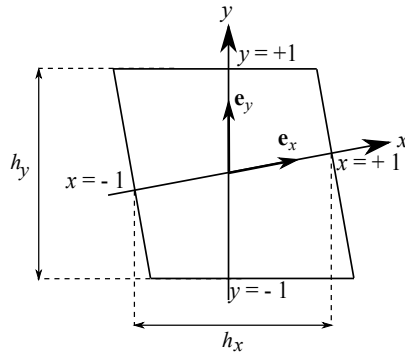


Figure 7.9: Four node parallelogram finite element geometry; definitions of element lengths  $h_x$  and  $h_y$  used in eq. (7.56). For more general quadrilaterals, a proposition is given in Section 7.2.4.

### 7.2.3.2 Analytical solution for high Péclet numbers

The two-dimensional diffusion-convection problem (7.54) can be re-written into a new coordinate system for an isotropic diffusivity  $\alpha_T$ , where  $\xi$  is aligned with the flow direction and  $\eta$  is perpendicular,

$$v_\xi \frac{\partial T}{\partial \xi} + v_\eta \frac{\partial T}{\partial \eta} = \alpha_T \left( \frac{\partial^2 T}{\partial \xi^2} + \frac{\partial^2 T}{\partial \eta^2} \right). \quad (7.57)$$

By assuming that diffusion in the flow direction  $\xi$  is much less important than convection, and that no convection occurs perpendicular to the flow, the problem reduces to,

$$v_\xi \frac{\partial T}{\partial \xi} = \alpha_T \frac{\partial^2 T}{\partial \eta^2} \quad \Leftrightarrow \quad \frac{\partial T}{\partial t} = \alpha_T \frac{\partial^2 T}{\partial \eta^2}, \quad (7.58)$$

which becomes equivalent to a transient conduction problem in which time  $t$  is replaced by  $\xi/v_\xi$  (Raithby, 1976).

The closed form solution of the simplified problem (7.58) is sought for a bounded square domain presented in Figure 7.10 (top-left). The velocity vector  $\mathbf{v}$  is uniform and skew to the grid. Let us define a solid line, which is parallel to the velocity vector, and which passes through the center of the domain. The thermal boundary conditions are  $\varphi = 1$  above the solid line and  $\varphi = 0$  under. When the solid line intersects a boundary node of the mesh, a value of  $\varphi = 0.5$  is assigned to this node.

The analytical solution (Carslaw and Jaeger, 1959) for the specific problem is (Raithby, 1976):

$$\begin{aligned} \varphi(x^*, y^*) &= \frac{T(x^*, y^*) - T_0}{T_L - T_0} \\ &= 0.5 \left[ 1 + \operatorname{erf} \left\{ \sqrt{\frac{\operatorname{Pe}_g}{2}} \left( \frac{(y^* - y_c^*)v_x^* - x^*v_y^*}{\sqrt{(y^* - y_c^*)v_y^* + x^*v_x^*}} \right) \right\} \right] \end{aligned} \quad (7.59)$$

in which  $T_0$  is equal to 273 K and  $T_L$  is equal to  $T_0 + 50$  K. The superscript \* indicates dimensionless values, such as,

$$x^* = \frac{x}{h_x}, \quad y^* = \frac{y}{h_y}, \quad y_c^* = \frac{y_c}{h_y}, \quad v_x^* = \frac{v_x}{\|\mathbf{v}\|}, \quad v_y^* = \frac{v_y}{\|\mathbf{v}\|}, \quad (7.60)$$

with,

$$\|\mathbf{v}\| = \sqrt{v_x^2 + v_y^2}. \quad (7.61)$$

and where  $y_c^*$  is indicated on Figure 7.10 (top-left). This solution is valid for  $\tilde{\alpha}_T \gg 1$  and far enough from the upstream boundary conditions ( $x = 0$  m in Figure 7.10, top-left).

### 7.2.3.3 Simulation results

The grid has a dimension of  $10 \times 10 \text{ m}^2$  and is discretised with a  $10 \times 10$  mesh of equal sized square elements ( $h_x = h_y = 1$ ). The grid Péclet number is set equal to  $\text{Pe}_{g_x} = \text{Pe}_{g_y} = 10^6$  and the diffusivity of the fluid (water) is equal to  $\alpha_T = 1.4 \times 10^{-6} \text{ m}^2/\text{s}$  resulting in a velocity  $\|\mathbf{v}\| = 2.8 \text{ m/s}$ .

In Figures 7.10 and 7.11, the analytical solution eq. (7.59) is compared with the finite element responses with SUPG and without SUPG (Galerkin method) to evaluate the influence of the angle  $\theta$  between the velocity direction and the  $x$ -direction on the accuracy of the SUPG method. Because the global Péclet number is equal to  $\text{Pe} = 2 \times 10^7$ , the solution is essentially one of pure convection.

For  $\theta = 0^\circ$ , the analytical solution matches that of the SUPG method as the artificial diffusivity  $\tilde{\alpha}_T$  reduces to the one-dimensional one, which provides a nodally exact solution in one-dimension. As the angle  $\theta$  is increased from  $0^\circ$  to  $45^\circ$ , the SUPG procedure stabilises the spurious wiggles and a good agreement with the analytical solution is obtained. Brooks and Hughes (1982) observed that for the particular case of  $\theta = 45^\circ$  the SUPG method with a two-by-two quadrature provides a less accurate solution than a one point Gaussian quadrature.

Nevertheless, the case  $\theta = 45^\circ$  is the exception. In general, the SUPG method with a two-by-two quadrature provides a better response than the SUPG method with a one point quadrature and than the Galerkin approach. Furthermore, the SUPG method enjoys the absence of spurious crosswind diffusion unlike the upwind method.

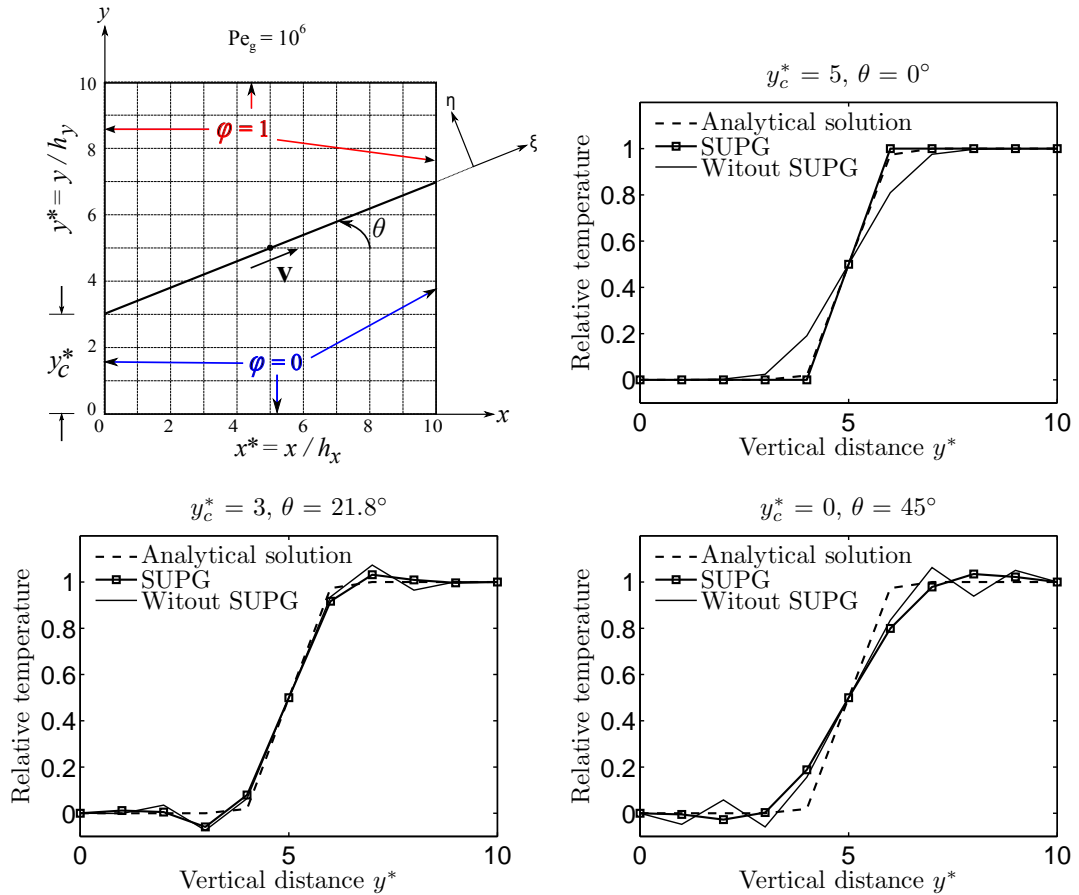


Figure 7.10: Relative temperature profiles along the vertical direction  $y^*$ , at  $x^* = 5$  and for a convective flow skewed to the mesh,  $Pe_g = 10^6$ . The tests are run for three values of  $y_c^*$  which correspond to three angles  $\theta$  of the velocity with the grid lines:  $\theta = 0^\circ$ ,  $\theta = 21.8^\circ$  and  $\theta = 45^\circ$ . The analytical solution is compared with the finite element response with and without SUPG. The SUPG procedure provides satisfactory results and stabilises well the response compared with the Galerkin method (without SUPG). When the angle is  $\theta = 0^\circ$ , the SUPG response is in perfect agreement with the analytical response. As the angle  $\theta$  increases from 0 to  $45^\circ$ , the SUPG response slightly comes away from the step but remains quite smooth in comparison with the non-stabilised response. The stabilisation effect of the SUPG method is mainly visible for  $\theta = 45^\circ$ .

#### 7.2.4 Two-dimensional transient diffusion-convection problems

Again, a unique optimal stabilisation parameter is sought for a two-dimensional *transient* diffusion-convection problem which is extended from the optimum parameter found for one-dimensional transient problems (that is accounting for a transient limit contribution) rather than from the previous two-dimensional steady state proposition which segregates the  $x$ -direction from the  $y$ -contribution. No analytical solution has been found for this problem and the numerical response is compared for various weighting functions for a flow skewed to the mesh.

The two-dimensional transient diffusion-convection partial differential equation is extended from Section (7.2.3),

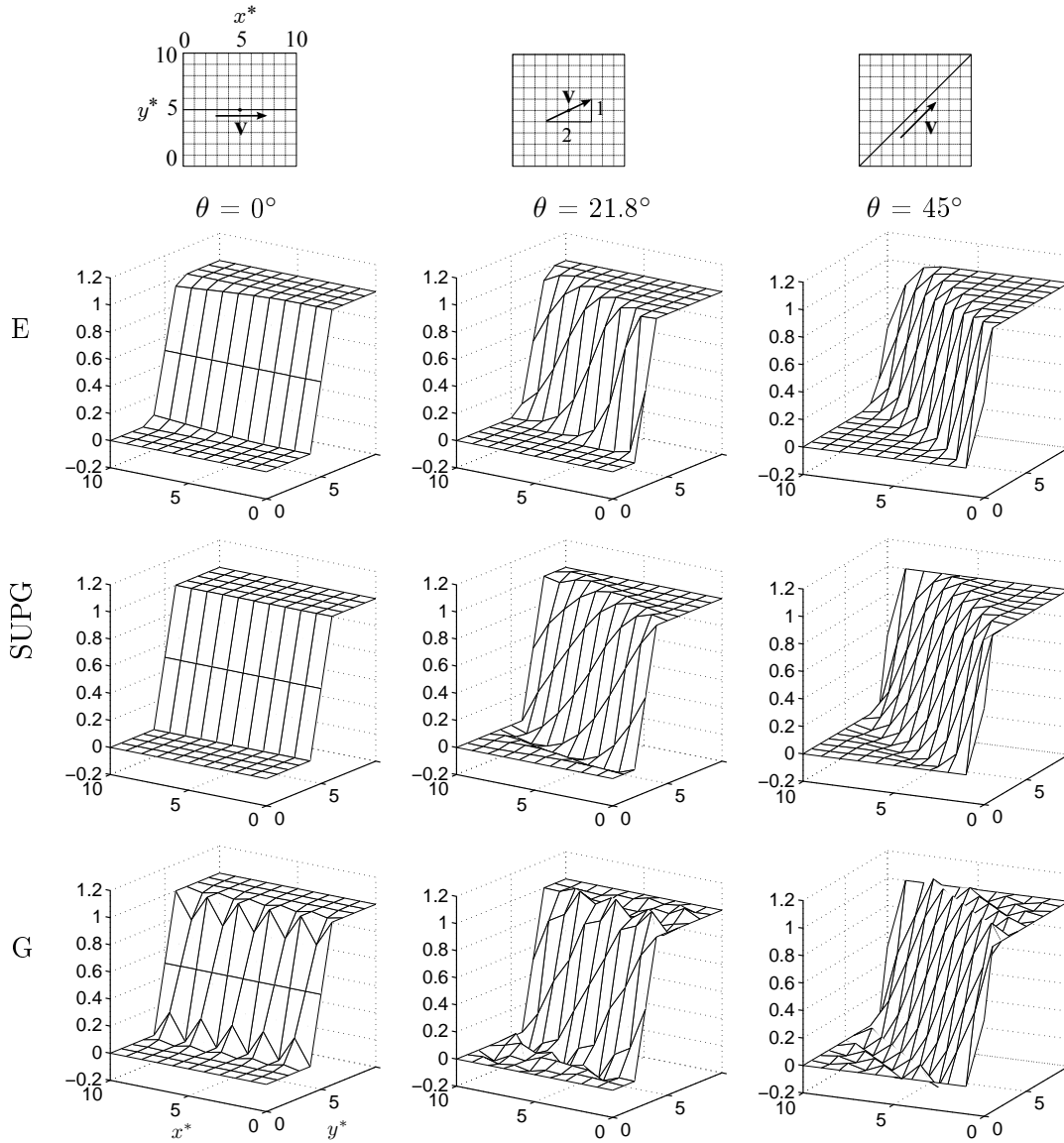


Figure 7.11: Relative temperature profiles in the plane  $(x^*, y^*)$ , for a convective flow skew to the mesh,  $\text{Pe}_g = 10^6$ . E illustrates the exact solution of a convection-dominated problem, from eq. (7.59). SUPG stands for the finite element response accounting for the SUPG method which demonstrates the stabilisation effect of the method. G represents the finite element response with no stabilisation (Galerkin method): spurious wiggles disturb the solution. The SUPG method significantly improves upon the Galerkin method as it efficiently cures the spurious wiggles. In addition, a good agreement with the exact solution is obtained for all the proposed angles.

$$\frac{\partial T}{\partial t} + \mathbf{v} \cdot \nabla T = \text{div}(\alpha_T \nabla T), \quad (7.62)$$

where  $\mathbf{v}$  is the velocity vector. The weak formulation of eq. (7.62) when using the SUPG method and linear shape functions  $\mathbf{N}_T$ , becomes,

$$\sum_{e=1}^{nel} [\delta \mathbf{T}^e]^T \left[ \int_{V^e} \mathbf{N}_T^T \left( \frac{\partial T}{\partial t} + \mathbf{v} \cdot \nabla T - \operatorname{div}(\alpha_T \nabla T) \right) dV^e + \int_{V^e} \tau (\mathbf{v} \cdot \nabla \mathbf{N}_T)^T \left( \frac{\partial T}{\partial t} + \mathbf{v} \cdot \nabla T \right) dV^e \right] = 0, \quad (7.63)$$

where the stabilisation is applied to all terms of eq. (7.62) except the diffusion term which vanishes on the element's interior.

#### 7.2.4.1 Multidimensional transient stabilisation parameter

Tezduyar and Osawa (2000) proposed an comprehensive way of computing the stabilisation parameter  $\tau$  for multidimensional and transient diffusion-convection problems. In their contribution,  $\tau$  is based on the element-level matrices and vectors and is computed at an element level. Their approach is followed throughout this section; except that the stabilisation parameter is computed at the node level. The main advantage of the formulation is that it automatically takes into account the transition between the transient-dominated period, the diffusion-dominated and the convection-dominated periods. This section taps on the work of Tezduyar and Osawa (2000) and we should refer to them for more detailed explanations.

A compact notation of the element matrices is introduced as following,

$$\begin{aligned} \mathbf{m}^e &= \int_{V^e} \mathbf{N}_T^T \frac{\partial T}{\partial t} dV^e, \\ \mathbf{c}^e &= \int_{V^e} \mathbf{N}_T^T \mathbf{v} \cdot \nabla T dV^e, & \tilde{\mathbf{c}}^e &= \int_{V^e} (\mathbf{v} \cdot \nabla \mathbf{N}_T)^T \frac{\partial T}{\partial t} dV^e, \\ \mathbf{k}^e &= \int_{V^e} \nabla \mathbf{N}_T^T \cdot \alpha_T \nabla T dV^e, & \tilde{\mathbf{k}}^e &= \int_{V^e} (\mathbf{v} \cdot \nabla \mathbf{N}_T)^T \mathbf{v} \cdot \nabla T dV^e. \end{aligned} \quad (7.64)$$

From these element-level matrices, the element-level *dimensionless* Reynolds and Courant<sup>2</sup> numbers are defined;

$$\begin{aligned} \operatorname{Re}^e &= \frac{\|\mathbf{v}\|^2 \|\mathbf{c}^e\|}{\alpha_T \|\tilde{\mathbf{k}}^e\|}, & \operatorname{Cr}_{\mathbf{u}}^e &= \frac{\|\mathbf{c}^e\|}{\|\mathbf{m}^e\|}, \\ \operatorname{Cr}_{\alpha}^e &= \frac{\|\mathbf{k}^e\|}{\|\mathbf{m}^e\|}, & \operatorname{Cr}_{\tilde{\alpha}}^e &= \tau \frac{\|\tilde{\mathbf{k}}^e\|}{\|\mathbf{m}^e\|}, \end{aligned} \quad (7.65)$$

in which the Courant numbers can be used to determinate the maximum time step  $\Delta t$  (see Section 7.2.5). The components of the element-based  $\tau$  are defined as follows;

<sup>2</sup>The Courant numbers presented here are adapted from Tezduyar and Osawa (2000) to enforce the dimensionless feature.

$$\begin{aligned}\tau_{S1} &= \frac{\|\mathbf{c}^e\|}{\|\tilde{\mathbf{k}}^e\|}, & \tau_{S2} &= \frac{\|\mathbf{c}^e\|}{\|\tilde{\mathbf{c}}^e\|}, \\ \tau_{S3} &= \tau_{S1} \times \text{Re}^e,\end{aligned}\tag{7.66}$$

in which  $\tau_{S1}$  is related to convection-dominated limit,  $\tau_{S2}$  is related to transient-dominated limit and  $\tau_{S3}$  is related to diffusion-dominated limit. Tezduyar and Osawa (2000) proposed the following formulation for  $\tau$ ,

$$\tau_{\text{SUPG}} = \left( \frac{1}{\tau_{S1}^r} + \frac{1}{\tau_{S2}^r} + \frac{1}{\tau_{S3}^r} \right)^{-1/r},\tag{7.67}$$

which is the inverse of the  $r$ -norm of the vector with components  $1/\tau_{S1}$ ,  $1/\tau_{S2}$  and  $1/\tau_{S3}$ . The higher the value of  $r$  the sharper the switch from one period to the other. The definition of  $\tau_{\text{SUPG}}$  in eq. (7.67) can be seen as an implicit definition because of its dependency on the solution.

An alternative proposal of  $\tau_{\text{SUPG}}$  (7.66) follows by extending the one-dimensional expression (7.45),

$$\left. \begin{aligned}\tau_{S1} &= \frac{h}{2\|\mathbf{v}\|} \\ \tau_{S2} &= \frac{\Delta t}{2} \\ \tau_{S3} &= \frac{h^2}{4\alpha_T}\end{aligned}\right\} \tau_{\text{SUPG}} = \left( \frac{1}{\tau_{S1}^2} + \frac{1}{\tau_{S2}^2} + \frac{1}{\tau_{S3}^2} \right)^{-1/2},\tag{7.68}$$

in which  $h$  is the ‘element length’ defined as Tezduyar and Osawa (2000),

$$h = 2\|\mathbf{v}\| \left( \sum_{a=1}^{n_{ne}} |\mathbf{v} \cdot \nabla \mathbf{N}_T^a| \right)^{-1},\tag{7.69}$$

and  $n_{ne}$  is the number of element node. Assuming that the velocity  $\mathbf{v}$  is given, the definition of  $\tau_{\text{SUPG}}$  in eq. (7.68) has no dependency on the solution.

Finally, the two proposals (7.67) and (7.68) have been compared for a transient diffusion-convection problem by Tezduyar and Osawa (2000) with square elements and a constant in time and uniform in space velocity; their performances are almost identical.

In the sequel, the form (7.68) is used in view of its coding simplicity.

### 7.2.4.2 Simulation results

The example used to test the two-dimensional transient diffusion-convection problem is the same as in Section 7.2.3.3, with a fixed angle of  $\theta = 21.8^\circ$ . The problem statement is illustrated in Figure 7.10 (top-left).

The time steps  $\Delta t$  are calculated according to a logarithmic law, up to the maximum value of  $10^4$  seconds. In other words, the calculated times are  $t = [1, 2, \dots, 9, 10, 20, \dots, 90, 100, 200, \dots, 900, \dots, 10000, 20000, \dots, 90000, 100000, 110000, \text{etc}]$ . This pattern is particularly useful to produce historical graphics with the  $\log(\text{time})$  in abscissa, which allows to visualise on the same figure the early period, the intermediate period and the late period.

Two numerical tests are presented in Figures 7.12 and 7.13: for a very high grid Péclet number  $\text{Pe}_g = 10^6$  which almost represents pure convection and for a high grid Péclet number  $\text{Pe}_g = 10^2$  which illustrates a convection-dominated flow, respectively.

For each test, the relative temperature response of the SUPG method is compared with that of the Galerkin method. To assess the influence of the transient contribution in the stabilisation parameter proposed by Tezduyar and Osawa (2000), eq. (7.68), the temperature profiles are also compared with the response produced by the stabilisation parameter without transient contribution eq. (7.56).

For ‘pure’ convection  $\text{Pe}_g = 10^6$  (Figure 7.12), the addition of the transient contribution in the stabilisation parameter seems to disturb the curing effect of the SUPG method at all times. Therefore, the use of the standard stabilisation parameter is recommended for very high grid Péclet numbers.

For standard convection-dominated flows  $\text{Pe}_g = 10^2$  (Figure 7.13), the addition of the transient contribution in the definition of  $\tau$  has a beneficial effect at early times *only*. Hence, if the response at early time is not sought and if the loading conditions can bear a stiff increase, the use of the stabilisation parameter with no transient contribution should be favored.

To summarise, the introduction of a transient contribution in the stabilisation parameter is only useful to describe the early period. The price to pay is quite heavy, since the spurious wiggles are not completely cured. Importantly, no optimum stabilisation parameter exists for two-dimensional transient problems.



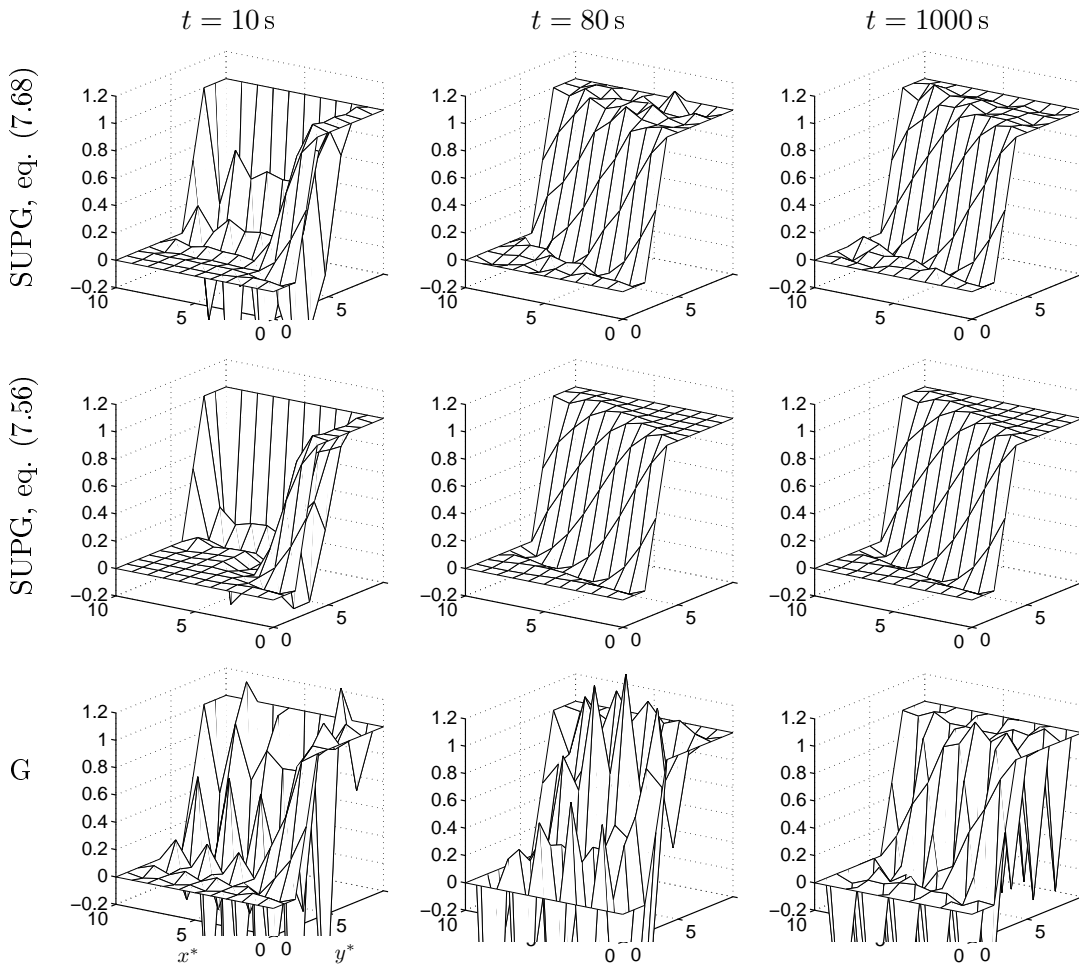
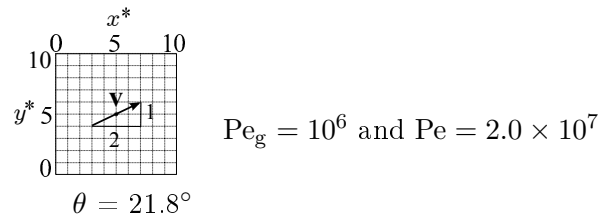


Figure 7.12: Relative temperature profiles in the plane  $(x^*, y^*)$ , for a convective flow skew to the mesh and a very high grid Péclet number  $Pe_g = 10^6$ . SUPG stands for the finite element response accounting for the SUPG method; whereas G represents the finite element response with no stabilisation on the weighting function, that is the standard Galerkin method, which displays a heavily disturbed response. The SUPG method using eq. (7.56) produces better results (at all times) than when accounting for a transient contribution eq. (7.68). This is due to the high grid Péclet number  $Pe_g = 10^6$ , which induces the transient contribution of (7.68) to be equal or smaller than the convection contribution. Therefore, for high grid Péclet numbers, the stabilisation parameter with no transient contribution (7.56) is more efficient.

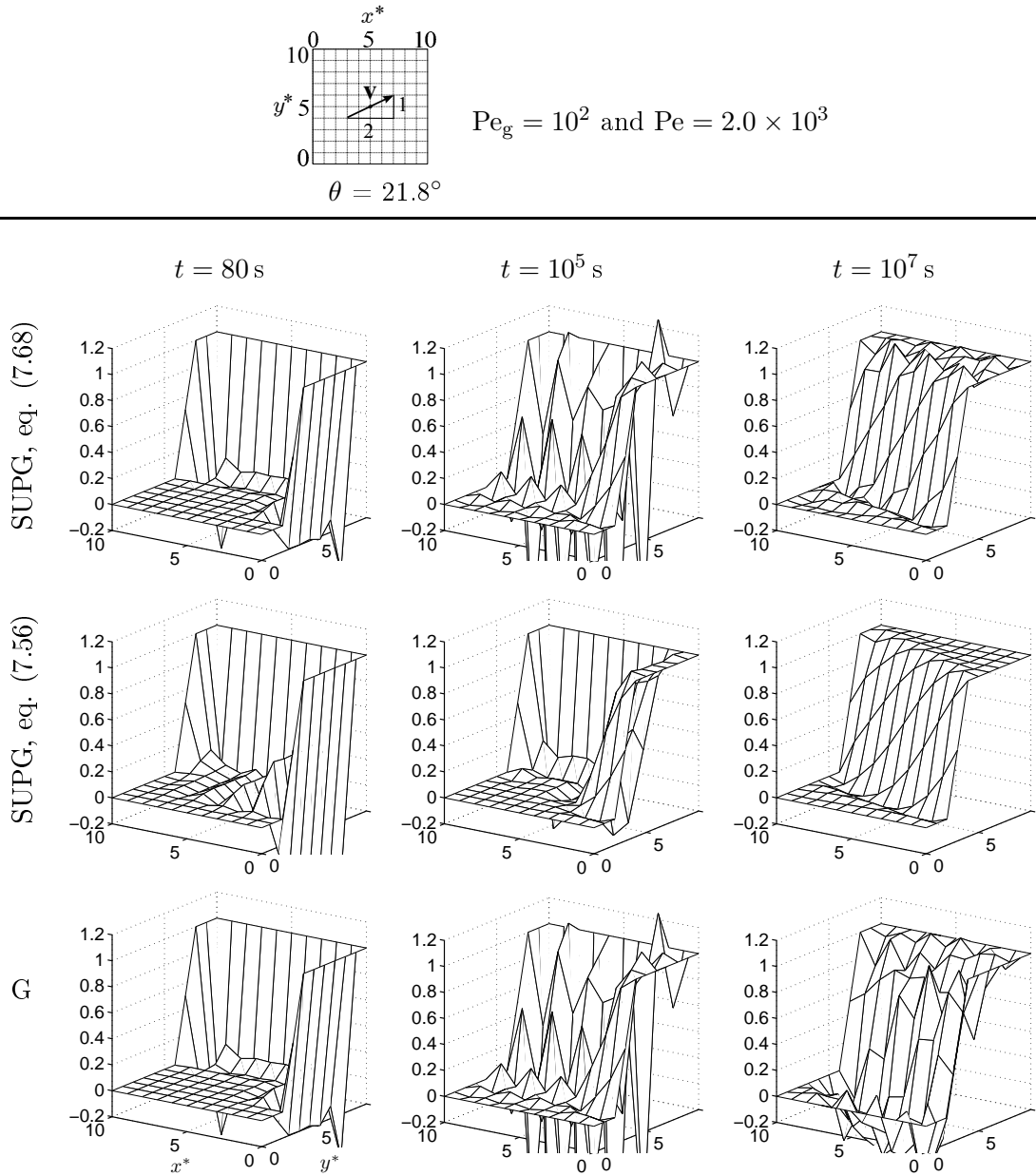


Figure 7.13: Same as Figure 7.12 for a smaller grid Péclet number:  $Pe_g = 10^2$ . At early times (left), the SUPG method with eq. (7.68) displays a smoother temperature profile than the SUPG method with eq. (7.56), thanks to the transient contribution. On the other, during the intermediate and the late periods, the SUPG method with eq. (7.56) produces smoother results than Tezduyar and Osawa's proposition. The description of the early period is better viewed by using eq. (7.68); whereas the description of the intermediate and of the latter periods is better reproduced with eq. (7.56). No optimum stabilisation parameter exists for two-dimensional transient problems.

### 7.2.5 Stability requirements

An algorithm for which stability imposes a time step restriction is called *conditionally stable*; whereas an algorithm for which there is no time step restriction imposed by stability is called *unconditionally stable*. Usually, unconditionally stable algorithms are preferred.

The semi-discretised finite element matrix form of the coupled thermo-hydro-mechanical model, eq. (2.319)-(2.324), can be expressed as a function of the diffusion matrix  $\mathbb{D}$ , the stiffness matrix  $\mathbb{K}$  and the convection matrix  $\mathbb{C}_{\text{conv}}$ , by (Section 4.2.4.4),

$$\mathbb{D} \mathbf{V} + \mathbb{K} \mathbf{X} + \mathbb{C}_{\text{conv}} \mathbf{X} = 0. \quad (7.70)$$

Consistency and stability are linked to a certain problem *and* to a certain type of time marching scheme. In this work, a predictor-multi-corrector algorithm with all contributions being *implicit* is used to discretise the diffusion-convection equation (presented in Section 4.3.2.2). The integration parameter is chosen equal to  $\alpha = 2/3$ . Importantly, no stability information is given for this general case, that is the diffusion matrix  $\mathbb{D}$ , the stiffness matrix  $\mathbb{K}$  and the convection matrix  $\mathbb{C}_{\text{conv}}$  are *non-symmetric* and do not respect the orthogonality property (Brooks and Hughes, 1982; Belytschko and Hughes, 1983). Hence, conditional stability characterises non-linear transient Newton-Raphson schemes and the time step is limited by the various diffusive limits, yielding the classical result,

$$\Delta t \leq \frac{L^2}{\alpha_k}, \quad (7.71)$$

in which  $L$  is the diffusion length and  $\alpha_k = \{\alpha_{H,p}, \alpha_{H,f}, \alpha_{T,s}, \alpha_{T,p}, \alpha_{T,f}\}$  represents in turn the hydraulic and the thermal diffusivities.

The particular case of a *fully explicit* multi-corrector algorithm (with a lumped mass matrix) is presented by Brooks and Hughes (1982, Section 4.3) and is summarised in Remark 7.5. Furthermore, more information on stability concepts for time marching schemes for diffusion-convection problems are presented in Belytschko and Hughes (1983) (see Remark 7.6).

**Remark 7.5.** *Stability conditions for an explicit ('lumped' diffusion matrix) multi-corrector algorithm are presented in Brooks and Hughes (1982) to discretise a one-dimensional constant coefficient convection-diffusion equation, while maintaining a good phase accuracy. Note that explicit algorithms are always conditionally stable, but can be more efficient than implicit algorithms for non-linear problems. With  $\alpha = 1/2$ , a uniform grid of element length  $h$  and no additional iterations in the multi-corrector algorithm, the following stability conditions hold on the Courant number  $\text{Cr} = \Delta t v/h$ , for the SUPG method:*

$$\left\{ \begin{array}{l} \text{Diffusive limit :} \\ \text{Diffusion-convection limit:} \end{array} \right. \quad \begin{array}{l} \text{Cr} \leq \text{Pe}_{\text{geff}} = \frac{1}{2} \frac{v h}{\alpha_T + \tilde{\alpha}_T}, \\ \text{Cr} \leq 1, \end{array} \quad (7.72)$$

and for the Galerkin method:

$$\left\{ \begin{array}{l} \text{Diffusive limit :} \\ \text{Diffusion-convection limit:} \end{array} \right. \quad \begin{array}{l} \text{Cr} \leq \text{Pe}_g = \frac{v h}{2\alpha_T}, \\ \text{Cr} \leq 1/\text{Pe}_g. \end{array} \quad (7.73)$$

**Remark 7.6.** In Belytschko and Hughes (1983, p. 150), the von Neumann method is used to analyse the stability of the Navier-Stokes equations discretised with a Galerkin method and the generalised trapezoidal method. Unconditional stability is maintained for the generalised trapezoidal scheme as long as the integration parameter  $\alpha \geq 1/2$ , the same as when the convective term is absent. However, no conclusion can be drawn regarding cases in which  $\alpha < 1/2$ .

## 7.3 Beyond SUPG

The next step after validating the implementation of the SUPG method (Section 7.2), is to assess the influence of convection-dominated diffusion-convection flow on the full comprehensive model involving cross-coupling phenomena. In the previous section, spurious oscillations have been observed in different conditions. Hence, a summary of the different spurious oscillations mechanisms is provided here. Then, the limitations of the SUPG method are presented and particular attention is given to unsteady, coupled and non-linear systems. A short review of the implementation of the SUPG method as part of larger thermo-mechanical and chemo-mechanical models is considered. Finally, the discontinuity capturing method is presented to remedy the remaining instabilities of the SUPG method.

### 7.3.1 Mechanisms of numerical ‘noise’ and spurious oscillations

Spurious numerical oscillations arise when sharp temperature gradients are applied or develop in the medium. Three problems are segregated:

1. In transient diffusion-dominated diffusion-convection problems, oscillations arise during the early times due to a sharp temperature gradient applied at the boundary (analogous to a shock front) (Idelsohn et al., 1998). This sharp gradient disappears after a few time steps if the problem is diffusion-dominated. In order to overcome these oscillations, the mesh can be refined at the vicinity of the perturbation, without

affecting the accuracy of the response as no mesh-dependent stabilisation method is required. Alternatively, the time scheme can be modified with various time-stepping algorithms to artificially damp the noise to an acceptable level (Wood and Lewis, 1975).

2. In steady convection-dominated diffusion-convection problems, spurious oscillations are induced by a sharp temperature gradient applied at the boundary (Figure 7.2, b). As presented above, the SUPG method is designed to cure the unwanted wiggles and a nodally exact solution is proposed by Brooks and Hughes (1982) for homogeneous meshes. These oscillations are induced by a high grid Péclet number, characterizing the local limit between a smooth temperature gradient and a sharp temperature gradient, with respect to the chosen mesh.
3. In transient convection-dominated diffusion-convection problems, two types of sharp gradients are encountered. The first sharp gradient occurs during the early times because of the transient solution (shock front) Yin et al. (2010).

The second sharp gradient arise when the thermal front hits a prescribed boundary condition (therefore at later times, as the thermal front needs to travel into the medium before hitting the boundary), see Figure 7.5. Again the grid Péclet number defines the local limit between smooth and sharp gradients.

### 7.3.2 The limitations of the SUPG method

Concerning unsteady, multidimensional, coupled and non-linear diffusion-convection systems, the limitations of the SUPG method are identified in the literature and many improvements have been proposed:

- The regular/homogeneous mesh is a constraint imposed by the SUPG method to obtain a good accuracy with a given stabilisation parameter. One limitation of the SUPG method is that for a regular/homogeneous mesh, oscillations arise during early times because of the transient solution (a sharp gradient analogous to a shock front) (Yin et al., 2010). Wellbore stability analyses are usually conducted during the early period. Unfortunately, both the SUPG method and the Galerkin/least square method fail to circumvent the oscillation phenomenon at early times. Therefore, wellbore stability analyses accounting for high convection can not be predicted by the SUPG method: the oscillations on the temperature response will spoil the pressures and the stress responses. One way to overcome these spurious temperature oscillations, is to replace the transient diffusion-convection problem by an diffusion-convection-reaction problem, which is then efficiently addressed by a stabilised finite element approach, the subgrid scale/gradient subgrid scale method (SGS/GSGS)

(Yin et al., 2010). The main drawback of this method is that the SGS/GSGS method displays a larger dispersion than the SUPG method for late times.

- For more complicated systems than steady diffusion-convection, the solution possesses *unresolved internal* and *boundary layers*, which are small subregions where the derivatives of the solution are very large. The widths of these layers are usually significantly smaller than the mesh size and hence overshooting and undershooting oscillations remain in narrow regions along sharp layers (see Figure 7.10 for  $\theta \neq 0$ ).

Although the remaining non-physical oscillations are usually small in magnitude, they are not permissible in many applications, such as (John and Knobloch, 2007):

1. Chemically reacting flows where it is essential to guarantee that the concentrations of all species are non-negative.
2. Free-convection computations where temperature oscillations create spurious sources and sinks of momentum that affect the computation of the flow field.
3. Numerical simulations of compressible flow problems, where the solution may develop discontinuities (for example shock waves) whose poor resolution may affect the global stability of the numerical calculations.

In order to improve the SUPG method to smoothly resolve sharp layers, the introduction of a *discontinuity capturing* or *shock capturing* operator was proposed by Hughes et al. (1986) and Johnson et al. (1990). The generalisation of the discontinuity-capturing operator to systems has proven to be an essential ingredient for accurately capturing shock waves (Hughes, 1987b), with enhanced stability and equal consistency. A comprehensive review of these discontinuity capturing methods is proposed in John and Knobloch (2007).

Since the mid of the 1980s, a number of methods have been proposed to improve the SUPG method by removing (or at least diminishing) the spurious wiggles at unresolved layers. As presented by Franca et al. (2006), the SUPG method has inspired other stabilisation methods, such as the Galerkin/Least-Squares method (GLS), the Galerkin/Gradient-Least-Squares method (GGLS) and the Unusual Stabilised Finite Element Method (USFEM). The latter is also suggested by static condensation of bubbles added to the finite element space. These stabilisation methods address many problems such as diffusion-convection, reaction-diffusion and diffusion-convection-reaction scalar equations; and also Stokes, incompressible Navier-Stokes and compressible Navier-Stokes equations.

Aside from the Eulerian techniques cited above, Eulerian-Lagrangian Methods (ELMs), or characteristics methods, have been developed to address diffusion-convection problems. The basic concept of ELMs is to solve the transport equation in a Lagrangian form ‘along’ characteristic lines, effectively decoupling convection and diffusion terms (Oliveira and

Baptista, 1995). Points within the Eulerian grid are tracked backward (or forward) along the characteristic lines over the time step, thereby forming a Lagrangian grid. The method retains the convenience of a fixed computational Eulerian grid. A significant advantage of these ELMs is that, owing to the Lagrangian nature of the convection step, the restriction on the time step size (*via* the local Courant number) is relaxed (Kaazempur-Mofrad and Ethier, 2002). Although attractive, questions remain about the robustness of the ELMs, for example there is no inherent mass preservation. From the literature, ELMs seem to apply to uncoupled diffusion-convection problems and to chemical convection (usually called advection) rather than thermal convection.

Nevertheless, the scope of this study is restricted to the implementation of the SUPG method applied to the generalised diffusion-convection energy equations presented in the fully coupled model (2.4). The limitation that is most likely to appear in our case is that overshooting and undershooting oscillations may induce even greater spurious ‘noise’ on the pressure and stresses profiles. In that case, the introduction of a *discontinuity capturing* operator will become necessary.

### 7.3.3 The SUPG method applied to porous media: a short literature review

The subject of flow and heat in porous media has been studied for many decades. Likewise, little research has been done on forced convection in porous media (Nield and Bejan, 2006). Several models have been developed, for example dual porosity models (Bai and Rogiers, 1994), homogenization methods (Royer et al., 2002) and local thermal non-equilibrium models (Polyaev et al., 1996).

In many references (Nair et al., 2004; Bataillé et al., 2006), although the constitutive model is detailed, no or little information is given on the implementation of the convective term. Nevertheless, the implementation of forced convection in porous media as part of a coupled constitutive model has rarely been studied. Very often, the heat transport equation is uncoupled from the rest of the model. The few papers which include a finite element formulation and use the SUPG method are now presented:

- Zhou et al. (2009) present a partially decoupled poro-thermoelastic model to assess the variation of *in-situ* stresses and induced seismicity with cold water injection into a geothermal reservoir. On one hand, the pore fluid diffusion and heat transfer in the pore matrix are assumed to be 3-D, and are modeled with a boundary integral equation method: therefore the 3-D reservoir does not need to be discretised. On the other hand, the fluid flow and the convective heat transfer in the fracture are modeled with a finite element method. The two methods are coupled and share the same mesh on the fracture plane. This setup provides the advantage of resolving a 3-D problem with only a 2-D mesh which results in less computational efforts; however the main drawback is the partial decoupling of the pressures and the temperature

fields.

In this decoupled model, the SUPG method is used to solve the purely convective heat transport equation in the fracture. The modified weighting functions are applied to the convective term, whereas the weighting functions of the heat source intensity term are not modified. This feature does ensure the accuracy of the method as the weighting function is not applied to all the terms of the weak form; unless the heat source intensity term vanishes on the element interior. The ‘upwind’ parameter  $\tilde{\tau}$  is determined as in Brooks and Hughes (1982).

- Gajo (2002) studied a non-linear analysis of non-isothermal wave propagation in fluid-saturated porous media. The thermo-mechanical law developed here is derived from the work of Pecker and Deresiewicz (1973) which accounts for both the temperature of the solid and the temperature of the fluid in the definition of the effective stress. This strong hypothesis is opposite to our assumption that only the solid phase would control the overall thermal dilatation of the mixture. An original contribution is introduced by Gajo (2002) in the form of a second initial temperature for the fluid in order to account only for the variation in fluid temperature occurring inside the element, whereas the variation in fluid temperature occurring outside the element is not desirable. This second initial temperature is then treated as a primary unknown and allows the convection terms to be separated from the balance of energy of the fluid phase. The SUPG method is correctly implemented on the resulting pure convective equation. Some small wiggles are visible on the temperature response, however no information is given on the influence of these disturbances on the pressure response. Overall, the complexity of the balance of energy equation for the fluid phase with convection (Gajo, 2002, eq. 5) has been overcome by the introduction of the second initial temperature for the fluid phase. Such ‘trick’ can not be applied to our work as our thermo-mechanical constitutive law is significantly different.
- Finite element simulations of chemo-mechanical coupling in elastic-plastic homoionic expansive clays have been studied by Gajo and Loret (2003). A diffusion-convection equation, accounting for the appropriate couplings, describes the convective transport of salt and the SUPG method is used to cure the spurious wiggles during the finite element discretisation. The modified weighting function is appropriately applied to the convective term. However, the shape function of the pressure, the mass and the time dependent contributions in the balance of mass of salt are not modified. Again, accuracy of the SUPG method is not ensured, as only the generalised diffusion terms vanish on the elements interior. This omission is illustrated in Gajo and Loret (2003, Figure 22) where the *advection with SUPG* curve does not match with the *advection without SUPG* curve for the three first times (No sharp boundary has been encountered yet and the wiggles-cure is useless). As a result the *advection with SUPG* curve is over-diffusive. However, the latter omission is understandable owing to the



complexity of the fully coupled model which requires a robust non-linear algorithm (line-search algorithm).

Two additional papers have accurately implemented the SUPG method as part of a coupled model Li et al. (2006); Fachinotti et al. (2006); however it remains unclear if convection is dominant or not in their applications and if the stabilisation method is actually required or not.

The SUPG method is used on the fully coupled model (outlined in Section 2.4) to stabilise the fluids energy equations due to the presence of convection terms. To implement *accurately* the SUPG method, the perturbation is applied to all terms of the energy equations (Section 8.1).

### 7.3.4 The discontinuity capturing method

In order to improve the SUPG method to smoothly resolve sharp layers, the introduction of a *discontinuity capturing* or *shock capturing* operator was proposed by Hughes et al. (1986) and Hughes (1987b). The method is briefly resumed and the main results are then presented.

#### 7.3.4.1 The weighting function

The discontinuity capturing method suggests in place of (7.5), the weighting function of the form,

$$\mathbf{W}_T = \mathbf{N}_T + \tau_1 \mathbf{v} \cdot \nabla \mathbf{N}_T + \tau_2 \mathbf{v}_{\parallel} \cdot \nabla \mathbf{N}_T, \quad (7.74)$$

in which  $\mathbf{v}_{\parallel}$  is the projection of  $\mathbf{v}$  on  $\nabla T$ , defined by,

$$\mathbf{v}_{\parallel} = \begin{cases} \frac{(\mathbf{v} \cdot \nabla T)}{\|\nabla T\|^2} \nabla T, & \text{if } \nabla T \neq \mathbf{0}, \\ \mathbf{0}, & \text{if } \nabla T = \mathbf{0}. \end{cases} \quad (7.75)$$

and  $\nabla T$  is obtained through the discretised form  $\nabla \mathbf{N}_T T^e$ .  $\|\cdot\|$  denotes the 2-norm, also called the Euclidean norm. This method is seen to be non-linear since  $\mathbf{v}_{\parallel} = \mathbf{v}_{\parallel}(T^e)$ . The interaction of equation (7.74) with the convection term  $\mathbf{v} \cdot \nabla T$  brings,

$$\begin{aligned} \mathbf{W}_T^T \mathbf{v} \cdot \nabla T &= \mathbf{N}_T^T \mathbf{v} \cdot \nabla T + \nabla \mathbf{N}_T^T \tau_1 \mathbf{v}^T \mathbf{v} \cdot \nabla T + \nabla \mathbf{N}_T^T \tau_2 \mathbf{v}_{\parallel}^T \mathbf{v} \cdot \nabla T, \\ &= \mathbf{N}_T^T \mathbf{v} \cdot \nabla T + \nabla \mathbf{N}_T^T \tau_1 \mathbf{v}^T \mathbf{v} \cdot \nabla T + \nabla \mathbf{N}_T^T \tau_2 \mathbf{v}_{\parallel}^T \mathbf{v}_{\parallel} \cdot \nabla T, \end{aligned} \quad (7.76)$$

due to  $\mathbf{v}_{\parallel} \cdot \nabla T = \mathbf{v} \cdot \nabla T$  from (7.75),

$$\mathbf{W}_T^T \mathbf{v} \cdot \nabla T = \mathbf{N}_T^T \mathbf{v} \cdot \nabla T + \underbrace{\nabla \mathbf{N}_T^T \tau_1 \mathbf{v}^T \mathbf{v} \cdot \nabla T}_{\text{streamline operator}} + \underbrace{\nabla \mathbf{N}_T^T \tau_2 \mathbf{v}_{\parallel}^T \mathbf{v}_{\parallel} \cdot \nabla T}_{\text{discontinuity-capturing operator}}. \quad (7.77)$$

The streamline matrix  $\mathbf{v}^T \mathbf{v}$  is a rank-1 positive-semidefinite matrix which acts only in the streamline direction; and the discontinuity capturing matrix  $\mathbf{v}_{\parallel}^T \mathbf{v}_{\parallel}$  is also a rank-1 positive-semidefinite matrix which acts only in the direction of the discrete solution gradient.

The discontinuity capturing method is experimented with four sets of parameters: DC1, in this case,

$$\tau_1 = \tau \quad \text{and} \quad \tau_2 = \tau_{\parallel}, \quad (7.78)$$

The main drawback of eq. (7.78) is obvious if  $\mathbf{v} = \mathbf{v}_{\parallel}$ ; the doubling of the stabilisation parameter  $\tau$  is engendered. To avoid this, DC2 has been proposed to remove the component  $\tau \mathbf{v}^T \mathbf{v}$  in the direction  $\nabla T$ , in this case

$$\tau_1 = \tau \quad \text{and} \quad \tau_2 = \max(0, \tau_{\parallel} - \tau). \quad (7.79)$$

$\tau_{\parallel}$  is defined in a similar way than  $\tau$  but through the parallel velocity  $\mathbf{v}_{\parallel}$ , as presented in Table 7.1, in which  $\xi = \xi(x)$  is the inverse mapping and  $|\mathbf{b}|_p$  is the ‘length’ of  $\mathbf{b}$  with respect to the p-norm, denoted,

$$|\mathbf{b}|_p = \left( \sum_{i=1}^{n_{sd}} |\mathbf{b}_i|^p \right)^{1/p}, \quad \text{with} \quad b_i = v_j \frac{\partial \xi_i}{\partial x_j}. \quad (7.80)$$

$h$  and  $h_{\parallel}$  are the element mesh parameters describing the length of the element in the direction of the velocity  $\mathbf{v}$  and in the direction of the temperature gradient  $\nabla T$ , respectively.

Tezduyar and Park (1986) proposed to redefine the stabilisation parameter  $\tau_2$  in eq. (7.74), which leads to the scheme denoted EC1,

$$\tau_2 = \frac{h_{\parallel}}{2 \|\mathbf{v}_{\parallel}\|} \eta \left( \frac{\|\mathbf{v}_{\parallel}\|}{\|\mathbf{v}\|} \right), \quad (7.81)$$

$\tau$	$\tau_{\parallel}$
$\mathbf{b} = (\mathbf{v} \cdot \nabla)\xi$	$\mathbf{b}_{\parallel} = (\mathbf{v}_{\parallel} \cdot \nabla)\xi$
$h = 2 \ \mathbf{v}\  /  \mathbf{b} _p$	$h_{\parallel} = 2 \ \mathbf{v}_{\parallel}\  /  \mathbf{b}_{\parallel} _p$
$\text{Pe}_{\mathbf{g}} = \ \mathbf{v}\  h / 2\alpha_T$	$\text{Pe}_{\mathbf{g}_{\parallel}} = \ \mathbf{v}_{\parallel}\  h_{\parallel} / 2\alpha_T$
$\tilde{\xi} = \tilde{\xi}(\text{Pe}_{\mathbf{g}})$	$\tilde{\xi}_{\parallel} = \tilde{\xi}(\text{Pe}_{\mathbf{g}_{\parallel}})$
$\tau = h\tilde{\xi} / 2\text{Pe}_{\mathbf{g}}$	$\tau_{\parallel} = h_{\parallel}\tilde{\xi}_{\parallel} / 2\text{Pe}_{\mathbf{g}_{\parallel}}$

Table 7.1: Comparison between the stabilisation parameter related to the streamline operator  $\tau$  and the stabilisation parameter related to discontinuity-capturing operator  $\tau_{\parallel}$ .

with,

$$h_{\parallel} = \frac{2 \|\mathbf{v}_{\parallel}\|}{\sum_a |\mathbf{v}_{\parallel} \cdot \nabla \mathbf{N}_T^a|} \quad \text{and} \quad \eta(x) = 2x(1-x). \quad (7.82)$$

Note that the function  $\eta$  vanishes at the end of its domain; that is whenever the velocity and the solution gradient vectors are either perpendicular or parallel, the function is designed to become zero  $\eta = 0$ ,

$$\frac{\|\mathbf{v}_{\parallel}\|}{\|\mathbf{v}\|} = \frac{\mathbf{v}}{\|\mathbf{v}\|} \cdot \frac{\nabla T}{\|\nabla T\|} \begin{cases} = 0 & \text{if } \mathbf{v} \perp \nabla T, \\ = 1 & \text{if } \mathbf{v} // \nabla T. \end{cases} \quad (7.83)$$

By selecting  $\eta = 1$  and  $\eta = 1 - \|\mathbf{v}_{\parallel}\| / \|\mathbf{v}\|$ , the discontinuity capturing method DC1 and DC2 from Hughes et al. (1986) are recovered, respectively. The proposition of Tezduyar and Park (1986) ensures that the stabilisation is not doubled if  $\mathbf{v}_{\parallel} = \mathbf{v}$  and is a generalisation of the *ad hoc* proposition introduced by Hughes et al..

In addition to EC1, Tezduyar and Park (1986) introduced the scheme EC2 which depends not only on the direction of  $\nabla T$  but also on its magnitude,

$$\tau_2 = \frac{h_{\parallel}}{2 \|\mathbf{v}_{\parallel}\|} \eta \left( \frac{\|\mathbf{v}_{\parallel}\|}{\|\mathbf{v}\|} \right) h_{\parallel} \frac{\|\nabla T\|}{T_{\text{ref}}}, \quad (7.84)$$

where  $T_{\text{ref}}$  is a global scaling of the unknown  $T$ .

Note that the ‘element length’ (7.82) introduced by Tezduyar and Park (1986) is easier to compute than the one presented by Hughes et al. (1986) in Table 7.1 and is used for all the methods (John and Knobloch, 2007).

#### 7.3.4.2 Simulation results

The problem to be solved is the convection of a single phase in a steady flow skew to the mesh with downwind essential boundary condition (Hughes et al., 1986; Tezduyar and Ganjoo, 1986; John and Knobloch, 2007). The thermal diffusivity is assumed to be very small; i.e. the grid Péclet number is very large. A  $10 \times 10$  square mesh is employed. The inflow boundary conditions involve a discontinuity resulting in an internal discontinuity skew to the mesh. The outflow boundary conditions induce spurious sharp boundary layers at the downwind boundary. The fluid velocity is positioned according to three different angles. In two cases, the internal and external boundary layers intersect at a corner. In the third case, only one internal sharp boundary remains.

The flow fields are given as  $v_y/v_x = 2$ ,  $v_y/v_x = 1$  and  $v_y/v_x = 0.5$  (Figures 7.14 and 7.15). The results for the Galerkin formulation are not shown due to their large oscillations. The SUPG response cures most of the spurious wiggles, nevertheless oscillations about the internal layer and the downwind boundary remain. The effect of the discontinuity capturing method is manifest. For DC1 the solution does not exhibit the strong overshoots of the SUPG solution at the boundary layers; in addition improvements are also observed at the internal discontinuity. The lack of accuracy is most probably due to the doubling effect between the SUPG method and the discontinuity capturing method, when  $\mathbf{v} = \mathbf{v}_{\parallel}^3$ . This drawback is effectively removed by the DC2 solution which is quite good with all the layers and the plateau apparent. Nevertheless, few overshooting nodes remain for DC2.

The solutions EC1 and EC2 proposed by Tezduyar and Park (1986) also provide a good improvement of the overshoots compared with the SUPG method alone. Improvements are observed both at the downwind boundary and at the internal discontinuity. Note that the reference temperature in eq. (7.84) is taken equal to  $T_{\text{ref}} = 30^\circ\text{C}$ .

EC1 and EC2 are preferred to DC1 and DC2 since the responses are smoother with fewer overshoots.

---

<sup>3</sup>In addition, the tolerance required for convergence is relatively large: 0.01 for both the residual norm and for the temperatures.

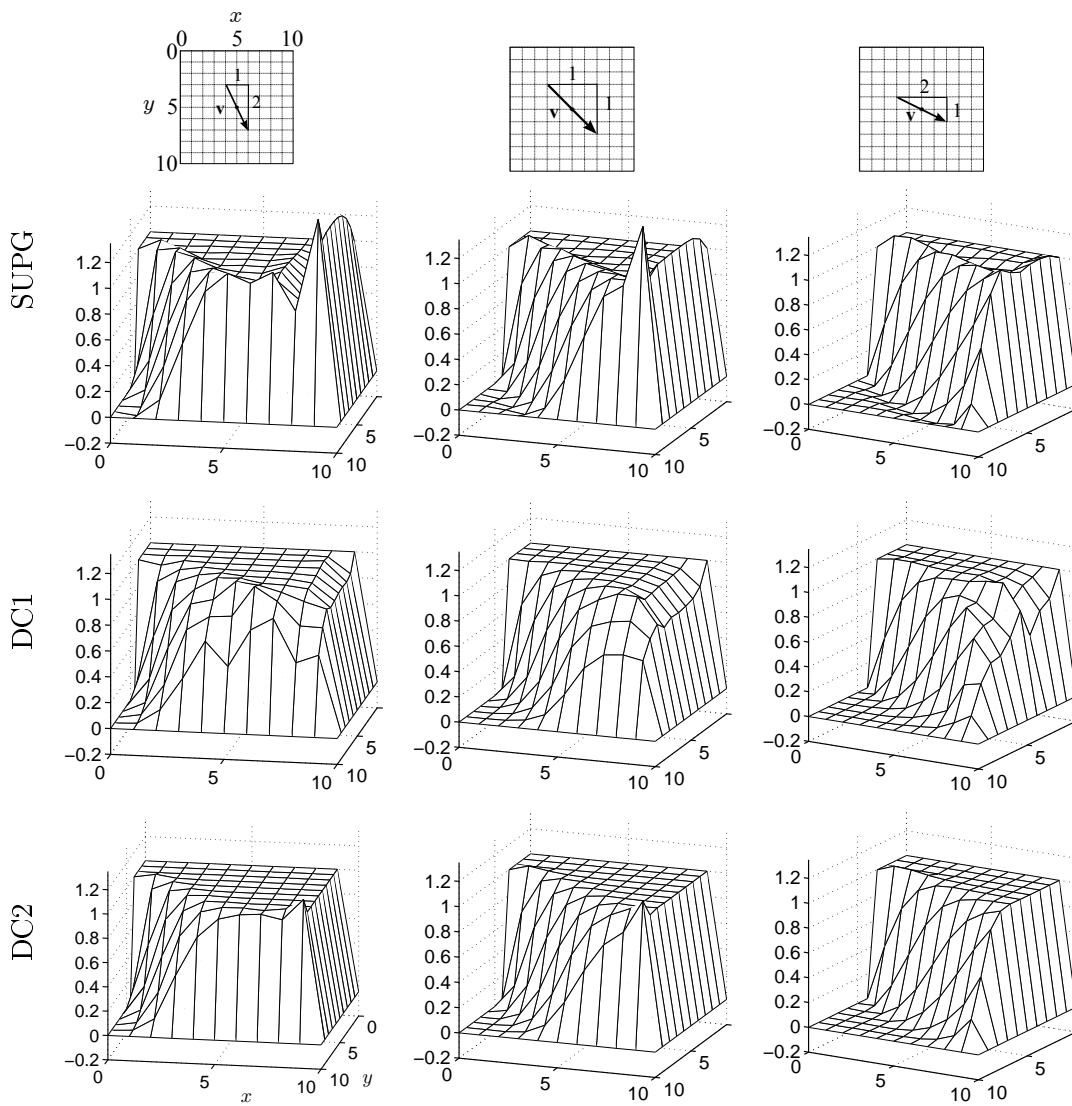


Figure 7.14: Relative temperature profiles for a convective flow skewed to the mesh. SUPG stands for the finite element response accounting for the SUPG method. DC1 and DC2 stand for the finite element response with the discontinuity capturing method (added to SUPG) with  $\tau_2 = \tau_{\parallel}$  and  $\tau_2 = \max(0, \tau_{\parallel} - \tau)$ , respectively. The significant improvements of the discontinuity capturing methods over SUPG are manifest: the solutions do not exhibit the overshoots of the SUPG at the downwind boundary; in addition the overshoots at the internal discontinuity are reduced. The DC2 response exhibits less artificial diffusion when  $\mathbf{v} = \mathbf{v}_{\parallel}$  and therefore a smoother response.

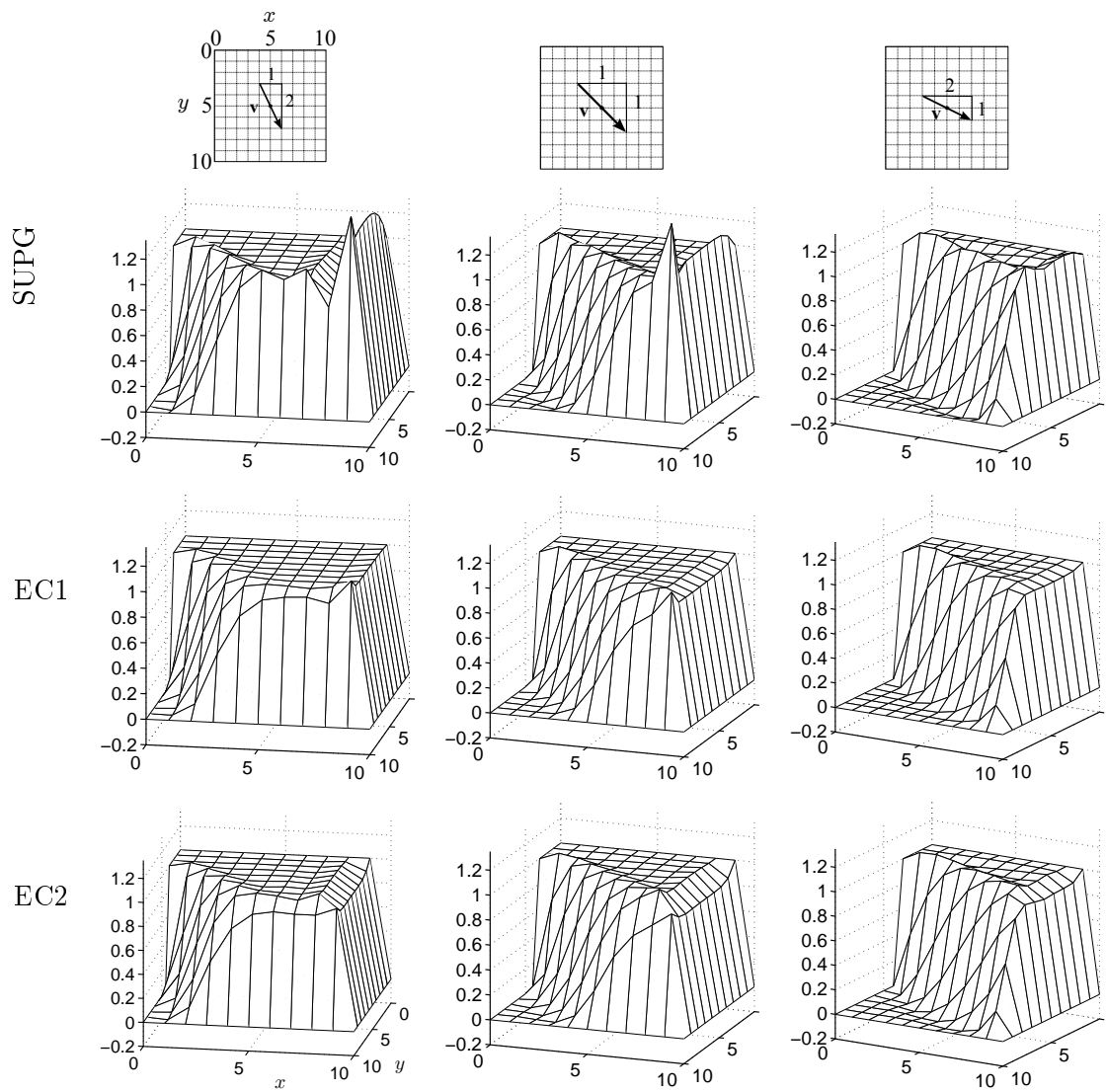


Figure 7.15: Relative temperature profiles for a convective flow skew to the mesh. SUPG stands for the finite element response accounting for the SUPG method. EC1 and EC2 stand for the finite element response with the discontinuity capturing method (added to SUPG) with eq. (7.81) and (7.84), respectively. The overshoots at the downwind boundary are effectively removed with both EC1 and EC2 methods. Minor improvements are observed also at the internal boundary.

## Chapter 8

# Simulation of heat extraction in geothermal reservoirs

Heat extraction in geothermal reservoirs, also called hot dry rock (HDR), can be described with a continuum mixture only if local thermal non-equilibrium (LTNE) within the mixture is accounted for. With the local thermal non-equilibrium assumption, heat transport is correctly described in each phase. Thermal transport within the fissure phase is dominated by forced convection with respect to conduction, owing to previous hydraulic stimulation. On the other hand, conduction is the dominant heat transport mechanism within the porous block (the solid phase and the pore fluid phase).

Convection dominated diffusion convection equations display spurious oscillations when implemented with classic numerical methods such as the Galerkin method or the finite difference method. A method to stabilise these equations has been developed by Brooks and Hughes (1982) and is called the streamline-upwind/Petrov-Galerkin method (Chapter 7).

In Section 8.1, the streamline-upwind/Petrov-Galerkin method is extended to stabilise the fully coupled thermo-hydro-mechanical model for dual porous media. The weak formulation is presented for both a mixture in local thermal non-equilibrium and for a mixture in local thermal equilibrium.

In Section 8.2, preliminary results with forced convection in a fully coupled thermo-hydro-mechanical model are displayed. The model is simplified to a single porosity in local thermal equilibrium to provide a first insight on the coupled response. To this respect, the SUPG method as part of a fully coupled model is tested. Results are satisfactory and wiggles are cured efficiently. Finally, the analytical solution of a problem in LTNE is compared with the finite element response and the LTNE assumption is clearly identified as unavoidable.

In Section 8.3, thermal recovery from a single porous medium in local thermal non-equilibrium is investigated. A parametric analysis is carried out to evaluate the influence of the LTNE assumption on the fluid outlet history, from a hot dry rock reservoir. The

main contribution is the ascertainment that the temperature outlet profile in thermal local non-equilibrium is characterised by a double-step pattern; representing the response of the reservoir respectively by, (1) the initial convection of the fluid (stage 1), (2) the transfer of heat between the solid and the fluid (stage 2), and (3) the final depletion of the mixture (stage 3). Next, the model is calibrated with data from the Fenton Hill hot dry rock reservoir. Temperature predictions compare favorably with experimental data for various setups. *In fine*, thermo-hydro-mechanical behaviour of the reservoir is described and tensile induced effective stress are observed owing to the thermal contraction of the rock. The results presented in this section will be submitted for publication in a near future.

In Section 8.4, the latter results are extended to a dual porous medium. The comprehensive framework used to define the constitutive behaviour of fractured porous media in LTNE is summarised from Chapter 2. Particular emphasis is laid on both mass and energy exchanges between the cavities which is controlled by the modified chemical potential difference and by the coldness difference, respectively. Again, three parameters of the model are calibrated, successively, with the thermal outputs of the Fenton Hill and of the Rosemanowes hot dry rock reservoirs. The solid-to-fracture fluid heat transfer parameter, which controls the local thermal non-equilibrium between the porous block and the fracture fluid, is found in the range  $35 < \kappa_{sf} < 120 \text{ mW/m}^3 \cdot \text{K}$ . Next, the calibrated model is used to describe the long term behaviour of the Fenton Hill hot dry rock reservoir. The thermally induced effective stress and the mechanisms for fluid loss are targeted. A parametric analysis is carried out to evaluate the influences of the dual porosity concept and of the fracture spacing on the effective stress response and on the permeation of fluid into the porous block. The thermally induced effective stress is found to be less tensile with the dual porosity model compared with the single porosity response illustrating the protective effect of the pore pressure drop which becomes more significant for large fracture spacings. The results presented in this section will also be submitted for publication in a near future.

## 8.1 The stabilisation process for a THM model

The comprehensive model involves six types of unknowns, namely the solid displacements, the fluid pressures, the temperatures of the solid, of the pore fluid and of the fissure fluid; and six types of field equations: 1. the balance of momentum for the solid skeleton 2 the balance of mass of the pore fluid 3. the balance of mass of the fissure fluid 4. the balance of energy of the solid 5. the balance of energy of the pore fluid and 6. the balance of energy of the fissure fluid. These equations are coupled as shown in Section 2.4.

The stabilisation of a THM model with the SUPG method is now considered for two sub-problems: I. the stabilisation of the balance of energy equations for a mixture in local thermal non-equilibrium (LTNE) and II. the stabilisation for the particular case of local thermal equilibrium, which displays only one balance of energy equation for the mixture as a whole.



The equations that display the convection-diffusion phenomenon have been addressed in the previous chapter, i.e. the balance of energy of the fluid phases. The balance of energy of the solid phase does not need to be stabilised in LTNE since no convective term is involved. Similarly, the balance of mass of the fluid phases are disregarded for the same reason.

### 8.1.1 Stabilisation for a mixture in LTNE

Referring to Section 7.1.1, the semi-discretised form of the balance of energy for the fluids  $k = p, f$ ,

$$\sum_{e=1}^{\text{nel}} [\delta \mathbf{T}^e]^T \int_{V^e} \mathbf{W}_{T_k}^T (\mathcal{L}_k T_k - f) dV^e = 0, \quad \text{with} \quad \mathcal{L}_{\text{conv},k} T_k = \mathbf{v}_{\text{conv},k} \cdot \nabla H_k, \quad (8.1)$$

involves the Petrov-Galerkin weighting function  $\mathbf{W}_{T_k}$ , defined as a function of the shape function vector  $\mathbf{N}_T$  and a rather *ad-hoc* stabilisation parameter  $\tau_{\text{conv},k}$  (Section 7.2.2.2),

$$\mathbf{W}_{T_k} = \mathbf{N}_T + \tau_{\text{conv},k} \mathcal{L}_{\text{conv},k} \mathbf{N}_T, \quad k = p, f; \quad (8.2)$$

the generic differential operator  $\mathcal{L}_k$  and  $\mathcal{L}_{\text{conv},k}$  the convective part of the operator  $\mathcal{L}_k$ . The balance of energy equations for solid and the fluids, in the case of a mixture in local thermal non-equilibrium, are summarised below (Section 2.4),

$$\begin{aligned} \mathcal{L}_s T_s &= -\frac{\partial}{\partial x_i} \left( n_s \Lambda_s \frac{\partial T_s}{\partial x_i} \right) + a_{T_s T_s} \frac{\partial T_s}{\partial t} + a_{T_s p} \frac{\partial p_p}{\partial t} + a_{T_s f} \frac{\partial p_f}{\partial t} + a_{T_s \epsilon} \frac{\partial^2 u_i}{\partial t \partial x_i} \\ &\quad + \kappa_{sp} (T_s - T_p) + \kappa_{sf} (T_s - T_f), \end{aligned} \quad (8.3)$$

$$\begin{aligned} \mathcal{L}_p T_p &= -\frac{\partial}{\partial x_i} \left( T_p n_p \Theta_p \frac{\partial p_p}{\partial x_i} + n_p \Lambda_p \frac{\partial T_p}{\partial x_i} \right) + a_{T_p T_p} \frac{\partial T_p}{\partial t} + a_{T_p p} \frac{\partial p_p}{\partial t} \\ &\quad + a_{T_p f} \frac{\partial p_f}{\partial t} + a_{T_p \epsilon} \frac{\partial^2 u_i}{\partial t \partial x_i} + a_{T_p T_s} \frac{\partial T_s}{\partial t} + \kappa_{sp} (T_p - T_s) + \kappa_{pf} (T_p - T_f) \\ &\quad + \hat{\rho}^p H_p + \underbrace{\mathbf{M}_p \cdot \nabla H_p}_{\text{convective term}}, \end{aligned} \quad (8.4)$$

$$\mathcal{L}_f T_f = -\frac{\partial}{\partial x_i} \left( T_f n_f \Theta_f \frac{\partial p_f}{\partial x_i} + n_f \Lambda_f \frac{\partial T_f}{\partial x_i} \right) + a_{T_f T_f} \frac{\partial T_f}{\partial t} + a_{T_f f} \frac{\partial p_f}{\partial t}$$

$$\begin{aligned}
& + a_{T_f p} \frac{\partial p_p}{\partial t} + a_{T_f \epsilon} \frac{\partial^2 u_i}{\partial t \partial x_i} + a_{T_f T_s} \frac{\partial T_s}{\partial t} + \kappa_{sf} (T_f - T_s) + \kappa_{pf} (T_f - T_p) \\
& + \hat{\rho}^f H_f + \underbrace{\mathbf{M}_f \cdot \nabla H_f}_{\text{convective term}}, \tag{8.5}
\end{aligned}$$

in which the coefficients of the model are presented in Table 2.9, p. 179. The convective parts of the balance of energy equations for the fluids (8.4)-(8.5), may also be expressed in terms of volume fluxes  $\mathbf{J}_k$ , for  $k = p, f$ ,

$$\mathbf{M}_p \cdot \nabla H_p = \rho_p \mathbf{J}_p \cdot \nabla H_p \quad \text{and} \quad \mathbf{M}_f \cdot \nabla H_f = \rho_f \mathbf{J}_f \cdot \nabla H_f. \tag{8.6}$$

The gradient of the fluid enthalpies (for constant thermal expansion coefficients  $c_{kT}$ ) are defined by (Note that the increment definitions are arbitrary),

$$\begin{aligned}
\nabla H_p &= v_0 (1 - T_0 c_{pT}) \nabla p_p + C_{p,p} \nabla T_p, \\
\nabla H_f &= v_0 (1 - T_0 c_{fT}) \nabla p_f + C_{f,p} \nabla T_f, \tag{8.7}
\end{aligned}$$

in which  $C_{k,p}$  is the heat capacity at constant pressure of the fluid  $k$  defined by,

$$C_{k,p} = C_{k,v} + \frac{c_{kT}^2}{\rho_p c_{kH}} T_0, \quad k = p, f. \tag{8.8}$$

By replacing in (8.6) the gradient of the fluid enthalpies by (8.7), the convective parts of the balance of energy equations are reformulated to,

$$\begin{aligned}
\mathbf{M}_p \cdot \nabla H_p &= b_{T_p p} (\mathbf{v}_p - \mathbf{v}_s) \cdot \nabla p_p + b_{T_p T_p} (\mathbf{v}_p - \mathbf{v}_s) \cdot \nabla T_p, \\
\mathbf{M}_f \cdot \nabla H_f &= b_{T_f f} (\mathbf{v}_f - \mathbf{v}_s) \cdot \nabla p_f + b_{T_f T_f} (\mathbf{v}_f - \mathbf{v}_s) \cdot \nabla T_f, \tag{8.9}
\end{aligned}$$

in which,

$$\begin{aligned}
b_{T_p p} &= n_p (1 - c_{pT} T_0), & b_{T_f f} &= n_f (1 - c_{fT} T_0), \\
b_{T_p T_p} &= n_p \rho_p C_{p,p}, & b_{T_f T_f} &= n_f \rho_f C_{f,p}. \tag{8.10}
\end{aligned}$$

### 8.1.1.1 The weighting function

It is important to notice that for this fully coupled model, the convective contributions are linked to two primary variables: the pressures  $p_k$  and the fluid temperatures  $T_k$ , eq. (8.9). This writing makes the application of the SUPG method delicate, indeed the artificial diffusivity  $\tilde{\alpha}_{\text{conv},T_k}$  (used in the calculation of  $\tau_{\text{conv},k}$ , for the fluid  $k$ ) is harder to identify. Two options arise:

1. The format of the convective terms in eq (8.4) and (8.5) suggests to use the enthalpies  $H_k$  as primary variables, instead of either the temperature  $T_k$  or the pressure  $p_k$ . The ensuing algebraic manipulations may not be un-tractable but they change the structure that we have in mind from the start.
2. The coupled terms in the definition of the convective parts of the balance of energy equations are neglected *in view of* the definition of  $\tau_{\text{conv},k} = \tilde{\alpha}_{\text{conv},T_k} / \|\mathbf{v}_{\text{conv},k}\|^2$ ,

$$\begin{aligned} \mathbf{M}_p \cdot \nabla H_p &\approx b_{T_p T_p} (\mathbf{v}_p - \mathbf{v}_s) \cdot \nabla T_p, \\ \mathbf{M}_f \cdot \nabla H_f &\approx b_{T_f T_f} (\mathbf{v}_f - \mathbf{v}_s) \cdot \nabla T_f. \end{aligned} \quad (8.11)$$

For simplicity, the second option is chosen. The fluid diffusivities used in the streamline upwind diffusivity equations (7.68) are,

$$\tilde{\alpha}_{\text{conv},T_p} = \frac{n_p \Lambda_p}{b_{T_p T_p}}, \quad \tilde{\alpha}_{\text{conv},T_f} = \frac{n_f \Lambda_f}{b_{T_f T_f}}, \quad (8.12)$$

and the convective fluid velocities are,

$$\mathbf{v}_{\text{conv},p} = \mathbf{v}_p - \mathbf{v}_s, \quad \mathbf{v}_{\text{conv},f} = \mathbf{v}_f - \mathbf{v}_s. \quad (8.13)$$

### 8.1.1.2 The weak formulation

Recall that the field equations containing convective terms, for a mixture in local thermal non-equilibrium, are the balance of energy for the two fluids  $k = p, f$ . The elementary weak contributions to the three balance of energy equations are considered in turn.

Elementary contribution to the balance of energy for the solid phase:

$$\begin{aligned}
& \int_{V^e} -\nabla \mathbf{N}_T^T n_s \Lambda_s \nabla \mathbf{N}_T \mathbf{T}_s^e - \mathbf{N}_T^T \mathbf{N}_T a_{T_s T_s} \dot{\mathbf{T}}_s^e \\
& + \int_{V^e} -\mathbf{N}_T^T \mathbf{N}_p (a_{T_s p} \dot{\mathbf{p}}_p^e + a_{T_s f} \dot{\mathbf{p}}_f^e) dV^e - \mathbf{N}_T^T \nabla \mathbf{N}_u a_{\epsilon T_s} \dot{\mathbf{u}}^e \\
& + \int_{V^e} -\mathbf{N}_T^T \mathbf{N}_T (\kappa_{sp} (\mathbf{T}_s^e - \mathbf{T}_p^e) + \kappa_{sf} (\mathbf{T}_s^e - \mathbf{T}_f^e)) dV^e - \int_{\partial V^e} \mathbf{N}_T^T \mathbf{q}_s \cdot \hat{\mathbf{n}} dS^e,
\end{aligned} \tag{8.14}$$

in which no stabilisation is required since no convective term appears in this balance equation. *The elementary contribution to the balance of energy for the pore fluid,*

$$\begin{aligned}
& \int_{V^e} -\nabla \mathbf{N}_T^T n_p \Lambda_p \nabla \mathbf{N}_T \mathbf{T}_p^e - \nabla \mathbf{N}_T^T T_p n_p \Theta_p \nabla \mathbf{N}_p \mathbf{p}_p^e dV^e \\
& + \int_{V^e} -\mathbf{W}_{T_p}^T \mathbf{N}_T (a_{T_p T_p} \dot{\mathbf{T}}_p^e + a_{T_p T_s} \dot{\mathbf{T}}_s^e) - \mathbf{W}_{T_p}^T \mathbf{N}_p (a_{T_p p} \dot{\mathbf{p}}_p^e + a_{T_p f} \dot{\mathbf{p}}_f^e) dV^e \\
& + \int_{V^e} -\mathbf{W}_{T_p}^T \nabla \mathbf{N}_u a_{T_p \epsilon} \dot{\mathbf{u}}^e - \mathbf{W}_{T_p}^T \mathbf{N}_T (\kappa_{sp} (\mathbf{T}_p^e - \mathbf{T}_s^e) + \kappa_{pf} (\mathbf{T}_p^e - \mathbf{T}_f^e)) dV^e \\
& + \int_{V^e} +\mathbf{N}_T \mathbf{T}_0^e \rho_p^2 \eta \mathbf{W}_{T_p}^T \left[ \frac{G_p (\mathbf{N}_p \mathbf{p}_p^e, \mathbf{N}_T \mathbf{T}_p^e)}{\mathbf{N}_T \mathbf{T}_p^e} - \frac{G_f (\mathbf{N}_p \mathbf{p}_f^e, \mathbf{N}_T \mathbf{T}_f^e)}{\mathbf{N}_T \mathbf{T}_f^e} \right] \\
& \quad \times H_p (\mathbf{N}_p \mathbf{p}_p^e, \mathbf{N}_T \mathbf{T}_p^e) dV^e \\
& + \int_{V^e} -\mathbf{W}_{T_p}^T (\mathbf{v}_p - \mathbf{v}_s) \cdot (\nabla \mathbf{N}_p b_{T_p p} \mathbf{p}_p^e + \nabla \mathbf{N}_T b_{T_p T_p} \mathbf{T}_p^e) dV^e \\
& - \int_{\partial V^e} \mathbf{N}_T^T \mathbf{q}_p \cdot \hat{\mathbf{n}} dS^e,
\end{aligned} \tag{8.15}$$

and the elementary contribution to the balance of energy for the fissure fluid,

$$\begin{aligned}
& \int_{V^e} -\nabla \mathbf{N}_T^T n_f \Lambda_f \nabla \mathbf{N}_T \mathbf{T}_f^e - \nabla \mathbf{N}_T^T T_f n_f \Theta_f \nabla \mathbf{N}_p \mathbf{p}_f^e dV^e \\
& + \int_{V^e} -\mathbf{W}_{T_f}^T \mathbf{N}_T (a_{T_f T_f} \dot{\mathbf{T}}_f^e + a_{T_f T_s} \dot{\mathbf{T}}_s^e) - \mathbf{W}_{T_f}^T \mathbf{N}_p (a_{T_f p} \dot{\mathbf{p}}_p^e + a_{T_f f} \dot{\mathbf{p}}_f^e) dV^e
\end{aligned}$$

$$\begin{aligned}
& + \int_{V^e} -\mathbf{W}_{T_f}^T \nabla \mathbf{N}_u a_{T_f \epsilon} \dot{\mathbf{u}}^e - \mathbf{W}_{T_f}^T \mathbf{N}_T (\kappa_{sf}(\mathbf{T}_f^e - \mathbf{T}_s^e) + \kappa_{pf}(\mathbf{T}_f^e - \mathbf{T}_p^e)) dV^e \\
& + \int_{V^e} -\mathbf{N}_T \mathbf{T}_0^e \rho_p^2 \eta \mathbf{W}_{T_f}^T \left[ \frac{G_p(\mathbf{N}_p \mathbf{p}_p^e, \mathbf{N}_T \mathbf{T}_p^e)}{\mathbf{N}_T \mathbf{T}_p^e} - \frac{G_f(\mathbf{N}_p \mathbf{p}_f^e, \mathbf{N}_T \mathbf{T}_f^e)}{\mathbf{N}_T \mathbf{T}_f^e} \right] \\
& \quad \times H_f(\mathbf{N}_p \mathbf{p}_f^e, \mathbf{N}_T \mathbf{T}_f^e) dV^e \tag{8.16} \\
& + \int_{V^e} -\mathbf{W}_{T_f}^T (\mathbf{v}_f - \mathbf{v}_s) \cdot (\nabla \mathbf{N}_p b_{T_f f} \mathbf{p}_f^e + \nabla \mathbf{N}_T b_{T_f T_f} \mathbf{T}_f^e) dV^e \\
& - \int_{\partial V^e} \mathbf{N}_T^T \mathbf{q}_f \cdot \hat{\mathbf{n}} dS^e,
\end{aligned}$$

require stabilisation on *all* terms except the diffusive terms and the boundary terms (first and last lines) which cancel out to zero on the elements interior and do not require stabilisation (Brooks and Hughes, 1982, p. 211-212) since 1. the unknowns are interpolated with multi-linear isoparametric interpolation functions, 2. the material properties are isotropic and 3. the element domains are rectangular. For a general mesh, the diffusion terms also require stabilisation with  $\nabla \mathbf{W}_{T_k}^T$  instead of  $\nabla \mathbf{N}_T^T$ . However, for reasonable element shapes, the streamline upwind contribution on the diffusive terms is small and can be neglected (Brooks and Hughes, 1982, p. 212).

In the left-hand-side of eq. (4.68), the parameters related to the mass transfer contributions have been heavily linearised to become, eq. (2.317),

$$\begin{aligned}
\gamma_{T_p p} &= \eta \rho_0 \times [C_{p,p} T_0 - H_0], & \text{and} & \quad \gamma_{T_p T_p} = -\eta \rho_0^2 S_0 \times [C_{p,p} T_0 - H_0], \\
\gamma_{T_f f} &= -\eta \rho_0 \times [C_{f,p} T_0 - H_0], & \text{and} & \quad \gamma_{T_f T_f} = +\eta \rho_0^2 S_0 \times [C_{f,p} T_0 - H_0].
\end{aligned} \tag{8.17}$$

In addition, the following parameters cancel out to zero due to their very low order of magnitude compared with their neighbor parameters (in the same equation);

$$\begin{aligned}
a_{T_p f} &= 0, & a_{T_p T_s} &= 0, & \text{and} & \quad a_{T_p \epsilon} &= 0, \\
a_{T_f p} &= 0, & a_{T_f T_s} &= 0, & \text{and} & \quad a_{T_f \epsilon} &= 0.
\end{aligned} \tag{8.18}$$

### 8.1.2 Stabilisation for a mixture in thermal equilibrium

Referring to Section 7.1.1, the semi-discretised form of a *coupled* problem in local thermal equilibrium

$$\sum_{e=1}^{\text{nel}} [\delta \mathbf{T}^e]^T \int_{V^e} \mathbf{W}_T^T (\mathcal{L} T - f) dV^e = 0, \quad \text{with} \quad \mathcal{L}_{\text{conv}} T = \sum_{k=p,f} \mathbf{v}_{\text{conv},k} \cdot \nabla H_k; \quad (8.19)$$

involves the Petrov-Galerkin weighting function  $\mathbf{W}_T$ , defined as a function of the shape function vector  $\mathbf{N}_T$ ,

$$\mathbf{W}_T = \mathbf{N}_T + \tau_{\text{conv}} \mathcal{L}_{\text{conv}} \mathbf{N}_T. \quad (8.20)$$

The balance of energy equation *for the mixture as a whole*, in the particular case of local thermal equilibrium, reduces to

$$\begin{aligned} \mathcal{L} T = & -\frac{\partial}{\partial x_i} \left( T n_p \Theta_p \frac{\partial p_p}{\partial x_i} + T n_f \Theta_f \frac{\partial p_f}{\partial x_i} + \Lambda \frac{\partial T}{\partial x_i} \right) + a_{TT} \frac{\partial T}{\partial t} + a_{Tp} \frac{\partial p_p}{\partial t} \\ & + a_{Tf} \frac{\partial p_f}{\partial t} + a_{T\epsilon} \frac{\partial^2 u_i}{\partial t \partial x_i} \underbrace{+ \mathbf{M}_p \cdot \nabla H_p + \mathbf{M}_f \cdot \nabla H_f}_{\text{convective terms}}, \end{aligned} \quad (8.21)$$

where the mass transfer contributions cancel out ( $\hat{\rho}^p = -\hat{\rho}^f$  in local thermal equilibrium only); and the convective terms are gathered on the second line as functions of the fluid enthalpies. Upon linearisation around the reference state with the initial enthalpy  $S_0 = 0$  (Table 2.9 and Remark 2.15), the coefficients are,

$$\begin{aligned} a_{Tf} &= T [(n_f - \xi_f) c_T - n_f c_{T,f}], & a_{Tp} &= T [(n_p - \xi_p) c_T - n_p c_{T,p}], \\ a_{TT} &= \rho C_p, & a_{T\epsilon} &= T c_T / c, \end{aligned} \quad (8.22)$$

in which  $\rho C_p = \rho^s C_{s,p} + \rho^p C_{p,p} + \rho^f C_{f,p}$ . The convective parts of the balance of energy (8.21), when the mass fluxes  $\mathbf{M}_k$  are replaced by the volume fluxes  $\mathbf{J}_k$ , for  $k = p, f$ , are,

$$\mathbf{M}_p \cdot \nabla H_p + \mathbf{M}_f \cdot \nabla H_f = \rho_p \mathbf{J}_p \cdot \nabla H_p + \rho_f \mathbf{J}_f \cdot \nabla H_f. \quad (8.23)$$

By substituting in (8.23) the gradient of the fluid enthalpies by their definitions (8.7) in thermal equilibrium, the convective part of the balance of energy is reformulated to,

$$\begin{aligned} \mathbf{M}_p \cdot \nabla H_p + \mathbf{M}_f \cdot \nabla H_f &= b_{T_p p} (\mathbf{v}_p - \mathbf{v}_s) \cdot \nabla p_p + b_{T_f f} (\mathbf{v}_f - \mathbf{v}_s) \cdot \nabla p_f \\ &+ (b_{T_p T_p} (\mathbf{v}_p - \mathbf{v}_s) + b_{T_f T_f} (\mathbf{v}_f - \mathbf{v}_s)) \cdot \nabla T, \end{aligned} \quad (8.24)$$

in which the coefficients are detailed in eq. (8.10).

### 8.1.2.1 The weighting function

This time, the convective contributions of the balance of energy equation are now linked to three primary variables:  $p_p$ ,  $p_f$  and  $T$ , eq. (8.24). Again, the coupled effects are neglected in the definition of the Petrov-Galerkin weighting function, and eq. (8.24) is approximated to

$$\mathbf{M}_p \cdot \nabla H_p + \mathbf{M}_f \cdot \nabla H_f \approx (b_{T_p T_p} (\mathbf{v}_p - \mathbf{v}_s) + b_{T_f T_f} (\mathbf{v}_f - \mathbf{v}_s)) \cdot \nabla T \quad (8.25)$$

in view of the definitions of  $\tau_{\text{conv}} = \tilde{\alpha}_{\text{conv},T} / \|\mathbf{v}_{\text{conv}}\|^2$  and  $\mathbf{v}_{\text{conv}}$ :

$$\mathbf{W}_T = \mathbf{N}_T + \tau_{\text{conv}} \mathbf{v}_{\text{conv},T} \cdot \nabla \mathbf{N}_T \quad (8.26)$$

Nevertheless, two options remain:

1. The mixture can be stabilised with respect to the largest fluid velocity,

$$\begin{aligned} \text{if } \mathbf{v}_p \geq \mathbf{v}_f \quad \mathbf{v}_{\text{conv}} &= (\mathbf{v}_p - \mathbf{v}_s), \quad \tilde{\alpha}_{\text{conv},T} = \frac{n_p \Lambda_p}{b_{T_p T_p}}; \\ \text{if } \mathbf{v}_f > \mathbf{v}_p \quad \mathbf{v}_{\text{conv}} &= (\mathbf{v}_f - \mathbf{v}_s), \quad \tilde{\alpha}_{\text{conv},T} = \frac{n_f \Lambda_f}{b_{T_f T_f}}. \end{aligned} \quad (8.27)$$

2. Alternatively, both contributions can be used and scaled by  $\sqrt{b_{T_p T_p}^2 + b_{T_f T_f}^2}$ ,

$$\mathbf{v}_{\text{conv}} = \frac{(b_{T_p T_p} (\mathbf{v}_p - \mathbf{v}_s) + b_{T_f T_f} (\mathbf{v}_f - \mathbf{v}_s))}{\sqrt{b_{T_p T_p}^2 + b_{T_f T_f}^2}}, \quad \tilde{\alpha}_{\text{conv},T} = \frac{\Lambda}{\sqrt{b_{T_p T_p}^2 + b_{T_f T_f}^2}}. \quad (8.28)$$

The option n°2. is implemented in the finite element program, although both options are essentially the same if  $\mathbf{v}_f \gg \mathbf{v}_p$ , which is likely to be the case for dual porous media.

### 8.1.2.2 The weak formulation

*The elementary weak contribution to the balance of energy of a mixture in thermal equilibrium is:*

$$\begin{aligned}
& \int_{V^e} -\nabla \mathbf{N}_T^T \Lambda \nabla \mathbf{N}_T \mathbf{T}^e - \nabla \mathbf{N}_T^T T (n_p \Theta_p \nabla \mathbf{N}_p \mathbf{p}_p^e + n_f \Theta_f \nabla \mathbf{N}_p \mathbf{p}_f^e) dV^e \\
& + \int_{V^e} -\mathbf{W}_T^T \mathbf{N}_T a_{TT} \dot{\mathbf{T}}^e - \mathbf{W}_T^T \mathbf{N}_p (a_{Tp} \dot{\mathbf{p}}_p^e + a_{Tf} \dot{\mathbf{p}}_f^e) dV^e \\
& + \int_{V^e} -\mathbf{W}_T^T (\mathbf{v}_p - \mathbf{v}_s) \cdot (\nabla \mathbf{N}_T b_{TpTp} \mathbf{T}^e + \nabla \mathbf{N}_p b_{T_p p} \mathbf{p}_p^e) dV^e \\
& + \int_{V^e} -\mathbf{W}_T^T (\mathbf{v}_f - \mathbf{v}_s) \cdot (\nabla \mathbf{N}_T b_{T_f T_f} \mathbf{T}^e + \nabla \mathbf{N}_p b_{T_f p_f} \mathbf{p}_f^e) dV^e \\
& + \int_{V^e} -\mathbf{W}_T^T \nabla \mathbf{N}_u a_{T\epsilon} \dot{\mathbf{u}}^e dV^e - \int_{\partial V^e} \mathbf{N}_T^T \mathbf{q} \cdot \hat{\mathbf{n}} dS^e
\end{aligned} \tag{8.29}$$

in which the first and the last lines represent the diffusive terms and the boundary term. The remarks exposed in Section 8.1.1.2 on the structure of the weak equations apply here as well.

Note that once the SUPG stabilisation method is performed on the three-temperature model, the elementary weak contributions to the balance of energy do not reduce to that of a single-temperature model when enforcing the temperatures and the parameters to be equal pointwise. Nevertheless, both discretisation are correct and should lead to the same result upon refinement; since, for large Péclet numbers,  $\tau_{\text{conv}} = h/2v_{\text{conv}} \rightarrow 0$  when the element size  $h \rightarrow 0$ .

## 8.2 Preliminary results on forced convection in a coupled model

A first insight of heat extraction in geothermal reservoirs is provided below. First, the model is restricted to a single porosity model in local thermal equilibrium and is applied to the Soultz-sous-Forêt site. The fully coupled thermo-hydro-mechanical response is investigated in spite of the unrealistic assumption of LTE. Next, the nature of the thermal boundary condition between the reservoir and the surrounding formation is briefly outlined. The ability of the SUPG method to cure spurious wiggles is validated for coupled models in LTE. Finally, the LTNE hypothesis is scrutinised by comparison with an analytical solution. The LTNE assumption appears unavoidable to describe thermal depletion in geothermal reservoirs, in spite of the remaining uncertainties regarding the coefficient of volumetric inter-phase heat transfer  $\kappa_{sp}$ .

### 8.2.1 Problem setup at Soultz-sous-Forêts

The first HDR projects were initiated in different parts of the world, Fenton Hill (USA) starting in 1973, Rosemanowes (England) in 1977 and Hijiori (Japan) in 1989; now followed



by more elaborate Enhanced Geothermal Systems (EGS); projects at Soultz-sous-Forêts (France), Coso (USA) and Habanero (Australia).

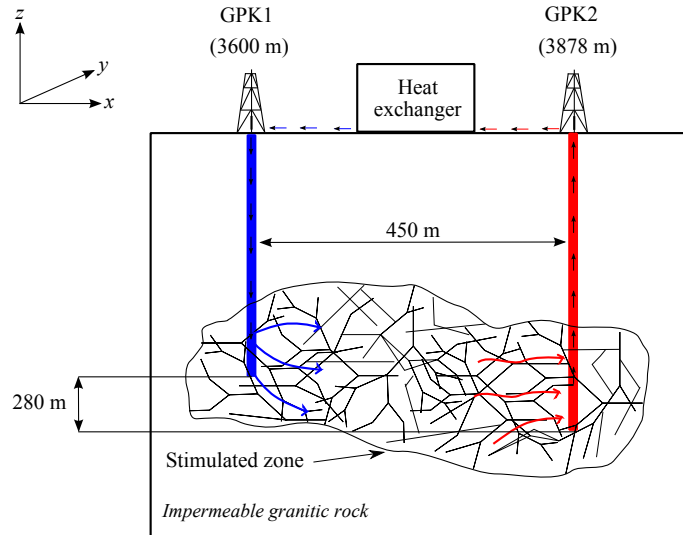


Figure 8.1: Fluid circulation in the geothermal reservoir at Soultz-sous-Forêts after hydraulic stimulation.

Preliminary numerical results are performed at Soultz-sous-Forêts (France), in the  $x-y$  plane. The injection well is named GPK1 and the production well is denoted GPK2 (Figure 8.1). The cold water injected into GPK1 is heated within the stimulated reservoir and is extracted in well GPK2. The hot produced fluid is cooled with water from a pond near GPK2 and is then re-introduced into GPK1 for a new circulation cycle. The reservoir has been artificially stimulated (hydraulically induced or chemically induced) prior to the circulation test. Artificial stimulation is not reproduced in this study, our main focus is rather on the circulation test itself. Gravity and free convection are not accounted for.

### 8.2.1.1 Material properties

The material properties of the Soultz-sous-Forêts reservoir are presented in Table 8.1, for a single porosity medium model. The subscript  $p$  is used to characterise the unique porosity with respect to the solid phase endowed with the subscript  $s$ .

In Table 8.1, the volumetric thermal expansion of the fluid is given for the initial temperature of  $80^\circ\text{C}$ . The volumetric thermal expansion of the fluid  $c_{pT}$  increases with temperature, see Figure 2.6 and eq. (2.171). Nevertheless, it may remain constant between  $80^\circ\text{C}$  and  $200^\circ\text{C}$  at a pressure of 60 MPa (Bataillé et al., 2006, p. 663).

The thermal diffusivity  $\alpha_T$  and hydraulic diffusivity  $\alpha_H$  of a single porosity medium, are defined by McTigue (1986),

Material parameter	Value	Unit	Reference
Drained elastic modulus $E$	54	GPa	3
Drained Poisson's ratio $\nu$	0.25	-	1
Bulk modulus of grains $K_s = 1/c_s$	50	GPa	3
Bulk modulus of the fluid $K_p = 1/c_{H,p}$	2.2	GPa	1
Dynamic viscosity of the fluid $\mu_p$	$3 \times 10^{-4}$	Pa.s	2
Overall network porosity* $n_p$	0.1003	-	2,3
Overall network permeability+ $k_p$	$1.0110^{-12}$	$\text{m}^2$	1
Thermal conductivity of the solid $\Lambda_s$	2.49	W/m.K	3
Thermal conductivity of the fluid $\Lambda_p$	0.6	W/m.K	1
Heat capacity of the solid $C_{s,v}$	1000	J/kg.K	3
Heat capacity of the fluid $C_{p,v}$	4200	J/kg.K	1
Density of the solid $\rho_s$	2910.2	$\text{kg}/\text{m}^3$	2,3
Density of the fluid $\rho_p$	980	$\text{kg}/\text{m}^3$	1
Volumetric thermal expansion of the solid $c_T$	$7.5 \times 10^{-6}$	1/K	2
Volumetric thermal expansion of the fluid $c_{pT}$	$1 \times 10^{-3}$	1/K	2

Table 8.1: Input parameters representative of the hot dry rock reservoir at Soultz-sous-Forêts (France). 1: Estimated parameters for water and granitic rock, 2: Bataillé et al. (2006) and 3: Evans et al. (2009). \*The porosity accounts for the fluid in the fissure network and in the rock matrix. +The permeability describes the interconnected fissure network post-stimulation.

$$\begin{aligned}
\alpha_T &= \frac{n_s \Lambda_s + n_p \Lambda_p}{n_s \rho_s C_{v,s} + n_p \rho_p C_{v,p}} = \frac{\Lambda}{\rho C_v}, \\
\alpha_H &= \frac{k_p}{\mu_p} \frac{2\mu^{DS}(1-\nu)}{1-2\nu} \left[ \frac{B^2(1+\nu_u)^2(1-2\nu)}{9(1-\nu_u)(\nu_u-\nu)} \right],
\end{aligned} \tag{8.30}$$

in which  $B$  is the Skempton coefficient and  $\nu_u$  is the undrained Poisson's ratio,

$$\frac{1}{B} = 1 + n_p \frac{c_{H,p} - c_s}{c - c_s}, \quad \nu_u = \frac{3\nu + B(1-2\nu)(1 - c_s/c)}{3 - B(1-2\nu)(1 - c_s/c)}. \tag{8.31}$$

For the material defined in Table 8.1, the thermal and hydraulic diffusivities are equal to  $\alpha_T = 7.59 \times 10^{-7} \text{ m}^2/\text{s}$  and  $\alpha_H = 66.80 \text{ m}^2/\text{s}$ . Therefore, the diffusivity ratio  $R = \sqrt{\alpha_H/\alpha_T}$  is equal to 9383  $\gg 1$  which illustrates that the hydraulic flow is faster than the heat flow. Note that the diffusivity ratio does not account for the dominant heat transportation phenomenon which is convection rather than diffusion, in the fissure network (macro-fissures). The characteristic times  $t = L^2/\alpha_k$ ,  $k = H, T$ , associated with a length of  $L = 450$  meters (distance separating the two wells) are equal to 8462.5 years for thermal diffusion and 0.84 hours for hydraulic diffusion.

### 8.2.1.2 Geometry

The 3-D dimensions of the hydraulically stimulated reservoir are approximately  $450 \times 36 \times 750$  as length, width and height ( $x, y, z$ ). The Soultz-sous-Forêts site is conceptualised by a reservoir composed of several fractured zones. Only one fracture zone is represented in this 2-D simplified model. The simulation of the circulation test is performed in the horizontal  $x - y$  plane of space as presented in Figure 8.2. The thickness of the fractured zone is assumed to be equal to 36 m (in the  $y$ -direction), which represents the width of the stimulated domain at the logging depth (Bataillé et al., 2006).

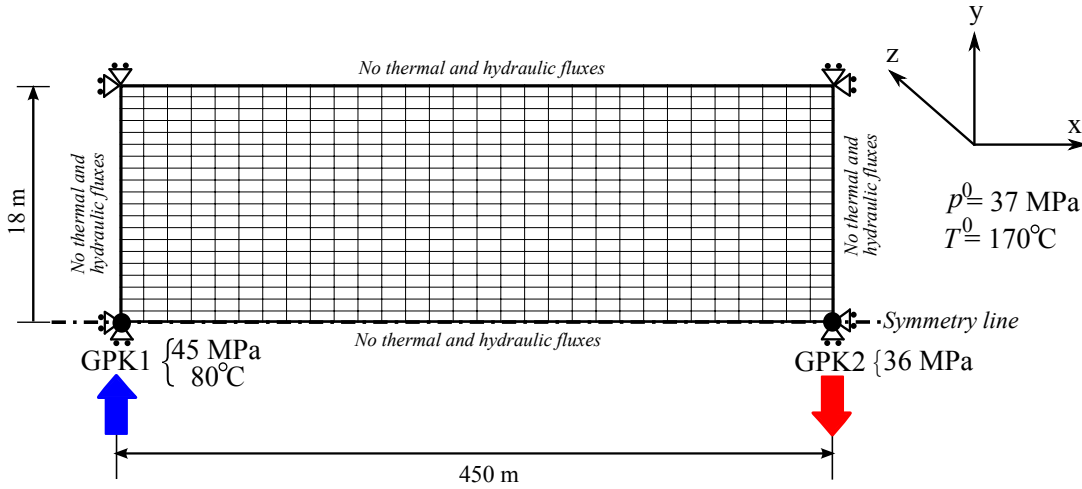


Figure 8.2: Conceptual model of the 2-D circulation test, at Soultz-sous-Forêts, in the horizontal  $x - y$  plane of space. Note that the above sketch is enlarged along the  $y$ -axis. The boundary conditions illustrated on this sketch are properly listed in Table 8.2.

### 8.2.1.3 Boundary conditions

The *in-situ* stresses defined in (Evans et al., 2009, p. 38-39), are disregarded in favor of a no-displacement boundary condition perpendicular to the walls of the mesh (Table 8.2). The influence of the overall behaviour on the stress field will generate *induced stresses* that could be later compared with a reference situation (non-zero initial stresses). Hence, the initial state is defined by zero initial stresses, the initial fluid pressure  $p_p^0 = 37$  MPa and the initial temperature  $T^0 = 170^\circ\text{C}$ , corresponding to a depth of  $z = 3.7$  km.

The injection temperature  $T_{\text{inj}} = 80^\circ\text{C}$  is applied at the injection well and the outlet temperature is sought. All the walls of the reservoir are insulated from the surroundings, that is  $\mathbf{q} \cdot \hat{\mathbf{n}} = 0$ .

The injection and production pressures are controlled manually. The injection pressure is equal to  $p_p = p_p^0 + 1$  MPa, whereas the production pressure is fixed to  $p_p = p_p^0 - 1$  MPa. All remaining boundaries are assumed impermeable, that is  $\mathbf{J}_p \cdot \hat{\mathbf{n}} = 0$ .

Type	Boundary	Condition
Displacements	r, l, t, b	No normal displacement
Fluid flow	r, l, t, b	Impermeable: $\mathbf{J}_p \cdot \hat{\mathbf{n}} = 0$
	injection well	$p_p = p_p^0 + 1 \text{ MPa}$
	production well	$p_p = p_p^0 - 1 \text{ MPa}$
Heat flow	r, l, t, b	Thermally insulated: $\mathbf{q} \cdot \hat{\mathbf{n}} = 0$
	injection well	$T_{\text{inj}} = 80^\circ\text{C}$

Table 8.2: Boundary conditions used for the circulating model, at Soultz-sous-Forêt. l = left, r = right, t = top, b = bottom boundary of Figure 8.2.

#### 8.2.1.4 A non-homogeneous velocity field

The boundary conditions of Table 8.2 applied to the geometry described in Figure 8.2 induce a realistic velocity field illustrated in Figure 8.3. The main characteristic of the field is its non-homogeneity in space.

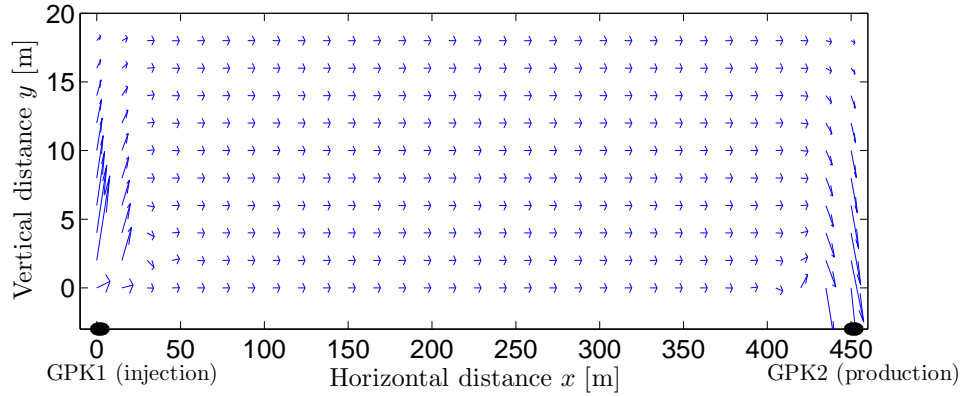


Figure 8.3: Scaled velocity vectors  $\mathbf{v}_p$  at steady state for an injection pressure equal to 1 MPa at GPK1 and a production pressure equal to -1 MPa at GPK2. The velocity field is non-homogeneous in space in the vicinity of the wells. The horizontal component of the velocity between the wells is equal to  $v_{p,x} = 1.44 \times 10^{-5} \text{ m/s}$  in average.

Note that the flow spreads all over the allowable volume (in the  $y$ -direction). This feature, which creates large gradients in the neighborhoods of the wells, could contribute to maintain the macro-fissures open, in spite of the thermal shrinkage induced by the cooling.

### 8.2.1.5 Mesh definition

The mesh is composed of 450 elements of size  $h_x \times h_y = 15 \text{ m} \times 2 \text{ m}$  and 510 nodes. The grid Péclet number is calculated with the *average* fluid velocity  $\|\mathbf{v}\| = 1.44 \times 10^{-5} \text{ m/s}$  (Bataillé et al., 2006) and the thermal diffusivity  $\alpha_T = \Lambda/\rho C_v = 7.5 \cdot 10^{-7} \text{ m}^2/\text{s}$  (Table 8.1),

$$\text{Pe}_g = \frac{h_x \|\mathbf{v}\|}{2\alpha_T} \quad (8.32)$$

that corresponds to a value of 142.3.

## 8.2.2 Influence of the thermo-hydro-mechanical couplings

The thermo-hydro-mechanical model is simplified to a single porosity model in local thermal equilibrium to provide a first understanding of the coupled response of convection-dominated mixtures. Since no hard boundary condition is imposed on the mesh, the SUPG method is not required. The analysis of its efficiency to cure spurious wiggles will be addressed in Subsection 8.2.3.

Recall that the model is simplified to a single porosity medium. In addition, gravity and local thermal non-equilibrium are disregarded. The fully coupled model (reduced to one equivalent porosity and one temperature) comprise the balance of momentum for the mixture, the balance of mass for the fluid and the balance of energy for the mixture,

$$\mu^{DS} \frac{\partial^2 u_i}{\partial x_j \partial x_j} + (\lambda^{DS} + \mu^{DS}) \frac{\partial^2 u_j}{\partial x_i \partial x_j} - \xi_p \frac{\partial p_p}{\partial x_i} - \frac{c_T}{c} \frac{\partial T}{\partial x_i} = 0, \quad (8.33)$$

$$\frac{\partial}{\partial x_i} \left( \frac{k_p}{\mu_p} \frac{\partial p_p}{\partial x_i} \right) = a_{pp} \frac{\partial p_p}{\partial t} + \xi_p \frac{\partial^2 u_i}{\partial t \partial x_i} + a_{pT} \frac{\partial T}{\partial t}, \quad (8.34)$$

$$\begin{aligned} \frac{\partial}{\partial x_i} \left( \Lambda \frac{\partial T}{\partial x_i} \right) &= a_{TT} \frac{\partial T}{\partial t} + T \left( a_{pT} \frac{\partial p_p}{\partial t} + \frac{c_T}{c} \frac{\partial^2 u_i}{\partial t \partial x_i} \right) \\ &\quad + b_{T_p T_p} \cdot \nabla T_p + b_{T_p p} \cdot \nabla p_p. \end{aligned} \quad (8.35)$$

By using the material parameters of Table 8.1, and the definitions of  $b_{T_p T_p}$  and  $b_{T_p p}$  in eq. (8.10); one can observe that  $b_{T_p T_p} \nabla T \gg b_{T_p p} \nabla p_p$  (for  $\nabla T = 90^\circ \text{C}/450 \text{ m}$  and  $\nabla p_p$

= 2 MPa/450 m). Therefore the coupling contribution in the convective contributions is negligible. On the other hand, if the enthalpy definition  $H_p$ ,

$$\nabla H_p = v_0 (1 - T_0 c_{pT}) \nabla p_p + C_{p,p} \nabla T, \quad (8.36)$$

is approximated by assuming that the fluid is incompressible and non-dilatable, that is  $C_{p,p} = C_{p,v} = \text{constant}$  and  $c_{pT} = 0.0$ ,

$$\nabla H_p = C_{p,v} \nabla T, \quad (8.37)$$

the convective contribution would be strongly underestimated:  $n_p \rho_p C_{p,v} \ll b_{T_p T_p}$ , and a slower propagation of the thermal front would be obtained.

The profile responses of the temperature, the fluid pressure and the horizontal displacement are plotted in Figures 8.4 and 8.5, for four different times. The effective stress responses are presented in Figure 8.6. The temperature results along the horizontal distance  $x$  are presented in terms of a dimensionless temperature  $\varphi$  defined to be equal to one when the *in-situ* temperature  $T$  is equal to the initial temperature  $T^0 = 170^\circ\text{C}$  and equal to zero when  $T$  is equal to the injection temperature  $T_{\text{inj}} = 80^\circ\text{C}$ ,

$$\varphi = \frac{T - T_{\text{inj}}}{T^0 - T_{\text{inj}}}. \quad (8.38)$$

The overall mechanism is controlled by the propagation of the cooled thermal front (Figure 8.4, left) which induces the mixture to contract (see Figure 8.5). The perturbation of the temperature profiles at 7.63 months is most probably due to the non-monotonic velocity around the producing well GPK2 (Figure 8.3). Note that the rate of propagation of the cooled front is not realistic due to the local thermal equilibrium assumption. A more realistic thermal assumption will be presented in a subsequent example (Subsection 8.2.4 and Section 8.3). The influence of the pressure field and of the mechanical field on the temperature response are negligible.

Importantly, the pressure profile is *not* influenced by the propagation of the cooled front. Hence, the fluid pressure is unlikely to influence in turn the temperature response *via* the convective velocity  $\mathbf{v}_p$ . It should be noted that the thermo-hydraulic couplings arise though the transient terms  $\partial p_p / \partial t$  and  $\partial T / \partial t$ , but also though the velocity term controlling the amount of convection  $\mathbf{M}_p$ .

The influence of the temperature on the displacement is significant and non-monotonic (Figure 8.5). The horizontal displacement profiles describe (1) first that the rock contracts close to the injection point, (2) second that this contraction involves the left-hand-side points as time goes on and as the thermal front propagates toward the right; and (3) third that the conjunction of rigid boundaries and homogeneous temperature repartition allows

the elastic contraction to recover its initial state. Logically, the largest displacements arise when the thermal front is almost in the middle of the wells, where all the points move away from the rigid walls.

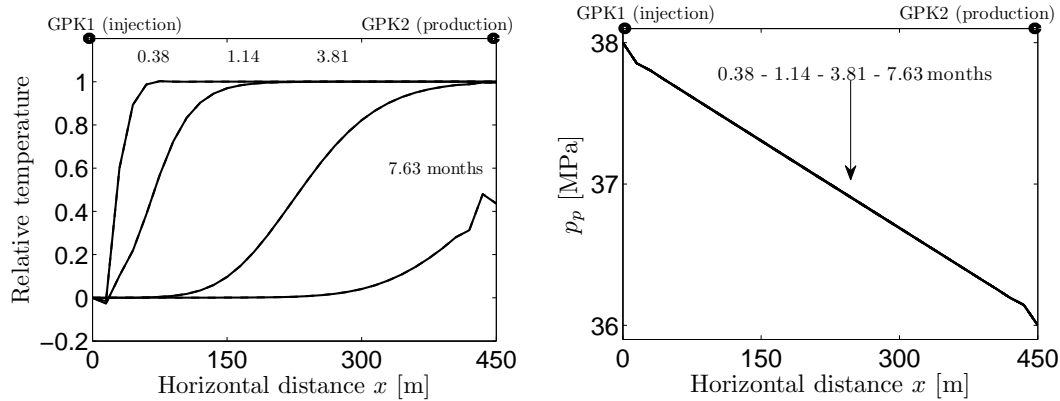


Figure 8.4: (left) Relative temperature profiles and (left) pressure profiles, on the Soultz-sous-Forêts site at  $y = 0$  m. The thermal front propagates towards the production well at a high *unrealistic* rate due to the local thermal equilibrium assumption. The pressure field is undisturbed by the cooling front. Furthermore, the influence of the mechanical couplings on the temperature and on the pressure fields are negligible.

The overall contraction of the sample is controlled by the volumetric thermal expansion coefficient of the solid phase  $c_T$  (see Remark 2.13, p. 117). Because the volumetric thermal expansion coefficient of water  $c_{pT}$  is about 3 to 4 times larger than that of the solid matrix  $c_T$ , the fluid pressure should decrease to compensate the small contraction imposed by the solid. However, the fluid pressure variations are very small (a few kPa) owing to the large permeability of the fissured reservoir.

The effective stress profiles are displayed in Figure 8.6, where tensile effective stress increases as time goes by. This tensile induce-stress is the direct consequence of the thermal contraction of the solid skeleton. The effective stress is continuously increasing in spite of the relaxation of the horizontal deformation and of the pore pressure over time, which indicates that the thermal strain is continuously increasing until it will reach a plateau.

In this section, the permeability of the voids remained constant. However, in view of the coupled thermo-hydro-mechanical behaviour, the issue of the permeability variation will need to be addressed. From a general point of view, the thermal contraction of the solid skeleton could slowly increase the permeability of the fracture network. Whereas, the decreasing fluid pressure tends to decrease the permeability. Since the competition between the pressure contribution and the thermal contribution on the overall deformation can not be analytically measured, numerical tests are required to understand the change in hydraulic aperture. For such a high permeability, the influence of the pore pressure on the displacement is small or negligible and thermal contraction rules the mechanism for propagating flow paths (Willis-Richards and Wallroth, 1995). Nonetheless, the competition between the pressure contribution and the thermal contribution on the overall deformation

will be scrutinised in Sections 8.3 and 8.4, for the single porosity concept and the dual porosity concept, respectively.

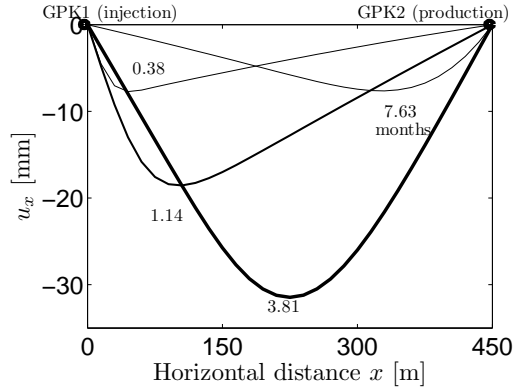


Figure 8.5: Horizontal displacement profile; on the Soultz-sous-Forêts site at  $y = 0$  m. The horizontal displacement is controlled by the propagation of the cooled thermal front.

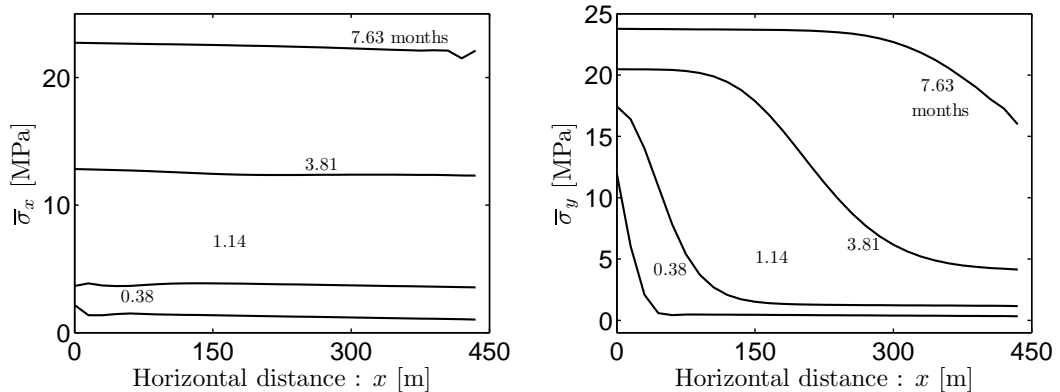


Figure 8.6: Effective stresses profiles  $\bar{\sigma}_x$  (left) and  $\bar{\sigma}_y$  (right) on the Soultz-sous-Forêts site at  $y = 0$  m. Tensile stresses are counted positive. Cooling induces thermal contraction of the solid skeleton, which induces an increase of tensile effective stress.

### 8.2.3 Influence of the thermal boundary conditions

The type of thermal boundary condition imposed at the boundaries of enhanced geothermal reservoir may have a great influence on the overall response of a coupled thermo-hydro-mechanical test. These conditions describe the amount of heat that the reservoir exchanges with its surroundings, usually an impermeable semi-infinite rock. If too much heat is supplied from the surroundings to the reservoir, the economic viability of the reservoir is overestimated and conversely. In a geomechanical context with no radiation, the four possible types of thermal boundary conditions are:

1. *The Dirichlet boundary condition* that is imposed on the temperature field,



$$T = T_{\text{known}} \quad \text{at } t > 0, \quad \text{on } \partial V. \quad (8.39)$$

2. *The Neumann boundary condition* that is imposed on the conductive flux,

$$\mathbf{Q} = \mathbf{Q}_{\text{known}} \quad \text{at } t > 0, \quad \text{on } \partial V. \quad (8.40)$$

3. *The convective boundary condition* that uses a convective heat transfer parameter  $h_{sf}$  [W/m<sup>2</sup>.K] and describes the amount of energy of a convective fluid heating a solid wall of temperature  $T_{\text{known}}$ ,

$$\mathbf{Q} = h_{\text{conv}}(T_{\text{known}} - T) \quad \text{at } t > 0, \quad \text{on } \partial V. \quad (8.41)$$

4. *The Robin boundary condition* that is a linear combination of Dirichlet and Neumann boundary conditions,

$$aT + b\mathbf{Q} = \mathbf{R}_{\text{known}} \quad \text{at } t > 0, \quad \text{on } \partial V \quad (8.42)$$

and is a general form of the insulating boundary condition for diffusion-convection equations. However, Brooks and Hughes (1982, p. 211) advise against the use of such a boundary condition as it is not suitable for certain numerical simulation, in favor of the classic Neumann condition on the convective flux.

Note that the Robin boundary condition is not a *mixed boundary condition* which indicates that different boundary conditions are used on different parts of the domain.

Thermal boundary conditions of enhanced geothermal reservoir have been described in various ways in the literature. Reservoirs can be simply described by one unique fracture interacting with a conductive infinite surrounding (Gringarten et al., 1975; Cheng et al., 2001), or heavily embedded in an impermeable buffer rock (Bataillé et al., 2006).

The Dirichlet boundary condition is often employed at a certain distance from the reservoir boundaries (Bataillé et al., 2006). This boundary condition assumes that the rock surrounding the reservoir is impermeable (or endowed with a very low permeability compared with the stimulated zone), i.e. thermal diffusion is dominant over convection. This surrounding rock describes the hot formation, at least during the time of the simulation. The main drawback of such a condition is that the formation around the reservoir needs to be modeled which significantly increases the number of elements.

The Neumann boundary condition is usually employed on the reservoir or the fracture edges. Often a heat conduction equation is used to represent the conductive heat flux

between the reservoir and the impermeable rock in the direction perpendicular to the reservoir slot (Kolditz and Diersch, 1993; Cheng et al., 2001). Whereas adiabatic conditions can be employed on the reservoir edges in the direction of the flow. The conductive heat flux may either be defined as an explicit function of time (Kolditz and Diersch, 1993) or as an explicit function of time and space (Cheng et al., 2001).

Alternatively, a convective boundary condition is rarely employed. This boundary condition is used when a convective fluid heats a solid wall remaining at a fixed temperature  $T_{\text{known}}$ . The main drawback of this boundary condition is the identification of the convective heat transfer parameter  $h_{\text{conv}}$  (Section 3.3.2).

The behaviour of a thermo-hydro-mechanical model with insulated boundaries (a Neumann boundary condition) has been scrutinised in Section 8.2.2. The contribution of the external heat supply is now assessed by comparing the previous results with a Dirichlet boundary condition (applied on a piece of formation added on top of the reservoir). The convective boundary condition will be analysed later in Section 8.3.

### 8.2.3.1 The Dirichlet boundary condition

When a piece of formation is added on the side of the reservoir, the velocity field in the reservoir is not modified due to the low permeability of the formation  $k_p = 10^{-20} \text{ m}^2$  (Figure 8.7). A Dirichlet boundary condition  $T = T^0$  is used on the formation at  $y = H$ , which has been calibrated so that  $T(x, H, t)$  would remain equal to  $T^0$  over the life time of the reservoir  $\approx 40$  years (Remark 8.1); hence,

$$H = \sqrt{t_{\text{lifetime}} \times \alpha_T} \approx 30 \text{ m.} \quad (8.43)$$

The injection temperature is applied at GPK1 and all the other boundaries are assumed to be insulated. The hydraulic and mechanical boundary conditions remain the same as in the previous section. The profile responses of the temperature, the horizontal displacement and the effective stresses are plotted in Figures 8.7 and 8.8, for four different times. Stability issues are illustrated in Figure 8.10.

The temperature propagates in the porous medium at the same rate as in the previous section regardless of the additional heat contribution brought by the piece of formation (Figure 8.8, left).

The pressure variation is not influenced by the thermal front (not shown) and remains the same as in Figure 8.4, right.

The horizontal displacement profile is similar to the one in the previous section but with a lower magnitude (Figure 8.8, right). This is due to the fact that two thermal fronts propagate in the reservoir which distribute the displacement contribution along the

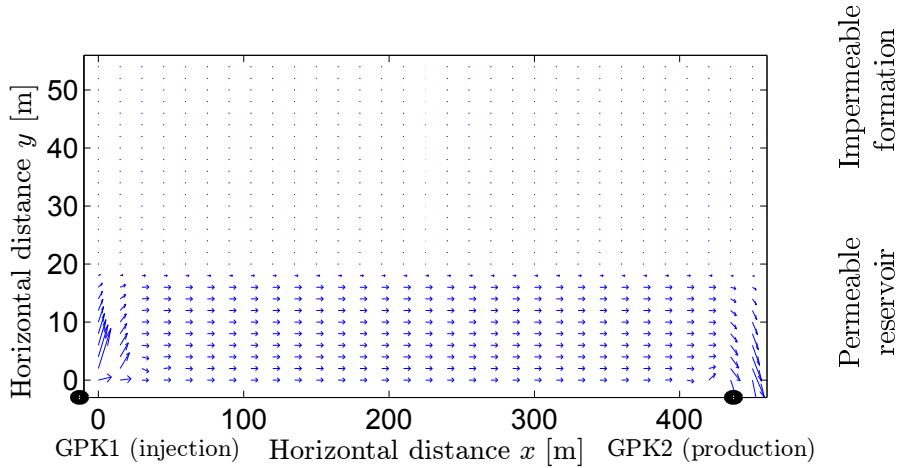


Figure 8.7: Scaled velocity vectors  $\mathbf{v}_p$  of a 18 m reservoir with a 36 m piece of formation located at  $(x, 18 < y < 36 \text{ m})$ . The velocity field is non-monotonic in the vicinity of the wells and the x-component of the velocity between the wells is equal to  $v_{p,x} = 1.44 \times 10^{-5} \text{ m/s}$  in average.

$x$ -direction and the  $y$ -direction. The effective stresses are also influenced by this  $x - y$  non uniform repartition (Figure 8.9). Thermal contraction is visible along both directions, as tensile effective stress increases behind the thermal front.

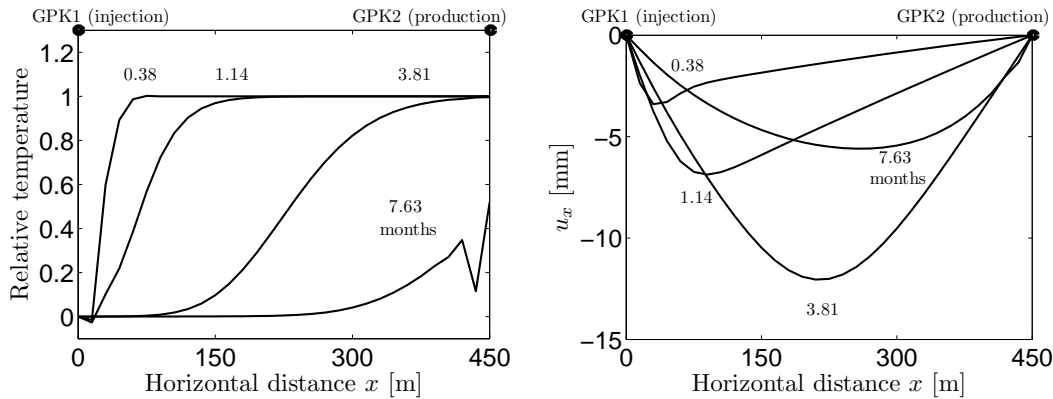


Figure 8.8: Relative temperature profiles (left) and horizontal displacement profiles  $u_x$  (right) on the Soultz-sous-Forêts site at  $y = 0 \text{ m}$ , with a piece of formation on the  $y$ -boundary of the reservoir. The hot formation does not modify significantly the temperature profile; whereas the horizontal displacements are significantly reduced compared with Figure 8.4.

**Remark 8.1.** *It should be noted that the thermal propagation in the formation is not influenced (during the time of the simulation) by the type of boundary condition applied on the  $y$ -boundary of the formation since the permeability of the formation is very low, that is the thermal propagation is diffusion-dominant as opposed to convection-dominant in the reservoir. The influence of such a boundary condition at  $y = H$  of the formation might become significant at very large times 20-30 years and with a lower average velocity.*

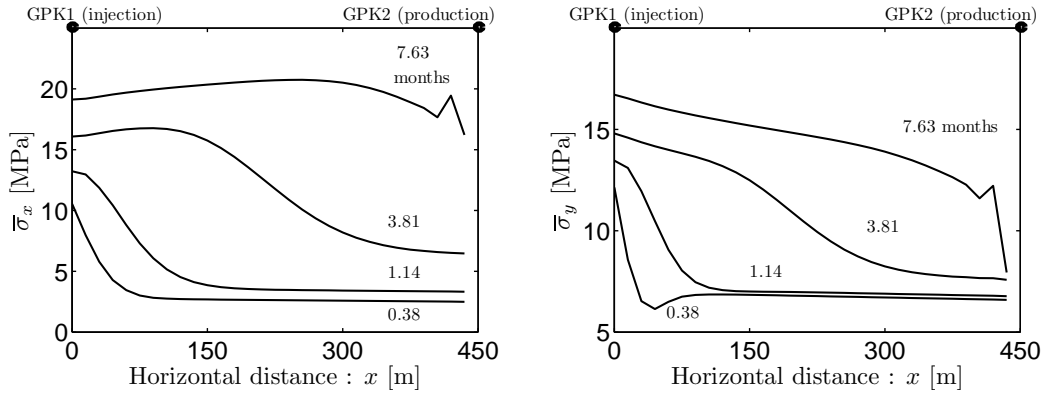


Figure 8.9: Horizontal effective stresses profiles  $\bar{\sigma}_x$  (left) and  $\bar{\sigma}_y$  (right) on the Soultz-sous-Forêts site at  $y = 0$  m, with a piece of formation on the  $y$ -boundary of the reservoir. The hot formation reduces the thermally induced increase in effective stress compared with Figure 8.6.

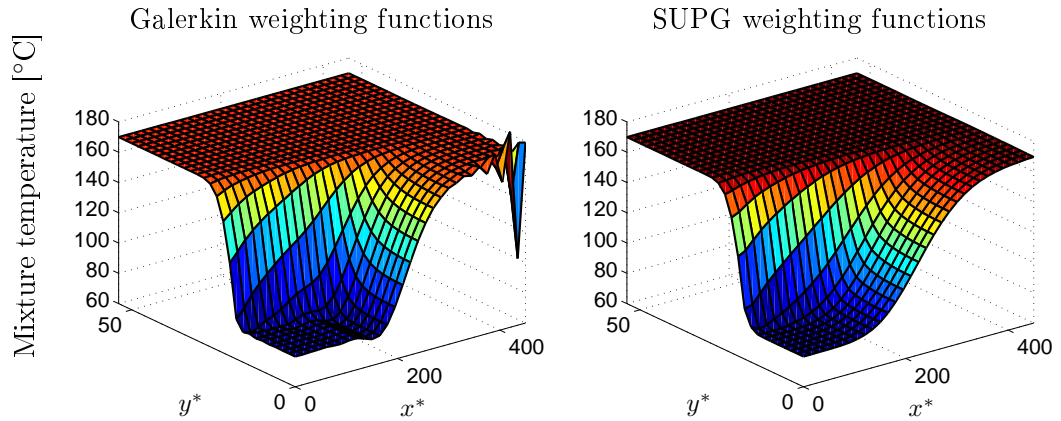


Figure 8.10: Contour of the mixture temperature  $T$  [°C], with a piece of formation on the  $y$ -boundary of the reservoir, at 3.81 months. The buffer zone brings a sharp internal layer that requires the use of the SUPG stabilisation method.

Finally, two-dimensional contours of the temperature response are presented in Figure 8.10 which compare the use of a Galerkin weighting function with a SUPG weighting function. The formation is so impermeable that the cool front does not penetrate above  $y = 18$  m, at least during the duration of the simulation. Therefore the formation acts like a Dirichlet boundary condition at the border between the formation and the reservoir; and a sharp internal layer arises. This sharp internal layer induces spurious wiggles when the balance of energy equation is not stabilised with the SUPG method. The stabilisation parameter is defined by eq. (7.67), as proposed by Tezduyar and Osawa (2000) for transient problems, with a maximum allowed time step of  $\Delta t_{\max} = 10^6 \text{ s} < h_x^2 / 2\alpha_T$  and which does not compromise the effect of the stabilisation parameter during the convection-dominated period (see Remark 7.4, p. 324).

The differences between the two proposed thermal boundary conditions remain negligible (at least when the mixture is in local thermal equilibrium) and suggests that the heat transfer mechanisms in side the reservoir overcome that of the reservoir with the surroundings. The validity of this hypothesis will be investigated for a mixture in local thermal non-equilibrium in Section 8.3.

#### 8.2.4 Influence of local thermal non-equilibrium

If local thermal non-equilibrium is not accounted for, the balance of energy equation of the mixture is likely to describe the temperature behaviour of the fluid in the fractures (heat transported by convection), rather than that of the mixture in local thermal non-equilibrium; hence, the temperature of the mixture will propagate at a time scale imposed by the velocity of the fluid in the fractures. To illustrate this, the analytical solution of heat propagation of a unique crack embedded in an impermeable rock (Gringarten et al., 1975) is compared with the numerical response of the equivalent single porosity model in local thermal equilibrium (LTE) and in local thermal non-equilibrium (LTNE) (Figure 8.12).

The context of the analytical solution is framed so as to best adapt the finite element analysis. Gringarten et al. (1975) proposed a study of a 2-D reservoir, of length  $L = 300$  m in the  $x$ -direction and of infinite extent in the  $y$ -direction which holds a unique crack of aperture  $b = 0.3$  m. Therefore, the distance separating two potential cracks is infinite. By further assuming 1-D convection in the fracture in the  $x$ -direction, and 1-D conduction in the impermeable rock in the  $y$ -direction, the analytical solution of the fluid temperature in the fracture  $T_p(x, 0, t)$  can be found by utilizing a Laplace transform (Gringarten et al., 1975; Cheng et al., 2001),

$$\frac{T_p(x, 0, 0) - T_p(x, 0, t)}{T_p(x, 0, 0) - T_p(0, 0, t)} = \begin{cases} \operatorname{erfc} \left[ \frac{\Lambda_s x}{v_p b \rho_p C_{p,v}} \sqrt{\frac{v \rho_s C_{s,v}}{\Lambda_s (vt - x)}} \right], & \text{for } x \leq vt, \\ 0, & \text{for } x \geq vt, \end{cases} \quad (8.44)$$

in which  $v_p$  is the velocity of the fluid in the fracture along the  $x$ -direction and the fluid conductivity is enforced to zero  $\Lambda_p = 0$ . A dimensionless time  $t_d$  is introduced to accurately compare the temperature history,

$$t_d = \frac{(\rho_p C_{p,v})^2}{\Lambda_s \rho_s C_{s,v}} \left( \frac{v_p b}{x} \right)^2 \left( t - \frac{x}{v_p} \right). \quad (8.45)$$

The finite element setup for a continuous fissured porous medium is adapted from the analytical setup proposed by Gringarten for a single crack embedded in a semi-infinite

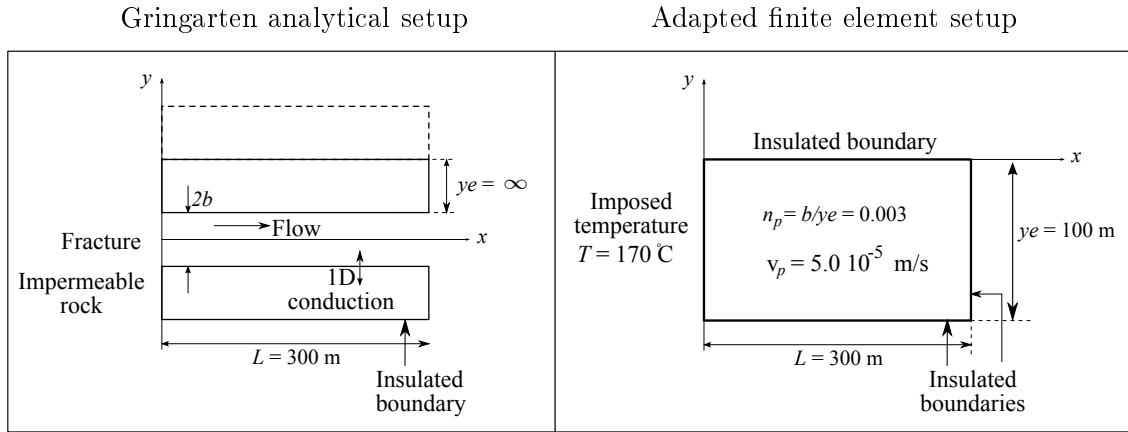


Figure 8.11: (left) Gringarten analytical setup for a single crack embedded in a semi-infinite impermeable rock. (right) A continuous single porous medium setup for the finite element analysis. The reservoir is modeled with 30 elements of size  $10 \times 100 \text{ m}^2$  forming a total volume of  $300 \times 100 \text{ m}^2$ .  $n_p$  is fixed to 0.003. The imposed fluid velocity along  $x$  is equal to  $v_p = 5 \times 10^{-5} \text{ m/s}$ .

impermeable rock, as illustrated in Figure 8.11. The fractured porous medium is reduced to one porosity and the temperature field alone is simulated, i.e. the pressure field and the mechanical field are disregarded. In order to best fit the analytical result of Gringarten, the fluid conductivity  $\Lambda_p$  is enforced to zero and the solid conductivity  $\Lambda_s$  is reduced to a 1-D conductivity in the  $y$ -direction. Insulated boundary conditions are applied along  $y = 0 \text{ m}$ ,  $y = ye$  and  $x = L$  on both phases. The *in-situ* temperature is chosen equal to  $T_p^0 = T_s^0 = T^0 = 80^\circ\text{C}$ , the injection temperature  $T_p = 170^\circ\text{C}$  is imposed instantaneously at  $x = 0 \text{ m}$  on the fluid phase *only*; and the production temperature at  $x = L \text{ m}$  is sought.

Since symmetry is observed around the  $x$ -axis, half of the reservoir only is implemented. The length of the reservoir and the aperture of the cracks are chosen equal to Gringarten setup,  $L = 300 \text{ m}$  and  $b = 0.3 \text{ m}$ . The height of the reservoir is chosen equal to  $ye = 100 \text{ m}$ . Since the semi-infinite rock surrounding the crack is assumed to be impermeable in Gringarten study,  $ye$  is calibrated so that the critical time for conduction in the  $y$ -direction is greater than the life-time of the reservoir. The porosity  $n_p$  is simply calculated by assuming that  $b$  represents the cumulative aperture of the fissured network over the distance  $ye$ . Hence,  $n_p = b/ye = 0.003$ .

Finally, the fluid velocity  $v_p$  is imposed, constant, uni-directional along the  $x$ -axis and null along the  $y$ -axis. The value of the fluid velocity is arbitrarily chosen to  $v_p = 5 \times 10^{-5} \text{ m/s}$  which corresponds to a pressure gradient of  $\nabla p_p = 4.5 \times 10^3 \text{ Pa/m}$  for an overall permeability of  $k_p = 1 \times 10^{-14} \text{ m}^2$  and a fluid viscosity of  $\mu_p = 0.3 \times 10^{-3} \text{ Pa.s}$ . In other words, the pressure drawdown would be equal to 1.35 MPa over the 300 m separating the injection point and the production point.

The temperature history and the temperature profile of a mixture in thermal equilibrium are characterised by step-like curves describing a convection-dominated behaviour;

whereas the temperature curves of the analytical results are characterised by a less stiff slopes which correspond to a less convective behaviour (Figure 8.12). The LTNE fluid temperature displays an intermediate response between the LTE response and the analytical solution. The solid and the fluid temperature remain in LTNE until  $t_d = 20$  (see Figure 8.13).

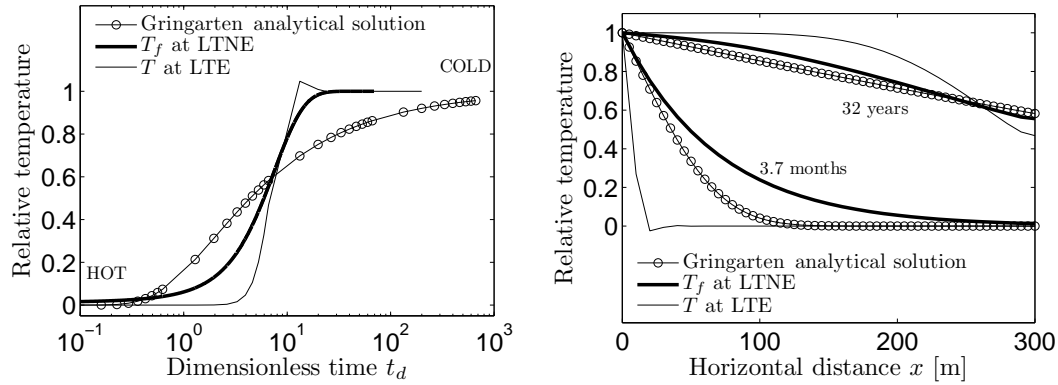


Figure 8.12: (Left) Relative outlet temperature versus dimensionless time. (Right) Relative temperature profile at times 3.7 months and 32 years. Gringarten analytical solution is presented in eq. (8.44). LTE stands for local thermal equilibrium and LTNE for local thermal non-equilibrium. The LTNE simulation uses an inter-phase heat transfer  $\kappa_{sp} = 1.0 \times 10^{-2} \text{ W/m}^3 \cdot \text{K}$  found by trial and error to ‘best fit’ the analytical response. The gap between the analytical solution and the LTNE response is attributed to the estimation of the fluid porosity  $n_p$ . In spite of the significant difference between the curves, the LTNE response is closer to the analytical solution compared with the LTE response.

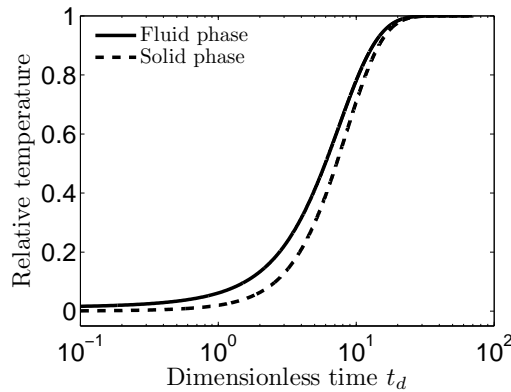


Figure 8.13: Relative outlet temperatures of the solid and the fluid phases versus dimensionless time. The solid and the fluid phase remain in LTNE until  $t_d = 20$ .

The LTNE response is endowed with a *volumetric* coefficient of inter-phase heat transfer  $\kappa_{sp} = 1.0 \times 10^{-2} \text{ W/m}^3 \cdot \text{K}$ , which has been found by trial and error to ‘best fit’ Gringarten analytical results. The coefficient of volumetric inter-phase heat transfer  $\kappa_{sp}$  is linked to a specific surface  $S_{sp}^s$  [ $\text{m}^2/\text{m}^3$ ] and to a inter-phase heat transfer  $h_{sp}$  [ $\text{W}/\text{m}^2 \cdot \text{K}$ ],

$$\kappa_{sp} = S_{sp}^s \times h_{sp}, \quad (8.46)$$

in which the inter-phase heat transfer parameter  $h_{sp}$  is related to a solid-fluid system. The latter coefficient also accounts for the regime of the dominant heat transport of the fluid, so that a rock-water diffusion-dominated system will have a different inter-phase heat transfer parameter than a rock-water convection-dominated system.  $\kappa_{sp}$  illustrates the rate at which a solid-fluid system reaches thermal equilibrium.

It is uneasy to compare the validity of  $\kappa_{sp}$  with the literature since this parameter represents both the material parameters of the mixture and the geometric disposition of the fracture network. Therefore, a discussion is presented below; (1) first on the evaluation of  $S_{sp}^s$  and (2) second on the validity of  $h_{sp}$  by comparison with empirical formulas.

(1) The specific surface of a solid-fluid system can be calculated in two different ways; either considering the specific surface of the fracture network, or that of the solid blocks (Section 3.3.2):

- i. In the first case, the fractures are grouped in a plate shape (rectangular box) of size  $L \times b \times H \text{ m}^3$ . The overall specific surface of the fracture network is then calculated with the formula  $S_{sp}^s = (2LH + 2Lb + 2bH)/LbH = 8.67 \text{ m}^{-1}$  (for  $H = 1 \text{ m}$ ); and the solid to fluid inter-phase heat transfer  $h_{sp}$  is equal to  $2.88 \times 10^{-3} \text{ W/m}^2.\text{K}$ .
- ii. In the second case, the solid blocks are grouped in a plate shape (rectangular box) of size  $L \times (ye - b) \times H \text{ m}^3$ , the overall specific surface of the fracture network can be calculated with the formula  $S_{sp}^s = (2LH + 2L(ye - b) + 2(ye - b)H)/L(ye - b)H = 2.02 \text{ m}^{-1}$  (for  $H = 1 \text{ m}$ ); and the solid to fluid inter-phase heat transfer  $h_{sp}$  is equal to  $1.23 \times 10^{-2} \text{ W/m}^2.\text{K}$ .

As a partial conclusion, the evaluation of the specific area allows to enclose the coefficient of inter-phase heat transfer within a minimum and a maximum:

$$1.15 \cdot 10^{-3} \text{ W/m}^2.\text{K} < h_{sp} < 4.95 \cdot 10^{-3} \text{ W/m}^2.\text{K}. \quad (8.47)$$

(2) This result can be compared with an empirical formula, (Bejan, 1993, p. 37), in which the overall heat transfer coefficient  $h_{sp}$  of a convective liquid along a wall of thickness  $(ye - b) = 99.7 \text{ m}$  is,

$$\frac{1}{h_{sp}} = \frac{1}{h_{\text{conv}}} + \frac{ye - b}{\Lambda_s}, \quad \rightarrow \quad h_{sp} = 2.88 \cdot 10^{-2} \text{ W/m}^2.\text{K}, \quad (8.48)$$

in which  $h_{\text{conv}}$  is the convective heat transfer coefficient of water under forced convection equal to  $1000 \text{ W/m}^2.\text{K}$ , (Bejan, 1993, p. 24). Note that the order of magnitude of the



inter-phase heat transfer parameter in eq. (8.48) is only one degree of magnitude above the upper boundary of eq. (8.47). Therefore, the LTNE response with a solid to fluid inter-phase heat transfer  $h_{sp}$  equal to  $4.95 \times 10^{-3} \text{ W/m}^2.\text{K}$  gives a better insight on Gringarten's formula and in the possibility of reproducing such a behaviour with a continuum model in local thermal non-equilibrium.

Finally, the literature provides comprehensive results on the maximum boundary of the inter-phase heat transfer  $h_{sp}$  (Minkowycz et al., 1999; Nield et al., 2002). Departure from local thermal non-equilibrium due to a rapidly changing heat source, such as a convective flux, is significant for the ratio of the Sparrow number over the Péclet number  $\text{Sp}/4\text{Pe}$  smaller than unity (definitions of Pe and Sp are provided in Section 3.4),

$$\frac{\text{Sp}}{4\text{Pe}} \left[ n_p + (1 - n_p) \frac{\Lambda_s}{\Lambda_p} \right] < 1 \quad \rightarrow \quad h_{sp} < 1.38 \text{ W/m}^2.\text{K}. \quad (8.49)$$

in which the specific area is  $S_{sp}^s = 2.02 \text{ m}^{-1}$ , the solid conductivity is  $\Lambda_s = 2.87 \text{ W/m.K}$ , the fluid conductivity is  $\Lambda_f = 0.6 \text{ W/m.K}$  and the Péclet number  $\text{Pe} = 1.029 \times 10^5$ .

In this section, the analytical solution of a porous medium subjected to a convective heat flow has been compared to the simulation response of a continuum model, first in local thermal equilibrium and second in local thermal non-equilibrium. The response in local thermal non-equilibrium, with a volumetric inter-phase heat transfer equal to  $\kappa_{sp} = 1.0 \times 10^{-2} \text{ W/m}^3.\text{K}$ , gives a more satisfactory response to the problem than the response in local thermal equilibrium. The inferred inter-phase heat transfer coefficient  $h_{sp}$  [ $\text{W/m}^2.\text{K}$ ] has been compared with the literature with a mixed success. On the other hand, the transition limit between LTE and LTNE has been identified for  $h_{sp} < 1.38 \text{ W/m}^2.\text{K}$ . Hence, all the proposed coefficients of inter-phase heat transfer  $h_{sp}$ , which magnitude are ranking from  $O(10^{-3})$  to  $O(10^{-1})$ , fall easily into the LTNE limit.

If it seems clear that the proposed application can only be described with a continuum mixture in local thermal non-equilibrium, the identification of the volumetric inter-phase heat transfer parameter remains uneasy. One way to avoid such problem is to calibrate  $\kappa_{sp}$  with experimental data. The issue of the identification of the volumetric inter-phase heat transfer parameter for enhanced geothermal reservoirs is discussed later in Section 8.3.

### 8.3 A single porosity medium in local thermal non-equilibrium

The work presented in this section has been submitted to the *International Journal for Numerical and Analytical Methods in Geomechanics* under the title *Thermal recovery from a fractured medium in local thermal non-equilibrium*, by the following authors, in order, Rachel Gelet, Benjamin Lorete and Nasser Khalili.

The motivation of this second publication is to describe the thermal depletion of a fractured reservoir in a coupled thermo-hydro-mechanical context. The main contribution of this work is the use of a continuum model in local thermal non-equilibrium. The volumetric inter-phase heat transfer  $\kappa_{sf}$  [W/m<sup>3</sup>.K] of a given geothermal reservoir is the least well-available of the required input parameters. In this work, experimental data from Fenton Hill HDR reservoir (Figure 8.14) are used to calibrate the model.

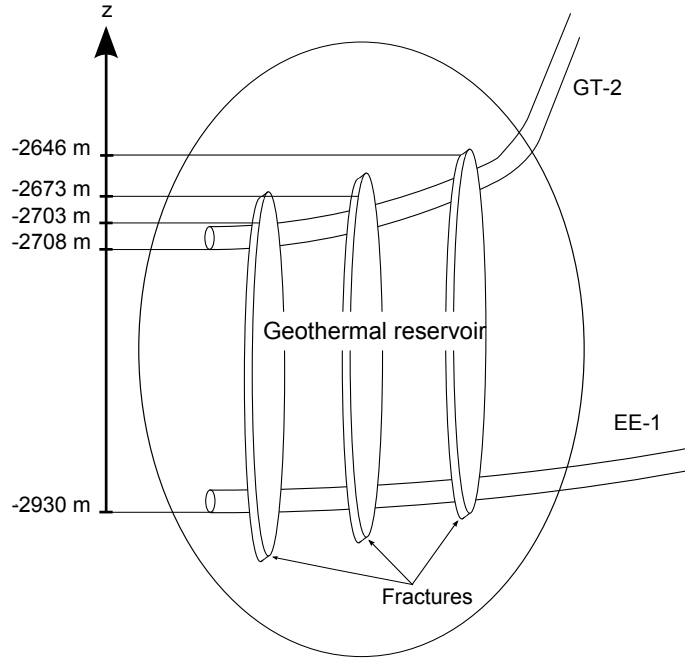


Figure 8.14: Conceptual representation of the Fenton Hill reservoir, inspired from Zyvoloski et al. (1981, Figure 3-2). The injection well is denoted EE-1 and the production well is denoted GT-2. The extent and the amount of fractures linking the two wells are not precisely known and are indicated here for the illustration.

### 8.3.1 Introduction

Geothermal extraction from deep hot dry rock (HDR) reservoirs may become a viable alternative to grey energies in the “far future” (Tenzer, 2001). The production of geothermal energy is achieved by cold water injection, in fractured igneous rocks (originally with low matrix permeability), at sites where the vertical temperature gradient is favorable. Of crucial importance to the economic viability of these enhanced geothermal systems (EGS) is the knowledge of thermal output evolution, induced thermal stress and fluid loss, at various time scales of the circulation tests (Armstead and Tester, 1987).

Thermo-poro-elastic mechanisms in addition to chemical, damage and plastic processes can play a significant role on the overall behavior of the HDR reservoirs (Evans et al., 2009)

Closed form solutions for the prediction of uncoupled reservoir depletion have been presented by a number of investigators, where heat transfer is dominated by convection in the fluid phase and by conduction in the solid phase (Gringarten et al., 1975; Elsworth,

1989; Cheng et al., 2001). Ghassemi et al. (2005) provided an uncoupled three-dimensional integral equation for calculating thermally induced stresses, highlighting the importance of induced thermal stress, without the burden of discretizing the reservoir. Notable contributions have also been made by Wang and Dusseault (2003) on the effects of convective-conductive heat flow on the stresses near a cylindrical wellbore.

Coupled thermo-hydro-mechanical analyses for geothermal systems are scarce (Hayashi et al., 1999) and focus mainly on partially coupled systems in an effort to implement a precise fracture network through a system of discrete discontinuities (DuTeaux et al., 1996; Bruel, 2002), to couple free and forced convection (Bataillé et al., 2006), or to characterize joint closure with a stress dependent law (Kohl et al., 1995; Bower and Zyvoloski, 1997).

Alternatively, comprehensive fully coupled thermo-hydro-mechanical formulations based on the mixture theory have been presented by Loret and Khalili (2000a) and Khalili and Loret (2001) for unsaturated porous media, with emphasis on the importance of an appropriate definition of the effective stress.

A key factor influencing geothermal energy recovery is the difference in characteristic times between diffusion in the solid phase and convection in the fluid phase. The thermally induced effective stress which results from these two contributions may lead to permeability change and fluid loss. Thermal shrinkage and pressure drop, across the body of the reservoir, occur at various time scales and the understanding of their interaction requires the simulation of a continuum mixture in local thermal non-equilibrium (Aifantis, 1980a; Willis-Richards and Wallroth, 1995).

This paper is aimed at presenting a fully coupled finite element formulation for a thermo-elastic fractured medium in local thermal non-equilibrium. The fractured medium is described as a porous mixture composed of a solid phase and a fluid phase. The solid matrix is made of impermeable solid blocks surrounded by saturated fractures. Numerical solutions are obtained by enforcing the balances of mass, momentum and energy. A summary of the governing differential equations is provided in Sect. 8.3.2. The weak form of the governing equations, the discretization and time-integration procedures to solve the coupled equations through a finite element method are detailed in Sect. 8.3.3. The primary variables are the displacements, the pressure of the fluid, the temperature of the solid phase and the temperature of the fluid. The resulting system of equations is used to address a generic HDR reservoir subjected to temperature gradients and to various external heat supplies (Sect. 8.3.4). An attempt to define a dimensionless threshold above which a LTNE analysis is required is exposed (Sect. 8.3.5). The threshold embodies local physical properties of the mixture, elements of the geometry of the reservoir and the production flow rate. When interpreted with help of this threshold, the simulations of geothermal energy recovery highlight quite distinct time profiles of the outlet temperature, depending whether local thermal equilibrium (LTE) or local thermal non-equilibrium (LTNE) hold in the reservoir. The calibrated model is used to obtain the thermal output and the thermally induced effective stress response to circulation tests, which are compared with data obtained at the Fenton Hill HDR reservoir (Sect. 8.3.6).

### 8.3.2 The two temperature thermoporoelastoc model

Geothermal energy is produced by circulating a fluid through the fracture reservoir within a single porosity conceptual framework. This continuum treatment requires the mixture to be in thermal non-equilibrium so that the processes acting on the fluid phase and on the solid phase are properly accounted for.

#### 8.3.2.1 Model assumptions

Local thermal non-equilibrium between the phases holds at all points of the simulated zone. Each phase  $k$  is endowed with its own temperature  $T_k$  and its own material properties. Local thermal non-equilibrium (LTNE) emanates from the contrast between the rapid convection of heat by the moving fluid in the fractures and the slow diffusion of heat through the solid matrix. Indeed, the characteristic time associated with convection is several orders of magnitude smaller than the characteristic times of diffusion in both solid skeleton and fluid, Sect. 8.3.3.3.

In order to concentrate efforts on the heat exchange between phases, a number of restrictions are adopted in the development of the model:

1. The material properties of each phase, namely, the porosities, the permeabilities, the densities, the viscosities, the conductivities, the specific heat capacities, the hydraulic compressibility, the coefficients of thermal expansion, as well as the solid-fluid specific heat transfer coefficient, are assumed to remain constant with time;
2. Density driven convection and gravity effects are neglected. In addition, the thermal boundary resistance (Kapitza resistance), the solid surface wettability and the lagging response (Virto et al., 2009) are considered negligible in the lifetime of the reservoir;
3. The additional stiffness induced by the initial fluid pressure is not accounted for either;
4. The flow regime remains laminar.

#### 8.3.2.2 Governing equations

With the indices  $s$  and  $f$  referring to the solid and to the fluid respectively, the governing field equations of the two phase mixture in local thermal non-equilibrium enforce the balance of momentum of the mixture as a whole, the balance of mass for the fluid phase and the balances of energy of the solid and fluid phases (Eringen and Ingram, 1965; Bowen

and Chen, 1975),

$$\begin{aligned}
\operatorname{div} \boldsymbol{\sigma} + \rho \mathbf{g} &= \mathbf{0}, \\
\operatorname{div} \mathbf{J}_f + \mathcal{J}_f &= 0, \quad \mathcal{J}_f \equiv n_f \frac{1}{\rho_f} \frac{d^f \rho_f}{dt} + \frac{1}{V} \frac{d^s V_f}{dt}, \\
\operatorname{div} \mathbf{q}_s + \mathcal{Q}_s &= 0, \quad \mathcal{Q}_s \equiv T_s \frac{d^s s^s}{dt} + \hat{e}_{sf}, \\
\operatorname{div} \mathbf{q}_f + \mathcal{Q}_f &= 0, \quad \mathcal{Q}_f \equiv T_f \frac{d^s s^f}{dt} - \hat{e}_{sf} + \rho_f \mathbf{J}_f \cdot \nabla H_f,
\end{aligned} \tag{8.50}$$

where  $\boldsymbol{\sigma}$  is the total stress,  $\mathbf{g}$  is the gravity,  $\mathbf{J}_f$  is the apparent volumetric flux of the fluid relative to the solid skeleton, and  $\mathbf{q}_k$  is the apparent heat flux through the phase  $k$ . The rate of energy transfer (or exchange) from the solid phase to the fluid phase  $\hat{e}_{sf}$  is defined by the constitutive equation (8.62) below.

The field equations feature intrinsic quantities like the mass density  $\rho_k$ , the specific entropy  $S_k$  [J/kg·K] and the specific enthalpy  $H_k$  [J/kg] of phase  $k$ . At variance, with  $n_k = V_k/V$  the volume fraction of phase  $k$  in the mixture,  $\rho^k = n_k \rho_k$  and  $s^k = \rho^k S_k$  are *apparent* quantities that represent respectively the mass and entropy of the phase  $k$  per unit current volume of mixture. Finally,  $\mathbf{u}$  denotes the displacement vector of the solid skeleton, while  $\mathbf{v}_k$  denotes the velocity vectors of any phase  $k$ , so that the apparent volumetric flux of the fluid relative to the solid skeleton  $\mathbf{J}_f$  is equal to  $n_f (\mathbf{v}_f - \mathbf{v}_s)$ .

The initial configuration, which serves as a reference, represents a state in mechanical and thermal equilibrium in which stress, strain and fluid pressure maybe non-zero. The solid temperature and the fluid temperature are initially equal to  $T^0$ . Departure from this reference state is denoted by the symbol  $\Delta(\cdot)$ .

The thermo-elastic mixture remains isotropic in both elastic and thermal properties. The shear behavior is accounted for by the second Lamé's constant  $\mu^{DS}$  of the drained solid skeleton while the fluid does not react to shear stresses. The elastic relationship links the elastic strain  $\boldsymbol{\epsilon}^{el}$  to the effective stress  $\bar{\boldsymbol{\sigma}}$ ,

$$\operatorname{tr} \boldsymbol{\epsilon}^{el} = c \frac{\operatorname{tr} \bar{\boldsymbol{\sigma}}}{3}, \quad \operatorname{dev} \boldsymbol{\epsilon}^{el} = \frac{\operatorname{dev} \bar{\boldsymbol{\sigma}}}{2 \mu^{DS}}, \tag{8.51}$$

where  $\operatorname{tr}$  and  $\operatorname{dev}$  denote respectively the trace and deviator operators. Actually, the total stress  $\boldsymbol{\sigma}$  and the effective stress  $\bar{\boldsymbol{\sigma}}$ ,

$$\bar{\boldsymbol{\sigma}} = \boldsymbol{\sigma} + \xi_f p_f \mathbf{I}, \tag{8.52}$$

have identical deviatoric parts. Here  $p_f$  is the fluid pressure, and  $\xi_f = 1 - c_s/c$  is Biot's coefficient expressed in terms of the compressibilities [1/Pa] of the solid skeleton  $c$  and of the solid constituent  $c_s$ . The compressibility  $c$  and the Lamé's constants [Pa] of the drained solid  $\lambda^{DS}$  and  $\mu^{DS}$  are associated with the drained Young's modulus  $E$  and the drained Poisson's ratio  $\nu$  through the standard relationships,

$$c = \frac{3(1-2\nu)}{E}, \quad \lambda^{DS} = \frac{E\nu}{(1+\nu)(1-2\nu)}, \quad \mu^{DS} = \frac{E}{2(1+\nu)}. \tag{8.53}$$

The total strain of the solid skeleton derives from the displacement vector  $\mathbf{u} = (u_i)$ , namely componentwise  $\epsilon_{ij} = \frac{1}{2}(\partial u_i/\partial x_j + \partial u_j/\partial x_i)$ . It is contributed additively by the elastic strain and by the thermal strain,

$$\boldsymbol{\epsilon} = \boldsymbol{\epsilon}^{el} + c_T \Delta T_s \mathbf{I}, \quad (8.54)$$

with  $c_T$  [1/K] the volumetric thermal expansion coefficient of the solid skeleton.

Aside the deviatoric components which are governed by (8.51)<sub>2</sub>, the mixed thermo-mechanical constitutive system relates the isotropic part of the total stress  $\text{tr}\boldsymbol{\sigma}/3$ , the volume of the fluid  $v^f = V_f/V^0$ , and the entropy of the solid  $s^s$  to the isotropic part of the total strain  $\text{tr}\boldsymbol{\epsilon}$ , to the fluid pressure  $p_f$  and to the solid temperature  $T_s$  by Loret (2008)

$$\begin{aligned} -\frac{\text{tr}\boldsymbol{\sigma}}{3} &= -\frac{1}{c} \text{tr}\boldsymbol{\epsilon} + \xi_f p_f + \frac{c_T}{c} \Delta T_s, \\ \Delta v^f &= \xi_f \text{tr}\boldsymbol{\epsilon} + (\xi_f - n_f)(c_s p_f - c_T \Delta T_s), \\ \Delta s^s &= \frac{c_T}{c} \text{tr}\boldsymbol{\epsilon} - (\xi_f - n_f) c_T p_f + \frac{\rho^s C_{s,v}}{T^0} \Delta T_s, \end{aligned} \quad (8.55)$$

in which  $C_{s,v}$  [J/kg.K] is the intrinsic specific heat capacity of the solid, i.e. per unit mass of solid, at constant volume and fluid pressure.

The thermodynamic potentials of the fluid are built separately. Assuming that the hydraulic compressibility, the thermal expansion coefficient and the heat capacity are constant, the change of the apparent entropy of the fluid is expressed as,

$$\Delta s^f = -n_f c_{fT} \Delta p_f + \frac{\rho^f C_{f,p}}{T_f} \Delta T_f, \quad (8.56)$$

where  $C_{f,p}$  [J/kg.K] is the intrinsic specific heat capacity of the fluid, i.e. per unit mass of the fluid, at constant pressure. The fluid enthalpy  $H_f$  and the fluid density  $\rho_f$  depend on the pressure and temperature only, so that the enthalpy gradient has the format,

$$\nabla H_f = (1 - T_f c_{fT}) \frac{\nabla p_f}{\rho_f} + C_{f,p} \nabla T_f, \quad (8.57)$$

while the change of the intrinsic mass density,

$$\frac{1}{\rho_f} \frac{d^f \rho_f}{dt} = c_{fH} \frac{d^f p_f}{dt} - c_{fT} \frac{d^f T_f}{dt}, \quad (8.58)$$

expresses in terms of the hydraulic compressibility  $c_{fH}$  [1/Pa] and of the coefficient of thermal expansion  $c_{fT}$  [1/K],

$$c_{fH} = \frac{1}{\rho_f} \left. \frac{d^f \rho_f}{dp_f} \right|_{T_f}, \quad c_{fT} = -\frac{1}{\rho_f} \left. \frac{d^f \rho_f}{dT_f} \right|_{p_f}. \quad (8.59)$$

Fluid flow and heat diffusion are defined by uncoupled Darcy's law and Fourier's law respectively. Darcy's law of seepage through the solid skeleton,

$$\mathbf{J}_f = -\frac{k_f}{\mu_f} (\nabla p_f - \rho_f \mathbf{g}), \quad (8.60)$$

expresses in terms of the macroscopic permeability of the fracture network  $k_f$  [m<sup>2</sup>] and of the dynamic viscosity  $\mu_f$  [Pa.s], while Fourier's law of heat transfer through phase  $k$ ,

$$\mathbf{q}_k = -n_k \Lambda_k \nabla T_k, \quad k = s, f. \quad (8.61)$$

requires the intrinsic thermal conductivity  $\Lambda_k$  [W/m.K].

Finally, the rate of energy transfer from the solid to the fluid,

$$\hat{e}_{sf} = \kappa_{sf} (T_s - T_f), \quad (8.62)$$

is simply proportional to the temperature differential. It agrees with 'Newton's law of cooling' which states that the rate of temperature decrease of a body immersed in a fluid is at all times proportional to the body-fluid temperature difference. Satisfaction of the thermodynamics of irreversible processes requires the specific inter-phase heat transfer coefficient between the solid phase and the fluid  $\kappa_{sf} \geq 0$  [W/m<sup>3</sup>.K] to be positive.

### 8.3.3 Finite element discretization

The finite element formulation considers the displacement vector  $\mathbf{u}$ , fluid pressure  $p_f$ , temperature of the solid skeleton  $T_s$  and temperature of the fluid  $T_f$  as primary unknowns. The finite element code written in FORTRAN has been developed as part of this work.

#### 8.3.3.1 The semi-discrete equations

Within the generic element  $e$ , the primary unknowns,

$$\mathbf{u} = \mathbf{N}_u \mathbf{u}^e, \quad p_f = \mathbf{N}_p p_f^e, \quad T_k = \mathbf{N}_T T_k^e, \quad k = s, f, \quad (8.63)$$

are interpolated in terms of nodal values through the respective interpolation functions  $\mathbf{N}_u$ ,  $\mathbf{N}_p$ ,  $\mathbf{N}_T$ . Multiplying the field equations (8.50) by the virtual fields  $\delta \mathbf{u}$ ,  $\delta p$ ,  $\delta T_s$  and  $\delta T_f$ , and integrating by parts over the body  $V$ , provides the weak form of the problem,

$$\begin{aligned} \int_V \nabla(\delta \mathbf{u}) : \boldsymbol{\sigma} - \delta \mathbf{u} \cdot \rho \mathbf{g} \, dV &= \int_{\partial V} \delta \mathbf{u} \cdot \boldsymbol{\sigma} \cdot \hat{\mathbf{n}} \, dS, \\ \int_V \nabla(\delta p) \cdot \mathbf{J}_f - \delta p \mathcal{J}_f \, dV &= \int_{\partial V} \delta p \mathbf{J}_f \cdot \hat{\mathbf{n}} \, dS, \\ \int_V \nabla(\delta T_s) \cdot \mathbf{q}_s - \delta T_s \mathcal{Q}_s \, dV &= \int_{\partial V} \delta T_s \mathbf{q}_s \cdot \hat{\mathbf{n}} \, dS, \\ \int_V \nabla(\delta T_f) \cdot \mathbf{q}_f - \delta T_f \mathcal{Q}_f \, dV &= \int_{\partial V} \delta T_f \mathbf{q}_f \cdot \hat{\mathbf{n}} \, dS, \end{aligned} \quad (8.64)$$

where  $\hat{\mathbf{n}}$  is the unit outward normal to the boundary  $\partial V$ . A standard Galerkin procedure is adopted for the balances of momentum (8.64)<sub>1</sub>, the balance of mass of the fluid (8.64)<sub>2</sub> and the balance of energy of the solid (8.64)<sub>3</sub>. On the other hand, the streamline-upwind/Petrov-Galerkin procedure (SUPG) devised by Brooks and Hughes (1982) is adopted for the treatment of the convective term  $\rho^f \mathbf{v}_{\text{conv}} \cdot \nabla H_f$  in the balance of energy of the fluid phase (8.64)<sub>4</sub>. The convective velocity  $\mathbf{v}_{\text{conv}}$  is identified as the diffusion velocity  $\mathbf{v}_f - \mathbf{v}_s$ . The virtual field  $\delta T_f$  is interpolated via the function  $\mathbf{W}_T$ ,

$$\mathbf{W}_T = \mathbf{N}_T + \tau_{\text{SUPG}} \mathbf{v}_{\text{conv}} \cdot \nabla \mathbf{N}_T, \quad (8.65)$$

in which the perturbation is weighted by the time-like parameter  $\tau_{\text{SUPG}}$ . The modified interpolation function  $\mathbf{W}_T$  applies to the whole differential equation. This procedure ensures that consistency is enforced from the beginning which distinguishes the SUPG method from the artificial diffusion method (Brooks and Hughes, 1982; Fries and Matthies, 2004). By summing the elementary contributions over the total number of elements  $n_{\text{el}}$ , the semi-discretized form of eqn (8.64)<sub>4</sub> may be transformed to,

$$\begin{aligned} \sum_{e=1}^{n_{\text{el}}} \int_{V^e} (\delta \mathbf{T}_f^e)^T ((\nabla \mathbf{N}_T)^T \mathbf{q}_f - (\mathbf{W}_T)^T \mathcal{Q}_f) dV^e = \\ \sum_{e=1}^{n_{\text{el}}} \int_{\partial V^e} (\delta \mathbf{T}_f^e)^T (\mathbf{N}_T)^T \mathbf{q}_f \cdot \hat{\mathbf{n}} dS^e. \end{aligned} \quad (8.66)$$

The stabilization contribution is restricted to the element interiors, since the conductivity  $\Lambda_f$  is isotropic and bi-linear elements are used (Brooks and Hughes, 1982). The stabilization parameter  $\tau_{\text{SUPG}}$  devised by Tezduyar and Osawa (2000),

$$\tau_{\text{SUPG}} = \left( \frac{1}{\tau_{S1}^2} + \frac{1}{\tau_{S2}^2} + \frac{1}{\tau_{S3}^2} \right)^{-\frac{1}{2}}, \quad (8.67)$$

is built from the three times  $\tau_{S1}$ ,  $\tau_{S2}$ ,  $\tau_{S3}$  associated respectively with convection-dominated, transient-dominated and diffusion-dominated flows,

$$\tau_{S1} = \frac{h}{2|\mathbf{v}_{\text{conv}}|}, \quad \tau_{S2} = \frac{\Delta t}{2}, \quad \tau_{S3} = \frac{h^2}{4\alpha_{T,f}}. \quad (8.68)$$

Here  $\alpha_{T,f}$  is the thermal diffusivity of the fluid and  $h$  is the ‘element length’ in the direction of the flow defined as (Tezduyar and Osawa, 2000)

$$h = 2|\mathbf{v}_{\text{conv}}| \left( \sum_{a=1}^{n_{\text{ne}}} |\mathbf{v}_{\text{conv}} \cdot \nabla \mathbf{N}_T^a| \right)^{-1}, \quad (8.69)$$

and  $n_{\text{ne}}$  is the number of element nodes. Note that the definition of  $\tau_{\text{SUPG}}$  in eqn (8.67) does not depend of the solution  $T_f$  but is dependent on the velocity  $\mathbf{v}_{\text{conv}}$  and on the time step  $\Delta t$ . The stabilization parameter (8.67) reduces to the exact form for 1-dimensional



and steady state problems  $\tau_{S1} = h/2|v_{\text{conv}}|$  if the grid Péclet number  $\text{Pe}_g = h|v_{\text{conv}}|/2\alpha_{T,f}$  is high, that is for a convection-dominated flow (Brooks and Hughes, 1982). The term  $\tau_{S2}$  smooths the response at early times. The diffusion-dominated limit  $\tau_{S3}$  is three times the value of the latter reference.

The resulting non-linear first-order semi-discrete equations for the unknown vector  $\mathbb{X}$ ,

$$\mathbb{X} = [\mathbf{u} \quad \mathbf{p}_f \quad \mathbf{T}_s \quad \mathbf{T}_f]^T, \quad (8.70)$$

with maximum nodal length = dimension of space + 3, imply the residual  $\mathbb{R}$ ,

$$\mathbb{R} = \mathbb{F}^{\text{grav}} + \mathbb{F}^{\text{surf}}(\mathbb{S}, \mathbb{X}) - \mathbb{F}^{\text{int+conv}}\left(\mathbb{X}, \frac{d\mathbb{X}}{dt}\right) = \mathbb{O}, \quad (8.71)$$

to vanish. Here  $\mathbb{F}^{\text{int+conv}}$  is the vector that contains the internal forces together with the convective contributions including the SUPG stabilization, appearing on the left-hand-side of eqns (8.64),  $\mathbb{F}^{\text{surf}}$  is the vector of surface loadings denoted collectively  $\mathbb{S}$  and  $\mathbb{F}^{\text{grav}}$  is the vector contributed by gravity (Appendix G.1). The residual vector includes terms associated with the four physical phenomena of interest,

$$\mathbb{R} = [\mathbf{R}_u \quad \mathbf{R}_{p_f} \quad \mathbf{R}_{T_s} \quad \mathbf{R}_{T_f}]^T. \quad (8.72)$$

### 8.3.3.2 Time integration

The semi-discrete equations are integrated through a generalized trapezoidal rule defined by a scalar  $\alpha \in ]0, 1]$ . At step  $n + 1$ , the equations are enforced at time  $t_{n+\alpha} = t_n + \alpha \Delta t$ , with  $\Delta t = t_{n+1} - t_n$ , namely,

$$\mathbb{R}_{n+\alpha} = \mathbb{F}^{\text{grav}} + \mathbb{F}^{\text{surf}}(\mathbb{S}_{n+\alpha}, \mathbb{X}_{n+\alpha}) - \mathbb{F}^{\text{int+conv}}(\mathbb{X}_{n+\alpha}, \mathbb{V}_{n+\alpha}) = \mathbb{O}. \quad (8.73)$$

In the above relation,  $\mathbb{Z} = \mathbb{S}, \mathbb{X}, \mathbb{V}$  is defined as  $\mathbb{Z}_{n+\alpha} = (1 - \alpha)\mathbb{Z}_n + \alpha\mathbb{Z}_{n+1}$ , and  $\mathbb{X}_{n+1}$  and  $\mathbb{V}_{n+1}$  are approximations of  $\mathbb{X}(t_{n+1})$  and  $(d\mathbb{X}/dt)(t_{n+1})$ , respectively.

The system (8.73) is solved iteratively by an explicit-implicit operator split, namely at iteration  $i + 1$ ,

$$\mathbb{R}_{n+\alpha}^{i+1} = \mathbb{F}_E^{\text{grav}} + \mathbb{F}_E^{\text{surf}}(\mathbb{S}_{n+\alpha}, \mathbb{X}_{n+\alpha}^i) - \mathbb{F}_I^{\text{int+conv}}(\mathbb{X}_{n+\alpha}^{i+1}, \mathbb{V}_{n+\alpha}^{i+1}) = \mathbb{O}. \quad (8.74)$$

The global iteration process uses a full Newton-Raphson procedure. The Newton direction  $\Delta\mathbb{V}$  is sought by setting eqn (8.74) to zero,

$$\mathbb{C}(\alpha \Delta\mathbb{V}) = \mathbb{R}_{n+\alpha}^i, \quad (8.75)$$

in which the *effective diffusion matrix*  $\mathbb{C}$  can be expressed in terms of the global diffusion matrix  $\mathbb{D} = \mathbb{D}(\mathbb{X}, \mathbb{V})$  and of the global stiffness-convection matrix  $\mathbb{K} = \mathbb{K}(\mathbb{X}, \mathbb{V})$ ,

$$\mathbb{C} = \mathbb{D} + \mathbb{K} \alpha \Delta t. \quad (8.76)$$

The global diffusion and stiffness-convection matrices are obtained by assembling the element contributions which have the following block structure,

$$\mathbb{D}^e = \begin{bmatrix} 0 & 0 & 0 & 0 \\ \mathbf{D}_{p_f \mathbf{u}}^e & \mathbf{D}_{p_f p_f}^e & \mathbf{D}_{p_f T_s}^e & \mathbf{D}_{p_f T_f}^e \\ \mathbf{D}_{T_s \mathbf{u}}^e & \mathbf{D}_{T_s p_f}^e & \mathbf{D}_{T_s T_s}^e & 0 \\ 0 & * \mathbf{D}_{T_f p_f}^e & 0 & * \mathbf{D}_{T_f T_f}^e \end{bmatrix}; \quad (8.77)$$

$$\mathbb{K}^e = \begin{bmatrix} \mathbf{K}_{\mathbf{u}\mathbf{u}}^e & \mathbf{K}_{\mathbf{u}p_f}^e & \mathbf{K}_{\mathbf{u}T_s}^e & 0 \\ 0 & \mathbf{K}_{p_f p_f}^e & 0 & 0 \\ 0 & 0 & \mathbf{K}_{T_s T_s}^e & \mathbf{K}_{T_s T_f}^e \\ 0 & * \mathbf{K}_{T_f p_f}^e & * \mathbf{K}_{T_f T_s}^e & * \mathbf{K}_{T_f T_f}^e \end{bmatrix}. \quad (8.78)$$

The detailed expressions of these matrices are given in Appendix G.2. Convection terms that require a special treatment are highlighted with the superscript \*.

The four-node element (Q4) is used to interpolate all unknowns. For all simulations, element sizes of  $10 \times 10 \text{ m}^2$  are used. The number of integration points is equal to two (for each space dimension), for all matrices and all residuals including the convective contributions.

Each component of the residual vector  $\mathbb{R}$  is scaled by a reference value:  $\mathbf{R}_{\mathbf{u},\text{ref}} = 75.0 \cdot 10^6 \text{ N}$  for the balance of momentum contributions,  $\mathbf{R}_{p_f,\text{ref}} = 1.0 \cdot 10^{-6} \text{ m}^3/\text{s}$  for the balance of mass contribution and  $\mathbf{R}_{T_s,\text{ref}} = \mathbf{R}_{T_f,\text{ref}} = 1.26 \text{ W}$  for the balance of energy contributions.  $\mathbf{R}_{\mathbf{u},\text{ref}}$  represents the overburden stress,  $\mathbf{R}_{p_f,\text{ref}}$  the maximum fluid flow and  $\mathbf{R}_{T_s,\text{ref}} = \mathbf{R}_{T_f,\text{ref}}$  the maximum heat flow; all four quantities referring to a unit area of one square meter. The norm of the residual at each iteration  $i$  is then calculated by summing the neq contributions (neq = number of equations),

$$|\mathbb{R}^i| = \sum_{a=1}^{\text{neq}} \left| \frac{\mathbf{R}_a}{\mathbf{R}_{a,\text{ref}}} \right|. \quad (8.79)$$

Iterations are stopped when the tolerances below involving both the *overall scaled* residual and unknowns are satisfied:

- $|\mathbb{R}^i| / |\mathbb{R}^1| < 0.001$
- $|x^i - x^{i-1}| / |x^i| < 0.001$ , for  $x = u_j, p_f, T_s, T_f$ .

The average number of Newton-Raphson iterations per time step has been observed to remain around 3.

### 8.3.3.3 Characteristic times

The time integration parameter  $\alpha$  is taken equal to  $2/3$ . Conditional stability characterizes non-linear transient convective-diffusive problems discretized with a full Newton-Raphson

scheme (Belytschko and Hughes, 1983). The time step  $\Delta t$  is increased by fits and starts in the range  $[\Delta t_{\min}, \Delta t_{\max}]$  in order to keep the computation time within acceptable limits. The lower bound  $\Delta t_{\min}$  is associated with the fastest diffusion time, that is the hydraulic diffusion of the fluid and is maintained constant until hydraulic steady state is reached.  $\Delta t_{\max}$  is obtained with respect to the slowest remaining diffusion, that is the thermal diffusion of the solid. The hydraulic diffusivity  $\alpha_H$  depends on the seepage and mechanical properties,

$$\alpha_H = \frac{k_f}{\mu_f} \frac{2\mu^{DS}(1-\nu)}{1-2\nu} \left[ \frac{A^2(1+\nu_u)^2(1-2\nu)}{9(1-\nu_u)(\nu_u-\nu)} \right], \quad (8.80)$$

in which  $A$  is the Skempton coefficient,

$$\frac{1}{A} = 1 + n_f \frac{c_{fH} - c_s}{c - c_s}, \quad (8.81)$$

and  $\nu_u$  is the undrained Poisson's ratio,

$$\nu_u = \frac{3\nu + A(1-2\nu)(1-c_s/c)}{3 - A(1-2\nu)(1-c_s/c)}. \quad (8.82)$$

The thermal diffusivities  $\alpha_{T,s}$ ,  $\alpha_{T,f}$  through the solid and the fluid, respectively, involve only thermal properties,

$$\alpha_{T,s} = \frac{n_s \Lambda_s}{\rho^s C_{s,v}}, \quad \alpha_{T,f} = \frac{n_f \Lambda_f}{\rho^f C_{f,p}}. \quad (8.83)$$

Heat transport in the fluid phase is dominated by convection due to the high permeability of the fracture network; whereas heat transport in the solid phase is controlled by diffusion. The characteristic time associated with convection at speed of  $v_{f,z}$  is proportional to the distance traveled  $L$ ,

$$t_{\text{conv}} = \frac{L}{v_{f,z}}. \quad (8.84)$$

On the other hand, the characteristic times associated with seepage and with thermal diffusion in phase  $k$  depend on the square of the distance traveled  $L$ ,

$$t_{\text{Hdiff}} = \frac{L^2}{\alpha_H}, \quad t_{\text{Tdiff},k} = \frac{L^2}{\alpha_{T,k}}. \quad (8.85)$$

In the tests reported in Sections 8.3.5 and 8.3.6, and in geothermal tests in general, the fluid velocity  $v_{f,z}$  ranges from  $O(10^{-6})$  m/s to  $O(10^{-3})$  m/s, the hydraulic diffusivity of water typically of the order  $O(10^1)$  m<sup>2</sup>/s is much larger than the thermal diffusivity of the solid about  $O(10^{-6})$  m<sup>2</sup>/s which is itself an order of magnitude larger than the thermal diffusivity of water  $O(10^{-7})$  m<sup>2</sup>/s. Consequently, over a diffusion length of  $L =$

230m separating the injection and production wells (see Sections 8.3.5 and 8.3.6), the characteristic times associated with convection and diffusion, through the solid phase and the fluid phase, range as follows,

$$\begin{aligned}
 t_{\text{Hdiff}} &\approx 1 \text{ hour}, \\
 t_{\text{conv}} &\in [2.66 \text{ days}, 7.31 \text{ years}], \\
 t_{\text{Tdiff},s} &\approx 1,500 \text{ years}, \\
 t_{\text{Tdiff},f} &\approx 10,000 \text{ years}.
 \end{aligned}
 \tag{8.86}$$

Hence, in absence of heat transfer across the solid-fluid interface, the rate of the temperature propagation, and its impacts on pressure and displacement fields, can be up to  $10^5$  times faster in the convection-dominated fracture network than in the diffusion-dominated solid skeleton. Therefore local thermal equilibrium is unlikely to be established before the late period of the circulation test, and the overall thermo-hydro-mechanical behavior of the mixture can only be accurately modeled if local thermal non-equilibrium between the solid phase and the fluid phase is accounted for.

**Remark 8.2.** *According to (8.84), the stabilization parameter for convection-dominated flows  $\tau_{S1}$ , eqn (8.68), can be interpreted as the time required for a particle to be convected over half the length of the element.*

### 8.3.4 HDR reservoir analysis

The fully coupled thermo-hydro-mechanical model is used in the subsequent sections to investigate the thermal drawdown of a generic hot dry rock reservoir in local thermal non-equilibrium. Information on the geometry, initial and boundary conditions considered are provided first.

#### 8.3.4.1 Geometry of the HDR reservoir

An artificially fractured reservoir with horizontal injection and production wells is considered (Fig. 8.15). The simulations assume a plane strain analysis. The finite element mesh includes half of the reservoir and a portion of the surrounding low permeability rock formation. The HDR fractured reservoir is idealized by a single porosity saturated medium. The material properties and constitutive equations characterizing the processes involved are described in Sect. 8.3.2.2.

Adding the surrounding low permeability formation in the analysis allows to assess the influence of the external heat supply which is presented in Sect. 8.3.5.5. The width of this surrounding domain  $X_F - X_R$  is chosen so that the characteristic time of heat diffusion, eqn (8.85), is greater than the life-time of the reservoir ( $\approx 20$  years). The formation is endowed with the same material properties as the reservoir except for the permeability.

The injection and the production wells are located at the bottom and at the top of the reservoir, respectively. The length of the wells is a key parameter that governs the flow path and the heat transfer between the rock and the fluid. Two setups are considered:

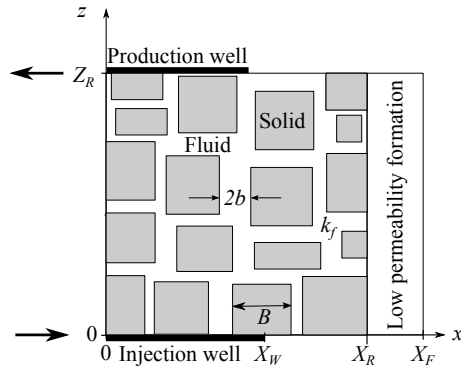


Figure 8.15: Representation of a generic HDR reservoir (not at scale). The permeability  $k_f$  of the reservoir depends on the average fracture spacing  $B$  and on the average fracture aperture  $2b$ . The simulations assume a plane strain analysis, in the  $x - z$  plane, and symmetry with respect to  $z$ -axis.

1. in one case, the wells penetrate horizontally into the entire reservoir, that is  $X_W = X_R$ . Consequently, the velocity of the fluid  $\mathbf{v}_f$  is vertical and uniform between the two wells, Fig. 8.20, left;
2. in the second case, the wells penetrate into one third of the reservoir, leading to non-uniform velocity field, Fig. 8.20, right.

#### 8.3.4.2 The specific inter-phase heat transfer coefficient $\kappa_{sf}$

The coefficient of *specific* inter-phase heat transfer  $\kappa_{sf}$  [W/m<sup>3</sup>.K] controls the rate at which the two phase system (solid-fluid) reaches thermal equilibrium. The higher this coefficient, the faster thermal equilibrium is reached. The coefficient of specific inter-phase heat transfer is defined by the product of the solid-fluid specific surface  $S_{sf}^s$  [m<sup>2</sup>/m<sup>3</sup>] with the coefficient of solid-fluid heat transfer  $h_{sf}$  [W/m<sup>2</sup>.K],

$$\kappa_{sf} = S_{sf}^s \times h_{sf}. \quad (8.87)$$

For a square block of size  $B$  bordered by a fracture fluid of width  $b$ , the volume fractions of the solid and fluid are equal to

$$n_s = \frac{B^2}{(B + 2b)^2}, \quad n_f = \frac{4b(B + b)}{(B + 2b)^2}. \quad (8.88)$$

The specific surface  $S_{sf}^s$  is the total surface area of the interstitial voids divided by the total volume of the medium,

$$S_{sf}^s = \frac{4B}{(B + 2b)^2}. \quad (8.89)$$

For  $2b \ll B$ , the specific surface area simplifies to

$$S_{sf}^s = \frac{2n_f}{2b} = \frac{4}{B}. \quad (8.90)$$

$S_{sf}^s$  vanishes if the fracture porosity tends to zero  $n_f \rightarrow 0$ , for a constant aperture  $2b$ , or if the fissure spacing tends towards infinity  $B \rightarrow \infty$ . A discussion on the theoretical formulation of the specific surface area (8.90) is provided in Appendix G.3.

The coefficient of solid-fluid heat transfer  $h_{sf}$  (also known as the particle-to-fluid heat transfer coefficient) depends of the nature of the solid, the nature of the fluid and the dominant regime of heat transport. By assuming that the effect of convection in the fracture fluid phase (perpendicular to the solid-fracture interface) is negligible, the coefficient of solid-fluid heat transfer may be quantitatively characterized by the sum of the thermal resistances of the two phases in series (Bejan, 1993),

$$\frac{1}{h_{sf}} = \frac{2b}{2n_f\Lambda_f} + \frac{B}{2n_s\Lambda_s}. \quad (8.91)$$

The general form of the *specific* coefficient of heat transfer between the solid and the fluid phase  $\kappa_{sf}$  is non-linearly related to  $B$  and  $b$  through eqs (8.87), (8.89), (8.91). This general form should be used when the ratio between the fracture aperture and the fracture spacing is in constant evolution, for example during comminution. On the other hand, in geothermal applications, the fracture width is much smaller than the fracture spacing, namely  $2b \ll B$ . Then the specific coefficient of heat transfer between the solid and the fluid phase is linearly related to  $B^{-2}$ ,

$$\kappa_{sf} = \frac{8}{B^2} \frac{2n_s\Lambda_s\Lambda_f}{n_s\Lambda_s + 2\Lambda_f}. \quad (8.92)$$

The thermal conductivities of the two phases are involved. Alternatively, assuming  $n_s\Lambda_s \ll 2\Lambda_f$ , the above relation would reduce to,

$$\kappa_{sf} = 8 \frac{n_s\Lambda_s}{B^2}, \quad (8.93)$$

where the two phases are not treated symmetrically, *à la* Warren and Root (1963), with emphasis on the most insulating material. For a geothermal reservoir, typical values entail  $n_s \approx 1$ ,  $\Lambda_s = 2.71$  W/m.K and  $\Lambda_f = 0.6$  W/m.K, and the two phases are seen to contribute to the overall conductivity.

Correlations of the solid-fluid heat transfer coefficient  $h_{sf}$  have been proposed in the literature with the Nusselt number (Wakao and Kaguei, 1982) and with a capillary tube model (Zanotti and Carbonell, 1984). Few experimental works have investigated the magnitude of the solid-fluid heat transfer coefficient  $h_{sf}$  (Pecker and Deresiewicz, 1973; Jiang et al., 2006). Instead, here, a sensitivity analysis is performed to determine the threshold value that separates local thermal equilibrium from the local thermal non-equilibrium (Minkowycz et al., 1999; Nield et al., 2002). A calibration of the model, and hence of the specific inter-phase heat transfer coefficient, with help of data provided from the Fenton Hill HDR reservoir is proposed in Sect. 8.3.6.

### 8.3.4.3 Initial conditions

Prior to the circulation test, the reservoir is assumed to be in local thermal equilibrium, and the solid and fluid have identical temperatures  $T_s^0 = T_f^0 = T^0$ . The geothermal gradient is neglected since the height of the reservoir is small with respect to its average depth  $H$ . The initial pressure of the fluid  $p_f^0 = \rho_f g H$  is assumed proportional to the depth of the point of interest  $H$ , the fluid density  $\rho_f$  and the gravity  $g$ , i.e. the hydrostatic gradient is also neglected. The initial stress state is due to the overburden stress and to the lateral earth stress.

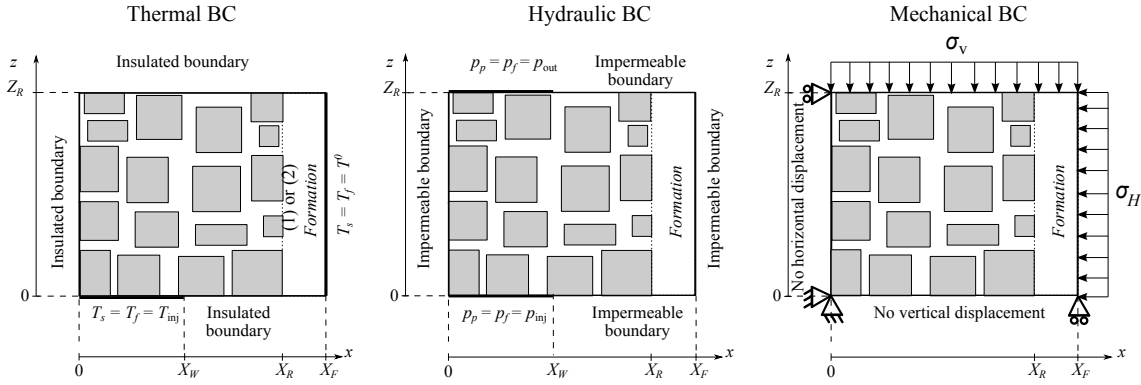


Figure 8.16: Thermal, hydraulic and mechanical boundary conditions.

### 8.3.4.4 Boundary conditions

A sketch of the thermal, hydraulic and mechanical boundary conditions is shown in Fig. 8.16.

The injection temperature  $T_{inj}$  is applied to all the phases along the injection well. The outlet temperature  $T_{f,out}$  along the producing well is an output of the simulations. The remaining horizontal and vertical boundaries are thermally insulated from the surroundings, that is  $\mathbf{q}_s \cdot \hat{\mathbf{n}} = \mathbf{q}_f \cdot \hat{\mathbf{n}} = 0$ .

The injection and production pressures,  $p_{f,inj}$  and  $p_{f,out}$  respectively, are both specified along the injection and production wells. The remaining boundaries are hydraulically impermeable, i.e.  $\mathbf{J}_f \cdot \hat{\mathbf{n}} = 0$ .

The vertical stress  $\sigma_z = \sigma_z^0$  remains constant along the top boundary  $z = Z_R$ , and so does the horizontal stress  $\sigma_x = \sigma_x^0$  along the lateral boundary  $x = X_F$ . The displacements on the other boundaries are specified,  $u_x(x = 0, z) = 0$  and  $u_z(x, z = 0) = 0$ .

At the contact between the reservoir and the surrounding rock  $x = X_R$ , two types of interactions are considered: (1) the reservoir is thermally insulated from the rock formation; (2) the reservoir exchanges heat with the formation which remains at the initial temperature  $T^0$ , namely  $T_s = T_f = T^0$  along  $x = X_F$ .

### 8.3.5 The double-step pattern of thermal depletion in LTNE

This section focuses on the influence of the LTNE assumption on the time profiles of the fluid temperature (at the producing well). The reservoir response in terms of fluid pressure, displacement and effective stress will be presented in Sect. 8.3.6.

In the context of a fluid saturated fractured medium, reservoir performances can be expressed in a general form in terms of the fracture porosity  $n_f$  and two dimensionless parameters (Gringarten et al., 1975). These parameters reflect the overwhelming importance of the characteristic lengths of the fracture network, namely the average aperture  $2b$  and the average spacing  $B$ .

(1) The dimensionless temperature  $T_D$  built from the outlet fluid temperature  $T_{f,\text{out}}$ , the initial temperature  $T^0$  and the injection temperature  $T_{\text{inj}}$ ,

$$T_D = \frac{T^0 - T_{f,\text{out}}}{T^0 - T_{\text{inj}}}, \quad (8.94)$$

ranges between 0 ( $T_{f,\text{out}} = T^0$ ) at early time and 1 ( $T_{f,\text{out}} = T_{\text{inj}}$ ) ultimately.

(2) Adapted from the work of Minkowycz et al. (1999) and Nield et al. (2002), the dimensionless parameter  $\eta_D$  that serves to delineate LTE and LTNE,

$$\eta_D = \frac{1}{n_f} \frac{\text{Sp}}{\text{Pe}}, \quad (8.95)$$

is defined in terms of the fracture porosity  $n_f$ , of a modified Sparrow number  $\text{Sp}$  which measures the relative weights of heat transfer across the system and heat conduction through the porous medium, and of the Péclet number  $\text{Pe}$ , which measures the relative weights of convection and thermal conduction,

$$\text{Sp} = \frac{\kappa_{sf} Z_R^2}{n_s \Lambda_s + n_f \Lambda_f}, \quad \text{Pe} = \frac{Z_R v^\infty}{\alpha_{T,f}}. \quad (8.96)$$

The general form of the dimensionless LTNE parameter  $\eta_D$  expresses in terms of the thermal properties of the porous medium,  $\Lambda_s$ ,  $\Lambda_f$  and  $\alpha_{T,f}$ , the fluid porosity  $n_f$ , the diffusion-convection length  $Z_R$ , the aperture of the fracture network  $2b$  and the steady state velocity  $v^\infty$  through eqns (8.90) and (8.92). For  $n_s \Lambda_s \gg n_f \Lambda_f$  and for  $n_s \approx 1$ , the above dimensionless LTNE parameter simplifies to

$$\eta_D = \frac{1}{n_f} \frac{16 \Lambda_f}{\Lambda_s + 2 \Lambda_f} \frac{Z_R \alpha_{T,f}}{v^\infty B^2}. \quad (8.97)$$

Of prime interest for the economical success of a HDR reservoir is the knowledge of the time profile of the temperature drawdown  $T_{f,\text{out}}$  for representative pumping/production rates  $\mathbf{J}_f$ . The fracture porosity  $n_f$  for igneous and metamorphic rocks ranges from 0.0005 to 0.01 (Evans et al., 2009; Elsworth, 1989; Bataillé et al., 2006).



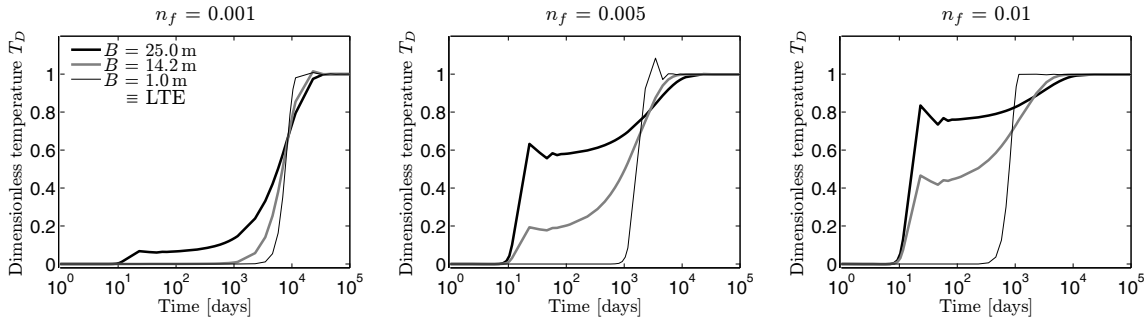


Figure 8.17: Dimensionless temperature outlet  $T_D$  as a function of time for three porosities  $n_f$  and three fracture spacings  $B$ . All results are for  $Z_R = 230$  m,  $v^\infty = 2 \cdot 10^{-4}$  m/s and thermal properties from Table 8.4. In LTNE, time profiles display a double-step pattern, whereas in LTE, time profiles display a continuous pattern. The thresholds between LTE and LTNE are associated with the fracture spacings  $B_T = 6$  m (left),  $B_T = 2.5$  m (middle) and  $B_T = 2$  m (right). The corresponding dimensionless values of  $\eta_D$  are equal respectively to 11, 13 and 10. Therefore, LTE is associated with  $\eta_D$  larger than, say 13, while values of  $\eta_D$  smaller than 13 requires a LTNE analysis. The late overshooting oscillations are numerical artifacts due to an imperfect damping of the convective contribution, see Remark 8.3.

First, thermal drawdown curves are observed to show a single-step pattern for small fracture spacings  $B$  and double-step patterns for large fracture spacings (Sect. 8.3.5.1). The threshold values between LTNE and LTE are sought in terms of the fracture spacing  $B_T$  for an average steady state velocity and several fluid porosities in Sect. 8.3.5.2. These thresholds define the onset of LTNE in which thermal drawdown curves change from a single-step pattern to a double-step pattern. A hyperbolic dependency between  $(B_T)^2$  and  $n_f$  is observed which matches with eqn (8.97) for  $n_f$  over the range of interest. Sect. 8.3.5.3 addresses the influence of the pumping rate on the fracture spacing thresholds  $B_T$ . The hyperbolic relation between  $(B_T)^2$  and  $v^\infty$  suggested by eqn (8.97) is well recovered by the finite element simulations.

Attention is restricted to a uniform and vertical flow, while the reservoir is insulated from the rock formation. Departures from this setting are considered in Sects. 8.3.5.4 and 8.3.5.5. The issue of fluid loss is ignored throughout and will be addressed in a subsequent Section 8.4.

### 8.3.5.1 Single- versus double-step patterns

A change of time profile is observed as the fracture spacing  $B$  increases. Time profiles for small  $B$  are clearly dominated by convection and display a characteristic single-step pattern. Conversely, the time profiles for large  $B$  display three stages and typical double-step patterns.

(1) In the first stage, the strong increase of the dimensionless temperature corresponds to the abrupt propagation of the injection temperature dominated by convection. This effect is mostly attributed to the difference in characteristic times between forced convection in the fracture network and diffusion of heat in the solid matrix. Accordingly for each fracture porosity  $n_f$ , the magnitude of the dimensionless temperature  $T_D$  at the end of this first

stage is increasing as a function of  $B$ . Thus, the smaller  $B$  (the larger the specific solid-fluid heat transfer  $\kappa_{sf}$ ), the higher the ‘instantaneous damping’ of the cooled fluid front by the solid phase. On the other hand, the duration of the first stage is independent of  $B$ , and it is about equal to the characteristic time for a particle of fluid to flow the length  $Z_R$  at the steady velocity  $v^\infty$ ,

$$t_c^{\text{stage 1}} = \frac{Z_R}{v^\infty} \approx 2 \times \tau_{S1} = 13 \text{ days}. \quad (8.98)$$

(2) During the second stage, the dimensionless temperature remains constant and displays a plateau. Heat transfer between the solid and the fluid phases takes place partly at constant fluid temperature.

(3) The third stage is characterized by a second strong increase of the temperature. The time required for the outlet temperature  $T_{f,\text{out}}$  to reach 95% of the injection temperature  $T_{\text{inj}}$  is higher for a model in LTNE than in LTE. In other words, the response of the mixture is delayed by the transfer of heat from the solid phase to the fluid phase. This type of behavior is characteristic of the response of reactive flows and of phases in non-equilibrium: as an example, the consolidation time of a dual porosity medium is delayed compared with a single porosity medium (Khalili et al., 1999).

### 8.3.5.2 Influence of the fracture porosity $n_f$

The influence of the fracture porosity, in the range of  $0.001 < n_f < 0.01$ , is mainly visible during the first and the second stage of the double-step pattern (Fig. 8.17).

(1) For each fracture spacing  $B$ , the magnitude of  $T_D$  at the end of this first stage is increasing as a function of the fluid volume ratio  $n_f$ , i.e. the larger the volume of cooled fluid, the smaller the temperature outlet. Since  $n_s \approx 1$ , the rate of heat transfer can be considered as constant, eqn (8.92), as opposed to the overall amount of heat supply in the system. In addition, the duration of the first stage is independent of  $n_f$  in agreement with eqn (8.98).

(2) Time profiles in Fig. 8.17 indicate that increasing the porosity of the fracture network  $n_f$  reduces the time length of the second stage and, hence, speeds up thermal depletion. An increase of fluid porosity modifies the phase and the heat repartitions in the system and hence reduces the overall amount of heat to be transferred by the solid to the fluid. Since the rate of heat transfer is almost independent of the fluid porosity, see eqn (8.92) in which  $n_s \approx 1$ , the heat transfer period requires less time.

In terms of fracture spacing, the threshold between LTE and LTNE decreases with increasing fluid porosity,  $B_T = 6 \text{ m}$  ( $n_f = 0.001$ ),  $B_T = 2.5 \text{ m}$  ( $n_f = 0.005$ ) and  $B_T = 2 \text{ m}$  ( $n_f = 0.01$ ), due to the increasing amount of cooled fluid. Those values are obtained by trial and error and correspond to  $T_s = T_f$ , at the reservoir outlet, over the entire circulation test. For smaller fracture spacings  $B < B_T$ , the local thermal non-equilibrium responses are indistinguishable from the responses in equilibrium and display overshooting

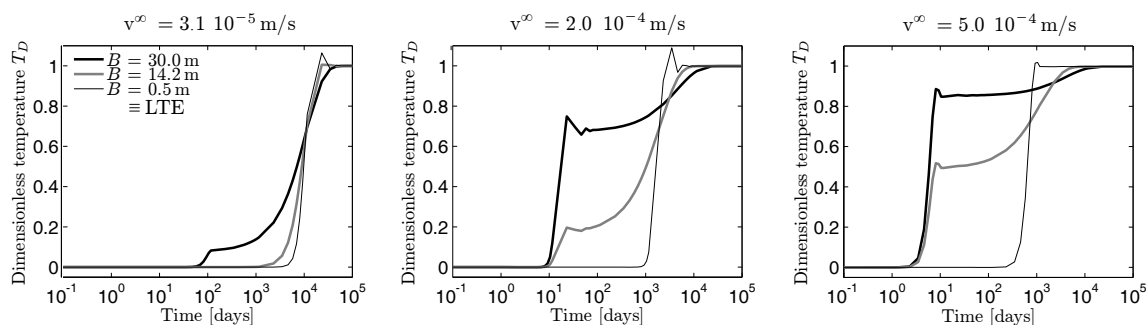


Figure 8.18: Dimensionless temperature outlet  $T_D$  as a function of time, for a porosity  $n_f = 0.005$ , three flow rates  $v^\infty$  and three fracture spacings  $B$ . All results are for  $Z_R = 230$  m and thermal properties from Table 8.4. In LTNE, time profiles display a double-step pattern, whereas, in LTE ( $B = 0.5$  m), time profiles display a continuous pattern. The thresholds between LTE and LTNE express in terms of fracture spacing  $B_T = 7.5$  m (left),  $B_T = 2.5$  m (middle),  $B_T = 1.5$  m (right). The resulting dimensionless threshold  $\eta_D \simeq 13$  applies to all velocities.

oscillations due to an imperfect damping of the convective contribution, see Remark 8.3. The corresponding dimensionless values of  $\eta_D$  are equal respectively to 11 ( $n_f = 0.001$ ), 13 ( $n_f = 0.005$ ) and 10 ( $n_f = 0.01$ ). Within the range of interest  $0.001 \leq n_f \leq 0.01$ , dimensionless values  $\eta_D \geq 13$  are likely to represent LTE and  $\eta_D < 13$  represents LTNE.

The response of a reservoir endowed with a porosity  $n_f = 0.005$  is scrutinized next (Sect. 8.3.5.3) for several pumping rates. To maintain LTNE characterized by  $\eta_D = 13$ , we expect the fracture spacing threshold  $B_T = 2.5$  m to decrease for larger pumping rates, in view of eqn (8.97).

**Remark 8.3.** Results corresponding to  $B = 1$  m in Fig. 8.17 are obtained with a model in LTNE and display high overshootings at large times if a standard Galerkin approach is used. These overshootings are associated with the large specific solid-fluid heat transfer coefficient  $\kappa_{sf}$  which plays the role of a penalty coefficient in eqn (8.62), and induces the development of local sharp temperature gradients. These numerical wiggles are damped by the SUPG and Discontinuity Capturing (DC) methods albeit not perfectly. The simulations have also been performed with a mixture in thermal equilibrium, namely a single temperature. The curves superpose, to within the fact that the single temperature simulations do not show overshootings.

### 8.3.5.3 Influence of the pumping rate

For the forced convection phenomenon to be dominant over conduction and for the economical viability of a given reservoir, the fluid velocity in the fracture network should be in the range of  $1.0 \cdot 10^{-7}$  m/s  $< v^\infty < 1.0 \cdot 10^{-3}$  m/s (Evans et al., 2009; Elsworth, 1989; Cheng et al., 2001). Within this range of fluid velocity and for a fracture spacing from 0.5 to 30 m (so as to capture the LTE threshold for all velocities, see Sect. 8.3.5.2), the relevance of the LTNE hypothesis is scrutinized by using the double-step pattern as an indicator.

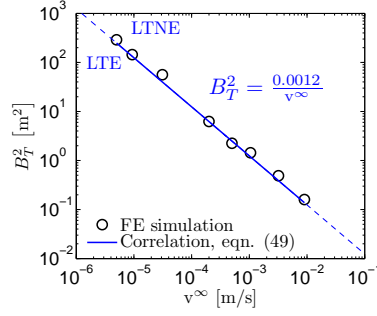


Figure 8.19: Square of the fracture spacing threshold  $B_T^2$  as a function of the average fluid velocity at steady state  $v^\infty$ , for a porosity  $n_f = 0.005$ , a uniform flow path and an insulated reservoir. All results are for  $Z_R = 230$  m and thermal properties from Table 8.4. The hyperbolic relationship defined by eqn (8.99) is represented by a blue line. It is well captured by the finite element (FE) simulation.

Results for time profiles with a constant fracture porosity  $n_f = 0.005$  are reported in Fig. 8.18 for three fluid velocities  $v^\infty$  and three fracture spacings  $B$ .

For an average fluid velocity  $v^\infty = 2.0 \cdot 10^{-4}$  m/s, the fracture spacing thresholds between LTNE and LTE remains  $B_T = 2.5$  m. As expected, this threshold is reduced for larger fluid velocities, for e.g.  $B_T = 1.5$  m for  $v^\infty = 5.0 \cdot 10^{-4}$  m/s and is increased for smaller fluid velocities, for e.g.  $B_T = 7.5$  m for  $v^\infty = 3.1 \cdot 10^{-5}$  m/s. Below the threshold values, the rate of thermal convection-diffusion in the fractures is comparable to the thermal diffusion in the rock matrix and hence a local thermal non-equilibrium analysis is not required. Consistently, the double-step pattern, in which heat transfer between the solid phase and the fluid phase is characterized by a plateau, is observed from approximately twice those values. The double-step pattern does not provide an accurate tool to identify the onset of LTNE and is rather a convenient visual control of established LTNE.

As expected, the above thresholds result from eqn (8.97),

$$(B_T)^2 = \frac{1}{\eta_D} \frac{1}{n_f} \frac{16 \Lambda_f}{\Lambda_s + 2 \Lambda_f} \frac{Z_R \alpha_{T,f}}{v^\infty}, \quad (8.99)$$

in which the dimensionless LTNE parameter  $\eta_D$  takes the value identified in Sect. 8.3.5.2 for  $n_f = 0.005$ , i.e.  $\eta_D = 13$ . A good agreement for the square of the fracture spacing threshold  $(B_T)^2$  as a function of the flow rate  $v^\infty$  is obtained between the numerical response and the above correlation, as illustrated in Fig. 8.19.

#### 8.3.5.4 Influence of the flow path

Results reported so far correspond to a uniform vertical flow (Fig. 8.20, left). The influence of a non-uniform flow path on the fracture spacing threshold  $B_T$  for  $n_f = 0.005$  is addressed for wells shorter than the horizontal extent of the reservoir (Fig. 8.20, center).

The limit between a single-step pattern and a double-step pattern is lowered to  $B_T = 16$  m ( $v^\infty = 2.0 \cdot 10^{-4}$  m/s) when the flow field is non-uniform. The reason is attributed to

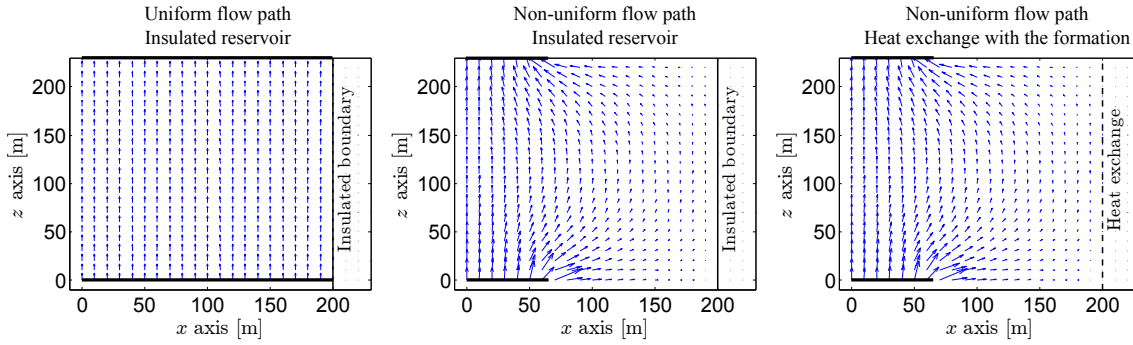


Figure 8.20: Scaled fluid velocity vectors in the reservoir. Wells (thick horizontal lines) penetrate the reservoir either totally (left) or partially (center, right). The reservoir is insulated from the rock formation (left, center) or exchanges heat with the formation (right).

the fluid velocity in the  $x$ -direction. For a non-uniform flow distribution, the fluid velocity in the  $x$ -direction is not negligible and the heat transport is convection-dominated in the  $x$ - and  $y$ -directions. This change in heat transport regime in the  $x$ -direction increases the rate of the thermal depletion of the solid phase and requires a smaller rate of heat transfer to maintain LTNE. The hyperbolic relation eqn (8.99) between the square of the fracture spacing threshold and the flow rate becomes  $(B_T)^2 = 0.051/v^\infty$ , which remains in very good agreement with the numerical data (not shown).

Overall, the comparison between a uniform and a non-uniform flow field yields the conclusion that the flow path (aside from the reservoir volume) has a marked influence on the dimensionless LTNE threshold. For a given reservoir (e.g.  $B_T = 2.5$  m is obtained from microseismic monitoring techniques), the above correlation provides valuable information on the minimum fluid velocity which should be  $v^\infty = 2.0 \cdot 10^{-4}$  m/s for a uniform flow field (the fracture network is fully penetrated by the wells) and  $v^\infty = 8.0 \cdot 10^{-3}$  m/s for a non-uniform flow field (the fracture network is larger than the wells).

### 8.3.5.5 Influence of the external heat supply

Heat recovered from a geothermal reservoir is captured a priori from the reservoir itself. However, the rock formation in contact with the reservoir may also contribute, depending on the thermal boundary condition. Two extreme situations are compared: (1) the reservoir is insulated from the rock formation boundary along the boundary  $x = X_R$  (Fig. 8.20, center); (2) the reservoir is in direct contact with the low permeability rock formation ( $k_f = 10^{-20}$  m<sup>2</sup>) which is continuously heated by the surrounding earth,  $T_s = T_f = T^0$ , along its boundary  $x = X_F$  (Fig. 8.20, right). In this case, the results are strongly influenced by the formation width  $X_F - X_R$ . If increased to infinity, the results will shift back to the case of an insulated reservoir, whereas if reduced, the additional heat transferred from the formation should influence further the fracture spacing threshold  $B_T$ . No experimental data are available to calibrate the width of the rock formation that thermally contributes

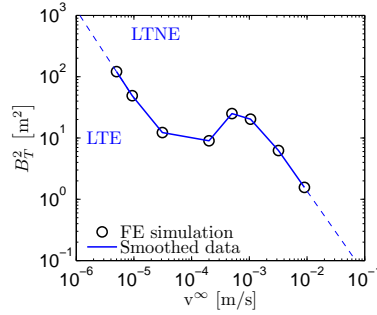


Figure 8.21: Same as Fig. 8.19 but for a non-uniform flow path and heat exchange with a formation of 30 m width. The drawdown results correspond to the tip of the production well, i.e.  $x = X_W = 60$  m. A non-linear non-monotonic response is obtained from the finite element (FE) simulations in opposition with the power response suggested by eqn (8.99). Heat exchange between the reservoir and the rock formation requires the use of the SUPG method, Remark 8.5.

to the reservoir (Sect. 8.3.6). The arbitrary value of  $X_F - X_R = 30$  m is discussed below.

For  $n_f = 0.005$  and non-uniform flow of  $v^\infty = 2.0 \cdot 10^{-4}$  m/s, the limit between a single-step pattern and a double-step pattern corresponds to  $B_T = 3$  m. The contribution of the rock formation reduces the rate of the thermal depletion of the fluid which may never reach  $T_D = 0.95$ , for small flow rates. The additional heat provided by the formation in the neighborhood of the production well is little affected by convection due to small fluid velocities in this area (Fig. 8.22, right). The relation between the square of the fracture spacing threshold and the inverse of the flow rate is no longer linear and even non-monotonic (Fig. 8.21). The non-monotonic behavior can be further explained by looking at the characteristic times. At high flow rates  $v^\infty > 10^{-3}$  m/s, the time required for the thermal depletion of the reservoir is much smaller than the characteristic time required by diffusion in the hot formation. The hot formation is merely equivalent to a zero heat flux boundary condition along the line  $x = X_R$ , for the time span over interest.

For intermediate flow rates, the characteristic times of diffusion in the rock formation and of thermal depletion in the reservoir are of similar magnitude. The externally supplied heat is mainly transported across the reservoir by the convective fluid so that the depletion time of the fluid phase is increased. Although the fluid velocity is increased, the fluid temperature remains high due to the external heat supply. Hence, the LTE threshold is only obtained for larger fracture spacings (smaller rates of heat transfer).

**Remark 8.4.** *Instead of including a rock formation in the finite element mesh, the influence of the hot formation can be introduced via a convective boundary condition,*

$$\mathbf{q}_k \cdot \hat{\mathbf{n}} = h_{k,\text{earth}}(T_k - T_{\text{earth}}), \quad k = s, f, \quad (8.100)$$

in which  $h_{k,\text{earth}}$  is the heat transfer coefficient [ $W/m^2.K$ ] between the phase  $k$  and earth, and  $T_{\text{earth}}$  is the constant temperature of the earth. The heat transfer coefficients are defined by the thermal conductivities weighted by a coefficient  $W$ :  $h_{f,\text{earth}} = W n_f \Lambda_f / (X_F - X_R)$ ,  $h_{s,\text{earth}} = W n_s \Lambda_s / (X_F - X_R)$  and  $T_{\text{earth}} = T^0$ . The case of a reservoir surrounded by a

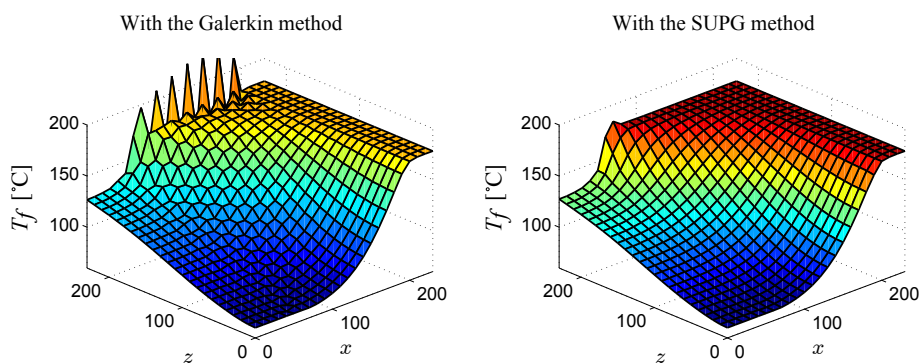


Figure 8.22: Fluid temperature contours for  $v^\infty = 2.0 \cdot 10^{-4}$  m/s, at  $t = 3.18$  years, accounting for heat transfer with the rock formation and for a non-uniform flow field. The Galerkin method (left) displays spurious numerical wiggles, which are partly cured by the SUPG method (right).

formation of width  $X_F - X_R = 30$  m is recovered for a precise value of  $W$ . For example, if the injection rate is  $v^\infty = 2.0 \cdot 10^{-4}$ , the weighting coefficient  $W$  is equal to 0.17 so as to recover the same thermal depletion curve. The convective boundary condition is particularly appropriate for industrial heat exchangers where the cooling/heating temperature  $T_{\text{earth}}$  is enforced at a known distance with a cooling/heating loop.

**Remark 8.5.** Heat exchange between the reservoir and the surrounding rock formation, by direct contact or via a convective boundary condition, requires the use of the SUPG method (Brooks and Hughes, 1982; Tezduyar and Osawa, 2000). Indeed, the boundary condition induces a sharp temperature gradient, which may lead to spurious numerical wiggles if the numerical response is not stabilized appropriately. The response for the Galerkin formulation is highly oscillatory, Fig. 8.22. However efficient, the SUPG method is not perfect (Hughes et al., 1986) and significant overshootings remain along the boundary. These overshootings may be damped by use of the discontinuity capturing method, Fig. G.1, see Appendix G.4. Still, the discontinuity capturing method has been experienced to be prone to instabilities for large velocities and large times.

Initial or boundary conditions	Value	Unit	Reference
Injection temperature $T_{f,\text{inj}}$	70	°C	1
Initial in-situ temperature $T^0$	178	°C	1
Initial production pressure $p_{f,\text{out}}^0 = \rho_f g H$ at $H = 2.673$ km	26.19	MPa	2
Initial injection pressure $p_{f,\text{inj}}^0 = \rho_f g H$ at $H = 2.903$ km	28.44	MPa	2
Injection overpressure	9.0	MPa	1
Overburden compressive stress	-75.0	MPa	3
Lateral earth stress	-37.5	MPa	3

Table 8.3: Initial and loading boundary conditions representative of Fenton Hill HDR reservoir, run segment 5. 1: Zyvoloski et al. (1981). 2: Sect. 8.3.4.3. 3: Murphy et al. (1977).

Material parameter	Value	Unit	Reference
Drained Young's modulus $E$	38.9	GPa	1
Drained Poisson's ratio $\nu$	0.3	-	1
Bulk thermal expansion coefficient $c_T$	$3.3 \cdot 10^{-6}$	1/K	2
Fissure network porosity $n_f$	$< 0.01$	-	1
Fissure network permeability $k_f$	$< 1.0 \cdot 10^{-13}$	$\text{m}^2$	1
Solid grains compressibility $c_s$	$2.7 \cdot 10^{-11}$	1/Pa	1
Solid thermal conductivity $\Lambda_s$	2.71	W/m.K	3
Solid specific heat capacity $C_{s,v}$	948.55	J/kg.K	†
Solid density $\rho_s$	2600	$\text{kg}/\text{m}^3$	†
Solid thermal diffusivity $\alpha_{T,s}$	$1.1 \cdot 10^{-6}$	$\text{m}^2/\text{s}$	-
Fluid hydraulic compressibility $c_{fH}$	$4.54 \cdot 10^{-10}$	1/Pa	†
Fluid thermal expansion coeff. $c_{fT}$	$1.0 \cdot 10^{-3}$	1/K	†
Fluid dynamic viscosity $\mu_f$ ‡	$3.0 \cdot 10^{-4}$	Pa.s	†
Fluid thermal conductivity $\Lambda_f$	0.6	W/m.K	†
Fluid specific heat capacity $C_{f,p}$	4275	J/kg.K	3
Fluid density $\rho_f$	980.0	$\text{kg}/\text{m}^3$	†
Fluid thermal diffusivity $\alpha_{T,f}$	$1.58 \cdot 10^{-7}$	$\text{m}^2/\text{s}$	-

Table 8.4: Input parameters representative of Fenton Hill HDR reservoir, run segment 5. 1: Murphy et al. (1977). 2: Zyvoloski et al. (1981). 3: Elsworth (1989). † Estimated parameters for water and granite. ‡ Although, fluid dynamic viscosity varies much with temperature and with viscosity-increasing additives or propping agents, the fluid dynamic viscosity  $\mu_f$  used throughout corresponds to pure water at 95°C, Table A.2.4 in de Marsily (1986).

### 8.3.6 Fenton Hill HDR reservoir

The thermal responses elicited from the thermo-hydro-mechanical model in LTNE may be compared with results from a 300-day circulation test at the Fenton Hill HDR reservoir, New Mexico, USA.

The circulation test was induced between depths 2903 m and 2667 m with an average reservoir height  $Z_R$  of 230 m (Zyvoloski et al., 1981). The horizontal half-width  $X_R$  of the permeable reservoir is arbitrary chosen equal to 200 m surrounded by a formation of width  $X_F - X_R = 30$  m. The horizontal half-width of the wells is equal to either (1)  $X_W = 200$  m or (2)  $X_W = 60$  m. Loading boundary conditions and material parameters are documented in Tables 8.3 and 8.4. The fluid pressures at the injection and the production wells are hydrostatic.

For a typical diffusion length  $Z_R$  of 230 m and the material parameters of Table 8.4, the characteristic times of seepage and of thermal diffusion through the solid skeleton, as defined by eqns (8.85), are equal to  $3500 \text{ s} \simeq 1$  hour and  $4.8 \cdot 10^{10} \text{ s} \simeq 1520$  years, respectively. Therefore, as indicated in Sect.8.3.3.3, the minimum and the maximum time steps are taken equal to  $\Delta t_{\min} = 1000 \text{ s}$  and  $\Delta t_{\max} = 10^{10} \text{ s} \simeq 317$  years.



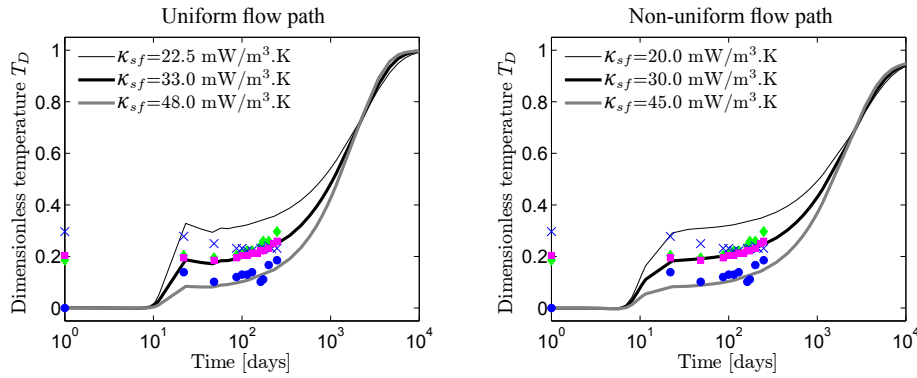


Figure 8.23: Relative temperature outlet  $T_D$  versus time  $t$  along the production well at  $x=60$  m. Experimental data pertain to different depths, namely  $\circ$  2703 m,  $\diamond$  2673 m,  $\times$  2626 m and  $\square$  in the casing 2660 m. Colors are available on the electronic version. The experimental temperatures at day one result from the spatial heterogeneity along the production well, see text. (left) Uniform flow field,  $k_f = 8.0 \cdot 10^{-15} \text{ m}^2$  and  $n_f = 0.005$ . Optimum specific inter-phase heat transfer coefficient  $\kappa_{sf} = 33.0 \text{ mW/m}^3 \cdot \text{K}$ . (right) *Non-uniform* flow field,  $k_f = 2.35 \cdot 10^{-14} \text{ m}^2$  and  $n_f = 0.005$ . Optimum specific inter-phase heat transfer coefficient  $\kappa_{sf} = 30.0 \text{ mW/m}^3 \cdot \text{K}$ .

### 8.3.6.1 Calibration of the model

The least well-defined of the required material parameters are the fracture permeability  $k_f$  after hydraulic stimulation, the fracture porosity  $n_f$  and the *specific* inter-phase heat transfer coefficient  $\kappa_{sf}$ .

Experimental data reported by Zyvoloski et al. (1981) are used to calibrate the above parameters based on the following procedure: (1) the fracture network permeability  $k_f$  is obtained so that the first stage of the thermal depletion curve, mainly due to the convection of the fluid, matches the field data; (2) the fracture network porosity  $n_f$  is adjusted so that the duration of the second stage of thermal depletion matches the rest of the response; finally (3) the optimum inter-phase heat transfer coefficient  $\kappa_{sf}$  is obtained by trial and error from the temperature magnitude at the start of the second stage of the field data, Fig. 8.23.

The calibration is considered for two different reservoir geometries: (i) for  $X_W = X_R$ , the flow field is uniform in space, Fig. 8.23, left; (ii) for  $X_W < X_R$ , the flow field is non-uniform in space, Fig. 8.23, right. In both cases, the reservoir is assumed to exchange heat with the formation. The mechanical boundary conditions are summarized in Sect. 8.3.4.4.

If the flow field is uniform, the calibration yields the fracture network permeability  $k_f = 8.0 \cdot 10^{-15} \text{ m}^2$ , the porosity  $n_f = 0.005$ , and the optimum specific inter-phase heat transfer coefficient  $\kappa_{sf} = 33 \text{ mW/m}^3 \cdot \text{K}$ , corresponding to a block width  $B = 14.2 \text{ m}$  in agreement with the magnitude used in Fig. 3.2 in Zyvoloski et al. (1981). If the flow field is non-uniform, the calibration yields a higher permeability  $k_f = 2.35 \cdot 10^{-14} \text{ m}^2$ , the same porosity  $n_f = 0.005$  and a slightly smaller specific inter-phase heat transfer coefficient  $\kappa_{sf} = 30 \text{ mW/m}^3 \cdot \text{K}$ .

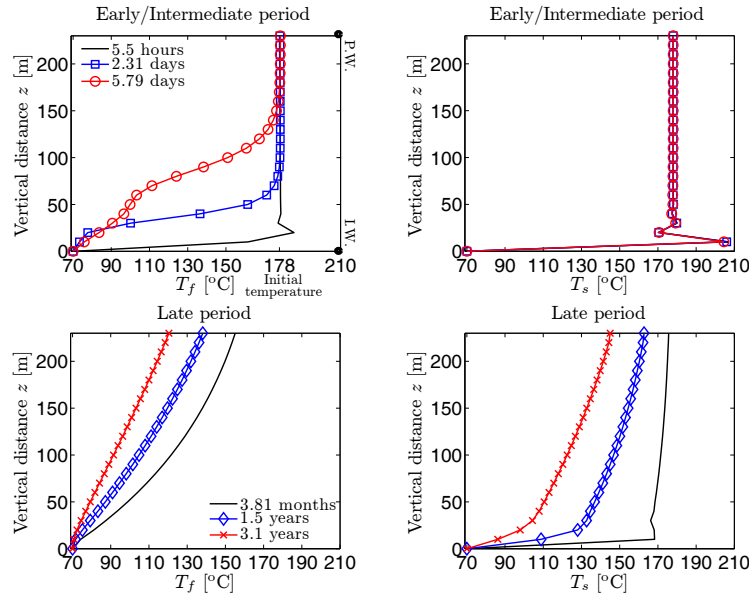


Figure 8.24: Profiles, along the  $z$ -axis at  $x = 60$  m, of fluid temperature (left) and solid temperature (right), with  $n_f = 0.005$ ,  $k_f = 8.0 \cdot 10^{-15} \text{ m}^2$ ,  $\kappa_{sf} = 33.0 \text{ mW/m}^3 \cdot \text{K}$  and a uniform flow field. P.W. stands for production well and I.W. for injection well. The early wiggles near the injection well are numerical artifacts due to an imperfect damping of the convective contribution, see text. The thermal depletion of the fluid phase is significantly ahead of the thermal depletion of the solid phase.

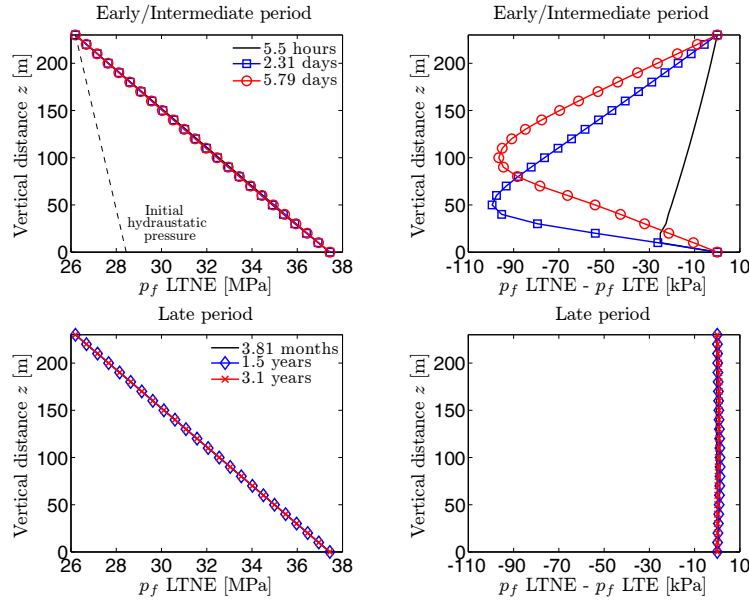


Figure 8.25: Profiles, along the  $z$ -axis at  $x = 60$  m, of fluid pressure  $p_f$  (left) and relative fluid pressure with respect to the LTE response (right). Same parameters as Fig. 8.24. The fluid pressure reaches quickly steady state and remains undisturbed in spite of the thermal depletion of the fluid phase and of the thermal contraction of the solid phase.

The inferred fracture network permeability is found to depend strongly on the spatial characteristics of the flow field. As expected, the non-uniform flow field setup requires a

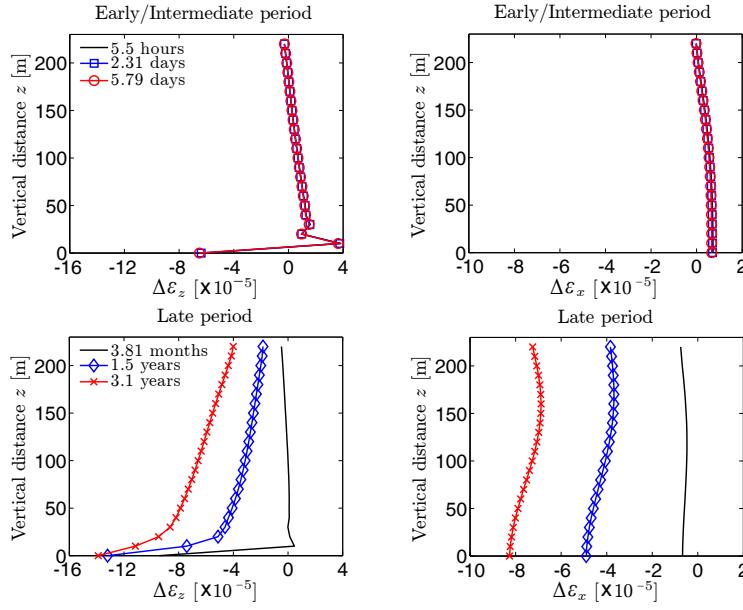


Figure 8.26: Profiles, along the  $z$ -axis at  $x = 60$  m, of vertical strain (left) and lateral strain (right). Same parameters as Fig. 8.24. Extension is counted positive. The simulations assume a plane strain analysis,  $\epsilon_y = 0$ . Contraction of the solid phase,  $\Delta\epsilon_z < 0$  and  $\Delta\epsilon_x < 0$ , is controlled by the solid temperature response and, thus, develops in the late period.

higher permeability  $k_f$ , that is a higher average fluid velocity  $v^\infty$ . Overall, both types of flow fields show a good correspondence with the experimental data and provide the same magnitude for the specific inter-phase heat transfer coefficient  $\kappa_{sf} \approx O(10)$  mW/m<sup>3</sup>.K.

Data provided by Zyvoloski et al. (1981) display spatially heterogeneous initial temperatures. This situation may be explained by the hydraulic stimulation tests previously undergone by the reservoir. The initial temperature  $T^0$  used in Fig. 8.23 represents the initial temperature at 2703 m depth, i.e. at the lowest point of the production well. If  $T^0$  is chosen equal to the average temperature of the production well, the results of Fig. 8.23 hold for higher values of  $\kappa_{sf}$ . The overall response remains the same but the second stage of thermal depletion begins at a lower dimensionless temperature  $T_D$ .

The initial response (stage 1) is dominated by the immediate response of the convective fluid while stage 2 corresponds to the transfer between the fluid and the solid phase. Only later thermal history ( $> 300$  days) is influenced by the external heat supply from the surroundings. Hence, the circulation test is too brief to yield a conclusive comparison on the thermal boundary condition at the reservoir-formation vertical interface, even with a non-uniform flow field.

If, from Fig. 8.23, left, which is associated with uniform flow, a fracture permeability of  $k_f = 8.0 \cdot 10^{-15}$  m<sup>2</sup> ( $v^\infty = 2.0 \cdot 10^{-4}$  m/s) is assumed, the entire thermal drawdown history may be determined directly from Fig. 8.17 for various porosities and heat transfer parameters. Similarly, if a porosity of  $n_f = 0.005$  is assumed for this physical system, the full thermal drawdown history may be determined directly from Fig. 8.18 for various flow rates and heat transfer parameters.

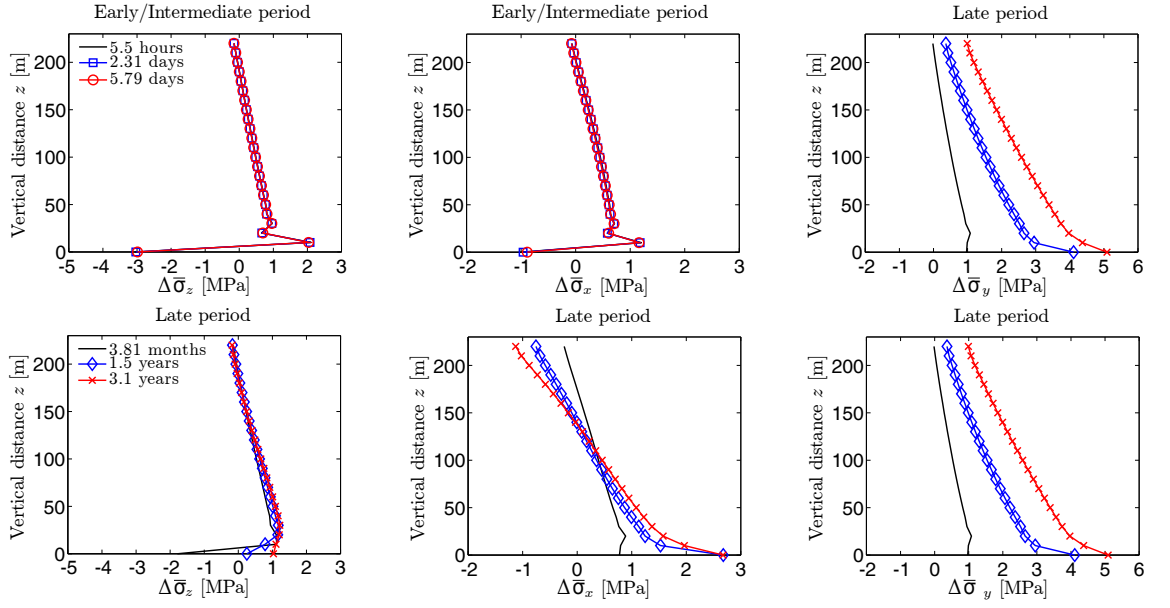


Figure 8.27: Profiles, along the  $z$ -axis at  $x = 60$  m, of the induced change in vertical effective stress (left), lateral effective stress (center) and out of plane effective stress (right). Same parameters as Fig. 8.24. Tensile stresses are counted positive. The contraction of the solid phase induces the effective lateral stress to be tensile near the injection well ( $z < 120$  m) and compressive near the production well ( $z > 120$  m).

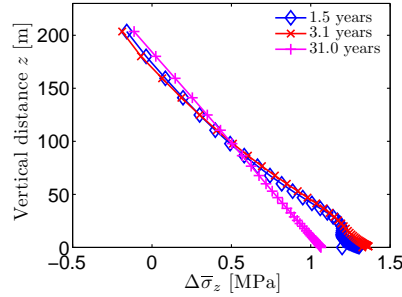


Figure 8.28: Same as Fig. 8.27 but with a refined mesh in the vicinity of the injection well. The profile at 31.0 years corresponds to the complete cooling of the reservoir.

### 8.3.6.2 THM coupled behavior

The LTNE model is used to predict the coupled thermo-hydro-mechanical behavior of the Fenton Hill HDR reservoir. The material parameters matching the experimental data for a uniform flow field are used, that is  $k_f = 8.0 \cdot 10^{-15} \text{ m}^2$ ,  $n_f = 0.005$  and  $\kappa_{sf} = 33.0 \text{ mW/m}^3 \cdot \text{K}$ . The reservoir is assumed to exchange heat with the rock formation, although the results are not affected by the external heat supply for the specific case considered. The mechanical boundary conditions prior to the circulation test are presented in Sect. 8.3.4.3 and are maintained constant throughout the simulations.

The coupled behavior of porous media in LTNE is governed by the difference in characteristic times between the thermal depletion of the fluid phase and that of the solid phase, Fig. 8.24. For example, at roughly 5.8 days the thermal depletion of the fluid phase has

already started to propagate inside the reservoir, whereas the thermal depletion of the solid phase is confined to the immediate vicinity of the injection well. However, as heat transfer between the two constituents gets completed, the mixture tends to thermal equilibrium.

This early significant difference in time depletion rates is due to the volume difference between the solid skeleton and the fluid. Indeed, the fluid porosity is  $n_f = 0.005$ , and the fracture aperture is  $2b = 0.035$  m for a typical fracture spacing of  $B = 14.2$  m. Hence, although local thermal equilibrium is ‘almost’ instantaneous along the fracture walls, the width of the solid blocks (perpendicular to the fractures) is much larger than the aperture of the fractures; and therefore at the scale of the solid blocks the time required to cool down the solid phase (by diffusion of heat from the solid block) is much larger than that for the fluid phase.

In transient convection-dominated diffusion convection problems, two types of numerical noises are encountered: (1) the first type is observed during the initial times due to the application of a sharp temperature gradient at the injection well which, analogous to a shock front, disappears after a few time steps (Idelsohn et al., 1998; Yin et al., 2010); (2) the second type is observed later when the thermal front hits a prescribed boundary condition. The SUPG method was initially designed to cure the second type of numerical noise for steady state convection-dominated diffusion convection problems (Brooks and Hughes, 1982). However, if the SUPG method is used for transient convection-dominated diffusion convection problems, the magnitude of the early time noise is enlarged compared with the Galerkin approximation. This problem is tackled using the method proposed by Tezduyar and Osawa (2000), eqn (8.67): the magnitude of the first kind of numerical noise is decreased with respect to a Galerkin approximation and the second type of noise is efficiently cured.

This issue is particularly important in coupled problems since the early numerical noise in the fluid temperature may pollute the response of the other fields, see Figs. 8.24 to 8.27 during the early/intermediate period.

The pressure field reaches steady state within 1 hour due to the high hydraulic diffusivity of the fracture network, Fig. 8.25, left. To highlight the influence of the LTNE assumption, the pressure responses in LTNE ( $\kappa_{sf} = 33$  W/m<sup>3</sup>.K) and in LTE ( $\kappa_{sf} = 100$  W/m<sup>3</sup>.K) are compared in Fig. 8.25. The very little difference (during the early/intermediate period) is associated with distinct rates of thermal depletion of the fluid phase. The pressure drops at  $t = 2.31$  and 5.79 days are induced by the fact that the fluid phase is embedded in a more rigid solid skeleton, thermally undisturbed at short times. Indeed, the drained thermal expansion/contraction of the mixture is controlled locally by the solid phase and is independent of the change in fluid temperature, until energy exchange between the phases takes place, giving rise to a solid temperature variation. However, these thermally induced pressure drops remain very small in magnitude, i.e. a few kPa, due to the large permeability of the fracture network.

The strain response is associated with the thermal depletion of the solid phase, Fig. 8.26. The latter takes place during the late period and induces a contraction of the solid skeleton

in both lateral and vertical directions. The contractive strains increase over time but remain largest near the injection well where cooling takes place first. Consequently, the strains remain small during the early/intermediate periods. The slight noise due to the overshooting of the temperature of the solid phase has limited impact. Note that the absence of noise in the lateral strain profile is due to a smooth temperature gradient in the  $x$ -direction.

The effective stresses are similarly governed by the thermal depletion of the solid phase during the late period, Fig. 8.27. Cooling of the lower part of the reservoir induces contractive strains and tensile stresses. A sort of arching develops in the upper part of the reservoir where a compressive effective horizontal stress develops in time. The limit response of the reservoir is reached at about 30 years, as might be guessed from the stress profile at a later time displayed on Fig. 8.28.

Tensile stresses induced by the contraction of the rock may cause the aperture of the fractures to increase or/and could initiate new vertical fractures in the  $x - z$  and  $y - z$  planes from the solid phase. Conversely, compressive stresses induced by the pull-in near the production well can cause the aperture of the fractures to reduce. None of these coupled effects are accounted for in this study. The potential increase in permeability of the voids (or micro-fractures) perpendicular to the main flow path may lead to an increase of fluid loss. Conversely, an increase of fracture aperture in the  $x - z$  plane would favor the ‘growth’ of the reservoir.

It is worth noting that a variation of aperture could significantly influence the fluid distribution and the rate of thermal depletion. If the injection is controlled by a constant pressure gradient, a variation of aperture would modify the convective velocity through the balance of mass of the fluid. Hence, the above predictions of heat extraction are valid if the thermally stress-induced aperture change is negligible. However, if the injection is controlled by a constant flow rate, a variation of aperture would only modify the fluid pressure (Ghassemi et al., 2008). Hence, the thermal predictions would remain unchanged since the pressure contribution was found to be small.

### 8.3.7 Conclusions

Diffusion and forced convection mechanisms between two phases have been studied in the context of heat extraction from a fractured hot dry rock reservoir. A model describing the behavior of poroelastic fractured media has been extended to account for local thermal non-equilibrium. The fully coupled thermo-hydro-mechanical system has been specified for single porosity mixtures. The nonlinear field equations associated with a Galerkin finite element discretization have been stabilized with a Petrov-Galerkin method and solved using a full Newton-Raphson procedure. This finite element analysis has been employed to investigate the response of a generic hot dry rock reservoir.

A parametric analysis has been carried out to study the influences of the solid-fluid heat transfer coefficient, the fluid porosity and the flow rate. As a typical feature of local thermal non-equilibrium, the temperature outlet profile displays a double-step pattern, representing the three-stage response of the reservoir, namely 1. the initial convection of

the fluid; 2. the transfer of heat between the solid and the fluid, and 3. the final depletion of the mixture. The solid-fluid heat transfer coefficient controls the characteristic time to recover local thermal equilibrium. Porosity influences the duration of stage 2. Large flow rates favor the time difference between heat propagation in the fluid and in the solid, and therefore the double-step pattern. The influences of the spatial uniformity of the flow path and of the external heat supply on the thermal depletion of the reservoir have also been scrutinized. The performance of the system appears very sensitive to the spatial distribution of the flow path and less sensitive to the amount of external heat supply.

The model is used to describe the thermo-hydro-mechanical behavior of a long term circulation test on the Fenton Hill HDR reservoir. The least well-defined material parameters have been calibrated with experimental data and the comparison with the numerical results demonstrates a local thermal non-equilibrium response. It has been found that the thermally induced fluid pressure drop is very small in magnitude and is confined to the early time response. Later, the thermally induced effective stresses are tensile near the injection well due to the thermal contraction of the solid, suggesting a possible increase of fracture aperture, and compressive near the production well due to the pull-in of the producing area.

Here, the solid blocks are endowed with their own temperature, but they are impermeable to fluid. A more general model would account for permeable porous blocks, and thus introduce the temperatures of the solid, the temperature of the fluid of the pores and the temperature of the fluid of the fracture, as well as the pressures associated with these two fluids. Still, in a geothermal context, the seepage of fluid through the porous blocks may be considered so slow, that the temperatures of the fluid of the pores and the solid are equal. Consequently, the improved model would introduce the pressure of the pores as an additional unknown. The retardation of the flow induced by the seepage of the fluid through porous blocks remains to be quantified.

## 8.4 A dual porosity medium in local thermal non-equilibrium

The work presented in this section will be submitted to the *Journal of Geophysical Research* in a near future under the title *A thermo-hydro-mechanical coupled model in local thermal non-equilibrium for fractured HDR reservoir*, by the following authors, in order, Rachel Gelet, Benjamin Loret and Nasser Khalili.

The motivation of this third publication is to present the comprehensive framework used to define the constitutive behavior of fractured media in LTNE within the dual porosity concept. The thermo-mechanical secant constitutive matrix and the generalized diffusion and transfer constitutive relations are summarised from Chapter 2. Particular emphasis is laid on both mass and energy exchanges between the cavities which are controlled by the modified chemical potential difference and by the coldness difference, respectively. The finite element approximation of the governing equations uses the displacement vector, the two fluid pressures and the three temperatures as primary variables. It is applied to the

analysis of a generic hot dry rock (HDR) geothermal reservoir. Three parameters of the model are calibrated from the thermal outputs of the Fenton Hill and Rosemanowes HDR reservoirs. The solid-to-fracture fluid heat transfer coefficient  $\kappa_{sf}$ , which controls the rate of heat exchange between the porous blocks and the fracture fluid, is found in the range 33 to 120 mW/m<sup>3</sup>.K. The calibrated model is next applied to simulate circulation tests at the Fenton Hill HDR reservoir. The finer thermo-hydro-mechanical response provided by the dual porosity model with respect to a single porosity model is highlighted in a parameter analysis. Emphasis is put on the influence of the fracture spacing, on the effective stress response and on the permeation of the fluid into the porous blocks. The dual porosity model yields a thermally induced effective stress that is less tensile compared with the single porosity response, reflecting distinct pore pressure contributions. This effect becomes significant for large fracture spacings. In agreement with field data, fluid loss is observed to be high initially and to decrease with time.

### 8.4.1 Introduction

Geothermal energy resources initially tested at Los Alamos National Laboratory (Murphy et al., 1981) continue to attract a significant amount of attention in present-day commercial prototypes (Tenzer, 2001). The development of constitutive models for energy extraction from artificially fractured hot dry rock (HDR) reservoirs requires three main ingredients: (1) a proper thermo-hydro-mechanical coupled model developed from a rational thermodynamic framework; (2) a theory of mixtures for a solid skeleton and one (or several) fluid(s), and (3) local thermal non-equilibrium (LTNE).

The purpose of this work is to contribute to a framework of understanding of the thermo-hydro-mechanical response of fractured media, where, at each geometrical point, the solid skeleton displays two fluid cavities and the temperatures of the solid and fluids are independent. Field observations of pressure buildup and depletion history of reservoirs have demonstrated that standard poro-elasticity may be too crude for modelling purpose. A more elaborate formulation, such as the dual porosity concept, is needed to provide a reliable description of the effective stress and of the fluid pressures in fractured reservoirs (Warren and Root, 1963; Kazemi, 1969; Zhang and Roegiers, 2005).

As for geothermal energy applications, focus so far has been on partially coupled systems in an effort to implement a network of discrete discontinuities (DuTeaux et al., 1996; Bruel, 2002), to couple free and forced convection (Bataillé et al., 2006), or to characterize joint closure with a stress dependent law (Kohl et al., 1995). The closed form solutions by Ghassemi et al. (2005) of the thermally induced stress, in geothermal reservoirs where heat transport is dominated by convection in the fluid phase and by conduction in the solid phase, are worth notice. Still, the influence of a second porosity, which is not participating to forced convection owing to its low permeability, has been systematically disregarded.

Indeed, in spite of their importance in the fields of petroleum engineering, reservoir engineering and geothermal energy extraction, as stressed by e.g. Hayashi et al. (1999),



thermo-hydro-mechanical coupling effects in media with double porosity have rarely been investigated to the exception of (Bai and Rogiers, 1994; Bower and Zyvoloski, 1997; Masters et al., 2000; Khalili and Selvadurai, 2003; Nair et al., 2004). Crucially, the extension of the effective stress concept to media with multiple porosity, and cavities saturated either by liquids or gases, has been an open question for a while. Two propositions remain today: (1) the double effective stress concept (Elsworth and Bai, 1992) and (2) the extension of Biot's relationship to dual porosity (Khalili and Valliappan, 1996). Hydro-mechanical dual porosity models, based on the double effective stress concept, have been extended to account for thermal effects, (Bai and Rogiers, 1994; Bower and Zyvoloski, 1997; Masters et al., 2000; Nair et al., 2004). On the other hand, Khalili and Selvadurai (2003) presented a thermo-hydro-mechanical model for elastic media with double porosity, using a systematic macroscopic approach based on a single effective stress concept. This model, assuming local thermal equilibrium (LTE), has been applied to wellbore stability in the context of enhanced heavy-oil recovery by hot water injection in Chapter 6. The importance of an appropriate definition of the effective stress is illustrated in the thermo-hydro-mechanical formulations developed for unsaturated porous media (Loret and Khalili, 2000b,a; Khalili and Loret, 2001).

A key factor in geothermal energy recovery is the difference in the characteristic times between diffusion of heat in the porous blocks and forced convection in the fracture network, a feature that motivates an analysis that allows for local thermal non-equilibrium. In fact, Section 8.3 show that continuum models displaying a single porosity can adequately predict the thermal depletion of hot dry rock reservoirs if LTNE between the solid skeleton and the fluid is accounted for. Still, to the exception of the above work, none of the constitutive models accounting for LTNE in mixtures including a solid and a fluid, namely Bowen and Garcia (1970); Pecker and Deresiewicz (1973); Aifantis (1980a,b); De La Cruz and Spanos (1989); Hsu (1999), have targeted geothermal reservoirs. Mechanical engineering applications have addressed packed beds (Minkowycz et al., 1999; Nield et al., 2002). Quantifying the inter-phase heat transfer coefficient is essentially an open question in the domain of deformable saturated dual porosity media.

Of crucial importance to the economical viability of enhanced geothermal systems is the knowledge of the induced thermal stresses and of the permeation losses into the porous matrix (Armstead and Tester, 1987). Provided that the injection and production wells are appropriately connected, water loss is mainly attributed to the uncontrolled thermal contraction of the rock. According to Richards et al. (1994), water loss may occur according to three mechanisms: steady state diffusive loss, transient loss into storage and loss due to reservoir growth (propagation of the fracture network). To the exceptions of Zyvoloski et al. (1981); Tenma et al. (2008); Ghassemi et al. (2008), few studies really address fluid losses into the matrix, permeation being usually imposed by a continuous leak-off into the formation. In contrast, the present approach quantifies the contributions of the two fluid pressures on the thermally induced effective stress and identifies a mechanism of fluid loss.

A fully coupled finite element formulation for a thermo-elastic fractured medium in

local thermal non-equilibrium is exposed here. The fractured medium is described as a dual porosity mixture composed of a solid phase and two fluid phases. While Gelet et al. (2011) consider a single porosity model with one pore pressure and two temperatures, the dual porosity model displays two pore pressures and three temperatures. The solid phase has a special role as it provides the matrix skeleton and encloses the fluid phases in the porous blocks and the fracture network. The three phase model is embedded within a rational thermodynamic framework. The balance equations and the Clausius-Duhem inequality are presented in Sect. 8.4.2. Even if the mixture is in LTNE, a single Clausius-Duhem inequality is required for the whole mixture. Three types of contributions, each with its own physical interpretation, are identified in the dissipation (Sect. 8.4.3). The resulting three inequalities motivate the form and structure of the constitutive equations, namely (1) the thermo-mechanical equations linking generalized stresses to generalized strains; (2) the constitutive equations for mass and energy transfers (exchanges) and (3) the constitutive equations for generalized diffusion. The weak form of the field equations, the spatial discretization and time integration procedures to solve the coupled equations through a finite element procedure are summarized in Sect. 8.4.5. The primary variables are the displacements, the two pressures of the fluids, the three temperatures of the solid and of the fluid phases. The resulting system of equations is used to address a generic HDR reservoir subjected to the injection of a cool fluid and tested for various fracture spacings (Sect. 8.4.6). Comparisons between field data and the simulated response are used to calibrate three parameters of the model so as to match the thermal output (Sect. 8.4.7). Particular attention is laid on the magnitude of the specific solid-to-fracture fluid heat transfer coefficient. Once calibrated, the model is used to simulate circulation tests, and the reservoir response is examined in terms of the effective stress and of the permeation of fluid through the porous blocks (Sect. 8.4.8). A parametric analysis is performed to explore the response of the model, with special emphasis on the fracture spacing.

Compact or index tensor notation is used throughout. Vector and tensor quantities are identified by bold face letters, e.g. the total stress is denoted  $\boldsymbol{\sigma}$ , and  $\mathbf{I}$  represents the second order identity tensor.  $\text{tr}(\cdot)$  denotes the trace of a second order tensor,  $\nabla(\cdot)$  the gradient operator and  $\text{div}(\cdot)$  the divergence operator. The subscripts  $s$ ,  $p$ ,  $f$  refer to the solid skeleton, the pore fluid and the fracture fluid, respectively. Unless stated otherwise, the convention of summation over repeated indices is *not* used.

### 8.4.2 Balance equations for the three phase mixture

Each of the three phases is endowed with its own kinematics, mass and energy content. Accordingly, the thermo-hydro-mechanical response of the mixture requires the partial differential equations in space and time expressing the balances of momentum, the balances of mass and the balances of energy to be satisfied pointwise.

### 8.4.2.1 Basic definitions

Dual porous media are made of three phases, a solid, a fluid in the pores and a fluid in the fractures. Although the fluids are identical, typically water, the two fluid phases are segregated by their spatial location and are therefore viewed as separate constituents endowed with their own independent pressures and temperatures. In the context of the theory of mixtures, the three phases are viewed as three independent overlapping continua. Furthermore, the solid phase, also referred to as the solid skeleton, has a special role as it serves as a reference (Biot, 1977). Each phase contains a single constituent, or species, and therefore the two terms could be used interchangeably. However, the term *constituent* will be used to refer to the individual properties of a species while the term *phase* refers to its contribution to the mixture.

At each point of each phase are defined intrinsic quantities, labeled by subscripts, and apparent or partial quantities, labeled by superscripts. At each point of the fractured porous medium of volume  $V$ , the phase  $k$  is introduced along with its intrinsic properties of mass  $M_k$  and volume  $V_k$ . The volumes  $V_k$  of the phases sum up to the total volume  $V = V_s + V_p + V_f$  of the mixture. The set of all phases is noted by  $\mathcal{K} = \{s, p, f\}$  while  $\mathcal{K}^* = \{p, f\}$  refers to the set of species which diffuse through the solid skeleton. Each phase  $k$  is endowed with a volume fraction  $n_k$ , an *intrinsic* density  $\rho_k$ , a *partial* density  $\rho^k$ ,

$$n_k = \frac{V_k}{V}; \quad \rho_k = \frac{M_k}{V_k}; \quad \rho^k = \frac{M_k}{V} = n_k \rho_k, \quad k \in \mathcal{K}, \quad (8.101)$$

and an absolute velocity  $\mathbf{v}_k$ . The volume fractions sum up to one,  $n_s + n_p + n_f = 1$ . The total mass density of the mixture  $\rho$  is the sum of the apparent contributions,

$$\rho = \sum_{k \in \mathcal{K}} \rho^k. \quad (8.102)$$

At the reference time  $t = 0$ , the total volume  $V$  is denoted  $V^0$ . The volume content and the mass content of the fluid phase  $k$  per unit reference volume of porous medium are denoted by  $v^k$  and  $m^k$ , respectively,

$$v^k = \frac{V_k}{V^0} = n_k \frac{V}{V^0}, \quad m^k = \frac{M_k}{V^0} = \rho_k v^k = \rho^k \frac{V}{V^0}, \quad k \in \mathcal{K}. \quad (8.103)$$

The reference and current volumes,  $V^0$  and  $V$  respectively, are related by the determinant of the deformation gradient  $\mathbf{F}$ , which linearizes to  $1 + \text{tr} \boldsymbol{\epsilon}$  for small strains,

$$\frac{V}{V^0} = \det \mathbf{F} \sim 1 + \text{tr} \boldsymbol{\epsilon}. \quad (8.104)$$

The mass flux  $\mathbf{M}_k$  and the volume flux  $\mathbf{J}_k$  per unit current area of the mixture measure the relative velocity of the fluid phase  $k$  with respect to the solid,

$$\mathbf{M}_k = \rho_k \mathbf{J}_k = \rho^k (\mathbf{v}_k - \mathbf{v}_s), \quad k \in \mathcal{K}^*. \quad (8.105)$$

The solid phase is endowed with its own (infinitesimal) strain tensor  $\boldsymbol{\epsilon} = \frac{1}{2}(\nabla \mathbf{u} + (\nabla \mathbf{u})^T)$ , which is defined from the macroscopic displacement vector  $\mathbf{u}$  and which is constitutively decomposed into an elastic contribution  $\boldsymbol{\epsilon}^e$  and a thermal contribution  $\boldsymbol{\epsilon}^\theta$ ,

$$\boldsymbol{\epsilon} = \boldsymbol{\epsilon}^e + \boldsymbol{\epsilon}^\theta. \quad (8.106)$$

The partial stress and pressures of the three phases,  $\boldsymbol{\sigma}^s$  and pressures  $p^k$ , which are linked to the intrinsic stress  $\boldsymbol{\sigma}_s$  and pressures  $p_k$  of the associated phases through the volume fractions,

$$\boldsymbol{\sigma}^s = n_s \boldsymbol{\sigma}_s, \quad \boldsymbol{\sigma}^k = -n_k p_k \mathbf{I}, \quad k \in \mathcal{K}^*, \quad (8.107)$$

sum up to the total stress,

$$\boldsymbol{\sigma} = \boldsymbol{\sigma}^s + \boldsymbol{\sigma}^p + \boldsymbol{\sigma}^f. \quad (8.108)$$

The total stress  $\boldsymbol{\sigma}$  and the effective stress  $\bar{\boldsymbol{\sigma}}$  may be decomposed into a spherical part and a deviatoric part  $\mathbf{s}$ , by use of the mean stresses  $p = -\frac{1}{3} \text{tr} \boldsymbol{\sigma}$  and  $\bar{p} = -\frac{1}{3} \text{tr} \bar{\boldsymbol{\sigma}}$ ,

$$\boldsymbol{\sigma} = -p \mathbf{I} + \mathbf{s}, \quad \bar{\boldsymbol{\sigma}} = -\bar{p} \mathbf{I} + \mathbf{s}. \quad (8.109)$$

The stress components are positive in tension so that the mean stresses  $p$  and  $\bar{p}$  are counted positive in compression. The elastic strain  $\boldsymbol{\epsilon}^e = \mathbf{C}^{DS} \bar{\boldsymbol{\sigma}}$  is by definition linked by a one-to-one relationship with the effective stress  $\bar{\boldsymbol{\sigma}}$  through the drained compliance tensor  $\mathbf{C}^{DS}$ . In an isotropic context,

$$\text{tr} \boldsymbol{\epsilon}^e = -c \bar{p}, \quad \text{dev} \boldsymbol{\epsilon}^e = \frac{\mathbf{s}}{2\mu^{DS}}, \quad (8.110)$$

in which  $c$  is the drained compressibility of the solid skeleton and  $\mu^{DS}$  its shear modulus.  $\text{dev} \boldsymbol{\epsilon}^e$  denotes the deviatoric part of the elastic strain  $\boldsymbol{\epsilon}^e = \frac{1}{3} \text{tr} \boldsymbol{\epsilon}^e \mathbf{I} + \text{dev} \boldsymbol{\epsilon}^e$ . In this isotropic context, the deviatoric parts of the elastic and total strains,  $\text{dev} \boldsymbol{\epsilon}^e$  and  $\text{dev} \boldsymbol{\epsilon}$  respectively, are equal.

Furthermore, the thermodynamical state of each fluid constituent is measured by its pressure  $p_k$ , its temperature  $T_k$ , its entropy  $S_k$  and thermodynamic potentials per unit current mass of the constituent such as the internal energy  $U_k$ , the free energy  $E_k$ , the enthalpy  $H_k$ , and the chemical potential  $G_k$ , also called free enthalpy,

$$E_k = U_k - T_k S_k, \quad H_k = U_k + \frac{p_k}{\rho_k}, \quad G_k = H_k - T_k S_k, \quad k \in \mathcal{K}^*. \quad (8.111)$$

Thermodynamic potentials per unit current volume are denoted by a lower letter, e.g.  $e^k = \rho^k E_k$  for the free energy and  $s^k = \rho^k S_k$  for the entropy.

### 8.4.2.2 Balances of momentum, mass and energy

A single balance of momentum is required for the mixture as a whole,

$$\operatorname{div} \boldsymbol{\sigma} + \rho \mathbf{g} = \mathbf{0}, \quad (8.112)$$

the body force  $\rho \mathbf{g}$  due to gravity  $\mathbf{g}$ , the mass density  $\rho = \sum_{k \in \mathcal{K}} \rho^k$  being contributed additively by all constituents of the mixture. Since the mass of the solid constituent is constant, a balance of mass is required for the fluid phases only,

$$\operatorname{div} \mathbf{J}_k + f_k = 0, \quad f_k \equiv n_k \frac{1}{\rho_k} \frac{d\rho_k}{dt} + \frac{1}{V} \frac{dV_k}{dt} - \frac{\hat{\rho}^k}{\rho_k}, \quad k \in \mathcal{K}^*. \quad (8.113)$$

Mass conservation implies the rates of mass change  $\hat{\rho}^k$  to sum up to zero,

$$\sum_{k \in \mathcal{K}^*} \hat{\rho}^k = 0, \quad \hat{\rho}^f = -\hat{\rho}^p. \quad (8.114)$$

This study aims to describe the transient period, referred to as local thermal non-equilibrium (LTNE), before the system reaches local thermal equilibrium (LTE). Hence, a balance of energy is required for each phase. Besides terms which are standard for single phases, the energy equations display terms that embody the rates of energy exchanges  $\hat{e}^k = \hat{e}_{\mathcal{M}}^k \cdot \mathbf{v}_s - \hat{e}_{\mathcal{U}}^k = X_k^{(4)}$ ,  $k \in \mathcal{K}$ . The balance of energy for the solid phase accounts for the flux of thermal energy due to conduction  $\mathbf{q}_s$ , the rate of solid entropy and the rate of energy exchange between the solid phase and the other phases,

$$\operatorname{div} \mathbf{q}_s + \mathcal{L}_s = 0, \quad \mathcal{L}_s \equiv T_s \frac{ds^s}{dt} + \hat{e}^s. \quad (8.115)$$

The balance of energy for the fluid phase  $k$  accounts for the flux of thermal energy due to conduction  $\mathbf{q}_k$ , the rate of fluid entropy, the rates in free energy due to mass transfer and forced convection, and the transfer of energy between the fluid phase  $k$  and the other phases,

$$\operatorname{div} \mathbf{q}_k + \mathcal{L}_k = 0, \quad \mathcal{L}_k \equiv T_k \frac{ds^k}{dt} + \hat{\rho}^k H_k + \mathbf{M}_k \cdot \nabla H_k + \hat{e}^k, \quad k \in \mathcal{K}^*. \quad (8.116)$$

Energy conservation implies the rates of energy transfer  $\hat{e}^k$  to sum up to zero,

$$\sum_{k \in \mathcal{K}} \hat{e}^k = 0, \quad \hat{e}^s = -\hat{e}^p - \hat{e}^f. \quad (8.117)$$

### 8.4.2.3 The Clausius-Duhem inequality

A single dissipation inequality is required at the mixture level. The dissipation associated with each phase is obtained by inserting the balance of energy into the balance of entropy of each species. The entropy productions of the phases are next summed *without* multiplying by the phase temperatures. The resulting inequality, referred to as Clausius-Duhem

inequality, proves a useful guide to restrict the form of the constitutive couplings (Eringen and Ingram, 1965; Bowen and Garcia, 1970). The Clausius-Duhem inequality may be advantageously rewritten in a form that highlights the thermo-mechanical, transfer and diffusion contributions,  $dD = dD_1 + dD_2 + dD_3 \geq 0$ , namely,

$$\begin{aligned}
\frac{dD_1}{dt} &= \sum_{k \in \mathcal{K}} \frac{1}{T_k} \left( -\frac{de^k}{dt} + (\boldsymbol{\sigma}^k - e^k \mathbf{I}) : \nabla \mathbf{v}_s - s^k \frac{dT_k}{dt} \right) \\
&\quad + \sum_{k \in \mathcal{K}^*} \frac{1}{\det \mathbf{F}} \frac{G_k}{T_k} \frac{dm^k}{dt} \geq 0, \\
\frac{dD_2}{dt} &= - \sum_{k \in \mathcal{K}^*} \left( G_k + \frac{1}{2} (\mathbf{v}_k - \mathbf{v}_s)^2 - \frac{1}{2} \mathbf{v}_s^2 \right) \frac{1}{T_k} \hat{\rho}^k - \sum_{k \in \mathcal{K}} \hat{e}_S^k \\
&\quad + \sum_{k \in \mathcal{K}} \frac{1}{T_k} \hat{e}^k \geq 0, \\
\frac{dD_3}{dt} &= - \sum_{k \in \mathcal{K}^*} \mathbf{J}_k \cdot \frac{1}{T_k} \left( \nabla p_k + \rho_k \left( \frac{d^k \mathbf{v}_k}{dt} - \mathbf{b}_k \right) \right) - \sum_{k \in \mathcal{K}} \mathbf{q}_k \cdot \frac{\nabla T_k}{T_k^2} \geq 0,
\end{aligned} \tag{8.118}$$

which are required to be positive individually (Loret, 2008). Note that the rate of entropy exchange between phase  $k$  and the other phases of the mixture  $\hat{e}_S^k$  appears to have no work conjugate variable. The mixture has been assumed to be closed with respect to momentum, eq (8.112), to mass, eq (8.114), and to energy, eq (8.117). Similarly, it is assumed to be closed with respect to entropy, so that the sum of the rates of entropy transfer vanish,

$$\sum_{k \in \mathcal{K}} \hat{e}_S^k = 0. \tag{8.119}$$

Therefore the constitutive equations of individual rates of entropy transfer are not needed here. On the other hand, constitutive equations need to be developed for the rates of mass transfer  $\hat{\rho}^k$  and the rates of energy transfer  $\hat{e}^k$ . Although not made explicit here, the momentum transfer of individual phases could also be retrieved from Darcy's law.

The set of independent variables used so far has tacitly included the strain, the pressures and the temperatures. Alternatively, the total stress might be substituted to the strain as an independent variable. The modification is realized by performing a partial Legendre transform of the elastic potential of the mixture  $\Psi(\boldsymbol{\epsilon}, p_p, p_f, T_s, T_p, T_f) = m^s E_s - \sum_{k \in \mathcal{K}^*} v^k p_k$  that yields the complementary potential  $\Psi_c$ ,

$$\Psi_c(\boldsymbol{\sigma}, p_p, p_f, T_s, T_p, T_f) = \Psi(\boldsymbol{\epsilon}, p_p, p_f, T_s, T_p, T_f) - \det \mathbf{F} \boldsymbol{\sigma} : \boldsymbol{\epsilon}. \tag{8.120}$$

A reference configuration is identified, in which the temperatures of the three phases are equal. Departure from this reference state is denoted by the symbol  $\Delta(\cdot)$ .

The Clausius-Duhem inequality is linearized by (1) neglecting the inertial terms in the transfer contributions  $dD_2$  and in the diffusion contributions  $dD_3$ ; (2) identifying the current and reference configurations so that  $\det \mathbf{F}$  may be set to 1. Within an updated

Lagrangian analysis, the volume content  $v^k$  and the volume fraction  $n_k$  are equal at each time, but their rates differ, namely  $dv^k = dn_k + n_k \operatorname{tr} \epsilon$ . The same remark applies to the mass content  $m^k$  and apparent mass density  $\rho^k$ . The thermo-mechanical contribution to the Clausius-Duhem inequality  $dD_1$ , eqn (8.118)<sub>1</sub>, is modified by multiplying by the temperature of the solid constituent  $T_s$ ,

$$\begin{aligned} T_s \frac{dD_1}{dt} &= -\frac{d\Psi_c}{dt} - \frac{d\boldsymbol{\sigma}}{dt} : \boldsymbol{\epsilon} - s^s \frac{dT_s}{dt} - \sum_{k \in \mathcal{K}^*} v^k \frac{dp_k}{dt} \geq 0, \\ \frac{dD_2}{dt} &= -\sum_{k \in \mathcal{K}^*} \frac{G_k}{T_k} \hat{\rho}^k + \sum_{k \in \mathcal{K}} \frac{1}{T_k} e^k \geq 0, \\ \frac{dD_3}{dt} &= -\sum_{k \in \mathcal{K}^*} \mathbf{J}_k \cdot \frac{\nabla p_k}{T_k} - \sum_{k \in \mathcal{K}} \mathbf{q}_k \cdot \frac{\nabla T_k}{T_k^2} \geq 0. \end{aligned} \quad (8.121)$$

Thermo-mechanical constitutive assumptions and simplifications are motivated in the next section.

### 8.4.3 Constitutive equations

The Clausius-Duhem inequalities (8.121) serve as guidelines to develop the constitutive equations:

- (1) the thermo-mechanical behavior is constructed in order the thermo-mechanical dissipation  $dD_1$  to *exactly vanish*, Sect. 8.4.3.1. The thermo-mechanical behavior of a single fluid  $k$  is introduced separately from the thermo-mechanical elastic equations, Sect. 8.4.3.2;
- (2) the energy dissipation is due exclusively to the transfers of mass and energy between phases, to diffusion of fluids through the solid skeleton and to conduction and convection of heat;
- (3) the constitutive equations of mass and energy exchanges are expressed in a format that ensures the second dissipation  $dD_2$  to be positive, Sect. 8.4.3.3;
- (4) the constitutive equations of thermal and hydraulic diffusions enforce the third dissipation  $dD_3$  to be positive as well, Sect. 8.4.3.4.

#### 8.4.3.1 Thermo-mechanical elastic equations

At constant total stress and pore pressures, the sole change of solid temperature leads to a volume change of the solid skeleton, the strain is uniform over the phases, and the volume change of each of the three phases is proportional to its volume fraction (Loret and Khalili, 2000b). Therefore the complementary energy depends on the restricted set of variables  $\{\boldsymbol{\sigma}, p_p, p_f, T_s\}$ . Then, the vanishing of  $dD_1$  implies that the complementary energy  $\Psi_c(\boldsymbol{\sigma}, p_p, p_f, T_s)$  can be used as a thermo-elastic potential, that delivers the work conjugate variables  $\{\boldsymbol{\epsilon}, v^p, v^f, s^s\}$ ,

$$\boldsymbol{\epsilon} = -\frac{\partial \Psi_c}{\partial \boldsymbol{\sigma}}; \quad -v^k = \frac{\partial \Psi_c}{\partial p_k}, \quad k \in \mathcal{K}^*; \quad -s^s = \frac{\partial \Psi_c}{\partial T_s}. \quad (8.122)$$

The complementary energy is assumed to be an isotropic quadratic function of the stress, and the sum of a quadratic function and of an affine function of the pressures and solid temperature,

$$\begin{aligned} \Psi_c(\boldsymbol{\sigma}, p_p, p_f, T_s) = & -\frac{1}{2} (c_{ss} p^2 + c_{pp} p_p^2 + c_{ff} p_f^2 + 2 c_{sp} p p_p + 2 c_{sf} p p_f \\ & + 2 c_{pf} p_p p_f) - \frac{|\mathbf{s}|^2}{4 \mu^{DS}} \\ & - \frac{1}{2} c_{TT} \Delta T_s^2 - \Delta T_s (c_{Ts} p + c_{Tp} p_p + c_{Tf} p_f) \\ & - \sum_{k \in \mathcal{K}^*} (v^k)^0 p_k - (s^s)^0 T_s. \end{aligned} \quad (8.123)$$

Therefore the deviatoric stress and strain are proportional, and the scalar work conjugate variables  $(-p, \text{tr}\boldsymbol{\epsilon})$ ,  $(p_p, v^p)$ ,  $(p_f, v^f)$ , and  $(s^s, T_s)$  are related by a symmetric and constant matrix,

$$\begin{bmatrix} -\text{tr}\boldsymbol{\epsilon} \\ \Delta v^p \\ \Delta v^f \\ \Delta s^s \end{bmatrix} = \begin{bmatrix} c_{ss} & c_{sp} & c_{sf} & c_{sT} \\ c_{ps} & c_{pp} & c_{pf} & c_{pT} \\ c_{fs} & c_{fp} & c_{ff} & c_{fT} \\ c_{Ts} & c_{Tp} & c_{Tf} & c_{TT} \end{bmatrix} \begin{bmatrix} p \\ p_p \\ p_f \\ \Delta T_s \end{bmatrix}, \quad \text{dev } \boldsymbol{\epsilon} = \frac{\mathbf{s}}{2\mu^{DS}}. \quad (8.124)$$

The identification of the constitutive coefficients is best addressed *via* the equivalent mixed format,

$$\begin{bmatrix} p \\ \Delta v^p \\ \Delta v^f \\ \Delta s^s \end{bmatrix} = \begin{bmatrix} -1/c & \xi_p & \xi_f & c_T/c \\ \xi_p & c_{22} & c_{23} & (n_p - \xi_p) c_T \\ \xi_f & c_{32} & c_{33} & (n_f - \xi_f) c_T \\ c_T/c & (n_p - \xi_p) c_T & (n_f - \xi_f) c_T & \rho^s C_{s,v}/T_s \end{bmatrix} \begin{bmatrix} \text{tr}\boldsymbol{\epsilon} \\ p_p \\ p_f \\ \Delta T_s \end{bmatrix}. \quad (8.125)$$

The thermo-mechanical constitutive relations extend the concept of effective stress (Biot, 1941) to dual porosity,

$$\frac{\text{tr}\boldsymbol{\sigma}}{3} + \xi_p p_p + \xi_f p_f = \frac{1}{c} (\text{tr}\boldsymbol{\epsilon} - c_T \Delta T_s). \quad (8.126)$$

The effective stress coefficients  $\xi_p$  and  $\xi_f$  and the other mechanical coefficients have been identified *via* a loading decomposition (Khalili and Valliappan, 1996),

$$\begin{aligned} \xi_p &= (c_p - c_s)/c, \\ \xi_f &= 1 - c_p/c, \\ c_{22} &= (\xi_f - n_f)(c_p - c_s) + c_s(\xi_p - n_p), \\ c_{33} &= (\xi_f - n_f)(c_p - c_s) + c_s(\xi_f - n_f), \\ c_{23} &= c_{32} = -(\xi_f - n_f)(c_p - c_s). \end{aligned} \quad (8.127)$$



The relations (8.125) and (8.127) use the drained compressibility of the solid skeleton  $c$  [1/Pa], the compressibility of the porous blocks  $c_p$ , the compressibility of the solid grains  $c_s$ , the volumetric thermal expansion coefficient of the solid phase  $c_T$  [1/K], and the heat capacity of the solid  $C_{s,v}$  per unit mass of solid, at constant strain and fluid pressures [J/kg.K].

The constitutive equations for the apparent entropies of the fluids are expressed separately from the thermo-mechanical relations (8.125) in Sect. 8.4.3.2.

### 8.4.3.2 Thermo-mechanical properties of the single fluid $k$

The entropy  $S_k$ , the chemical potential  $G_k$  and the enthalpy  $H_k$  of the fluids enter the balance of energy (8.116). The variation of the specific volume  $v_k = 1/\rho_k$  for a compressible and dilatable fluid  $k$ ,

$$\frac{dv_k}{v_k} = c_{kT} dT_k - c_{kH} dp_k, \quad (8.128)$$

introduces the compressibility  $c_{kH}$  [1/Pa] and the thermal expansion coefficient  $c_{kT}$  [1/K],

$$\begin{aligned} c_{kH} &= -\frac{1}{v_k} \left( \frac{\partial v_k}{\partial p_k} \right)_{|T_k} = \frac{1}{\rho_k} \left( \frac{\partial \rho_k}{\partial p_k} \right)_{|T_k}, \\ c_{kT} &= \frac{1}{v_k} \left( \frac{\partial v_k}{\partial T_k} \right)_{|p_k} = -\frac{1}{\rho_k} \left( \frac{\partial \rho_k}{\partial T_k} \right)_{|p_k}. \end{aligned} \quad (8.129)$$

For constant coefficients  $c_{kT}$  and  $c_{kH}$ , the specific volume results as a non-linear function of the departures of pressure and temperature from the reference state labeled by a zero superscript,

$$v_k = v_k^0 \exp(-c_{kH}(p_k - p_k^0) + c_{kT}(T_k - T_k^0)). \quad (8.130)$$

Moreover, as  $(\partial S_k / \partial v_k)_{|T_k} = c_{kT} / c_{kH}$ , the differential of the entropy  $dS_k$ ,

$$T_k dS_k = T_k \frac{c_{kT}}{c_{kH}} dv_k + C_{k,v} dT_k, \quad (8.131)$$

integrates to,

$$S_k - S_k^0 = \frac{c_{kT}}{c_{kH}} (v_k - v_k^0) + C_{k,v} \text{Ln} \frac{T_k}{T_k^0}, \quad (8.132)$$

the heat capacity at constant volume  $C_{k,v} = T_k (\partial S_k / \partial T_k)_{|v_k}$  [J/kg.K] being assumed constant.

The incremental variations of the chemical potential  $G_k$  and of the enthalpy  $H_k$  express in terms of the specific volume  $v_k$  and of the entropy  $S_k$ ,

$$dG_k = v_k dp_k - S_k dT_k, \quad dH_k = v_k dp_k + T_k dS_k, \quad (8.133)$$

and integrate to,

$$\begin{aligned}
G_k - G_k^0 &= -\frac{v_k - v_k^0}{c_{kH}} + \left( C_{k,v} + \frac{c_{kT}}{\rho_k c_{kH}} - S_k^0 \right) (T_k - T_k^0) \\
&\quad - C_{k,v} T_k \text{Ln} \frac{T_k}{T_k^0}, \\
H_k - H_k^0 &= -\frac{v_k - v_k^0}{c_{kH}} (1 - T_k c_{kT}) + \left( C_{k,v} + \frac{c_{kT}}{\rho_k c_{kH}} \right) (T_k - T_k^0).
\end{aligned} \tag{8.134}$$

In spite of the third law of thermodynamics (Kestin, 1968), the reference potentials  $G_k^0$ ,  $H_k^0$  and  $S_k^0$  are conventional, and need to be assigned.

The enthalpy may alternatively be expressed as a function of pressure and temperature,

$$dH_k = v_k(1 - T_k c_{kT}) dp_k + C_{k,p} dT_k, \tag{8.135}$$

through the heat capacity at constant pressure  $C_{k,p}$  [J/kg.K],

$$C_{k,p} = C_{k,v} + \frac{T_k c_{kT}^2}{\rho_k c_{kH}}. \tag{8.136}$$

Note that the differential operator  $d$  appearing in the relations above is arbitrary, i.e. it may refer to time or space.

#### 8.4.3.3 Constitutive equations for mass and heat transfers

The constitutive equations of mass and energy exchanges are defined by enforcing the second term of the Clausius-Duhem inequality  $dD_2$  to be positive, eqn (8.121). For that purpose, the rate of mass exchange  $\hat{\rho}^k$  and the rate of energy exchange  $\hat{e}^k$  are viewed as work-conjugated respectively to the chemical potential scaled by the temperature  $-G_k/T_k$  and to the coldness (inverse temperature)  $1/T_k$ . Due to a lack of *in situ* measurements and as a first approximation, no coupling is assumed between mass transfer and energy transfer. In other words, the transfer counterparts of the thermo-osmosis and of the isothermal heat transfer in the diffusion constitutive equations developed in Section 8.4.3.4 are not introduced.

The transfers satisfy the closure relations (8.114) and (8.117) so that a single mass rate, e.g. the rate  $\hat{\rho}^p$  of the pore fluid, and two rates of energy exchange, e.g. the rates  $\hat{e}^p$  and  $\hat{e}^f$  associated with the fluids, are needed. Consequently, equation (8.121) may be rearranged to highlight the driving forces of the transfer mechanisms, namely the jumps in scaled chemical potential  $-G_k/T_k$  across the fluid phases and in coldness  $1/T_k$  across the three phases,

$$\begin{aligned}
\text{mass transfer : } & -\hat{\rho}^p \left( \frac{G_p}{T_p} - \frac{G_f}{T_f} \right) \geq 0; \\
\text{heat transfer : } & -\hat{e}^p \left( \frac{1}{T_p} - \frac{1}{T_s} \right) - \hat{e}^f \left( \frac{1}{T_f} - \frac{1}{T_s} \right) \geq 0.
\end{aligned} \tag{8.137}$$

The first inequality is satisfied by setting

$$\hat{\rho}^p = -\eta \rho_p^2 T_p^0 \left( \frac{G_p}{T_p} - \frac{G_f}{T_f} \right) = -\hat{\rho}^f. \quad (8.138)$$

This constitutive equation for mass transfer extends the existing isothermal formulation where the mass transfer is controlled by the difference of pressures between the cavities. The actual leakage parameter  $\eta$  is defined in Sect. 8.4.6.3. The dissipation inequality (8.137)<sub>1</sub> is clearly satisfied for  $\eta \geq 0$ .

The constitutive relations of energy transfer assume the simple linear format,

$$\begin{aligned} \hat{e}^s &= \kappa_{sp}(T_s - T_p) + \kappa_{sf}(T_s - T_f), \\ \hat{e}^p &= \kappa_{sp}(T_p - T_s) + \kappa_{pf}(T_p - T_f), \\ \hat{e}^f &= \kappa_{sf}(T_f - T_s) + \kappa_{pf}(T_f - T_p). \end{aligned} \quad (8.139)$$

These relations extend the proposition of Bowen and Chen (1975) for porous media with a single porosity. The coefficients  $\kappa_{ab}$ ,  $ab = sp, sf, pf$ , are the *volumetric* or *specific* inter-phase heat transfer coefficients [W/m<sup>3</sup>.K]. The second inequality, in eqn (8.137), can be written as a sum of terms  $\kappa_{ab}(T_a - T_b)^2/(T_a T_b)$  over  $ab = sp, sf, pf$ , so that the inequality is satisfied if the three *specific* inter-phase heat transfer coefficients are positive, namely  $\kappa_{sp} \geq 0$ ,  $\kappa_{sf} \geq 0$  and  $\kappa_{pf} \geq 0$ .

#### 8.4.3.4 Constitutive equations for hydraulic and heat diffusions

The diffusion constitutive equations are similarly defined by enforcing the third term of the Clausius-Duhem inequality  $dD_3$  to be positive. The volume flux  $\mathbf{J}_k$  is seen as work-conjugated to the hydraulic gradient  $-\nabla p_k/T_k$  and the heat flux  $\mathbf{q}_k$  is conjugated to the thermal gradient  $\nabla(1/T_k)$ . Since the fluids are segregated by their spatial location, no coupling between the pore fluid diffusion and the fracture fluid diffusion is physically appropriate. For each fluid  $k$ , the *extended Darcy's law* equation describing hydraulic diffusion under combined hydraulic and thermal gradients assumes the coupled format,

$$\mathbf{J}_k = -T_k \frac{k_k}{\mu_k} \cdot \left( \frac{\nabla p_k - \rho_k \mathbf{g}}{T_k} \right) - n_k T_k^2 \Theta_k \left( \frac{\nabla T_k}{T_k^2} \right), \quad k \in \mathcal{K}^*, \quad (8.140)$$

where  $k_k$  is the intrinsic permeability [m<sup>2</sup>],  $\mu_k$  is the dynamic viscosity of the fluid [Pa.s] and  $\Theta_k$  the thermo-osmosis coupling coefficient [m<sup>2</sup>/s.K].

Similarly, the *extended Fourier's law* defining the heat fluxes  $\mathbf{q}_k$ ,  $k \in \mathcal{K}$ , under combined hydraulic and thermal gradients displays no coupling over phases, but *a priori* it includes an internal thermo-hydraulic coupling,

$$\begin{aligned} \mathbf{q}_s &= -n_s T_s^2 \Lambda_s \left( \frac{\nabla T_s}{T_s^2} \right), \\ \mathbf{q}_k &= -n_k T_k^2 \Phi_k \left( \frac{\nabla p_k - \rho_k \mathbf{g}}{T_k} \right) - n_k T_k^2 \Lambda_k \left( \frac{\nabla T_k}{T_k^2} \right), \quad k \in \mathcal{K}^*. \end{aligned} \quad (8.141)$$

The  $\Phi_k$ 's are called the isothermal heat flow coefficients [ $\text{m}^2/\text{s.K}$ ], and the  $\Lambda_k$ 's are the thermal conductivities [ $\text{W}/\text{m.K}$ ]. Along Onsager's reciprocity principle, the generalized diffusion matrix linking the vector of fluxes  $\{\mathbf{J}_p, \mathbf{J}_f, \mathbf{q}_s, \mathbf{q}_p, \mathbf{q}_f\}$  to the driving gradients  $\{-\nabla p_p/T_p, -\nabla p_f/T_f, -\nabla T_s/T_s^2, -\nabla T_p/T_p^2, -\nabla T_f/T_f^2\}$  is assumed symmetric so that the thermo-osmosis coefficients are equal to the isothermal heat flux coefficients:  $\Theta_k = \Phi_k$ ,  $k \in \mathcal{K}^*$ . The Clausius-Duhem inequality (8.121)<sub>3</sub> is satisfied if the generalized diffusion matrix is positive semi-definite, which is ensured by the inequalities,

$$\Lambda_k \geq 0, \quad k \in \mathcal{K}; \quad \frac{k_k}{\mu_k} \geq 0, \quad k \in \mathcal{K}^*; \quad \Lambda_k \frac{k_k}{\mu_k} - n_k T_k \Theta_k^2 \geq 0, \quad k \in \mathcal{K}^*. \quad (8.142)$$

#### 8.4.4 The coupled field equations

Inserting the thermo-mechanical constitutive equations (8.106) and (8.125)<sub>1</sub> into the balance of momentum (8.112) yields three coupled partial differential equations involving the displacement vector, the pressures and the solid temperature,

$$\mu^{DS} \nabla^2 \mathbf{u} + (\lambda^{DS} + \mu^{DS}) \nabla(\text{div } \mathbf{u}) - \xi_p \nabla p_p - \xi_f \nabla p_f - \frac{cT}{c} \nabla T_s - \rho \mathbf{g} = \mathbf{0}. \quad (8.143)$$

The drained compressibility of the solid skeleton  $c$  and the Lamé's constants of the drained solid  $\lambda^{DS}$  and  $\mu^{DS}$  are deduced from the drained Young's modulus  $E$  and Poisson's ratio  $\nu$  through the standard relationships,

$$c = \frac{3(1-2\nu)}{E}, \quad \lambda^{DS} = \frac{E\nu}{(1+\nu)(1-2\nu)}, \quad \mu^{DS} = \frac{E}{2(1+\nu)}. \quad (8.144)$$

A field equation describing seepage is obtained by inserting the constitutive relations (8.125)<sub>2</sub>, (8.125)<sub>3</sub>, (8.128) and (8.140) into the balance of mass (8.113), yielding in turn for the pores and for the fractures,

$$\begin{aligned} \text{div} \left( \frac{k_p}{\mu_p} (\nabla p_p - \rho_p \mathbf{g}) + n_p \Theta_p \nabla T_p \right) &= a_{pp} \frac{\partial p_p}{\partial t} + a_{pf} \frac{\partial p_f}{\partial t} + \xi_p \text{div} \frac{\partial \mathbf{u}}{\partial t} \\ &+ a_{pT_s} \frac{\partial T_s}{\partial t} + a_{pT_p} \frac{\partial T_p}{\partial t} - \frac{\hat{\rho}^p}{\rho_p}, \end{aligned} \quad (8.145)$$

$$\begin{aligned} \text{div} \left( \frac{k_f}{\mu_f} (\nabla p_f - \rho_f \mathbf{g}) + n_f \Theta_f \nabla T_f \right) &= a_{ff} \frac{\partial p_f}{\partial t} + a_{pf} \frac{\partial p_p}{\partial t} + \xi_f \text{div} \frac{\partial \mathbf{u}}{\partial t} \\ &+ a_{fT_s} \frac{\partial T_s}{\partial t} + a_{fT_f} \frac{\partial T_f}{\partial t} - \frac{\hat{\rho}^f}{\rho_f}, \end{aligned} \quad (8.146)$$

the rates of mass transfer being defined by the non-linear constitutive laws (8.134)<sub>1</sub> and (8.138).

Heat flow, forced convection and heat transfer in presence of local thermal non-equilibrium are obtained by inserting the constitutive equations (8.125)<sub>4</sub>, (8.135), (8.131), (8.141) into

the equations of balance of energy (8.115) and (8.116), resulting in turn for the solid, pore fluid and fracture fluid to,

$$\begin{aligned} \operatorname{div} (n_s \Lambda_s \nabla T_s) &= a_{T_s T_s} \frac{\partial T_s}{\partial t} + T_s \frac{c_T}{c} \operatorname{div} \frac{\partial \mathbf{u}}{\partial t} \\ &+ T_s a_{p T_s} \frac{\partial p_p}{\partial t} + T_s a_{f T_s} \frac{\partial p_f}{\partial t} \\ &+ \kappa_{sp} (T_s - T_p) + \kappa_{sf} (T_s - T_f) , \end{aligned} \quad (8.147)$$

$$\begin{aligned} \operatorname{div} (n_p \Lambda_p \nabla T_p + T_p n_p \Theta_p (\nabla p_p - \rho_p \mathbf{g})) &= a_{T_p T_p} \frac{\partial T_p}{\partial t} + T_p a_{p T_p} \frac{\partial p_p}{\partial t} \\ &+ \mathbf{M}_p \cdot \nabla H_p + \hat{\rho}^p H_p \\ &+ \kappa_{sp} (T_p - T_s) + \kappa_{pf} (T_p - T_f) , \end{aligned} \quad (8.148)$$

$$\begin{aligned} \operatorname{div} (n_f \Lambda_f \nabla T_f + T_f n_f \Theta_f (\nabla p_f - \rho_f \mathbf{g})) &= a_{T_f T_f} \frac{\partial T_f}{\partial t} + T_f a_{f T_f} \frac{\partial p_f}{\partial t} \\ &+ \mathbf{M}_f \cdot \nabla H_f + \hat{\rho}^f H_f \\ &+ \kappa_{sf} (T_f - T_s) + \kappa_{pf} (T_f - T_p) . \end{aligned} \quad (8.149)$$

The enthalpies of the fluids  $H_p$  and  $H_f$  are defined by eqns (8.134)<sub>2</sub>. Note that the term  $\hat{\rho}^p (H_p - H_f)$  vanishes when the fracture spacing  $B$  tends to zero, i.e. when hydraulic and thermal equilibria are recovered. The coefficients appearing in equations (8.145) to (8.149) are identified in terms of known properties,

$$\begin{aligned} a_{kk} &= n_k c_{H,k} + (\xi_k - n_k) c_s - a_{pf}, \quad k = p, f; \quad a_{pf} = -(\xi_f - n_f)(c_p - c_s), \\ a_{k T_s} &= (n_k - \xi_k) c_T, \quad k = p, f; \quad a_{k T_k} = -n_k c_{T,k}, \quad k = p, f; \\ a_{T_s T_s} &= n_s \rho_s C_{s,v}; \quad a_{T_k T_k} = n_k \rho_k C_{k,p}, \quad k = p, f . \end{aligned} \quad (8.150)$$

In a HDR reservoir context, if the fractured medium is described with a single porosity model, the fluid in the porous blocks is motionless with respect to the solid. In other words, the pores introduce a residual porosity, isolated from the fracture network. On the other hand, the pores contribute to the diffusion of heat. A comparison with a single porosity model serves to highlight the influence of the dual porosity concept on the overall reservoir response.

The single porosity model is recovered by setting the pore volume fraction  $n_p$  to zero, which implies  $c_p = c_s$ . Consequently,  $\xi_p = 0$  and  $\xi_f = 1 - c_s/c$ , and Biot's effective stress is recovered. Details pertaining to the single porosity model are postponed to Appendix H.1.

### 8.4.5 Finite element discretization

The finite element formulation is developed for the following primary unknowns: displacement vector  $\mathbf{u}$ , pressure of the pore fluid  $p_p$ , pressure of the fracture fluid  $p_f$ , temperature

of the solid skeleton  $T_s$ , temperatures of the pore fluid  $T_p$  and of the fracture fluid  $T_f$ . These primary unknowns are interpolated within the generic element  $e$ , in terms of nodal values through the interpolation functions  $\mathbf{N}_u$ ,  $\mathbf{N}_p$ ,  $\mathbf{N}_T$ , respectively,

$$\mathbf{u} = \mathbf{N}_u \mathbf{u}^e, \quad p_p = \mathbf{N}_p \mathbf{p}_p^e, \quad p_f = \mathbf{N}_p \mathbf{p}_f^e, \quad T_k = \mathbf{N}_T \mathbf{T}_k^e, \quad k \in \mathcal{K}. \quad (8.151)$$

Multiplying equations (8.112)-(8.116) by the virtual fields  $\delta \mathbf{u}$ ,  $\delta p$ , and  $\delta T$ , and integrating by parts over the body  $V$ , provides the weak form of the problem,

$$\int_V \nabla(\delta \mathbf{u}) : \boldsymbol{\sigma} - \delta \mathbf{u} \cdot \rho \mathbf{g} \, dV = \int_{\partial V} \delta \mathbf{u} \cdot \boldsymbol{\sigma} \cdot \hat{\mathbf{n}} \, dS, \quad (8.152)$$

$$\int_V \nabla(\delta p) \cdot \mathbf{J}_k - \delta p f_k \, dV = \int_{\partial V} \delta p \mathbf{J}_k \cdot \hat{\mathbf{n}} \, dS, \quad k \in \mathcal{K}^* \quad (8.153)$$

$$\int_V \nabla(\delta T) \cdot \mathbf{q}_k - \delta T \mathcal{L}_k \, dV = \int_{\partial V} \delta T \mathbf{q}_k \cdot \hat{\mathbf{n}} \, dS, \quad k \in \mathcal{K}, \quad (8.154)$$

where  $\hat{\mathbf{n}}$  is the unit outward vector normal to the boundary  $\partial V$ . A standard Galerkin procedure is adopted for the whole system of equations (8.152)-(8.154). Specific stabilization *ad hoc* for forced convection, such as the Streamline Upwind / Petrov-Galerkin method, is required only if a hard outflow boundary condition is applied on the temperature field. The resulting non-linear first-order semi-discrete equations for the unknown vector  $\mathbb{X}$ ,

$$\mathbb{X} = [\mathbf{u} \quad \mathbf{p}_p \quad \mathbf{p}_f \quad \mathbf{T}_s \quad \mathbf{T}_p \quad \mathbf{T}_f]^T \quad (8.155)$$

with maximum nodal length = dimension of space + 5, imply the residual  $\mathbb{R}$  to vanish:

$$\mathbb{R} = \mathbb{F}^{\text{grav}} + \mathbb{F}^{\text{surf}}(\mathbb{S}, \mathbb{X}) - \mathbb{F}^{\text{int+conv}}\left(\mathbb{X}, \frac{d\mathbb{X}}{dt}\right) = \mathbb{O}, \quad (8.156)$$

Here  $\mathbb{F}^{\text{int+conv}}$  is the vector that contains the internal forces together with the convective contributions appearing on the left-hand-side of eqn (8.152)-(8.154),  $\mathbb{F}^{\text{surf}}$  is the vector of surface loadings denoted collectively  $\mathbb{S}$  and  $\mathbb{F}^{\text{grav}}$  is the vector contributed by gravity (Appendix H.2). The semi-discrete equations are integrated through a generalized trapezoidal rule defined by a scalar  $\alpha \in ]0, 1]$ . At step  $n + 1$ , the equations are enforced at time  $t_{n+\alpha} = t_n + \alpha \Delta t$ , with  $\Delta t = t_{n+1} - t_n$ , namely,

$$\mathbb{R}_{n+\alpha} = \mathbb{F}^{\text{grav}} + \mathbb{F}^{\text{surf}}(\mathbb{S}_{n+\alpha}, \mathbb{X}_{n+\alpha}) - \mathbb{F}^{\text{int+conv}}(\mathbb{X}_{n+\alpha}, \mathbb{V}_{n+\alpha}) = \mathbb{O}. \quad (8.157)$$

In the above relation,  $\mathbb{Z} = \mathbb{S}, \mathbb{X}, \mathbb{V}$  are defined as  $\mathbb{Z}_{n+\alpha} = (1 - \alpha)\mathbb{Z}_n + \alpha\mathbb{Z}_{n+1}$ , and  $\mathbb{X}_{n+1}$  and  $\mathbb{V}_{n+1}$  are approximations of  $\mathbb{X}(t_{n+1})$  and  $(d\mathbb{X}/dt)(t_{n+1})$ , respectively. The system (8.157) is solved iteratively by an explicit-implicit operator split (Hughes, 1987a), namely at step  $n$ , iteration  $i + 1$ ,

$$\mathbb{R}_{n+\alpha}^{i+1} = \mathbb{F}_E^{\text{grav}} + \mathbb{F}_E^{\text{surf}}(\mathbb{S}_{n+\alpha}, \mathbb{X}_{n+\alpha}^i) - \mathbb{F}_I^{\text{int+conv}}(\mathbb{X}_{n+\alpha}^{i+1}, \mathbb{V}_{n+\alpha}^{i+1}) = \mathbb{O}. \quad (8.158)$$

The partition shown in equation (8.158) is motivated by two observations: (1) the dependence of the vector of external forces on the solution is weak; (2) the vector of internal forces depends non-linearly on the solution  $\mathbb{X}$  through the non-linear field equations (8.143)-(8.149). The global iteration process uses a full Newton-Raphson procedure. The Newton direction  $\Delta\mathbb{V}$  is sought by setting the residual eqn (8.158) to zero,

$$\mathbb{R}_{n+\alpha}^{i+1} = \mathbb{R}_{n+\alpha}^i - \mathbb{C} (\alpha \Delta\mathbb{V}) = \mathbb{O}. \quad (8.159)$$

$\mathbb{R}_{n+\alpha}^i$  represents the *exact* non-linear contributions of the comprehensive model, whereas the *effective diffusion matrix*  $\mathbb{C}$  is expressed in terms of the global diffusion matrix  $\mathbb{D} = \mathbb{D}(\mathbb{X}, \mathbb{V})$  and of the global stiffness-convection matrix  $\mathbb{K} = \mathbb{K}(\mathbb{X}, \mathbb{V})$ ,

$$\mathbb{C} = \mathbb{D} + \mathbb{K} \alpha \Delta t. \quad (8.160)$$

The global diffusion and stiffness-convection matrices are obtained by assembling the element contributions which have the following block structure,

$$\mathbb{D}^e = \begin{bmatrix} 0 & 0 & 0 & 0 & 0 & 0 \\ \mathbf{D}_{pp}^e \mathbf{u} & \mathbf{D}_{pp}^e p_p & \mathbf{D}_{pp}^e p_f & \mathbf{D}_{pp}^e T_s & \mathbf{D}_{pp}^e T_p & 0 \\ \mathbf{D}_{pf}^e \mathbf{u} & \mathbf{D}_{pf}^e p_p & \mathbf{D}_{pf}^e p_f & \mathbf{D}_{pf}^e T_s & 0 & \mathbf{D}_{pf}^e T_f \\ \mathbf{D}_{Ts}^e \mathbf{u} & \mathbf{D}_{Ts}^e p_p & \mathbf{D}_{Ts}^e p_f & \mathbf{D}_{Ts}^e T_s & 0 & 0 \\ 0 & \mathbf{D}_{Tp}^e p_p & 0 & 0 & \mathbf{D}_{Tp}^e T_p & 0 \\ 0 & 0 & \mathbf{D}_{Tf}^e p_f & 0 & 0 & \mathbf{D}_{Tf}^e T_f \end{bmatrix}, \quad (8.161)$$

$$\mathbb{K}^e = \begin{bmatrix} \mathbf{K}_{uu}^e & \mathbf{K}_{up_p}^e & \mathbf{K}_{up_f}^e & \mathbf{K}_{uT_s}^e & 0 & 0 \\ 0 & \mathbf{K}_{p_p p_p}^e & \mathbf{K}_{p_p p_f}^e & 0 & \mathbf{K}_{p_p T_p}^e & \mathbf{K}_{p_p T_f}^e \\ 0 & \mathbf{K}_{p_f p_p}^e & \mathbf{K}_{p_f p_f}^e & 0 & \mathbf{K}_{p_f T_p}^e & \mathbf{K}_{p_f T_f}^e \\ 0 & 0 & 0 & \mathbf{K}_{T_s T_s}^e & \mathbf{K}_{T_s T_p}^e & \mathbf{K}_{T_s T_f}^e \\ 0 & \mathbf{K}_{T_p p_p}^e & \mathbf{K}_{T_p p_f}^e & \mathbf{K}_{T_p T_s}^e & \mathbf{K}_{T_p T_p}^e & \mathbf{K}_{T_p T_f}^e \\ 0 & \mathbf{K}_{T_f p_p}^e & \mathbf{K}_{T_f p_f}^e & \mathbf{K}_{T_f T_s}^e & \mathbf{K}_{T_f T_p}^e & \mathbf{K}_{T_f T_f}^e \end{bmatrix}. \quad (8.162)$$

The detailed expression of these matrices is provided in Appendix H.3. The finite element code has been developed as part of this work. The four-node element (QUAD4) is used to interpolate all unknowns. The number of integration points is equal to two (in each spatial dimension), for all matrices and all residuals including the convective contributions. Iterations (index  $i$ ) are stopped when the tolerances below involving both the *overall scaled* residual and unknowns are satisfied:

$$\text{tol}_1: \quad |\mathbb{R}^i| / |\mathbb{R}^1| < 0.001$$

$$\text{tol}_2: \quad |x^i - x^{i-1}| / |x^i| < 0.001, \quad \text{for } x = u_j, p_p, p_f, T_s, T_p, T_f.$$

Each component of the residual vector is scaled by a representative value for the problem at hand as detailed in Section 8.3.

The time integration parameter  $\alpha$  is taken equal to  $2/3$ . Conditional stability characterizes non-linear transient convective-diffusive problems discretized with a full Newton-Raphson scheme (Belytschko and Hughes, 1983). The time step  $\Delta t$  is increased by fits and starts in the range  $[\Delta t_{\min}, \Delta t_{\max}]$  in order to keep the computation time within acceptable limits. The average number of Newton-Raphson iterations per time step has been observed to remain around 5. The lower bound  $\Delta t_{\min}$  is associated with the fastest diffusion time and is maintained constant until hydraulic steady state is reached, whereas  $\Delta t_{\max}$  is associated with the slowest remaining diffusion process.

To increase the accuracy of the solution in the vicinity of the injection well, the mesh is graded along the vertical direction according to a logarithmic rule.

### 8.4.6 HDR reservoir analysis

The thermo-hydro-mechanical constitutive equations are now used to investigate generic HDR reservoirs with various fracture spacings  $B$  subjected to hydraulic gradients and thermal loadings.

#### 8.4.6.1 Geometry of the HDR reservoir

An artificially fractured reservoir with horizontal injection and production wells is considered (Figure 8.29). The injection and the production wells are located at the bottom and at the top of the reservoir, respectively, and they penetrate the entire horizontal extent of the problem domain  $x_R$ . The problem definition requires information on the horizontal and vertical extents of the reservoir  $x_R$  and  $z_R$  respectively, on the average fracture spacing  $B$ , on the average fracture aperture  $2b$  and on the average permeability of the porous blocks  $k_p$ , which provide second porosity. The simulations assume a plane strain analysis, and the finite element mesh includes only half of the reservoir.

#### 8.4.6.2 Initial and boundary conditions

Prior to the circulation test, the reservoir is assumed to be in local thermal equilibrium, and the solid and the fluids have identical temperatures  $T^0 = T_s^0 = T_p^0 = T_f^0$ . Geothermal gradient is neglected. The initial pressures of the fluids  $p_p^0 = p_f^0 = \rho_f g z$  are assumed to be in hydrostatic equilibrium, proportional to the depth  $z$ , with the fluid densities  $\rho_p = \rho_f$ . The initial stress state is due to the overburden stress  $\sigma_z^0 = \sigma_v$  and to the lateral earth stress  $\sigma_x^0 = \sigma_H$ . Since, the fluids are initially in local thermal and hydraulic equilibria, the reference thermodynamic potentials of the fluids are equal:  $S^0 = S_p^0 = S_f^0$ ,  $G^0 = G_p^0 = G_f^0$ , and  $H^0 = H_p^0 = H_f^0$ .

The thermal, hydraulic and mechanical boundary conditions (BC) are shown in Figure 8.30.



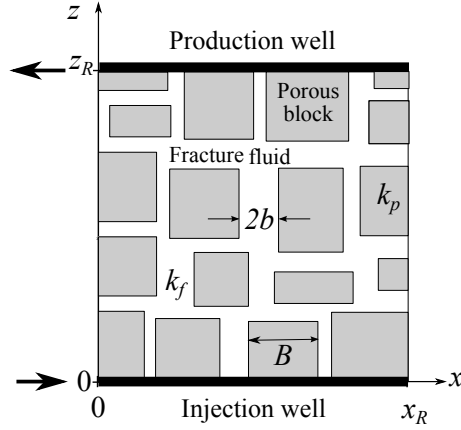


Figure 8.29: Representation of a generic HDR reservoir. The exact convective flow path is unknown and only the average fracture spacing  $B$  and  $n_f$  the porosity of the fracture network are required to obtain the average fracture aperture  $2b$ , eqn (8.165).  $k_p$  and  $k_f$  denote the permeabilities of the porous blocks and of the fracture network, respectively. The simulations assume a plane strain analysis, in the  $x - z$  plane. Symmetry with respect to  $z$ -axis is assumed.

(1) *Thermal boundary conditions:*

The injection temperature is applied to all the phases along the injection well ( $x \in [0, x_R], z = 0$ ). The remaining boundaries ( $x = 0, z \in ]0, z_R[$ ), ( $x \in [0, x_R], z = z_R$ ) and ( $x = x_R, z \in ]0, z_R[$ ) are insulated from the surroundings, that is  $\mathbf{q}_s \cdot \hat{\mathbf{n}} = \mathbf{q}_p \cdot \hat{\mathbf{n}} = \mathbf{q}_f \cdot \hat{\mathbf{n}} = 0$ ,  $\hat{\mathbf{n}}$  being the local unit outward normal to the reservoir.

(2) *Hydraulic boundary conditions:*

The injection and production pressures, denoted  $p_{\text{inj}}$  and  $p_{\text{out}}$ , are specified along the injection and the production wells, respectively, for the two fluid phases so that  $p_p(x \in [0, x_R], z = 0) = p_f(x \in [0, x_R], z = 0) = p_{\text{inj}}$  and  $p_p(x \in [0, x_R], z = z_R) = p_f(x \in [0, x_R], z = z_R) = p_{\text{out}}$ . The remaining boundaries ( $x = 0, z \in ]0, z_R[$ ) and ( $x = x_R, z \in ]0, z_R[$ ) are impermeable, i.e.  $\mathbf{J}_p \cdot \hat{\mathbf{n}} = \mathbf{J}_f \cdot \hat{\mathbf{n}} = 0$ .

(3) *Mechanical boundary conditions:*

The vertical stress  $\sigma_z = \sigma_z^0$  remains constant along the top boundary ( $x \in [0, x_R], z = z_R$ ) and similarly for the horizontal stress  $\sigma_x = \sigma_x^0$  along the lateral boundary ( $x = x_R, z \in [0, z_R]$ ), while the displacements on the other boundaries are specified as  $u_x(x = 0, z \in [0, z_R]) = 0$  and  $u_z(x \in [0, x_R], z = 0) = 0$ .

The influences of the spatial uniformity of the flow path and of the external heat supply on the thermal depletion of the reservoir have been addressed in Section 8.3. They are disregarded herein so as to focus on the specific influence of the dual porosity model.

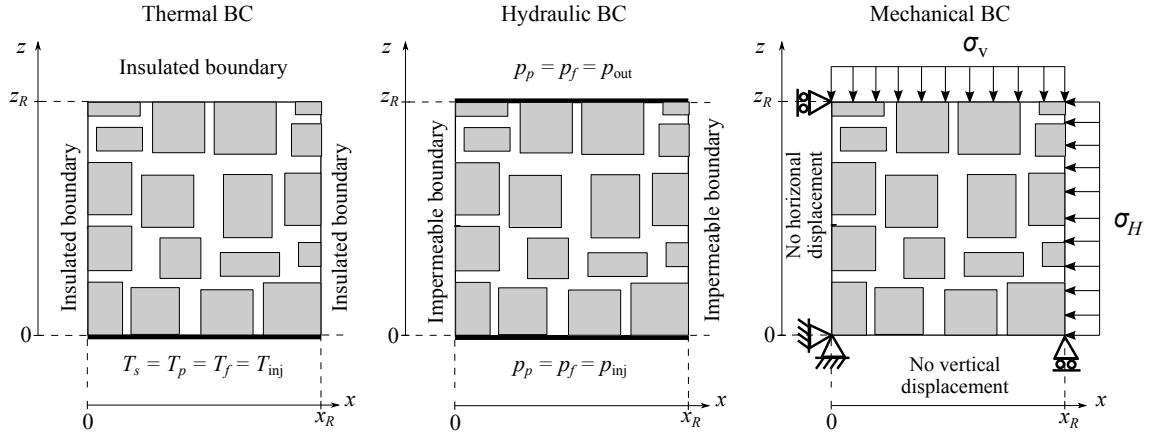


Figure 8.30: Thermal, hydraulic and mechanical boundary conditions (BC). Symmetry with respect to  $z$ -axis is assumed.

#### 8.4.6.3 Parameters related to the fracture spacing $B$

The fracture spacing  $B$  influences three material parameters used in the model, namely (1) the leakage parameter  $\eta$  [1/Pa.s], (2) the specific solid-to-fracture fluid heat transfer coefficient  $\kappa_{sf}$  [W/m<sup>3</sup>.K] and (3) the specific pore fluid-to-fracture fluid heat transfer coefficient  $\kappa_{pf}$  [W/m<sup>3</sup>.K].

(1) The leakage parameter  $\eta = \bar{\alpha} k_p / \mu_p \geq 0$  that controls the flow between the porous blocks and the fracture network draws from Barenblatt et al. (1960). In this double porosity context, the leakage parameter does not treat the two cavities symmetrically, and puts emphasis on the permeability of the porous blocks  $k_p$  which is lower than the permeability of the fracture network. The aperture factor  $\bar{\alpha}$  [1/m<sup>2</sup>] corresponding to the lowest permeable phase has been introduced by Warren and Root (1963),

$$\eta = \bar{\alpha} \frac{k_p}{\mu_p}, \quad \text{with} \quad \bar{\alpha} = \frac{4n(n+2)}{B^2}, \quad (8.163)$$

in which  $n = 2$  represents the space dimension.

(2) The specific solid-to-fracture fluid heat transfer coefficient  $\kappa_{sf}$  is usually defined as the product of the solid-to-fracture fluid specific surface  $S_{sf}^s$  [m<sup>2</sup>/m<sup>3</sup>] with the coefficient of solid-to-fracture fluid heat transfer  $h_{sf}$  [W/m<sup>2</sup>.K],

$$\kappa_{sf} = h_{sf} \times S_{sf}^s, \quad \text{with} \quad S_{sf}^s = \frac{4n_s}{B} \quad \text{for} \quad 2b \ll B. \quad (8.164)$$

where the specific surface  $S_{sf}^s$  is obtained by considering a porous block square of size  $B$  bordered by a fracture fluid of width  $b$ . The specific surface  $S_{sf}^s$  represents the ratio of the wetted solid surfaces over the total volume (de Marsily, 1986). The volume fraction  $n_f$  of the fracture fluid is then equal to

$$n_f = \frac{2 \times 2b}{B} \quad \text{for} \quad 2b \ll B, \quad (8.165)$$

so that, for a given fracture porosity  $n_f$ , the average fracture aperture  $2b$  increases with the fracture spacing  $B$ . By assuming that the effect of convection in the fracture fluid phase (perpendicular to the solid-fracture fluid interface) is negligible, the coefficient of solid-to-fracture fluid heat transfer  $h_{sf}$  may be quantitatively characterized by the sum of the thermal resistances of the two phases in series (Bejan, 1993),

$$\frac{1}{h_{sf}} = \frac{2b}{2n_f\Lambda_f} + \frac{B}{2n_s\Lambda_s}. \quad (8.166)$$

By inserting eqs (8.165) and (8.166) in eqn (8.164), the specific coefficient of heat transfer between the solid and the fracture fluid  $\kappa_{sf}$  is, in turn, linearly related to  $B^{-2}$ ,

$$\kappa_{sf} = \frac{8n_s}{B^2} \frac{n_s\Lambda_s \times 2\Lambda_f}{n_s\Lambda_s + 2\Lambda_f}. \quad (8.167)$$

It is worth noting that if  $n_s\Lambda_s \ll 2\Lambda_f$ , the above relation reduces to  $\kappa_{sf} = 8(n_s)^2\Lambda_s/B^2$  where the formulation does not treat the two phases symmetrically, *à la* Warren and Root (1963), and puts emphasis on the most insulating phase.

(3) Similarly, the specific pore fluid-to-fracture fluid heat transfer coefficient  $\kappa_{pf}$  is defined as the product of the pore fluid-to-fracture fluid specific surface  $S_{pf}^s$  [ $\text{m}^2/\text{m}^3$ ] with the coefficient of pore fluid-to-fracture fluid heat transfer  $h_{pf}$  [ $\text{W}/\text{m}^2\cdot\text{K}$ ],

$$\begin{aligned} \kappa_{pf} &= h_{pf} \times S_{pf}^s = \frac{8(n_p)^2\Lambda_p}{B^2}, \quad \text{with} \\ S_{pf}^s &= \frac{n_p}{n_s} \times S_{sf}^s \quad \text{and} \quad h_{pf} \approx \frac{2n_p\Lambda_p}{B}, \end{aligned} \quad (8.168)$$

for  $\Lambda_p = \Lambda_f$ ,  $2b \ll B$  and  $n_p \ll 1$ .

Consequently, the three coefficients  $\eta$ ,  $\kappa_{sf}$  and  $\kappa_{pf}$  scale with the inverse of the square of the fracture spacing  $B^{-2}$ , as illustrated in Table 8.5.

Parameter	Unit	Eqn	Fracture spacing $B$ [m]				
			0.01	1	10	13	20
$\eta$	[1/Pa.s]	(8.163)	$3.2 \cdot 10^{-12}$	$3.2 \cdot 10^{-16}$	$3.2 \cdot 10^{-18}$	$1.88 \cdot 10^{-18}$	$8.0 \cdot 10^{-19}$
$\kappa_{sf}$	[W/m <sup>3</sup> .K]	(8.167)	$6.18 \cdot 10^4$	6.18	$6.18 \cdot 10^{-2}$	$3.30 \cdot 10^{-2}$	$1.54 \cdot 10^{-2}$
$\kappa_{pf}$	[W/m <sup>3</sup> .K]	(8.168)	$1.2 \cdot 10^2$	$1.2 \cdot 10^{-2}$	$1.2 \cdot 10^{-4}$	$7.07 \cdot 10^{-5}$	$3.0 \cdot 10^{-5}$

Table 8.5: Sensitivity of the leakage parameter  $\eta$ , the specific solid-to-fracture fluid heat transfer coefficient  $\kappa_{sf}$  and the specific pore fluid-to-fracture fluid heat transfer coefficient  $\kappa_{pf}$  to the fracture spacing  $B$  for a two-dimensional fracture network  $n = 2$  endowed with a pore permeability  $k_p = 10^{-20} \text{m}^2$ , a fracture porosity  $n_f = 0.005$  and a pore porosity  $n_p = 0.05$ . The other material parameters are taken from Table 8.8.

Correlations of the solid-to-fracture fluid heat transfer coefficient  $h_{sf}$  have been proposed in the literature, with the Nusselt number (Wakao and Kaguei, 1982) and with a

capillary tube model (Zanotti and Carbonell, 1984). Few experimental works have investigated the magnitude of this coefficient (Pecker and Deresiewicz, 1973; Jiang et al., 2006). Instead, here, a calibration of the model with help of data provided from the two HDR reservoirs of Fenton Hill and Rosemanowes is proposed (Section 8.4.7). A sensitivity analysis is performed in Subsection 8.4.8.2 to determine the influence of the fracture spacing  $B$  on the results.

Boundary conditions	Value	Unit	Reference
Injection temperature $T_{\text{inj}}$	70	°C	Fig. 6-1 in 1
Initial in-situ temperature $T_s^0 = T_p^0 = T_f^0$	178	°C	Fig. 6-3 in 1
Initial production pressure $p_{\text{out}}^0 = \rho_f g z$ at $z = 2.673$ km	26.19	MPa	-
Initial injection pressure $p_{\text{inj}}^0 = \rho_f g z$ at $z = 2.903$ km	28.44	MPa	-
Imposed production overpressure	0.0	MPa	-
Imposed injection overpressure	9.0	MPa	Fig. 4-1 in 1
Overburden compressive stress $\sigma_v$	-75.0	MPa	2
Earth compressive stress $\sigma_H$	-37.5	MPa	2

Table 8.6: Initial and loading boundary conditions representative of Fenton Hill HDR reservoir, run segment 5. 1: Zylvoski et al. (1981). 2: Murphy et al. (1977).

Boundary conditions	Value	Unit	Reference
Injection temperature $T_{\text{inj}}$	23	°C	1
Initial in-situ temperature $T_s^0 = T_p^0 = T_f^0$	83.5	°C	2
Initial production pressure $p_{\text{out}} = \rho_f g z$ at $z = 2.160$ km	21.12	MPa	-
Initial injection pressure $p_{\text{inj}} = \rho_f g z$ at $z = 2.490$ km	24.35	MPa	-
Imposed production overpressure	0.0	MPa	-
Imposed injection overpressure	10.0	MPa	Fig. 6 in 2
Overburden compressive stress $\sigma_v$ at $z_{\text{av}} = 2.325$ km	-60.4	MPa	3
Earth compressive stress $\sigma_H$ at $z_{\text{av}} = 2.325$ km	-65.11	MPa	3

Table 8.7: Initial and loading boundary conditions representative of Rosemanowes HDR reservoir, RH12/RH15 system. 1: Hicks et al. (1996). 2: Richards et al. (1994). 3: Bruel (1995).

Unless the fracture spacing tends to zero, the dual porosity model will *not* recover the response of the single porosity model since it accounts for the presence of the pore fluid in the balance of momentum and in the balance of energy equations, while the single porosity model does not recognize the pore fluid.

#### 8.4.7 Calibration with field data

The thermal response obtained from the thermo-hydro-mechanical model may be compared with field results from the literature. Two hot dry rock reservoirs are investigated: (1) Fenton Hill, New Mexico, USA, and (2) Rosemanowes, Cornwall, UK. The time profiles of the fracture fluid temperature (at the production well) are scrutinized alone in Figure

Material parameter	Value	Unit	Reference
Drained Young's modulus $E$	38.9	GPa	1
Drained Poisson's ratio $\nu$	0.3	-	1
Volumetric thermal expansion $c_T$	$3.3 \times 10^{-6}$	1/K	2
Compressibility ratio $c_p/c$	0.9	-	3
Fracture network porosity $n_f$	$< 0.01$	-	1
Porosity of the porous blocks $n_p$	$10 \times n_f$	-	4
Fracture network permeability $k_f$	$< 10^{-13}$	m <sup>2</sup>	1
Permeability of the porous blocks $k_p$	$\geq 10^{-20}$	m <sup>2</sup>	1
	$\leq 10^{-18}$	m <sup>2</sup>	1
Solid grains compressibility $c_s$	$2.7 \times 10^{-11}$	1/Pa	1
Solid thermal diffusivity $\alpha_{T,s}$	$1.1 \times 10^{-6}$	m <sup>2</sup> /s	5
Solid thermal conductivity $\Lambda_s$	2.71	W/m.K	5
Solid specific heat capacity $C_{s,v}$	948.55	J/kg.K	6
Solid density $\rho_s$	2600	kg/m <sup>3</sup>	6
Fluid compressibilities $c_{pH} = c_{fH}$	$4.54 \times 10^{-10}$	1/Pa	6
Fluid thermal expansion $c_{pT} = c_{fT}$	$10^{-3}$	1/K	6
Fluid dynamic viscosities $\mu_p = \mu_f$	$3 \times 10^{-4}$	Pa.s	6
Fluid thermal conductivities $\Lambda_p = \Lambda_f$	0.6	W/m.K	6
Thermo-osmosis coefficients $\Theta_p = \Theta_f$	0	m <sup>2</sup> /s.K	6
Fluid specific heat capacities $C_{p,p} = C_{f,p}$	4275	J/kg.K	5
Fluid densities $\rho_p = \rho_f$	980.0	kg/m <sup>3</sup>	6
Fluid thermal diffusivities $\alpha_{T,p} = \alpha_{T,f}$	$1.58 \times 10^{-7}$	m <sup>2</sup> /s	-
Solid-to-pore fluid heat transfer coef. $\kappa_{sp}$	$10^4$	W/m <sup>3</sup> .K	7

Table 8.8: Input parameters representative of Fenton Hill HDR reservoir, run segment 5. 1: Murphy et al. (1977). 2: Zyvoloski et al. (1981). 3: Wilson and Aifantis (1982). 4: First estimation owing to the rather high pressure of the overburden rock. 5: Elsworth (1989). 6: Estimated parameters for water. 7: Local thermal equilibrium is enforced between the pore fluid phase and the solid phase owing to the absence of convection, to their similar thermal diffusivities  $\alpha_{T,s} \approx \alpha_{T,p} \times 10$ , and to the large specific surface  $S_{sp}^s$ .

8.31, even if the numerical results presented in this section describe a complete thermo-hydro-mechanical problem. The response in terms of fluid pressures and effective stress will be studied in Section 8.4.8 for Fenton Hill HDR reservoir only. The reservoirs are described with a dual porosity model in LTNE and the simulations assume a plane strain analysis. Furthermore, the triple point of water is used as a reference (Kestin, 1968, p. 513) so that the reference entropy and chemical potential are set to  $S^0 = 2.101$  kJ/K.kg and  $G^0 = -187.6$  kJ/kg, respectively.

For a LTNE analysis, the time profile of the temperature depletion is characterized by three stages: (a) the first stage represents the abrupt propagation of the injection temperature dominated by convection; (b) the second stage characterizes the heat transfer between the fracture fluid phase and the porous blocks and (c) the third stage represents the final thermal depletion of the porous medium. The least well-defined of the material parameters required for a thermo-hydro-mechanical simulation in LTNE are the fracture

Material parameter	Value	Unit	Reference
Drained Young's modulus $E$	40.0	GPa	1
Drained Poisson's ratio $\nu$	0.25	-	2
Volumetric thermal expansion $c_T$	$3.3 \times 10^{-6}$	1/K	3
Compressibility ratio $c_p/c$	0.9	-	4
Fracture network porosity $n_f$	$< 0.01$	-	5
Porosity of the porous block $n_p$	$10 \times n_f$	-	6
Fracture network permeability $k_f$	$\leq 10^{-13}$	m <sup>2</sup>	1
Permeability of the porous block $k_p$	$10^{-18}$	m <sup>2</sup>	5
Solid grains compressibility $c_s$	$2.0 \times 10^{-11}$	1/Pa	3
Solid thermal diffusivity $\alpha_{T,s}$	$1.29 \times 10^{-6}$	m <sup>2</sup> /s	-
Solid thermal conductivity $\Lambda_s$	2.8	W/m.K	1
Solid specific heat capacity $C_{s,v}$	822.1	J/kg.K	7
Solid density $\rho_s$	2642	kg/m <sup>3</sup>	7
Fluid hydraulic compressibilities $c_{pH} = c_{fH}$	$4.54 \times 10^{-10}$	1/Pa	3
Fluid thermal compressibilities $c_{pT} = c_{fT}$	$0.65 \times 10^{-3}$	1/K	3
Fluid dynamic viscosities $\mu_p = \mu_f$	$6 \times 10^{-4}$	Pa.s	5
Fluid thermal conductivities $\Lambda_p = \Lambda_f$	0.68	W/m.K	7
Thermo-osmosis coefficients $\Theta_p = \Theta_f$	0	m <sup>2</sup> /s.K	3
Fluid specific heat capacities $C_{p,p} = C_{f,p}$	4219.8	J/kg.K	7
Fluid densities $\rho_p = \rho_f$	978.0	kg/m <sup>3</sup>	7
Fluid thermal diffusivities $\alpha_{T,p} = \alpha_{T,f}$	$1.67 \times 10^{-7}$	m <sup>2</sup> /s	-
Solid-to-pore fluid heat transfer coefficient $\kappa_{sp}$	$10^4$	W/m <sup>3</sup> .K	8

Table 8.9: Input parameters representative of Rosemanowes HDR reservoir. 1: Bruel (1995). 2: Armstead and Tester (1987). 3: Estimated parameters for water or granite. 4: Wilson and Aifantis (1982). 5: Richards et al. (1994). 6: First estimation owing to the rather high pressure of the overburden rock. 7: Kolditz and Clauser (1998). 8: Local thermal equilibrium is enforced between the pore fluid phase and the solid phase owing to the absence of convection, to their similar thermal diffusivities  $\alpha_{T,s} \approx \alpha_{T,p} \times 10$ , and to the large specific surface  $S_{sp}^s$ .

permeability  $k_f$ , the fracture porosity  $n_f$  and the solid-to-fracture fluid *specific* heat transfer coefficient  $\kappa_{sf}$ . These coefficients are calibrated so that the numerical response matches the field response based on the following procedure: (i) the fracture network permeability  $k_f$  is obtained so that the end of the first stage matches the field data; (ii) the fracture network porosity  $n_f$  is adjusted so that the duration of the second stage matches the rest of the response and (iii) the optimum solid-to-fracture fluid heat transfer coefficient  $\kappa_{sf}$  is obtained so that the temperature magnitude of the second stage best fits the field data.

#### 8.4.7.1 Fenton Hill reservoir

The circulation test was induced between the depths 2903 m and 2667 m with an average reservoir height of  $z_R = 230$  m. Experimental results for the test 'segment-5' are reported in Zyvoloski et al. (1981). The horizontal half-width of the permeable reservoir is arbitrarily

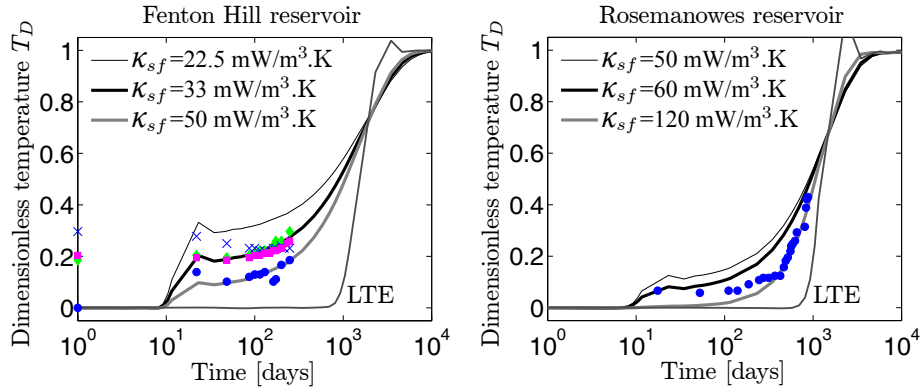


Figure 8.31: Relative temperature outlet  $T_D = (T^0 - T_f(z = z_R))/(T^0 - T_{inj})$  versus time in days. LTE stands for local thermal equilibrium and is obtained for  $\kappa_{sf} = 100$  W/m<sup>3</sup>.K. Colors are available on the electronic version. (left) Fenton Hill hot dry rock reservoir with  $k_f = 8.0 \cdot 10^{-15}$  m<sup>2</sup> and  $n_f = 0.005$ . Field data pertain to  $\circ$  2703 m,  $\diamond$  2673 m,  $\times$  2626 m and  $\square$  in the casing 2660 m (Zyvoloski et al., 1981). The optimum specific solid-to-fracture fluid heat transfer coefficient  $\kappa_{sf}$  is equal to 33 mW/m<sup>3</sup>.K. (right) Rosemanowes hot dry rock reservoir with  $k_f = 3.2 \cdot 10^{-14}$  m<sup>2</sup>,  $n_f = 0.005$ . Field data pertain to  $\circ$  the casing shoe of the production well ( $\approx 2125$  m in true vertical depth) (Kolditz and Clauser, 1998). The optimum specific solid-to-fracture fluid heat transfer coefficient  $\kappa_{sf}$  lies in the range 60 to 120 mW/m<sup>3</sup>.K. The late overshooting oscillations for the LTE solution are due to an imperfect damping of the convective contribution (Section 8.3).

chosen equal to  $x_R = 200$  m. Loading boundary conditions and material parameters are documented in Tables 8.6 and 8.8, in which the hydrostatic pressure gradient between the injection and the production wells is imposed.

The thermo-hydro-mechanical model for this LTNE analysis recovers well the field response for the combination of fracture permeability  $k_f = 8.0 \cdot 10^{-15}$  m<sup>2</sup>, fracture porosity  $n_f = 0.005$  and *specific* solid-to-fracture fluid heat transfer coefficient  $\kappa_{sf} = 33$  mW/m<sup>3</sup>.K. This set of calibrated parameters is the same as for a single porosity model if the thermal diffusivity of the solid phase is replaced by the thermal diffusivity of the porous blocks (the ‘equivalent’ solid phase).

If the calibrated material parameters are considered suitable, the fracture spacing can be calculated with eqn (8.167),  $B = 13$  m which matches well the 10 m magnitude proposed in Figure 3.2 of Zyvoloski et al. (1981). Furthermore, the solid-to-fracture fluid heat transfer coefficient  $h_{sf}$  can be estimated to  $h_{sf} = 0.12$  W/m<sup>2</sup>.K.

It is worth noting that the field data for Fenton Hill reservoir display spatially heterogeneous initial rock temperatures (Zyvoloski et al., 1981). This situation is attributed to circulation in the hot dry rock reservoir before the circulation tests. The initial temperature  $T^0$  used to calculate the relative temperature  $T_D$  and to perform the calibrations in Figure 8.31, left, represents the temperature at the lowest outlet point  $z = 2703$  m. If the initial temperature  $T^0$  is chosen at a higher outlet point  $z > 2703$  m, the calibrations hold for higher values of the solid-to-fracture fluid heat transfer  $\kappa_{sf}$ .

#### 8.4.7.2 Rosemanowes reservoir

This second circulation test was performed between the depths 2490 m and 2160 m with an average reservoir height of  $z_R = 330$  m. The horizontal half-width of the permeable reservoir is also chosen equal to  $x_R = 200$  m. Loading boundary conditions and material parameters are documented in Tables 8.7 and 8.9. The setup and the boundary conditions are similar to the Fenton Hill simulation so as to simplify the implementation. The experimental results for the RH12/RH15 system reported in Kolditz and Clauser (1998), their Figure 5, provide the data for the calibration.

The thermo-hydro-mechanical LTNE model recovers well the field response for the combination of fracture permeability  $k_f = 3.2 \cdot 10^{-14} \text{ m}^2$ , fracture porosity  $n_f = 0.005$  and *specific* solid-to-fracture fluid heat transfer coefficient  $\kappa_{sf}$  in the range 60 to 120 mW/m<sup>3</sup>.K. The lack of accuracy of the calibration is most probably due to the simplified setup assumed for the numerical simulations: in the field, the wells are not horizontal and the fracture permeability is not uniform within the reservoir. Furthermore, significant water loss (45%) was generated owing to the unconfined nature of the reservoir (Brown et al., 1999), and to its lack of stability (Bruel, 2002) leading to the development of short-circuit flow paths.

The calibration of the specific solid-to-fracture fluid heat transfer coefficient  $\kappa_{sf}$  yields the same order of magnitude for both hot dry rock reservoirs, which indicates that the order of magnitude is reliable. The comparisons between the field results and the model simulations demonstrate responses in local thermal non-equilibrium, characterized by three stages, which again provides confidence in the LTNE model.

#### 8.4.8 Thermo-hydro-mechanical response

The calibration of the thermo-hydro-mechanical model is now used to perform coupled simulations on the Fenton Hill HDR reservoir. Emphasis is laid on delineating the differences in the response of the geothermal system in terms of temperatures, fluid pressures and effective stress, as inferred by the single and dual porosity models. Special attention is devoted to the fracture spacing  $B$ . Some details of the constitutive model are also addressed, including the influence of the thermodynamic potentials  $S^0$  and  $G^0$  and the unconnected porosity limit.

For the material parameters associated with Fenton Hill reservoir, we hypothesize that the dual porosity concept will provide a response in the range of a single porosity model and of a dual porosity model endowed with a low pore permeability (lower than the expected value presented in Table 8.8). Furthermore, the dual porosity model is endowed with a mass transfer law which allows the permeation of fluid from the fractures towards the pores. It is expected that large fracture spacings reduce the thermally induced tensile stress and fluid loss: this phenomenon highlights a key feature of sparsely fractured reservoirs with respect to densely fractured reservoirs.

For the circulation tests simulated, the energy exchanges due to mass transfer  $\hat{\rho}_p H_p$  and  $\hat{\rho}_f H_f$  appearing in the energy equations of the fluids (8.148) and (8.149) have been



checked to have virtually no influence on the overall response.

Results are presented in Figures 8.32 to 8.40. The sign convention of continuum mechanics is used, compressive stresses being negative.

#### 8.4.8.1 Dual porosity model versus single porosity model

The thermo-hydro-mechanical response of fractured media in a LTNE analysis can be sought with two types of models: (2P) models developed for dual porous media involving two pressures and three temperatures or (1P) models developed for single porous media as summarized in Appendix H.1 and involving one pressure and two temperatures. Both types are used to predict the thermo-hydro-mechanical behavior of the Fenton Hill HDR reservoir in Figures 8.32 and 8.33. As a simplification here, the (2P) model assumes the temperatures of the solid and of the pore fluid to be identical. Still, two sub-options are considered: (i) the pores are connected to each other with a large permeability  $k_p = 10^{-18} \text{ m}^2$  and (ii) the pores are connected to each other with a low permeability  $k_p = 10^{-21} \text{ m}^2$  so that both the diffusive flow in the pores and the mass transfer are small.

The dual porosity response with a large pore permeability (and hence large mass transfer) is expected to range between the response of the single porosity model (1P), since no pore pressure counterbalance effect is accounted for in the effective stress, and the dual porosity response with a low pore permeability, since the induced pore pressure will dissipate slowly due to the small mass transfer.

The material parameters matching field data for the Fenton Hill HDR reservoir are used, that is, permeability of the fracture network  $k_f = 8.0 \cdot 10^{-15} \text{ m}^2$ , volume fraction of the fracture fluid  $n_f = 0.005$  and specific solid-to-fracture fluid heat transfer coefficient  $\kappa_{sf} = 33 \text{ mW/m}^3 \cdot \text{K}$ . The triple point of water is used as a reference. The initial and loading boundary conditions are detailed in Sect. 8.4.6.2. The leakage parameter  $\eta$  is estimated from (8.163) for the material parameters presented in Table 8.8 and for the average fracture spacing  $B = 13 \text{ m}$  (Sect. 8.4.7.1). The vertical profiles at time  $t = 1.9$  years of the temperatures, fluid pressures and stress changes from the initial state  $\Delta \bar{\sigma} = \bar{\sigma} - \bar{\sigma}^0$  plotted in Figures 8.32 and 8.33 illustrate the late time of the numerical test. The coupled thermo-hydro-mechanical response at early time  $t = 34.72$  days is presented next in Figure 8.34.

The coupled behavior of fractured media in thermal and hydraulic non-equilibria is governed by the difference in characteristic times between the thermal depletion of the fracture fluid phase and of the solid/pore fluid phases (Figure 8.32, top). The significant difference in temperature between the fracture fluid and the porous blocks correlates with their highly distinct masses and volumes. Indeed, heat diffuses by conduction in the porous blocks which are endowed with a large volume  $n_s + n_p = 0.995$ . On the other hand, the temperature of the fracture fluid propagates by convection and thermal depletion is much faster than in the porous blocks.

The solid temperature responses provided by the single porosity model (1P), the dual

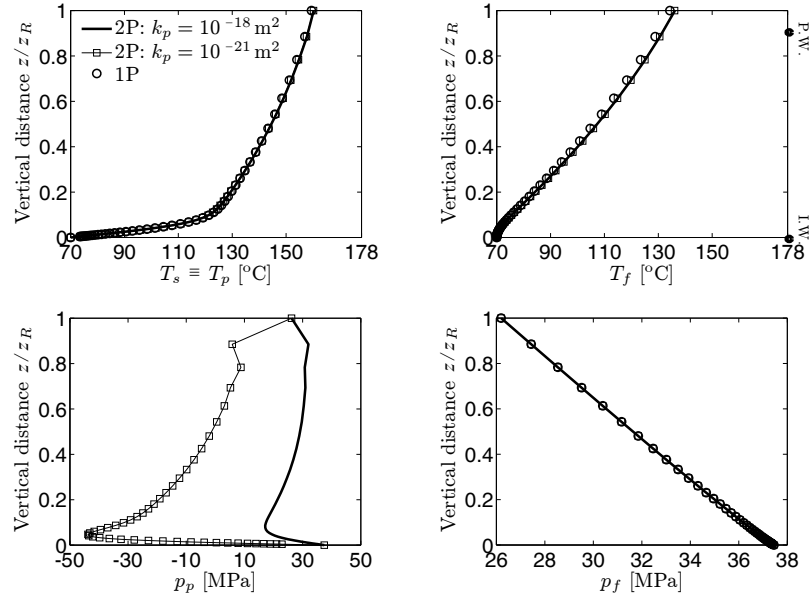


Figure 8.32: Fenton Hill reservoir, late time ( $t = 1.9$  years) vertical profiles of the temperatures of solid and pore fluid (top-left), the temperature of fracture fluid (top-right), the pressure of pore fluid (bottom-left), and the pressure of fracture fluid (bottom-right) for  $k_f = 8.0 \cdot 10^{-15} \text{ m}^2$ ,  $n_f = 0.005$ ,  $\kappa_{sf} = 33 \text{ mW/m}^3 \cdot \text{K}$  and  $B = 13 \text{ m}$  (Sect. 8.4.7.1). I.W. stands for injection well and P.W. for production well. The responses of the various models match for the temperatures and for the fracture fluid pressure. On the other hand, the pore pressure response of the dual porosity model displays a pressure drop near the injection point. The magnitude of the pressure drop is controlled by the diffusivity ratio  $R_p$  and is larger for smaller pore permeability ( $k_p = 10^{-21} \text{ m}^2$ ). The single porosity model leaves out of account the pore pressure response. Regarding the pore pressure, the dual porosity response for  $k_p = 10^{-18} \text{ m}^2$  is bounded by the dual porosity response for smaller pore permeabilities and by the fracture fluid pressure (1P), close to the injection well  $z/z_R < 0.3$ .

porosity model (2P) with a large pore permeability ( $k_p = 10^{-18} \text{ m}^2$ ) and with a small pore permeability ( $k_p = 10^{-21} \text{ m}^2$ ) almost match and are not influenced by the pressure and the strain fields. Hence, the calibration proposed in Sect. 8.4.7 remains valid for all models.

As expected from the large fracture permeability  $k_f = 8.0 \cdot 10^{-15} \text{ m}^2$ , the response of the fracture fluid pressure varies little from one model to the other as opposed to that of the pore fluid pressure. The single porosity model disregards the pore fluid pressure. The dual porosity model displays a decrease in pore pressure induced by the thermal contraction of the solid phase. Indeed, since (1) the pore fluid is embedded into the solid phase which controls fully the magnitude of the thermal contraction and (2) the coefficient of thermal expansion of the fluid  $c_{pT}$  is approximatively 300 times greater than that of the solid phase  $c_T$ , the pore pressure decrease is governed by the thermal depletion of the solid phase.

On the other hand, the magnitude of the pore pressure peak is controlled by the hydraulic to thermal diffusivity ratio  $R_p = \sqrt{\alpha_{H,p}/\alpha_{T,p}}$ . The lower  $R_p$ , the greater the pore fluid pressure response. Hence, for the dual porosity model with  $k_p = 10^{-21} \text{ m}^2$ ,  $R_p$  is small and the pore pressure drop is large compared with the dual porosity model with

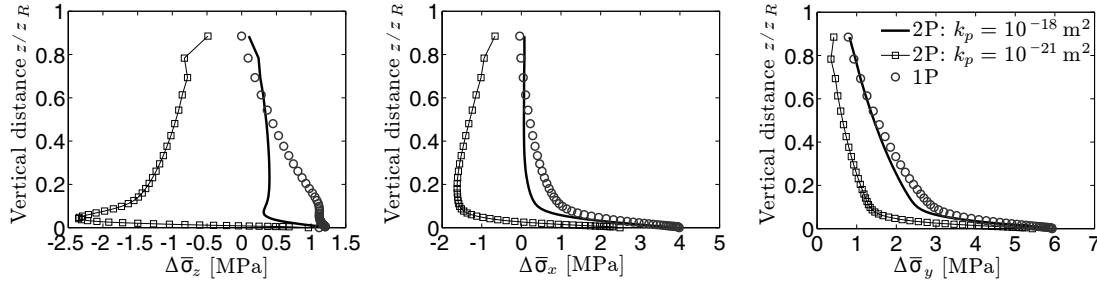


Figure 8.33: Fenton Hill reservoir, late time ( $t = 1.9$  years) vertical profiles of the changes in vertical effective stress (left), lateral effective stress (middle) and out-of-plane effective stress (right). Tensile stresses are counted positive. Owing to the pore pressure contribution, the stress responses described by the single porosity model (1P) are not equivalent to the responses described by the dual porosity model. The single porosity model predicts a thermally induced tensile stress in the vicinity of the injection well, whereas the dual porosity model predicts a smaller tensile stress ( $\Delta\bar{\sigma}_x$  and  $\Delta\bar{\sigma}_y$ ) and an increase of compressive stress ( $\Delta\bar{\sigma}_z$ ). The pore pressure drop counterbalances the contraction induced by the solid temperature. As expected, the dual porosity response with  $k_p = 10^{-18} \text{ m}^2$  is bounded by the single porosity and by the dual porosity with  $k_p = 10^{-21} \text{ m}^2$  responses, close to the injection well  $z/z_R < 0.3$ .

$k_p = 10^{-18} \text{ m}^2$  in which the pore pressure drop dissipates through the connected pores and through mass transfer with the fracture network.

While the thermal depletion of the various phases is the same for all the proposed models, the vertical effective stress is significantly influenced by the pore pressure contribution which tends to damp ( $k_p = 10^{-18} \text{ m}^2$ ) or to suppress ( $k_p = 10^{-21} \text{ m}^2$ ) the thermally induced tensile stress (1P) (Figure 8.33). Interestingly, the effective stress response predicted by the dual porosity model for a large pore permeability is bounded by the single porosity response and by the dual porosity response for a small pore permeability, close to the injection well  $z/z_R < 0.3$ .

The response of the dual porosity model is fully recovered by the single porosity model in the particular case of small fracture spacings  $B \rightarrow 0$  as presented in the next subsection in Figure 8.35. This phenomenon is consistent with the fact that, for very small fracture spacings  $B$ , fractured media lose their spatial and time scale separation characteristics, which are the two main hypotheses of the dual porosity concept. Once local thermal and hydraulic equilibria are reached, the dual porosity model is indeed expected to reduce to a single porosity model in LTE with porosity equal to the sum of the fracture and pore porosities and permeability equal to the sum of the fracture and pore permeabilities.

Moreover, the early mechanism of fluid loss is a consequence of the law of mass transfer induced by the jump in scaled chemical potentials between the two fluids. During the early time  $t = 34.72$  days, the thermal front propagates in the fracture fluid only, while the porous blocks are almost thermally undisturbed as shown in Figure 8.34 for  $k_p = 10^{-21} \text{ m}^2$ . Consequently, the thermally induced contraction of the pore fluid is small and restricted to the vicinity of the injection well. On the other hand, the temperature difference between the pore fluid and the fracture fluid leads to a large mass transfer from the fractures towards

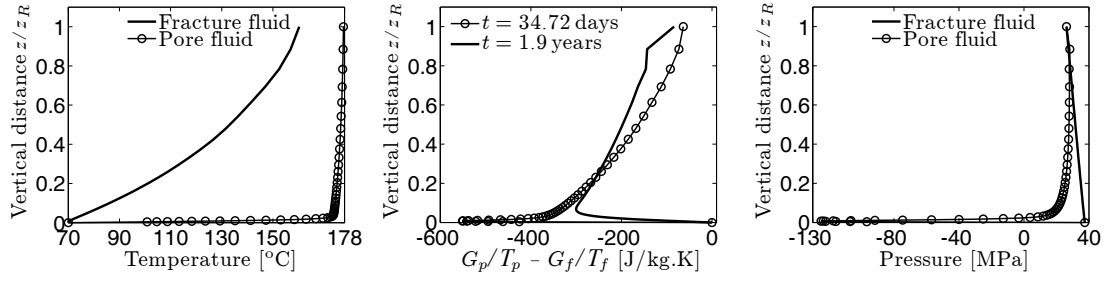


Figure 8.34: Fenton Hill reservoir, early time ( $t = 34.72$  days) vertical profiles of fluid temperatures (left), and fluid pressures (right), and jump in scaled chemical potential at early and late times (middle). At early time, the temperature of the fracture fluid decreases, whereas the temperature of the pore fluid remains high. This large difference associated with a negative difference in scaled chemical potentials  $G_p/T_p - G_f/T_f < 0$  induces a large transfer of mass from the fracture network towards the porous blocks, which is characterized by a significant pore pressure drop, while the fracture fluid pressure remains undisturbed as in Figure 8.32. This behavior matches the observations of field experiments Murphy et al. (1981).

the porous blocks. This large mass transfer is characterized by a large pore pressure drop, to which the thermal contraction contributes a little, and by an increase in compressive effective stress. This model response matches with typical field observations: Murphy et al. (1981) report that the permeation of fluid to the porous blocks is large during the early time and decreases with time.

In summary, the dual porosity model allows a more accurate description of the coupled thermo-hydro-mechanical behavior of fractured reservoirs compared with a single porosity model. In particular, the distinct responses between early time and late time provide information on the permeation mechanism and on the stress path history, which is a key element in view of damage prediction.

#### 8.4.8.2 Influence of the fracture spacing $B$

In Subsection 8.4.6.3, the leakage parameter  $\eta \propto B^{-2}$ , the specific solid-to-fracture fluid heat transfer coefficient  $\kappa_{sf} \propto B^{-2}$  and the specific pore fluid-to-fracture fluid heat transfer coefficient  $\kappa_{pf} \propto B^{-2}$  have been estimated based on the fracture spacing  $B$ . The latter controls *simultaneously* the mass transfer and the heat transfer. The influence of the fracture spacing  $B$  is considered in the range from 0 to 20 m, so that the lower bound recovers the single porosity response and the upper bound represents a realistic large value (Table 8.5).

The material parameters matching field data for the Fenton Hill HDR reservoir are used, that is  $k_f = 8.0 \cdot 10^{-15} \text{ m}^2$  and  $n_f = 0.005$ . Again, the triple point of water is used as reference. The boundary conditions are detailed in Section 8.4.6.2. The vertical profiles of the temperatures and of the fluid pressures are plotted in Figure 8.35 for the late time  $t = 1.9$  years. The effective stress and the strain responses are presented in Figures 8.36 and 8.37, respectively.

For small values of  $B$ , LTE between the solid phase and the fluid phases is enforced.

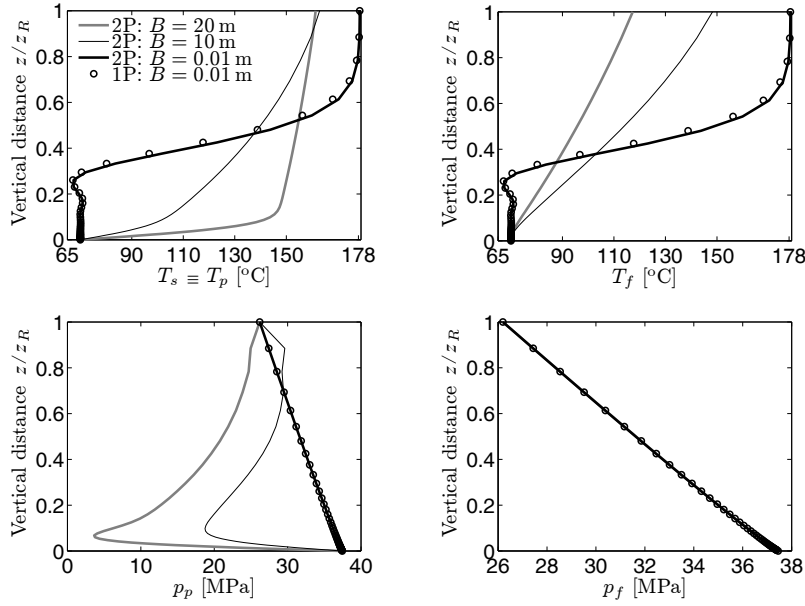


Figure 8.35: Fenton Hill reservoir, late time ( $t = 1.9$  years) vertical profiles of solid and pore fluid temperatures (top-left), fracture fluid temperature (top-right), pore fluid pressure (bottom-left) and fracture fluid pressure (bottom-right) for  $k_f = 8.0 \cdot 10^{-15} \text{ m}^2$ ,  $k_p = 10^{-20} \text{ m}^2$  and  $n_f = 0.005$ . A small fracture spacing  $B$  represents a dense fracture network that overlaps the response of the single porosity model, whereas a large  $B$  represents a sparsely fractured reservoir. The fracture spacing  $B$  controls the departure from *both* hydraulic and thermal equilibria. Hydraulic equilibrium is not recovered unless thermal equilibrium is attained, which takes place only for  $B \rightarrow 0$ . Solely, the fracture fluid pressure is not influenced by the fracture spacing  $B$ . The overshooting oscillations for the temperature solutions near  $z/z_R = 0.2$  are again due to an imperfect damping of the convective contribution, Sec. 8.3, which slightly pollutes the stress and the strain responses (Figures 8.36 and 8.37).

Indeed, a small  $B$  represents a dense fracture network and reduces the spatial scale and the time scale separation between the porous blocks and the fracture network. Conversely, a large fracture spacing  $B = 10 \text{ m}$  reduces the specific surface area between the solid phase and the fracture fluid phase so that a LTNE model is required.

The fracture spacing  $B$  influences greatly the pore pressure response for the reasons explained earlier, whereas, the fracture fluid pressure remains undisturbed owing to its large permeability. It is worth noting that hydraulic equilibrium is not recovered unless thermal equilibrium is attained which *only* takes place for  $B \rightarrow 0$  or at large times. This situation is due to the fact that the force driving mass transfer is a non-linear contribution in the form of a difference in scaled chemical potentials,  $G_p/T_p - G_f/T_f$ , between the pore fluid and the fracture fluid.

The change in effective stress results from the deformation and the solid temperature contributions. When both hydraulic and thermal equilibria are reached ( $B \rightarrow 0$ ), the effective stress components become more tensile close to the injection area  $z/z_R < 0.3$ , the final state being more tensile than the initial state. An increase of fracture spacing  $B$  induces simultaneously (1) a departure from thermal equilibrium and thus a slower

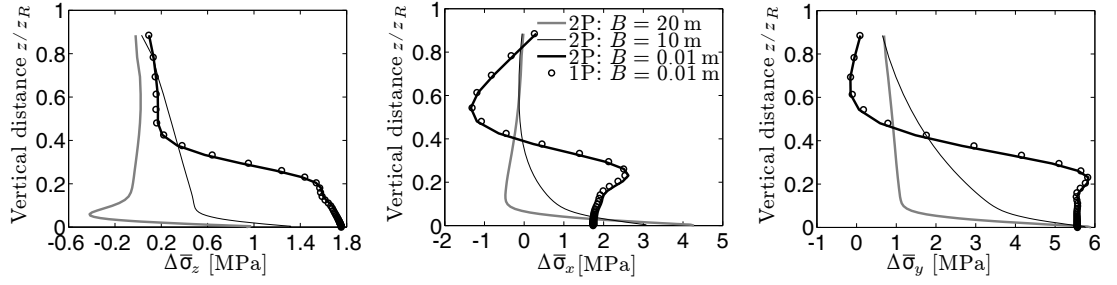


Figure 8.36: Fenton Hill reservoir, late time ( $t = 1.9$  years) vertical profiles of the changes in vertical effective stress (left), in lateral effective stress (middle) and in out-of-plane effective stress (right) for  $k_f = 8.0 \cdot 10^{-15} \text{ m}^2$ ,  $k_p = 10^{-20} \text{ m}^2$  and  $n_f = 0.005$ . For small fracture spacings  $B \rightarrow 0$ , hydraulic and thermal equilibria are reached and the changes in effective stress are tensile close to the injection area  $z/z_R < 0.3$ . In addition, the single porosity response is well recovered. The dual porosity model reveals that large fracture spacings  $B$  reduce the pore pressure and therefore the effective stress  $\bar{\sigma} = \sigma + \xi_p p_p \mathbf{I} + \xi_f p_f \mathbf{I}$  is more compressive.

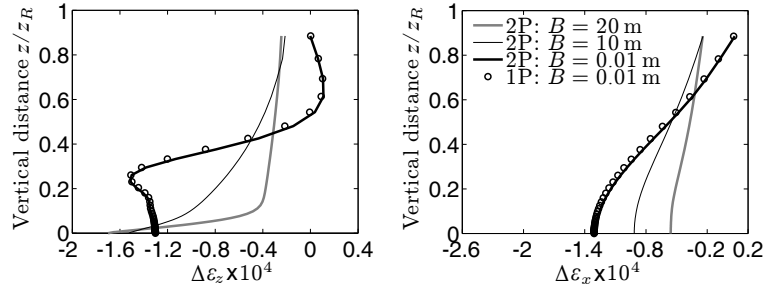


Figure 8.37: Fenton Hill reservoir, late time ( $t = 1.9$  years) vertical profiles of the changes in vertical strain (left) and in lateral strain (right) with the same parameters as in Figure 8.36. For small fracture spacings  $B \rightarrow 0$ , hydraulic and thermal equilibria are reached and negative strains close to the injection area  $z/z_R < 0.3$  characterize a sharp thermally induced contraction. In addition, the single porosity response is well recovered. The dual porosity model reveals that large fracture spacings  $B$  reduce the thermally induced contraction of the rock in the vicinity of the injection well and thereby the potential for aperture enlargement of the micro-fractures or pores.

thermal depletion of the solid phase, and (2) a departure from hydraulic equilibrium and consequently a larger drop in pore pressure. These two contributions entail the change in effective stress by reducing (1) the rate of thermally induced stress and (2) the thermally induced tensile effective stress near the injection point.

The thermally induced contraction of the rock may have two adverse effects, a beneficial effect by increasing the aperture of fractures and a negative effect by increasing the aperture of the micro-fractures or pores. The first effect may favor the growth of the reservoir, whereas the second effect may favor fluid loss. The dual porosity model reveals that large fracture spacings  $B$  reduce significantly the thermally induced contraction of the rock in the vicinity of the injection well (Figure 8.37) and thereby the aforementioned effects, in particular the second negative effect. This observation advises against fracture clouds composed of many fractures with small spacings and argues in favor of multiple fracture systems with large fracture spacings (Tenzer, 2001, Figure 2).

### 8.4.8.3 Influence of the reference thermodynamic potentials $S^0$ and $G^0$

The chemical potential (8.134) controls the rate of mass transfer (8.138). It is defined in terms of the reference thermodynamic potentials  $S^0$  and  $G^0$ . A sensitivity analysis is proposed for two sets of reference thermodynamic potentials:

- (1) for the first set, the injection state of the circulation test is used as reference:  $S_{\text{inj}} = 0.0$  and  $G_{\text{inj}} = 0.0$  for  $T_{\text{inj}} = 70^\circ\text{C}$ ,  $p_{\text{inj}} = 27.44\text{ MPa}$  ;
- (2) for the second set, the triple point of water is used as reference:  $S_{\text{TPW}} = 0.0$  and  $G_{\text{TPW}} = 0.0$  for  $T_{\text{TPW}} = 0.01^\circ\text{C}$ ,  $p_{\text{TPW}} = 611.2\text{ Pa}$ .

reference state	$S^0$ (kJ/K.kg)	$G^0$ (kJ/kg)
injection of the circulation test	1.136	-79.3
triple point of water	2.101	-187.6

Table 8.10: Two possible definitions of the reference thermodynamic potentials.

The ensuing thermodynamic potentials are listed in Table 8.10. The contours of the scaled chemical potential displayed in Figure 8.38 show a quantitative, rather than qualitative, influence of the reference potentials  $S^0$  and  $G^0$ .

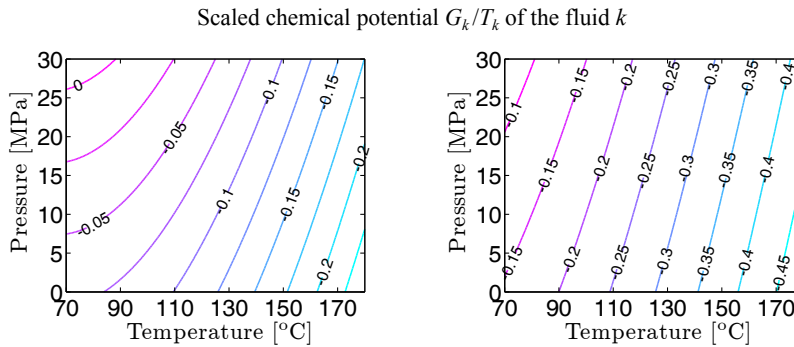


Figure 8.38: Scaled chemical potential [ $\text{J}/\text{kg.K.10}^3$ ] as a function of temperature and pressure in a range appropriate to the present analysis. The material data are issued from Tables 8.6 and 8.8. (left): the injection state of the circulation test is taken as reference; (right): the triple point of water is taken as a reference.

The tests of the previous subsection have been re-run, with the same material parameters, boundary conditions and initial conditions as detailed in Table 8.6. If the injection state of the circulation test is used as reference, mass transfer reduces in magnitude. However, the consequences on the various elements of the reservoir response, temperatures, pressures and stresses, are quite small at the late time  $t = 1.9$  years as shown in Figure 8.39. Hence, the conclusions provided in subsections 8.4.8.1 and 8.4.8.2 are not affected.

### 8.4.8.4 Unconnected porosity

If the pore permeability tends to zero  $k_p \rightarrow 0$ , the response obtained with a single porosity model detailed in Appendix H.1 should be recovered. This is the case if the porous block

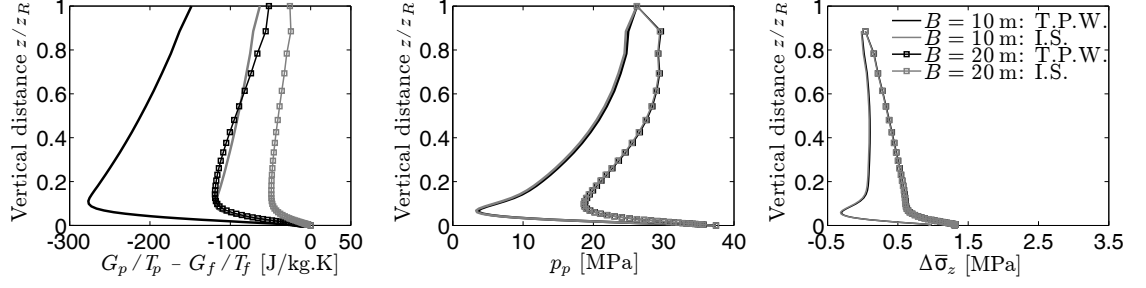


Figure 8.39: Fenton Hill reservoir, late time ( $t = 1.9$  years) vertical profiles of jump in scaled chemical potentials (left), pore fluid pressure (middle), and change in vertical effective stress (right) for  $k_f = 8.0 \cdot 10^{-15} \text{ m}^2$ ,  $k_p = 10^{-20} \text{ m}^2$  and  $n_f = 0.005$ . I.S. : the injection state of the circulation test is used as a reference. T.P.W. : the triple point of water is used as a reference. Mass transfer is larger for T.P.W. Although the pore pressure drop dissipates more effectively for larger mass transfer, the consequences on the reservoir response are quite small. For the pore fluid pressure and the change in vertical effective stress, the T.P.W. and the I.S. responses superpose.

compressibility  $c_p$  is adequately estimated.  $c_p$  characterizes the intermediate stress-state of a loading decomposition problem (Khalili and Valliappan, 1996) which can be represented by the hydraulic characteristic time needed for the pore fluid to exit the porous block,

$$t_H = \frac{B^2}{4\alpha_H}, \quad \alpha_H = \frac{k_p}{\mu_p} \frac{2\mu^{DS}(1-\nu)}{1-2\nu} \left[ \frac{A^2(1+\nu_u)^2(1-2\nu)}{9(1-\nu_u)(\nu_u-\nu)} \right], \quad (8.169)$$

in which  $\alpha_H$  is the hydraulic diffusivity of the porous blocks,  $A$  is the Skempton coefficient and  $\nu_u$  is the undrained Poisson's ratio,

$$\frac{1}{A} = 1 + n_f \frac{c_{p,H} - c_s}{c - c_s}, \quad \nu_u = \frac{3\nu + A(1-2\nu)(1 - c_s/c)}{3 - A(1-2\nu)(1 - c_s/c)}. \quad (8.170)$$

For geothermal reservoirs, the maximum time scale of the problem would be approximately  $t_{\max} \approx 30$  years, so that during the time span of interest, the porous block will remain undrained if  $t_H > t_{\max}$  and  $c_p = c_s$  should be enforced. The latter time constraint provides a bound to the permeability,

$$k_p < \frac{B^2}{4} \frac{\mu_p}{t_{\max}} \frac{1-2\nu}{2\mu^{DS}(1-\nu)} \left[ \frac{9(1-\nu_u)(\nu_u-\nu)}{A^2(1+\nu_u)^2(1-2\nu)} \right] \approx 2.3 \times 10^{-23} \text{ m}^2 \quad (8.171)$$

below which a single porosity model can be safely used, i.e. the pore pressure influence can be disregarded. For higher permeabilities, the dual porosity model should be used to capture the correct stress evolution. It should be noted that for  $t \approx t_H$ , the pore pressure (induced by both early mass transfer and by thermal contraction) remains large and negative (Figure 8.40) which means that further fracturing cannot occur in the porous blocks and that any opening will be confined to the existing fractures. These aspects cannot be predicted using a single porosity model which will indicate tensile stresses irrespective of the situation in the blocks.



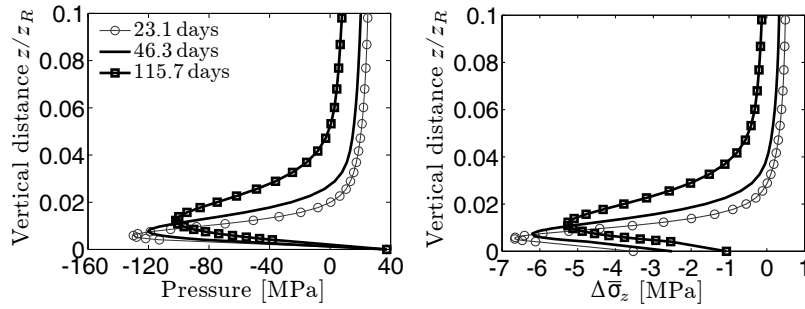


Figure 8.40: Fenton Hill reservoir close to the injection well  $z/z_R \leq 0.1$ , vertical profiles of pore pressure (left) and change in vertical effective stress (right) for  $k_f = 8.0 \cdot 10^{-15} \text{ m}^2$ ,  $k_p = 10^{-21} \text{ m}^2$ ,  $B = 13 \text{ m}$  and  $n_f = 0.005$ . The hydraulic characteristic time is  $t_H \approx 40$  days. For times close to  $t_H$ , the pore pressure remains high and negative. However, for  $t > t_H$  the excessive pore pressure can dissipate in the fracture network.

### 8.4.9 Conclusions

The main concern here has been to develop thermo-hydro-mechanical constitutive equations that exhibit key features of fractured media in local thermal non-equilibrium. A model describing the behavior of poro-elastic dual porous media has been extended to account for thermal contributions within a rational thermodynamics framework. The constitutive equations have been motivated and restricted by the Clausius-Duhem inequality to characterize the thermo-mechanical transfer and diffusion constitutive relations. Earlier poro-mechanical analyses, starting from Barenblatt et al. (1960), have considered the fluid transfer between the two cavities to be driven by the pressure jump. The extension to a mixture in local thermal non-equilibrium indicates that the driving engine for this mass transfer is the jump of the scaled chemical potential.

A finite element approximation has been developed that accounts for these constitutive features, and the thermo-hydro-mechanical couplings. The primary variables are the displacements, the pressures in the two cavities and the temperatures of the three phases. The non-linear field equations are solved using a full Newton-Raphson procedure. This finite element analysis has been employed to investigate the mechanisms of deformation, diffusion, forced convection and transfer in the context of heat extraction from a fractured hot dry rock reservoir.

Prior to the description of long term circulation tests, three parameters of the model have been calibrated with field data from two instrumented HDR reservoirs, namely from the Fenton Hill and Rosemanowes sites. Simulations highlight a local thermal non-equilibrium response characterized by three stages.

A sensitivity analysis has been carried out to study the influences of the dual porosity model and of the fracture spacing on the phase temperatures, the fluid pressures, and the effective stress. As expected, the dual porosity model provides, close to the injection well, a thermo-hydro-mechanical response which is bounded by the single porosity response and by the dual porosity response endowed with a low pore permeability. The drop in the thermally induced pore pressure is more pronounced when the fracture spacing is large.

Hence, large fracture spacings tend to increase the compressive effective stress. In view of potential fluid loss due to the thermally induced rock contraction, the aforementioned effect advises against densely fractured reservoirs in favor of multiple fracture systems with large fracture spacings.

Accounting only for the fracture fluid and disregarding the pore pressure contribution, the single porosity approach overestimates the thermal contraction of fractured reservoirs. A dual porosity approach delivers information, (1) on fluid permeation in the porous matrix; (2) on the beneficial effect of the pore pressure contribution towards thermally induced stress; (3) on the history of the stress path and (4) on the optimum fracture spacing to reduce fluid loss induced by thermal contraction. Actually, the dual porosity response recovers well the field observations, e.g. Murphy et al. (1981), that fluid loss is high at the beginning of the circulation test and decreases with time.

# Summary and conclusions

## General

The main objective of this study was to develop a constitutive model for the fully coupled analysis of heat flow, hydraulic flow and deformation in saturated dual porous media. The main tasks accomplished were: (1) formulation of the governing equations for the coupled thermo-poro-elastic deformation, generalised flows and generalised transfer processes within a mixture in local thermal non-equilibrium, (2) interpretation and identification of the constitutive parameters, (3) implementation of the comprehensive equations in a finite element code using a non-linear numerical scheme, (4) validation of the proposed model and of the corresponding numerical code using analytical solutions from the literature, (5) application of the model to a borehole stability analysis, (6) implementation of the streamline-upwind/Petrov-Galerkin method to treat the convective terms and (7) application of the model to the prediction of heat extraction in enhanced geothermal reservoirs.

## A thermo-hydro-mechanical model for dual porous media

A constitutive model was developed as part of this investigation to describe the coupled behaviour of fully saturated, dual porous media subject to thermo-hydro-mechanical loadings including those able to cause local thermal non-equilibrium.

The field equations were developed using the theory of mixtures. The deformation equation for the mixture as a whole was derived by satisfying the equation of momentum. The equations governing the flow of fluids were established from the conservation equations of mass for each sub-cavity, namely the porous block and the fissure network. The equations governing the flow of heat were established from the balance equations of energy for each phase of the mixture.

The constitutive equations were obtained within a rational thermodynamic framework. The entropy inequality, also called the Clausius-Duhem inequality, was stated for the mixture as a whole so as to motivate and to provide restrictive informations on coupling phenomena in between phases. Three types of constitutive equations were required by the thermodynamic theory: (1) The thermo-mechanical constitutive equations which describe a reversible process governed by the thermo-poro-elastic theory; (2) the generalised

diffusion equations and (3) the generalised transfer equations which describe irreversible processes and were simplified by assuming symmetry properties.

The thermo-poro-elastic constitutive law was obtained through the effective concept which was identified within a loading decomposition of a planar element. The generalised diffusion constitutive law was obtained by coupling Darcy's law and Fourier's law. The uncoupled mass and energy transfer constitutive laws were obtained so as to recover the same transfer fluxes when reducing to a hydro-mechanical model and to a single porosity model, respectively.

The comprehensive equations were written using a mixed formulation where the basic variables were solid matrix displacement vector, fluid pressures of the porous block and of the fissure network, and temperatures of solid and of the fluids.

## **Constitutive parameters: interpretation and identification**

Particular attention was given to identification and determination of the model parameters. A range of values of these parameters for typical soils, rocks and water were gathered from the literature. The constitutive parameters characteristic of dual porous media were expressed in terms of constants measurable through experiments performed at different scales. Extensive parameters were described within a typical range of temperature to restrict appropriately the thermodynamic potentials. The coefficients of thermo-osmosis and of volumetric inter-phase heat transfer were investigated through experimental data and theoretical correlations which highlighted the difficulties to identify their magnitude.

## **The numerical implementation: finite element method**

Numerical solution to the comprehensive equations was obtained using the finite element approach. The fully coupled governing equations were discretised using the Galerkin method, while time integration of the rate equations was accomplished using a predictor-multi-corrector algorithm. Two explicit/implicit partitions were proposed with a particular focus on the convection contributions. The non-linear first-order semi-discrete equations were solved so as to force the exact form of the residual to vanish; whereas, the global effective diffusion matrix, central in the implementation, was linearised.

## **Preliminary numerical results**

The thermal contributions of the proposed model were validated using several numerical examples. A simplified single porosity mixture in local thermal equilibrium with no convection was considered. Numerical predictions were compared with analytical solutions from the literature for a semi-infinite one-dimensional column of porous media subject to (1) a fixed temperature loading and (2) a fixed thermal flux loading, for both (i) a drained

boundary and (ii) an undrained boundary. The results were satisfactory and showed the model was highly sensitive to thermal shocks which required a step loading function to achieve acceptable accuracy. Furthermore, an axi-symmetric boundary value problem was analysed in a purely mechanical context and an optimisation of the mesh was proposed to minimise the errors on the displacement, the strain and the stress.

## **A borehole stability analysis: focus on diffusion and mass transfer**

A borehole stability problem of a fractured reservoir in a thermally enhanced oil recovery context was addressed which highlighted the importance of the difference between the characteristic times of the diffusion phenomena. A parametric analysis was developed to study the influence of the leakage parameter on the pore pressure, the fissure network pressure and the effective stresses in the vicinity of the wellbore. Numerical solutions showed the effective stress was mostly controlled by the pore pressure, which induced a reduction in compressive effective stress for low leakage parameter values. It was found that dual porosity media displayed a higher failure potential compared with an associated single porosity medium. This result was strengthened if a semi-permeable boundary condition on the porous block was applied compared with a permeable boundary condition at the wellbore lining.

## **The streamline-upwind/Petrov-Galerkin method**

Numerical solution to the energy equations containing convection terms required stabilisation. The streamline-upwind/Petrov-Galerkin approach was implemented and tested for various uncoupled convection-dominated diffusion-convection problems for which optimum stabilisation parameters were sought. Numerical predictions were compared with analytical solutions from the literature for (1) a one-dimension steady case, (2) a one-dimension transient case, (3) a two-dimension steady case and (4) a two-dimension transient case. The results were satisfactory and showed that the accuracy of the thermal response was highly sensitive to the *ad-hoc* stabilisation parameter. The streamline-upwind/Petrov-Galerkin method may require additional support in the form of the discontinuity capturing method to accurately damp overshooting/undershooting oscillations. Few numerical works have investigated the implementation of the streamline-upwind/Petrov-Galerkin method as part of a coupled constitutive model for porous media.

## **Simulation of heat extraction in geothermal reservoirs**

The coupled thermo-hydro-mechanical model developed specifically for saturated dual porous media was applied to the simulation of heat extraction in geothermal reservoirs.

The streamline-upwind/Petrov-Galerkin method was extended to stabilise the model and the weak formulation was developed for both a mixture in local thermal non-equilibrium and for a mixture in local thermal equilibrium. The stabilisation and the convergence of the numerical results were then tested within a simplified single porosity mixture in local thermal equilibrium.

Thermal recovery from a hot dry rock reservoir described with a fractured medium in local thermal non-equilibrium was investigated. The characteristic time before local thermal equilibrium is established, referred to as local thermal non-equilibrium, was controlled by the volumetric solid-to-fracture fluid heat transfer coefficient. A parametric analysis was carried out to study the influence of the local thermal non-equilibrium assumption on the fluid thermal output response. The numerical temperature response was characterised, at the outlet of the reservoir, by a double-step pattern. The latter was representing successively (1) the initial convection of the fluid, (2) the transfer of heat between the solid and the fluid, and (3) the final depletion of the mixture. The model was then used to describe the thermo-hydro-mechanical behaviour of a long term circulation test on the Fenton Hill hot dry rock reservoir. The least well-defined material parameters were calibrated with experimental data and the comparison with the numerical results demonstrated a local thermal non-equilibrium response. Although calibrated, the numerical predictions were able to match, with great accuracy, the experimental data.

With a single porosity model, the thermally induced fluid pressure drop was very small in magnitude and was confined to the early time response. Later, the thermally induced effective stresses were tensile near the injection well due to the thermal contraction of the solid, suggesting a possible increase of fracture aperture, and compressive near the production well due to the pull-in of the producing area.

On the other hand, the dual porosity model predicts a significant thermally induced pore pressure drop during the late response, for sparsely fractured media. This situation is due to the mass transfer force that is the difference in modified chemical potentials between the pore fluid and the fissure fluid. The dual porosity model suggests that sparsely fractured media are less sensitive to thermal contraction and to fluid losses than heavily fractured media. This conclusion would explain partially the relative success of the Fenton Hill hot dry rock reservoir and of the Soultz-sous-Forêt project as opposed to the Rosemanowes hot dry rock reservoir. Furthermore, the new transfer law recovered well field observations that fluid losses were large initially and decreased with time.

## **Recommendations for further research**

Three topics worthy of further research are described below.

The first topic is to investigate the effects of forced convection for a borehole stability problem of a fractured reservoir in a thermally enhanced oil recovery context. It is expected that the thermally induced pore pressure increase would induce a significant increase of porous block permeability which would favor the transportation of the fracture fluid in the

vicinity of the well. To investigate this effect it would be worthwhile to perform further numerical tests on typical tight reservoirs so as to evaluate the influences of stiff thermal loadings.

The second topic stems from the idea that the specific surface area of the porous block - fracture fluid system varies proportionally to the fracture fluid porosity and to the inverse of the fracture aperture. This empirical formula, which is used throughout the study of heat extraction in enhanced geothermal reservoirs, requires verification against experimental data. Laboratory experiments on saturated fractured igneous rocks may be performed using testing techniques capable of measuring dual porosity material parameters.

The third topic involves performing adequate experimental tests so as to measure the pore pressure variation in igneous fractured rocks with forced convection in a context of heat extraction from an enhanced geothermal reservoir. Ideally, the tests would be compared with numerical results to calibrate accurately the mass transfer law, that is the reference entropy and the reference chemical potential. This would allow a proper prediction of the optimum fracture spacing so as to minimise fluid losses from thermal contraction. However, pressure and stress results of field tests, in the vicinity of the wells and deep into the reservoirs, would also be of great interest.

# Bibliography

- Y. Abousleiman and S. Ekbote. Solutions for the inclined borehole in a porothermoelastic transversely isotropic medium. *ASME Journal of Applied Mechanics*, 72:102–114, 2005.
- P.M. Adler and J.F. Thovert. *Fractures and fracture networks*. Kluwer Academic Publishers, 1999.
- E.C. Aifantis. Introducing a multi-porous medium. *Developments in Mechanics*, 8:209–211, 1977.
- E.C. Aifantis. On the response of fissured rocks. *Developments in Mechanics*, 10:249–253, 1979.
- E.C. Aifantis. On the problem of diffusion in solids. *Acta Mechanica*, 37:265–296, 1980a.
- E.C. Aifantis. Further comments on the problem of heat extraction from hot dry rocks. *Mechanics Research Communications*, 7(4):219–226, 1980b.
- E.C. Aifantis and D.E. Beskos. Heat extraction from hot dry rocks. *Mechanics Research Communications*, 7(3):165–170, 1980.
- T. Aktan and F. Ali. Finite element analysis of temperature and thermal stresses induced by hot water injection. In *Conference: Spring meeting of the Society of Petroleum Engineers, Amsterdam, the Netherlands*, 1976.
- B. Alazmi and K. Vafai. Analysis of variants within the porous media transport models. *Journal of heat transfer*, 122:303–327, 2000.
- K.F. Alexander and K. Wirtz. Thermal osmosis in aqueous systems. *Z. Physik. Chem*, 195:165, 1950.
- H.C.H. Armstead and J.W. Tester. *Heat mining*. Methuen Inc., New York, NY, 1987.
- R.J. Atkin and R.E. Craine. Continuum theories of mixtures: basic theory and historical development. *The Quarterly Journal of Mechanics and Applied Mathematics*, 29(2):209, 1976.
- J.L. Auriault and C. Boutin. Deformable porous media with double porosity. quasi-statics. i: Coupling effects. *Transport in Porous Media*, 7:63–82, 1992.



- J.L. Auriault and C. Boutin. Deformable porous media with double porosity. quasi-statics. ii: Memory effects. *Transport in Porous Media*, 10:153–169, 1993.
- B. Bai. Thermal consolidation of layered porous half-space to variable thermal loading. *Applied Mathematics and Mechanics*, 27(11):1531–1539, 2006.
- M. Bai and Y. Abousleiman. Thermoporoelastic coupling with application to consolidation. *International Journal for Numerical and Analytical Methods in Geomechanics*, 21:121–132, 1997.
- M. Bai and J.C. Rogiers. Fluid flow and heat flow in deformable fractured porous media. *International Journal of Engineering Science*, 32:1615–1633, 1994.
- M. Bai, D. Elsworth, and J.C. Rogiers. Modeling of naturally fractured reservoirs using deformation dependent flow mechanism. *International Journal of Rock Mechanics and Mining Sciences*, 30:1185–1191, 1993.
- M. Bai, J.C. Roegiers, and D. Elsworth. Poromechanical response of fractured-porous rock masses. *Journal of Petroleum Science and Engineering*, 13(3-4):155–168, 1995.
- M. Bai, Y. Abousleiman, L. Cui, and J. Zhang. Dual-porosity poroelastic modeling of generalized plane strain. *International Journal of Rock Mechanics and Mining Sciences*, 36:1087–1094, 1999.
- G.I. Barenblatt, U.P. Zheltov, and G.H. Kochina. Basic concepts in the theory of seepage of homogeneous liquids in fissured rocks. *Journal of Applied Mathematics and Mechanics, English Translation*, 24:1286–1303, 1960.
- A. Bataillé, P. Genthon, M. Rabinowicz, and B. Fritz. Modeling the coupling between free and forced convection in a vertical permeable slot: implications for the heat production of an Enhanced Geothermal System. *Geothermics*, 35(5-6):654–682, 2006.
- J. Bear and Y. Bachmat. *Introduction to modeling of transport phenomena in porous media*. Springer the Netherlands, 1991.
- J. Bear and M.Y. Corapcioglu. A mathematical model for consolidation in a thermoelastic aquifer due to hot water injection or pumping. *Water Resources Research*, 17:723–736, 1981.
- A. Bejan. *Heat Transfer*. John Wiley & Sons, Inc., 1993.
- T. Belytschko and T.J.R. Hughes. *Computational methods for transient analysis*. Amsterdam, North-Holland (Computational Methods in Mechanics), 1983.
- M.A. Biot. General theory of three-dimensional consolidation. *Journal of Applied Physics*, 12:155–164, 1941.

- M.A. Biot. Variational Lagrangian-thermodynamics of nonisothermal finite strain mechanics of porous solids and thermomolecular diffusion. *International Journal of Solids and Structures*, 13(6):579–597, 1977.
- D. Bourdet and A.C. Gringarten. Determination of fissure volume and block size in fractured reservoirs by type-curve analysis. In *Paper SPE 9293 presented at the SPE Annual Technical Conference and Exhibition, Dallas*, 1980.
- R.M. Bowen and P.J. Chen. Waves in a binary mixture of linear elastic materials. *Journal de Mécanique*, 14:237–266, 1975.
- R.M. Bowen and D.J. Garcia. On the thermodynamics of mixtures with several temperatures. *International Journal of Engineering Science*, 8:63–83, 1970.
- K.M. Bower and G. Zyzolowski. A numerical model for thermo-hydro-mechanical coupling in fractured rock. *International Journal of Rock Mechanics and Mining Sciences*, 34(8):1201–1211, 1997.
- A.N. Brooks and T.J.R. Hughes. Streamline upwind/ Petrov-galerkin formulations for convection dominated flows with particular emphasis on the incompressible Navier-Stokes equations. *Computer Methods in Applied Mechanics and Engineering*, 32:199–259, 1982.
- D. Brown, R. DuTeaux, P. Kruger, D. Swenson, and T. Yamaguchi. Fluid circulation and heat extraction from engineered geothermal reservoirs. *Geothermics*, 28(4-5):553–572, 1999.
- D.H. Jr. Brownell, S.K. Garg, and J.W. Pritchett. Governing equations for geothermal reservoirs. *Water Resources Research*, 13:929–934, 1977.
- D. Bruel. Heat extraction modelling from forced fluid flow through stimulated fractured rock masses: application to the Rosemanowes hot dry rock reservoir. *Geothermics*, 24(3):361–374, 1995.
- D. Bruel. Impact of Induced Thermal Stresses During Circulation Tests in an Engineered Fractured Geothermal Reservoir: Example of the Soultz-sous-Forêts European Hot Fractured Rock Geothermal Project, Rhine Graben, France. *Oil & Gas Science and Technology*, 57(5):459–470, 2002.
- J. Burger, P. Sourieau, and M. Combarous. *Thermal methods of oil recovery*. Éditions Technip, 1985.
- R. Burridge and J.B. Keller. Poroelasticity equations derived from microstructure. *The Journal of the Acoustical Society of America*, 70:1140, 1981.
- C. Callari and F. Federico. Fem validation of a double porosity elastic model for consolidation of structurally complex clayey soils. *International Journal for Numerical and Analytical Methods in Geomechanics*, 24:367–402, 2000.

- C.L. Carnahan. Thermodynamic coupling of heat and matter flows in near-field regions of nuclear waste repositories. *Materials Research Society Proc. Symp.*, 26:1023–1030, 1984.
- H.S. Carslaw and J.C. Jaeger. *Conduction of Heat in Solids*. Oxford University Press 2nd edn., 1959.
- G. Chen and R.T. Ewy. Thermoporoelastic effect on wellbore stability. *Society of Petroleum Engineers Journal*, 10(2):121–129, 2005.
- G. Chen, M.E. Chenevert, M.M. Sharma, and M. Yu. A study of wellbore stability in shales including poroelastic, chemical, and thermal effects. *Journal of Petroleum Science and Engineering*, 38:167–176, 2003.
- H.Y. Chen and L. Teufel. Coupling fluid-flow and geomechanics in dual-porosity modeling of naturally fractured reservoirs. In *SPE Annual Technical Conference and Exhibition*, 1997.
- X. Chen, C.P. Tan, and C.M. Haberfield. Guidelines for efficient wellbore stability analysis. *International Journal of Rock Mechanics & Mining Sciences*, 34:3–4, 1997.
- A.H.D. Cheng, A. Ghassemi, and E. Detournay. Integral equation solution of heat extraction from a fracture in hot dry rock. *International Journal for Numerical and Analytical Methods in Geomechanics*, 25(13):1327–1338, 2001.
- R.M. Christensen. *Mechanics of Composite Materials*. Wiley, New York, 1979.
- B.D. Coleman and W. Noll. The thermodynamics of elastic materials with heat conduction and viscosity. *Archive for Rational Mechanics and Analysis*, 13(1):167–178, 1963.
- S.C. Cowin. Summary of discussion on fluid infiltrated geomaterials. In *Mechanics of Geomaterials*, Z.P. Bazant, pages 581–582. Wiley, New York, 1985.
- S.C. Cowin. *Bone Mechanics Handbook*. CRC Press LLC, 2001.
- V. De La Cruz and T.J.T. Spanos. Thermomechanical coupling during seismic wave propagation in a porous medium. *Journal of Geophysical Research*, 94(B1):637–642, 1989.
- G. de Marsily. *Quantitative Hydrogeology*. Academic Press, Masson Paris, 1986.
- J.E. Dendy. Two methods of galerkin-type achieving optimum  $l^2$  rates of convergence for first order hyperbolics. *SIAM Journal on Numerical Analysis*, 11:637–653, 1974.
- E. Detournay and A.H.D. Cheng. *Fundamentals of poroelasticity in Comprehensive rock engineering: principles, practice and projects, vol. II*. Pergamon Press, New York, 1993.
- C. Dirksen. Thermo-osmosis through compacted saturated clay membranes. *Soil Science Society of America Proc.*, 33:821–826, 1969.

- D.C. Drucker and W. Prager. Soil mechanics and plastic analysis for limit design. *Quarterly of Applied Mathematics*, 10(2):157–165, 1952.
- D.S. Drumheller. *Introduction to wave propagation in nonlinear fluids and solids*. Cambridge University Press, 1998.
- R. DuTeaux, D. Swenson, and B. Hardeman. Insight from modelling discrete fractures using GEOCRACK. Technical report, Mechanical Engineering, Kansas State University, Manhattan, KS, 1996.
- A. Dybbs and R.V. Edwards. *Fundamentals of Transport Phenomena in Porous Media*, chapter A new look at porous media fluid mechanics—Darcy to turbulent, pages 199–254. Martinus Nijhoff, Dordrecht, 1984.
- D. Elsworth. Theory of Thermal Recovery From a Spherically Stimulated Hot Dry Rock Reservoir. *Journal of Geophysical Research*, 94(B2):1927–1934, 1989.
- D. Elsworth and M. Bai. Flow-deformation response of dual-porosity media. *Journal of Geotechnical Engineering*, 118(1):107–124, 1992.
- A.C. Eringen and J.D. Ingram. A continuum theory of chemically reacting media. *International Journal of Engineering Science*, 3:197–212, 1965.
- K. Evans, B. Valley, M. Häring, R.J. Hopkirk, C. Baujard, T. Kohl, T. Mégel, L. André, S. Portier, and F.D. Vuataz. Studies and support for the EGS reservoirs at Soultz-sous-Forêts. Final report April 2004 - May 2009, 2009.
- V.D. Fachinotti, S. Le Corre, N. Triolet, M. Bobadilla, and M. Bellet. Two-phase thermo-mechanical and macrosegregation modelling of binary alloys solidification with emphasis on the secondary cooling stage of steel slab continuous casting processes. *International Journal for Numerical Methods in Engineering*, 67(10):1341–1384, 2006.
- L.P. Franca, G. Hauke, and A. Masud. Revisiting stabilized finite element methods for the advective-diffusive equation. *Computer Methods in Applied Mechanics and Engineering*, 195(13-16):1560–1572, 2006.
- Bertrand Francois. *Thermo-plasticity of fine-grained soils at various saturation states: application to nuclear waste disposal*. PhD thesis, Ecole Polytechnique Fédérale de Lausanne, 2008.
- T.P. Fries and H.G. Matthies. A review of petrov-galerkin stabilization approaches and an extension to meshfree methods. In *Informatikbericht-Nr. 2004-01*, Technical University Braunschweig, Brunswick, 2004.
- A. Gajo. A non-linear analysis of non-isothermal wave propagation in linear-elastic fluid-saturated porous media. *International Journal of Plasticity*, 18:313–344, 2002.

- A. Gajo and B. Loret. Finite element simulations of chemo-mechanical coupling in elastic-plastic homoionic expansive clays. *Computer Methods in Applied Mechanics and Engineering*, 192:3489–3530, 2003.
- H. Gebrande. Elasticity of rocks and minerals. In *Numerical data and Functional Relationship in Science and Technology. Group V: Geophysics and Space Research (1B)*, Springer, Berlin: 1-99, 1982.
- R. Gelet, B. Loret, and N. Khalili. Thermal recovery from a fractured medium in local thermal non-equilibrium. *International Journal of Heat and Mass transfer*, Submitted: ?, 2011.
- J.G. Georgiadis and I. Catton. Stochastic modeling of unidirectional fluid transport in uniform and random packed beds. *Physics of Fluids*, 30:1017–1022, 1987.
- H. Gercek. Poisson's ratio values for rocks. *International Journal of Rock Mechanics and Mining Sciences*, 44(1):1–13, 2007.
- H.R. Ghafouri and W. Lewis. A finite element double porosity model for heterogeneous deformable porous media. *International Journal for Numerical and Analytical Methods in Geomechanics*, 20:831–844, 1996.
- A. Ghassemi and A. Diek. Porothermoelasticity for swelling shales. *Journal of Petroleum Science and Engineering*, 34:123–135, 2002.
- A. Ghassemi, S. Tarasovs, and A.H.D. Cheng. Integral equation solution of heat extraction-induced thermal stress in enhanced geothermal reservoirs. *International Journal for Numerical and Analytical Methods in Geomechanics*, 29(8):829–844, 2005.
- A. Ghassemi, A. Nygren, and A. Cheng. Effects of heat extraction on fracture aperture: A poro-thermoelastic analysis. *Geothermics*, 37(5):525–539, 2008.
- A.C. Gringarten, P.A. Witherspoon, and Y. Ohnishi. Theory of heat extraction from fractured hot dry rock. *Journal of Geophysical Research*, 80:1120–1124, 1975.
- S.R. De Groot and P. Mazur. *Nonequilibrium thermodynamics*. Amsterdam: NorthHolland, 1962.
- R. Haase and H. Schönert. Diffusion und Sedimentation in Mehrstoffgemischen. *Zeitschrift für Elektrochemie, Berichte der Bunsengesellschaft für physikalische Chemie*, 64(10): 1155–1163, 1960.
- K. Hayashi, J. Willis-Richards, R.J. Hopkirk, and Y. Niibori. Numerical models of HDR geothermal reservoirs—a review of current thinking and progress. *Geothermics*, 28(4-5): 507–518, 1999.

- T.W. Hicks, R.J. Pine, J. Willis-Richards, S. Xu, A.J. Jupe, and N.E.V. Rodrigues. A hydro-thermo-mechanical numerical model for HDR geothermal reservoir evaluation. In *International journal of rock mechanics and mining sciences & geomechanics abstracts*, volume 33, pages 499–511. Elsevier, 1996.
- C. Hirsch. *Numerical Computation of Internal and External Flows: Fundamentals of Numerical Discretization*, volume 1. John Wiley & Sons, 1988.
- U. Hornung. *Homogenization and porous media*. Springer Verlag, 1997.
- S.T. Horseman and T.J. McEwen. Thermal constraints on disposal of heat-emitting waste in argillaceous rocks. *Engineering Geology*, 41:5–16, 1996.
- C.T. Hsu. A closure model for transient heat conduction in porous media. *Journal of Heat Transfer*, 121:733–739, 1999.
- T.J.R. Hughes. *The Finite Element Method. Linear Static and Dynamic Finite Element Analysis*. Prentice-Hall, INC., Englewood Cliffs, New Jersey 07632, 1987a.
- T.J.R. Hughes. Recent progress in the development and understanding of SUPG methods with special reference to the compressible Euler and Navier-Stokes equations. *International Journal for Numerical Methods in Fluids*, 7(11):1261–1275, 1987b.
- T.J.R. Hughes and A.N. Brooks. A multidimensional upwind scheme with no crosswind diffusion. In Ed. Hughes T.J.R., editor, *ASME Monograph AMD-34*, volume 34. ASME, New York, NY, 1979.
- T.J.R. Hughes, M. Mallet, and A. Mizukami. A new finite element formulation for computational fluid dynamics: II. Beyond SUPG. *Computer Methods in Applied Mechanics and Engineering*, 54(3):341–355, 1986.
- S.R. Idelsohn, J.C. Heinrich, and E. Oñate. Petrov-Galerkin methods for the transient advective-diffusive equation with sharp gradients. *International Journal for Numerical Methods in Engineering*, 39(9):1455–1473, 1998.
- P.X. Jiang, R.N. Xu, and W. Gong. Particle-to-fluid heat transfer coefficients in miniporous media. *Chemical Engineering Science*, 61:7213–7222, 2006.
- V. John and P. Knobloch. On spurious oscillations at layers diminishing (SOLD) methods for convection-diffusion equations: Part I-A review. *Computer Methods in Applied Mechanics and Engineering*, 196(17-20):2197–2215, 2007.
- C. Johnson, A. Szepessy, and P. Hansbo. On the convergence of shock-capturing streamline diffusion finite element methods for hyperbolic conservation laws. *Mathematics of Computation*, 54:107–129, 1990.

- MR Kaazempur-Mofrad and CR Ethier. An efficient characteristic Galerkin scheme for the advection equation in 3-D. *Computer Methods in Applied Mechanics and Engineering*, 191(46):5345–5363, 2002. ISSN 0045-7825.
- M. Kaviany. *Principles of Heat Transfer in Porous media*. Springer, 1995.
- H. Kazemi. Pressure transient analysis of naturally fractured reservoirs with uniform fracture distribution. *Society of Petroleum Engineers Journal*, 9(4):451–462, 1969.
- H. Kazemi, K.L. Porterfield, and P.R. Zeman. Numerical simulation of water-oil flow in naturally fractured reservoirs. *Old SPE Journal*, 16(6):317–326, 1976.
- D.W. Kelly, S. Nazakawa, O.C. Zienkiewicz, and J.C. Heinrich. A note of upwinding and anisotropic balancing dissipation in finite element approximations to convective diffusion problems. *International Journal for Numerical Methods in Engineering*, 15:1705–1711, 1980.
- J. Kestin. *A Course in Thermodynamics Vols. 1 and 2*. Blaisdell, Waltham, Mass, 1968.
- M.Y. Khaled. *Infiltration of a two-state compressible fluid through a linearly deformed, porous, elastic, fissured rock*. PhD thesis, University of Illinois at Urbana-Champaign, 1980.
- M.Y. Khaled, D.E. Beskos, and E.C. Aifantis. On the theory of consolidation with double porosity-iii a finite element formulation. *International Journal for Numerical and Analytical Methods in Geomechanics*, 8:101–123, 1984.
- N. Khalili. Coupling effects in double porosity media with deformable matrix. *Geophysical Research Letters*, 30(22):2153, 2003.
- N. Khalili. Two-phase fluid flow through fractured porous media with deformable matrix. *Water Resources Research*, 44:1–12, 2008.
- N. Khalili and B. Loret. An elasto-plastic model for non-isothermal analysis of flow and deformation in unsaturated porous media formulation. *International Journal of Solids and Structures*, 38:8305–8330, 2001.
- N. Khalili and A.P.S. Selvadurai. A fully coupled constitutive model for thermo-hydro-mechanical analysis in elastic media with double porosity. *Geophysical Research Letters*, 30(24):1–5, 2003.
- N. Khalili and S. Valliappan. Unified theory of flow and deformation in double porous media. *European Journal of Mechanics - A/Solids*, 15(2):321–336, 1996.
- N. Khalili, S. Valliappan, and C.F. Wan. Consolidation of fissured clays. *Géotechnique*, 49(1):75–89, 1999.
- N. Khalili, R. Witt, L. Laloui, L. Vulliet, and A. Koliji. Effective stress in double porous media with two immiscible fluids. *Geophysical Research Letters*, 32(L15309):1–5, 2005.

- N. Khalili-Naghadeh. *Numerical Modeling of Flow through Fractured Media*. PhD thesis, University of New South Wales, Sydney, 1991.
- T. Kohl and R.J. Hopkirk. “FRACure” - A simulation code for forced fluid flow and transport in fractured, porous rock. *Geothermics*, 24(3):333–343, 1995.
- T. Kohl, K.F. Evansi, R.J. Hopkirk, and L. Rybach. Coupled hydraulic, thermal and mechanical considerations for the simulation of hot dry rock reservoirs. *Geothermics*, 24(3):345–359, 1995. ISSN 0375-6505.
- O. Kolditz and C. Clauser. Numerical simulation of flow and heat transfer in fractured crystalline rocks: Application to the hot dry rock site in Rosemanowes (UK). *Geothermics*, 27(1):1–23, 1998.
- O. Kolditz and H.J. Diersch. Quasi-steady-state strategy for numerical simulation of geothermal circulation in hot dry rock fractures. *International Journal of Non-Linear Mechanics*, 28(4):467–481, 1993.
- M. Kurashige. A thermoelastic theory of fluid-filled porous materials. *International Journal of Solids and Structures*, 25(9):1039–1052, 1989.
- L. L. Lake, R. L. Schmidt, and P. B. Venuto. A niche for enhanced oil recovery in the 1990s. Technical report, Schlumberger Oilfield Review: January, pp. 55-61, 1992.
- B. Ledésert, J. Dubois, B. Velde, A. Meunier, A. Genter, and A. Badri. Geometrical and fractal analysis of a three-dimensional hydrothermal vein network in a fractured granite. *Journal of Volcanology and Geothermal Research*, 56(3):267–280, 1993.
- R.W. Lewis and B.A. Schrefler. *The finite element method in the static and dynamic deformation and consolidation of media*. Wiley, England, 1998.
- X. Li, R. Li, and B.A. Schrefler. A coupled chemo-thermo-hygro-mechanical model of concrete at high temperature and failure analysis. *International Journal for Numerical and Analytical Methods in Geomechanics*, 30(7):635–681, 2006.
- B. Loret. Biomechanical aspects of soft tissues. Unpublished lecture notes, 2008.
- B. Loret and N. Khalili. A three-phase model for unsaturated soils. *International Journal for Numerical and Analytical Methods in Geomechanics*, 24:893–927, 2000a.
- B. Loret and N. Khalili. *Thermo-mechanical potentials for unsaturated Soils*. CISM Courses and Lectures Advanced Numerical Applications and Plasticity in Geomechanics no. 426, Udine, 2000b.
- B. Loret and E. Rizzi. Strain localization in fluid-saturated anisotropic elastic-plastic porous media with double porosity. *Journal of the Mechanics and Physics of Solids*, 47: 503–530, 1999.



- B. Loret and F. Simões. A framework for deformation, generalized diffusion, mass transfer and growth in multi-species multi-phase biological tissues. *European Journal of Mechanics - A/Solids*, 24:757–781, 2005.
- M. Lu and L.D. Connell. A dual-porosity model for gas reservoir flow incorporating adsorption behaviour-part i. theoretical development and asymptotic analyses. *Transport in porous media*, 68(2):153–173, 2007.
- L.E. Malvern. *Introduction to the Mechanics of a continuous Medium*. Prentice-hall, Inc., 1969.
- J. Mandel. *Introduction à la mécanique des milieux continus déformables*. PWN Editions Scientifiques de Pologne, Varsovie, Pologne., 1974.
- I. Masters, W.K.S. Pao, and R.W. Lewis. Coupling temperature to a double-porosity model of deformable porous media. *International Journal for Numerical Methods in Engineering*, 49:421–438, 2000.
- V. Maury and C. Zurdo. Drilling Induced Lateral Shifts Along Pre Existing Fractures: A Common Cause of Drilling Problems. In *SPE Drilling & Completion, March*, pages 17–23, 1996.
- D.F. McTigue. Thermoelastic response of fluid-saturated porous rock. *Journal of Geophysical Research*, 91:9533–9542, 1986.
- D.F. McTigue. Flow to a heated borehole in porous thermoelastic rock: analysis. *Water Resources Research*, 26(8):1763–1774, 1990.
- W.J. Minkowycz, A. Haji-Sheikh, and K. Vafai. On departure from local thermal equilibrium in porous media due to a rapidly changing heat source: the Sparrow number. *International Journal of Heat and Mass Transfer*, 42(18):3373–3385, 1999.
- J.K. Mitchell. *Fundamentals of Soil Behavior*. Wiley, the Netherlands, 1993.
- H.D. Murphy, R.G. Lawton, J.W. Tester, R.M. Potter, DW Brown, and RL Aamodt. Preliminary assessment of a geothermal energy reservoir formed by hydraulic fracturing. *SPE Journal*, 17(4):317–326, 1977.
- H.D. Murphy, J.W. Tester, C.O. Grigsby, and R.M. Potter. Energy extraction from fractured geothermal reservoirs in low-permeability crystalline rock. *Journal of Geophysical Research*, 86(B8):7145–7158, 1981.
- R. Nair, Y. Abousleiman, and M. Zaman. An application of the dual-porosity porothermoelastic approach in naturally fractured porous media. In *Poromechanics II, Auriault et al (eds.) (Second Biot Conference on Poromechanics, Grenoble, France, August 26-28, 2002, Swets & Zeitlinger)*, pages 509–514, 2002.

- R. Nair, Y. Abousleiman, and M. Zaman. A finite element porothermoelastic model for dual-porosity media. *International Journal for Numerical Methods in Engineering*, 28: 875–898, 2004.
- D.A. Nield and A. Bejan. *Convection in porous media*. Springer Verlag, 2006.
- D.A. Nield, A.V. Kuznetsov, and M. Xiong. Effect of local thermal non-equilibrium on thermally developing forced convection in a porous medium. *International Journal of Heat and Mass Transfer*, 45(25):4949–4955, 2002.
- A. Nur and J. D. Byerlee. An exact effective stress law for elastic deformation of rock with fluids. *Journal of Geophysical Research*, 76:6414–6419, 1971.
- A. Oliveira and A.M. Baptista. A comparison of integration and interpolation Eulerian-Lagrangian methods. *International Journal for Numerical Methods in Fluids*, 21(3): 183–204, 1995.
- W.K.S. Pao, R.W. Lewis, and I. Masters. A fully coupled hydro-thermo-poro-mechanical model for black oil reservoir simulation. *International Journal for Numerical and Analytical Methods in Geomechanics*, 25:1229–1256, 2001.
- P.R. Paslay and J.B. Cheatham. Rock stresses induced by flow of fluids into boreholes. *Society of Petroleum Engineers Journal*, 3:85, 1963.
- C. Pecker and H. Deresiewicz. Thermal effects on wave propagation in liquid-filled porous media. *Acta Mechanica*, 16:45–64, 1973.
- G. Philipponnat, B. Hubert, and A. Isnard. *Fondations et ouvrages en terre*. Eyrolles Paris, France, 2003.
- V.M. Polyakov, A.P. Mozhaev, B.M. Galitseysky, and A.L. Lozhkin. A study of internal heat transfer in nonuniform porous structures. *Experimental Thermal and Fluid Science*, 12(4):426–432, 1996.
- M.K. Rahman, D. Naseby, and S.S. Rahman. Borehole collapse analysis incorporating time-dependent pore pressure due to mud penetration in shales. *Journal of Petroleum Science and Engineering*, 28:13–31, 2000.
- G.D. Raithby. Skew upstream differencing schemes for problems involving fluid flow. *Computer Methods in Applied Mechanics and Engineering*, 9:153–164, 1976.
- D.A. Randall. *General Circulation Model Development: Past, Present, and Future*. Academic Press, 2000.
- W.H. Raymond and A. Garder. Selective damping in a galerkin method for solving wave problems with variable grids. *Monthly Weather Review*, 104:1583–1590, 1976.

- J.R. Rice. Pore pressure effects in inelastic constitutive formulations for fissured rock masses. In *Advances in Civil Engineering Through Engineering Mechanics (Proc. 2nd ASCE Engineering Mechanics Specialty Conference, Raleigh, N.C., 1977)*, ASCE, N.Y., pages 295–297, 1977.
- J.R. Rice and M.P. Cleary. Some basic stress diffusion solutions for fluid-saturated elastic porous media with compressible constituents. *Reviews of geophysics and space physics*, 14:227–241, 1976.
- H.G. Richards, R.H. Parker, A.S.P. Green, R.H. Jones, J.D.M. Nicholls, D.A.C. Nicol, M.M. Randall, S. Richards, R.C. Stewart, and J. Willis-Richards. The performance and characteristics of the experimental hot dry rock geothermal reservoir at Rosemanowes, Cornwall (1985-1988). *Geothermics*, 23(2):73–109, 1994.
- P. Royer, J.L. Auriault, J. Lewandowska, and C. Serres. Continuum modelling of contaminant transport in fractured porous media. *Transport in Porous Media*, 49(3):333–359, 2002.
- R.L. Schiffman. A thermoelastic theory of consolidation. *Environmental and Geophysical Heat Transfer*, 25(4):78–83, 1971.
- F. Shakib, T.J.R. Hughes, and Z. Johan. A new finite element formulation for computational fluid dynamics: X. the compressible euler and navier-stokes equations. *Computer Methods in Applied Mechanics and Engineering*, 89:141–219, 1991.
- J.C. Slattery. Flow of viscoelastic fluids through porous media. *Journal of American Institute of Chemical Engineers*, 13:1066–1071, 1967.
- J.M. Soler. The effect of coupled transport phenomena in the opalinus clay and implications for radionuclide transport. *Journal of Contaminant Hydrology*, 53:63–84, 2001.
- D.C. Spanner. *Introduction to thermodynamics*. London : New York : Academic press, 1964.
- R.C. Srivastava and P.K. Avasthi. Non-equilibrium thermodynamics of thermo-osmosis of water through kaolinite. *Journal of Hydrology*, 24:11–120, 1975.
- S.S. Suthersan. *Remediation engineering: Design concepts*. CRC, 1997.
- N. Tenma, T. Yamaguchi, and G. Zyvoloski. The Hijiori Hot Dry Rock test site, Japan:: Evaluation and optimization of heat extraction from a two-layered reservoir. *Geothermics*, 37(1):19–52, 2008.
- H. Tenzer. Development of hot dry rock technology. *Bulletin Geo-Heat Center*, 32(4): 14–22, 2001.
- K. Terzaghi. Die Berechnung der Durchlässigkeitsziffer des Tones aus dem Verlauf der hydrodynamischen Spannungserscheinungen, Sitzungsber. *Akad. Wiss. Wien Math. Naturwiss. Kl. Abt.*, 132:105–125, 1923.

- T.E. Tezduyar and D.K. Ganjoo. Petrov-galerkin formulations with weighting functions dependent upon spatial and temporal discretization: applications to transient convection-diffusion problems. *Computer Methods in Applied Mechanics and Engineering*, 59:49–71, 1986.
- T.E. Tezduyar and Y. Osawa. Finite element stabilization parameters computed from element matrices and vectors. *Computer Methods in Applied Mechanics and Engineering*, 190:411–430, 2000.
- T.E. Tezduyar and Y.J. Park. Discontinuity-capturing finite element formulations for nonlinear convection-diffusion-reaction equations. *Computer Methods in Applied Mechanics and Engineering*, 59(3):307–325, 1986.
- C. Truesdell. Sulle basi della termomeccanica, *Rend. Lincei*, 22:33–38,1158–1166, 1957.
- C. Truesdell. *Rational Thermodynamics*. Springer-Verlag New York Inc. Composition House Ltd., Salisbury, England, 1984.
- C.A. Truesdell and R.A. Toupin. *The classical field theories*. Handbuch der Physik, Flugge, S., 1960.
- D.O. Uldrich and J. Ershaghi. A method for estimating the interporosity flow parameter in naturally fractured reservoirs. *Society of Petroleum Engineers Journal*, 29:324, 1979.
- S. Valliappan and N. Khalili-Naghadeh. Flow through fissured porous media with deformable matrix. *International Journal for Numerical Methods in Engineering*, 29:1079–1094, 1990.
- L. Virto, M. Carbonell, R. Castilla, and P.J. Gamez-Montero. Heating of saturated porous media in practice: Several causes of local thermal non-equilibrium. *International Journal of Heat and Mass Transfer*, 52(23-24):5412–5422, 2009. ISSN 0017-9310.
- N. Wakao and S. Kaguei. *Heat and Mass Transfer in Packed Beds*. Gordon and Breach Science, 1982.
- C.C. Wang and C. Truesdell. *Introduction to rational elasticity*. Publishing, Leyden Noordhoff International, 1973.
- Y. Wang and M.B. Dusseault. A coupled conductive-convective thermo-poroelastic solution and implications for wellbore stability. *Journal of Petroleum Science*, 38:187–198, 2003.
- Y. Wang and E. Papamichos. Conductive heat flow and thermally induced fluid flow around a well bore in a poroelastic medium. *Water Resources Research*, 30(12):3375–3384, 1994.
- J.B. Warren and P.J. Root. The behaviour of naturally fractured reservoirs. *Society of Petroleum Engineers Journal*, 228:245–255, 1963.
- S. Whitaker. Diffusion and dispersion in porous media. *Journal of American Institute of Chemical Engineers*, 13:420–427, 1967.

- S. Whitaker. Advances in theory of fluid motion in porous media. *Industrial & Engineering Chemistry*, 61(12):14–28, 1969.
- J. Willis-Richards and T. Wallroth. Approaches to the modelling of HDR reservoirs: a review. *Geothermics*, 24(3):307–332, 1995.
- S.M. Willson, N.C. Last, M.D. Zoback, and D. Moos. Drilling in South America: a wellbore stability approach for complex geologic conditions. In *Latin American and Caribbean Petroleum Engineering Conference*, 1999.
- R.K. Wilson and E.C. Aifantis. On the theory of consolidation with double porosity. *International Journal of Engineering Science*, 20(9):1009–1035, 1982.
- WL Wood and RW Lewis. A comparison of time marching schemes for the transient heat conduction equation. *International Journal for Numerical Methods in Engineering*, 9(3):679–689, 1975.
- S. Yin, B.F. Towler, M.B. Dusseault, and L. Rothenburg. Fully Coupled THMC Modeling of Wellbore Stability with Thermal and Solute Convection Considered. *Transport in Porous Media*, Article in Press:1–26, 2010.
- F. Zanotti and R.G. Carbonell. Development and transport equation for multi-phase systems-i-iii. *Chemical Engineering Science*, 39:263–278, 279–297, 299–311, 1984.
- D. Zhang, S. Weinbaum, and S.C. Cowin. Estimates of the peak pressures in bone pore water. *Journal of biomechanical engineering*, 120:697, 1998.
- J. Zhang and J.C. Roegiers. Double porosity finite element method for borehole modeling. *Rock Mechanics and Rock Engineering*, 38:217–242, 2005.
- J. Zhang, M. Bai, and J.C. Roegiers. Dual-porosity poroelastic analyses of wellbore stability. *International Journal of Rock Mechanics and Mining Sciences*, 40:473–483, 2003.
- X.X. Zhou, A. Ghassemi, and A.H.D. Cheng. A three-dimensional integral equation model for calculating poro- and thermoelastic stresses induced by cold water injection into a geothermal reservoir. *International Journal for Numerical and Analytical Methods in Geomechanics*, 33(14):1613–1640, 2009.
- Y. Zhou, R. Rajapakse, and J. Graham. A coupled thermoporoelastic model with thermo-osmosis and thermal-filtration. *International Journal of Solids and Structures*, 35:4659–4683, 1998.
- R.W. Zimmerman, T. Hadgu, and G.S. Bodvarsson. Development of a dual-porosity model for vapor-dominated fractured geothermal reservoirs using a semi-analytical fracture/matrix interaction term. In *Eighteenth Workshop on Geothermal Reservoir Engineering, Stanford University, Stanford, California*, January 26-28 1993.

G.A. Zyvoloski, R.L. Aamodt, and R.G. Aguilar. Evaluation of the second hot dry rock geothermal energy reservoir: results of Phase I, Run Segment 5. Technical report, Los Alamos National Lab., NM (USA), 1981.

## Appendix A

# Ray M. Bowen (1970) constitutive model

Bowen and Garcia (1970) developed a formulation of a thermo-mechanical theory of a mixture where each constituent has its own temperature field. Besides the multiple temperature mixture approach, the theory also contains the effects of non-linear elasticity, non-linear heat conduction, non-linear viscosity and diffusion. However, only the *linear isotropic* part of the theory is analysed here where each body has its own temperature field.

On one hand, the multiple temperature diffusion method implied by the theory of mixtures is briefly summarised. On the other hand, the multiple temperature linear isotropic theory (the linearised field equations appropriate to a mixture of one fluid and one isotropic solid) is analysed in detail from Bowen and Garcia (1970, Section 6) and Bowen and Chen (1975, Section 2). This appendix aims to provide a matrix form of the thermo-mechanical constitutive equation obtained by the authors so that the latter can be compared with our model (developed in Chapter 2) and simplified to single porosity media. The particular decoupling relating Bowen's model to Biot's approach are detailed.

**Notation:** In this appendix, Bowen's model is written with notations that are similar to the reference Bowen and Chen (1975). Whereas, our model is written with notations introduced in Loret (2008).

### A.1 Bowen Multiple temperature theory

In the work of Bowen and Garcia (1970), the authors first summarise the field equations governing the theory of mixtures: the balance of mass, linear momentum, moment of momentum, energy and entropy inequality. Finally, they rewrite the entropy inequality so as to obtain an equation in the form of (2.90). Their formulation appears to be more general than ours as they account for non-linearities such as non-linear elasticity. Two types of models can be segregated (Truesdell, 1984, Chap 5A):

- A mixture is said to be constrained if its constituents have a common temperature, say  $T$ . For constrained mixtures the Clausius-Duhem inequality reduces to: equation (2.90) times  $T$  greater or equal to zero. The Helmotz free energy is therefore used as potential.
- However for multiple temperature mixtures, Bowen and Garcia (1970) introduced a Massieu function for each species,

$$\Lambda_a = -\frac{\rho^a E_a}{T_a} \quad (\text{A.1})$$

where  $E_a$  is the free energy,  $\rho_a$  the apparent mass density and  $T_a$  the temperature of species  $a$ .

As a rule in ‘Rational Thermodynamics’ theories (Coleman and Noll, 1963; Truesdell, 1984), the constitutive equations which define the mixture are stated first. The choice of independent variables is naturally extended from the previous mixture theories where a single temperature was allowed.

Next, the appropriate thermodynamic restrictions are listed. The method leads to six relations that are necessary and sufficient in order that the Clausius-Duhem inequality be satisfied for every admissible thermodynamic process. The first two are: for each species  $a = 1, \dots, \mathcal{K}$

$$\bullet \quad \Lambda = \Lambda(\nu_b, \epsilon^b) \quad (\text{A.2})$$

$$\bullet \quad U_a = U_a(\nu_b, \epsilon^b) = -\frac{1}{\rho^a} \frac{\partial \Lambda}{\partial \nu_a}(\nu_b, \epsilon^b) \quad (\text{A.3})$$

where  $\nu_a$  is defined as the coldness and is equal to  $\nu_a = 1/T_a$ . Moreover, the method relates the partial stresses  $\sigma^a$  to the Massieu functions and to the partial strains  $\epsilon^a$ , through (for a linear isotropic theory)

$$\sigma^a = -\frac{1}{\nu_a} \Lambda_a \mathbf{I} - \frac{1}{\nu_a} \frac{\partial \Lambda}{\partial \epsilon^a} \quad \text{and} \quad \Lambda = \sum_{a=1}^{\mathcal{K}} \Lambda_a \quad (\text{A.4})$$

where  $\Lambda$  is the total Massieu function.

Finally, more restrictions are imposed upon the model by the axiom of material frame-indifference and by material symmetry (Truesdell, 1984, p. 230).



## A.2 Bowen's multiple temperature linear isotropic theory

In this section, the linearised expressions for the internal energies and stresses for a mixture of one fluid, subscript  $f$ , and one isotropic solid, subscript  $s$ , are presented. The phases are subjected to small coldness changes, small deformations and small departures from equilibrium.

Since the stresses in equilibrium and the internal energies are expressed as derivatives of the Massieu functions, it is convenient to expand the Massieu functions first to obtain the common coefficients. Expanding  $\Lambda_a$  about the reference state, and recalling that since  $\Lambda_a$  is an isotropic function of its arguments, the coefficients in its expansion must be isotropic tensors. Let us write for the fluid species (Bowen and Chen, 1975, eq. 2.1),

$$\begin{aligned}
\Lambda_f = & \Lambda_f^0 - \alpha_{ff} \Delta\nu_f - \alpha_{fs} \Delta\nu_s - \nu_0 \sigma_{ff} \frac{\text{tr } \boldsymbol{\epsilon}^f}{\rho^{f0}} - \nu_0 \sigma_{fs} \text{tr } \boldsymbol{\epsilon}^s + \frac{1}{2} v_{fff} \Delta\nu_f^2 \\
& + v_{ffs} \Delta\nu_f \Delta\nu_s + \frac{1}{2} v_{fss} \Delta\nu_s^2 + \tau_{fff} \Delta\nu_f \frac{\text{tr } \boldsymbol{\epsilon}^f}{\rho^{f0}} + \tau_{fsf} \Delta\nu_s \frac{\text{tr } \boldsymbol{\epsilon}^f}{\rho^{f0}} \\
& + \tau_{ffs} \Delta\nu_f \text{tr } \boldsymbol{\epsilon}^s + \tau_{fss} \Delta\nu_s \text{tr } \boldsymbol{\epsilon}^s - \frac{1}{2} \nu_0 \chi_{fff} \frac{\text{tr } \boldsymbol{\epsilon}^{f2}}{(\rho^{f0})^2} - \nu_0 \lambda_{ffs} \text{tr } \boldsymbol{\epsilon}^s \frac{\text{tr } \boldsymbol{\epsilon}^f}{\rho^{f0}} \\
& - \nu_0 \left( \frac{1}{2} \lambda_{fss} + \frac{1}{3} \mu_{fss} \right) (\text{tr } \boldsymbol{\epsilon}^s)^2 - \nu_0 \mu_{fss} (\text{dev } \boldsymbol{\epsilon}^s : \text{dev } \boldsymbol{\epsilon}^s) \quad (\text{A.5})
\end{aligned}$$

where,

$$\begin{aligned}
\text{tr } \boldsymbol{\epsilon}^f &= \rho^{f0} \left( \frac{1}{\rho^f} - \frac{1}{\rho^{f0}} \right) \quad (\text{Bowen and Chen, 1975, eq. 2.1}) \\
\boldsymbol{\epsilon}^s &= \text{tr } \boldsymbol{\epsilon}^s \frac{\mathbf{I}}{3} + \text{dev } \boldsymbol{\epsilon}^s \quad (\text{A.6})
\end{aligned}$$

$$\text{tr } ((\boldsymbol{\epsilon}^s)^2) = \frac{(\text{tr } \boldsymbol{\epsilon}^s)^2}{3} + \text{dev } \boldsymbol{\epsilon}^s : \text{dev } \boldsymbol{\epsilon}^s$$

and for the solid species, (Bowen and Chen, 1975, eq. 2.2)

$$\begin{aligned}
\Lambda_s = & \Lambda_s^0 - \alpha_{sf} \Delta\nu_f - \alpha_{ss} \Delta\nu_s - \nu_0 \sigma_{sf} \frac{\text{tr } \boldsymbol{\epsilon}^f}{\rho^{f0}} - \nu_0 \sigma_{ss} \text{tr } \boldsymbol{\epsilon}^s + \frac{1}{2} v_{sff} \Delta\nu_f^2 \\
& + v_{sfs} \Delta\nu_f \Delta\nu_s + \frac{1}{2} v_{sss} \Delta\nu_s^2 + \tau_{sff} \Delta\nu_f \frac{\text{tr } \boldsymbol{\epsilon}^f}{\rho^{f0}} + \tau_{ssf} \Delta\nu_s \frac{\text{tr } \boldsymbol{\epsilon}^f}{\rho^{f0}}
\end{aligned}$$

$$\begin{aligned}
& +\tau_{sfs} \Delta\nu_f \operatorname{tr} \epsilon^s + \tau_{sss} \Delta\nu_s \operatorname{tr} \epsilon^s - \frac{1}{2} \nu_0 \chi_{sff} \frac{\operatorname{tr} \epsilon^f{}^2}{(\rho^f{}^0)^2} - \nu_0 \lambda_{sfs} \operatorname{tr} \epsilon^s \frac{\operatorname{tr} \epsilon^f}{\rho^f{}^0} \\
& -\nu_0 \left( \frac{1}{2} \lambda_{sss} + \frac{1}{3} \mu_{sss} \right) (\operatorname{tr} \epsilon^s)^2 - \nu_0 \mu_{sss} (\operatorname{dev} \epsilon^s : \operatorname{dev} \epsilon^s)
\end{aligned} \tag{A.7}$$

The analysis of Bowen's multiple temperature linear isotropic theory proceed in six steps. The partial stresses (1) and the partial entropies (2), of the solid and the fluid phases, are derived in turn from the previous Massieu functions. (3) Next, the thermo-mechanical constitutive matrix is constructed. (4) Symmetry is enforced on the latter to allow the comparison with (5) our model which is presented in a fifth step. (6) Finally, the coefficients of the two models are compared.

(1) Partial stresses

Let us work with the isotropic part of the partial stresses, namely  $p^s$  and  $p^f$ , the isotropic part of the partial strains. Hence the partial stresses write,

$$p^a = -\frac{\operatorname{tr} \sigma^a}{3} = \frac{1}{\nu_a} \Lambda_a + \frac{1}{\nu_a} \frac{\partial \Lambda}{\partial \operatorname{tr} \epsilon^a} \quad \text{for} \quad a = s, f \tag{A.8}$$

Due to the linearisation process to first order around the reference configuration of the inverse coldness, the coldness of the solid writes,

$$\begin{aligned}
\frac{1}{\nu_s} &= \frac{1}{\nu_0} + \Delta \left( \frac{1}{\nu_s} \right) = \frac{1}{\nu_0} + \frac{\nu_0 - \nu_s}{\nu_0 \nu_s} \\
&= \frac{1}{\nu_0} - \frac{1}{\nu_s} \frac{\Delta \nu_s}{\nu_0} = \frac{1}{\nu_0} - \left( \frac{1}{\nu_0} + \Delta \left( \frac{1}{\nu_s} \right) \right) \frac{\Delta \nu_s}{\nu_0} \\
&= \frac{1}{\nu_0} - \frac{\Delta \nu_s}{\nu_0^2} + 0(\epsilon^2)
\end{aligned} \tag{A.9}$$

A similar relation can be obtained for  $1/\nu_f$ . Inserting this last result into equation (A.8) leads to,

$$p^a = \left( \frac{1}{\nu_0} - \frac{\Delta \nu_a}{\nu_0^2} \right) \left( \Lambda_a + \frac{\partial \Lambda}{\partial \operatorname{tr} \epsilon^a} \right) \quad \text{for} \quad a = s, f \tag{A.10}$$

After using MATLAB to expand equation (A.10) and neglecting the second order terms, the partial stresses reduce to,

$$\begin{aligned}
p^s &= \pi_s^0 - \left( \sigma_{ss} + \lambda_{ss} + \frac{2}{3} \mu_{ss} \right) \text{tr } \epsilon^s - (\sigma_{sf} + \lambda_{fs}) \frac{\text{tr } \epsilon^f}{\rho^{f0}} - (\alpha_{sf} - \tau_{fs}) \frac{\Delta \nu_f}{\nu_0} \\
&\quad - (\alpha_{ss} - \tau_{ss} + \pi_s^0) \frac{\Delta \nu_s}{\nu_0} + 0(\epsilon)^2 \\
p^f &= \pi_f^0 - \left( \sigma_{fs} + \frac{\lambda_{fs}}{\rho^{f0}} \right) \text{tr } \epsilon^s - \left( \sigma_{ff} + \frac{\chi_{ff}}{\rho^{f0}} \right) \frac{\text{tr } \epsilon^f}{\rho^{f0}} - \left( \alpha_{ff} - \frac{\tau_{ff}}{\rho^{f0}} + \pi_f^0 \right) \frac{\Delta \nu_f}{\nu_0} \\
&\quad - \left( \alpha_{fs} - \frac{\tau_{sf}}{\rho^{f0}} \right) \frac{\Delta \nu_s}{\nu_0} + 0(\epsilon)^2
\end{aligned} \tag{A.11}$$

in which

$$\pi_f^0 = \frac{\Lambda_f^0}{\nu_0} - \frac{(\sigma_{ff} + \sigma_{sf})}{\rho^{f0}} \quad \text{and} \quad \pi_s^0 = \frac{\Lambda_s^0}{\nu_0} - (\sigma_{ss} + \sigma_{fs}) \tag{A.12}$$

## (2) The partial entropies

By use of equation (A.3) and from the partial derivatives of the Massieu functions, the internal energies expression  $U_a$  can be deduced for each species,

$$U_a = -\frac{1}{\rho^a} \frac{\partial \Lambda}{\partial \nu_a} \quad \text{for} \quad a = s, f \tag{A.13}$$

In addition, the entropies  $\rho^a S_a$  relate to the Massieu functions through their definition (A.1),

$$\Lambda_a = \rho^a S_a - \nu_a \rho^a U_a \quad \text{for} \quad a = s, f \tag{A.14}$$

The relation between on one hand the entropy for the solid  $\rho^s S_s$  and the entropy for the fluid  $\rho^f S_f$ , and on the other hand the Massieu function and the coldnesses  $\nu_s$  and  $\nu_f$  is then obtained,

$$\rho^a S_a = \Lambda_a - (\nu_0 + \Delta \nu_a) \frac{\partial \Lambda}{\partial \Delta \nu_a} \quad \text{for} \quad a = s, f \tag{A.15}$$

After using MATLAB to expand equation (A.15) and neglecting the second order terms, the partial entropies reduce to,

$$\begin{aligned}\rho^s S_s &= \Lambda_s^0 + \nu_0 \alpha_s + \nu_0 (-\sigma_{sf} - \tau_{sf}) \frac{\text{tr } \epsilon^f}{\rho^f \nu_0} + \nu_0 (-\sigma_{ss} - \tau_{ss}) \text{tr } \epsilon^s \\ &\quad + (-\nu_0 v_{fs} - \alpha_{sf}) \Delta \nu_f + (-\nu_0 v_{ss} + \alpha_{fs}) \Delta \nu_s + 0 (\epsilon)^2\end{aligned}\quad (\text{A.16})$$

and,

$$\begin{aligned}\rho^f S_f &= \Lambda_f^0 + \nu_0 \alpha_f + \nu_0 (-\sigma_{ff} - \tau_{ff}) \frac{\text{tr } \epsilon^f}{\rho^f \nu_0} + \nu_0 (-\sigma_{fs} - \tau_{fs}) \text{tr } \epsilon^s \\ &\quad + (-\nu_0 v_{ff} + \alpha_{sf}) \Delta \nu_f + (-\nu_0 v_{fs} - \alpha_{fs}) \Delta \nu_s + 0 (\epsilon)^2\end{aligned}\quad (\text{A.17})$$

**Remark A.1.** The generalised stresses:  $p^s$ ,  $p^f$ ,  $\rho^s S_s$  and  $\rho^f S_f$  will be expressed as functions of the generalised strains:  $\text{tr } \epsilon^s$ ,  $\text{tr } \epsilon^f$ ,  $\Delta T_s$  and  $\Delta T_f$ . To do so, the coldness variation  $\Delta \nu_s$  will be replaced by the temperature variation  $\Delta T_s$ , by use of

$$\begin{aligned}\Delta \nu_s &= \nu_s - \nu_0 = \frac{1}{T_s} - \frac{1}{T_0} = \frac{T_0 - T_s}{T_s T_0} \\ &= \frac{-\Delta T_s}{T_s T_0} = \frac{-\Delta T_s}{T_0} \left( \frac{1}{T_0} + \Delta \left( \frac{1}{T_s} \right) \right) \\ &= -\frac{\Delta T_s}{T_0^2} + 0 (\epsilon)^2 \quad \rightarrow \quad \Delta \nu_s = -\Delta T_s \nu_0^2\end{aligned}\quad (\text{A.18})$$

The same relation stands for  $\Delta \nu_f = -\Delta T_f \nu_0^2$ .

### (3) Bowen's thermo-mechanical constitutive matrix

One form of the thermo-mechanical equation considers the primary variables to be apparent strains and temperatures; and the dependent variables to be the apparent stresses and entropies. A matrix links the partial stresses to the partial strains as:

$$\begin{bmatrix} p^s \\ p^f \\ \rho^s S_s \\ \rho^f S_f \end{bmatrix} - \begin{bmatrix} p_0^s \\ p_0^f \\ \rho^s S_s^0 \\ \rho^f S_f^0 \end{bmatrix} = - \begin{bmatrix} C_{11} & C_{12} & C_{13} & C_{14} \\ C_{21} & C_{22} & C_{23} & C_{24} \\ C_{31} & C_{32} & C_{33} & C_{34} \\ C_{41} & C_{42} & C_{43} & C_{44} \end{bmatrix} \begin{bmatrix} \text{tr } \epsilon^s \\ \text{tr } \epsilon^f \\ \Delta T_s \\ \Delta T_f \end{bmatrix}\quad (\text{A.19})$$

By gathering equations (A.11), (A.16) and (A.17) the thermo-mechanical constitutive relation may be written the following matrix form,

$$\begin{bmatrix} \Delta p^s \\ \Delta p^f \\ \Delta(\rho^s S_s) \\ \Delta(\rho^f S_f) \end{bmatrix} = - \begin{bmatrix} \sigma_{ss} + \lambda_{ss} + \frac{2}{3}\mu_{ss} & \frac{\sigma_{sf}}{\rho^{f0}} + \frac{\lambda_{fs}}{\rho^{f0}} & -\nu_0 (\alpha_{ss} + \pi_s^0) & -\nu_0 \alpha_{sf} \\ \sigma_{fs} + \frac{\lambda_{fs}}{\rho^{f0}} & \frac{\sigma_{ff}}{\rho^{f0}} - \frac{\chi_{ff}}{\rho^{f0^2}} & -\nu_0 \alpha_{fs} & -\nu_0 (\alpha_{ff} + \pi_f^0) \\ \nu_0 \sigma_{ss} + \nu_0 \tau_{ss} & \frac{\nu_0}{\rho^{f0}} \sigma_{sf} + \frac{\nu_0}{\rho^{f0}} \tau_{sf} & \nu_0^2 \alpha_{fs} & -\nu_0^2 \alpha_{sf} \\ \nu_0 \sigma_{fs} + \nu_0 \tau_{fs} & \frac{\nu_0}{\rho^{f0}} \sigma_{ff} + \frac{\nu_0}{\rho^{f0}} \tau_{ff} & -\nu_0^2 \alpha_{fs} & \nu_0^2 \alpha_{sf} \end{bmatrix} \begin{bmatrix} \text{tr } \epsilon^s \\ \text{tr } \epsilon^f \\ \Delta T_s \\ \Delta T_f \end{bmatrix} \tag{A.20}$$

in which

$$\begin{aligned} \pi_s^0 &= \frac{\Lambda_s^0}{\nu_0} - (\sigma_{ss} + \sigma_{fs}) & \pi_f^0 &= \frac{\Lambda_f^0}{\nu_0} - \frac{(\sigma_{sf} + \sigma_{ff})}{\rho^{f0}} \\ \Delta p^s &= p^s - \pi_0^s & \Delta p^f &= p^f - \pi_0^f \\ \Delta(\rho^s S_s) &= \rho^s S_s - (\Lambda_s^0 + \nu_0 \alpha_s) & \Delta(\rho^f S_f) &= \rho^f S_f - (\Lambda_f^0 + \nu_0 \alpha_f) \end{aligned} \tag{A.21}$$

In equation (A.20), the coefficients multiplying linear terms in the Massieu functions are gathered at a upper level; and the coefficients factor of quadratic terms are gathered at a lower level. Note that Bowen's thermo-mechanical matrix displays symmetry from the lower/quadratic coefficients point of view only. The non-symmetry is due to the upper/linear coefficients.

(4) Bowen's thermo-mechanical constitutive matrix: forced symmetry

When expanding the Massieu function, Bowen took into account all the linear and quadratic terms that are mathematically possible, regardless of the available field parameters and of the physical meaning of the introduced coefficients. Moreover, Bowen took great care not to neglect initial terms. It is worth noting that Bowen's model is the most *general* since all proposed terms are coherent and possible. For instance, from the terms  $\pi_s^0$  and  $\pi_f^0$  rigidity induced by initial apparent stress and pore pressure are taken into account.

This appendix aims to compare Bowen's non-symmetric general case to our particular symmetric constitutive model. Bowen's model is simplified so that the constitutive matrix becomes symmetric. Note that some information is lost during the symmetrization process.

When imposing symmetry to equation (A.20), the six following relations are enforced:

$$\begin{aligned}
\alpha_{sf} &= \alpha_{fs} & \frac{\sigma_{sf}}{\rho^{f0}} &= \sigma_{fs} \\
\alpha_{sf} &= -\sigma_{fs} & \frac{\sigma_{sf}}{\rho^{f0}} &= -\alpha_{fs} \\
\sigma_{fs} &= \alpha_{ss} + \frac{\Lambda_s^0}{\nu_0} & \frac{\sigma_{sf}}{\rho^{f0}} &= \alpha_{ff} + \frac{\Lambda_f^0}{\nu_0}
\end{aligned} \tag{A.22}$$

Hence, the thermo-mechanical constitutive relation forced to *symmetry* can be written in the following format,

$$\begin{bmatrix} \Delta p^s \\ \Delta p^f \\ \Delta(\rho^s S_s) \\ \Delta(\rho^f S_f) \end{bmatrix} = - \begin{bmatrix} \sigma_{ss} + (\lambda_{ss} + \frac{2}{3}\mu_{ss}) & -\alpha_{fs} + \frac{\lambda_{fs}}{\rho^{f0}} & \nu_0 \sigma_{ss} & -\nu_0 \alpha_{fs} \\ -\alpha_{fs} + \frac{\lambda_{fs}}{\rho^{f0}} & \frac{\sigma_{ff}}{\rho^{f0}} - \frac{\chi_{ff}}{\rho^{f0^2}} & -\nu_0 \alpha_{fs} & \frac{\nu_0}{\rho^{f0}} \sigma_{ff} \\ \nu_0 \sigma_{ss} + \nu_0 \tau_{ss} & -\nu_0 \alpha_{fs} + \frac{\nu_0}{\rho^{f0}} \tau_{sf} & \nu_0^2 \alpha_{fs} & -\nu_0^2 \alpha_{fs} \\ -\nu_0 \alpha_{fs} + \nu_0 \tau_{fs} & \frac{\nu_0}{\rho^{f0}} \sigma_{ff} + \frac{\nu_0}{\rho^{f0}} \tau_{ff} & -\nu_0^2 \alpha_{fs} & \nu_0^2 \alpha_{fs} \end{bmatrix} \begin{bmatrix} \text{tr } \epsilon^s \\ \text{tr } \epsilon^f \\ \Delta T_s \\ \Delta T_f \end{bmatrix} \tag{A.23}$$

Note that even after this forced symmetry, Bowen's TM constitutive matrix still displays upper/linear terms: Three terms are remaining in the matrix, namely  $\sigma_{ss}$ ,  $\sigma_{ff}$  and  $\alpha_{fs}$ . In addition, the initial stress values reduced to<sup>1</sup>,

$$\begin{aligned}
\pi_f^0 &= \frac{\Lambda_f^0}{\nu_0} - (-\alpha_{fs} + \frac{\sigma_{ff}}{\rho^{f0}}) & \pi_s^0 &= \frac{\Lambda_s^0}{\nu_0} - (\sigma_{ss} - \alpha_{fs}) \\
\Delta p^s &= p^s - \pi_0^s & \Delta p^f &= p^f - \pi_0^f \\
\Delta(\rho^s S_s) &= \rho^s S_s & \Delta(\rho^f S_f) &= \rho^f S_f
\end{aligned} \tag{A.24}$$

<sup>1</sup>Note that consequent to the symmetrization process, the initial entropies of the solid and the fluid phase reduces to zero.

(5) Our thermo-mechanical constitutive matrix

The latter result is compared with our thermo-mechanical constitutive matrix. For simplicity, the potential is imposed to be quadratic in the generalised partial strains. As no linear terms nor initial ones are taken into account in our potential, less coefficients arise compared with Bowen. In order to compare Biot's thermo-mechanical constitutive matrix to equation (A.23), the relation needs to be expressed with the same strain and stress vectors. From Loret (2008), the thermo-mechanical constitutive matrix writes,

$$\begin{bmatrix} -p^s \\ -p^f \\ -\rho^s \eta_s \\ -\rho^f \eta_f \end{bmatrix} = \begin{bmatrix} K^{ss} & \lambda & -K^{ss} c_T & -\lambda c_{Tf} \\ \lambda & L & -\lambda c_T & -L c_{Tf} \\ -K^{ss} c_T & -\lambda c_T & -C_m^s/T_s^0 & \lambda c_T c_{Tf} \\ -\lambda c_{Tf} & -L c_{Tf} & \lambda c_T c_{Tf} & -C_v^f/T_f^0 \end{bmatrix} \begin{bmatrix} \text{tr } E_s \\ \text{tr } E_f \\ \Delta T_s \\ \Delta T_f \end{bmatrix} \quad (\text{A.25})$$

where,

$$\begin{aligned} M^{-1} &= \frac{n_f}{K_f} + \frac{1-n_f}{K_s} - \frac{K}{K_s^2} & L &= M (n_f)^2 \\ K^{ss} &= K + L \left( -n_s + \frac{K}{K_s} \right)^2 & \lambda &= -\frac{L}{n_f} \left( -n_s + \frac{K}{K_s} \right) \\ C_m^s &= C_\sigma^s - c_T : K^{ss} : c_T T_s^0 & C_v^f &= C_p^f - M(n_f)^2 (c_{Tf})^2 T_f^0 \end{aligned} \quad (\text{A.26})$$

in which  $n_s$  and  $n_f$  are the volume fractions of the solid phase and the fluid phase, respectively;  $K_s$ ,  $K_f$  and  $K$  are the bulk modulus of the solid grains, the fluid and of the mixture as a whole, respectively;  $c_T$  and  $c_{Tf}$  are the thermal dilatation coefficients of the mixture as a whole and of the fluid phase, respectively. Finally,  $C_\sigma^s$  is the partial heat capacity of the solid phase at constant stress and  $C_p^f$  is the partial heat capacity of the fluid phase at constant pressure.

(6) Identification and interpretation

Equations (A.23) and (A.25) are compared; due to the symmetry, ten equalities are obtained. However, Bowen's matrix displays thirteen terms. Hence, all the coefficients

introduced by Bowen and Chen (1975) can not be identified at once. To find an issue, the quadratic/lower coefficients are assumed more important than the linear ones and will be identified in priority. No restriction will be imposed on the linear coefficient and they will be considered arbitrary. Let us start the identification process by the mechanical part only,

$$\begin{aligned}
\text{Bowen's coef.} &= \text{Biot's coef.} + \text{arbitrary coef.} \\
(\lambda_{ss} + \frac{2}{3}\mu_{ss}) &= K^{ss} + \sigma_{ss} \\
\frac{\lambda_{fs}}{\rho^{f0}} &= \lambda + \alpha_{fs} \\
-\frac{1}{\rho^{f0}} \frac{\chi_{ff}}{\rho^{f0}} &= L + \frac{\sigma_{ff}}{\rho^{f0}}
\end{aligned} \tag{A.27}$$

Secondly, from the rest of the matrix (A.23) the following equalities are obtained:

$$\begin{aligned}
\text{Bowen's coef.} &= \text{Our coef.} + \text{arbitrary coef.} \\
\tau_{ss} &= \frac{K^{ss} c_T}{\nu_0} + \sigma_{ss} \\
\frac{\tau_{sf}}{\rho^{f0}} &= -\frac{\lambda c_T}{\nu_0} + \alpha_{fs} \\
\tau_{fs} &= -\frac{\lambda c_{Tf}}{\nu_0} + \alpha_{fs} \\
\frac{\tau_{ff}}{\rho^{f0}} &= -\frac{L c_{Tf}}{\nu_0} + \frac{\sigma_{ff}}{\rho^{f0}} \\
v_{fs} &= -\frac{\lambda c_{Tf} c_T}{\nu_0^2} + \alpha_{fs} \\
v_{ss} &= -\frac{C_m^s}{T_s^0 \nu_0^3} + \frac{\alpha_{fs}}{\nu_0} \\
v_{ff} &= -\frac{C_v^f}{T_f^0 \nu_0^3} + \frac{\alpha_{fs}}{\nu_0}
\end{aligned} \tag{A.28}$$

Bowen's quadratic coefficients have all been related to our coefficients. Note that no contradiction arises during the identification process. The problem being under-constrained, any value can be assigned to the arbitrary coefficients.

In classical thermo-elasticity, the coefficient  $\alpha_{fs}$  is usually chosen equal to zero  $\alpha_{fs} = 0$  (Bowen and Chen, 1975, eq. 2.36). Furthermore, the initial values of the Massieu functions may be chosen equal to zero due to their potential nature.



However, great care should be taken when choosing  $\pi_s^0 = -\sigma_{ss}$  and  $\pi_f^0 \equiv -\sigma_{ff}$ . Their value strongly depends on the definition of the reference state. When choosing  $\pi_s^0 = \sigma_{ss} = \pi_f^0 = \sigma_{ff} = 0$  no stiffness induced by initial stresses can be taken into account.

As a conclusion, the arbitrary coefficients  $\sigma_{ss}$  and  $\sigma_{ff}$  will be assumed to be zero, if and only if the reference state is defined as an *equilibrium state* in which the mixture is submitted to vanishing initial apparent stresses.

## Appendix B

# Pecker and Deresiewicz (1973) constitutive model

Pecker and Deresiewicz (1973) presented a formulation to account for the effects of temperature on the behaviour of fluid-saturated rocks. The model describes a single porous medium before thermal equilibrium occurs, each phase is endowed with its own temperature. No phase change is accounted for here.

The constitutive model presented by Pecker and Deresiewicz (1973) is discussed in four sections. First, the Clausius-Duhem inequality which provides useful restriction on the choice of stress/strain variables is described. Then the partial stress/strain formulation is presented in a matrix form and compared to our model (developed in Chapter 2) and simplified to single porosity media. This constitutive formulation is then transformed to an equivalent total stress/strain formulation and is once more compared with our thermo-mechanical constitutive model. Finally, a reflexion is proposed on the physical meaning of the thermo-elastic couplings terms  $\alpha_{sf}$  and  $\alpha_{fs}$  introduced and measured by Pecker and Deresiewicz (1973).

**Notations:** To ease the comparison, the notations introduced by Pecker and Deresiewicz (1973) are kept when describing their work and the notations introduced in Section 2.2.2 are used when describing the constitutive model developed as part of this study.

### B.1 The Clausius-Duhem inequality

Following the model of Pecker and Deresiewicz (1973), the elastic strain in the solid phase is noted  $e_{ij}$ , and  $e_{ii} = e$ . The strain of the liquid phase is noted  $\epsilon_{ii} = \epsilon$ . They represent the respective dilatations of the phases. The partial stresses, namely the stress in the solid and liquid phases measured per unit area of bulk, are noted  $\sigma_{ij}$  for the solid phase and  $\sigma = -\beta p$  for the fluid phase,  $p$  being the fluid pressure and  $\beta$  the porosity.

Pecker and Deresiewicz (1973) *assumed* the change of internal energy per unit volume  $E$  to be function of four variables: the solid strain, the fluid strain and the entropies of the

solid and fluid phases per unit volume,  $\eta_s$  and  $\eta_f$ ,

$$E = E(e_{ij}, \epsilon, \eta_s, \eta_f) \quad (\text{B.1})$$

The following derivative relation is a consequence of the assumed functional dependence of the internal energy,

$$\dot{E} = \frac{\partial E}{\partial e_i} \dot{e}_i + \frac{\partial E}{\partial \eta_s} \dot{\eta}_s + \frac{\partial E}{\partial \eta_f} \dot{\eta}_f \quad (\text{B.2})$$

Therefore, after insertion of the conservation of energy into the balance of entropy, the thermo-mechanical part of the Clausius-Duhem equation, takes to following form,

$$\sum_{i=1}^1 \left( \sigma_i - \frac{\partial E}{\partial e_i} \right) \dot{e}_i + \left( \bar{T}_s - \frac{\partial E}{\partial \eta_s} \right) \dot{\eta}_s + \left( \bar{T}_f - \frac{\partial E}{\partial \eta_f} \right) \dot{\eta}_f = 0 \quad (\text{B.3})$$

where  $\bar{T}_s$  and  $\bar{T}_f$  denote the solid and fluid temperatures. The thermo-mechanical part of the Clausius-Duhem equation is equal to zero as no dissipation occurs in the elastic domain. Hence, it is sufficient for any process that,

$$\sigma_i = \frac{\partial E}{\partial e_i}, \quad \bar{T}_s = \frac{\partial E}{\partial \eta_s}, \quad \bar{T}_f = \frac{\partial E}{\partial \eta_f} \quad (\text{B.4})$$

The previous equation describes the functional dependence of the stresses and of the temperatures on the strains and on the entropies. In addition, the relations (B.4) may be written in totally inversed form, assuming the inversion is possible,

$$\begin{aligned} e_i &= e_i(\sigma_i, \bar{T}_s, \bar{T}_f), \\ \eta_s &= \eta_s(\sigma_i, \bar{T}_s), \\ \eta_f &= \eta_f(\sigma_i, \bar{T}_f) \end{aligned} \quad (\text{B.5})$$

Note that in this model, the strains depend on the stresses and on both the solid and the fluid temperature variation, contrary to the entropies which depend on the stresses and on their respective phase temperature. Compared to Bowen's systematic procedure, equations (B.5)<sub>2</sub> and (B.5)<sub>3</sub> can appear as a restrictive result.

## B.2 A partial stress/strain formulation

Their development proceeded by obtaining, next, the stress-strain-temperature relations. A partial stress-strain approach is adopted. To ease the comparison, the model proposed by Pecker and Deresiewicz (1973) is reduced to its isotropic part. The matrix form relating the generalised stresses: partial stresses of the solid and of the fluid phases, namely  $\sigma_i/3$  and  $\sigma$ , and entropies of the solid and the fluid phases, namely  $-\eta_s$  and  $-\eta_f$ ; to the generalised strains:  $e$ ,  $\epsilon$ ,  $\Delta T_s$  and  $\Delta T_f$ , where  $\Delta T_s$  and  $\Delta T_f$  are deviations from equilibrium temperature in the two phases, is *symmetric*:

$$\begin{bmatrix} \sigma_i/3 \\ \sigma \\ -\eta_s \\ -\eta_f \end{bmatrix} = \begin{bmatrix} P/3 & Q & -R_{11} & -R_{12} \\ Q & R & -R_{21} & -R_{22} \\ -R_{11} & -R_{21} & -C_s/T_0 + 3\alpha_s R_{11} + \alpha_{fs} R_{21} & 3\alpha_s R_{12} + \alpha_{fs} R_{22} \\ -R_{12} & -R_{22} & \alpha_f R_{21} + 3\alpha_{sf} R_{11} & -C_f/T_0 + \alpha_f R_{22} + 3\alpha_{sf} R_{12} \end{bmatrix} \begin{bmatrix} e \\ \epsilon \\ \Delta T_s \\ \Delta T_f \end{bmatrix} \quad (\text{B.6})$$

where  $P$ ,  $Q$  and  $R$  are the classic elastic moduli introduced by Biot.  $C_s$  and  $C_f$  are the specific heats per unit volume of bulk at constant stress and pressure.  $\alpha_s$  and  $\alpha_f$  represent the usual (isobaric) coefficients of thermal expansion for the individual phases, and  $\alpha_{sf}$ ,  $\alpha_{fs}$  are seen to be thermo-elastic coupling terms:  $\alpha_{sf}$  is the strain in the matrix due to a unit change of temperature in the liquid phase and  $\alpha_{fs}$  is the dilatation of the fluid due to a unit change in matrix temperature. Moreover the remaining coefficients are related to these by,

$$\begin{aligned} R_{11} &= \alpha_s P + \alpha_{fs} Q & R_{21} &= 3\alpha_s Q + \alpha_{fs} R \\ R_{12} &= \alpha_{sf} P + \alpha_f Q & R_{22} &= 3\alpha_{sf} Q + \alpha_f R \end{aligned} \quad (\text{B.7})$$

Note that, in addition to the usual isobaric coefficient of thermal expansion of each phase, two new coefficients appear  $\alpha_{sf}$  and  $\alpha_{fs}$  which represent measures of dilation of each phase caused by the temperature change of the other phase.

Due to the fact that this thermo-mechanical constitutive system is expressed in partial stresses and strains, it can be compared with the system A.25. The parameter identification leads to,

Pecker and Deresiewicz (1973)	Loret (2008)
$3 \alpha_s$	$c_T$
$\alpha_f$	$c_{Tf}$
$\alpha_{sf}$	0
$\alpha_{fs}$	0
$P/3$	$K^{ss}$
$Q$	$\lambda$
$R$	$L$

(B.8)

Note that if  $\alpha_{sf} = \alpha_{fs} = 0$  Pecker and Deresiewicz's model reduces to our formulation. As a first conclusion, one may suppose that our model is a particular case of the one proposed by Pecker and Deresiewicz.

### B.3 The equivalent total stress/strain formulation

Furthermore, the thermo-mechanical constitutive model, presented in Section 2.2.2 and expressed *in a total stress-strain form*, is now compared with the model presented by Pecker and Deresiewicz (1973) one in order to highlight our theoretical differences.

The equivalent total stress/strain formulation can be deduced from the partial stress/strain relation, equation (B.6). The total stress/strain system relates the following generalised stresses: the total isotropic stress  $p^I$ , the volume content variation of the fluid  $\Delta v^f$ ,  $\eta_s$  and  $\eta_f$ ; to their respective generalised strains:  $e$ , the fluid pressure  $p_f$ ,  $\Delta T_s$  and  $\Delta T_f$ .

The transformation processes in four steps:

1. The total isotropic stress  $p^I$  is defined by the same definition as equation (2.125). Therefore,  $p^I$  is obtained by summing the partial isotropic stresses of each phase, namely,

$$\begin{aligned}
 p^I &= - \left( \frac{\sigma_{ii}}{3} + \sigma \right) \\
 &= - \left( \frac{P}{3} + Q \right) e - (Q + R) \epsilon + (R_{11} + R_{21}) \Delta T_s + (R_{12} + R_{22}) \Delta T_f \quad (\text{B.9})
 \end{aligned}$$

2. The partial stress of the fluid phase  $\sigma$  can be related to the fluid pressure  $p_f$  through its definition and the porosity  $\beta$ . As no initial stress nor strains are introduced in the formulation, there is no need to decompose the porosity and to linearise the calculation. Hence,

$$p_f = \frac{1}{\beta} (-\sigma)$$

$$= \frac{1}{\beta} (-Q e - R \epsilon + R_{21} \Delta T_s + R_{22} \Delta T_f) \quad (\text{B.10})$$

The entropy equations remain unchanged and can be deduced from equation (B.6),

$$\begin{aligned} \eta_s &= R_{11} e + R_{21} \epsilon + (C_s/T_0 - 3 \alpha_s R_{11} - \alpha_{fs} R_{21}) \Delta T_s \\ &\quad - (3 \alpha_s R_{12} + \alpha_{fs} R_{22}) \Delta T_f \\ \eta_f &= R_{12} e + R_{22} \epsilon - (3 \alpha_{sf} R_{11} + \alpha_f R_{21}) \Delta T_s \\ &\quad + (C_f/T_0 - 3 \alpha_{sf} R_{12} - \alpha_f R_{22}) \Delta T_f \end{aligned} \quad (\text{B.11})$$

3. Next, the strain of the fluid phase  $\epsilon$  is replaced by its volume content variation  $\Delta v^f$ . The volume content definition may be rearranged as below,

$$v^f = \frac{V_f}{V_0} = \frac{V_f}{M_f} \frac{M_f}{V_0} = \frac{V_f}{M_f} \frac{M_f}{V} \frac{V}{V_0} = \frac{\rho^f}{\rho_f} \det \mathbf{F} \quad (\text{B.12})$$

Hence, the derivative of the volume content can be written,

$$\begin{aligned} d v^f &= \frac{d\rho^f}{\rho_f} \det \mathbf{F} + \frac{\rho^f}{\rho_f} d(\det \mathbf{F}) - \frac{\rho^f}{\rho_f^2} \det \mathbf{F} d(\rho_f) \\ &= \frac{d\rho^f}{\rho_f} \det \mathbf{F} + \frac{\rho^f}{\rho_f} e - \frac{\rho^f}{\rho_f} \det \mathbf{F} (c_{Hf} dp_f - c_{Tf} dT_f) \end{aligned} \quad (\text{B.13})$$

Since the derivation process is finished, the little deformation hypothesis  $\det \mathbf{F} = 1$  can safely be applied. Moreover, the hypothesis of incompressible fluids is made, namely  $c_{Hf} dp_f \ll c_{Tf} dT_f$ . Finally, since the increment  $\Delta(\cdot)$  and the derivative  $d(\cdot)$  relations are equivalent, the volume content reduces to,

$$\begin{aligned} \Delta v^f &= \frac{\Delta\rho^f}{\rho_f} + \frac{\rho^f}{\rho_f} e + \frac{\rho^f}{\rho_f} c_{Tf} \Delta T_f \\ &= \left( \frac{1}{\rho_{f0}} + \Delta \left( \frac{1}{\rho_f} \right) \right) (\rho^{f0} + \Delta\rho^f) (e - \epsilon + c_{Tf} \Delta T_f) \end{aligned} \quad (\text{B.14})$$

due to the definition,

$$\rho^{f0} = \rho^f (1 + \epsilon) \quad \rightarrow \quad \rho^f - \rho^{f0} = \Delta\rho^f = -\rho^f \epsilon \quad (\text{B.15})$$

After linearisation at the first order of  $\Delta v^f$  around the reference configuration, the following relations are obtained:

$$\Delta v^f = \beta_0 (e - \epsilon + c_{Tf} \Delta T_f) \quad \rightarrow \quad \epsilon = -\frac{\Delta v^f}{\beta_0} + e + c_{Tf} \Delta T_f \quad (\text{B.16})$$

One can now replace the strain of the fluid phase  $\epsilon$  by its volume content variation  $\Delta v^f$ , through equation (B.16) into equations (B.9), (B.10) and (B.11). In a matrix form, the following *non-symmetric* system is obtained,

$$\begin{bmatrix} p^I \\ -p_f \\ \eta_s \\ \eta_f \end{bmatrix} = \begin{bmatrix} -\left(\frac{P}{3} + 2Q + R\right) & \frac{Q+R}{\beta_0} & R_{11} + R_{21} & R_{12} + R_{22} \\ \frac{Q+R}{\beta_0} & -\frac{R}{\beta_0^2} & -\frac{R_{21}}{\beta_0} & -c_{Tf}(Q+R) \\ R_{11} + R_{21} & -\frac{R_{21}}{\beta_0} & C_s/T_0 - 3\alpha_s R_{11} & \frac{c_{Tf}R - R_{22}}{\beta_0} \\ R_{12} + R_{22} & -\frac{R_{22}}{\beta_0} & -\alpha_f R_{21} & C_f/T_0 - \alpha_f R_{22} \end{bmatrix} \begin{bmatrix} e \\ \Delta v^f \\ \Delta T_s \\ \Delta T_f \end{bmatrix} \quad (\text{B.17})$$

4. Finally, the second line of the system (B.17) is reversed and the following *non-symmetric* relation is obtained after rearranging,

$$\begin{bmatrix} p^I \\ \Delta v^f \\ \eta_s \\ \eta_f \end{bmatrix} = \begin{bmatrix} -K & \beta_0 \left(\frac{Q+R}{R}\right) & 3\alpha_s K & 3\alpha_{sf} K \\ \beta_0 \left(\frac{Q+R}{R}\right) & \frac{\beta_0^2}{R} & -\beta_0 \frac{R_{21}}{R} & -\beta_0 3\alpha_{sf} \frac{Q}{R} \\ 3\alpha_s K & -\beta_0 \frac{R_{21}}{R} & C_s/T_0 - 9\alpha_s^2 K & -9\alpha_s \alpha_{sf} K \\ 3\alpha_{sf} K & -\beta_0 \frac{R_{22}}{R} & -9\alpha_{sf} \alpha_s K & C_f/T_0 - 9\alpha_{sf}^2 K \end{bmatrix} \begin{bmatrix} e \\ p_f \\ \Delta T_s \\ \Delta T_f \end{bmatrix} \quad (\text{B.18})$$

where,

$$\begin{aligned}
K &= \left( \frac{P}{3} - \frac{Q^2}{R} \right) \\
R_{21} &= 3 \alpha_s Q + \alpha_{fs} R \\
R_{22} &= 3 \alpha_{sf} Q + \alpha_f R
\end{aligned} \tag{B.19}$$

The constitutive model proposed by Pecker and Deresiewicz (1973) can be compared with our model (2.204) reduced to a single porosity medium,

$$\begin{bmatrix} p^I \\ \Delta v^f \\ \eta_s \\ \eta_f \end{bmatrix} = \begin{bmatrix} -1/c & 1 - \frac{c_s}{c} & \gamma_T & 0 \\ 1 - \frac{c_s}{c} & c_s(1 - \frac{c_s}{c} - n_f) & -c_T(1 - \frac{c_s}{c} - n_f) & 0 \\ \gamma_T & -c_T(1 - \frac{c_s}{c} - n_f) & C_p^s/T_0 & 0 \\ \hline 0 & -n_f c_{Tf} & 0 & C_p^f/T_0 \end{bmatrix} \begin{bmatrix} e \\ p_f \\ \Delta T_s \\ \Delta T_f \end{bmatrix} \tag{B.20}$$

Note that by use of the relations (A.26), with  $K_f = 0$  to respect the incompressible fluid hypothesis and (B.8), the two systems are found identical, except that in our model the coefficients  $\alpha_{sf} = \alpha_{fs} = 0$  are assumed to be null. Furthermore, the comparison holds if the volume content  $\Delta v^f$  is replaced by the mass content  $\Delta m^f/\rho_f$  yielding a symmetric matrix, for  $\alpha_{sf} = \alpha_{fs} = 0$ .

## B.4 Reflexion on the physical meaning of the terms $\alpha_{sf}$ and $\alpha_{fs}$

Here, a reflexion on the physical meaning of the coefficients  $\alpha_{sf}$  and  $\alpha_{fs}$  is proposed, which are the thermo-mechanical coupling terms introduced and measured by Pecker and Deresiewicz (1973). First, the implications of Biot's approach on both models are scrutinised. Next, the measurement of the terms  $\alpha_{sf}$  and  $\alpha_{fs}$  is commented.

Our model stems from *Biot's approach*: the solid skeleton is paid a special role. The species being in the interstitial porosity are viewed as flowing through the solid skeleton



matrix. Therefore, the hypothesis of a continuous grain path crossing the porous medium from side to side is assumed to hold for every application.

To ease our reasoning, a thought experiment is proposed. A single porous medium fully saturated is said to be in a transient thermal state. The temperature variation from equilibrium in the solid phase is  $\Delta T_s$  and the temperature in the fluid phase is  $\Delta T_f$ . In order to focus our attention on the thermo-mechanical behaviour only and not on the inter-phase heat transfer, the two phases are separated by a thermally insulated barrier. Since a continuous grain path relating the extremities of our sample is assumed, the deformation of the porous medium is said to be equal to the deformation of the solid skeleton. Due to the thermally insulated barrier, the solid skeleton is only influenced by the solid skeleton temperature  $\Delta T_s$ . If  $\Delta T_s > 0$  the deformation of the medium increases thanks to the solid skeleton volumetric expansion coefficient. Due to the continuous grain path assumption, the variation of volume content of the fluid phase is driven by the solid skeleton deformation and is logically proportional to the solid skeleton volumetric dilatation by its porosity  $\beta_0$ . Therefore, by considering a continuous grain path, under zero stress and zero pressure assumptions, our thermo-mechanical constitutive model reduces to,

$$\begin{cases} e &= & 3 \alpha_s & T_s & + & 0 & T_f \\ \Delta v^f &= & \beta_0 3 \alpha_s & \Delta T_s & + & 0 & \Delta T_f \end{cases} \quad (\text{B.21})$$

By using the hypothesis of a continuous grain path, the thermo-mechanical behaviour appears to be independent on the fluid temperature. This supposition recovers successfully the results of the ‘thermodynamic of irreversible processes’ approach, see Section 2.2.2.

When considering an unstressed state (zero stress and zero pressure), Pecker and Dere-siewicz’s model reduces to the following system,

$$\begin{cases} e &= & 3 \alpha_s & \Delta T_s & + & 3 \alpha_{sf} & \Delta T_f \\ \Delta v^f &= & \beta_0(3 \alpha_s - \alpha_{fs}) & \Delta T_s & + & \beta_0 3 \alpha_{sf} & \Delta T_f \end{cases} \quad (\text{B.22})$$

The dependence of the solid and the fluid strains on the fluid temperature is induced by the functional dependence of the internal energy  $E$ . However, if this coupling is possible from a systematic point of view, it is incompatible with the continuous grain path hypothesis.

The value of  $\alpha_{sf}$  appears to be one order of magnitude lower than its corresponding direct coefficient  $\alpha_s$ , the ratio being exactly of -0.1. Since no indication on the precision of the measurement and no other measurements to compare this result is available, no conclusion can be made.

The procedure carried out to measure  $\alpha_{fs}$  is based on the variation of the *mass* content of the whole saturated sample at different temperatures rather than on the variation of

the *volume* content of the fluid phase. As presented in Remark 2.18, on page 140, the thermo-mechanical formulation involving the volume content and the mass content are not equivalent. In fact, the formulation with the mass content variation is dependent on the fluid temperature variation, see equation (2.207).

Overall, more measurements should be made to estimate the validity of the continuous grain path assumption and of the independence of the thermo-mechanical behaviour with the fluid temperature variation.

In conclusion, our thermo-mechanical constitutive system is not a particular case of Pecker and Deresiewicz's (1973) model, as the independence of the thermo-mechanical behaviour on the fluid temperature is imposed by the thermo-mechanical part of the Clausius-Duhem inequality, in agreement with the continuous grain path assumption.

## Appendix C

# McTigue (1986) constitutive model

McTigue (1986) presented a linear theory for a fluid saturated poro-thermo-elastic medium. McTigue's theoretical model allows for the compressibility and thermal expansion of both the fluid and solid constituents. The model describes a single porosity medium fully saturated: the mixture is composed of two phases a solid phase and a fluid phase. Moreover, the model is assumed to be in thermal equilibrium. Hence, a single temperature is defined for the whole mixture. In this context, no mass transfer nor energy transfer are defined.

The presented field equations are the balance of mass of the fluid, the momentum balance equation for the mixture and the balance of energy equation for the mixture. The thermo-mechanical constitutive behaviour is based on Biot's poro-elasticity theory and can be seen as a direct extension of the isothermal theory of Rice and Cleary (1976) thus allowing for compressible fluid and solid constituents, as well as thermal expansion of both phases. Similarly to our model, the thermal expansion of the porous medium is controlled by the solid skeleton only. In addition to our model, McTigue takes into account *the presence of unconnected porosity* through a second solid constituent bulk modulus  $K_s''$  that is different from the solid constituent bulk modulus  $K_s'$ . Moreover they account for the difference between the thermal response of the drained porous medium  $\alpha_s'$  and that of the solid constituent alone  $\alpha_s''$ . If the following simplifications are considered  $K_s' = K_s''$  and  $\alpha_s' = \alpha_s''$ , McTigue's thermo-mechanical behaviour relations reduce to ours. The generalised diffusion constitutive equations are equivalent to Darcy's law and to Fourier's law. No coupling between the mass flux and the heat flux is accounted for. The energy balance equation for the mixture presents a highly reduced form of the complete energy balance: convective transport and thermo-elastic couplings are neglected so as to obtain a tractable analytical solution.

Close form solutions are sought. Drained and undrained thermoelastic limits have been identified. The first is obtained when the pore fluid pressure vanishes, in which case the medium behaves as a simple thermo-elastic body with the properties of the solid skeleton. The undrained limit is obtained when the 'change in fluid content' is null. In this case, the medium again behaves as a simple thermo-elastic body, but exhibits effective properties

modified by the presence of the fluid. These limiting cases are strongly associated with the ratio of the hydraulic and thermal diffusivities,  $c/\kappa$  (where  $c$  is directly proportional to the permeability over the viscosity and  $\kappa$  is equal to the ratio of the thermal conductivity over the volumetric heat capacity). When  $c/\kappa \rightarrow \infty$  (e.g. for large permeability) the fluid pressure relaxes rapidly in comparison to the rate of temperature change, and the material exhibits a drained response. For  $c/\kappa \rightarrow 0$  (e.g. for very small permeability) the fluid is immobilised on the time scale of heat transfer, and undrained behaviour is obtained.

The theory has been specialised to the case of one dimensional deformation, and exact solutions for several illustrative problems have been found. These include the heating of a half-space with either a constant temperature or a constant heat flux boundary. Both drained (zero pressure) and impermeable (zero flux) conditions on the fluid have been considered. One of the main result is the observation that the coupling between heat transfer fluid flow and deformation is strongest *for thermal and fluid diffusivity of like order*, namely  $R = (c/\kappa)^{1/2}$ ; large contrasts result in the drained and undrained limiting behaviour are obtained as discussed previously. Two candidate materials for nuclear waste isolation, deep-sea sediment and rock salt remarkably display a ratio of fluid to thermal diffusivity of like order (McTigue, 1986, Table 1).

## Appendix D

### Appendices of Chapter 2.3.3

To obtain the final form of the balance of energy equations several substitutions are involved. To this end, two demonstrations are gathered in this Appendix. The first one describes the balance of energy equations for a mixture in local thermal non-equilibrium, whereas the second describes the balance of energy for a mixture in local thermal equilibrium. Note that  $\mathcal{K}$  represents all the species, namely the solid skeleton, the pore fluid and the fissure fluid, whereas  $\mathcal{K}^*$  represents *only* the pore fluid and the fissure fluid.

**Demonstration D.1.** *Demonstration balance of energy equations for a mixture in local thermal non-equilibrium. The procedure stands in four steps:*

*i. The first step aims at writing the balance of energy equation for species with respect to the mass center. The generic energy equation is obtained by inserting the balance of momentum in the basic initial relation to have an expression with no momentum transfer contributions  $\hat{\mathbf{p}}_k \cdot \mathbf{v}_k$ ,*

$$\rho^k \frac{d^k U_k}{dt} - \boldsymbol{\sigma}^k : \nabla \mathbf{v}_k + \operatorname{div} \mathbf{q}_k - r_k = \hat{\rho}^k \left( \tilde{U}_k - U_k + \frac{1}{2} (\tilde{\mathbf{v}}_k - \mathbf{v}_k)^2 \right) + \hat{u}_k \quad (\text{D.1})$$

*First, let us substitute the first term  $\rho^k \frac{d^k U_k}{dt}$  to express the time derivative with respect to the mass center,*

$$\frac{d^s}{dt} (\rho^k U_k) = \left( \frac{d^s}{dt} \rho^k \right) U_k + \rho^k \left( \frac{d^k U_k}{dt} + \nabla U_k \cdot (\mathbf{v}_s - \mathbf{v}_k) \right) \quad (\text{D.2})$$

*Expressing the balance of mass (2.21) with respect to the mass center leads to,*

$$\frac{d^s \rho^k}{dt} + \underbrace{\operatorname{div} (\rho^k (\mathbf{v}_k - \mathbf{v}_s))}_{\operatorname{div} \mathbf{M}_k} + \rho^k \operatorname{div} \mathbf{v}_s = \hat{\rho}^k \quad (\text{D.3})$$

*Replacing  $\frac{d^s \rho^k}{dt}$  from equation (D.3) into equation (D.2) and rearranging brings,*

$$\begin{aligned}
\frac{d^s}{dt} (\rho^k U_k) &= \left( \hat{\rho}^k - \operatorname{div} \mathbf{M}_k - \rho^k \operatorname{div} \mathbf{v}_s \right) U_k + \rho^k \frac{d^k U_k}{dt} - \nabla U_k \cdot \mathbf{M}_k \\
&= \left( \hat{\rho}^k - \rho^k \operatorname{div} \mathbf{v}_s \right) U_k + \rho^k \frac{d^k U_k}{dt} - \operatorname{div} (U_k \mathbf{M}_k)
\end{aligned} \tag{D.4}$$

Finally replacing  $\rho^k \frac{d^k U_k}{dt}$  into equation (D.1), leads to the following form of the balance of energy,

$$\begin{aligned}
\frac{d^s}{dt} (\rho^k U_k) + \operatorname{div} (U_k \mathbf{M}_k) + \rho^k U_k \operatorname{div} \mathbf{v}_s - \boldsymbol{\sigma}^k : \nabla \mathbf{v}_k + \operatorname{div} \mathbf{q}_k - r_k = \\
\hat{\rho}^k \left( \tilde{U}_k + \frac{1}{2} (\tilde{\mathbf{v}}_k - \mathbf{v}_k)^2 \right) + \hat{u}_k
\end{aligned} \tag{D.5}$$

Equation (D.5) may also be written with respect to the species motion,

$$\begin{aligned}
\frac{d^k}{dt} (\rho^k U_k) + \rho^k U_k \operatorname{div} \mathbf{v}_k - \boldsymbol{\sigma}^k : \nabla \mathbf{v}_k + \operatorname{div} \mathbf{q}_k - r_k = \\
\hat{\rho}^k \left( \tilde{U}_k + \frac{1}{2} (\tilde{\mathbf{v}}_k - \mathbf{v}_k)^2 \right) + \hat{u}_k
\end{aligned} \tag{D.6}$$

ii. The second step aims at writing the definition of the internal energy for the solid  $m^s U_s$  as a function of the elastic potential of the mixture in the reference configuration  $\underline{\Psi}$ . The definition of the elastic potential of the mixture in the reference configuration  $\underline{\Psi}$  has been previously introduced in equation (2.110),

$$\begin{aligned}
\underline{\Psi} &= m^s E_s - \sum_{p,f} v_k p_k \\
&= m^s U_s - T_s m^s S_s - \sum_{p,f} v_k p_k
\end{aligned} \tag{D.7}$$

Hence, the internal energy of the solid may be written in the following formats, due to equation (2.117),

$$\begin{aligned}
m^s U_s &= \underline{\Psi} + T_s m^s S_s + \sum_{p,f} v_k p_k \\
\rho^s U_s &= \underline{\Psi}^a + T_s \rho^s S_s + \sum_{p,f} n_k p_k, \quad \text{with } \underline{\Psi} = \det \mathbf{F} \underline{\Psi}^a.
\end{aligned} \tag{D.8}$$

iii. Let us focus on the balance of energy equation for the solid phase. First, the derivative of  $\rho^s U_s$  is expressed in an explicit manner with respect to the mass center. Under braced numbers are positioned to emphasis the simplifications. The internal energy of the solid written in the actual configuration can not be derived first. To obtain the correct result, the equations need to be kept in the reference configuration. The simplification by  $\det \mathbf{F}$  can be done after the derivation process only. Hence,

$$\begin{aligned}
d(m^s U_s) &= \frac{\partial \underline{\Psi}}{\partial \boldsymbol{\epsilon}} : d\boldsymbol{\epsilon} + \underbrace{\frac{\partial \underline{\Psi}}{\partial T_s} dT_s}_{(1)} + \underbrace{\sum_{k \in \mathcal{K}^*} \frac{\partial \underline{\Psi}}{\partial p_k} dp_k}_{(2)} - T_s d\left(\frac{\partial \underline{\Psi}}{\partial T_s}\right) - \underbrace{\frac{\partial \underline{\Psi}}{\partial T_s} dT_s}_{(1)} \\
&\quad - \sum_{k \in \mathcal{K}^*} d\left(\frac{\partial \underline{\Psi}}{\partial p_k}\right) p_k - \underbrace{\sum_{k \in \mathcal{K}^*} \frac{\partial \underline{\Psi}}{\partial p_k} dp_k}_{(2)}
\end{aligned} \tag{D.9}$$

After reorganization and simplification, the derivative of  $m^s U_s$  reduces to,

$$\begin{aligned}
d(m^s U_s) &= \frac{\partial \underline{\Psi}}{\partial \boldsymbol{\epsilon}} : d\boldsymbol{\epsilon} - T_s d\left(\frac{\partial \underline{\Psi}}{\partial T_s}\right) - \sum_{k \in \mathcal{K}^*} d\left(\frac{\partial \underline{\Psi}}{\partial p_k}\right) p_k \\
&= \boldsymbol{\tau} : d\boldsymbol{\epsilon} + T_s d(\rho^s S_s) + \sum_{k \in \mathcal{K}^*} p_k dv_k
\end{aligned} \tag{D.10}$$

Since the derivation process is finished, one can safely simplify equation (D.10), using  $dm_s = d\rho_s \det \mathbf{F} + \rho_s \det \mathbf{F} \operatorname{div} \mathbf{v}$ , by  $\det \mathbf{F}$ ,

$$\begin{aligned}
d(\rho^s U_s) &= -\rho^s U_s \mathbf{I} : d\boldsymbol{\epsilon} + \boldsymbol{\sigma} : d\boldsymbol{\epsilon} + T_s (\rho^s S_s \mathbf{I} : d\boldsymbol{\epsilon} + d(\rho^s S_s)) \\
&\quad + \sum_{k \in \mathcal{K}^*} p_k (n_k \mathbf{I} : d\boldsymbol{\epsilon} + dn_k) \\
&= (\boldsymbol{\sigma} + p_k n_k \mathbf{I} + T_s \rho^s S_s \mathbf{I} - \rho^s U_s \mathbf{I}) : d\boldsymbol{\epsilon} + T_s d(\rho^s S_s) + \sum_{k \in \mathcal{K}^*} p_k dn_k
\end{aligned}$$

$$= (\boldsymbol{\sigma}^s - \rho^s E_s \mathbf{I}) : d\boldsymbol{\epsilon} + T_s d(\rho^s S_s) + \sum_{k \in \mathcal{K}^*} p_k dn_k \quad (\text{D.11})$$

In the further development, the following definitions are used,

$$\left. \begin{aligned} \sigma &= \frac{\partial \underline{\Psi}^a}{\partial \boldsymbol{\epsilon}} + \underline{\Psi}^a \mathbf{I} \\ &= \sigma^s + \sum_{k \in \mathcal{K}^*} (-p^k) \mathbf{I} \\ \underline{\Psi}^a &= \rho^s E_s - \sum_{k \in \mathcal{K}^*} n_k p_k \end{aligned} \right\} \rightarrow \sigma^s - \rho^s E_s \mathbf{I} = \frac{\partial \underline{\Psi}^a}{\partial \boldsymbol{\epsilon}}, \quad (\text{D.12})$$

and,

$$\text{div } \mathbf{v}_s = \frac{d(\text{tr } \boldsymbol{\epsilon})}{dt}. \quad (\text{D.13})$$

Let us now rewrite the four first terms of equation (D.5) using equations (D.10) and (D.12). The deviatoric part of the strain  $\text{dev } \boldsymbol{\epsilon}$  is dropped here, since the shear behaviour is accounted for fully by the shear modulus of the drained solid. To highlight the simplifications, underbraced numbers are positioned,

$$\begin{aligned} \frac{d(\rho^s U_s)}{dt} + \rho^s U_s \text{div } \mathbf{v}_s - \sigma^s : \frac{d\boldsymbol{\epsilon}}{dt} &= \underbrace{\frac{\partial \underline{\Psi}^a}{\partial(\text{tr } \boldsymbol{\epsilon})}}_{(1)} : \frac{d(\text{tr } \boldsymbol{\epsilon})}{dt} + T_s \frac{d\rho^s S_s}{dt} + \sum_{k \in \mathcal{K}^*} p_k \frac{dn_k}{dt} \\ &+ \left( \underbrace{\frac{\underline{\Psi}^a}{(2)}}_{(2)} + T_s \rho^s S_s + \underbrace{\sum_{k \in \mathcal{K}^*} n_k p_k}_{(3)} \right) \frac{d(\text{tr } \boldsymbol{\epsilon})}{dt} - \left( \underbrace{\frac{\partial \underline{\Psi}^a}{\partial(\text{tr } \boldsymbol{\epsilon})}}_{(1)} + \sum_{k \in \mathcal{K}^*} \underbrace{p^k \mathbf{I}}_{(3)} + \underbrace{\underline{\Psi}^a \mathbf{I}}_{(2)} \right) \frac{d(\text{tr } \boldsymbol{\epsilon})}{dt} \end{aligned} \quad (\text{D.14})$$

Finally, by rearranging equation (D.14), the final form of the balance of energy equation for the solid phase may be written in the following format,

$$\begin{aligned} T_s \frac{d^s(\rho^s S_s)}{dt} + T_s \rho^s S_s \text{div } \mathbf{v}_s + \sum_{k \in \mathcal{K}^*} p_k \frac{d^s n_k}{dt} + \text{div } \mathbf{q}_s - r_s \\ = \hat{\rho}^s \left( \tilde{U}_s + \frac{1}{2} (\tilde{\mathbf{v}}_s - \mathbf{v}_s)^2 \right) + \hat{u}_s = \underbrace{\frac{\hat{\rho}^s}{2} \mathbf{v}_s^2}_{\text{mass transfer}} + \underbrace{\hat{e}_{\text{energy}}^s - \mathbf{v}_s \cdot \hat{e}_{\mathcal{M}}^s}_{\text{energy transfer}} \end{aligned} \quad (\text{D.15})$$

Note that the mass transfer of the solid phase  $\hat{\rho}^s$  vanishes in the double porosity model,



$$T_s \frac{d^s(\rho^s S_s)}{dt} + T_s \rho^s S_s \operatorname{div} \mathbf{v}_s + \sum_{k \in \mathcal{K}^*} p_k \frac{d^s n_k}{dt} + \operatorname{div} \mathbf{q}_s - r_s = \hat{u}_s \quad (\text{D.16})$$

iv. Let us focus on the balance of energy equation for the fluid phases. First, the internal energy per unit volume for species  $\rho^k U_k$  is defined by use of Table (2.1),

$$\rho^k U_k = \rho^k G_k - p^k + T_k \rho^k S_k \quad (\text{D.17})$$

Let us work on the three first terms of equation (D.6) to highlight some simplifications. By use of equation (D.17) several substitutions are made,

$$\begin{aligned} \frac{d^k}{dt} (\rho^k U_k) + \rho^k U_k \operatorname{div} \mathbf{v}_k + p^k \operatorname{div} \mathbf{v}_k &= \frac{d^k}{dt} (\rho^k G_k - p^k + \rho^k T_k S_k) + (\rho^k G_k - p^k + \rho^k T_k S_k) \operatorname{div} \mathbf{v}_k \\ &\quad + p^k \operatorname{div} \mathbf{v}_k \\ &= G_k \frac{d^k}{dt} \rho^k + \rho^k \frac{d^k G_k}{dt} - \frac{d^k p^k}{dt} + T_k \frac{d^k (\rho^k S_k)}{dt} + \rho^k S_k \frac{d^k T_k}{dt} \\ &\quad + \left( \rho^k G_k - \underbrace{p^k}_{(1)} + \rho^k T_k S_k \right) \operatorname{div} \mathbf{v}_k + \underbrace{p^k \operatorname{div} \mathbf{v}_k}_{(1)} \end{aligned} \quad (\text{D.18})$$

After reorganization and simplification by use of the balance of mass equation (2.21), the three first terms of the generic balance of energy for the species  $k$  reduce to,

$$\begin{aligned} \frac{d^k}{dt} (\rho^k U_k) + \rho^k U_k \operatorname{div} \mathbf{v}_k + p^k \operatorname{div} \mathbf{v}_k &= \hat{\rho}^k G_k + \rho^k \frac{d^k G_k}{dt} - \frac{d^k p^k}{dt} + T_k \frac{d^k}{dt} (\rho^k S_k) \\ &\quad + \rho^k S_k \left( \frac{d^k T_k}{dt} + T^k \operatorname{div} \mathbf{v}_k \right) \end{aligned} \quad (\text{D.19})$$

Moreover, the derivative  $\frac{d^k}{dt} (\rho^k S_k)$  is written with respect to the mass center,

$$\frac{d^k}{dt} (\rho^k U_k) + \rho^k U_k \operatorname{div} \mathbf{v}_k + p^k \operatorname{div} \mathbf{v}_k = \hat{\rho}^k G_k + \rho^k \frac{d^k G_k}{dt} - \frac{d^k p^k}{dt} \quad (\text{D.20})$$

$$+\rho^k S_k \left( \frac{d^k T^k}{dt} + T_k \operatorname{div} \mathbf{v}_k \right) + T_k \left[ \frac{d(\rho^k S_k)}{dt} + \nabla(\rho^k S_k) \cdot (\mathbf{v}_k - \mathbf{v}_s) \right]$$

The definition of the chemical potential total derivative is obtained from Table 2.1,

$$d^k G_k = \frac{d^k p_k}{\rho_k} - S_k d^k T_k \quad \rightarrow \quad d^k p_k = \rho_k (d^k G_k + S_k d^k T_k) \quad (\text{D.21})$$

in which the derivative of the partial pressure writes,

$$d^k p^k = p_k d^k n_k + n_k d^k p_k \quad \rightarrow \quad \rho^k \frac{d^k G_k}{dt} - \frac{d^k p^k}{dt} + \rho^k S_k \frac{d^k T^k}{dt} = -p_k \frac{d^k n_k}{dt} \quad (\text{D.22})$$

By replacing equation (D.22) and simplifying, equation (D.20) may now be cast in the following form,

$$\begin{aligned} \frac{d^k}{dt} (\rho^k U_k) + \rho^k U_k \operatorname{div} \mathbf{v}_k + p^k \operatorname{div} \mathbf{v}_k &= T_k \frac{d^s}{dt} (\rho^k S_k) \\ + T_k \operatorname{div} (S_k \mathbf{M}_k) + T_k \rho^k S_k \operatorname{div} \mathbf{v}_s - p_k \frac{d^k n_k}{dt} + \hat{\rho}^k G_k & \quad (\text{D.23}) \end{aligned}$$

Finally, the balance of energy equation for the fluid phases displays the following form,

$$\begin{aligned} T_k \frac{d^s}{dt} (\rho^k S_k) + T_k \operatorname{div} (S_k \mathbf{M}_k) + T_k \rho^k S_k \operatorname{div} \mathbf{v}_s - p_k \frac{d^k n_k}{dt} + \operatorname{div} \mathbf{q}_k - r_k \\ + \hat{\rho}^k \left( G_k - \tilde{U}_k - \frac{1}{2} (\tilde{\mathbf{v}}_k - \mathbf{v}_k) \right) - \hat{u}_k = 0 \end{aligned} \quad (\text{D.24})$$

Note that the balance of energy equation for the fluid phases may be written in a form that involves mass transfer, energy transfer and diffusion terms. The demonstration is provided in Remark D.1.

$$\begin{aligned} T_k \frac{d^s}{dt} (\rho^k S_k) + T_k \operatorname{div} (S_k \mathbf{M}_k) + T_k \rho^k S_k \operatorname{div} \mathbf{v}_s - p_k \frac{d^k n_k}{dt} + \underbrace{\operatorname{div} \mathbf{q}_k}_{\text{diffusion}} - r_k \\ + \hat{\rho}^k \left( \underbrace{G_k + \frac{1}{2} (\mathbf{v}_k - \mathbf{v}_s)^2 - \frac{1}{2} \mathbf{v}_s^2}_{\text{mass transfer}} + \underbrace{\mathbf{v}_s \cdot \hat{\mathbf{e}}_{\mathcal{M}}^k - \hat{\mathbf{e}}_{\text{energy}}^k}_{\text{energy transfer}} \right) \\ + \underbrace{\mathbf{J}_k \cdot \left( \frac{\nabla p_k}{n_k} + \rho_k \left( \frac{d^k \mathbf{v}_k}{dt} - \mathbf{b}_k \right) \right)}_{\text{convection}} = 0 \end{aligned} \quad (\text{D.25})$$

The term  $T_k \operatorname{div} (S_k \mathbf{M}_k)$  may be written in the following format,

$$\begin{aligned} T_k \operatorname{div} (S_k \mathbf{M}_k) &= T_k \nabla S_k \cdot \mathbf{M}_k + T_k S_k \operatorname{div} (\mathbf{M}_k) \\ &= T_k \rho_k \nabla S_k \cdot \mathbf{J}_k + T_k S_k \left( \hat{\rho}^k - \frac{d\rho^k}{dt} - \rho^k \operatorname{div} \mathbf{v}_s \right) \quad \text{eq. (2.26)} \end{aligned}$$

$$= T_k \rho_k \nabla S_k \cdot \mathbf{J}_k + T_k S_k \hat{\rho}^k - T_k S_k \left( \frac{1}{\det \mathbf{F}} \frac{dm^k}{dt} \right) \quad \text{eq. (2.89)}$$

Therefore, equation (D.25) can be rearranged by replacing the term  $T_k \operatorname{div} (S_k \mathbf{M}_k)$ ,

$$\begin{aligned} &T_k \frac{d^s}{dt} (\rho^k S_k) + T_k \rho^k S_k \operatorname{div} \mathbf{v}_s + T_k S_k \left( -\frac{1}{\det \mathbf{F}} \frac{dm^k}{dt} \right) - p_k \frac{d^s n_k}{dt} \\ &+ \underbrace{\operatorname{div} \mathbf{q}_k}_{\text{diffusion}} - r_k + \underbrace{\hat{\rho}^k \left( H_k + \frac{1}{2} (\mathbf{v}_k - \mathbf{v}_s)^2 - \frac{1}{2} \mathbf{v}_s^2 \right)}_{\text{mass transfer}} + \underbrace{(\mathbf{v}_s \cdot \hat{e}_{\mathcal{M}}^k - \hat{e}_{\mathcal{U}}^k)}_{\text{energy transfer}} \\ &+ \underbrace{\mathbf{M}_k \cdot \left( \nabla H_k + \left( \frac{d^k \mathbf{v}_k}{dt} - \mathbf{b}_k \right) \right)}_{\text{convection}} = 0 \end{aligned} \quad (\text{D.26})$$

**Remark D.1.** Proof of equation (D.25). The temporary notation  $C_{Tr}$  is used to represent the transfer terms of equation (D.25),

$$\begin{aligned} C_{Tr} &= \hat{\rho}^k \left( G_k - \tilde{U}_k - \frac{1}{2} (\tilde{\mathbf{v}}_k - \mathbf{v}_k) \right) - \hat{u}_k \\ &= \hat{\rho}^k \left( G_k - \frac{1}{2} \mathbf{v}_k^2 \right) + \mathbf{v}_k \cdot \hat{e}_{\mathcal{M}}^k - \hat{e}_{\mathcal{U}}^k \quad \text{by eq. (2.31) and (2.46)} \\ &= \hat{\rho}^k \left( G_k - \frac{1}{2} \mathbf{v}_k^2 \right) + \mathbf{v}_s \cdot \hat{e}_{\mathcal{M}}^k - \hat{e}_{\mathcal{U}}^k + (\mathbf{v}_k - \mathbf{v}_s) \cdot \hat{e}_{\mathcal{M}}^k \\ &= \hat{\rho}^k \left( G_k - \frac{1}{2} \mathbf{v}_k^2 \right) + \mathbf{v}_s \cdot \hat{e}_{\mathcal{M}}^k - \hat{e}_{\mathcal{U}}^k \\ &\quad + (\mathbf{v}_k - \mathbf{v}_s) \cdot \left( \nabla p^k + \rho^k \left( \frac{d^k \mathbf{v}_k}{dt} - \mathbf{b}_k \right) + \hat{\rho}^k \mathbf{v}_k \right) \quad \text{by eq. (2.32)} \end{aligned}$$

$$\begin{aligned}
&= \hat{\rho}^k \left( G_k + \frac{1}{2} \mathbf{v}_k^2 - \mathbf{v}_k \mathbf{v}_s \right) + \mathbf{v}_s \cdot \hat{e}_{\mathcal{M}}^k - \hat{e}_{\mathcal{U}}^k \\
&\quad + (\mathbf{v}_k - \mathbf{v}_s) \cdot \left( \nabla p^k + \rho^k \left( \frac{d^k \mathbf{v}_k}{dt} - \mathbf{b}_k \right) \right) \\
&= \hat{\rho}^k \left( G_k + \frac{1}{2} \mathbf{v}_k^2 - \mathbf{v}_k \mathbf{v}_s \right) + \mathbf{v}_s \cdot \hat{e}_{\mathcal{M}}^k - \hat{e}_{\mathcal{U}}^k \\
&\quad + \mathbf{J}_k \cdot \left( \frac{\nabla p^k}{n_k} + \rho_k \left( \frac{d^k \mathbf{v}_k}{dt} - \mathbf{b}_k \right) \right) \\
&= \underbrace{\hat{\rho}^k \left( G_k + \frac{1}{2} (\mathbf{v}_k - \mathbf{v}_s)^2 - \frac{1}{2} \mathbf{v}_s^2 \right)}_{\text{mass transfer}} + \underbrace{\mathbf{v}_s \cdot \hat{e}_{\mathcal{M}}^k - \hat{e}_{\mathcal{U}}^k}_{\text{energy transfer}} \\
&\quad + \underbrace{\mathbf{J}_k \cdot \left( \nabla p_k + \rho_k \left( \frac{d^k \mathbf{v}_k}{dt} - \mathbf{b}_k \right) \right)}_{\text{diffusion}} + p_k \nabla(n_k) \cdot (\mathbf{v}_k - \mathbf{v}_s) \tag{D.27}
\end{aligned}$$

**Demonstration D.2.** *Demonstration of the balance of energy for the mixture in thermal equilibrium, proof of equation (2.307).*

First, the following notations are introduced: the total entropy  $S$ , the total heat source and total heat flux of the mixture are equal to,

$$S = \sum_{k \in \mathcal{K}} \rho^k S_k, \quad \mathbf{q} = \mathbf{q}^I = \sum_{k \in \mathcal{K}} \mathbf{q}_k, \quad r = r^I = \sum_{k \in \mathcal{K}} r_k \tag{D.28}$$

If the species are in thermal equilibrium  $T_k = T_s = T$ , summing up the energy equations over the species, accounting for the closure relations (2.20), (2.31), (2.46), the energy equation for the mixture reduces to,

$$\begin{aligned}
T \frac{dS}{dt} + T S \operatorname{div} \mathbf{v}_s + \operatorname{div} \mathbf{q} - r &= - \sum_{p,f} \hat{\rho}^k \left( G_k + \frac{1}{2} (\mathbf{v}_k - \mathbf{v}_s)^2 \right) \\
&\quad - \sum_{p,f} T \operatorname{div} (S_k \mathbf{M}_k) - \sum_{p,f} \mathbf{J}_k \cdot \left( \nabla p_k + \rho_k \left( \frac{d^k \mathbf{v}_k}{dt} - \mathbf{b}_k \right) \right) \tag{D.29}
\end{aligned}$$

Upon expanding the divergence term  $\operatorname{div} (S_k \mathbf{M}_k)$ , the energy equation becomes,

$$T \frac{dS}{dt} + T S \operatorname{div} \mathbf{v}_s + \operatorname{div} \mathbf{q} - r = - \sum_{p,f} \hat{\rho}^k \left( G_k + \frac{1}{2} (\mathbf{v}_k - \mathbf{v}_s)^2 \right) \tag{D.30}$$

$$-\sum_{p,f} T S_k \operatorname{div}(\mathbf{M}_k) - \sum_{p,f} \mathbf{M}_k \cdot \left( \frac{\nabla p_k}{\rho_k} + T \nabla S_k + \left( \frac{d^k \mathbf{v}_k}{dt} - \mathbf{b}_k \right) \right)$$

The definition of the enthalpy and of the enthalpy gradient are obtained from Table (2.1),

$$H_k = G_k + T S_k \quad \text{and} \quad \nabla H_k = \frac{\nabla p_k}{\rho_k} + T \nabla S_k \quad (\text{D.31})$$

Furthermore, by use of the mass balance equation (2.26), the term  $\operatorname{div}(\mathbf{M}_k)$  is replaced,

$$\begin{aligned} T \frac{dS}{dt} + T S \operatorname{div} \mathbf{v}_s + \operatorname{div} \mathbf{q} - r = & - \sum_{p,f} \hat{\rho}^k \left( H_k + \frac{1}{2} (\mathbf{v}_k - \mathbf{v}_s)^2 \right) + \\ & - \sum_{p,f} T S_k \left( \frac{d\rho^k}{dt} + \rho^k \operatorname{div} \mathbf{v}_s \right) \sum_{p,f} \mathbf{M}_k \cdot \left( \nabla H_k + \left( \frac{d^k \mathbf{v}_k}{dt} - \mathbf{b}_k \right) \right) \end{aligned} \quad (\text{D.32})$$

Finally, by use of equation (2.89), the final form of the balance of energy for a mixture in thermal equilibrium is obtained,

$$\begin{aligned} T \frac{dS}{dt} + T S \operatorname{div} \mathbf{v}_s + \operatorname{div} \mathbf{q} - r + \sum_{p,f} \hat{\rho}^k \left( H_k + \frac{1}{2} (\mathbf{v}_k - \mathbf{v}_s)^2 \right) \\ - \sum_{p,f} T S_k \left( \frac{1}{\det \mathbf{F}} \frac{dm^k}{dt} \right) + \sum_{p,f} \mathbf{M}_k \cdot \left( \nabla H_k + \left( \frac{d^k \mathbf{v}_k}{dt} - \mathbf{b}_k \right) \right) = 0 \end{aligned} \quad (\text{D.33})$$

## Appendix E

# Appendices of Chapter 4

### E.1 Sub-matrices of the weak formulation

The detailed formulation of each sub-matrix introduced in the weak formulation is written below. Each unknown type is discretised with four functions of interpolation. For a plane strain problem, the sub-matrices of the weak formulation write,

$$\mathbf{u} = \begin{bmatrix} u_{x_1} \\ u_{x_2} \end{bmatrix} = \mathbf{N}_u \mathbf{u}^e, \quad (\text{E.1})$$

$$\mathbf{N}_u = \begin{bmatrix} N_u^1 & 0 & N_u^2 & 0 & N_u^3 & 0 & N_u^4 & 0 \\ 0 & N_u^1 & 0 & N_u^2 & 0 & N_u^3 & 0 & N_u^4 \end{bmatrix}, \quad (\text{E.2})$$

$$[\mathbf{u}^e]^T = [u_{x_1}^1 \quad u_{x_2}^1 \quad u_{x_1}^2 \quad u_{x_2}^2 \quad u_{x_1}^3 \quad u_{x_2}^3 \quad u_{x_1}^4 \quad u_{x_2}^4], \quad (\text{E.3})$$

$$p_k = \mathbf{N}_p \mathbf{p}_k^e, \quad \text{for } k = p, f, \quad (\text{E.4})$$

$$\mathbf{N}_p = [N_p^1 \quad N_p^2 \quad N_p^3 \quad N_p^4], \quad (\text{E.5})$$

$$[\mathbf{p}_k^e]^T = [p_k^1 \quad p_k^2 \quad p_k^3 \quad p_k^4], \quad \text{for } k = p, f, \quad (\text{E.6})$$

$$T_k = \mathbf{N}_T \mathbf{T}_k^e, \quad \text{for } k = s, p, f, \quad (\text{E.7})$$

$$\mathbf{N}_T = [N_T^1 \quad N_T^2 \quad N_T^3 \quad N_T^4], \quad (\text{E.8})$$

$$[\mathbf{T}_k^e]^T = [T_k^1 \ T_k^2 \ T_k^3 \ T_k^4], \quad \text{for } k = s, p, f, \quad (\text{E.9})$$

$$\mathbf{B}_u = \begin{bmatrix} \frac{\partial N_u^1}{\partial x_1} & 0 & \frac{\partial N_u^2}{\partial x_1} & 0 & \frac{\partial N_u^3}{\partial x_1} & 0 & \frac{\partial N_u^4}{\partial x_1} & 0 \\ 0 & \frac{\partial N_u^1}{\partial x_2} & 0 & \frac{\partial N_u^2}{\partial x_2} & 0 & \frac{\partial N_u^3}{\partial x_2} & 0 & \frac{\partial N_u^4}{\partial x_2} \\ \frac{\partial N_u^1}{\partial x_2} & \frac{\partial N_u^1}{\partial x_1} & \frac{\partial N_u^2}{\partial x_2} & \frac{\partial N_u^2}{\partial x_1} & \frac{\partial N_u^3}{\partial x_2} & \frac{\partial N_u^3}{\partial x_1} & \frac{\partial N_u^4}{\partial x_2} & \frac{\partial N_u^4}{\partial x_1} \end{bmatrix}, \quad (\text{E.10})$$

$$\nabla \mathbf{N}_u = \begin{bmatrix} \frac{\partial N_u^1}{\partial x_1} & \frac{\partial N_u^1}{\partial x_2} & \frac{\partial N_u^2}{\partial x_1} & \frac{\partial N_u^2}{\partial x_2} & \frac{\partial N_u^3}{\partial x_1} & \frac{\partial N_u^3}{\partial x_2} & \frac{\partial N_u^4}{\partial x_1} & \frac{\partial N_u^4}{\partial x_2} \end{bmatrix}, \quad (\text{E.11})$$

$$\nabla \cdot \mathbf{N}_u = \begin{bmatrix} \frac{\partial N_u^1}{\partial x_1} & 0 & \frac{\partial N_u^2}{\partial x_1} & 0 & \frac{\partial N_u^3}{\partial x_1} & 0 & \frac{\partial N_u^4}{\partial x_1} & 0 \\ 0 & \frac{\partial N_u^1}{\partial x_2} & 0 & \frac{\partial N_u^2}{\partial x_2} & 0 & \frac{\partial N_u^3}{\partial x_2} & 0 & \frac{\partial N_u^4}{\partial x_2} \end{bmatrix}, \quad (\text{E.12})$$

$$\nabla \mathbf{N}_p = \begin{bmatrix} \frac{\partial N_p^1}{\partial x_1} & \frac{\partial N_p^2}{\partial x_1} & \frac{\partial N_p^3}{\partial x_1} & \frac{\partial N_p^4}{\partial x_1} \\ \frac{\partial N_p^1}{\partial x_2} & \frac{\partial N_p^2}{\partial x_2} & \frac{\partial N_p^3}{\partial x_2} & \frac{\partial N_p^4}{\partial x_2} \end{bmatrix}, \quad (\text{E.13})$$

$$\nabla \mathbf{N}_T = \begin{bmatrix} \frac{\partial N_T^1}{\partial x_1} & \frac{\partial N_T^2}{\partial x_1} & \frac{\partial N_T^3}{\partial x_1} & \frac{\partial N_T^4}{\partial x_1} \\ \frac{\partial N_T^1}{\partial x_2} & \frac{\partial N_T^2}{\partial x_2} & \frac{\partial N_T^3}{\partial x_2} & \frac{\partial N_T^4}{\partial x_2} \end{bmatrix}, \quad (\text{E.14})$$

$$\mathbf{D}_{el} = \begin{bmatrix} \lambda^{DS} + 2\mu^{DS} & \lambda^{DS} & 0 \\ \lambda^{DS} & \lambda^{DS} + 2\mu^{DS} & 0 \\ 0 & 0 & \mu^{DS} \end{bmatrix}, \quad (\text{E.15})$$

$$\mathbf{v}_p = \begin{bmatrix} v_{p,x_1} \\ v_{p,x_2} \end{bmatrix}, \quad \mathbf{v}_f = \begin{bmatrix} v_{f,x_1} \\ v_{f,x_2} \end{bmatrix}.$$

Due to similarities between *axi-symmetric* and plane strain analyses, all the integrations necessary to develop the element stiffness matrix for an *axi-symmetric* analysis are very similar to that of plane strain analysis, except that

- The integration domain is over the volume of the body of revolution,  $dV^e = dx_1 dx_2 \rightarrow dV^e = 2\pi r dr dz$
- The  $\mathbf{D}_{\text{el}}$  matrix becomes of size  $4 \times 4$  and the  $\mathbf{B}_{\mathbf{u}}$  becomes of size  $4 \times 8$ .

For an axi-symmetric analysis,  $\mathbf{D}_{\text{el}}$  and  $\mathbf{B}_{\mathbf{u}}$  are defined by using cylindrical coordinates instead of Cartesian coordinates,

$$\mathbf{D}_{\text{el}} = \begin{bmatrix} \lambda^{DS} + 2\mu^{DS} & \lambda^{DS} & 0 & \lambda^{DS} \\ \lambda^{DS} & \lambda^{DS} + 2\mu^{DS} & 0 & \lambda^{DS} \\ 0 & 0 & \mu^{DS} & 0 \\ \lambda^{DS} & \lambda^{DS} & 0 & \lambda^{DS} + 2\mu^{DS} \end{bmatrix}, \quad (\text{E.16})$$

$$\mathbf{B}_{\mathbf{u}} = \begin{bmatrix} \frac{\partial N_{\mathbf{u}}^1}{\partial x_1} & 0 & \frac{\partial N_{\mathbf{u}}^2}{\partial x_1} & 0 & \frac{\partial N_{\mathbf{u}}^3}{\partial x_1} & 0 & \frac{\partial N_{\mathbf{u}}^4}{\partial x_1} & 0 \\ 0 & \frac{\partial N_{\mathbf{u}}^1}{\partial x_2} & 0 & \frac{\partial N_{\mathbf{u}}^2}{\partial x_2} & 0 & \frac{\partial N_{\mathbf{u}}^3}{\partial x_2} & 0 & \frac{\partial N_{\mathbf{u}}^4}{\partial x_2} \\ \frac{\partial N_{\mathbf{u}}^1}{\partial x_2} & \frac{\partial N_{\mathbf{u}}^1}{\partial x_1} & \frac{\partial N_{\mathbf{u}}^2}{\partial x_2} & \frac{\partial N_{\mathbf{u}}^2}{\partial x_1} & \frac{\partial N_{\mathbf{u}}^3}{\partial x_2} & \frac{\partial N_{\mathbf{u}}^3}{\partial x_1} & \frac{\partial N_{\mathbf{u}}^4}{\partial x_2} & \frac{\partial N_{\mathbf{u}}^4}{\partial x_1} \\ \hline \frac{N_{\mathbf{u}}^1}{r} & 0 & \frac{N_{\mathbf{u}}^2}{r} & 0 & \frac{N_{\mathbf{u}}^3}{r} & 0 & \frac{N_{\mathbf{u}}^4}{r} & 0 \end{bmatrix}. \quad (\text{E.17})$$

## E.2 Detailed elementary weak formulation

The elementary weak formulation, before assembling, writes as following. The sub-matrices are provided in Appendix E.1. The non-linear terms issued from convection are highlighted in green and the non-linear terms issued from the internal energy due to mass transfer are colored in blue.

Elementary contribution to the balance of momentum for the mixture:

$$\begin{aligned} & \int_{V^e} \mathbf{B}_{\mathbf{u}}^T \mathbf{D}_{\text{el}} \mathbf{B}_{\mathbf{u}} \mathbf{u}^e - \nabla \mathbf{N}_{\mathbf{u}}^T \mathbf{N}_p (\xi_p \mathbf{p}_p^e + \xi_f \mathbf{p}_f^e) - \nabla \mathbf{N}_{\mathbf{u}}^T \mathbf{N}_T \alpha_{\epsilon T_s} \mathbf{T}_s^e dV^e \\ & - \int_{V^e} \mathbf{N}_{\mathbf{u}}^T \rho \mathbf{b} dV^e - \int_{\partial V^e} \mathbf{N}_{\mathbf{u}}^T \boldsymbol{\sigma} \cdot \hat{\mathbf{n}} dS^e. \end{aligned} \quad (\text{E.18})$$



Elementary contribution to the balance of mass for the pore fluid:

$$\begin{aligned}
& \int_{V^e} -\nabla \mathbf{N}_p^\top \frac{k_p}{\mu_p} \nabla \mathbf{N}_p \mathbf{p}_p^e - \nabla \mathbf{N}_p^\top n_p \Theta_p \nabla \mathbf{N}_T \mathbf{T}_p^e \, dV^e \\
& \int_{V^e} -\mathbf{N}_p^\top \mathbf{N}_p (a_{pp} \dot{\mathbf{p}}_p^e + a_{pf} \dot{\mathbf{p}}_f^e) \, dV^e \\
& + \int_{V^e} -\mathbf{N}_p^\top \mathbf{N}_T (a_{pT_s} \dot{\mathbf{T}}_s^e + a_{pT_p} \dot{\mathbf{T}}_p^e) - \mathbf{N}_p^\top [1 \quad 1] \nabla \cdot \mathbf{N}_u \xi_p \dot{\mathbf{u}}^e \, dV^e \\
& + \int_{V^e} -\mathbf{N}_T \mathbf{T}_0^e \rho_p \eta \mathbf{N}_p^\top \left[ \frac{G_p(\mathbf{N}_p \mathbf{p}_p^e, \mathbf{N}_T \mathbf{T}_p^e)}{\mathbf{N}_T \mathbf{T}_p^e} - \frac{G_f(\mathbf{N}_p \mathbf{p}_f^e, \mathbf{N}_T \mathbf{T}_f^e)}{\mathbf{N}_T \mathbf{T}_f^e} \right] \, dV^e \\
& - \int_{\partial V^e} \mathbf{N}_p^\top \mathbf{J}_p \cdot \hat{\mathbf{n}} \, dS^e + \int_{V^e} \nabla \mathbf{N}_p^\top \frac{k_p}{\mu_p} \rho_p \mathbf{g} \, dV^e.
\end{aligned} \tag{E.19}$$

in which the chemical potential  $G_k(\mathbf{N}_p \mathbf{p}_k^e, \mathbf{N}_T \mathbf{T}_k^e)$  of the fluid  $k$  is defined in eq. (2.160)<sub>2</sub>.

Elementary contribution to the balance of mass for the fissure fluid:

$$\begin{aligned}
& \int_{V^e} -\nabla \mathbf{N}_p^\top \frac{k_f}{\mu_f} \nabla \mathbf{N}_p \mathbf{p}_f^e - \nabla \mathbf{N}_p^\top n_f \Theta_f \nabla \mathbf{N}_T \mathbf{T}_f^e \, dV^e \\
& \int_{V^e} -\mathbf{N}_p^\top \mathbf{N}_p (a_{ff} \dot{\mathbf{p}}_f^e + a_{pf} \dot{\mathbf{p}}_p^e) \, dV^e \\
& + \int_{V^e} -\mathbf{N}_p^\top \mathbf{N}_T (a_{fT_s} \dot{\mathbf{T}}_s^e + a_{fT_f} \dot{\mathbf{T}}_f^e) - \mathbf{N}_p^\top [1 \quad 1] \nabla \cdot \mathbf{N}_u \xi_f \dot{\mathbf{u}}^e \, dV^e \\
& + \int_{V^e} +\mathbf{N}_T \mathbf{T}_0^e \rho_p \eta \mathbf{N}_p^\top \left[ \frac{G_p(\mathbf{N}_p \mathbf{p}_p^e, \mathbf{N}_T \mathbf{T}_p^e)}{\mathbf{N}_T \mathbf{T}_p^e} - \frac{G_f(\mathbf{N}_p \mathbf{p}_f^e, \mathbf{N}_T \mathbf{T}_f^e)}{\mathbf{N}_T \mathbf{T}_f^e} \right] \, dV^e \\
& - \int_{\partial V^e} \mathbf{N}_p^\top \mathbf{J}_f \cdot \hat{\mathbf{n}} \, dS^e + \int_{V^e} \nabla \mathbf{N}_p^\top \frac{k_f}{\mu_f} \rho_f \mathbf{g} \, dV^e.
\end{aligned} \tag{E.20}$$

Elementary contribution to the balance of energy for the solid phase:

$$\begin{aligned}
& \int_{V^e} -\nabla \mathbf{N}_T^\top n_s \Lambda_s \nabla \mathbf{N}_T \mathbf{T}_s^e - \mathbf{N}_T^\top \mathbf{N}_T a_{T_s T_s} \dot{\mathbf{T}}_s^e \, dV^e \\
& + \int_{V^e} -\mathbf{N}_T^\top \mathbf{N}_p (a_{T_s p} \dot{\mathbf{p}}_p^e + a_{T_s f} \dot{\mathbf{p}}_f^e) - \mathbf{N}_T^\top [1 \quad 1] \nabla \cdot \mathbf{N}_u a_{T_s \epsilon} \dot{\mathbf{u}}^e \, dV^e \\
& + \int_{V^e} -\mathbf{N}_T^\top \mathbf{N}_T (\kappa_{sp}(\mathbf{T}_s^e - \mathbf{T}_p^e) + \kappa_{sf}(\mathbf{T}_s^e - \mathbf{T}_f^e)) \, dV^e \\
& - \int_{\partial V^e} \mathbf{N}_T^\top \mathbf{q}_s \cdot \hat{\mathbf{n}} \, dS^e.
\end{aligned} \tag{E.21}$$

Elementary contribution to the balance of energy for the pore fluid:

$$\begin{aligned}
& \int_{V^e} -\nabla \mathbf{N}_T^T n_p \Lambda_p \nabla \mathbf{N}_T \mathbf{T}_p^e - \nabla \mathbf{N}_T^T T_p n_p \Theta_p \nabla \mathbf{N}_p \mathbf{p}_p^e \, dV^e \\
& + \int_{V^e} -\mathbf{N}_T^T \mathbf{N}_T (a_{T_p T_p} \dot{\mathbf{T}}_p^e + a_{T_p T_s} \dot{\mathbf{T}}_s^e) - \mathbf{N}_T^T \mathbf{N}_p (a_{T_p p} \dot{\mathbf{p}}_p^e + a_{T_p f} \dot{\mathbf{p}}_f^e) \, dV^e \\
& + \int_{V^e} -\mathbf{N}_T^T [1 \quad 1] \nabla \cdot \mathbf{N}_u a_{T_p \epsilon} \dot{\mathbf{u}}^e \, dV^e \\
& + \int_{V^e} -\mathbf{N}_T^T \mathbf{N}_T (\kappa_{sp} (\mathbf{T}_p^e - \mathbf{T}_s^e) + \kappa_{pf} (\mathbf{T}_p^e - \mathbf{T}_f^e)) \, dV^e \\
& + \int_{V^e} +\mathbf{N}_T \mathbf{T}_0^e \rho_p^2 \eta \mathbf{N}_T^T \left[ \frac{G_p (\mathbf{N}_p \mathbf{p}_p^e, \mathbf{N}_T \mathbf{T}_p^e)}{\mathbf{N}_T \mathbf{T}_p^e} - \frac{G_f (\mathbf{N}_p \mathbf{p}_f^e, \mathbf{N}_T \mathbf{T}_f^e)}{\mathbf{N}_T \mathbf{T}_f^e} \right] \\
& \quad \times H_p (\mathbf{N}_p \mathbf{p}_p^e, \mathbf{N}_T \mathbf{T}_p^e) \, dV^e \\
& + \int_{V^e} -\mathbf{N}_T^T (\mathbf{v}_p - \mathbf{v}_s) \cdot (\nabla \mathbf{N}_p b_{T_p p} \mathbf{p}_p^e + \nabla \mathbf{N}_T b_{T_p T_p} \mathbf{T}_p^e) \, dV^e \\
& - \int_{\partial V^e} \mathbf{N}_T^T \mathbf{q}_p \cdot \hat{\mathbf{n}} \, dS^e + \int_{V^e} \nabla \mathbf{N}_T^T n_p T_p \Theta_p \rho_p \mathbf{g} \, dV^e.
\end{aligned} \tag{E.22}$$

in which the enthalpy  $H_k(\mathbf{N}_p \mathbf{p}_k^e, \mathbf{N}_T \mathbf{T}_k^e)$  of the fluid  $k$  is defined in eq. (2.160)<sub>3</sub>. Elementary contribution to the balance of energy for the fissure fluid:

$$\begin{aligned}
& \int_{V^e} -\nabla \mathbf{N}_T^T n_f \Lambda_f \nabla \mathbf{N}_T \mathbf{T}_f^e - \nabla \mathbf{N}_T^T T_f n_f \Theta_f \nabla \mathbf{N}_p \mathbf{p}_f^e \, dV^e \\
& + \int_{V^e} -\mathbf{N}_T^T \mathbf{N}_T (a_{T_f T_f} \dot{\mathbf{T}}_f^e + a_{T_f T_s} \dot{\mathbf{T}}_s^e) - \mathbf{N}_T^T \mathbf{N}_p (a_{T_f p} \dot{\mathbf{p}}_p^e + a_{T_f f} \dot{\mathbf{p}}_f^e) \, dV^e \\
& + \int_{V^e} -\mathbf{N}_T^T [1 \quad 1] \nabla \cdot \mathbf{N}_u a_{T_f \epsilon} \dot{\mathbf{u}}^e \, dV^e \\
& + \int_{V^e} -\mathbf{N}_T^T \mathbf{N}_T (\kappa_{sf} (\mathbf{T}_f^e - \mathbf{T}_s^e) + \kappa_{pf} (\mathbf{T}_f^e - \mathbf{T}_p^e)) \, dV^e \\
& + \int_{V^e} -\mathbf{N}_T \mathbf{T}_0^e \rho_p^2 \eta \mathbf{N}_T^T \left[ \frac{G_p (\mathbf{N}_p \mathbf{p}_p^e, \mathbf{N}_T \mathbf{T}_p^e)}{\mathbf{N}_T \mathbf{T}_p^e} - \frac{G_f (\mathbf{N}_p \mathbf{p}_f^e, \mathbf{N}_T \mathbf{T}_f^e)}{\mathbf{N}_T \mathbf{T}_f^e} \right] \\
& \quad \times H_f (\mathbf{N}_p \mathbf{p}_f^e, \mathbf{N}_T \mathbf{T}_f^e) \, dV^e \\
& + \int_{V^e} -\mathbf{N}_T^T (\mathbf{v}_f - \mathbf{v}_s) \cdot (\nabla \mathbf{N}_p b_{T_f p} \mathbf{p}_f^e + \nabla \mathbf{N}_T b_{T_f T_f} \mathbf{T}_f^e) \, dV^e \\
& - \int_{\partial V^e} \mathbf{N}_T^T \mathbf{q}_f \cdot \hat{\mathbf{n}} \, dS^e + \int_{V^e} \nabla \mathbf{N}_T^T n_f T_f \Theta_f \rho_f \mathbf{g} \, dV^e.
\end{aligned} \tag{E.23}$$

### E.3 Sub-matrices of the effective convection-diffusion matrix

The identification of the sub-matrices of the stiffness matrix  $\mathbb{K}^e$ , of the diffusion matrix  $\mathbb{D}^e$  and of the convection matrix  $\mathbb{C}_{\text{conv}}^e$  is obtained by comparing equations (4.38) to (4.43),

$$\begin{aligned}
\mathbf{K}_{\mathbf{u}\mathbf{u}}^e &= \mathbf{E}_{\mathbf{u}\mathbf{u}}^e, & \mathbf{K}_{\mathbf{u}p_p}^e &= -\xi_p \mathbf{C}_{\mathbf{u}p}^e, \\
\mathbf{K}_{\mathbf{u}p_f}^e &= -\xi_f \mathbf{C}_{\mathbf{u}p}^e, & \mathbf{K}_{\mathbf{u}T_s}^e &= -a_{\epsilon T_s} \mathbf{C}_{\mathbf{u}T}^e, \\
\mathbf{K}_{p_p p_p}^e &= -\mathbf{J}_{k_p}^e - \gamma_{pp} \mathbf{M}_{pp}^e, & \mathbf{K}_{p_p p_f}^e &= \gamma_{pp} \mathbf{M}_{pp}^e, \\
\mathbf{K}_{p_p T_p}^e &= -\mathbf{J}_{\Theta_p}^e - \gamma_{pT} \mathbf{M}_{pT}^e, & \mathbf{K}_{p_p T_f}^e &= \gamma_{pT} \mathbf{M}_{pT}^e, \\
\mathbf{K}_{p_f p_f}^e &= -\mathbf{J}_{k_f}^e - \gamma_{pp} \mathbf{M}_{pp}^e, & \mathbf{K}_{p_f p_p}^e &= \gamma_{pp} \mathbf{M}_{pp}^e, \\
\mathbf{K}_{p_f T_f}^e &= -\mathbf{J}_{\Theta_f}^e - \gamma_{pT} \mathbf{M}_{pT}^e, & \mathbf{K}_{p_f T_p}^e &= \gamma_{pT} \mathbf{M}_{pT}^e, \\
\mathbf{K}_{T_s T_s}^e &= -\mathbf{Q}_{\Lambda_s}^e - (\kappa_{sp} + \kappa_{sf}) \mathbf{M}_{TT}^e, & \mathbf{K}_{T_s T_p}^e &= \kappa_{sp} \mathbf{M}_{TT}^e, \\
\mathbf{K}_{T_s T_f}^e &= \kappa_{sf} \mathbf{M}_{TT}^e, & & \\
\mathbf{K}_{T_p p_p}^e &= -\mathbf{Q}_{\Theta_p}^e - \gamma_{T_p p} [\mathbf{M}_{pT}^e]^\top, & \mathbf{K}_{T_p p_f}^e &= \gamma_{T_p p} [\mathbf{M}_{pT}^e]^\top, \\
\mathbf{K}_{T_p T_s}^e &= \kappa_{sp} \mathbf{M}_{TT}^e, & \mathbf{K}_{T_p T_f}^e &= (\kappa_{pf} + \gamma_{T_p T_p}) \mathbf{M}_{TT}^e, \\
\mathbf{K}_{T_p T_p}^e &= -\mathbf{Q}_{\Lambda_p}^e - (\kappa_{sp} + \kappa_{pf} + \gamma_{T_p T_p}) \mathbf{M}_{TT}^e, & & \\
\mathbf{K}_{T_f p_f}^e &= -\mathbf{Q}_{\Theta_f}^e + \gamma_{T_f f} [\mathbf{M}_{pT}^e]^\top, & \mathbf{K}_{T_f p_p}^e &= -\gamma_{T_f f} [\mathbf{M}_{pT}^e]^\top, \\
\mathbf{K}_{T_f T_s}^e &= \kappa_{sf} \mathbf{M}_{TT}^e, & \mathbf{K}_{T_f T_p}^e &= (\kappa_{pf} - \gamma_{T_f T_f}) \mathbf{M}_{TT}^e, \\
\mathbf{K}_{T_f T_f}^e &= -\mathbf{Q}_{\Lambda_f}^e - (\kappa_{sf} + \kappa_{pf} - \gamma_{T_f T_f}) \mathbf{M}_{TT}^e. & &
\end{aligned} \tag{E.24}$$

The identification of the sub-matrices of the diffusion matrix  $\mathbb{D}^e$  brings,

$$\begin{aligned}
\mathbf{D}_{p_p \mathbf{u}}^e &= -\xi_p [\mathbf{C}_{\mathbf{u}p}^e]^\top, & \mathbf{D}_{p_p p_p}^e &= -a_{pp} \mathbf{M}_{pp}^e, \\
\mathbf{D}_{p_p p_f}^e &= -a_{pf} \mathbf{M}_{pp}^e, & \mathbf{D}_{p_p T_s}^e &= -a_{pT_s} \mathbf{M}_{pT}^e, \\
\mathbf{D}_{p_p T_p}^e &= -a_{pT_p} \mathbf{M}_{pT}^e, \\
\hline
\mathbf{D}_{p_f \mathbf{u}}^e &= -\xi_f [\mathbf{C}_{\mathbf{u}p}^e]^\top, & \mathbf{D}_{p_f p_p}^e &= -a_{pf} \mathbf{M}_{pp}^e, \\
\mathbf{D}_{p_f p_f}^e &= -a_{ff} \mathbf{M}_{pp}^e, & \mathbf{D}_{p_f T_s}^e &= -a_{fT_s} \mathbf{M}_{pT}^e, \\
\mathbf{D}_{p_f T_f}^e &= -a_{fT_f} \mathbf{M}_{pT}^e, \\
\hline
\mathbf{D}_{T_s \mathbf{u}}^e &= -a_{T_s \epsilon} [\mathbf{C}_{\mathbf{u}T}^e]^\top, & \mathbf{D}_{T_s p_p}^e &= -a_{T_s p} [\mathbf{M}_{pT}^e]^\top, \\
\mathbf{D}_{T_s p_f}^e &= -a_{T_s f} [\mathbf{M}_{pT}^e]^\top, & \mathbf{D}_{T_s T_s}^e &= -a_{T_s T_s} \mathbf{M}_{TT}^e, \\
\hline
\mathbf{D}_{T_p \mathbf{u}}^e &= -a_{T_p \epsilon} [\mathbf{C}_{\mathbf{u}T}^e]^\top, & \mathbf{D}_{T_p p_p}^e &= -a_{T_p p} [\mathbf{M}_{pT}^e]^\top, \\
\mathbf{D}_{T_p p_f}^e &= -a_{T_p f} [\mathbf{M}_{pT}^e]^\top, & \mathbf{D}_{T_p T_s}^e &= -a_{T_p T_s} \mathbf{M}_{TT}^e, \\
\mathbf{D}_{T_p T_p}^e &= -a_{T_p T_p} \mathbf{M}_{TT}^e, \\
\hline
\mathbf{D}_{T_f \mathbf{u}}^e &= -a_{T_f \epsilon} [\mathbf{C}_{\mathbf{u}T}^e]^\top, & \mathbf{D}_{T_f p_p}^e &= -a_{T_f p} [\mathbf{M}_{pT}^e]^\top, \\
\mathbf{D}_{T_f p_f}^e &= -a_{T_f f} [\mathbf{M}_{pT}^e]^\top, & \mathbf{D}_{T_f T_s}^e &= -a_{T_f T_s} \mathbf{M}_{TT}^e, \\
\mathbf{D}_{T_f T_f}^e &= -a_{T_f T_f} \mathbf{M}_{TT}^e; \\
\hline
\end{aligned} \tag{E.25}$$

and the identification of the sub-matrices of the convection matrix  $\mathbf{C}_{\text{conv}}^e$  introduces the approximated terms,

$$\begin{aligned}
\mathbf{C}_{T_p p_p}^e &= -b_{T_p p} \mathbf{C}_{T_p, v_p}^e, & \mathbf{C}_{T_p T_p}^e &= -b_{T_p T_p} \mathbf{C}_{TT, v_p}^e, \\
\mathbf{C}_{T_f p_f}^e &= -b_{T_f f} \mathbf{C}_{T_p, v_f}^e, & \mathbf{C}_{T_f T_f}^e &= -b_{T_f T_f} \mathbf{C}_{TT, v_f}^e. \\
\hline
\end{aligned} \tag{E.26}$$

# Appendix F

## Appendices of Chapter 6

### F.1 Finite element sub-matrices

The finite element sub-matrices of the compact weak formulation in equations (6.19-6.22) are listed below.

- the four element matrices contributing to the balance of momentum of the mixture,

$$\begin{aligned}
 \mathbf{E}_{\mathbf{u}\mathbf{u}}^e &= \int_{V^e} \mathbf{B}_{\mathbf{u}}^T \mathbf{D}_{\text{el}} \mathbf{B}_{\mathbf{u}} dV^e, & \mathbf{C}_{\mathbf{u}p}^e &= \int_{V^e} \nabla \mathbf{N}_{\mathbf{u}}^T \mathbf{N}_p dV^e \\
 \mathbf{C}_{p\mathbf{u}}^e &= \int_{V^e} \mathbf{N}_p^T [1 \quad 1] \nabla \cdot \mathbf{N}_{\mathbf{u}} dV^e, & \mathbf{C}_{\mathbf{u}T}^e &= \int_{V^e} \nabla \mathbf{N}_{\mathbf{u}}^T \mathbf{N}_T dV^e, \\
 \mathbf{C}_{T\mathbf{u}}^e &= \int_{V^e} \mathbf{N}_T^T [1 \quad 1] \nabla \cdot \mathbf{N}_{\mathbf{u}} dV^e;
 \end{aligned} \tag{F.1}$$

- the matrices describing the hydraulic conductivity and the thermal conductivity,

$$\begin{aligned}
 \mathbf{J}_{k_p}^e &= \int_{V^e} \nabla \mathbf{N}_p^T \frac{k_p}{\mu_p} \nabla \mathbf{N}_p dV^e, & \mathbf{J}_{k_f}^e &= \int_{V^e} \nabla \mathbf{N}_p^T \frac{k_f}{\mu_f} \nabla \mathbf{N}_p dV^e \\
 \mathbf{Q}_{\Lambda}^e &= \int_{V^e} \nabla \mathbf{N}_p^T \Lambda \nabla \mathbf{N}_p dV^e
 \end{aligned} \tag{F.2}$$

- the three mass matrices,

$$\begin{aligned}
 \mathbf{M}_{pp}^e &= \int_{V^e} \mathbf{N}_p^T \mathbf{N}_p dV^e, & \mathbf{M}_{TT}^e &= \int_{V^e} \mathbf{N}_T^T \mathbf{N}_T dV^e \\
 \mathbf{M}_{pT}^e &= \int_{V^e} \mathbf{N}_p^T \mathbf{N}_T dV^e
 \end{aligned} \tag{F.3}$$

- the element force vectors,

$$\mathbf{F}_{\mathbf{u}}^e = \int_{\partial V^e} \mathbf{N}_{\mathbf{u}}^T \boldsymbol{\sigma} \cdot \hat{\mathbf{n}} \, dS^e + \int_{V^e} \mathbf{N}_{\mathbf{u}}^T \mathbf{F} \, dV^e \quad (\text{F.4})$$

$$\mathbf{F}_{p_p}^e = \int_{\partial V^e} \mathbf{N}_p^T \mathbf{J}_p \cdot \hat{\mathbf{n}} \, dS^e$$

$$\mathbf{F}_{p_f}^e = \int_{\partial V^e} \mathbf{N}_p^T \mathbf{J}_f \cdot \hat{\mathbf{n}} \, dS^e \quad (\text{F.5})$$

$$\mathbf{F}_T^e = \int_{\partial V^e} \mathbf{N}_T^T \mathbf{q} \cdot \hat{\mathbf{n}} \, dS^e$$

in which,

$$\mathbf{N}_{\mathbf{u}} = \begin{bmatrix} N^1 & 0 & N^2 & 0 & N^3 & 0 & N^4 & 0 \\ 0 & N^1 & 0 & N^2 & 0 & N^3 & 0 & N^4 \end{bmatrix}$$

$$\mathbf{N}_p = \mathbf{N}_T = [ N^1 \quad N^2 \quad N^3 \quad N^4 ], \quad (\text{F.6})$$

where  $N^1, N^2, N^3$  and  $N^4$  are the shape functions.  $\mathbf{D}_{\text{el}}$  is the drained stiffness matrix,

$$\mathbf{D}_{\text{el}} = \begin{bmatrix} \lambda^{DS} + 2\mu^{DS} & \lambda^{DS} & 0 & \lambda^{DS} \\ \lambda^{DS} & \lambda^{DS} + 2\mu^{DS} & 0 & \lambda^{DS} \\ 0 & 0 & \mu^{DS} & 0 \\ \lambda^{DS} & \lambda^{DS} & 0 & \lambda^{DS} + 2\mu^{DS} \end{bmatrix}, \quad (\text{F.7})$$

and  $\mathbf{B}_{\mathbf{u}}$  is the strain displacement matrix,

$$\mathbf{B}_{\mathbf{u}} = \begin{bmatrix} \frac{\partial N^1}{\partial r} & 0 & \frac{\partial N^2}{\partial r} & 0 & \frac{\partial N^3}{\partial r} & 0 & \frac{\partial N^4}{\partial r} & 0 \\ 0 & \frac{\partial N^1}{\partial z} & 0 & \frac{\partial N^2}{\partial z} & 0 & \frac{\partial N^3}{\partial z} & 0 & \frac{\partial N^4}{\partial z} \\ \frac{\partial N^1}{\partial z} & \frac{\partial N^1}{\partial r} & \frac{\partial N^2}{\partial z} & \frac{\partial N^2}{\partial r} & \frac{\partial N^3}{\partial z} & \frac{\partial N^3}{\partial r} & \frac{\partial N^4}{\partial z} & \frac{\partial N^4}{\partial r} \\ \hline \frac{N^1}{r} & 0 & \frac{N^2}{r} & 0 & \frac{N^3}{r} & 0 & \frac{N^4}{r} & 0 \end{bmatrix}, \quad (\text{F.8})$$

where  $r$  and  $z$  are the radial and the axial coordinates for the axi-symmetric case. Note that in equations (F.6), the shape functions are the same for all primary variables.

## F.2 Definition of the matrices $\mathbf{K}$ and $\mathbf{D}$ in eq. (6.24)

Identification of the sub-matrices of the stiffness matrix  $\mathbb{K}$  and of the diffusion matrix  $\mathbb{D}$ , equation (6.24).

$$\begin{aligned}
\mathbf{K}_{\mathbf{u}\mathbf{u}}^e &= \mathbf{E}_{\mathbf{uu}}^e, & \mathbf{K}_{\mathbf{u}p_p}^e &= -\xi_p \mathbf{C}_{\mathbf{up}}^e \\
\mathbf{K}_{\mathbf{u}p_f}^e &= -\xi_f \mathbf{C}_{\mathbf{up}}^e, & \mathbf{K}_{\mathbf{u}T}^e &= -c_T/c \mathbf{C}_{\mathbf{u}T}^e \\
\mathbf{K}_{p_p p_p}^e &= -\mathbf{J}_{k_p}^e - \eta \mathbf{M}_{pp}^e, & \mathbf{K}_{p_p p_f}^e &= \eta \mathbf{M}_{pp}^e \\
\mathbf{K}_{p_f p_f}^e &= -\mathbf{J}_{k_f}^e - \eta \mathbf{M}_{pp}^e, & \mathbf{K}_{p_f p_p}^e &= \eta \mathbf{M}_{pp}^e \\
\mathbf{K}_{TT}^e &= -\mathbf{Q}_{\Lambda}^e.
\end{aligned} \tag{F.9}$$

and,

$$\begin{aligned}
\mathbf{D}_{p_p \mathbf{u}}^e &= -\xi_p \mathbf{C}_{p\mathbf{u}}^e, & \mathbf{D}_{p_p p_p}^e &= -a_{pp} \mathbf{M}_{pp}^e \\
\mathbf{D}_{p_p p_f}^e &= -a_{pf} \mathbf{M}_{pp}^e, & \mathbf{D}_{p_p T}^e &= -a_{pT} \mathbf{M}_{pT}^e
\end{aligned} \tag{F.10}$$

$$\begin{aligned}
\mathbf{D}_{p_f \mathbf{u}}^e &= -\xi_f \mathbf{C}_{p\mathbf{u}}^e, & \mathbf{D}_{p_f p_p}^e &= -a_{pf} \mathbf{M}_{pp}^e \\
\mathbf{D}_{p_f p_f}^e &= -a_{ff} \mathbf{M}_{pp}^e, & \mathbf{D}_{p_f T}^e &= -a_{fT} \mathbf{M}_{pT}^e \\
\mathbf{D}_{T \mathbf{u}}^e &= -T c_T/c [\mathbf{C}_{\mathbf{u}T}^e]^T, & \mathbf{D}_{T p_p}^e &= -T a_{pT} [\mathbf{M}_{pT}^e]^T \\
\mathbf{D}_{T p_f}^e &= -T a_{fT} [\mathbf{M}_{pT}^e]^T, & \mathbf{D}_{TT}^e &= -a_{TT} \mathbf{M}_{TT}^e
\end{aligned} \tag{F.11}$$

## Appendix G

### Appendices of Section 8.3

#### G.1 Definition of the vectors $\mathbb{F}^{\text{grav}}$ and $\mathbb{F}^{\text{surf}}$

$\mathbb{F}^{\text{grav}}$  comprises the gravity contributions to the weak form of the problem (8.64),

$$\mathbb{F}^{\text{grav}} = \begin{bmatrix} \int_V \mathbf{N}_u^T \rho \mathbf{g} \, dV \\ - \int_V (\nabla \mathbf{N}_p)^T \frac{k_f}{\mu_f} \rho_f \mathbf{g} \, dV \\ 0 \\ 0 \\ 0 \end{bmatrix}, \quad (\text{G.1})$$

while the surface contributions are gathered in

$$\mathbb{F}^{\text{surf}} = \begin{bmatrix} \int_{\partial V} \mathbf{N}_u^T \boldsymbol{\sigma} \cdot \hat{\mathbf{n}} \, dS \\ \int_{\partial V} \mathbf{N}_p^T \mathbf{J}_f \cdot \hat{\mathbf{n}} \, dS \\ \int_{\partial V} \mathbf{N}_T^T \mathbf{q}_s \cdot \hat{\mathbf{n}} \, dS \\ \int_{\partial V} \mathbf{N}_T^T \mathbf{q}_f \cdot \hat{\mathbf{n}} \, dS \end{bmatrix}. \quad (\text{G.2})$$

#### G.2 Definition of the matrices $\mathbb{K}^e$ and $\mathbb{D}^e$ in eqn (8.77)

The submatrices of the element generalized stiffness and diffusion matrices of the finite element formulation (8.77) are built from constitutive matrices, namely for the generalized



stiffness-convection matrix,

$$\begin{aligned} \mathbf{K}_{\mathbf{uu}}^e &= \mathbf{E}_{\mathbf{uu}}^e, & \mathbf{K}_{\mathbf{u}p_f}^e &= -\xi_f \mathbf{C}_{\mathbf{up}}^e, \\ \mathbf{K}_{\mathbf{u}T_s}^e &= -c_T/c \mathbf{C}_{\mathbf{u}T}^e, & \mathbf{K}_{p_f p_f}^e &= -k_f/\mu_f \mathbf{Q}_p^e, \\ \mathbf{K}_{T_s T_s}^e &= -n_s \Lambda_s \mathbf{Q}_T^e - \kappa_{sf} \mathbf{M}_{TT}^e, & \mathbf{K}_{T_s T_f}^e &= \kappa_{sf} \mathbf{M}_{TT}^e. \end{aligned} \quad (\text{G.3})$$

and for the generalized diffusion matrix,

$$\begin{aligned} \mathbf{D}_{p_f \mathbf{u}}^e &= -\xi_f (\mathbf{C}_{p\mathbf{u}}^e)^\top, & \mathbf{D}_{p_f p_f}^e &= -a_{ff} \mathbf{M}_{pp}^e, \\ \mathbf{D}_{p_f T_s}^e &= -a_{fT_s} \mathbf{M}_{pT}^e, & \mathbf{D}_{p_f T_f}^e &= -a_{fT_f} \mathbf{M}_{pT}^e, \\ \mathbf{D}_{T_s \mathbf{u}}^e &= -T_s c_T/c (\mathbf{C}_{\mathbf{u}T}^e)^\top, & \mathbf{D}_{T_s p_f}^e &= -T_s a_{fT_s} (\mathbf{M}_{pT}^e)^\top, \\ \mathbf{D}_{T_s T_s}^e &= -a_{T_s T_s} \mathbf{M}_{TT}^e. \end{aligned} \quad (\text{G.4})$$

Some sub-matrices of the element matrices  $\mathbb{K}^e$  and  $\mathbb{D}^e$  are discretized with the SUPG method namely,

$$\begin{aligned} {}^* \mathbf{K}_{T_f p_f}^e &= -n_f (1 - T_f c_{fT}) {}^* \mathbf{C}_{Tp}^e, & {}^* \mathbf{K}_{T_f T_s}^e &= \kappa_{sf} {}^* \mathbf{M}_{TT}^e, \\ {}^* \mathbf{K}_{T_f T_f}^e &= -n_f \Lambda_f \mathbf{Q}_T^e - \kappa_{sf} {}^* \mathbf{M}_{TT}^e - n_f \rho_f C_{f,p} {}^* \mathbf{C}_{TT}^e, \\ {}^* \mathbf{D}_{T_f p_f}^e &= -T_f a_{fT_f} {}^* \mathbf{M}_{Tp}^e, & {}^* \mathbf{D}_{T_f T_f}^e &= -a_{T_f T_f} {}^* \mathbf{M}_{TT}^e. \end{aligned} \quad (\text{G.5})$$

The material properties have been aggregated in the coefficients,

$$\begin{aligned} a_{ff} &= n_f c_{fH} + (\xi_f - n_f) c_s, & a_{fT_s} &= -(\xi_f - n_f) c_T, \\ a_{fT_f} &= -n_f c_{fT}, & a_{T_s T_s} &= n_s \rho_s C_{s,v}, \\ a_{T_f T_f} &= n_f \rho_f C_{f,p}. \end{aligned} \quad (\text{G.6})$$

The finite element sub-matrices of the compact weak formulation in equations (G.3) to (G.5) are now provided in explicit form. First, the three matrices involved in the elementary contribution to the balance of momentum of the mixture,

$$\begin{aligned} \mathbf{E}_{\mathbf{uu}}^e &= \int_{V^e} (\mathbf{B}_{\mathbf{u}})^\top \mathbf{D}_{el} \mathbf{B}_{\mathbf{u}} dV^e, & \mathbf{C}_{\mathbf{up}}^e &= \int_{V^e} (\nabla \mathbf{N}_{\mathbf{u}})^\top \mathbf{N}_p dV^e, \\ \mathbf{C}_{\mathbf{u}T}^e &= \int_{V^e} (\nabla \mathbf{N}_{\mathbf{u}})^\top \mathbf{N}_T dV^e, \end{aligned} \quad (\text{G.7})$$

where  $\mathbf{D}_{el}$  is the drained stiffness matrix and  $\mathbf{B}_{\mathbf{u}}$  is the strain displacement matrix. Next, the matrices involved in the diffusion phenomena,

$$\mathbf{Q}_p^e = \int_{V^e} (\nabla \mathbf{N}_p)^\top \nabla \mathbf{N}_p dV^e, \quad \mathbf{Q}_T^e = \int_{V^e} (\nabla \mathbf{N}_T)^\top \nabla \mathbf{N}_T dV^e. \quad (\text{G.8})$$

The mass matrices below are discretized with the Galerkin method,

$$\begin{aligned} \mathbf{M}_{pp}^e &= \int_{V^e} (\mathbf{N}_p)^\top \mathbf{N}_p dV^e, & \mathbf{M}_{TT}^e &= \int_{V^e} (\mathbf{N}_T)^\top \mathbf{N}_T dV^e, \\ \mathbf{M}_{pT}^e &= \int_{V^e} (\mathbf{N}_p)^\top \mathbf{N}_T dV^e, \end{aligned} \quad (\text{G.9})$$

while the following matrices are discretized with the SUPG method,

$${}^* \mathbf{M}_{TT}^e = \int_{V^e} (\mathbf{W}_T)^T \mathbf{N}_T dV^e, \quad {}^* \mathbf{M}_{Tp}^e = \int_{V^e} (\mathbf{W}_T)^T \mathbf{N}_p dV^e. \quad (\text{G.10})$$

Two convective matrices associated with the element contributions of the balance of energy of the fluid phase are required:

$$\begin{aligned} {}^* \mathbf{C}_{TT}^e &= \int_{V^e} (\mathbf{W}_T)^T \mathbf{v}_{\text{conv}} \cdot \nabla \mathbf{N}_T dV^e, \\ {}^* \mathbf{C}_{Tp}^e &= \int_{V^e} (\mathbf{W}_T)^T \mathbf{v}_{\text{conv}} \cdot \nabla \mathbf{N}_p dV^e. \end{aligned} \quad (\text{G.11})$$

The  $[1 \times 4]$  vectors of shape functions,

$$\mathbf{N}_p = \mathbf{N}_T = [N^1 \ N^2 \ N^3 \ N^4], \quad (\text{G.12})$$

are identical for the pressure and temperature fields.  $N^1$ ,  $N^2$ ,  $N^3$  and  $N^4$  are the shape functions of the Q4 elements;  $\mathbf{N}_u$  is the expanded shape function vector of size  $[2 \times 8]$ .

### G.3 An expression for the specific surface

The empirical expression of the specific surface described in the literature applies to fluid flow through packed beds. The starting point is the specific area of a solid sphere bathed in fluid at maximum density in a cube of side length  $d_p$ ,

$$S_{sf}^s = \frac{\text{solid area}}{\text{total volume}} = \frac{\pi d_p^2}{d_p^3}. \quad (\text{G.13})$$

In this situation, the solid porosity  $n_s$  is equal to  $\pi/6$ . Hence, by assuming that the wetted surface is equal to the solid-fluid specific surface, the specific surface is related to the solid porosity  $n_s$  and to the solid characteristic dimension  $d_p$ ,

$$S_{sf}^s = \frac{6 n_s}{d_p}. \quad (\text{G.14})$$

Although satisfactory for small particles (Nield et al., 2002; ?; Nield and Bejan, 2006) eqn (G.14) is not adapted for the solid-fluid specific surface area of HDR reservoirs endowed with rock blocks with a spacing larger than aperture  $B \gg 2b$ . To the best knowledge of the authors, no experimental result is available to evaluate  $S_{sf}^s$  for HDR reservoirs. A theoretical formula *ad-hoc* to our 2D plane strain problem is proposed. The specific surface  $S_{sf}^s$  is obtained by considering four fluid rectangles of size  $b \times (B + b)$  surrounding a solid square of area  $B^2$  and of wetted length  $4 \times B$  in a surface  $S = (B + 2b)^2$ ,

$$S_{sf}^s = \frac{\text{fluid length}}{\text{total surface}} = \frac{4 \times B}{S}. \quad (\text{G.15})$$

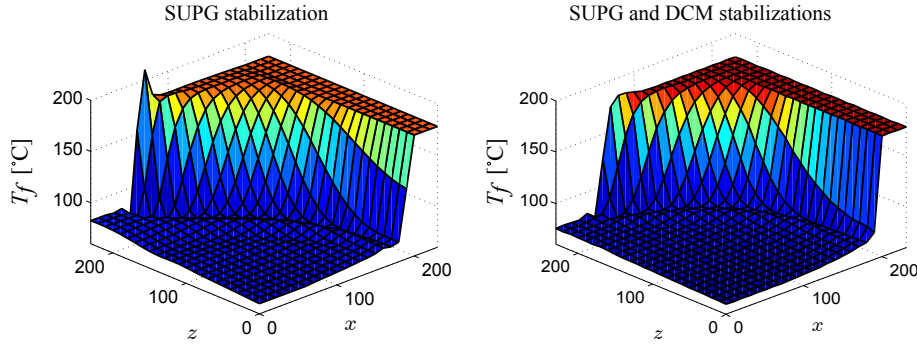


Figure G.1: Contours of fluid temperature for a dimensionless flux  $v^\infty = 9.0 \cdot 10^{-3}$  m/s at time  $t = 0.38$  hour, accounting for heat transfer with the surrounding, with the SUPG stabilization (left) and with the SUPG and DC stabilizations (right). The DC stabilization effectively cures some overshootings that are not taken care of by the SUPG method.

The total surface may be substituted by the fluid porosity  $n_f = 4b(B+b)/S$ , leading to (8.90) for  $2b \ll B$ . This relation highlights the importance, at constant aperture  $2b$ , of the fluid porosity  $n_f$  in the heat transfer mechanism. Still, note that its validity has not been tested experimentally.

## G.4 The discontinuity capturing method

The shock capturing operator proposed by Tezduyar and Ganjoo (1986) aims at improving the SUPG stabilization to smoothly resolve sharp layers. The discontinuity capturing (DC) stabilization suggests, in place of (8.65), the weighting function of the form,

$$\mathbf{W}_T = \mathbf{N}_T + \tau_{\text{SUPG}} \mathbf{v}_{\text{conv}} \cdot \nabla \mathbf{N}_T + \tau_{\text{DC}} \mathbf{v}_{\text{conv}\parallel} \cdot \nabla \mathbf{N}_T, \quad (\text{G.16})$$

in which  $\mathbf{v}_{\text{conv}\parallel}$  is the projection of  $\mathbf{v}_{\text{conv}}$  on the direction of the gradient  $\mathbf{i} = \nabla T_f / |\nabla T_f|$  if  $\nabla T_f \neq \mathbf{0}$ , namely,

$$\mathbf{v}_{\text{conv}\parallel} = (\mathbf{v}_{\text{conv}} \cdot \mathbf{i}) \mathbf{i}, \quad (\text{G.17})$$

and  $\nabla T_f$  is obtained consistently with the element discretization  $T_f = \mathbf{N}_T T_f^e$ . If  $\nabla T_f$  vanishes, then so does  $\mathbf{v}_{\text{conv}\parallel}$ . This method is seen to be non-linear since the projection depends on the solution.

Tezduyar and Ganjoo (1986) proposed to define the stabilization parameter  $\tau_{\text{DC}}$  as a function of the direction  $\nabla T_f$  with respect to the flow and of its magnitude as,

$$\tau_{\text{DC}} = \frac{h_{\parallel}}{2|\mathbf{v}_{\text{conv}\parallel}|} h_{\parallel} \frac{|\nabla T_f|}{T_{\text{ref},f}} \eta(p), \quad (\text{G.18})$$

where  $T_{\text{ref},f}$  is a reference value of the unknown  $T_f$  and  $h_{\parallel}$  is the element size in the direction of the thermal gradient,

$$h_{\parallel} = \frac{2 |\mathbf{v}_{\text{conv}\parallel}|}{\sum_a |\mathbf{v}_{\text{conv}\parallel} \cdot \nabla N_T^a|}. \quad (\text{G.19})$$

The argument  $p = |\mathbf{v}_{\text{conv}\parallel}|/|\mathbf{v}_{\text{conv}}|$  of the function  $\eta$  remains in the interval  $[0, 1]$ , and the function  $\eta(p)$  is designed to vanish at the end of its domain, that is, whenever the velocity  $\mathbf{v}_{\text{conv}}$  and the gradient  $\nabla T_f$  are either perpendicular ( $p = 0$ ) or parallel ( $p = 1$ ). Tezduyar and Ganjoo (1986) take  $\eta(p) = 2p(1 - p)$ . The DC method acts only on thermal gradient oblique to the flow. For a thermal gradient orthogonal to the flow, both the velocity  $\mathbf{v}_{\text{conv}\parallel}$  and  $\eta$  vanish, and for a thermal gradient parallel to the flow,  $\eta = 0$  so that the SUPG stabilization is not doubled.

The discontinuity capturing method is illustrated by Fig.G.1. While it damps some overshootings which are not cured by the SUPG stabilization, the DC stabilization has also drawbacks: 1. the number of iterations per time step is heavily increased, and 2. the fully coupled thermo-hydro-mechanical model fails to converge at large times and large pumping rates.

# Appendix H

## Appendices of Section 8.4

### H.1 Reduction of the dual porosity model to a single porosity model

The dual porosity model reduces to a single porosity model by assuming that the volume fraction  $n_p$  of the pore fluid vanishes, which implies  $c_p = c_s$ . Consequently, the effective stress parameters reduce to,

$$\xi_p = 0, \quad \xi_f = 1 - \frac{c_s}{c}. \quad (\text{H.1})$$

Hence, the field equations (8.143) to (8.149) describe the balance of momentum of the mixture, the balance of mass of the fracture fluid, and the balances of energy of the solid and of the fracture fluid, namely,

$$\mu^{DS} \nabla^2 \mathbf{u} + (\lambda^{DS} + \mu^{DS}) \nabla(\text{div } \mathbf{u}) - \xi_f \nabla p_f - \frac{c_T}{c} \nabla T_s + \rho \mathbf{b} = \mathbf{0}, \quad (\text{H.2})$$

$$\text{div} \left( \frac{k_f}{\mu_f} \nabla p_f + n_f \Theta_f \nabla T_f \right) = a_{ff} \frac{\partial p_f}{\partial t} + \xi_f \text{div} \frac{\partial \mathbf{u}}{\partial t} + a_{fT_s} \frac{\partial T_s}{\partial t} + a_{fT_f} \frac{\partial T_f}{\partial t}, \quad (\text{H.3})$$

$$\text{div} (n_s \Lambda_s \nabla T_s) = a_{T_s T_s} \frac{\partial T_s}{\partial t} + T_s \frac{c_T}{c} \text{div} \frac{\partial \mathbf{u}}{\partial t} + T_s a_{fT_s} \frac{\partial p_f}{\partial t} + \kappa_{sf} (T_s - T_f), \quad (\text{H.4})$$

$$\begin{aligned} \text{div} (n_f \Lambda_f \nabla T_f + T_f n_f \Theta_f \nabla p_f) &= a_{T_f T_f} \frac{\partial T_f}{\partial t} + T_f a_{fT_f} \frac{\partial p_f}{\partial t} + \mathbf{M}_f \cdot \nabla H_f \\ &+ \kappa_{sf} (T_f - T_s), \end{aligned} \quad (\text{H.5})$$

while the balance of mass and the balance of energy of the pore fluid become elusive.

## H.2 Definition of the vectors $\mathbb{F}^{\text{grav}}$ and $\mathbb{F}^{\text{surf}}$

$\mathbb{F}^{\text{grav}}$  comprises the gravity contributions to the weak form of the problem (8.152)-(8.154),

$$\mathbb{F}^{\text{grav}} = \begin{bmatrix} \int_V \mathbf{N}_u^T \rho \mathbf{g} dV \\ - \int_V (\nabla \mathbf{N}_p)^T \frac{k_p}{\mu_p} \rho_p \mathbf{g} dV \\ - \int_V (\nabla \mathbf{N}_p)^T \frac{k_f}{\mu_f} \rho_f \mathbf{g} dV \\ 0 \\ - \int_V (\nabla \mathbf{N}_T)^T n^p T_p \Theta_p \rho_p \mathbf{g} dV \\ - \int_V (\nabla \mathbf{N}_T)^T n^f T_f \Theta_f \rho_f \mathbf{g} dV \end{bmatrix}, \quad (\text{H.6})$$

while the surface contributions are gathered in

$$\mathbb{F}^{\text{surf}} = \begin{bmatrix} \int_{\partial V} \mathbf{N}_u^T \boldsymbol{\sigma} \cdot \hat{\mathbf{n}} dS \\ \int_{\partial V} \mathbf{N}_p^T \mathbf{J}_p \cdot \hat{\mathbf{n}} dS \\ \int_{\partial V} \mathbf{N}_p^T \mathbf{J}_f \cdot \hat{\mathbf{n}} dS \\ \int_{\partial V} \mathbf{N}_T^T \mathbf{q}_s \cdot \hat{\mathbf{n}} dS \\ \int_{\partial V} \mathbf{N}_T^T \mathbf{q}_p \cdot \hat{\mathbf{n}} dS \\ \int_{\partial V} \mathbf{N}_T^T \mathbf{q}_f \cdot \hat{\mathbf{n}} dS \end{bmatrix}. \quad (\text{H.7})$$

## H.3 Definition of the element matrices $\mathbb{K}^e$ and $\mathbb{D}^e$

The submatrices of the element generalized stiffness-convection matrix (8.162) are built from the constitutive matrices, namely

$$\begin{aligned} \mathbf{K}_{uu}^e &= \mathbf{E}_{uu}^e, \\ \mathbf{K}_{up_p}^e &= -\xi_p \mathbf{C}_{up}^e, \\ \mathbf{K}_{up_f}^e &= -\xi_f \mathbf{C}_{up}^e, \\ \mathbf{K}_{uT_s}^e &= -c_T/c \mathbf{C}_{uT}^e; \end{aligned} \quad (\text{H.8})$$

$$\begin{aligned}
\mathbf{K}_{pppp}^e &= -\mathbf{J}_{k_p}^e - \gamma_{pp} \mathbf{M}_{pp}^e, \\
\mathbf{K}_{pppf}^e &= \gamma_{pp} \mathbf{M}_{pp}^e, \\
\mathbf{K}_{ppT_p}^e &= -\mathbf{J}_{\Theta_p}^e - \gamma_{pT} \mathbf{M}_{pT}^e, \\
\mathbf{K}_{ppT_f}^e &= \gamma_{pT} \mathbf{M}_{pT}^e;
\end{aligned} \tag{H.9}$$

$$\begin{aligned}
\mathbf{K}_{p_f p_f}^e &= -\mathbf{J}_{k_f}^e - \gamma_{pp} \mathbf{M}_{pp}^e, \\
\mathbf{K}_{p_f p_p}^e &= \gamma_{pp} \mathbf{M}_{pp}^e, \\
\mathbf{K}_{p_f T_f}^e &= -\mathbf{J}_{\Theta_f}^e - \gamma_{pT} \mathbf{M}_{pT}^e, \\
\mathbf{K}_{p_f T_p}^e &= \gamma_{pT} \mathbf{M}_{pT}^e;
\end{aligned} \tag{H.10}$$

$$\begin{aligned}
\mathbf{K}_{T_s T_s}^e &= -\mathbf{Q}_{\Lambda_s}^e - (\kappa_{sp} + \kappa_{sf}) \mathbf{M}_{TT}^e, \\
\mathbf{K}_{T_s T_p}^e &= \kappa_{sp} \mathbf{M}_{TT}^e, \\
\mathbf{K}_{T_s T_f}^e &= \kappa_{sf} \mathbf{M}_{TT}^e;
\end{aligned} \tag{H.11}$$

$$\begin{aligned}
\mathbf{K}_{T_p p_p}^e &= -\mathbf{Q}_{\Theta_p}^e - \gamma_{T_p p} (\mathbf{M}_{pT}^e)^T - b_{T_p p} \mathbf{C}_{T_p, v_p}^e, \\
\mathbf{K}_{T_p p_f}^e &= \gamma_{T_p p} (\mathbf{M}_{pT}^e)^T, \\
\mathbf{K}_{T_p T_s}^e &= \kappa_{sp} \mathbf{M}_{TT}^e, \\
\mathbf{K}_{T_p T_p}^e &= -\mathbf{Q}_{\Lambda_p}^e - (\kappa_{sp} + \kappa_{pf} + \gamma_{T_p T_p}) \mathbf{M}_{TT}^e - b_{T_p T_p} \mathbf{C}_{T_p, v_p}^e, \\
\mathbf{K}_{T_p T_f}^e &= (\kappa_{pf} + \gamma_{T_p T_p}) \mathbf{M}_{TT}^e;
\end{aligned} \tag{H.12}$$

$$\begin{aligned}
\mathbf{K}_{T_f p_p}^e &= -\gamma_{T_f f} (\mathbf{M}_{pT}^e)^T, \\
\mathbf{K}_{T_f p_f}^e &= -\mathbf{Q}_{\Theta_f}^e + \gamma_{T_f f} (\mathbf{M}_{pT}^e)^T - b_{T_f f} \mathbf{C}_{T_p, v_f}^e, \\
\mathbf{K}_{T_f T_s}^e &= \kappa_{sf} \mathbf{M}_{TT}^e, \\
\mathbf{K}_{T_f T_p}^e &= (\kappa_{pf} - \gamma_{T_f T_f}) \mathbf{M}_{TT}^e, \\
\mathbf{K}_{T_f T_f}^e &= -\mathbf{Q}_{\Lambda_f}^e - (\kappa_{sf} + \kappa_{pf} - \gamma_{T_f T_f}) \mathbf{M}_{TT}^e - b_{T_f T_f} \mathbf{C}_{T_p, v_f}^e,
\end{aligned} \tag{H.13}$$

in which the coefficients have been linearized around the reference configuration,

$$\begin{aligned}
\gamma_{pp} &= \eta, \quad \gamma_{pT} = -\eta \rho_p S^0, \\
\gamma_{T_p p} &= +\eta \rho_p \times (C_{p,p} T^0 - H^0), \quad \gamma_{T_p T_p} = -\eta \rho_p^2 S^0 \times (C_{p,p} T^0 - H^0), \\
\gamma_{T_f f} &= -\eta \rho_p \times (C_{f,p} T^0 - H^0), \quad \gamma_{T_f T_f} = +\eta \rho_p^2 S^0 \times (C_{f,p} T^0 - H^0), \\
b_{T_p p} &= n_p (1 - c_{pT} T^0), \quad b_{T_f f} = n_f (1 - c_{fT} T^0), \\
b_{T_p T_p} &= n_p \rho_p C_{p,p}, \quad b_{T_f T_f} = n_f \rho_f C_{f,p}.
\end{aligned} \tag{H.14}$$

The submatrices of the generalized diffusion matrix (8.161),

$$\begin{aligned}
\mathbf{D}_{p_p \mathbf{u}}^e &= -\xi_p \mathbf{C}_{p \mathbf{u}}^e, \quad \mathbf{D}_{p_p p_p}^e = -a_{pp} \mathbf{M}_{pp}^e, \\
\mathbf{D}_{p_p p_f}^e &= -a_{pf} \mathbf{M}_{pp}^e, \quad \mathbf{D}_{p_p T_s}^e = -a_{pT_s} \mathbf{M}_{pT}^e, \quad \mathbf{D}_{p_p T_p}^e = -a_{pT_p} \mathbf{M}_{pT}^e;
\end{aligned} \tag{H.15}$$

$$\begin{aligned} \mathbf{D}_{pf\mathbf{u}}^e &= -\xi_f \mathbf{C}_{p\mathbf{u}}^e, & \mathbf{D}_{pfpp}^e &= -a_{pf} \mathbf{M}_{pp}^e, \\ \mathbf{D}_{pfpf}^e &= -a_{ff} \mathbf{M}_{pp}^e, & \mathbf{D}_{pfT_s}^e &= -a_{fT_s} \mathbf{M}_{pT}^e, & \mathbf{D}_{pfT_f}^e &= -a_{fT_f} \mathbf{M}_{pT}^e; \end{aligned} \quad (\text{H.16})$$

$$\begin{aligned} \mathbf{D}_{T_s\mathbf{u}}^e &= -T_s c_T / c \mathbf{C}_{T\mathbf{u}}^e, & \mathbf{D}_{T_s pp}^e &= -T_s a_{pT_s} (\mathbf{M}_{pT}^e)^\top, \\ \mathbf{D}_{T_s pf}^e &= -T_s a_{fT_s} (\mathbf{M}_{pT}^e)^\top, & \mathbf{D}_{T_s T_s}^e &= -a_{T_s T_s} \mathbf{M}_{TT}^e; \end{aligned} \quad (\text{H.17})$$

$$\mathbf{D}_{T_p pp}^e = -T_p a_{pT_p} (\mathbf{M}_{pT}^e)^\top, \quad \mathbf{D}_{T_p T_p}^e = -a_{T_p T_p} \mathbf{M}_{TT}^e; \quad (\text{H.18})$$

$$\mathbf{D}_{T_f pf}^e = -T_f a_{fT_f} (\mathbf{M}_{pT}^e)^\top, \quad \mathbf{D}_{T_f T_f}^e = -a_{T_f T_f} \mathbf{M}_{TT}^e, \quad (\text{H.19})$$

involve coefficients defined in (8.150).

The finite element sub-matrices of the weak formulation in equations (H.8) to (H.19) are listed below, starting with the  $[1 \times 4]$  vectors of shape functions,

$$\mathbf{N}_p = \mathbf{N}_T = [ N^1 \quad N^2 \quad N^3 \quad N^4 ], \quad (\text{H.20})$$

which are identical for the pressure and temperature fields.  $N^1, N^2, N^3$  and  $N^4$  are the shape functions of the Q4 elements.  $\mathbf{N}_{\mathbf{u}}$  is the expanded shape function vector of size  $[2 \times 8]$  for the displacement.

Five matrices are involved in the balance of momentum of the mixture,

$$\begin{aligned} \mathbf{E}_{\mathbf{uu}}^e &= \int_{V^e} (\mathbf{B}_{\mathbf{u}})^\top \mathbf{D}_{\text{el}} \mathbf{B}_{\mathbf{u}} dV^e, \\ \mathbf{C}_{\mathbf{up}}^e &= \int_{V^e} (\nabla \mathbf{N}_{\mathbf{u}})^\top \mathbf{N}_p dV^e, \\ \mathbf{C}_{\mathbf{uT}}^e &= \int_{V^e} (\nabla \mathbf{N}_{\mathbf{u}})^\top \mathbf{N}_T dV^e. \\ \mathbf{C}_{p\mathbf{u}}^e &= \int_{V^e} (\mathbf{N}_p)^\top [1 \quad 1] \nabla \cdot \mathbf{N}_{\mathbf{u}} dV^e, \\ \mathbf{C}_{T\mathbf{u}}^e &= \int_{V^e} (\mathbf{N}_T)^\top [1 \quad 1] \nabla \cdot \mathbf{N}_{\mathbf{u}} dV^e. \end{aligned} \quad (\text{H.21})$$

where  $\mathbf{D}_{\text{el}}$  is the drained stiffness matrix and  $\mathbf{B}_{\mathbf{u}}$  is the strain displacement matrix. The next matrices pertain to hydraulic conductivity and heat conduction,

$$\begin{aligned} \mathbf{J}_{k_p}^e &= \int_{V^e} (\nabla \mathbf{N}_p)^\top \frac{k_p}{\mu_p} \nabla \mathbf{N}_p dV^e, \\ \mathbf{J}_{k_f}^e &= \int_{V^e} (\nabla \mathbf{N}_p)^\top \frac{k_f}{\mu_f} \nabla \mathbf{N}_p dV^e, \\ \mathbf{Q}_{\Lambda_s}^e &= \int_{V^e} (\nabla \mathbf{N}_T)^\top n_s \Lambda_s \nabla \mathbf{N}_T dV^e, \\ \mathbf{Q}_{\Lambda_p}^e &= \int_{V^e} (\nabla \mathbf{N}_T)^\top n_p \Lambda_p \nabla \mathbf{N}_T dV^e, \\ \mathbf{Q}_{\Lambda_f}^e &= \int_{V^e} (\nabla \mathbf{N}_T)^\top n_f \Lambda_f \nabla \mathbf{N}_T dV^e, \end{aligned} \quad (\text{H.22})$$



while the matrices below are involved in the thermo-osmosis and coupled isothermal heat flow,

$$\begin{aligned}
\mathbf{J}_{\Theta_p}^e &= \int_{V^e} (\nabla \mathbf{N}_p)^T n_p \Theta_p \nabla \mathbf{N}_T dV^e, \\
\mathbf{J}_{\Theta_f}^e &= \int_{V^e} (\nabla \mathbf{N}_p)^T n_f \Theta_f \nabla \mathbf{N}_T dV^e, \\
\mathbf{Q}_{\Theta_p}^e &= \int_{V^e} (\nabla \mathbf{N}_T)^T T_p n_p \Theta_p \nabla \mathbf{N}_p dV^e, \\
\mathbf{Q}_{\Theta_f}^e &= \int_{V^e} (\nabla \mathbf{N}_T)^T T_f n_f \Theta_f \nabla \mathbf{N}_p dV^e.
\end{aligned} \tag{H.23}$$

Three mass matrices are required in the general case,

$$\begin{aligned}
\mathbf{M}_{pp}^e &= \int_{V^e} (\mathbf{N}_p)^T \mathbf{N}_p dV^e, & \mathbf{M}_{TT}^e &= \int_{V^e} (\mathbf{N}_T)^T \mathbf{N}_T dV^e, \\
\mathbf{M}_{pT}^e &= \int_{V^e} (\mathbf{N}_p)^T \mathbf{N}_T dV^e.
\end{aligned} \tag{H.24}$$

Note that they actually reduce to a single matrix if the same shape function is used for the pressures and the temperatures, namely  $\mathbf{N}_p = \mathbf{N}_T$ .

The four convective matrices discretised with the Galerkin method adopt the format,

$$\begin{aligned}
\mathbf{C}_{TT, \mathbf{v}_p}^e &= \int_{V^e} (\mathbf{N}_T)^T (\mathbf{v}_p - \mathbf{v}_s) \cdot \nabla \mathbf{N}_T dV^e, \\
\mathbf{C}_{Tp, \mathbf{v}_p}^e &= \int_{V^e} (\mathbf{N}_T)^T (\mathbf{v}_p - \mathbf{v}_s) \cdot \nabla \mathbf{N}_p dV^e, \\
\mathbf{C}_{TT, \mathbf{v}_f}^e &= \int_{V^e} (\mathbf{N}_T)^T (\mathbf{v}_f - \mathbf{v}_s) \cdot \nabla \mathbf{N}_T dV^e, \\
\mathbf{C}_{Tp, \mathbf{v}_f}^e &= \int_{V^e} (\mathbf{N}_T)^T (\mathbf{v}_f - \mathbf{v}_s) \cdot \nabla \mathbf{N}_p dV^e.
\end{aligned} \tag{H.25}$$